"CURRENT PROBLEMS IN NUCLEAR PHYSICS AND ATOMIC ENERGY", Kyiv, 2012
Proceedings, part 2

NPAE
2012

September 3-7, 2012
Kyiv, Ukraine

The 4-th International Conference

Current Problems in Nuclear Physics and Atomic Energy

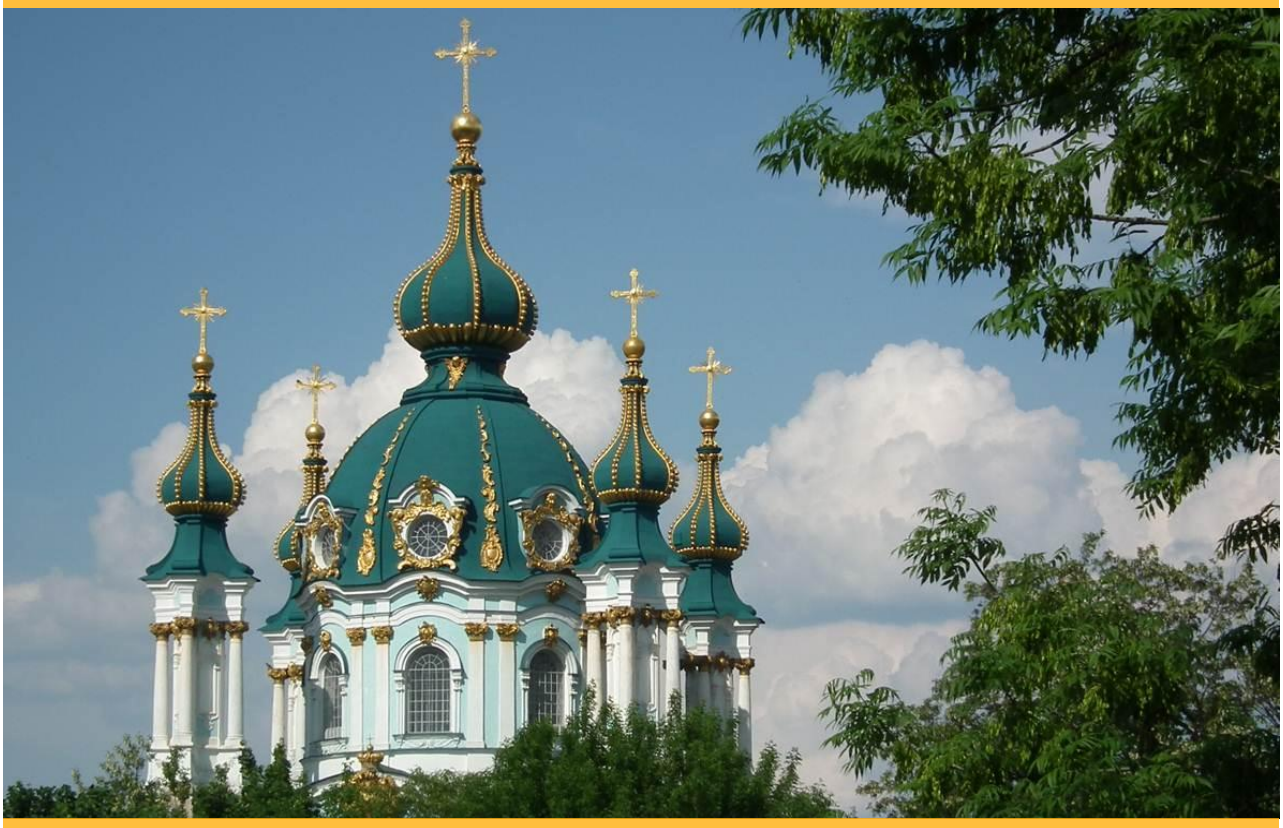

Proceedings









National Academy of Sciences of Ukraine
Institute for Nuclear Research

The 4-th International Conference

Current Problems in Nuclear Physics and Atomic Energy (NPAE-Kyiv2012)

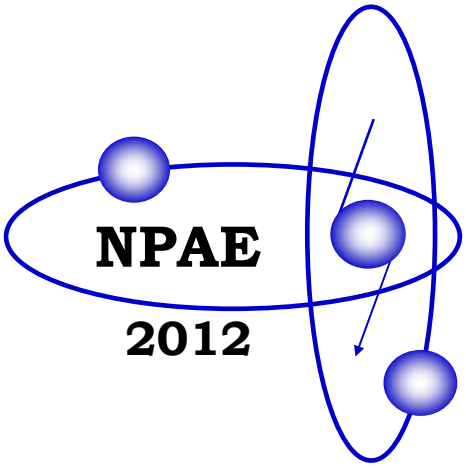

Proceedings

September 3 - 7, 2012
Kyiv, Ukraine

Part II

Kyiv 2013

International Advisory Committee

A. Barabash	ITEP, Russia	I. M. Neklyudov	KIPT, Ukraine
R. Bernabei	RU, Italy	V. E. Oberacker	VU, USA
S. Gales	GANIL, France	Yu. Ts. Oganessian	JINR, Russia
K.A. Gridnev	SPU, Russia	V. Pronyaev	IPPE, Russia
S. Hofmann	GSI, Germany	P. Ring	TUM, Germany
A. Iwamoto	JU, Japan	S. Shlomo	TAMU, USA
A. A. Korsheninnikov	KIAE, Russia	A. Sobiczewski	SINS, Poland
M. Lattuada	LNS, Italy	V. G. Zelevinsky	MSU, USA
W. Nazarewicz	ORNL, USA		

Organizing Committee

I. M. Vyshnevskyi – Chairman
L. A. Bulavin, V. M. Kolomietz – Vice-Chairs
V. Yu. Denisov – Scientific secretary

Scientific Program Committee:

L. A. Bulavin	NTSU, Kyiv	V. M. Pavlovych	KINR, Kyiv
F. A. Danevich	KINR, Kyiv	V. M. Pugatch	KINR, Kyiv
V. Yu. Denisov	KINR, Kyiv	A. T. Rudchyk	KINR, Kyiv
G. F. Filippov	BITF, Kyiv	N. F. Shulga	KIPT, Kharkiv
O. O. Gritzay	KINR, Kyiv	I. V. Simenog	BITF, Kyiv
V. F. Klepikov	IERT, Kharkiv	V. I. Slisenko	KINR, Kyiv
V. M. Kolomietz	KINR, Kyiv	I. M. Vyshnevskyi	KINR, Kyiv
V. A. Plujko	NTSU, Kyiv	S. N. Yezhov	NTSU, Kyiv

Local Organizing Committee (KINR, Kyiv)

O. O. Beliuskina, V. V. Davydovskyy, O. D. Grygorenko, T. V. Kovalinska, L. M. Lamonova, V. A. Nesterov, N. V. Olesova, V. V. Ostashko, N. A. Pilipenko, Yu. N. Stepanenko, V. P. Verbytskyi, V. V. Uleshchenko

The address of the Organizing Committee

Institute for Nuclear Research, 47, Pr. Nauky, 03680, Kyiv, Ukraine
Tel.: (38044)525-52-38, 525-14-56
Fax: (38044)525-44-63
E-mail: npae-kyiv2012@kinr.kiev.ua
Website: http://www.kinr.kiev.ua/NPAE-Kyiv2012

ISBN 978-966-02-6750-3 (загальний)
ISBN 978-966-02-6752-7 (Частина II)

CONTENTS

Part I

Plenary Sessions

Section 1. Collective Processes in Atomic Nuclei

Section 2. Nuclear Reactions

Section 3. Nuclear Structure and Decay Processes

Part II

Section 4. Rare Nuclear Processes

Section 5. Neutron and Reactor Physics, Nuclear Data

Section 6. Problems of Atomic Energy

Section 7. Applied Nuclear Physics, Experimental Facilities and Detection Techniques

Section 8. High Energy Physics

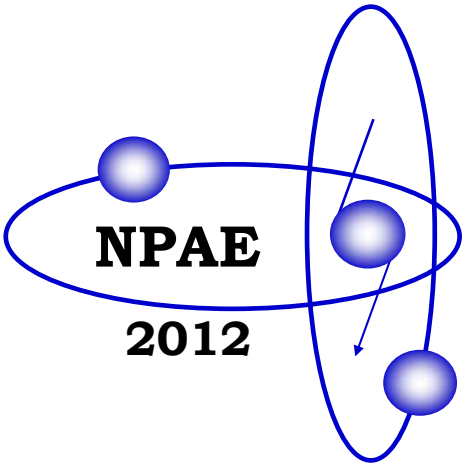

Section 4

Rare Nuclear Processes

DARK MATTER SEARCH WITH THE PICASSO EXPERIMENT

S. Archambault[1], E. Behnke[2], P. Bhattacharjee[3], S. Bhattacharya[3], X. Dai[4], M. Das[3], A. Davour[4], F. Debris[1], N. Dhungana[5], J. Farine[5], S. Gagnebin[6], G. Giroux[1], E. Grace[2], C. M. Jackson[1], A. Kamaha[4], C. Krauss[6], S. Kumaratunga[1], M. Lafreniere[1], M. Laurin[1], I. Lawson[7], L. Lessard[1], I. Levine[2], C. Levy[4], R. P. MacDonald[6], D. Marlisov[6], J.-P. Martin[1], P. Mitra[6], A. J. Noble[4], M.-C. Piro[1], R. Podviyanuk[5], S. Pospisil[8], S. Saha[3], O. Scallon[1], S. Seth[3], N. Starinski[1], I. Stekl[8], U. Wichoski[5], T. Xie[4], V. Zacek[1]

[1] Departement de Physique, Universite de Montreal, Montreal,Canada
[2] Department of Physics and Astronomy, Indiana University South Bend, South Bend, IN, USA
[3] Saha Institute of Nuclear Physics, Centre for AstroParticle Physics (CAPP), Kolkata, India
[4] Department of Physics, Queen's University, Kingston, Canada
[5] Department of Physics, Laurentian University, Sudbury, Canada
[6] Department of Physics, University of Alberta, Edmonton, Canada
[7] SNOLAB, Lively, ON, Canada
[8] Institute of Experimental and Applied Physics, Czech Technical University, Prague, Czech Republic

A low background PICASSO experiment to search for dark matter is in progress at the Sudbury Neutrino Observatory (Canada) by using 10 detectors with total target mass of 0.72 kg of ^{19}F and exposure time of 114 kgd. Recoil energy thresholds are 1.7 keV which allows the sensitivity to interactions from Weakly Interacting Massive Particles (WIMPs) with masses below 10 GeV/c^2. No dark matter signal was foundtill now. The limits in the spin dependent sector were obtained for WIMP masses of 20 GeV/c^2 with a cross section on protons of σ_p^{SD} =0.032 pb (90% C.L.), in the spin independent sector close to the low WIMP mass region of 7 GeV/c^2 with cross section on protons $\sigma_p^{SI} = 1.41 \cdot 10^{-4}$pb (90 % C.L.).

Introduction

The PICASSO detection principle based on superheated liquid droplets [1]. The presence of ^{19}F in the target liquid C_4F_{10} gives PICASSO an increased sensitivity to spin dependent WIMP interactions since, with the exception of neutralino scattering on free protons and ^3He, ^{19}F is the most favorable nucleus for direct detection [2]. The light target nucleus ^{19}F together with the low recoil detection threshold of 1.7 keV renders the experiment particularly sensitive to low WIMP masses below 15 GeV/c^2. This is especially interesting following the DAMA/LIBRA and recent CoGeNT and CRESST results [3 - 5] which are suggestive of a low mass WIMP solution of order 10 GeV/c^2.

PICASSO detector

The detector of the PICASSO experiment is 4.5 liter acrylic container with polymerized gel where 200 μm liquid droplets of C_4F_{10} are distributed. The average mass of C_4F_{10} in the detector is 90 g corresponds 72 g of ^{19}F. The droplets of C_4F_{10} (T_{boil} = -1.7^{0}C) are in superheated state at ambient temperature and pressure. In this state a heat spike due to the energy deposited by an ionizing particle can cause the formation of a vapour bubble. This phase transition produces the acoustic shock and accompanied by an acoustic signal in ultrasonic frequency range. This effect can be registered with help of piezoelectric transducers (piezo-sensors). Since the detector captures phase transitions, it performs as an energy threshold device which can be controlled by setting the temperature and/or pressure. The relation between the energy threshold and the operating temperature in C_4F_{10} has been determined by measurements using mono-energetic neutron beams and with emitters of known energies (Fig. 1, *A*). It allows a precise description of the temperature dependence of energy thresholds ranging from 0.8 keV up to 800 keV. Details of detector principle can be found in [6, 7]. The sensitivity of the detector to different particles can be adjusted by change of the temperature with fixed pressure (Fig. 1, *B*). Expected that WIMP inducted recoil energies can be smaller than 100 keV and become detectable from the temperature around 30^{0}C at ambient pressure. From the temperature 50 ^{0}Cdetector is sensitive to γ, β radiation and cosmic muons which produce sub-keV energy clusters and can be easily separated from strongly ionizing neutron and WIMP recoils. In case of alpha particle events there can be two different responses. First response is the curve with lower threshold energy which was obtained when the gel matrix was spiked with ^{241}Am. It means that only α-particle entering the droplets from the gel matrix can induce nucleation (Bragg peak trigger nucleation). The value of deposited energy is 71 keV. Second response is the curve with the higher alpha-energy threshold was obtained with ^{226}Ra spiked detectors. In this case ^{226}Ra daughter ^{222}Rn diffuses into the droplets and ^{210}Pb with the higher energy spikes droplets from inside. The value of recoil energy is 146 keV [8].

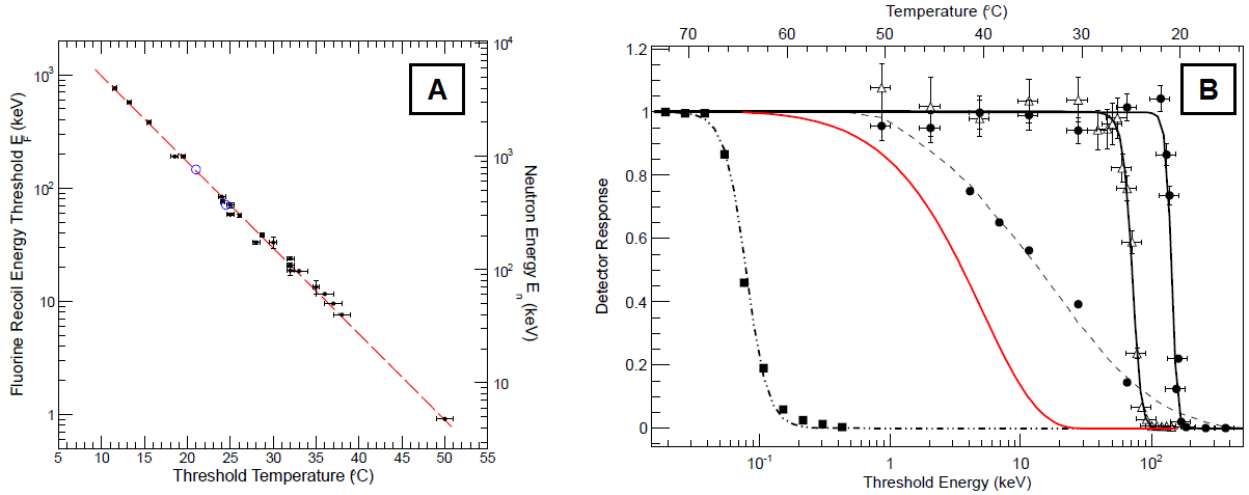

Fig. 1. *A* – Calibration curve for the energy threshold of ^{19}F recoils as a function of temperature obtained from measurements with mono-energetic neutrons; α-particle measurements are shown as open circles at 21 and 25 ^0C. *B* – Response to different kinds of particles in superheated C_4F_{10}. From left to right: 1.75 MeV γ-rays and minimum ionizing particles (dot-dashed); ^{19}F recoils modeled assuming the scattering of a 50 GeV/c^2 WIMP (red); poly-energetic neutrons from an AcBe source (dotted); α-particles at the Bragg peak from ^{241}Am decays (open triangles); and ^{210}Pb recoil nuclei from ^{226}Ra spikes (full dots).

Experimental setup

The name of four PICASSO detectors group is TPCS (Temperature and Pressure Control System). The PICASSO installation in SNOLAB consists of 8 TPCSs, totally 32 detectors. The temperature range from 20 to 50 ^0C can be adjusted with precision of ±0.1 ^0C [9]. The active mass of each detector known with precision of 1 % but mass of C_4F_{10} in detector can decrease due to diffusion of C_4F_{10} into the gel matrix. However active mass of detector and their sensitivities are verified with help of calibrated AmBe neutron source. Each detector has nine piezo-sensors with sensitivity 27 μV/μbar. The piezo-sensors placed outside of acrylic cylinder on three different positions of detector wall. The electronics of one TPCS consist of 4 × 9 preamplifier boards and 4 DAQ boards based on 400 kHz digitizers. PICASSO installation was surrounded by 30.5 cm water shield and located in SNOLAB on depth 2070 m (~6000 m.w.e.).On this depth, around 90 % of 5 keV fast neutrons produced by (α, n) reaction in the surrounding rock. The fast neutron flux was measured is around 3000 neutrons $m^{-2}d^{-1}$.

Background reduction

PICASSO detector is the temperature detector which means that different temperature can be used to discriminate different particle interactions in superheat liquids. The signals from detector can be separated on particle inducted and non-particle inducted. To discriminate different kind of signals the amplitude, waveform, frequency content and signal rise time analysis are using (Fig. 2).

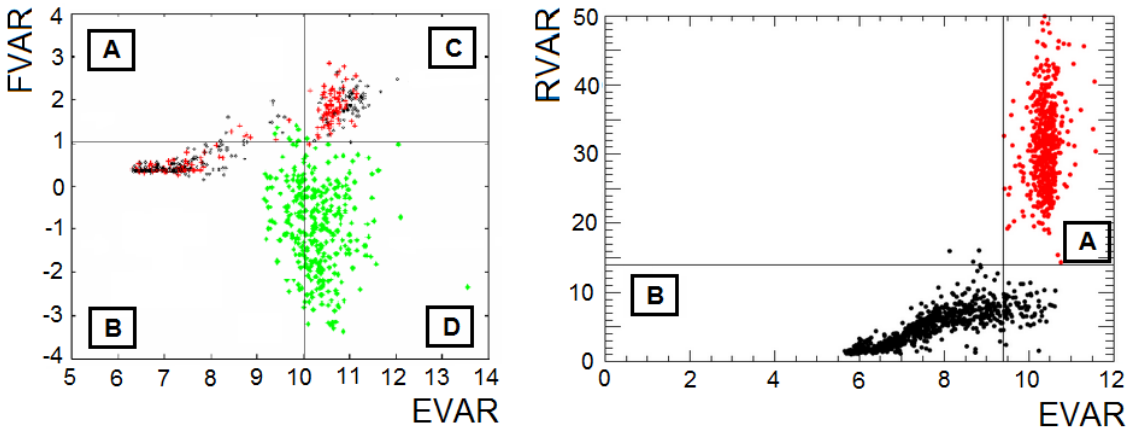

Fig. 2. Left: the frequency content analysis variable (FVAR) vs. signal energy (EVAR); sectors: *A* – acoustic noises and mine blasts; *B* – electromagnetic noises; *C* – fractures; *D* – particle inducted events. Right: the rise time (RVAR) vs. signal energy (EVAR); sectors: *A* – particle inducted events (neutrons); *B* – non-particle inducted events which produced different kind of activities in detector matrix.

Due to α-particles, neutrons and noises have different amplitudes the *amplitude analysis* is using to discriminate particles by the amplitudes. *Acoustic energy* (*EVAR*) analysis is using to discriminate particle inducted recoil events from non-particle inducted signals (electronic noises, air bubbles). *Frequency content* (*FVAR*) analysis is using to suppress of fractures or secondary events which have a deficit in signal power due to weakening of the gel matrix and mine blast events. Avariable FVAR is constructed by taking the logarithm of the ratio of signalpower in the intervals from 20 - 30 kHz and 45 - 55 kHz. *Signal rise time* (*RVAR*) is analysis of first 25 μs after pulse start. This variable is using for suppression of class of background events with slow rise time, but with an acoustic energy and frequency content comparable to particle events [10].

Data collection and analysis

The typically time of WIMP run is 40 h. After this the detectors are recompressed for 15 h with gauge pressure 6 bar. It prevents bubbles growth which could damage the gel matrix. The data of 10 "golden" (i.e. best) detectors from 32 detectors installed in SNOLAB was used for the data analysis. A total 264 WIMP runs were analysed gives the exposure of 114.3 kgd in background and signal regions.Approximately every three months calibration data have been taken at several temperatures with a weak AmBe neutron source (68.71 ± 0.74 s^{-1}), placed on distance 10 ± 2 cm from each detector [11]. The analysis process is the following:

- A list of golden runs is established for each detector. The run is "golden" when the duration of WIMP run exceeds 15 h, duration of calibration run exceeds 1 h, gauge pressure less than 0.1 bar of ambient pressure and six from nine channels of DAQ are working well;

Effect of the applied cuts on the trigger rate at 30 ^{0}C and 45 ^{0}C

	Number of events	
	30 ^{0}C	45 ^{0}C
Triggers/day	23.4 ± 0.9	60.5 ± 1.2
After 3 sec cut	15.8 ± 0.8	40.0 ± 1.0
After EVAR cut	2.3 ± 0.3	3.2 ± 0.3
After RVAR cut	2.2 ± 0.3	2.4 ± 0.3
After FVAR cut	2.1 ± 0.3	2.2 ± 0.2

- A selection to remove event bursts with <3 sec between successive triggers is applied;
- An event selection is performed on EVAR. For calibration run only first 200 neutron inducted events are selected because large quantity of bubbles which appear in the calibration are decreasing the amplitude of signals;
- The events have to pass a selection on RVAR;
- Finally the events have to pass a selection on FVAR.

The effects of the applied cuts for two temperatures on the trigger rates are illustrated for one of the detectors in the Table [10].

Results for spin dependent and spin independent sectors

The interaction of WIMPs with nuclei of ordinary particles in case of spin dependent interaction can be given as:

$$\sigma_A = 4G_F^2 \left(\frac{M_W M_A}{M_W + M_A}\right)^2 C_A F(q^2)\,, \tag{1}$$

where G_F is the Fermi constant, M_w and M_A are masses of WIMP and detector nuclei; C_A is an enhancement factor; $F(q^2)$ is the nuclear form factor [12]. The important parameter in formula below is enhancement factor which depends of WIMP interaction and can be calculated as:

$$C_A^{SD} = \left(\frac{8}{\pi}\right)\left(a_p\langle S_p\rangle + a_n\langle S_n\rangle\right)^2 \frac{(J+1)}{J}, \tag{2}$$

where a_p and a_n are effective proton and neutron strengths; $\langle S_p\rangle$ and $\langle S_n\rangle$ are the expectation values for nucleon spins in target nucleus: $\langle S_p\rangle = 0.44$, $\langle S_n\rangle = -0.19$ in ^{19}F; J is the nuclear spin [12 - 14]. Assuming that scattering of WIMPs on ^{19}F is dominated with protons, the cross section σ_p^{SD} on for scattering on protons:

$$\sigma_p^{SD} = \sigma_F \left(\frac{\mu_p}{\mu_F}\right)^2 \frac{C_p^{SD}}{C_{p(F)}^{SD}}, \tag{3}$$

where μ_p and μ_F are WIMP-proton reduced mass; C_p^{SD} and $C_{p(F)}^{SD}$ are enhancement factors for scattering on free proton and scattering on protons in ^{19}F nucleus. With (3) the result can be converted into cross sections on protons. The resulting curve for WIMP cross section on protons as function of WIMP mass for the case of *spindependent* interaction shown in Fig. 3 (left). In case of spin independent interaction the enhancement factor proportional to atomic mass: $C_A \propto A^2$. The resulting curve for *spinindependent* interaction showed on Fig. 3 (right).

Conclusions

The data taking and analysis is in progress.The purification technique of detectors production was improved which allow reducing of alpha background. The new variable RVAR was used to discriminate particle inducted events from non-particle inducted events.The sensitivity for low wimp mass region was improved which allowed to obtainthe

competitive results with spin independent mass. The limits in the spin dependent sector were obtained for WIMP masses of 20 GeV/c^2 with a cross section on protons of $\sigma_p^{SD} = 0.032$ pb (90 % C.L.), in the spin independent sector close to the low WIMP mass region of 7 GeV/c^2 with cross section on protons $\sigma_p^{SI} = 1.41 \cdot 10^{-4}$pb (90 % C.L.).

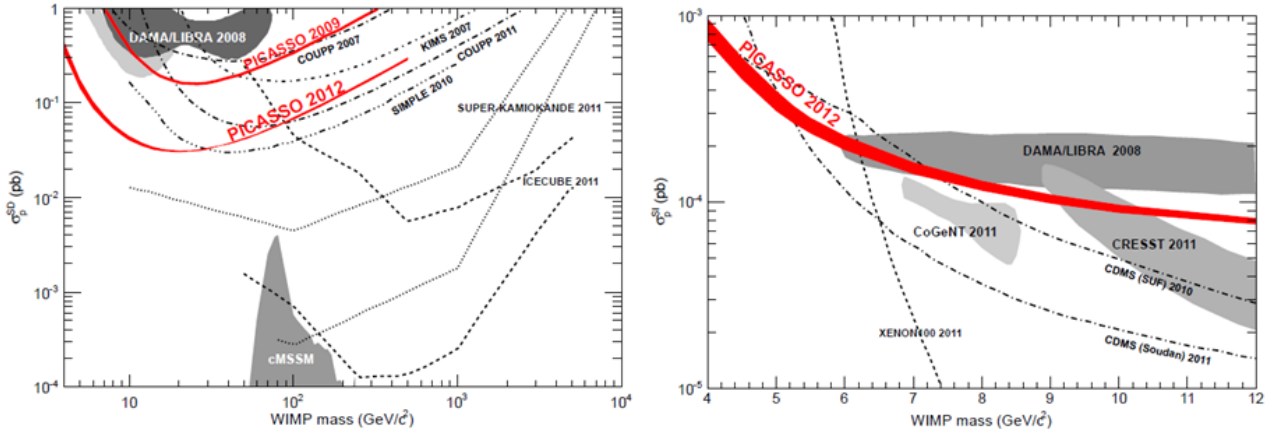

Fig. 3. Left: upper limits at 90 % C.L. on spin dependent WIMP-proton interactions. PICASSO limits are shown as full lines. Right: PICASSO limits in the spin independent sector (90% C.L.). Only the region of recent interest in the range of low WIMP masses is shown [10].

REFERENCES

1. *Glaser D.A.* // Phys. Rev. - 1952. - Vol. 87. - P. 665 - 665.
2. *Bednyakov V.A., Klapdor-Kleingrothaus H.V., Kovalenko S.G.* // Phys. Rev. D. - 1997. - Vol. 55. - P. 503 - 514.
3. *Bernabei R. et al.* // Eur. Phys. J. C. - 2010. - Vol. 67. - P. 39 - 49.
4. *Aalseth C.E. et al.* // Phys. Rev. Lett. - 2011. - Vol. 106. - P. 131301.
5. *Angloher G. et al*. Results from 730 kg days of the CRESST-II Dark Matter Search, 2011. ArXiv:1109.0702.
6. *Apfel R.E.* // Nucl. Instrum. and Methods. - 1979. - Vol. 162. - P. 603 - 608.
7. *Ing H., Noulty R., McLean T.* // Radiation Measurements. - 1997. - Vol. 27. - P. 1 - 11.
8. *Archambault S. et al.* // New J. Phys. - 2011. - Vol. 13. - P. 043006.
9. *Archambault S. et al.* // Phys. Lett. B. - 2009. - Vol. 682. - P. 185 - 192.
10. *Archambault S. et al.* // Phys. Lett. B. - 2012. - Vol. 711. - P. 153 - 161.
11. *Loach J.C.* Measurement of the flux of ^{8}B solar neutrinos at the Sudbury Neutrino Observatory: Ph.D. thesis. - University of Oxford, 2008.
12. *Jungman G., Kamionkowski M., Griest K.* // Physics Reports. - 1996. - Vol. 267. - P. 195 - 373.
13. *Engel J., Pittel S., Vogel P.* // Int. J. Mod. Phys. E. - 1992. - Vol. 1. - P. 1 - 37.
14. *Pacheco F., Strottman D.* // Phys. Rev. D. - 1989. - Vol. 40. - P. 2131 - 2133.

PREPARATION OF EXPERIMENT FOR SEARCH OF 0ν2β-DECAY OF ^{150}Nd

A. Ya. Balysh, A. B. D'yachkov, A. V. Labozin, S. M. Mironov, V. Ya. Panchenko, S. V. Semenov, V. A. Firsov, G. O. Tsvetkov, G. G. Shatalova

National Research Center "Kurchatov Institute", Moscow, Russia

State of work, which is being performed in NRC "Kurchatov Institute", aimed on construction of large-scale setup for search of ^{150}Nd neutrinoless double beta decay, is considered. Compact detector, consisting of thin scintillator plates on the base of polystyrene with ^{150}Nd foil between them is proposed. The ^{150}Nd isotope will be produced by laser separation method in the Institute for Molecular Physics of NRC "Kurchatov Institute". Calculations of 2ν2β background in the region of 0ν2β peak corresponding to different nuclear mechanisms of ^{150}Nd 2ν2β-decay are made.

1. Introduction

Search of neutrinoless double beta decay is now going on in many laboratories of the world [1, 2]. It should be noted, that till now the most sensitive experiments in this field are based on stable isotopes, such as ^{76}Ge, ^{82}Se, ^{100}Mo, ^{116}Cd, ^{136}Xe [3], which can be obtained in large amounts by the effective centrifugal method [4]. The necessary condition for isotope is to have gaseous compound, which allows one to produce centrifugal enrichment. However, nowadays considerable attention is attracted to the possibility of construction of large-scale setup for search of ^{150}Nd neutrinoless double beta decay The advantage of neodymium-150 as 2β-source is in its large energy release, $Q_{\beta\beta}$ = = 3.367 MeV, that together with high nuclear charge leads to the greatest among all isotopes 0ν2β-phase factor [5]. Estimations of nuclear matrix elements, based on modern models of nuclear structure [6, 7] show, that for fixed effective neutrino mass the ^{150}Nd 0ν2β-decay may be one of the most intensive. Also high transition energy provides better background conditions for neutrinoless double beta decay search. Several projects are proposed, which plan to use large masses of natural neodymium [8, 9]. The abundance of ^{150}Nd is 5.62%, so implementation of isotope enriched to 60 - 70 % can enlarge significantly the sensitivity of experiment. Moreover neodymium has no gaseous compound to use effectively centrifugal technique. In this situation laser separation method can be used for neodymium 2β-source production.

2. Laser separation of isotopes

Atomic vapour laser laser isotope separation (AVLIS) can by applied for rare-earth and other elements. AVLIS method is based on selective photoionization of atoms, as can be seen from Fig. 1, where enrichment scheme for Nd-150 is presented. Atoms pass through operation volume irradiated by laser were the isotope selective photoionization takes place. The target isotope photoions are extracted to the product collector by electric field. The neutral atoms of other isotopes follow the straight trajectory up to the waist collector. The selectivity of photoionization is based on isotope shift of energy levels of different isotopes. The isotope shift causes the difference of interlevel transition energy. So it is possible to tune the laser to excite the transition of specified isotope atoms. That is because the tunable dye lasers are traditionally used for AVLIS.

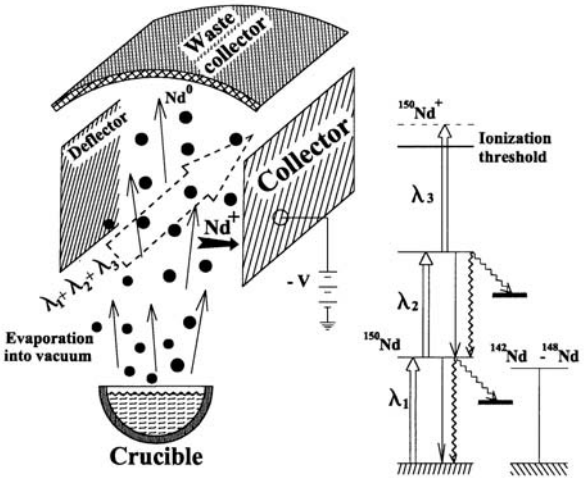

Fig. 1. AVLIS principal scheme.

Kurchatov Institute is the pioneer in optical isotope separation methods developement. The first discussions about selective photoionization were initiated by Prof. I. K. Kikoin and refer to 1968. Since 1974 AVLIS metod has been studied and significant result are achieved now not only in the main stream for uranium enrichment but also for stable isotopes. Selective photoionization was demonstrated for many elements including the case of disappearing isotope shift. The 90 % concentration of Ca-48 was received in photoionization experiments. In experiments, performed in the Institute for Molecular Physics of NRC Kurchatov Institute the versability of the AVLIS method had been established. The minimum changes required to convert our Nd facility to produce the weight amounts of Lu-176 that is so promising for medical applications.

The abundance of ^{176}Lu isotope is 2.59 %. As a result of exposition of ^{176}Lu in reactor neutron flux beta-active isotope ^{177}Lu(β^-) is produced due to reaction ^{176}Lu + n $\rightarrow$ ^{177}Lu + γ. ^{177}Lu with half-decay time 6.7 days is considered to be effective source of electrons for targeted radiotherapy.

The technical project of the industrial AVLIS setup for rear earth and other elements isotope separation is being designed in NRC "Kurchatov Institute" (Fig. 2). The work is intended to arrange commercial production of Lu-176

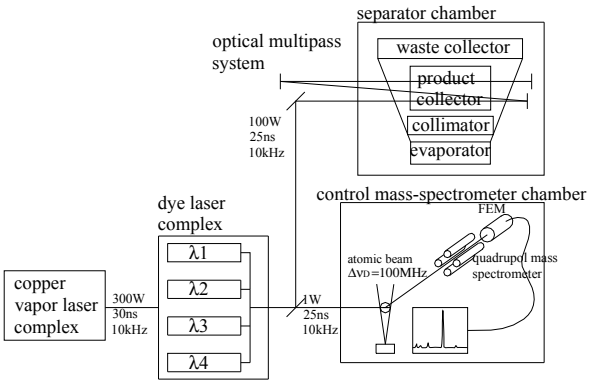

Fig. 2. AVLIS setup scheme.

isotope for medical application [10]. The setup is as well capable to produce 100 kg sample of Nd-150 with 60 % concentration for Russian double beta decay search experiment [11]. In 2005 we reported the development of the separation cell with productivity 1 g/day of Nd-150 [12]. At present the vacuum production unit, which gives the possibility to realize continuous work of separation cells is under construction. The new unit allows one to enlarge significantly the number of separation cells on one laser bulk. The production of 30 g of Lu-176 or 100 g of Nd-150 is planned during the new vacuum module test operation run.

3. Detector for search of neodymium-150 neutrinoless double beta-decay

The setup for search of ^{150}Nd 0ν2β transition is made as a set of thin (17 mm) scintillation plates on the basis of polystyrene with enriched neodymium foil with thickness 30 mg/cm^2 (up to 70 % in ^{150}Nd) located between them**.** The light is collected from four thin sides of plates for resolution enhancement. The path of electrons falls completely on one plate and registration of neutrinoless double beta decay will occur in one or two neighboring plates, directly being adjacent to the layer, where the decay had taken place. The background event, which is usually comprised of electron and accompanying gamma-quanta (for thallium-208 it is absolutely) are registered by several plates (see Fig. 2). The presence of great quantity of thin plates should maintain reliable separation of double beta decay processes.

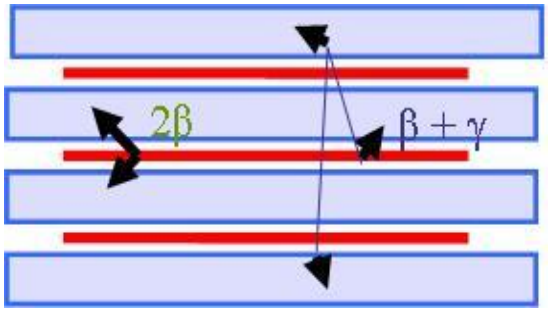

Fig. 3. Scheme of registration of 2β-decay electrons and internal radioactivity background.

The background was calculated by Monte Carlo method for bismuth-214 (cutoff energy ~ 3,27 MeV) and thallium-208 (cutoff energy ~ 5 MeV) isotopes, distributed uniformly in polystyrene and neodymium, being in equilibrium with uranium and thorium, because other long-living isotopes have smaller decay energies and do not give the contribution to the energy range under investigation. Results are normalized on the parents of radioactive numbers (uranium and thorium), in the assumption, that equilibrium of chains is not broken.

The actual size of setup will be determined on the base of optimization of spectrometric characteristics with the help of detector model. For the preliminary sensitivity estimation we choose the size of neodymium layer – 1.3 × 1.3 m^2, and plates 1.5 × 1.5 m^2. Then weight of one layer of neodymium will be ~ 500 g, weight of one plate ~ 40 kg, and for all setup the weight of polystyrene will be about 8 tons. The anticoincidence plates with size 1500 × 1500 × 300 mm are placed from below and from above. The number of neodymium layers equals 200. The light entering from one plate into another is excluded. The events, constrained by the neodymium layer size (1300 × × 1300 mm), were being extracted, (that is, event, accompanied by energy release in the peripheral 10 cm zone was considered to be background one).

Criterion of presence of neutrinoless mode is the triple excess of an error of the background. To this we add that here and in the following calculations the right side of distribution is used, i.e. energy window is equal 3σ the right of energy 3367 КэВ (ε ~ 40%). The event, imitating double beta decay was considered to be the one, which was registered in one or in two neighboring plates with energy release, falling in the energy window, corresponding to three sigma (the right part of neutrinoless mode peak distribution) and in the absence of signal from the rest part of detector. Minimal energy, which can be equals registered by the detector rest part is 50 keV. Threshold of single events registration is also 50 keV. As a result of calculations were obtained:

1. Spectra of bismuth and thallium, distributed in neodymium and polystyrene, registered by the whole detector integrally.

2. Spectra of bismuth and thallium, distributed in neodymium and polystyrene, registered only by one or two neighboring plates with anticoincidence with the rest part of detector. 3. The same as in item 2, but the primary event (in one or two neighboring plates) is registered in a square 10 or 5 cm on a side.

Spectra from ^{214}Bi and ^{208}Tl uniformly distributed in the polystyrene, for due to its great mass the requirements to radioactive impurities in polystyrene are stronger, are shown in Figs. 4, 5 (spectra for Nd appear to be similarly). Label “2” refers to the events, registered in two plates, “1” - in one plates, 10 or 5 cm refer to the size of event identification domain.

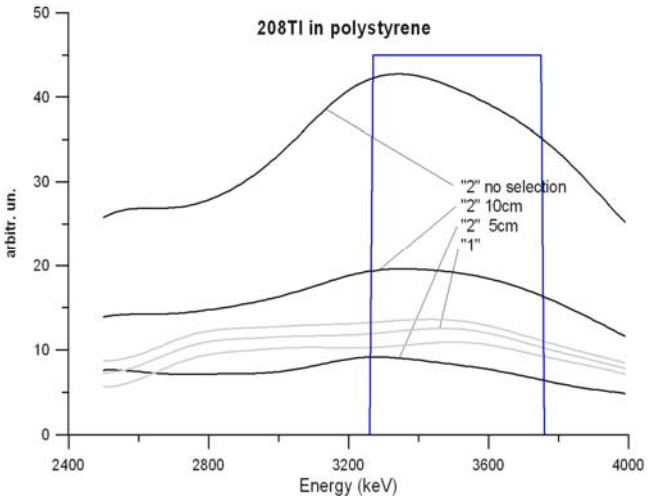

Fig. 4. Thallium-208 spectrum.

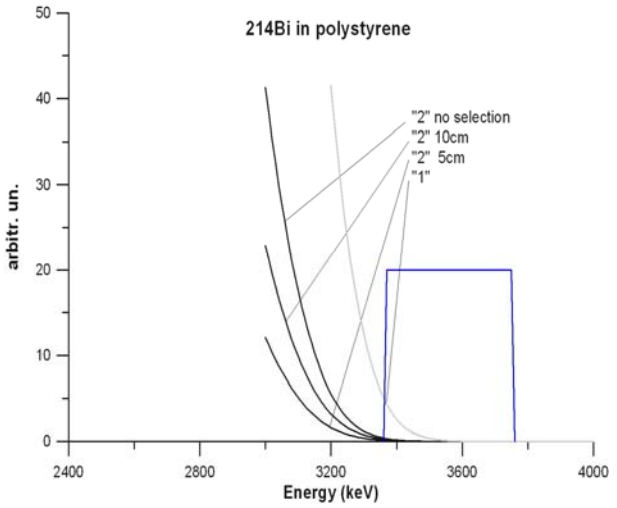

Fig. 5. Bismuth-214 spectrum.

It should be noted, that as it follows from the character of ^{208}Tl spectrum, the number of events in the energy region under investigation practically does not depend on the detector resolution, but it changes appreciably with the size of the identification region. As for ^{214}Bi, then, like a two-neutrino mode, the number of events in the energy window of interest decreases sharply with resolution improvement. The performed calculations enable us to estimate background magnitudes due to natural radioactive impurities. Thus supposing that uranium and thorium content in polystyrene and neodymium is on the level of 10^{-12} $g_{U,Th}/g$, the corresponding background rates are: (for thresholds 50 keV, resolution 8 % and identification region 5 × 5 cm^2)

Background counting from thallium-208 in polystyrene will be 111 events;

Background counting from thallium-208 in neodymium will be 1.6 events;

Background counting from bismuth-214 in polystyrene will be 23 events;

Background counting from bismuth-214 in neodymium will be 0.3 events.

So, total background from natural radioactivity equals 136 events for 5 years of measurements (3σ = 35 events) with the awaited effect of ~ 39 events for ^{150}Nd half-decay time 10^{25} yr.

In the presented calculations have not been taken into account the possibility of additional suppression of the background, due to the impurities in polystyrene (giving the main background contribution) by means of extraction of delayed coincidences between bismuth-214 decays and polonium- 214 alpha-decays (uranium chain) and bismuth-212 alpha-decays and thallium-208 beta-decays (thorium chain). On the other hand, the background from these isotopes, distributed in neodymium is not too large, and the requirements for the amounts of uranium and thorium impurities in neodymium can be moderated.

4. Calculation of background contribution from 2ν2β-transitions

The irremovable source of background for neutrinoless double beta decay experiments is due to two-neutrino channel. Thus for estimation of sensitivity of 0ν2β searches it is necessary to calculate exactly the contribution of 2ν2β - signals in the region of ^{150}Nd 0ν2β peak. The distribution $\frac{dI}{dT}$ of the sum of electron kinetic energies, $T = T_1 + T_2$, depends on nuclear mechanism of 2ν2β-decay and has the form [2, 13]:

$$\frac{dI}{dT} = \int_0^T I_{12}(T - T_2, T_2)dT_2 ,$$

where $I_{12}(T_1, T_2)$ contains summation over all 1^+ states of intermediate nucleus. There are two possible approaches to treat this sum. One can assume the dominance of higher lying states of intermediate nucleus in 2ν2β-amplitude, this is HSD-hypothesis. The alternative mechanism is based on suggestion, that 2ν2β-decays are determined by the two virtual beta-transitions via 1^+ intermediate state [15, 16]. This is the single state dominance (SSD) hypothesis. In [16] the fraction S_W of 2ν2β signals in the detector energy window in the region of 0ν2β peak was calculated according to HSD approach and it was noted, that it would be interesting to consider a model, where contributions of possible excited 1^+ - states of intermediate nucleus ^{150}Pm are taken into account. The recently observed low-lying 1^+ -states of ^{150}Pm, determined in charge-exchange reactions [17] confirm this suggestion. So, evaluation of electrons total energy distribution for SSD and HSD mechanisms can give the limits for background contribution, due to two-neutrino channel. The background counting N_b for 5 years of measurement, corresponding to two values of detector resolution R are the following: R = 7 % N_b(HSD) = 59, N_b(SSD) = 92; R = 8 % N_b(HSD) = 126, N_b(SSD) = 192. Here the lowest 1^+

state is taken into account in SSD calculations. The study of energy and angular distribution of outgoing electrons would give useful information on mechanism of 2ν2β transitions [18].

The work is supported by RFBR grants 11-02-12034-ofi-m-2011, 12-08-00561-a, 11-02-00882-a.

REFERENCES

1. *Klapdor-Kleingrothaus H.V.* Seventy Years of Double Beta Decay. - Singapore: World Scientific Publishing Co., 2010.
2. *Tretyak V., Zdesenko Y.* Tables of Double Beta Decay Data -An Update // At. Data and Nucl. Data Tables. - 2002. - Vol. 80. - P. 83 - 116.
3. *Barabash A.S.* Double-beta decay experiments // Particles and Nuclei. - 2011. - Vol. 42. - P. 1184 - 1205.
4. *Tikhomirov A.V.* Some aspects of centrifugal technology of stable isotopes separation // Isotopes Properties Production Application. - Moscow: Fizmatlit, 2005. - P. 208 - 228.
5. *Doi M., Kotani T., Takasugi E.* Double Beta Decay and Majorana Neutrino // Progr. Theor. Phys. Suppl. - 1985. - Vol. 83. - P. 1 - 175.
6. *Hirsch J.G., Castaños O, Hess P.O.* Neutrinoless double beta decay in heavy deformed nuclei // Nucl. Phys. A. - 1995. - Vol. 582. - P. 124 - 140.
7. *Rodin V.A. ,Faessler A., Šimkovic F, Vogel P.* Assessment of uncertainties in QRPA 0νββ- decay nuclear matrix elements // Nucl. Phys. A. - 2006. - Vol. 766. - P. 107 - 131.
8. *Barabanov I., Bezrukov L., Cattadori C. et al.* Characterization of Nd-loaded organic liquid scintillator for neutrinoless double beta decay of ^{150}Nd search with a 10-ton scale detector; arXiv:0909.2152v1 [physics.ins-det].
9. *Hartnell J.* Neutrinoless Double Beta Decay with SNO+; arXiv:1201.6169v1 [physics.ins- det].
10. *D'yachkov A.B., Kovalevich S.K., Labozin A.V. et al.* Investigation of selective photoionization of lutetium atoms // Proc. of the XI Int. Conf. "Physico-chemical Processes in Selection of Atoms and Molecules and in Laser, Plasma and Nanotechnologies". - Zvenigorod: TSNIIATOMINFORM, 2006. - P. 83 - 88; *D'yachkov A.B., Labozin V.P., Firsov V.A., Tsvetkov G.O.* Indication of AVLIS method relevance for modern high technologies // Ibid. - Zvenigorod: TSNIIATOMINFORM, 2008. - P. 153 - 158.
11. *Balysh A.Ya., Labozin V.P., Semenov S.V.* The proposal of experiment for search of double beta-decay of ^{150}Nd nuclei. - Dubna, 2008. - 20 p. - (Prep. / RRC "KI"; 6541/2); *Alyoshin V.I., Balysh A.Ya., Brudanin V.B. et al.* Search for neutronoless double beta-decay of^{150}Nd // Perspektivnye materialy. - 2010. - Special. Issue 8. - P. 351 - 360.
12. *Babichev A.P., Grigor'ev A.I., Grigor'ev I. S. et al.* Development of laser (AVLIS) method of weight amounts production of high-enriched ^{150}Nd isotope // Kvantovaya elektronika. - 2005. - Vol. 35. - P. 879 - 890.
13. *Tomoda T.* Double beta decay // Rep. Progr. Phys. - 1991. - Vol. 54. - P. 53 - 126.
14. *Abad J., Morales A., Nunez-Lagos R., Pacheco A.F.* // An. Fiz. A. - 1984. - Vol. 80. - P. 15 - 20.
15. *Civatarese O., Suhonen J.* Is the single-state dominance realized in double-β-decay transitions? // Phys. Rev. C. - 1998. - Vol. 58. - P. 1535 - 1538.
16. *Balysh A.Ya., Khruschov V.V., Labozin V.P. et al.* Calculation of 2ν2β amplitude for ^{100}Mo and ^{150}Nd // Proc. of the 3-rd Int. Conf. "Current Problems in Nuclear Physics and Atomic Energy" (Kyiv, 7 - 12 June 2010). - Kyiv, 2011. - P. 414 - 418.
17. *Guess C.J., Adachi T., Akimune H. et al.* The ^{150}Nd(^{3}He, t) and ^{150}Sm(t, ^{3}He) reactions with applications to ββ decay of ^{150}Nd // Phys. Rev. C. - 2011. - Vol. 83. - P. 064318.
18. *Šimkovic F., Domin P., Semenov S.V.* The single state dominance hypothesis and the two-neutrino double beta decay of 100Mo // J. Phys. G. - 2001. - Vol. 27. - P. 2233 - 2240.

FIRST RESULTS OF THE EXPERIMENT TO SEARCH FOR DOUBLE BETA DECAY OF ^{116}Cd WITH THE HELP OF ENRICHED $^{116}CdWO_4$ CRYSTAL SCINTILLATORS

A. S. Barabash[1], P. Belli[2], R. Bernabei[2,3], F. Cappella[4,5], V. Caracciolo[6], S. Castellano[6], R. Cerulli[6], D. M. Chernyak[7], F. A. Danevich[7], E. N. Galashov[8], A. Incicchitti[4,5], V. V. Kobychev[7], S. I. Konovalov[1], M. Laubenstein[6], D. V. Poda[7], R. B. Podviyanuk[7], O. G. Polischuk[5,7], V. N. Shlegel[8], V. I. Tretyak[7], V. I. Umatov[1], Ya. V. Vasiliev[8]

[1] *Institute of Theoretical and Experimental Physics, Moscow, Russia*
[2] *Dipartimento di Fisica, Università di Roma "Tor Vergata", Rome, Italy*
[3] *Istituto Nazionale di Fisica Nucleare, Sezione di Roma "Tor Vergata", Rome, Italy*
[4] *Dipartimento di Fisica, Università di Roma "La Sapienza", Rome, Italy*
[5] *Istituto Nazionale di Fisica Nucleare, Sezione di Roma "La Sapienza", Rome, Italy*
[6] *Laboratori Nazionali del Gran Sasso, Istituto Nazionale di Fisica Nucleare, Assergi (AQ), Italy*
[7] *Institute for Nuclear Research, National Academy of Sciences of Ukraine, Kyiv, Ukraine*
[8] *Nikolaev Institute of Inorganic Chemistry, Novosibirsk, Russia*

A low background experiment to search for the double β decay of ^{116}Cd is in progress at the Gran Sasso National Laboratories of the INFN (Italy) by using $^{116}CdWO_4$ crystal scintillators (≈ 1.2 kg) enriched in ^{116}Cd to 82 %. The energy resolution of the detector is FWHM ≈ 5.5% at $Q_{2\beta}$ of ^{116}Cd (2813 keV); the background rate is 0.28 counts/(yr × keV × kg) in the 2.7–2.9 MeV energy range. After ≈ 1 kg × yr of data taking, the half-life of ^{116}Cd relatively the 2ν2β decay was measured as $T_{1/2} = (2.5 \pm 0.5) \times 10^{19}$ yr and new improved limits on the 2β decay of ^{116}Cd to few excited levels of ^{116}Sn were set at level of 10^{21} - 10^{22} yr. In particular, 2ν2β transitions to 2^+ states (2112 and 2225 keV) of ^{116}Sn were restricted as $T_{1/2} \geq 6.0 \times 10^{20}$ yr and $T_{1/2} \geq 6.7 \times 10^{20}$ yr at 90% C.L., respectively, that is approximately one order of magnitude higher than those previously established.

1. Introduction

The neutrinoless double beta decay (0ν2β) is a powerful tool to check the lepton number conservation, to determine an absolute neutrino mass and its hierarchy, to establish the nature of the neutrino (Majorana or Dirac particle), to find the possible contribution of right-handed admixture to weak interaction and the existence of Nambu-Goldstone bosons (Majorons) [1].

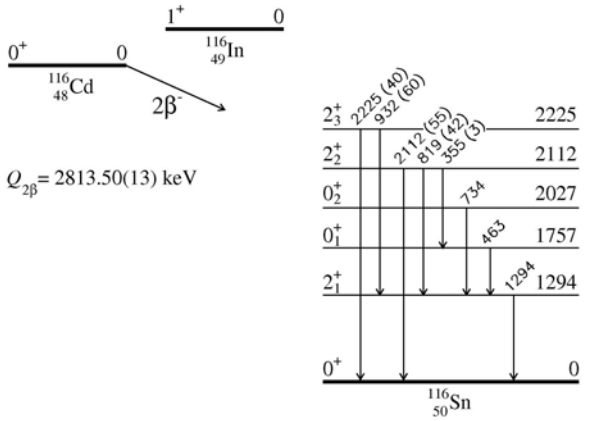

Fig. 1. Simplified decay scheme of ^{116}Cd [14]. The energies of the excited levels and of the emitted γ quanta are in keV (relative intensities of γ quanta are given in parentheses); $Q_{2\beta}$ is the double beta decay energy [2].

The ^{116}Cd isotope is one of the most favorable nuclides for 2β studies thanks to the large energy release ($Q_{2\beta}$ = (2813.50 ± 0.13) keV [2]), the high natural abundance (δ = (7.49 ± 0.18)% [3]), and the promising theoretical predictions [4, 5, 6]. The decay scheme of ^{116}Cd is presented in Fig. 1. The two neutrino (2ν) 2β decay of ^{116}Cd to the ground state of ^{116}Sn was registered by the ELEGANT V [7], by the Solotvina [8], by the NEMO-2 [9] and by the NEMO-3 [10] experiments. The weighted average value for the half-life is $T_{1/2} = (2.8 \pm 0.2) \times 10^{19}$ yr [11]. The strongest restrictions on the 0ν2β decay of ^{116}Cd, as well as 0ν2β processes with Majoron(s) emission were achieved in [8]. As regarding the 2β transitions of ^{116}Cd to the excited levels of ^{116}Sn, only $T_{1/2}$ limits in the range 10^{20} - 10^{22} yr were obtained; the strongest limits can be found in Refs. [8, 12, 13].

A low background detector with radiopure cadmium tungstate crystal scintillator enriched in ^{116}Cd ($^{116}CdWO_4$, mass of ≈ 1.2 kg, enrichment of ^{116}Cd is 82%) was developed to search for the 2β decay of ^{116}Cd at the Gran Sasso National Laboratories of the INFN (Italy) [15]. The first preliminary results of the experiment are presented here.

2. Low background experiment with the $^{116}CdWO_4$ detector

The development of the $^{116}CdWO_4$ crystal scintillators, its characterization, and the construction of the low background $^{116}CdWO_4$ detector can be found in Ref. [15]. Here we shortly outline the main features of the experiment.

Two $^{116}CdWO_4$ crystals (580 g and 582 g) are used in the experiment. The scintillators are fixed inside the cavities (filled with liquid scintillator) located in the central part of the light-guides (∅70 × 594 mm); they are viewed on

opposite sides by two low radioactive 3" PMTs (Hamamatsu R6233MOD). The light-guides are glued to polystyrene scintillators (the central parts $\varnothing 70 \times 194$ mm) and to two high purity quartz details ($\varnothing 70 \times 200$ mm). In particular, the light-guides with the $^{116}CdWO_4$ crystals are placed between two polystyrene plastic scintillators $500 \times 300 \times 120$ mm each. The plastic scintillators are viewed by low background 3" PMTs (ETL 9302FLA).

The detector is sealed in a low radioactive air-tight Cu box continuously flushed with high purity nitrogen gas to avoid the presence of environmental radon. The Cu box is surrounded by a passive shield made of high purity Cu (10 cm of thickness), 15 cm of low radioactive lead, 1.5 mm of cadmium and 4 to 10 cm of polyethylene/paraffin to reduce the external background. The shield is contained inside a Plexiglas box, also continuously flushed by high purity nitrogen. The set-up is installed deep underground (≈ 3600 m w.e.) at the Gran Sasso National Laboratories of the INFN (Italy).

An event-by-event data acquisition system based on a 1 GS/s 8 bit transient digitizer (Acqiris DC270) records the time of each event and the pulse shapes (in the time window of 50 μs) from the $^{116}CdWO_4$ detectors and from the plastic scintillator. The calibration of the detector was performed with ^{22}Na, ^{60}Co, ^{137}Cs, and ^{228}Th sources. The energy resolution of the detector is FWHM ≈ 5.5% at $Q_{2\beta}$ of ^{116}Cd.

The radioactive contamination of the $^{116}CdWO_4$ crystals is reported in [15]; the activities of ^{226}Ra and ^{228}Th are on the level < 0.005 mBq/kg and ≈ 0.06 mBq/kg, respectively, while the total α activity does not exceed 3 mBq/kg.

3. Results and discussion

The background energy spectrum of γ(β) events accumulated with the $^{116}CdWO_4$ detector over ≈ 7593 h is presented in Fig. 2. The γ(β) events were selected by the pulse-shape and the front edge analyzes described in [15]. The background is caused by radioactive contamination of the $^{116}CdWO_4$ scintillators and of the set-up. The main part of the counting rate below ≈ 0.65 MeV is caused by β decay of ^{113}Cd and ^{113m}Cd, while the background in the range 0.7 - 2.4 MeV is dominated by 2ν2β decay of ^{116}Cd. Possible components of the background (internal ^{40}K, ^{90}Sr-^{90}Y, ^{110m}Ag, radionuclides from U/Th chains, external γ from the details of the set-up, 2ν2β decay of ^{116}Cd) were simulated by using the EGS4 code [16]. Fit of the background spectrum and the main components of the background are presented in Fig. 2. The fit gives the half-life of ^{116}Cd relatively to the 2ν2β decay as $T_{1/2} = (2.5 \pm 0.5) \times 10^{19}$ yr in agreement with the results of the previous experiments [7, 8, 9, 10] (see also the Table) and world average value [11].

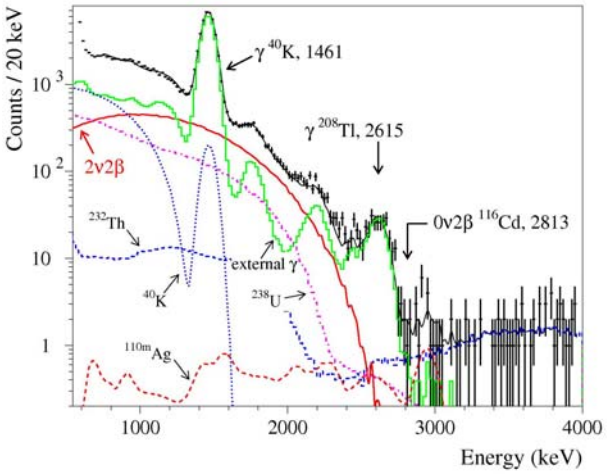

Fig. 2. The energy spectrum of γ(β) events measured with the $^{116}CdWO_4$ scintillation detector over 7593 h in the low-background set-up (points) together with the fit (solid black line). The main components of the background are also shown: 2ν2β decay of ^{116}Cd, the distributions of internal ^{40}K, ^{232}Th, ^{238}U, and cosmogenic ^{110m}Ag, the contribution from external γ quanta from the details of the set-up ("external γ") under these experimental conditions. The energies are in keV.

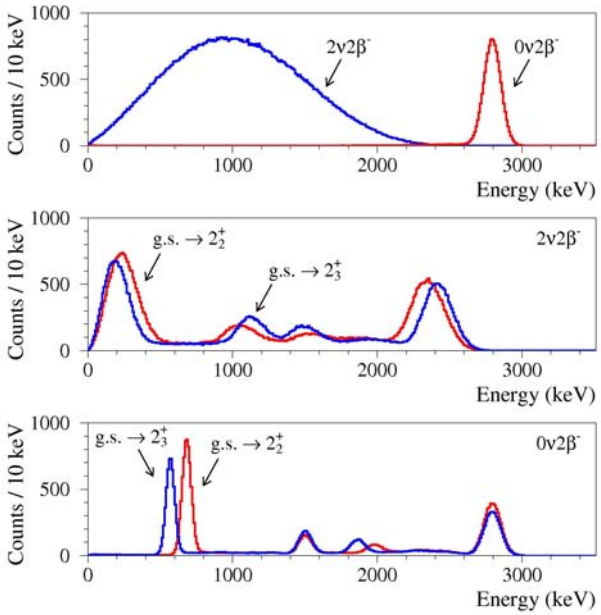

Fig. 3. Simulated response functions of the $^{116}CdWO_4$ detector to 2β processes in ^{116}Cd. There are (top) 2ν and 0ν 2β decay of ^{116}Cd to the ground state of ^{116}Sn; 2ν (middle) and 0ν (bottom) 2β transitions of ^{116}Cd to the 2^+_2 (2112 keV) and to the 2^+_3 (2225 keV) excited levels of ^{116}Sn.

There are no other peculiarities in the spectrum which could be ascribed to the 2β processes in ^{116}Cd (the Monte Carlo calculated distributions of some 2β processes in ^{116}Cd are presented in Fig. 3). Therefore only lower half-life limits were set according to formula: $\lim T_{1/2} = N \times \eta \times t \times \ln 2 / \lim S$, where N is the number of ^{116}Cd nuclei

(1.617×10^{24}), η is the detection efficiency, t is the measuring time, and lim$S$ is the number of events of the effect searched for which can be excluded at a given confidence level (C.L.). The values of lim$S$ were estimated by applying the Feldman-Cousins procedure [17] to the results of the fits. The fits allow us to set new limits on the 2β decay in ^{116}Cd to excited levels of ^{116}Sn (Table).

The half-lives of the 2β decay ^{116}Cd $\rightarrow$ ^{116}Sn.
Limits are given at 90 % C.L. except than those from [12] which are at 68 % C.L.

Decay channel	Level of ^{116}Sn	$T_{1/2}$, yr	
		Present work	Best previous limits and positive results
$2\nu2\beta^-$	g.s.	$= 2.5(5) \times 10^{19}$	$= (2.6\ ^{+0.9}_{-0.5}) \times 10^{19}$ [7] $= (2.9 \pm 0.06(\text{stat.})\ ^{+0.4}_{-0.3}(\text{syst.})) \times 10^{19}$ [8] $= (3.75 \pm 0.35(\text{stat.}) \pm 0.21(\text{syst.})) \times 10^{19}$ [9] $= (2.88 \pm 0.04(\text{stat.}) \pm 0.16(\text{syst.})) \times 10^{19}$ [10] $= (2.8 \pm 0.2) \times 10^{19}$ (average weighted value) [11]
	2^+_2 (2112)	$\geq 6.0 \times 10^{20}$	$\geq 1.7 \times 10^{20}$ [12]
	2^+_3 (2225)	$\geq 6.7 \times 10^{20}$	$\geq 1.0 \times 10^{20}$ [12]
$0\nu2\beta^-$	0^+_2 (2027)	$\geq 6.7 \times 10^{21}$	$\geq 6.0 \times 10^{21}$ [8]
	2^+_2 (2112)	$\geq 8.2 \times 10^{21}$	$\geq 1.7 \times 10^{20}$ [12]
	2^+_3 (2225)	$\geq 6.7 \times 10^{21}$	$\geq 1.0 \times 10^{20}$ [12]

The background rate of the $^{116}CdWO_4$ detector is 0.28(4) counts/(yr × keV × kg) in the 2.7 - 2.9 MeV energy range where peak of 0ν2β decay of ^{116}Cd is expected for (in the 2.8 - 3.0 MeV energy interval the background is 0.10(2) counts/(yr × keV × kg)). Fit of the energy spectrum of the $^{116}CdWO_4$ detector shows that the main components of the background in the energy range of interest are 2615 keV γ quanta of ^{208}Tl from contaminations of the PMTs (≈30 %) and the copper box (≈40 %) by ^{232}Th. The radioactive contamination of the $^{116}CdWO_4$ crystal scintillators gives about one-third of the counting rate (≈10 % due to ^{208}Tl and ≈20 % due to cosmogenic ^{110m}Ag). The background could be suppressed by the installation of an additional shield and the recrystallization of the $^{116}CdWO_4$ crystals to decrease thorium content. The activity of ^{110m}Ag is expected to be reduced due to relatively short decay time ($T_{1/2} \approx 250$ days).

To suppress the contribution from 2615 keV γ quanta of ^{208}Tl in the set-up, an R&D for an additional passive shield made of highly radio-pure copper, as well as of $PbWO_4$ crystal scintillators to replace some part of the plastic light-guides, is in progress. Such an upgrade of the set-up could suppress the background at least by a factor 3 in the vicinity of the energy region of interest for the 0ν2β decay of ^{116}Cd. Furthermore, our preliminary study confirms a rather low segregation of thorium in $CdWO_4$ crystal (much higher activity of ^{228}Th was detected by low background HPGe γ spectrometry in the scraps after the $^{116}CdWO_4$ crystal growth than that in the $^{116}CdWO_4$ crystals). Therefore recrystallization could decrease the activity of ^{228}Th in the scintillators, while the activity of ^{110m}Ag should be decreased in time due to the decay of this radionuclide. As a result we expect to reach a sensitivity to the neutrinoless 2β decay of ^{116}Cd on the level of $T_{1/2} \sim (0.5 - 1.5) \times 10^{24}$ yr over 5 years of the measurements. It corresponds, taking into account the recent calculations of the matrix elements, to the effective neutrino mass $\langle m_\nu \rangle \approx 0.4 - 1.4$ eV.

4. Conclusions

An experiment using a cadmium tungstate crystal scintillator enriched in ^{116}Cd up to 82 % is in progress at the Gran Sasso National Laboratories of the INFN (Italy). The exposure of the experiment is ≈ 1.2 kg × yr at end of August 2012. The energy resolution of the detector is FWHM ≈ 5.5 % at the $Q_{2\beta}$ of ^{116}Cd, the background counting rate is 0.28(4) counts/(yr × keV × kg) in the region of interest 2.7 - 2.9 MeV. The main components of the background in the vicinity of 0ν2β decay of ^{116}Cd are γ quanta of ^{208}Tl from the contamination of the set-up, from the internal contamination of the $^{116}CdWO_4$ crystal scintillators by ^{228}Th and from the cosmogenic ^{110m}Ag.

A sensitivity of the experiment to 0ν2β decay of ^{116}Cd after 5 yr of measurements is expected to be on the level of $T_{1/2} \sim (0.5 - 1.5) \times 10^{24}$ yr (which corresponds to the effective neutrino mass $\langle m_\nu \rangle \approx 0.4 - 1.4$ eV) after the improvement of the background due to the installation of an additional shield and recrystallization of $^{116}CdWO_4$ crystals. An R&D to improve the background conditions is in progress.

The half-life of ^{116}Cd relatively to the 2ν2β decay was measured as $T_{1/2} = (2.5 \pm 0.5) \times 10^{19}$ yr, which is in agreement with the positive results of previous experiments. New limits on the 2β transitions of ^{116}Cd to few excited states of ^{116}Sn were set on the level of 10^{21}–10^{22} yr. In particular, the 2ν2β decays of ^{116}Cd to 2^+ levels (2112 and 2225 keV) of ^{116}Sn were restricted as $T_{1/2} \geq 6.0 \times 10^{20}$ yr and $T_{1/2} \geq 6.7 \times 10^{20}$ yr at 90 % C.L., respectively, that is approximately one order of magnitude higher than those known previously.

REFERENCES

1. *Rodejohann W.* Neutrinoless double beta decay and neutrino physics // ArXiv:1206.2560v1 [hep-ph], 26 p.; *Vergados J.D., Ejiri H., Simkovic F.* Theory of neutrinoless double beta decay // ArXiv:1205.0649v2 [hep-ph], 104 p.; *Elliott S.R.* Recent progress in double beta decay // Mod. Phys. Lett. - 2012. - Vol. A27. - P. 1230009, 16 p.; *Rodejohann W.* Neutrino-less double beta decay and particle physics // Int. J. Mod. Phys. - 2011. - Vol. E20. - P. 1833 - 1930; *Barabash A.S.* Double beta decay experiments // Phys. Part. Nucl. - 2011. - Vol. 42. - P. 613 - 627; *Avignone III F.T., Elliott S.R., Engel J.* Double beta decay, Majorana neutrinos, and neutrino mass // Rev. Mod. Phys. - 2008. - Vol. 80. - P. 481- 516.
2. *Rahaman S., Elomaa V.-V., Eronen T. et al.* Double-beta decay Q values of ^{116}Cd and ^{130}Te // Phys. Lett. - 2011. - Vol. B703. - P. 412 - 416.
3. *Berglund M., Wieser M.E.* Isotopic compositions of the elements 2009 (IUPAC technical report) // Pure Appl. Chem. - 2011. - Vol. 83. - P. 397 - 410.
4. *Simkovic F. et al.* 0νββ-decay nuclear matrix elements with self-consistent short-range correlations // Phys. Rev. - 2009. - Vol. C79. - P. 055501, 10 p.
5. *Kortelainen M., Suhonen J.* Nuclear matrix elements of 0νββ decay with improved short-range correlations // Phys. Rev. - 2007. - Vol. C76. - P. 024315, 6 p.
6. *Rodrigez T.R., Martinez-Pinedo G.* Energy density functional study of nuclear matrix elements for neutrinoless ββ decay // Phys. Rev. Lett. - 2010. - Vol. 105. - P. 252503, 4 p.
7. *Ejiri H. et al.* Double beta decay of ^{116}Cd // J. Phys. Soc. Japan. - 1995. - Vol. 64. - P. 339 - 343.
8. *Danevich F.A. et al.* The research of 2β decay of ^{116}Cd with enriched $^{116}CdWO_4$ crystal scintillators // Phys. Lett. - 1995. - Vol. B344. - P. 72 - 78; *Danevich F.A. et al.* Search for 2β decay of cadmium and tungsten isotopes: Final results of the Solotvina experiment // Phys. Rev. – 2003. – Vol. C68. – P. 035501, 12 p.
9. *Arnold R. et al.* Observation of two neutrino double beta decay of ^{116}Cd with the tracking detector NEMO-2 // JETP Lett. - 1995. - Vol. 61. - P. 170 - 174; *Arnold R. et al.* Double-β decay of ^{116}Cd // Z. Phys. - 1996. - Vol. C72. - P. 239 - 247.
10. *Tretyak V.I. on behalf of the NEMO-3 collaboration.* The NEMO-3 results after completion of data taking // AIP Conf. Proc. - 2011. - Vol. 1417. - P. 125 - 128.
11. *Barabash A.S.* Precise half-life values for two-neutrino double-β decay // Phys. Rev. - 2010. - Vol. C81. - P. 035501, 7 p.
12. *Barabash A.S., Kopylov A.V., Cherehovsky V.I.* Search for double β-decay of ^{100}Mo and ^{116}Cd to the excited states of ^{100}Ru and ^{116}Sn // Phys. Lett. - 1990. - Vol. B249. - P. 186 - 190.
13. *Piepke A. et al.* Investigation of the ββ decay of ^{116}Cd into excited states of ^{116}Sn // Nucl. Phys. - 1994. - Vol. A577. - P. 493 - 510.
14. *Blachot J.* Nuclear Data Sheets for A = 116 // Nucl. Data Sheets - 2010. - Vol. 111. - P. 717 - 895.
15. *Barabash A.S. et al.* Low background detector with enriched $^{116}CdWO_4$ crystal scintillators to search for double β decay of ^{116}Cd // J. Instrum. - 2011. - Vol. 6. - P. P08011, 24 p.
16. *Nelson W.R. et al.* The EGS4 code system // SLAC-Report-265, Stanford, 1985. - 398 p.
17. *Feldman G.J., Cousins R.D.* Unified approach to the classical statistical analysis of small signals // Phys. Rev. - 1998. - Vol. D57. - P. 3873 - 3889.

FIRST SEARCH FOR DOUBLE BETA DECAY OF OSMIUM BY LOW BACKGROUND HPGe DETECTOR

P. Belli[1], R. Bernabei[1,2], F. Cappella[3,4], R. Cerulli[5], F. A. Danevich[6], S. d'Angelo[1], A. Di Marco[1], A. Incicchitti[3,4], G. P. Kovtun[7], N. G. Kovtun[7], M. Laubenstein[5], D. V. Poda[6], O. G. Polischuk[4,6], A. P. Shcherban[7], V. I. Tretyak[6]

[1] Dipartimento di Fisica, Università di Roma "Tor Vergata", Rome, Italy
[2] Istituto Nazionale di Fisica Nucleare, Sezione di Roma "Tor Vergata", Rome, Italy
[3] Dipartimento di Fisica, Università di Roma "La Sapienza", Rome, Italy
[4] Istituto Nazionale di Fisica Nucleare, Sezione di Roma "La Sapienza", Rome, Italy
[5] Istituto Nazionale di Fisica Nucleare, Laboratori Nazionali del Gran Sasso, Assergi (AQ), Italy
[6] Institute for Nuclear Research, National Academy of Sciences of Ukraine, Kyiv, Ukraine
[7] National Science Center "Kharkiv Institute of Physics and Technology", Kharkiv, Ukraine

A search for 2β decay of osmium was realized for the first time with the help of an ultra-low background HPGe γ detector at the underground Gran Sasso National Laboratories of the INFN (Italy). After 2741 h of data taking with 173 g osmium sample limits on 2β processes in ^{184}Os have been established on the level of $T_{1/2} \geq 10^{16}$ - 10^{17} yr at 90 % C.L. A possible resonant neutrinoless double electron capture in ^{184}Os to the excited 1322.2 keV level of ^{184}W was restricted as $T_{1/2} \geq 1.3 \cdot 10^{16}$ yr. A half-life limit $T_{1/2} \geq 3.7 \cdot 10^{19}$ yr was set for the 2β decay of ^{192}Os to the first excited level of ^{192}Pt. As a by-product of the experiment, α decays of ^{184}Os and ^{186}Os to the first excited levels of daughter nuclei were searched for. A half-life limit on α decay of ^{186}Os to the 2^+ state (100.1 keV) of ^{182}W is set as $T^{\alpha}_{1/2}(^{186}\text{Os}) \geq 4 \cdot 10^{16}$ yr. A peak in the energy spectrum at 103 ± 1 keV with an area 22 ± 14 counts may be considered as an indication for α decay of ^{184}Os to the 2^+ level (103.5 keV) of ^{180}W with the half-life $T^{\alpha}_{1/2}(^{184}\text{Os}) = 5^{+8}_{-2} \cdot 10^{14}$ yr. The experiment is in progress.

Introduction

The investigation of the neutrinoless double beta (0ν2β) decay is considered to-date as a way to probe physics beyond the Standard Model. The process is sensitive to the lepton number violation, the nature of neutrino (Majorana or Dirac particle), an absolute scale of neutrino mass and the neutrino mass hierarchy (see [1] and refs. therein). In particular, investigation of 0ν 2ε and $\varepsilon\beta^+$ processes could clarify the possible contribution of the right-handed currents to the $0\nu2\beta^-$ decay rate [2].

Osmium contains two potentially 2β active isotopes: ^{184}Os (energy of decay $Q_{2\beta}$ = 1451.2(1.0) keV, isotopic abundance δ = 0.02(1) %, allowed decay channels are 2ε and $\varepsilon\beta^+$) and ^{192}Os ($Q_{2\beta}$ = 412.4(2.9) keV, δ = 40.8(2) %, $2\beta^-$). The decay schemes of ^{184}Os and ^{192}Os are presented in Fig. 1. There is a possibility of a resonant enhancement of the 0ν double electron capture in ^{184}Os to a few excited levels of ^{184}W. The most promising of them is the level $(0)^+$ 1322.2 keV [3].

We have realized the first search for 2β processes in ^{184}Os and ^{192}Os with the help of an ultra-low background HPGe γ spectrometer. As a by-product of the experiment we have also performed a search for α decay of ^{184}Os (^{186}Os) to the first excited levels of ^{180}W (^{182}W). Preliminary results of the experiment are presented here.

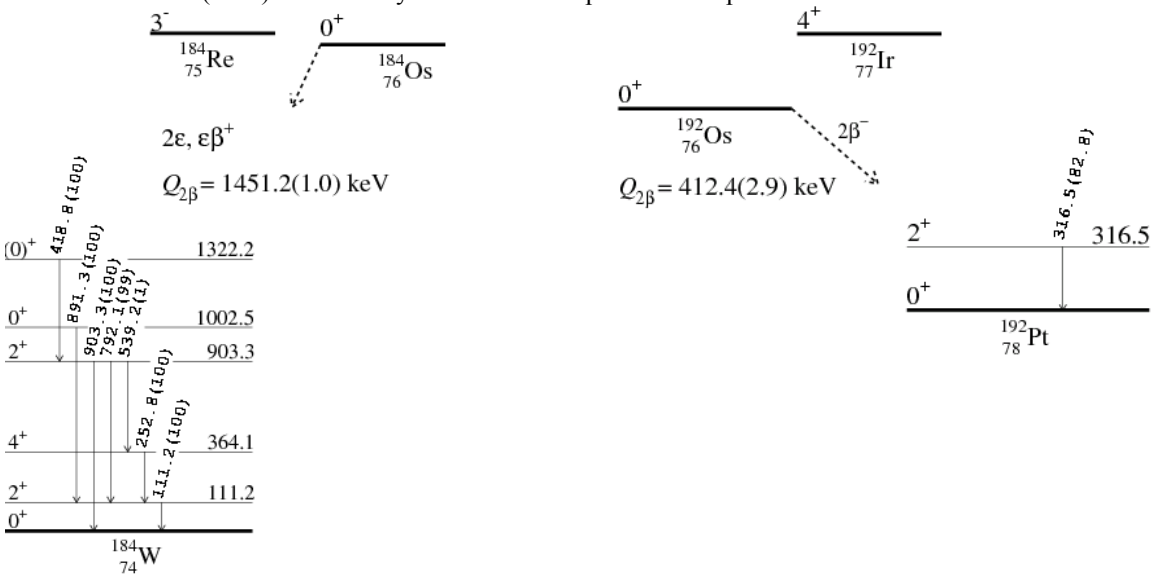

Fig. 1. Decay schemes of ^{184}Os [4] and ^{192}Os [5]. The energies of the excited levels and emitted γ quanta are in keV. $Q_{2\beta}$ is the double beta decay energy [6].

Experiment

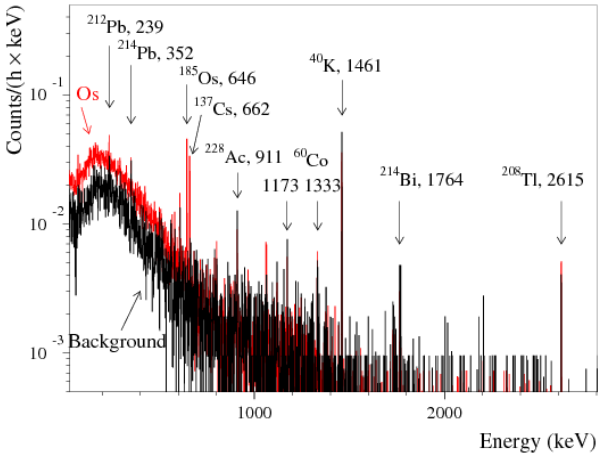

Fig. 2. Energy spectra measured with the osmium sample over 2741 h (Os) and without sample over 1046 h (Background) by ultra-low background HPGe γ spectrometer. The energy of the γ lines is in keV.

An ultra-pure osmium sample (more than 99.999% purity grade) with mass of 173 g was used in the experiment. The sample contains $1.1 \cdot 10^{20}$ nuclei of ^{184}Os and $2.2 \cdot 10^{23}$ nuclei of ^{192}Os. The experiment was carried out at the Gran Sasso National Laboratories of the INFN (Italy) with an ultra-low background HPGe detector GeCris, whose volume is 465 cm^3. The detector is shielded by lead (≈ 20 cm), copper (≈ 10 cm) and polyethylene (≈ 10 cm). The energy resolution of the spectrometer is FWHM = 2.0 keV at the 1333 keV γ line of ^{60}Co. The data with the sample were accumulated over 2741 h, while the background spectrum was taken over 1046 h. The spectra are presented in Fig. 2.

Radioactive contamination of the osmium sample

The peaks in the spectra can be ascribed to γ quanta of U/Th daughters, ^{40}K, ^{60}Co, ^{137}Cs. The response functions of the detector to decays of these nuclides as well as to the 2β processes in the osmium isotopes were simulated by EGS4 [7] and GEANT4 [8] packages with initial kinematics given by the DECAY0 event generator [9]. Both simulations gave consistent results[1]. Some excess of events in the 662 keV peak of ^{137}Cs was observed. The activity of ^{137}Cs as well as upper limits on contamination by ^{40}K and U/Th daughters are presented in Table 1. The radioactive ^{185}Os (EC decay, $T_{1/2}$ = 96.3 d [10]) was also detected in the sample with an activity (3.9 ± 0.4) mBq/kg. We assume that this radionuclide was generated before the installation of the sample into the set-up by capture of neutrons by ^{184}Os and by spallation processes induced by cosmic rays on heavier Os isotopes.

Table 1. **Radioactive contamination of the osmium sample measured with the HPGe detector. The upper limits are given at 68 % C.L.**

Chain	Nuclide (sub-chain)	γ emitters (E_γ, keV)	Activity, mBq/kg
	^{40}K	^{40}K (1460.8)	≤ 2.8
	^{137}Cs	^{137}Cs (661.6)	2.1 ± 0.4
	^{185}Os	^{185}Os (646.7, 717.2, 875.9, 880.9)	3.9 ± 0.4
^{232}Th	^{228}Ra	^{228}Ac (338.3, 911.2, 969.0)	≤ 0.9
	^{228}Th	^{212}Pb (238.6); ^{208}Tl (583.2, 2614.5)	≤ 15
^{238}U	^{226}Ra	^{214}Pb (295.2, 352.0); ^{214}Bi (609.3, 1764.5)	≤ 0.4

Search for double β processes in ^{184}Os and ^{192}Os

We do not observe any peaks in the spectrum accumulated with the osmium sample which could indicate 2β activity of ^{184}Os or ^{192}Os. Therefore only lower half-life limits (lim $T_{1/2}$) can be set according to the formula: $\lim T_{1/2} = \dfrac{N \cdot \eta \cdot t \cdot \ln 2}{\lim S}$, where N is the number of potentially 2β unstable nuclei, η is the detection efficiency, t is the measuring time, and lim S is the number of events of the effect searched for which can be excluded at given confidence level (C.L.).

One positron can be emitted in the εβ$^+$ decay of ^{184}Os with the energy up to (429 ± 1) keV. The annihilation of the positron should give two 511 keV γ's leading to an extra rate in the annihilation peak. To estimate lim S for the decay, the energy spectra were fitted in the energy interval 497 - 524 keV (Fig. 3). There are (52 ± 35) events in the 511 keV peak in the data with the sample. The area of the annihilation peak in the background spectrum is (22 ± 11) counts (normalized on the time of measurement with the sample). The difference in the areas of the annihilation peak with and without sample (30 ± 37 counts) gives no indication of the effect. In accordance with the Feldman-Cousins procedure [11] we should take lim S = 91 counts which can be excluded at 90% C.L. Taking into account the detection efficiency η = 9.0%, we have obtained the following limit on the half-life of ^{184}Os relatively to 2ν mode of εβ$^+$ decay: $T_{1/2}^{2\nu\varepsilon\beta^+}$ (^{184}Os, g.s. → g.s.) ≥ $2.4 \cdot 10^{16}$ yr. The detection efficiency in case of neutrinoless εβ$^+$ decay is slightly lower (8.9 %), which leads to the limit $T_{1/2}^{0\nu\varepsilon\beta^+}$ (^{184}Os, g.s. → g.s.) ≥ $2.3 \cdot 10^{16}$ yr.

[1] For example, the detection efficiency to the γ quanta with the energy 418.8 keV, expected to be irradiated in the resonant 0ν2ε process, in ^{184}Os is η = 3.14 % (3.12 %) with EGS4 (GEANT4).

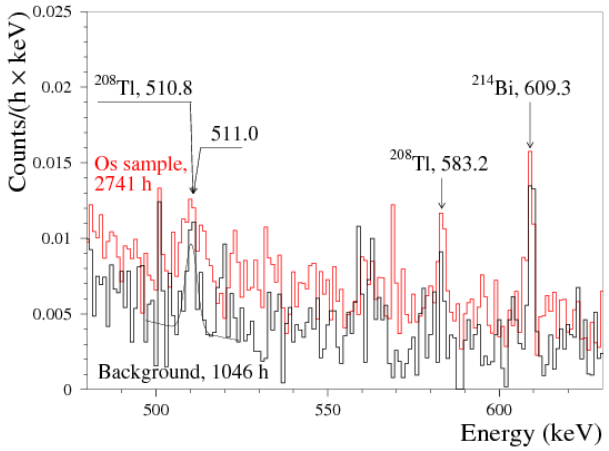

Fig. 3. Part of the energy spectra accumulated with osmium sample over 2741 h (Os sample) and without sample over 1046 h (Background) in the vicinity of annihilation peak. Fits of the data are shown by solid lines.

The $\varepsilon\beta^+$ decay of ^{184}Os is allowed to the first excited level of ^{184}W with the energy of 111.2 keV. To estimate a value of lim S for the effects searched for, the energy spectrum was fitted in the vicinity of the expected peak by the sum of a 1st degree polynomial function (the background) and Gaussian (to describe the expected γ peak). However, stronger limits were obtained by analysis of the annihilation peak. We have obtained the following limits for 2ν and 0ν modes of the decay: $T_{1/2}^{2\nu\varepsilon\beta^+}$ (^{184}Os, g.s. → 111.2 keV) ≥ $2.4 \cdot 10^{16}$ yr and $T_{1/2}^{0\nu\varepsilon\beta^+}$ (^{184}Os, g.s. → 111.2 keV) ≥ $2.3 \cdot 10^{16}$ yr.

To estimate limits on the 2ν2ε decay of ^{184}Os to the 903.3 keV and 1002.5 keV excited levels of ^{184}W, the energy spectrum accumulated with the osmium sample was fitted in the energy intervals where peaks from de-excitation of γ-rays are expected. The obtained results are presented in Table 2.

Table 2. **Half-life limits on 2β processes in ^{184}Os and ^{192}Os. Detection efficiency is denoted as η**

Process of decay	Decay mode	Level of daughter nucleus, keV	E_γ, keV	η	lim S	Experimental limit, $T_{1/2}$, yr
^{184}Os → ^{184}W						
$\varepsilon\beta^+$	2ν	g.s.	511.0	9.0 %	91	≥ $2.4 \cdot 10^{16}$
	0ν	g.s.	511.0	8.9 %	91	≥ $2.3 \cdot 10^{16}$
	2ν	2^+ (111.2)	511.0	9.0 %	91	≥ $2.4 \cdot 10^{16}$
	0ν	2^+ (111.2)	511.0	8.8 %	91	≥ $2.3 \cdot 10^{16}$
2ε	2ν	2^+ (903.3)	792.1	2.3 %	21	≥ $2.6 \cdot 10^{16}$
		0^+ (1002.5)	891.3	4.5 %	2.1	≥ $5.1 \cdot 10^{17}$
$2K$	0ν	g.s.	(1306 - 1318)	4.1 %	5.6	≥ $1.7 \cdot 10^{17}$
2ε		2^+ (903.3)	792.1	2.0 %	21	≥ $2.3 \cdot 10^{16}$
		0^+ (1002.5)	891.3	4.1 %	2.1	≥ $4.7 \cdot 10^{17}$
Res. KL	0ν	$(0)^+$ (1322.2)	418.8	3.1 %	55	≥ $1.3 \cdot 10^{16}$
^{192}Os → ^{192}Pt, $2\beta^-$	2ν + 0ν	2^+ (316.5)	316.5	3.0 %	39	≥ $3.7 \cdot 10^{19}$

In the neutrinoless double electron capture in addition to X-rays we suppose that only one bremsstrahlung γ quantum is emitted to take away the rest of the energy. In the case of 0ν2K decay the energy of the γ quantum is expected to be equal to $E_\gamma = Q_{2\beta} - 2E_K$, where E_K is the binding energy of the captured electrons on the K atomic shell of tungsten (E_K = 69.5 keV). Therefore, the expected energy of the γ quanta for the 0ν2K capture in ^{184}Os to the ground state of ^{184}W is E_γ = (1312.2 ± 1.0) keV. There are no clear peaks in the energy interval (1306 - 1318) keV. We have accepted 5.6 counts as the numbers of events which can be excluded at 90 % C.L., which leads to the half-life limit $T_{1/2}^{0\nu 2K}$ (^{184}Os, g.s. → g.s.) ≥ $1.7 \cdot 10^{17}$ yr.

The $Q_{2\beta}$ energy of ^{184}Os allows also the population of several excited levels of ^{184}W. The limits obtained for the processes of 0ν2ε decay are presented in Table 2. In particular, we set the following limit on the resonant 0νKL capture in ^{184}Os: $T_{1/2}^{0\nu KL}$ (^{184}Os, g.s. → 1322.2 keV) ≥ $1.3 \cdot 10^{16}$ yr.

To set a limit on the $2\beta^-$ transition of ^{192}Os to the 2^+ 316.5 keV excited level of ^{192}Pt, the energy spectrum was fitted by a straight line (which represents the background model) and a Gaussian at 316.5 keV (expected peak). Taking into account the detection efficiency (η = 3.0 %) we have obtained the following limit on the process searched for: $T_{1/2}^{(2\nu+0\nu)2\beta^-}$ (^{192}Os, g.s. → 316.5 keV) ≥ $3.7 \cdot 10^{19}$ yr.

All the limits on double β processes in Os are presented in Table 2.

Alpha decay of osmium

^{184}Os and ^{186}Os are potentially unstable relatively to α decay to excited levels of daughter nuclei with Q_α = 2963(4) and Q_α = 2823.1(1.2), respectively [6]. To search for the α decay of ^{184}Os to the excited 2^+ (103.5 keV) level of ^{180}W, the energy spectrum accumulated with the osmium sample was fitted in the energy interval 91 - 114 keV (Fig. 4). There is a peculiarity with the energy (103 ± 1) keV with an area (22 ± 14) counts, which might be considered as an indication

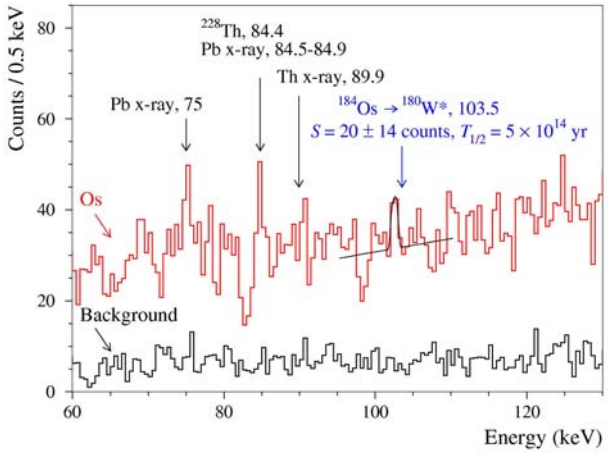

Fig. 4. A part of the energy spectrum accumulated with osmium sample over 2741 h. The fit of data in energy interval 91 - 114 keV is shown by solid line. The background, measured during 1046 h, is normalized here to 2741 h. The energies of *X*-rays and γ quanta are in keV.

for the α decay of ^{184}Os. Taking into account the detection efficiency (0.2%) and the yield of γ quanta for the transitions from the first excited 2^+ level (0.224), we have obtained the following value of half-life: $T^{\alpha}_{1/2}(^{184}\text{Os, g.s.} \rightarrow 103.5\text{ keV}) = 5^{+8}_{-2} \cdot 10^{14}$ yr. The result is near the theoretical estimations calculated here with the cluster model of Ref. [12] ($T_{1/2} = 1.2 \cdot 10^{15}$ yr) and with the semi-empirical formulae [13] based on liquid drop model and the description of the α decay as a very asymmetric fission process: $T_{1/2} = 2.6 \cdot 10^{15}$ yr.

In case of the α decay of ^{186}Os to the first excited 2^+ (100.1 keV) level of ^{182}W we have set only limit $T^{\alpha}_{1/2}(^{186}\text{Os, g.s.} \rightarrow 100.1\text{ keV}) \geq 4 \cdot 10^{16}$ yr.

Conclusions

The first experiment to search for 2β processes in ^{184}Os and ^{192}Os was carried out by using ultra-low background HPGe γ spectrometry. After 2741 h of data taking with 173 g ultra-pure osmium sample preliminary limits on double beta processes in ^{184}Os have been established at level of $T_{1/2} \geq 10^{16-17}$ yr at 90 % C.L. A possible resonant neutrinoless double electron capture in ^{184}Os to the excited 1322.2 keV level of ^{184}W is bounded as $T_{1/2} \geq 1.3 \cdot 10^{16}$ yr. The double β transition of ^{192}Os to the first excited level of ^{192}Pt is restricted as $T_{1/2} \geq 3.7 \cdot 10^{19}$ yr.

A search for α decay of osmium isotopes to the excited levels of daughter nuclei was realized as a by-product of the experiment. We have obtained an indication on the α decay of ^{184}Os to the 2^+ level (103.5 keV) of ^{180}W with the half-life $T^{\alpha}_{1/2}(^{184}\text{Os, g.s.} \rightarrow 103.5\text{ keV}) = 5^{+8}_{-2} \cdot 10^{14}$ yr. A half-life limit on the α decay of the ^{186}Os to the first excited level of ^{182}W was set as $T^{\alpha}_{1/2}(^{186}\text{Os, g.s.} \rightarrow 100.1\text{ keV}) \geq 4 \cdot 10^{16}$ yr.

REFERENCES

1. *Vergados J.D., Ejiri H., Simkovic F.* Theory of neutrinoless double beta decay // ArXiv:1205.0649v2 [hep-ph], 104 p.; *Elliott S.R.* Recent progress in double beta decay // Mod. Phys. Lett. - 2012. - Vol. A27. - P. 1230009, 16 p.; *Rodejohann W.* Neutrino-less double beta decay and particle physics // Int. J. Mod. Phys. - 2011. - Vol. E20. - P. 1833 - 1930.
2. *Hirsch M. et al.* Nuclear structure calculations of $\beta^+\beta^+$, β^+/EC and EC/EC decay matrix elements // Z. Phys. - 1994. - Vol. A347. - P. 151 - 160.
3. *Krivoruchenko M.I. et al.* Resonance enhancement of neutrinoless double electron capture // Nucl. Phys. - 2011. - Vol. A859. - P. 140 - 171.
4. *Baglin C.M.* Nuclear Data Sheets for A = 184 // Nuc. Data Sheets. - 2010. - Vol. 111 - P. 275 - 523.
5. *Baglin C.M.* Nuclear Data Sheets for A = 192 // Nucl. Data Sheets. - 2010. - Vol. 84. - P. 717 - 900.
6. *Audi G., Wapstra A.H., Thibault C.* The AME2003 atomic mass evaluation (II). Tables, graphs and references // Nucl. Phys. - 2003. - Vol. A729. - P. 337 - 676.
7. *Nelson W.R, Hirayama H., Rogers D.W.O.* The EGS4 code system // SLAC-Report-265, Stanford, 1985. - P. 1 - 398.
8. *Agostinelli S. et al.* GEANT4 - a simulation toolkit // Nucl. Instr. Meth. - 2003. - Vol. A506. - P. 250 - 303; *Allison J. et al.* GEANT4 developments and applications // IEEE Trans. Nucl. Sci. - 2006. - Vol. 53. - P. 270 - 278.
9. *Ponkratenko O.A., Tretyak V.I., Zdesenko Yu.G.* Event generator DECAY4 for simulating double-beta processes and decays of radioactive nuclei // Phys. Atom. Nucl. - 2000. - Vol. 63. - P. 1282 - 1287; [Yad. Phys. - 2000. - Vol. 63, No. 7. - P. 1355 - 1360]; *Tretyak V. I.*, in preparation.
10. *Firestone R.B. et al.* Table of isotopes / 8-th ed. // New York: John Wiley, 1996 and CD update (1998).
11. *Feldman G.J., Cousins R.D.* Unified approach to the classical statistical analysis of small signals // Phys. Rev. - 1998. - Vol. D57. - P. 3873 - 3889.
12. *Buck B., Merchant A.C., Perez S.M.* Ground state to ground state alpha decays of heavy even-even nuclei // J. Phys. - 1991. - Vol. G17. - P. 1223 - 1235.
13. *Poenaru D.N., Ivascu M.* Estimation of the alpha-decay half-lives // J. Phys. - 1983. - Vol. 44. - P. 791 - 796.

DOUBLE BETA PROCESSES IN ^{96}Ru AND ^{104}Ru

P. Belli[1], R. Bernabei[1,2], F. Cappella[3,4], R. Cerulli[5], F. A. Danevich[6], S. d'Angelo[1,2], A. Incicchitti[3,4], G. P. Kovtun[7], N. G. Kovtun[7], M. Laubenstein[5], D. V. Poda[5,6], O. G. Polischuk[6], A. P. Shcherban[7], D. A. Solopikhin[7], J. Suhonen[8], V. I. Tretyak[6]

[1]Dipartimento di Fisica, Università di Roma "Tor Vergata", Rome, Italy
[2] Dipartimento di Fisica, Università di Roma "La Sapienza", Rome, Italy
[3] Istituto Nazionale di Fisica Nucleare, Sezione di Roma "La Sapienza", Rome, Italy
[4] Dipartimento di Fisica, Università di Roma "La Sapienza",Rome, Italy
[5] Istituto Nazionale di Fisica Nucleare, Laboratori Nazionali del Gran Sasso, Assergi (AQ), Italy
[6] Institute for Nuclear Research, National Academy of Sciences of Ukraine, Kyiv, Ukraine
[7] National Science Center "Kharkiv Institute of Physics and Technology", Kharkiv, Ukraine
[8] Department of Physics, University of Jyväskylä, Jyväskylä, Finland

An experiment to search for double β decay processes in ^{96}Ru and ^{104}Ru has been realized in the underground (3600 m w.e.) Gran Sasso National Laboratories (LNGS) of the INFN (Italy). The ruthenium samples with masses of (0.5 - 0.7) kg were measured with the help of ultra-low background HPGe γ ray spectrometry. After 2162 h of data taking the samples were deeply purified to reduce the ^{40}K internal contamination and further measured during 5479 h. The new improved half life limits on the $2\beta^+/\varepsilon\beta^+/2\varepsilon$ processes in ^{96}Ru have been established at level of 10^{20} yr. The resonant neutrinoless double electron captures to the 2700 and 2713 keV excited states of ^{96}Mo are restricted at 90 % C.L. as $T_{1/2}(KL0\nu) \geq 2.0 \cdot 10^{20}$ yr and $T_{1/2}(2L0\nu) \geq 3.6 \cdot 10^{20}$ yr, respectively. In addition, the limit on the $2\beta^-$ decay of ^{104}Ru to the first excited state of ^{104}Pd has been obtained as $T_{1/2} \geq 6.5 \cdot 10^{20}$ yr.

1. Introduction

The double beta (2β) decay is a process of transformation of a nucleus (A, Z) to (A, $Z \pm 2$) with the simultaneous emission of two electrons e^- or positrons e^+. The two neutrino (2ν) double β decay, in which $e^\pm$ are emitted together with two (anti)neutrinos, is allowed in the Standard Model (SM); however, being a second order process in the weak interactions, it is characterized by very long half lives in the range: 10^{18} - 10^{24} yr [1]. To-date, two neutrino 2β decays are observed for several double β^- decaying nuclei [1, 2], while an indication on double electron capture (2ε) has been presented by geochemical experiments for ^{130}Ba [3].

The neutrinoless (0ν) mode of the 2β decay is forbidden in the SM because it violates the lepton number by 2 units. However, it is naturally expected in many SM extensions which describe neutrino as a Majorana particle with non-zero mass. The neutrino oscillation experiments indicate that the neutrino is massive, however, since they are sensitive to the difference in ν masses, the absolute ν mass scale is unknown [4]. The $2\beta0\nu$ decay is considered a powerful tool to check the lepton number conservation, to determine the absolute ν masses and their hierarchy, to establish the nature of the neutrino (Majorana or Dirac particle), to find the possible contribution of right-handed admixtures to weak interaction and the existence of Nambu-Goldstone bosons (Majorons) [1]. A particular analysis of data on ^{76}Ge has been presented in [5]; several experiments to investigate the existence of such decay are now in progress on that and on other isotopes.

The ^{96}Ru is one of the only six isotopes where the decay with emission of two positrons is allowed [2] thanks to the high energy release: $Q_{2\beta}$ = (2718 ± 8 keV) [6]. It has also a quite big natural abundance: δ = 5.54 % [7]. Moreover, in case of capture of two electrons from K and L shells (E_K = 20.0 keV; E_{L1} = 2.9 keV) or both from the L shell, the decay energies (2695 ± 8) keV and (2712 ± 8) keV are close to the energy of the excited levels of ^{96}Mo (E_{exc} = 2700 and 2713 keV [8]). Such a coincidence could give a resonant enhancement of the neutrinoless KL and $2L$ capture to the corresponding level of the daughter nucleus as a result of the energy degeneracy (see e.g. [9] and refs. therein). In addition, another isotope of ruthenium, the ^{104}Ru, is potentially unstable relatively to the $2\beta^-$ decay ($Q_{2\beta}$ = = (1301 ± 4) keV, δ = 18.62 %). The decay schemes of ^{96}Ru and ^{104}Ru are shown in Fig. 1.

Despite the high energy release, the high abundance and the potentiality to obtain in the experimental investigations of the $2\beta^+/\varepsilon\beta^+/2\varepsilon$ decays information supplementary to the $2\beta^-$, only one search for $2\beta^+/\varepsilon\beta^+$ processes in ^{96}Ru was performed in 1985, giving $T_{1/2}$ limits at level of 10^{16} yr [10]. The efforts were renewed only in 2009, when we measured a Ru sample with a mass of 473 g during 158 h with a HPGe detector (468 cm^3) in the underground conditions of the Gran Sasso National Laboratories of the INFN (3600 m w.e.) [11] (an updated statistics of 2162 h was then reported in [12]). The achieved sensitivity to the $2\beta^+/\varepsilon\beta^+/2\varepsilon$ decays was 10^{18} - 10^{19} yr; however the measurements showed that the sample was contaminated by ^{40}K at ≈3 Bq/kg, and better results are possible only with a purified Ru sample. Here we report the results of a search for $2\beta^+/\varepsilon\beta^+/2\varepsilon$ processes in ^{96}Ru and for $2\beta^-$ decay in ^{104}Ru obtained with a purified sample of Ru (720 g). Recently, a search for 2β decays of Ru was performed also in the HADES underground laboratory [13].

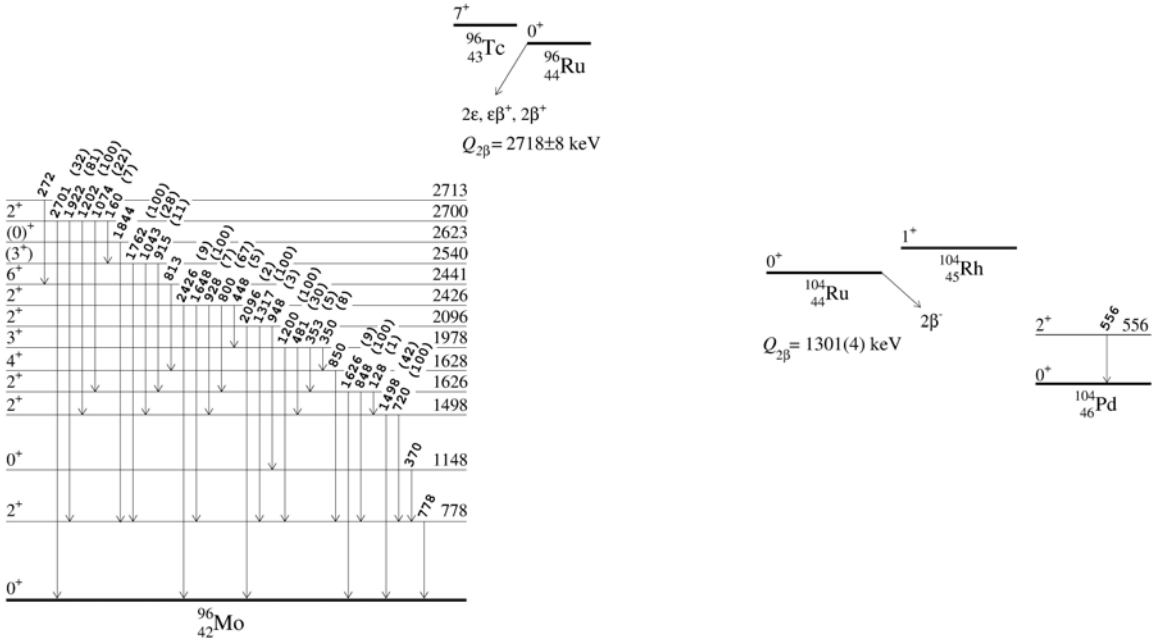

Fig. 1. Decay schemes of ^{96}Ru (*left*) and ^{104}Ru (*right*). Energies of the excited levels and emitted γ quanta are given in keV. The relative intensities of γ quanta are in parentheses [8].

2. Low background measurements

Ru sample with the total mass of 946 g was deeply purified by electron beam melting method; in result, five Ru samples (totally 719.5 g) were obtained. They were measured during 5479 h in the GeMulti set-up (made of four HPGe detectors; ≈225 cm^3 each one) installed deep underground at LNGS. The detectors were surrounded by a passive shield made of low radioactivity copper (≈10 cm thick), low radioactivity lead (≈20 cm), and polyethylene (≈10 cm). The set-up was continuously flushed by high purity nitrogen to remove radon present in the air. The typical energy resolution of the detectors is 2 keV at 1332 keV line of ^{60}Co. The energy spectra without samples were accumulated with the GeMulti spectrometer over 7862 h. The results of the measurements are presented in Fig. 2. Table 1 gives a summary of the measured radioactive contaminations in the used Ru before and after the purification process. As one can see, the purification allowed to decrease the ^{40}K presence by 20 times; other contaminations were also suppressed.

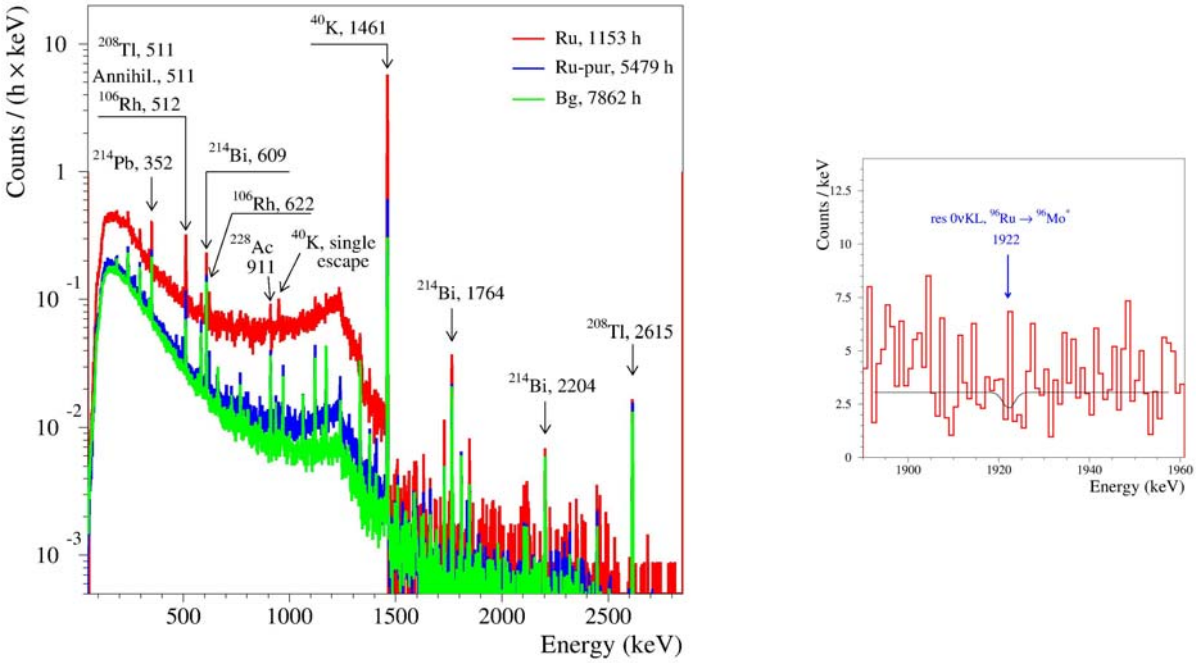

Fig. 2. *Left*: The energy spectra accumulated by the GeMulti set-up with the initial Ru sample (1153 h) and the purified Ru (5479 h) together with the background spectrum (7862 h) for comparison. *Right*: Example of a fit of the spectrum in the vicinity of the γ line with energy 1922 keV expected for the resonant *KL*0ν capture in ^{96}Ru. The energy of the γ quanta are given in keV.

Table 1. **Radioactive contamination of the Ru sample used in [11] (473 g, 158 h) and of the purified Ru sample (720 g, 5479 h, measured here). For comparison, the results of the sample used in [13] (149 g, 2592 h) are also presented. The limits are given at 90 % C.L. (95 % C.L. for [13])**

Chain	Nuclide	Activity, mBq/kg		
		Ru [11]	Purified Ru	Ru [13]
^{232}Th	^{228}Ra	≤ 7.1	≤ 1	8.7 ± 0.7
	^{228}Th	≤ 3.4	1.4 ± 0.4	8.8 ± 0.6
^{235}U	^{235}U	≤ 6.9	≤ 4	–
^{238}U	^{226}Ra	6.4 ± 1.7	1.0 ± 0.3	14.6 ± 0.7
	^{234}Th	≤ 390	–	≤ 36
	^{234m}Pa	≤ 260	≤ 23	–
	^{210}Pb	–	–	≤ 100
	^{40}K	3300 ± 600	153 ± 4	169 ± 7
	^{60}Co	≤ 1.7	≤ 0.1	≤ 0.2
	^{137}Cs	≤ 2.6	≤ 0.1	≤ 0.2
	^{106}Ru	24 ± 7	5.0 ± 0.6	≤ 1.7

3. Results and discussion

We did not observe any peak in the spectra accumulated with the ruthenium samples which could be unambiguously attributed to the 2β processes in ^{96}Ru and ^{104}Ru. Therefore only lower half life limits are derived by using the formula: $\lim T_{1/2} = N \cdot \eta \cdot t \cdot \ln 2 / \lim S$, where N is the number of potentially 2β unstable nuclei in the Ru sample ($N_{96} = 2.38 \times \times 10^{23}$, $N_{104} = 7.98 \cdot 10^{23}$), η is the detection efficiency, t is the measuring time, and $\lim S$ is the number of events of the effect searched for which can be excluded at a given confidence level (C.L.); all the limits in the present study are given at 90 % C.L. The efficiency of the detectors for the 2β processes in ^{96}Ru and ^{104}Ru has been calculated by using the EGS4 code [14] with initial kinematics given by the DECAY0 event generator [15]. The procedure of estimation of $\lim S$ value is described in detail in [11]. Let us give here two examples of calculation of $\lim S$: for the peak at 511 keV (relevant for $2\beta^+$ and $\varepsilon\beta^+$ decays of ^{96}Ru) and for the peak at 1922 keV expected for the resonant $KL0\nu$ capture in ^{96}Ru.

In case of $2\beta^+$ and $\varepsilon\beta^+$ decays of ^{96}Ru to the ground state of ^{96}Mo only annihilation γ quanta with energy 511 keV could be registered by our detectors. Thus, the possible extra rate in the annihilation peak of the spectrum accumulated with the purified sample was analyzed to search for the mentioned 2β channels. The area of the annihilation peak in the measurements with the purified Ru during 5479 h is equal to (1461 ± 39) counts, while in the background spectrum it is (535 ± 27) counts during 3362 h. There are also other contributions to the 511 keV peak:

1) the 511.8 keV γ line from ^{106}Rh which is daughter radionuclide of the cosmogenic ^{106}Ru; its contribution is estimated as (433±52) counts using the supplementary peak at 622 keV;

2) the e^+e^- pairs created by the 1461 keV γ quantum emitted in the ^{40}K decay; its contribution is estimated as (165±38) counts using the area of the 1461 keV peak;

3) the 510.8 keV γ line from ^{208}Tl; its contribution is estimated as (49±11) counts using the area of the 583 keV peak of ^{208}Tl.

The difference between the measured number of events in the 511 keV peak and the estimated contributions from the known sources (−58 ± 71 counts) can be ascribed to the effect searched for. Obviously, it gives no evidence of $2\beta^+$ and $\varepsilon\beta^+$ decays of ^{96}Ru to the ground state of ^{96}Mo. In accordance with the Feldman-Cousins procedure [16], it results in the limit $\lim S = 66$ counts for the effect which can be excluded at 90 % C.L. Taking into account the calculated efficiency for $2\beta^+$ decay (10.3%) and the number of the ^{96}Ru nuclei ($2.38 \cdot 10^{23}$), this gives:

$$T_{1/2}(2\beta^+0\nu + 2\beta^+2\nu, \text{g.s.} \rightarrow \text{g.s.}) > 1.6 \cdot 10^{20} \text{ yr at 90 \% C.L.}$$

In the resonant $KL0\nu$ capture in ^{96}Ru, the ^{96}Mo excited level with the energy 2700 keV is populated (see Fig. 1). Few γ's could be emitted in the deexcitation process, in particular γ's with $E_\gamma = 1922$ keV. Peak at this energy is absent in the experimental spectrum (Fig. 2). To find the $\lim S$ value, the spectrum was fitted in the vicinity of the 1922 keV peak by the sum of a straight line (representing the background) and a Gaussian with centre at 1922 keV (representing the effect). The obtained area of the peak is $S = (-2.4 \pm 3.7)$ counts that gives $\lim S = 3.9$ counts and, together with the calculated efficiency η = 0.60 %, leads to:

$$\lim T_{1/2} (\text{res. } KL0\nu, \text{g.s.} \rightarrow 2700 \text{ keV}) > 2.0 \cdot 10^{20} \text{ yr at 90 \% C.L.}$$

The limits for the other 2β decay channels were obtained in similar way; some results are summarized in Table 2.

Table 2. **Preliminary $T_{1/2}$ limits for the 2β processes in ^{96}Ru and ^{104}Ru. The previous best results [13] are given for comparison**

Process of decay	Decay mode	Level of daughter nucleus, E, keV	E_γ, keV	$T_{1/2}$, yr	
				[13]	Present work
^{96}Ru → ^{96}Mo					
$2\beta^+$	$0\nu + 2\nu$	g.s.	511	$>5.0 \cdot 10^{19}$	$>1.6 \cdot 10^{20}$
$\varepsilon\beta^+$	0ν	g.s.	511	$>5.5 \cdot 10^{19}$	$>9.3 \cdot 10^{19}$
	2ν	g.s.	511	$>5.5 \cdot 10^{19}$	$>9.7 \cdot 10^{19}$
	$0\nu + 2\nu$	2^+ 778	778	$>2.7 \cdot 10^{19}$	$>2.2 \cdot 10^{20}$
	$0\nu + 2\nu$	0^+ 1148	778	$>1.8 \cdot 10^{19}$	$>2.1 \cdot 10^{20}$
2K	0ν	g.s.	2678 ± 8	$>5.4 \cdot 10^{19}$	$>1.8 \cdot 10^{20}$
KL	0ν	g.s.	2695 ± 8	$>6.9 \cdot 10^{19}$	$>1.6 \cdot 10^{20}$
2L	0ν	g.s.	2713 ± 8	$>6.9 \cdot 10^{19}$	$>1.5 \cdot 10^{20}$
2ε	2ν	2^+ 778	778	$>6.5 \cdot 10^{19}$	$>2.6 \cdot 10^{20}$
		0^+ 1148	778	$>4.2 \cdot 10^{19}$	$>2.5 \cdot 10^{20}$
		2^+ 1498	778	$>3.0 \cdot 10^{19}$	$>1.7 \cdot 10^{20}$
		2^+ 1626	848	$>3.9 \cdot 10^{19}$	$>3.6 \cdot 10^{20}$
	0ν	2^+ 778	778	$>6.4 \cdot 10^{19}$	$>2.4 \cdot 10^{20}$
		0^+ 1148	778	$>4.1 \cdot 10^{19}$	$>2.3 \cdot 10^{20}$
		2^+ 1498	778	$>2.9 \cdot 10^{19}$	$>1.6 \cdot 10^{20}$
		2^+ 1626	848	$>3.8 \cdot 10^{19}$	$>3.3 \cdot 10^{20}$
Resonant *KL*	$0\nu + 2\nu$	2700	1922	$>2.7 \cdot 10^{19}$	$>2.0 \cdot 10^{20}$
Resonant 2*L*	$0\nu + 2\nu$	2713	813	$>2.0 \cdot 10^{19}$	$>3.6 \cdot 10^{20}$
^{104}Ru→^{104}Pd					
$2\beta^-$	$0\nu + 2\nu$	2^+ 556	556	$>1.9 \cdot 10^{20}$	$>6.5 \cdot 10^{20}$

In addition to the analysis of the 1-dimensional spectrum, the GeMulti set-up with its 4 HPGe detectors gives possibility to use the coincidence between different detectors for γ quanta emitted simultaneously (annihilation γ quanta in $2\beta^+$ and $\varepsilon\beta^+$ decays, and γ's from cascades in the deexcitation of the excited ^{96}Mo levels). The $T_{1/2}$ limits, obtained in this way, are comparable with those derived from the 1-dimensional spectrum, but in general are lower due to lower detection efficiency.

Theoretical estimates of the half lives can be found in compilations [2] and in recent works [17 - 19] (see also refs. therein). They are higher by few orders of magnitude than the experimental limits reached to-date. It should be also noted that the recent re-measurements [20] of the $Q_{2\beta}$ of ^{96}Ru: $Q_{2\beta} = (2714.51 \pm 0.13)$ keV, makes this nuclide a less perspective candidate for resonant $2\varepsilon 0\nu$ captures.

4. Conclusions

A low background experiment to search for 2β processes in ^{96}Ru and ^{104}Ru isotopes was carried out over more than 7.6 thousands hours in the underground Gran Sasso National Laboratories of the INFN by using ultra-low background HPGe detectors. Purification of the ruthenium sample by refining method allows to reduce the ^{40}K contamination by more than 20 times, and concentrations of other radionuclides was also decreased. The new improved half life limits on double beta processes in ^{96}Ru and ^{104}Ru have been set at the level of 10^{20} yr. All the results are 2 - 12 times higher than those recently published in [13]. However, the limits are still far from the theoretical predictions with the exception of the $\varepsilon\beta^+2\nu$ channel, for which $T_{1/2} = 10^{21} - 10^{22}$ yr has been estimated [18].

REFERENCES

1. *Avignone III F.T., Elliott S.R., Engel J.* Double beta decay, Majorana neutrinos, and neutrino mass // Rev. Mod. Phys. - 2008. - Vol. 80. - P. 481 - 516; *Barabash A.S.* Double beta decay experiments // Phys. Part. Nucl. - 2011. - Vol. 42. - P. 613 - 627; *Gomez-Cadenas J.J. et al.* The search for neutrinoless double beta decay // Riv. Nuovo Cim. - 2012. - Vol. 35. - P. 29 - 98.
2. *Tretyak V.I., Zdesenko Yu.G.* Tables of double beta decay data // At. Data Nucl. Data Tables - 1995. - Vol. 61. - P. 43 - 90; 2002. - Vol. 80. - P. 83 - 116.
3. *Meshik A.P. et al.* Weak decay of ^{130}Ba and ^{132}Ba: Geochemical measurements // Phys. Rev. - 2001. - Vol. C64. - P. 035205, 6 p.; *Pujol M. et al.* Xenon in Archean barite: Weak decay of ^{130}Ba, mass-dependent isotopic fractionation and implication for barite formation // Geochim. Cosmochim. Acta - 2009. - Vol. 73. - P. 6834 - 6846.
4. *Dore U., Orestano D.* Experimental results on neutrino oscillations // Rep. Prog. Phys. - 2008. - Vol. 71. -

P. 106201, 36 p.
5. *Klapdor-Kleingrothaus H.V., Krivosheina I.V.* The evidence for the observation of 0νββ decay: The identification of 0νββ events from the full spectra // Mod. Phys. Lett. - 2006. - Vol. A21. - P. 1547 - 1566.
6. *Audi G., Wapstra A.H., Thibault C.* The AME2003 atomic mass evaluation (II). Tables, graphs and references // Nucl. Phys. - 2003. - Vol. A729. - P. 337 - 676.
7. *Berglund M., Wieser M.E.* Isotopic compositions of the elements 2009 // Pure Appl. Chem. - 2011. - Vol. 83. - P. 397 - 410.
8. *Firestone R.B. et al.* Table of isotopes / 8-th ed. // New York: John Wiley, 1996 and CD update (1998).
9. *Belli P. et al.* Searches for neutrinoless resonant double electron captures at LNGS // J. Phys.: Conf. Ser. - 2012. - Vol. 375. - P. 042024, 4 p.
10. *Norman E.B.* Improved limits on the double beta decay half-lives of ^{50}Cr, ^{64}Zn, ^{92}Mo, and ^{96}Ru // Phys. Rev. - 1985. - Vol. C31. - P. 1937 - 1940.
11. *Belli P. et al.* Search for double-β decays of ^{96}Ru and ^{104}Ru by ultra-low background HPGe γ spectrometry // Eur. Phys. J. - 2009. - Vol. A42. - P. 171 - 177.
12. *Belli P. et al.* Search for double β decays of ^{96}Ru and ^{104}Ru with high purity Ge γ spectrometry // Nucl. Phys. At. Energy - 2010. - Vol. 11. - P. 362 - 366.
13. *Andreotti E. et al.* Study of the double beta decays of ^{96}Ru and ^{104}Ru // Appl. Rad. Isot. - 2012. - Vol. 70. - P. 1985 - 1989.
14. *Nelson W.R., Hirayama H., Rogers D.W.O.* The EGS4 code system // SLAC-Report-265, Stanford, 1985, 398 p.
15. *Ponkratenko O.A., Tretyak V.I., Zdesenko Yu.G.* Event generator DECAY4 for simulating double-beta processes and decays of radioactive nuclei // Phys. Atom. Nucl. - 2000. - Vol. 63. - P. 1282 - 1287.
16. *Feldman G.J., Cousins R.D.* Unified approach to the classical statistical analysis of small signals // Phys. Rev. - 1998. - Vol. D57. - P. 3873 - 3889.
17. *Krivoruchenko M.I. et al.* Resonance enhancement of neutrinoless double electron capture // Nucl. Phys. - 2011. - Vol. A859. - P. 140 - 171.
18. *Suhonen J.* Theoretical investigation of the double-β processes in ^{96}Ru // Phys. Rev. - 2012. - Vol. C86. - P. 024301, 10 p.
19. *Suhonen J.* On the double-beta decays of ^{70}Zn, ^{86}Kr, ^{94}Zr, ^{104}Ru, ^{110}Pd and ^{124}Sn // Nucl. Phys. - 2011 - Vol. A864. - P. 63 - 90.
20. *Eliseev S.* et al. Q values for neutrinoless double-electron capture in ^{96}Ru, ^{162}Er, and ^{168}Yb // Phys. Rev. - 2011. - Vol. C83. - P. 038501, 3 p.

NEUTRON BEAM IMAGING WITH MICROMEGAS DETECTORS IN COMBINATION WITH NEUTRON TIME-OF-FLIGHT AT THE n_TOF FACILITY AT CERN

F. Belloni[1], S. Andriamonje[2], E. Berthoumieux[1], M. Calviani[2], E. Chiaveri[2], N. Colonna[3], Y. Giomataris[1], C. Guerrero[2], F. Gunsing[1], F. J. Iguaz[1], M. Kebbiri[1], J. Pancin[1], T. Papaevangelou[1], A. Tsinganis[2,4], V. Vlachoudis[2], S. Altstadt[5], J. Andrzejewski[6], L. Audouin[7], M. Barbagallo[3], V. Bécares[8], F. Bečvář[9], J. Billowes[10], V. Boccone[2], D. Bosnar[11], M. Brugger[2], F. Calviño[12], D. Cano-Ott[8], C. Carrapiço[13], F. Cerutti[2], E. Chiaveri[1,2], M. Chin[2], G. Cortés[12], M. A. Corté-Giraldo[14], M. Diakaki[4], C. Domingo-Pardo[15], I. Duran[16], N. Dzysiuk[17], C. Eleftheriadis[18], A. Ferrari[2], K. Fraval[1], S. Ganesan[19], A. R. García[8], G. Giubrone[15], M. B. Gómez-Hornillos[12], I. F. Gonçalves[13], E. González-Romero[8], E. Griesmayer[20], P. Gurusamy[19], D. G. Jenkins[21], E. Jericha[20], Y. Kadi[2], F. Käppeler[22], D. Karadimos[4], P. Koehler[23], M. Kokkoris[4], M. Krtička[9], J. Kroll[9], C. Langer[5], C. Lederer[5,24], H. Leeb[20], L. S. Leong[7], R. Losito[2], A. Manousos[18], J. Marganiec[6], T. Marítnez[8], C. Massimi[25], P. F. Mastinu[17], M. Mastromarco[3], M. Meaze[3], E. Mendoza[8], A. Mengoni[26], P. M. Milazzo[27], F. Mingrone[25], M. Mirea[28], W. Mondalaers[29], C. Paradela[16], A. Pavlik[24], J. Perkowski[6], A. Plompen[29], J. Praena[14], J. M. Quesada[14], T. Rauscher[30], R. Reifarth[5], A. Riego[12], F. Roman[2,28], C. Rubbia[2,31], R. Sarmento[13], P. Schillebeeckx[29], S. Schmidt[5], G. Tagliente[3], J. L. Tain[15], D. Tarrío[16], L. Tassan-Got[7], S. Valenta[9], G. Vannini[25], V. Variale[3], P. Vaz[13], A. Ventura[26], R. Versaci[2], M. J. Vermeulen[21], V. Vlachoudis[2], R. Vlastou[4], A. Wallner[24], T. Ware[10], M. Weigand[5], C. Weiss[20], T. J. Wright[10], P. Žugec[11]

[1] CEA Saclay, DSM/IRFU/SPhN, Gif-sur-Yvette, France
[2] European Organization for Nuclear Research (CERN), Geneva, Switzerland
[3] Istituto Nazionale di Fisica Nucleare, Bari, Italia
[4] National Technical University of Athens, Athens, Greece
[5] Goethe Universität, Frankfurt, Germany
[6] Uniwersyte Łódzki, Lodz, Poland
[7] Centre National de la Recherche Scientifique/IN2P3, IPN, Orsay, France
[8] Centro de Investigaciones Energeticas Medioambientales y Tecnólgicas, Madrid, Spain
[9] Charles University, Prague, Czech Republic
[10] University of Manchester, Oxford Road, Manchester, United Kingdom
[11] Department of Physics, Faculty of Science, University of Zagreb, Croatia
[12] Universitat Politecnica de Catalunya, Barcelona, Spain
[13] Instituto Tecnológico e Nuclear, Instituto Superior Técnico, Universidade Técnica de Lisboa, Lisboa, Portugal
[14] Universidad de Sevilla, Sevilla, Spain
[15] Instituto de Fisica Corpuscular, CSIC-Universidad de Valencia, Spain
[16] Universidad de Santiago de Compostela, Santiago de Compostela, Spain
[17] Istituto Nazionale di Fisica Nucleare, Laboratori Nazionali di Legnaro, Legnaro, Italy
[18] Aristotle University of Thessaloniki, Thessaloniki, Greece
[19] Bhabha Atomic Research Centre, Mumbai, India
[20] Atominstitut, Technische Universität Wien, Austria
[21] University of York, Heslington, York, United Kingdom
[22] Karlsruhe Institute of Technology, Campus Nord, Institut für Kernphysik, Karlsruhe, Germany
[23] Oak Ridge National Laboratory, Oak Ridge, TN, USA
[24] University of Vienna, Faculty of Physics, Austria
[25] Dipartimento di Fisica, Università di Bologna, and Sezione INFN di Bologna, Italy
[26] Agenzia nazionale per le nuove tecnologie, l'energia e lo sviluppo economico sostenibile, Bologna, Italy
[27] Istituto Nazionale di Fisica Nucleare, Trieste, Italy
[28] Horia Hulubei National Institute of Physics and Nuclear Engineering, Bucharest-Magurele, Romania
[29] European Commission JRC, Institute for Reference Materials and Measurements, Department of Physics and Astronomy, Geel, Belgium
[30] University of Basel, Basel, Switzerland
[31] Laboratorio Nazionali del Gran Sasso, Istituto Nazionale di Fisica Nucleare, Assergi (AQ), Italy

A bulk micromegas detector with the anode segmented in 2 orthogonal directions and equipped with a neutron/charged particle converter is employed at the neutron time-of-flight (nTOF) facility at CERN to determine the incident neutron beam profile and beam interception factor as a function of the neutron energy determined by the time of flight. Discrepancies between experimental results and simulations in the values of the beam interception factor range up to 12 % and are to be ascribed to a defect in the mesh of the bulk. Nevertheless the detector proved to be really useful for checking the alignment of the neutron beam optics of the facility. Measurements with a new pixelized bulk detector for the determination of the beam interception factor are forseen before the end of 2012.

1. Introduction

The neutron time-of-flight (n_TOF) facility at CERN is a white neutron source based on spallation of 20 GeV/c proton beam with pulses 6 ns r.m.s. hitting a Pb target with a minimum repetition rate of 2.4 seconds. A 185 m long evacuated tube leads neutrons to an experimental area (EAR or EAR-1) equipped with several detectors for neutron-induced capture, fission and (n, α) cross sections. A detailed description of the facility can be found in [1].

Neutron-induced reaction measurements need an accurate knowledge of the incident flux. At n_TOF this is measured with a silicon monitor [2] and a Micro-mesh gaseous structure (micromegas) detector [3] of microbulk type [4], as well as a very accurate estimation of the spatial profile, determined with a micromegas detector of bulk type [5] in order to calculate the beam interception factor, i.e. the correction to be applied to the extracted neutron induced cross sections when the sample is smaller than the beam diameter. Micromegas detectors are a stack of one ionization chamber and one proportional chamber. A thin mesh separates the two communicating region, where two different electric fields are applied to obtain respectively the ionization and multiplication charge regimes. When the anode and the mesh of the detector are constructed into a single piece, this is called bulk. The main difference between bulks and microbulks is the thickness of the mesh, thinner in the latter thanks to the fabrication procedure.

2. Detector

The n_TOF beam profiler is a circular bulk of 4 cm radius with a typical bulk thickness of 128 μm. The readout is smaller than the anode itself and it is obtained by segmenting a square portion of 6 cm side of the anode in two orthogonal directions, called X and Y in the reference frame of the detector, by 106 strips. The detector allows therefore the determination of the beam image with a spatial resolution of 0.5 mm as a function of the time-of-flight. A 2 μm thick layer of BC_4 enriched in ^{10}B is deposited on the drift and acts as a neutron/charged particle converter through the $^{10}B(n,\alpha)^7Li$ reaction. The drift to mesh distance is 4 mm, and the detector is operated with and admixture of Ar (90 %), CF_4 (8 %) and C_4H_{10} (2 %). In order to reduce the number of channels necessary to collect the output of the strips and of the mesh, two gassiplex cards are employed.

3. Analysis

The analysis procedure consists in identifying signals caused by α particles or ^7Li particles produced by the interaction of neutrons with the converter and, for every interaction, associating to each strip of the detector its signal amplitude. The baseline level in each strip is determined through a measurement without beam, called pedestal run. The following step consists in subtracting, for each strip, the baseline level to the registered signals and identifying the strips with a leftover higher than a certain threshold. The set of these strips is called cluster and an algorithm to find the center of charge of each cluster is applied. By exploiting the time information of the mesh signal, a bi-dimensional histogram is filled with pairs of centers of charges calculated in the two orthogonal directions in time coincidence and the beam image is obtained as a function of time of flight. Since the axis of the detector are tilted of 135° with respect to the floor and walls of the experimental area, a rotation has to be applied to the beam image in order to visualize it in the reference system of the laboratory. A bi-dimensionnal Gaussian fit of the beam profile allows the study of its widths. In the end, the beam interception factor is extracted by calculating the ratio of the number of neutrons hitting the area covered by a sample to the number of neutrons in the whole beam.

4. Results

Data collected in the years 2009 - 2012 have been analyzed. In 2009 the study of the influence of the beam optics alignment on the beam profile was studied, allowing to detect a misalignment of the second collimator (Fig. 1).

A study of the gain of the detector showed that the distance between the mesh and the anode was not constant because of a slightly curved mesh plane, provoking differences in gain between different strips. This issue was partially solved by fitting experimental data to exclude the non operative strips. Nevertheless, given the fact that the problem concerns a large portion of the detector, it was not possible to totally correct for this.

Fig. 2 shows a comparison of the beam interception factor for a sample of 1 cm diameter obtained from simulations, from the measured data and from the Gaussian fit to the latter. Discrepancies between the results given by the fit to our data and simulations reach 12 %, but their trends are similar and in agreement with the expectations. Since the low energy neutrons are produced after several scatterings in the moderator of the spallation target (made of H_20), the neutron beam should be wider at low neutron energies than at high neutron energies, with the consequence that the beam interception factor increases with the neutron energy.

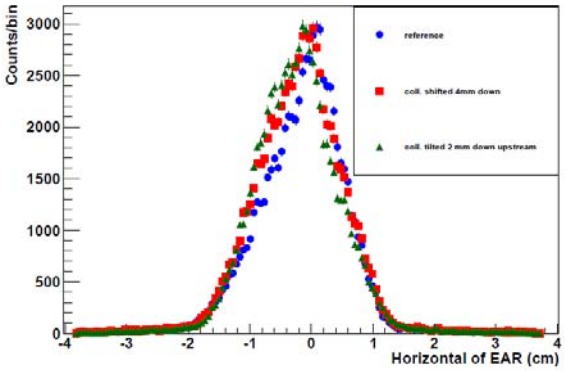

Fig. 1. Beam profile projected along the vertical axis in the reference system of the laboratory.

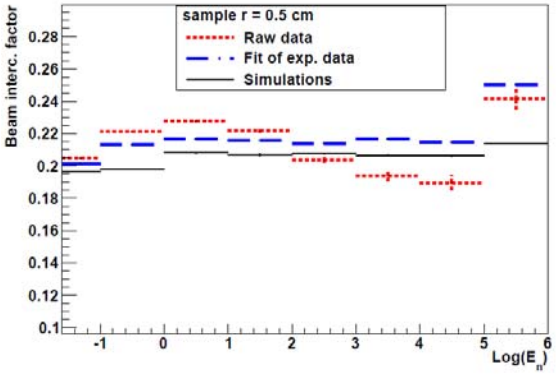

Fig 2. Beam interception factor for a sample of 1 cm diameter.

5. Conclusions

A study of the beam profile was performed at the n_TOF facility with a micromegas detector of bulk type. Thanks to these studies a misalignment of the second collimator was detected and corrected for. The trend of the extracted beam interception factor as a function of the incident neutron energy is in agreement with expectations, but always higher and discrepancies reach 12%. This is ascribed to a defect in the mesh of the detector and a measurement with a new pixelized micromegas detector of bulk type is already scheduled before the end of 2012.

REFERENCES

1. *The n_TOF Collaboration,* CERN n_TOF Facility: Performance Report // CERN/INTC-O-011, INTC-2002-037, CERN-SL-2002-053 ECT. - 2001.
2. *Marrone S. et al.* // Nuclear Instruments and Methods in Physics Research. - 2004. - Vol. A517. - P. 389 - 398.
3. *Giomataris Y., Rebourgeard Ph., Robert J.P., Charpak G.* Micromegas: a highgranularity position-sensitive gaseous detector for high particle-flux environments // Nucl. Instr. Meth. - 1996. - Vol. A376. - P. 29 - 35.
4. *Giomataris Y., De Oliveira R., Andriamonje S. et al.* Micromegas in a bulk // Nucl. Instr. Meth. - 2005. - Vol. A560. - P. 405 - 408.
5. *Andriamonje S., Attie D., Berthoumieux E. et al.* Development and performance of microbulk micromegas detectors // J. Instrum. - 2010. - Vol. 5. - P. 02001 - 02013.

EXO-200 RESULTS

V. A. Belov (for the EXO collaboration)

A. I. Alihanov Institute for Theoretical and Experimental Physics, Moscow, Russia

Status update and recent results from a second low background run of the double beta decay search experiment EXO-200 are presented here. Detector is a liquid xenon TPC with charge and light readout located underground in low-background environment (1600 m.w.e.). It contains 175 kg of xenon with 80.6 % abundance of ^{136}Xe. Data was taken from September 2011 till April 2012 and have total exposure of 32.5 kg·y. New enhanced signal reconstruction and estimation of energy from combined ionization and scintillation signals allowed to improve energy resolution dramatically. Analysis of new data results in a half-life for a $2\beta2\nu$ decay mode of $2.23 \cdot 10^{21}$ years that completely agree with previous value and with results of experiment KamLAND-Zen. Also are set a new limit for a $2\beta0\nu$ mode equal to $1.6 \cdot 10^{25}$ (90 % C.L.) and world-leading limit on effective Majorana neutrino mass.

1. Introduction

Nuclear beta decay is the familiar process in which a nucleon decays, releasing a electron (positron) and an electron antineutrino (or neutrino). For some even-even nuclei, this single beta decay is forbidden or highly suppressed and it becomes possible to observe double beta decay, in which two nucleons decay simultaneously. The half-lives for $\beta\beta$ decay are very long (typically of order $10^{18} \div 10^{21}$ years) since it is a second-order weak process. This decay has been observed in a number of isotopes. Xenon was one of the last unseen. The hypothetical neutrinoless ($0\nu\beta\beta$) decay mode can only occur if neutrino is massive Majorana particle [1]. This decay may be mediated by the exchange of a Majorana neutrino or by other new particles. The recent discovery of neutrino mass in oscillation experiments [2] makes the search for the Majorana nature of neutrinos particularly relevant and timely. The $0\nu\beta\beta$ decay rate is related to the square of an effective Majorana neutrino mass $\langle m \rangle_{\beta\beta}$ by the product of phase space and a nuclear matrix element squared. Direct kinematic measurements restrict the neutrino mass scale to be below ~1 eV [3 - 4], leading to $0\nu\beta\beta$ half lives beyond 10^{24} yr. In 2006 year a positive observation of $0\nu\beta\beta$ decay in ^{76}Ge has been claimed [5] with $T^{0\nu\beta\beta}_{1/2}$ (^{76}Ge) = $= (2.23^{+0.44}_{-0.31}) \cdot 10^{25}$ yr, implying $\langle m \rangle_{\beta\beta} = 0.32 \pm 0.03$ eV for given nuclear matrix element.

The exceedingly long half lives of interest for $0\nu\beta\beta$ decay require large detectors using isotopically enriched sources, radio-clean construction techniques and the ability to actively reject remaining backgrounds. The $0\nu\beta\beta$ decay results in a discrete electron sum energy distribution centered at the Q-value ($Q_{\beta\beta}$). The allowed, yet also rare, two neutrino double beta ($2\nu\beta\beta$) decay is characterized by a continuous sum energy spectrum ending at $Q_{\beta\beta}$. The sum energy of decay electrons allows discrimination between the two modes. The $2\nu\beta\beta$ decay has been observed in many isotopes [6] and, recently, in ^{136}Xe with the EXO-200 detector [7], later confirmed in [8]. Several experiments are running to test $0\nu\beta\beta$ decay discovery on ^{76}Ge but it is important to test this also with different nucleus like ^{136}Xe.

2. Detector

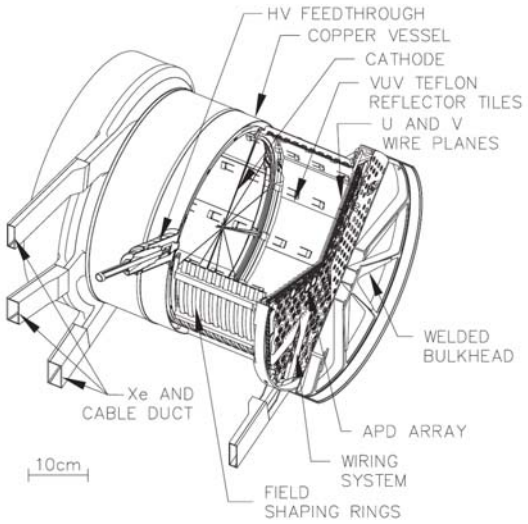

Fig. 1. Drawing of the EXO-200 TPC.
The chamber contains ~175 kg of liquid xenon.

EXO-200 was designed to be a state of the art double beta decay experiment and, at the same time, a technology test bed for a future, larger detector. In order to take advantage of event topology, xenon self-shielding, and the possibility of purifying a noble element before and during its use, EXO-200 uses the xenon as both source and detector in a single homogeneous volume (for a detailed description see [9]). In order to minimize the surface-to-volume ratio while maintaining a practical geometry, the detector is a double TPC, having the shape of a square cylinder. Of the 200 kg of enriched xenon available, 175 kg are in liquid phase, and 110 kg are in the active volume of the detector. Isotope composition is 80.6 % of the ^{136}Xe and the remaining 19.4 % is ^{134}Xe A cutaway view of the TPC is shown in Fig. 1. Gas system allows to recirculate and purify xenon continuously.

Charged particles produce energy depositions in the TPC. This energy through ionization and excitation of xenon atoms produce both ionization electrons and scintillation photons. In EXO-200 both the ionization and the scintillation signals are recorded. The cylindrical TPC is divided into two symmetric volumes separated by a cathode grid. Ionization electrons drift along applied electric field from center towards ends of the TPC. Each end of the TPC holds grid of 38 charge induction (V) and 38 charge collection (U) wire triplets. The U and V wire grids, oriented at 60◦ from each other, provide planar information for charge depositions. At each end of the TPC there are ~ 250 Large Area

Avalanche PhotoDiodes (LAAPDs) [10] that record the 178 nm xenon scintillation light and make 41 % of area coverage. The TPC configuration allows for three-dimensional topological and temporal reconstruction of individual energy depositions. This ability is essential for discriminating $\beta\beta$ decays from residual backgrounds dominated by gammas.

Because the rate of $0\nu\beta\beta$ is so small, two considerations were central in designing the detector: the need for good energy resolution at the double beta decay decay Q-value of 2457.8 keV [11], and the requirement to achieve exceedingly low backgrounds that can deposit energy near the ^{136}Xe Q-value. The attenuation length in LXe of 2.5 MeV γ-rays is quite large (~ 9 cm), so xenon self-shielding is not particularly effective, and the materials near the active xenon volume have to be intrinsically clean. Very low backgrounds are achieved by selecting ultra-low radioactivity construction materials, minimizing the masses of passive components through careful design, specially cleaning and storing components before assembly, and building the detector in progressively clean, shielded layers. The decision to use LAAPDs instead of photomultiplier tubes, unusual among large LXe detectors, is important because they combine high quantum efficiency for the scintillation light with ultra-low levels of radioactivity. The TPC was built using primarily copper and bronze for conductors and acrylic, PTFE and polyimide for dielectrics. Some of the specific materials used are reported in [12]. All TPC materials were degreased and etched to remove surface contamination. At least 50 cm of HFE-7000 fluid plus 10 cm of copper and 25 cm of low-activity lead shield the TPC from external radioactivity. The clean room module housing the TPC is surrounded on four sides by 50 mm thick plastic-scintillator cosmic-ray veto panels, which are (95.5 ±0.6) % efficient. To reduce cosmogenic and radioactive background EXO-200 is located at a depth of 1585^{+11}_{-6} m.w.e. at the WIPP salt mine in New Mexico, USA.

3. Reconstruction

Offline event reconstruction proceeds in three stages: signal finding, parameter estimation, and clustering. Charge signals on the U wires and scintillation signals on the two LAAPD planes are found using a matched filter technique. The filter yields time estimates for both ionization and scintillation channels. The time information from the U wires is used to search for induction signals in V wire waveforms. Candidate U wire signals are fit to template waveforms modeling the measured transfer functions so that the signal amplitudes can be extracted for energy estimation. Amplitudes are corrected, channel-by-channel, for electronic gains determined from radioactive source calibration.

U wire and V wire signals are then combined into charge clusters using timing information from the fits, and associated with the nearest (earlier in time) summed scintillation signal. Matching signals at two wire planes (U and V) provides planar coordinates for each ionization cluster. Three-dimensional position sensitivity is achieved by using the difference in the arrival time between the ionization and scintillation signals to calculate the electron drift time. Events with one charge cluster per one scintillation cluster are called single site events (SS) and events with many charge clusters per one scintillation cluster are called multiple site events (MS). The ability of the TPC to identify SS and MS interactions is used to separate β and ββ decays in the bulk xenon from multiple site γ interactions. The clustering, currently applied in 2D, has a separation resolution of 18 mm in the U-dimension and 6 mm in z (drift time).

Each cluster energy is corrected for position-dependent charge losses due to finite xenon purity and for the shielding grid inefficiency of the V wire plane. This procedure, introducing the only time-dependent correction, yields reconstructed ionization energy and three dimensional position information for each charge cluster. An efficiency loss is incurred by events for which 3D reconstruction is not possible as these are rejected from this analysis. The LAAPD sum signal gives total scintillation energy. It is corrected for variations of gain and spatial light collection efficiency within the TPC. A trilinear interpolation of the 2615 keV gammas SS full absorption peak scintillation signal, recorded for 1352 locations throughout the LXe during ^{228}Th calibration source deployments, is used to construct the correction function.

As first discussed in [13] anti-correlation of charge vs scintillation signal can be used to reduce energy reconstruction error. The 2D SS and MS energy spectra are independently rotated and projected onto a new (1D) energy variable in such a way as to minimize the width of the 2615 keV line.

4. Calibration

EXO-200 experiment utilizes various techniques to measure and track detector performance. Calibration runs are performed daily. It includes charge and light injection as well as in-situ measurements with gamma-ray sources. Individual wire and APD gains are measured and electronics stability and linearity is monitored with dedicated runs. Compact gamma sources are used for final energy calibration. We use three different isotopes to cover broad energy range. Namely they are ^{137}Cs, ^{60}Co, and ^{228}Th each with high and low activities. Delivery is organized with pipe going around detector inside cryostat and source connected to the end of low-friction cable. Position is controlled by a length of that delivery cable. Sources are placed in different known positions around detector to measure response for events in entire volume.

Energy spectra from sources are reconstructed, then the positions of the full absorption peaks at 662, 1173, 1333 and 2615 keV are fit (Fig. 2). The energy calibration function that converts the rotated energy estimator into keV is almost linear but has a small quadratic term. The energy resolution is parameterized as $\sigma^2 = a\sigma^2_e + bE + cE^2$. Here σ_e is the electronic noise contribution, bE represents statistical fluctuations in the ionization and scintillation, and cE^2 is a

position- and time-dependent broadening. It is found that σ/E = 1.67% (1.84%) for SS (MS) spectra at $Q_{\beta\beta}$, dominated by the noise and broadening terms.

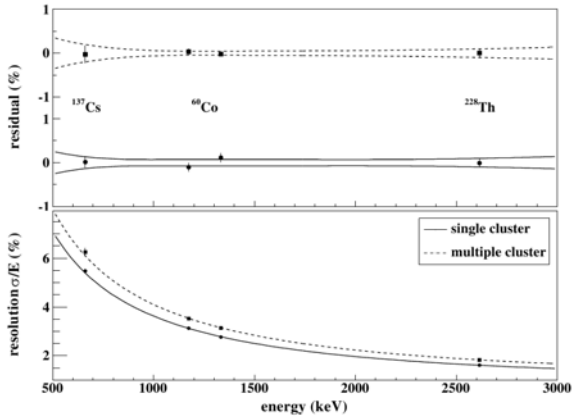

Fig. 2. *Top*: systematic uncertainty bands on the energy calibration residuals, for both SS (solid) and MS (dashed). *Bottom*: energy resolution along with a fit to the empirical model (see text).

5. Measurements

EXO-200 started taking low background data in late May 2011 and published first result in August 2011 [7]. The second run begun after upgrade and last from September 22, 2011 to April 15, 2012, for a total of 2,896.6 hours live time under low background conditions [14]. During the same period, 376.8 hours of calibration data were collected with three γ sources at three positions. Most of these data was taken with a ^{228}Th source for the primary purpose of measuring the free electron lifetime (τ_e) in the TPC. This is achieved by recording the charge collected for 2615 keV full absorption events occurring at di□erent z-positions. The resulting τ_e was ~200 μs for the summer 2011 [7] but climbed to ~3 ms upon increasing the Xe recirculation flow for the current dataset.

The fiducial volume used in this analysis contains 79.4 kg of ^{136}Xe ($3.52 \cdot 10^{26}$ atoms), corresponding to 98.5 kg of active ^{enr}LXe. The trigger is fully efficient above 700 keV. Specific cut eliminates a population of events due to interactions in the ^{enr}LXe region for which the charge collection efficiency is low, leading to an anomalous light-to-charge ratio. This cut also eliminates α decays from the low background data, but causes only a negligible loss of efficiency for γ- and β-like events. Cosmic-ray induced backgrounds are removed using three time-based cuts. Events preceded by a veto hit within 25 ms are removed (0.58 % dead time). Events occurring within 60 s after a muon track in the TPC are also eliminated (5.0 % dead time). Finally, any two events that occur within 1 s of each other are removed (3.3 % dead time). The combination of all three cuts incurs a total dead time of 8.6 %. The last cut, combined with the requirement that only one scintillation event per frame is observed, removes β-α decay coincidences due to the time correlated decay of the ^{222}Rn daughters ^{214}Bi and ^{214}Po. Alpha spectroscopic analysis finds 360 ± 65 μBq of ^{222}Rn in the ^{enr}LXe, that is constant in time.

6. Results

Using its first low-backround run of EXO-200 experiment a *2β2ν* decay mode of xenon was observed for the first time. This result was later confirmed by KamLAND-Zen [8]. In this new analysis an enhanced signal reconstruction was used. Also estimation of energy is now made from combined ionization and scintillation signals. This allowed to improve energy resolution dramatically. Namely it was decreased from 4.5% at 2614 keV for previous analysis [7] down to 1.67% now [14].

The obtained low background energy spectra both for SS and MS are shown in Fig. 3. The SS and MS spectra are compared to probability density functions (PDFs) generated by GEANT4 [15] Monte-Carlo simulations. Using a maximum likelihood estimator, those spectra are simultaneously fit with PDFs of the *2νββ* and *0νββ* of ^{136}Xe along with PDFs of dominating backgrounds. Background models were developed for various components of the detector. A possible energy offset and the resolution of the γ-like spectra are parameters in the fit and are constrained by the results of the source calibrations. Primarily due to bremsstrahlung, a fraction of ββ events are MS. The MC simulation predicts that 82.5% of *0νββ* events are SS. The ββ energy scale is a free parameter in the fit, so that it is constrained by the *2νββ* spectrum. The fit reports a scale factor of 0.995 ± 0.004. The uncertainty is inflated to ± 0.006 as a result of an independent study of the possible energy scale differences between γ- and ββ-like energy deposits. The fit reports $T^{2\nu\beta\beta}_{1/2} = (2.23 \pm 0.017 \text{ stat.} \pm 0.22 \text{ sys.}) \cdot 10^{21}$ yr, which is in complete agreement with previous value [7] and with results of experiment KamLAND-Zen [8].

For the best-fit energy scale and resolution the ±1σ and ±2σ regions around $Q_{\beta\beta}$ are shown in Fig. 4. The number of events observed in the SS spectrum is 1 and 5, respectively, with the 5 events in the ±2σ region accumulating at both edges of the interval. Therefore, no evidence for *0νββ* decay is found in the present data set. A background prediction from combined fit is 4.1 ± 0.3 background counts in the ±1σ region. It gives an expected background rate of $(1.5 \pm 0.1) \cdot 10^{-3}$ kg^{-1} yr^{-1} keV^{-1}. This is well below expected level and experiment goal.

The limit on $T^{0\nu\beta\beta}_{1/2}$ is obtained by the profile likelihood fit to the entire SS and MS spectra. Systematic uncertainties are incorporated as constrained nuisance parameters. The fit yields *0νββ* decay limits of < 2.8 counts at 90 % C.L. This corresponds to a $T^{0\nu\beta\beta}_{1/2} > 1.6 \cdot 10^{25}$ yr at 90 % C.L. Toy MC studies confirm the coverage of this method as suggested by [16]. The levels of contamination from γ-emitting nuclides are found to be consistent with material screening estimates [12]. The present result contradicts [5] at 68% C.L. (90 % C.L.) for the nominal values of all (most) matrix element calculations considered [14] and provides upper bounds to Majorana neutrino masses between 140 and 380 meV at 90 % C.L.

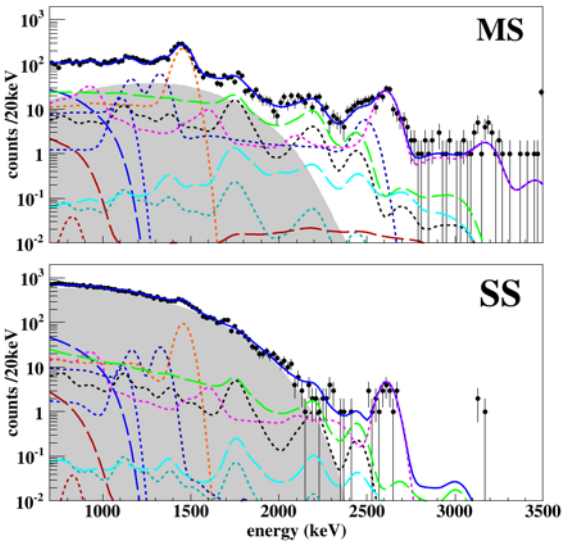

Fig. 3. MS (*top*) and SS (*bottom*) energy spectra. The best fit line (solid blue) is shown. The background components are 2νββ (grey region), ^{40}K (dotted orange), ^{60}Co(dotted dark blue), ^{222}Rn in the cryostat-lead air-gap (long-dashed green), ^{238}U in the TPC vessel (dotted black), ^{232}Th in the TPC vessel (dotted magenta), ^{214}Bi on the cathode(long-dashed cyan), ^{222}Rn outside of the field cage (dotted dark cyan), ^{222}Rn in active xenon (long-dashed brown), ^{135}Xe (long-dashed blue) and ^{54}Mn (dotted brown). The last bin on the right includes overflows (none in the SS spectrum).

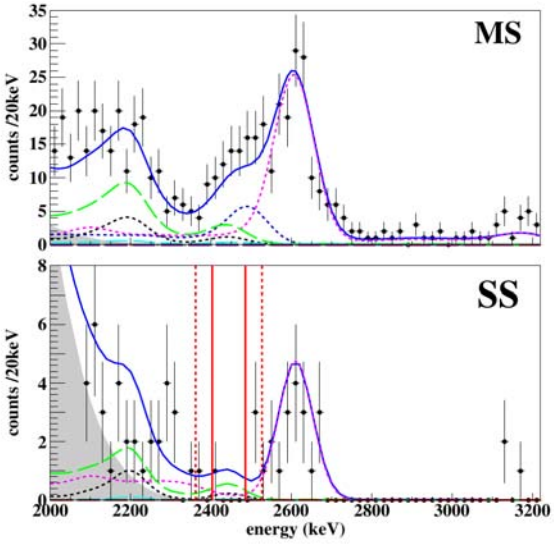

Fig. 4. Energy spectra in the ^{136}Xe $Q_{\beta\beta}$ region for MS (*top*) and SS (*bottom*) events. The 1 (2)σ regions around $Q^{\beta\beta}$ are shown by solid (dashed) vertical lines. The *0νββ* PDF from the fit is not visible. The fit results have the same meaning as in Fig. 3.

ACKNOWLEDGEMENTS

EXO-200 is supported by DoE and NSF in the United States, NSERC in Canada, SNF in Switzerland, NRF in Korea and RFBR in Russia. This research used resources of the National Energy Research Scientific Computing Center (NERSC). The collaboration gratefully acknowledges the WIPP for the hospitality and G. Walther (Stanford) for discussions on statistical methods.

REFERENCES

1. *Schechter J., Valle J.W.F.* Neutrinoless double-β decay in SU(2)×U(1) theories // Phys. Rev. - 1982. - Vol. D25. - I.11 - 2951.
2. *Nakamura K. et al.* (*Particle Data Group*) Review of particle physics // J. Phys. - 2010. - Vol. G37. - P. 075021.
3. *Aseev V.N. et al.* Upper limit on the electron antineutrino mass from the Troitsk experiment // Phys. Rev. - 2011. - Vol. D84. - I.11 - 112003.
4. *Kraus Ch. et al.* Final results from phase II of the Mainz neutrino mass searching tritium b decay // Eur. Phys. J. - 2005. - Vol. C40. - No. 4. - P. 447.
5. *Klapdor-Kleingrothaus H.V., Krivosheina I.V.* The evidence for the observation of 0νββ decay: the identification of 0νββ events from the full spectra // Mod. Phys. Lett. - 2006. - Vol. A21. - I. 20 - 1547; Private communication H.V. Klapdor-Kleingrothaus.
6. *Barabash A.S.* Double beta decay experiments // Phys. Part. Nucl. - 2011. - Vol. 42. - P. 613.
7. *Ackerman N. et al.* Observation of Two-Neutrino Double-Beta Decay in 136Xe with the EXO-200 Detector // Phys. Rev. Lett. - 2011. - Vol. 107. - I.21 - 212501.
8. *Gando A.et al.* Measurement of the double-β decay half-life of 136Xe with the KamLAND-Zen experiment // Phys. Rev. - 2012. - Vol. C85. - I.4 - 045504.
9. *Auger M. et al.* The EXO-200 detector, part I: detector design and construction // JINST. - 2012. - Vol. 7. - P. 05010.
10. *Neilson R. et al.* Characterization of large area APDs for the EXO-200 detector // Nucl. Instr. Meth. - 2009. - Vol. A608. - I.1 - 68.
11. *Redshaw M. et al.* Mass and Double-Beta-Decay Q Value of 136Xe // Phys. Rev. Lett. - 2007. - Vol. 98. - I.5 - 053003.
12. *Leonard D.S.et al.* Systematic study of trace radioactive impurities in candidate construction materials for EXO-200 // Nucl. Instr. Meth. - 2008. - Vol. A591. - I.3 - 490.
13. *Conti E. et al.* Correlated fluctuations between luminescence and ionization in liquid xenon // Phys. Rev. - 2003. -

Vol. B68. - I.5 - 054201.
14. *Auger M.et al.* Search for neutrinoless double-beta decay in 136Xe with EXO-200 // Phys. Rev. Lett. - 2012. - Vol. 109. - I.3 - 032505.
15. *Agostinelli S. et al.* Geant4 - a simulation toolkit // Nucl. Inst. Meth. - 2003. - Vol. A506. - I.3 - 250.
16. *Rolke W.A., Lopez A.M., J. Conrad.* Limits and confidence intervals in the presence of nuisance parameters // Nucl. Inst. Meth. - 2005. - Vol. A551. - I.2-3 - 493.

CRYOGENIC ZINC MOLYBDATE SCINTILLATING BOLOMETERS TO SEARCH FOR NEUTRINOLESS DOUBLE BETA DECAY OF ^{100}Mo

D. M. Chernyak[1,2], F. A. Danevich[1], E. N. Galashov[3], A. Giuliani[2], V. V. Kobychev[1], S. Marnieros[2], C. Nones[4], E. Olivieri[2], V. N. Shlegel[3], M. Tenconi[2], V. I. Tretyak[1], Ya. V. Vasiliev[3]

[1] *Institute for Nuclear Research, National Academy of Sciences of Ukraine, Kyiv, Ukraine*
[2] *Centre de Spectrométrie Nucléaire et de Spectrométrie de Masse, Orsay, France*
[3] *Nikolaev Institute of Inorganic Chemistry, 630090 Novosibirsk, Russia*
[4] *Service de Physique des Particules, CEA Saclay, Gif sur Yvette, France*

Zinc molybdate ($ZnMoO_4$) crystals of improved quality were grown by the low-thermal gradient Czochralski technique. A prototype scintillating bolometer with a 23.8 g $ZnMoO_4$ crystal was tested at temperature 18 mK. The scintillation light was read out by a thin Ge bolometer equipped with an NTD Ge thermistor, while the phonon signals were collected by the same type of sensor directly coupled to the scintillating crystal. Intrinsic energy resolution of the heat channel was ≈ 1.3 keV (FWHM), the α/β rejection factor was achieved better than 99.9% in the energy region of interest (≈ 3 MeV). Pulse shape discrimination technique was developed to suppress background from the random coincidence of 2ν2β decay events in $ZnMoO_4$ cryogenic scintillating bolometer. Large $ZnMoO_4$ crystal scintillator (313 g of mass) was produced and tested as scintillating bolometer. A next generation experiment applying enriched $Zn^{100}MoO_4$ crystal with unprecedented sensitivity to neutrinoless 2β decay of ^{100}Mo (on the level of $\lim T_{1/2} \approx 10^{27}$ yr) is discussed.

1. Introduction

Observations of neutrino oscillations [1] give a clear evidence that neutrino is a massive particle, which provides strong motivation to search for neutrinoless double beta decay (0ν2β) of atomic nuclei. Double beta decay is a rare nuclear transition which changes the nuclear charge by two units. Two neutrino double beta decay (2ν2β) is allowed by the Standard Model and has been already observed for 11 isotopes. Neutrinoless 2β decay violates the lepton number and is possible only if the neutrino is a massive Majorana particle. The 0ν2β decay, if observed, will establish the Majorana nature of the neutrino, test lepton number conservation and, in case of transition mediated by light neutrino exchange, determine the absolute scale of neutrino masses [2]. Moreover, this process could clarify the presence of right-handed currents in weak interaction and the existence of Majorons [2]. Taking into account ambiguity of the theoretical estimations [3, 4], development of experimental methods for different 2β isotopes is highly requested.

^{100}Mo is one of the most promising 2β isotopes because of its large transition energy $Q_{2\beta}$ = 3034.40(17) keV [5] and a considerable natural isotopic abundance δ = 9.67(20) % [6]. The decay scheme of ^{100}Mo is presented in Fig. 1. From the experimental point of view a large $Q_{2\beta}$ value simplifies the problem of background induced by natural radioactivity and cosmogenic activation.

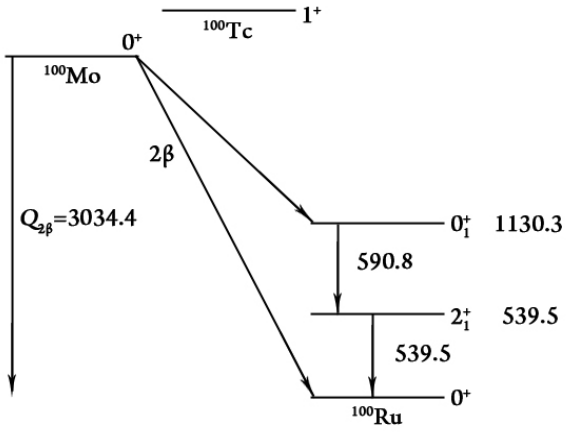

Fig. 1. Decay scheme of ^{100}Mo. Energies of the level and γ quanta are in keV. $Q_{2\beta}$ is the 2β decay energy.

At present the best sensitivity to 0ν2β decay of ^{100}Mo was reached by the NEMO-3 experiment [7] with ≈ 7 kg of foil enriched in ^{100}Mo. The experiment gave a half-life limit $T_{1/2}^{0\nu2\beta} > 4.6 \cdot 10^{23}$ yr at 90 % C.L. However, the NEMO technique has two disadvantages that limit its sensitivity: the low detection efficiency (≈ 14 % to 0ν2β events) and rather poor energy resolution (≈ 10 % at the energy of $Q_{2\beta}$ of ^{100}Mo). The detection efficiency can be improved up to 80 - 90 % by using detector containing molybdenum (so-called source = detector technique). Only cryogenic bolometers and semiconductor HP Ge detectors can provide high enough energy resolution (a few keV) [8]. Furthermore, simultaneous detection of phonon and scintillation signals in cryogenic scintillating bolometers allows efficient particle discrimination, important to reject background caused by radioactive contamination of crystal scintillators.

There are several inorganic scintillators containing molybdenum. The most promising of them are molybdates of Calcium ($CaMoO_4$), Cadmium ($CdMoO_4$), Lead ($PbMoO_4$), and Lithium (Li_2MoO_4). However, $CaMoO_4$ contains the 2ν2β active isotope ^{48}Ca with $Q_{2\beta}$ = 4274 keV which, even if present in natural Ca with a very small abundance of δ = 0.187 % [6], creates background at $Q_{2\beta}$ energy of ^{100}Mo. $CdMoO_4$ contains the β active ^{113}Cd ($T_{1/2}^{\beta} = 8.04 \cdot 10^{15}$ yr [9], δ = 12.22 % [6]) which has a very high cross section to capture thermal neutrons. The concentration of molybdenum in $PbMoO_4$ is rather low (27 % by mass), Li_2MoO_4 has low light yield. $ZnMoO_4$ crystals were developed recently [10, 11, 12]. An important advantage of $ZnMoO_4$ is the absence of heavy and radioactive elements, and high concentration of molybdenum (43 %).

2. A $ZnMoO_4$ scintillating bolometer prototype

High quality $ZnMoO_4$ crystals were developed in the Nikolaev Institute of Inorganic Chemistry (Novosibirsk, Russia) from deeply purified molybdenum. $ZnMoO_4$ crystals up to 25 mm in diameter and 60 mm in length were grown by the low-thermal-gradient Czochralski technique in platinum crucible.

Detector prototype of the cryogenic scintillating bolometer with a $ZnMoO_4$ scintillating crystal was constructed and tested in the Centre de Spectrométrie Nucléaire et de Spectrométrie de Masse (Orsay, France). Detector consists of near cylindrical $ZnMoO_4$ crystal with a mass of 23.8 g, faced from one side by the thin light-detecting ultrapure germanium slab. Bolometer was surrounded by a highly reflective polymeric multilayer foil (Radiant Mirror Film VM2000/VM2002 from 3M). The thermal signals from the $ZnMoO_4$ crystal and the germanium slab were read out by two nominally identical sensors, consisting of neutron transmutation doped (NTD) germanium thermistors, with a mass of ≈ 10 mg. The thermistors resistances and sensitivities were tuned for an optimal operation at the 18 mK.

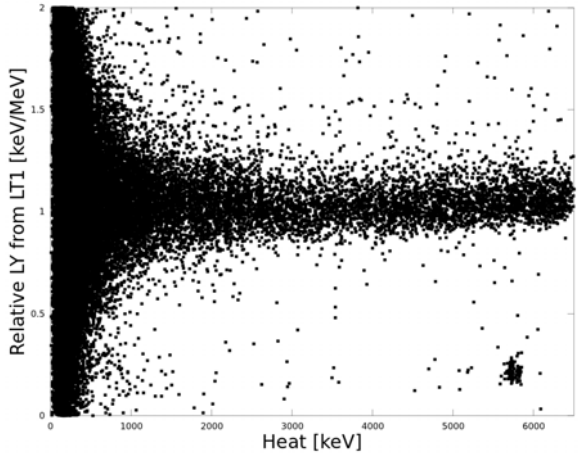

Fig. 2. The ratio of the light-to-heat energy as a function of the heat energy obtained with a 23.8 g $ZnMoO_4$ crystal working as a cryogenic bolometer. The upper band (caused by β/γ and cosmic muon events) and isolated lower band (populated by α decays of ^{210}Po) are clearly separated.

The signals from the $ZnMoO_4$ crystal (the heat channel) corresponded to voltage pulses with an amplitude of ≈ 100 μV for 1 MeV deposited energy at 19 mK. The time structure was characterized by ≈ 10 ms risetime and ≈ 40 ms decaytime (respectively from 10 to 90 % and from 90 to 30% of the signal maximum amplitude). Intrinsic energy resolution of the heat channel (corresponding to the FWHM baseline fluctuations) was at the level of 1.3 keV. The α/β rejection factor was achieved better than 99.9 % in the energy region of interest for ^{100}Mo (Fig. 2).

3. Random coincidence of 2ν2β decay events as a background source

A disadvantage of cryogenic bolometers is their slowness which causes poor time resolution. This can lead to a background component at the energy $Q_{2\beta}$ due to random coincidences of lower energy signals, in particular those due to the unavoidable two-neutrino double β decay events.

The pile-up phenomenon was studied by generating light pulses with the observed experimental shape on top of experimental noisy baselines. Pulse shapes and noise were used from a real light detector coupled to a $ZnMoO_4$ scintillating crystal. In particular, pairs of pulses were generated with random time distances with a flat distribution up to 10 ms.

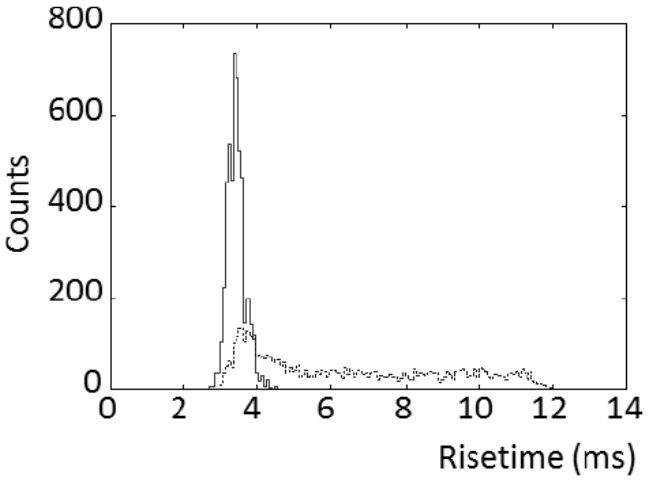

Fig. 3. Risetime distribution for two populations of 5000 generated events each. The solid line refers to single pulses; the dashed line is obtained with piled-up pulses separated by a time distance uniformly covering the interval [0, 10] ms, with amplitudes sampling the 2ν2β spectrum and adding so as to fall in the region of the 0ν2β expected peak [14].

As a first step, we defined a 90 % efficiency in accepting a pulse from the light detector as a potentially good 0ν2β pulse using opportune signal filtering and three different pulse-shape indicators: (1) the risetime from 15 to 90 % of the maximum amplitude; (2) the χ^2 evaluated using an average pulse as a standard shape function; (3) the pulse shape parameter defined in [13], which also uses a standard pulse-shape function. The rejection efficiency of piled-up pulses was then tested. In each pulse pair, the amplitude of the first pulse A_1 was extracted by sampling the 2ν2β distribution, while the amplitude of the second pulse A_2 was chosen as $Q_{2\beta}(^{100}\text{Mo}) - A_1 + \Delta E$, where ΔE is a random component in the interval [−5, +5] keV.

The generated pulse amplitudes were chosen so as to fix the signal-to-noise ratio at the level expected for a 0ν2β signal, i.e., of the order of 30. In fact, the typical light energy collected by the light detectors in $ZnMoO_4$ scintillating bolometers realized so far is of the order of 1 keV for 1 MeV energy in the heat channel, while the typical root mean square (RMS) noise of the light detector can be conservatively taken as 100 eV. The piled-up pulses generated in the simulation were analyzed with the mentioned pulse-shape indicators. Using the risetime method, excellent pile-up rejection efficiency was obtained. A comparison between the risetime distribution for genuine

single pulses and piled-up pulses generated as described above is shown in Fig. 3. More quantitatively, the same procedure that retains 90 % of genuine single pulses rejects 80 % - 90 % of piled-up pulses when their sum amplitude is in the region of $Q_{2\beta}$ and the difference between the arrival times of the two pulses covers uniformly the interval [0, 10] ms. For example, the analysis of the sample reported in Fig. 3 excludes 83 % of piled-up pulses when accepting 90 % of single pulses. The other two indicators provide equivalent or even better results. However, we prefer here to consider conservatively the results obtained with the method of the risetime, since this parameter is an intrinsic property of each signal that does not require the comparison with a standard shape.

4. Potential of $ZnMoO_4$ scintillating bolometers to search for 0v2β decay of ^{100}Mo

Large $ZnMoO_4$ crystal scintillator (313 g of mass) was produced using the low-thermal-gradient Czochralski technique in the Nikolaev Institute of Inorganic Chemistry (Novosibirsk, Russia). Cryogenic scintillating bolometer with the $ZnMoO_4$ crystal was developed, constructed and tested at the aboveground level in the Centre de Spectrométrie Nucléaire et de Spectrométrie de Masse (Orsay, France) (Fig. 4, *a*). Preliminary measurements with the detector have shown possibility to use large $ZnMoO_4$ crystals as cryogenic bolometers (Fig. 4, *b*). Measurements and further investigation are in progress.

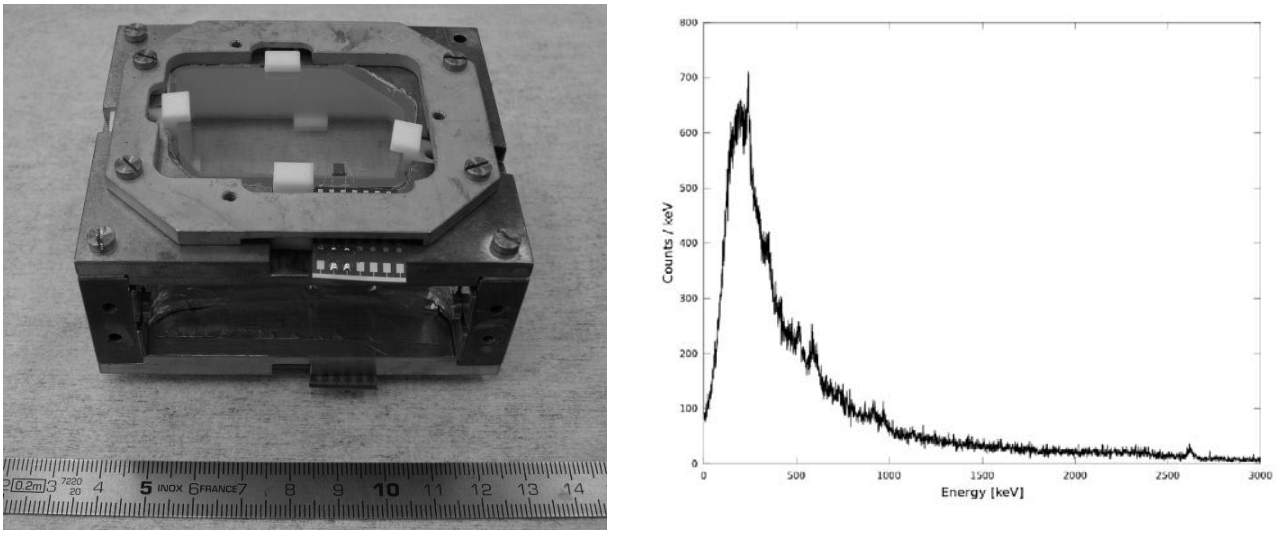

a *b*

Fig. 4. *a*: Copper holder with a 313 g $ZnMoO_4$ scintillating crystal developed for the cryogenic scintillating bolometer; *b*: Calibration of the 313 g $ZnMoO_4$ scintillating bolometer with a ^{232}Th source. Energy resolution 1.2 % for 2615 keV is limited by pile-up due to aboveground operation.

According to the current study of a $ZnMoO_4$ scintillating bolometer prototype and the simulation of the background for a close-packed array of such devices made in [15], we can evaluate the sensitivities of future 0v2β searches in realistic configurations, as reported in the Table. We consider both the use of enriched and natural material, given the reasonably high isotopic abundance of ^{100}Mo (9.67 %). For the next tests an enriched 200 g $ZnMoO_4$ crystal is in preparation. The low-thermal-gradient Czochralski technique minimizes the loss of material during crystal growth. In case of a positive outcome of the 200 g test, four large crystals of about 400 - 500 g each will be produced and measured in one of the existing underground low-activity dilution refrigerators in Modane or Gran Sasso underground laboratories (option (1) in the Table).

Sensitivity (at 90 % C.L.) of experiments based on $ZnMoO_4$ scintillating bolometers searching for 0v2β of ^{100}Mo. The live time is 5 yr and the energy window 6 keV. The enrichment level is 97 % (except for the third option, where natural molybdenum is considered) and the detection efficiency to 0v2β of ^{100}Mo is 90%, compatible with the single module structure. The range in $m_{\beta\beta}$ takes into account three different approaches to the evaluation of the nuclear matrix elements (QRPA [16], ISM [17], IBM-2 [18])

Option	Number of ≈ 0.4 kg crystals	Total isotope mass, kg	Half-life sensitivity, 10^{26} yr	$m_{\beta\beta}$ sensitivity, eV
(1)	4	0.68	0.05	0.1 - 0.5
(2)	40	6.8	0.5	0.05 - 0.2
(3)	2000 (nat.)	33	1.5	0.03 - 0.09
(4)	2000	338	10	0.01 - 0.04

This pilot experiment would have sensitivities comparable to present searches and would constitute the general test bench for scaling up this technology. A further step could exploit existing enriched material, of the order of several kg. This search (option (2) in the Table) would approach the inverted hierarchy (IH) region and could be housed by the former Cuoricino refrigerator or by a cryogenic set-up with equivalent capability. A major extension is required to substantially cover the IH mass pattern. Molybdenum can be enriched by centrifugation at reasonable prices and with reasonable throughput. The production of ≈ 350 kg of ^{100}Mo fits the time and budget scale of a large next-generation 0ν2β search. Bolometric masses of the order of 1 ton could be housed, after the completion of the TeO_2 program, by the CUORE dilution refrigerator (under construction) or by the EURECA dilution refrigerator (under design), which could share dark matter and 0ν2β searches (options (3) and (4) in the Table [15]).

5. Conclusions

Large volume $ZnMoO_4$ crystals of improved quality were grown by the low-thermal gradient Czochralski technique. Development of $Zn^{100}MoO_4$ crystal scintillators from enriched ^{100}Mo is in progress.

Detector prototypes of the cryogenic scintillating bolometers with a 23.8 g and 313 g $ZnMoO_4$ scintillating crystals were constructed and tested. Both of them prove the possibility of the large-scale next-generation experiment with $ZnMoO_4$ crystals.

The present bolometric detector technologies enable to control 2ν2β decay form of background at the required level, in particular the case of bolometers searching for the 0ν2β decay of ^{100}Mo, which is characterized by a relatively short 2ν2β decay half-life.

$ZnMoO_4$ scintillating bolometers are extremely promising detectors for a next-generation 0ν2β experiment capable to explore the inverted hierarchy region of the neutrino mass pattern.

REFERENCES

1. *Mohapatra R.N. et al.* Theory of neutrinos: a white paper // Rep. Prog. Phys. - 2007. - Vol. 70. - P. 1757 - 1867.
2. *Avignone III F.T., Elliott S.R., Engel J.* Double beta decay, Majorana neutrinos, and neutrino mass // Rev. Mod. Phys. - 2008. - Vol. 80. - P. 481 - 516; *Rodejohann W.* Neutrino-less double beta decay and particle physics // Int. J. Mod. Phys. - 2011. - Vol. E20. - P. 1833 - 1930; *Elliott S.R.* Recent progress in double beta decay // Mod. Phys. Lett. - 2012. - Vol. A27. - P. 1230009, 16 p.; *Vergados J. D., Ejiri H. and Simkovic F.* Theory of neutrinoless double-beta decay // Rep. Prog. Phys. - 2012. - Vol. 75 - P. 106301, 52 p.
3. *Simkovic F. et al.* Anatomy of nuclear matrix elements for neutrinoless double-beta decay // Phys. Rev. - 2008. - Vol. C77. -P. 045503, 11 p.
4. *Menendez J. et al.* Disassembling the Nuclear Matrix Elements of the Neutrinoless double beta Decay // Nucl. Phys. - 2009. -Vol. A818. - P. 139 - 151.
5. *Rahaman S. et al.* Q values of the ^{76}Ge and ^{100}Mo double-beta decays // Phys. Lett. - 2008. - Vol. B662. - P. 111 - 116.
6. *Bohlke J.K. et al.* Isotopic Compositions of the Elements, 2001 // J. Phys. Chem. Ref. Data. - 2005. - Vol. 34. - P. 57 - 67.
7. *Arnold R. et al.* First Results of the Search for Neutrinoless Double-Beta Decay with the NEMO 3 Detector // Phys. Rev. Lett. - 2005. - Vol. 95. - P. 182302, 5 p.
8. *Giuliani A.* Neutrino Physics with Low-Temperature Detectors // Journal of Low Temperature Physics. - 2012. - Vol. 167. - P. 991 - 1003.
9. *Belli P. et al.* Investigation of beta decay of ^{113}Cd // Phys. Rev. - 2007. - Vol. C76. - P. 064603, 10 p.
10. *Ivleva L.I. et al.* Growth and properties of $ZnMoO_4$ single crystals // Crystallography Reports. - 2008. - Vol. 53. - P. 1087 - 1090.
11. *Nagornaya L.L. et al.* Tungstate and Molybdate Scintillators to Search for Dark Matter and Double Beta Decay // IEEE Trans. Nucl. Sci. - 2009. - Vol. 56. - P. 2513 - 2518.
12. *Gironi L. et al.* Performance of $ZnMoO_4$ crystal as cryogenic scintillating bolometer to search for double beta decay of molybdenum // JINST. - 2010. - Vol. 5. - P. 11007, 12 p.
13. *Fazzini T. et al.* Pulse-shape discrimination with $CdWO_4$ crystal scintillators // Nucl. Instrum. Methods Phys. Res. - 1998. - Vol. A410. - P. 213 - 219.
14. *Chernyak D.M. et al.* Random coincidence of 2ν2β decay events as a background source in bolometric 0ν2β decay experiments // Eur. Phys. J. - 2012. - Vol. C72. - P. 1989 - 1995.
15. *Beeman J.W. et al.* A next-generation neutrinoless double beta decay experiment based on $ZnMoO_4$ scintillating bolometers // Phys. Lett. - 2012. - Vol. B710. - P. 318 - 323.
16. *Simkovic F. et al.* 0νββ-decay nuclear matrix elements with self-consistent short-range correlations // Phys. Rev. - 2009. - Vol. C79. - P. 055501, 10 p.; *Civitarese O., Suhonen J.* Nuclear matrix elements for double beta decay in the QRPA approach: A critical review // J. Phys.: Conf. Ser. - 2009. - Vol. 173. - P. 012012, 7 p.
17. *Menendez J. et al.* Novel nuclear structure aspects of the 0νββ-decay // J. Phys.: Conf. Ser. - 2011. - Vol. 267. - P. 012058, 6 p.
18. *Barea J., Iachello F.* Neutrinoless double-β decay in the microscopic interacting boson model // Phys. Rev. - 2009. - Vol. C79. - P. 044301, 16 p.

NEW OBSERVATIONS FOR THE TRIGGERING OF ^{178m2}Hf ISOMER EMBEDDED IN Ta MATRIX BY 30 keV ELECTRONS

A. M. Dovbnya[1], S. S. Kandybey[1], V. I. Kirischuk[2], Yu. N. Ranyuk[1], O. S. Shevchenko[1], N. V. Strilchuk[2]

[1] National Science Center "Kharkiv Institute of Physics and Technology", Kharkiv, Ukraine
[2] Institute for Nuclear Research, National Academy of Sciences of Ukraine, Kyiv, Ukraine

^{178m2}Hf isomer triggering has been studied using the upgraded experimental setup developed in Kharkiv National University and installed at Kyiv Institute for Nuclear Research. The target that presented a single Ta foil of 300 μm thickness with ^{178m2}Hf isomeric activity of about 100 Bq has been irradiated by 30 keV electron beam. The enhanced counting rates of all the ground-state band transitions have been observed. Our data are consistent with an estimate for the triggering effect of 2.9 ± 0.7 % and the electron induced triggering cross-section can be estimated as 1.1 b, which is about four times less than the upper limit for the photon induced triggering cross-section 4.7 b.

1. Background and introduction

The 16^+ four-quasiparticle state of the nucleus ^{178}Hf, a K isomer with the excitation energy 2.4474 MeV and half-life $T_{½}$ = 31 years, is considered for a long time as the most promising on the way to create gamma-ray sources controlled by low energy photons and a gamma ray laser as well. Having so high excitation energy and the longest half-life among all known highly excited nuclear isomers, ^{178m2}Hf isomer is absolutely unique nuclear isomer and the most perspective for the triggering experiments. Consequently, this isomer has become the subject of intense experimental study for possible mechanisms that could trigger its decay. Since 1998 a number of experiments have been performed, nevertheless the obtained positive results completely exclude the negative results and vice versa yet [1, 2].

The recent experiment on NEET observation in ^{197}Au [3] and following theoretical calculations [4] have revealed some NEET features registered in ^{178m2}Hf isomer triggering experiments increasing the prospects of classical NEET to be responsible for the triggering. At the same time, the current theoretical study of possible NEET effect for ^{178m2}Hf isomer in the frame of strict collision theory [5] indicates that the above-mentioned controversy is not as drastic as it has been considered before as well [6, 7].

The new ^{178m2}Hf isomer triggering experiment has recently been conducted using the experimental setup developed in Kharkiv National University and installed at Kiyv Institute for Nuclear Research allowing the irradiation of isomeric targets directly by electrons (or by x-rays when corresponding converters are used) with the energy of 1 - 25 keV and currents 0 - 150 μA. The target presenting a single Ta foil of 100 μm thickness with ^{178m2}Hf isomeric activity of 5 Bq has been irradiated by 25 keV electron beam. The enhanced counting rates of all the ground-state band (GSB) transitions, just as γ89 keV isomeric and γ216 keV 8^--state band transitions have been observed. The obtained data are consistent with an estimate for the triggering effect of 2.83 ± 0.81 % and corresponding triggering cross-section can qualitatively be estimated as $\sigma_{trig} = 5.4 \cdot 10^{-27}$ cm^2 [8].

2. Target, experimental setup and results

The given ^{178m2}Hf isomer triggering experiment has been conducted using as a target the Ta foil of 300 μm thickness with about 250 Bq isomeric activity which was exploited many years ago as the converter at Kharkiv 1.2 GeV linac. Such target has been irradiated directly by electrons at maximal currents without any risk to be overheated and evaporated into vacuum, moreover the bremsstrahlung radiation and Ta fluorescence x-rays could be used with maximal efficiency while the isomer is embedded in Ta matrix.

Taking into account that the used isomeric target is 3 times thicker than in the first ^{178m2}Hf isomer triggering experiment [8] the experimental setup has been upgraded to the energy 1 - 30 keV and currents 0 - 250 μA and the second triggering experiment has been carried out with 30 keV electron beam at the average current higher than 200 μA. The diameter of the beam spot at the target was about 8 mm – around the same size as the areas of two available spots with practically the same ^{178m2}Hf isomer activity in the target. The γ-ray spectra have been acquired using HPGe coaxial detector mounted on the opposite side of the target in the horizontal plane and at 180° to the horizontally incident electron beam. In our experiment GC 2018 (CANBERRA) detector with the efficiency 20 % and energy resolution at γ1332 keV peak of ^{60}Co better than 1.8 keV and the standard acquisition system based on CANBERRA InSpector 2000 unit have been used. The distance from the detector front face to the target taking into account the thickness of the experimental setup wall was less than 5 mm. The acquisition rate in γ213 keV peak of ^{178m2}Hf isomer even taking into consideration its essential absorption in Ta and additional absorption in the experimental setup wall and the detector cap was around 4.3 counts/s.

L_x lines of Hf cannot be detected in our experiment, consequently the bremsstruhlung radiation with the endpoint energy of 30 keV has been used as the beam-on monitor of electron currents at the target in all runs of measurements ensuring that the experimental luminosity remain at the expected values during the irradiations (Fig. 1, *a*). At the same time, bremsstruhlung radiation rate registered by the detector was low enough for x-ray coincidence detection (see Fig. 1, *b*).

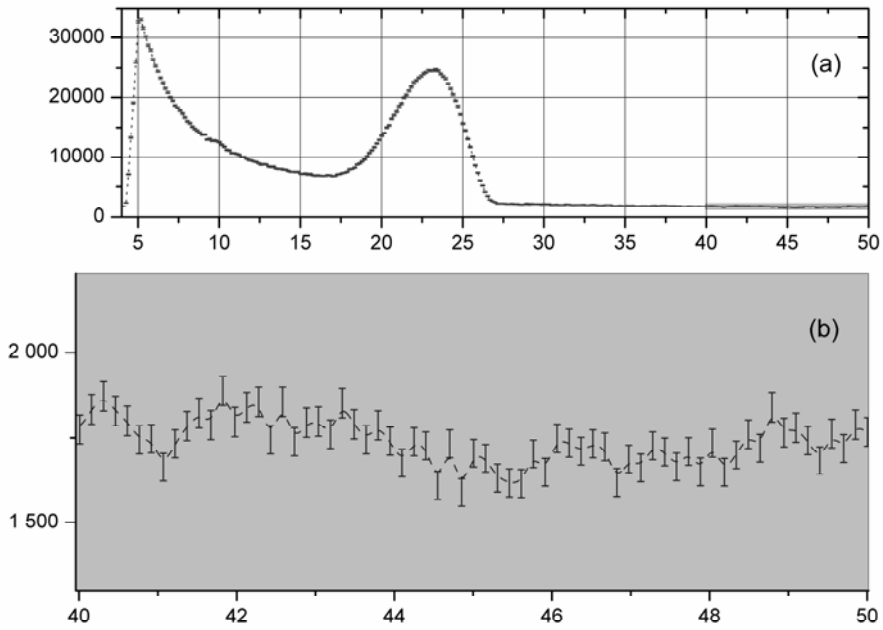

Fig. 1. Bremsstruhlung radiation with the endpoint energy of 30 keV used as the beam-on monitor of electron currents at the target in all runs of the irradiations. *a*: Due to the essential absorption of low-energy x-rays the bremsstruhlung radiation is registered by HPGe detector as a peak with the maximum at the energy about 7 keV lower than the endpoint energy. *B*: Bremsstruhlung radiation rate registered by the detector was too low to produce the summing peak.

Table 1. **The counting rates of all GSB transitions obtained in the beam-off runs conducted before and after the irradiations.**

Transition	Intensity before the irradiation	Intensity after the irradiation	Averaged intensity
γ93 keV	0.208(2)	0.215(2)	0.212(4)
γ213 keV	4.27(2)	4.28(3)	4.28(2)
γ325 keV	3.77(1)	3.79(1)	3.78(1)
γ426 keV	3.01(1)	3.03(1)	3.02(1)

The entire series of measurements have involved a number of runs of beam-on measurements with the absolutely stable measurement geometry and the total acquisition period of about 8 hours. In order to monitor the stability of measurement geometry, several runs of beam-off measurements have been conducted before and after the irradiations, just as between the separate beam-on measurements each accumulating data over the periods from a few hours to around 20 hours. Table 1 shows the counting rates of all GSB transitions acquired in the beam-off runs conducted before and after the irradiations used to obtain the averaged values for above-mentioned counting rates. The accuracies of obtained counting rates are better than 1 % even in the case of γ93 keV transition having the lowest intensity and reaches 0.3 % for the transitions with the highest intensities. In the event when the statistical uncertainty of averaged intensity turned out to be less than the data spread obtained before and after the irradiations the latter has been taken as the uncertainty for the corresponding averaged intensity.

Table 2. **The enhanced beam-on counting rates of all GSB transitions compared to the averaged beam-off counting rates**

Transition	Beam-on intensity	Beam-off intensity	Enhancement
γ93 keV	0.215(5)	0.212(4)	+ 0.003(6)
γ213 keV	4.33(2)	4.28(2)	+ 0.05(3)
γ325 keV	3.84(2)	3.78(1)	+ 0.06(2)
γ426 keV	3.07(1)	3.02(1)	+ 0.05(2)
Beam-on total GSB transition counting rate			11.45(3)
Beam-off total GSB transition counting rate			11.29(2)
Averaged enhancement			+ 0.17(4)
Relative enhancement			+ 1.47(34) %

The beam-induced decay of the isomer has resulted in the increase of the GSB transition intensities compared to the beam-off measurements (Table 2). Similar to the ^{178m2}Hf isomer triggering experiment conducted with 25 keV electron beam [8], any new γ-ray peaks not observed in the spontaneous decay of ^{178m2}Hf isomer have not been detected in this experiment as well and such result allows to use the total counting rate of mentioned above cascade transitions as a measure of the triggering effect. The total counting rates of all transitions triggered in the decay of ^{178m2}Hf isomer have been registered at the levels 11.451 ± 0.032 and 11.285 ± 0.021 decays per second for the beam-on and beam-off spectra, respectively, thus the enhancement factor can be estimated as 1.47 ± 0.34 %. Taking into account that only one from two available spots with practically the same ^{178m2}Hf isomer activity in the target has been irradiated, the triggering effect is two fold higher 2.9 ± 0.7 %.

Table 3. **The counting rates of the γ88 keV isomeric and 8^- band transitions obtained in the beam-off runs conducted before and after the irradiations.**

Transition	Intensity before the irradiation	Intensity after the irradiation	Averaged intensity
γ88 keV	0.674(3)	0.679(4)	0.676(3)
γ216 keV	3.52(2)	3.55(2)	3.53(2)
γ237 keV	0.433(3)	0.423(4)	0.429(5)
γ257 keV	0.791(5)	0.803(4)	0.797(6)
γ297 keV	0.417(5)	0.416(5)	0.416(4)
γ454 keV	0.565(3)	0.571(4)	0.567(3)
γ495 keV	2.034(8)	2.034(7)	2.034(5)
γ534 keV	0.253(2)	0.250(3)	0.252(2)
γ574 keV	2.114(6)	2.131(7)	2.122(8)

Table 4. **The non-enhanced beam-on counting rates of the γ88 keV isomeric and 8^- band transitions compared to the averaged beam-off counting rates**

Transition	Beam-on intensity	Beam-off intensity	Enhancement
γ88 keV	0.673(6)	0.676(3)	- 0.003(7)
γ216 keV	3.53(3)	3.53(3)	- 0.005(29)
γ237 keV	0.421(9)	0.429(5)	- 0.01(1)
γ257 keV	0.790(6)	0.797(6)	- 0.007(9)
γ297 keV	0.427(5)	0.416(4)	+ 0.011(6)
γ454 keV	0.565(5)	0.567(3)	- 0.002(6)
γ495 keV	2.038(9)	2.034(5)	+ 0.004(10)
γ534 keV	0.256(4)	0.252(2)	+ 0.004(4)
γ574 keV	2.15(1)	2.122(5)	+ 0.028(11)
Averaged enhancement			+0.022(37)

In particular, this has resulted in the enhanced counting rates of all GSB transitions compared to the counting rates of the γ88 keV isomeric and 8^--state band transitions as well. Table 3 shows the counting rates of the γ88 keV isomeric and all 8^- band transitions (save for γ277 keV transition since its intensity is about order of magnitude lower than the intensity of the weakest transition in the list) acquired in the beam-off runs conducted before and after the irradiations used to obtain the averaged values for above-mentioned counting rates. The accuracies of obtained counting rates are better than 1 % even in the case of γ534 keV transition having the lowest intensity and reaches 0.25 % for the transitions with the highest intensities. In the event when the statistical uncertainty of averaged intensity turned out to be less than the data spread obtained before and after the irradiations the latter has been taken as the uncertainty for the corresponding averaged intensity.

The beam-induced decay of the isomer has resulted in the non-enhanced beam-on counting rates of the γ88 keV isomeric and 8^- band transitions compared to the averaged beam-off counting rates (Table 4) and the non-enhancement factor can be estimated as + (0.0221 ± ± 0.0366) %.

On the contrary to ^{178m2}Hf isomer triggering experiment conducted with 25 keV electron beam [8], in the case of 30 keV electrons the line widths have much more significantly broadened in the beam-on spectra compared to the beam-off spectra. Such broadening has produced very strong differentiation effect in the difference spectrum not allowing especially taking into account about twice lower enhancement to illustrate visually the ^{178m2}Hf isomer triggering in the difference spectrum. All the reasons for the differentiation are quite clearly shown in Fig. 2.

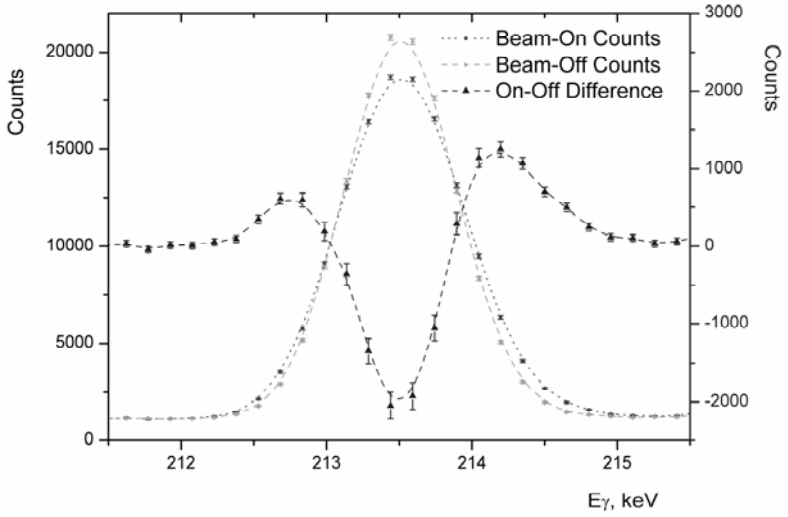

Fig. 2. Notably broadened line widths observed in the beam-on spectra compared to the beam-off spectra are a reason why the very strong differentiation is clearly seen in the difference spectrum. The channel widths are ~ 0.152 keV/channel.

3. Discussions and conclusions

In summary, we have repeated the initial ^{178m2}Hf isomer triggering experiments using the isomeric source not used before and the new experimental setup upgraded for this experiment. We see the evidence for the triggering of ^{178m2}Hf isomer by observing the enhanced counting rates of all ground-state band transitions. Our data are consistent with an

estimate for the triggering effect of 2.9 ± 0.7 %. In order to be compatible absolutely with the previous ^{178m2}Hf isomer triggering experiment when 25 keV electron beam was used the γ88 keV isomeric and γ216 keV 8^- band transitions can be taken into consideration as well. In this event our data are consistent with an estimate for the triggering effect of 2.7 ± 0.7 % and 2.1 ± 0.6 % when only the γ88 keV isomeric transition and both above-mentioned transitions have been taken into account, respectively.

In the same manner to that used in the previous works we can estimate, at least qualitatively and ignoring many unknown effects including all the absorption factors, the triggering cross-section as well. The enhancement factor S can be expressed through the triggering cross-section from the relation

$$S\ (N/\tau) = (N/A)\ F\ \sigma_{trig}\,, \qquad (1)$$

where N is the number of isomeric states in the target, τ is the lifetime of the isomeric state ($1.4 \cdot 10^9$ s), A is the area of the target, F is the number of incident electrons, and σ_{trig} is the triggering cross-section for the isomer de-excitation. N/τ is the normal decay rate of the isomeric nuclei in the target. This then gives

$$\sigma_{trig} = S\ [A/(\tau \cdot F)]. \qquad (2)$$

As a result, for the triggering effect S = 2.9 with the values of A = 0.8 cm^2 and F = $4 \cdot 10^{15}$ e/c (~200 μA), the cross-section estimate $\sigma_{trig} = 4.2 \cdot 10^{-27}$ cm^2, which is in good agreement with the value obtained in the previous ^{178m2}Hf isomer triggering experiment when 25 keV electron beam was used [8], can be deduced.

In order to estimate quantitatively the cross-section of electron induced triggering some assumptions should be made. It looks quite reasonable to suppose that the electron flux is linearly absorbed in the target, thus the averaged electron flux over the range of 30 keV electrons in Ta, which is about 2.15 μm, is one half of the incident electron flux F/2 = 2×10^{15} e/s. Taking into account that ^{178m2}Hf isomers should be uniformly distributed over the target thickness, only 2.15/300 = 0.76 % of total number of ^{178m2}Hf isomers in the target have really been irradiated. This then gives the size of electron induced triggering cross-section 1.1 b that is about four times less than the upper limit for the magnitude of photon induced triggering cross-section 4.7 b obtained in [7].

Additionally, it has been demonstrated that even using rather weak isomeric source the sensitivity of our ^{178m2}Hf isomer triggering experiments is much better than in the initial triggering experiments with dental x-ray machine.

More detailed conclusions can be made when much stronger isomeric source will be prepared and ready for use. In this case the increased emission of γ-rays could be detected in every separate transition supplying exclusively valuable information about possible scenarios and mechanisms of the induced acceleration of ^{178m2}Hf isomer decay. It would allow to conduct the coincidence measurements as well.

ACKNOWLEDGMENTS

We are indebted to Prof. Valentine V. Chorny and his colleagues for their help in the development of new experimental setup and to Prof. Aleksey I. Feoktistov and Dr. Vladimir T. Kupryashkin for their help in various aspects of these measurements. Special thanks to Prof. Victor A. Zheltonozhskiy, Dr. Anatoly P. Lashko, Dr. Leonid P. Sidorenko and Dr. Andrey N. Savrasov for their encouragement of this investigation.

REFERENCES

1. *Kirischuk V.I., McDaniel P., Collins C.B. et al.* Status and perspectives for the experimental investigation of ^{178m2}Hf isomer triggering by low-energy photons // Proc. of the 7th AFOSR Workshop “Isomers and Quantum Nucleonics” (June 26 - July 1, 2005, Dubna, Russia) / Ed. by S.A. Karamian, J.J. Carroll, E.A. Cherepanov. - JINR, Dubna, 2006. - P. 99 - 103; See also the references to our earlier papers in *Collins C.B., Zoita N.C., Rusu A.C. et al.* Accelerated decay of the 31-yr isomer of Hf-178 induced by low-energy photons and electrons // Laser Physics. - 2004. - Vol. 14. - No. 2. P. 154 - 165.
2. *Ahmad I., Banar J.C., Becher J.A. et al.* Search for x-ray induced decay of the 31-yr isomer of ^{178}Hf using synchrotron radiation // Phys. Rev. C. - 2005. - Vol. 71. - P. 024311 - 024326. See all the references to the previous papers inside as well.
3. *Kishimoto S., Yoda Y., Kobayashi Y. et al.* Nuclear excitation by electron transition on ^{197}Au by photoionization around the K-absorption edge // Phys. Rev. C. - 2006. - Vol. 74. - P. 031301-1 - 031301-4 (R).
4. *Dzyublik A.Ya.* Photo-induced nuclear excitation by electron transition // JETP Lett. - 2011. - Vol. 93. - P. 489 - 494.
5. *Dzyublik A.Ya.* Nuclear excitation at electron transition // Private communication.
6. *Harston M.R., Carroll J.J.* Limits on Nuclear Excitation and Deexcitation of ^{178}Hf^{m2} by Electron-Nucleus Coupling // Laser Physics - 2005. - Vol. 15. - P. 487 - 491.
7. *Carroll J.J., Karamian S.A., Propri R. et al.* Search for low-energy induced depletion of ^{178}Hf^{m2} at the Spring-8 synchrotron // Phys. Lett. B. - 2009. - Vol. 679. - P. 203 - 208.
8. *Kirischuk V.I., Strilchuk N.V.* New observations for the triggering of ^{178m2}Hf isomer embedded in Ta matrix by 25 keV electrons // Proc. of the 4-th Int. Conf. “Current Problems in Nuclear Physics and Atomic Energy” (Kyiv, Sept. 3 - 7, 2012). - Kyiv, 2013. - Part II. - P. 396 - 399.

ATOMIC IONIZATION AT POSITRON-ELECTRON ANNIHILATION AT β^+-DECAY

S. N. Fedotkin

Institute for Nuclear Research, National Academy of Sciences of Ukraine, Kyiv, Ukraine

The role of the nuclear charge screening and corrections to the Born approximation for the flying from atom electron in a process of atomic ionization at annihilation of positron with another electron of daughter's atom at β^+ - decay is studied. It was considered the processes of ionization of different atomic shells (n = 1, 2, 3, 4) at annihilation of positron, emitted at β^+ - decay with K- electron of daughter's atom. It is shown that the screening effect is important only for shell with n = 4. While corrections to the Born approximation plays the essential role for all shells. It is shown that the most probable process is related with emission of the another K- electron.

Introduction

When the positron beam fall on the atom may exist the one photon annihilation as well as the radiationless processes of atomic shell [1] or nuclear excitation [2 - 5]. Similar processes may occur also and at the β^+ -decay. In this case the process of β^+ -decay can be accompanied by nuclear or atomic shell excitation if happens annihilation of positron and atomic electron. The first process was studied experimentally [6] and theoretically [7] at β^+ -decay of $^{45}_{22}$Ti and the following excitation of nucleus $^{45}_{21}$Sc .

In papers [8, 9] was studied process of positron - K-electron annihilation at β^+ - decay which accompanied energy passing to other s-electron from K, L, M or N- shells. As result the last electron leaves the atom. The similar processes of the atomic ionization at electron capture were studied in [10]. For the wave functions of atomic electrons in a paper [9] was used the wave functions of hydrogen atom. But it is necessary to study the application of such consideration since the interaction between electrons in a case of high quantum numbers n plays the essential role. In the present paper this interaction is taking into account in some approximation by means of using of the effective charges.

The role of screening in process of atomic ionization at positron-electron annihilation in β^+ -decay

Let as consider process when occurs the annihilation of the β^+ - decay's positron with K-electron and energy released herewith is passed to another s-electron from K, L, M or N-shell (the corresponding quantum numbers are n = 1, 2, 3, 4). In the Figure is shown the Feynman diagram corresponding to this process:

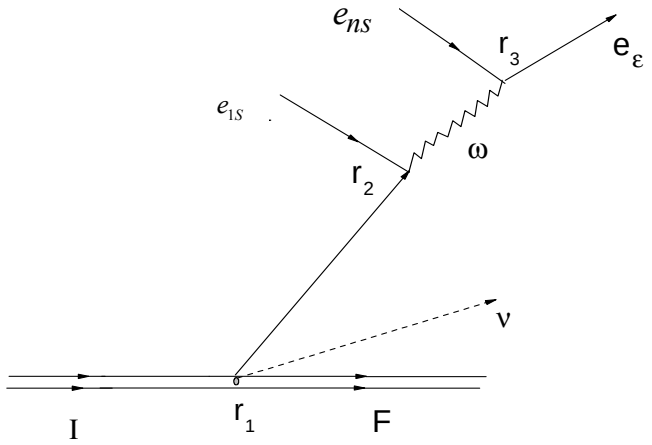

Annihilation of β^+ -decay's positron with K-shell electron
and following energy ω passing to other s-electron of n-shell.

Here I and F are initial and final nuclear states; e_{1S} and e_{ns} are the s-electrons of K- and n-atomic shells; e_ε is electron with energy ε and momentum $\mathbf{p}_\varepsilon$ which left atom, ν is neutrino. The probability amplitude for this process may be written as

$$S_{fi} = -\frac{ie^2}{16\pi^3} G_V \, M^{\beta}_{FI} \, \bar{\psi}_\nu \int\int d\mathbf{r}_2 \, d\mathbf{r}_3 \, (\bar{\psi}_\varepsilon(\mathbf{r}_3)\gamma_\mu \psi_{ns}(\mathbf{r}_3)) \frac{e^{i\omega|\mathbf{r}_2-\mathbf{r}_3|}}{|\mathbf{r}_2-\mathbf{r}_3|} (S_{E_{03}}(\mathbf{r}_2)\gamma_\mu \psi_{1s}(\mathbf{r}_2)) \delta(\mathrm{E}_3 - \varepsilon - p_\nu) \quad . \qquad (1)$$

Here ψ_{ns}, $\bar{\psi}_{\varepsilon}$ are the wave functions of s-electron from shell with quantum number n and of electron which left the atom respectively; $\bar{\psi}_{\nu}$ is the neutrino wave functions; M^{β}_{FI} is the nuclear matrix element; e is the electron charge; G_V is constant of the vector part of weak interaction. The maximum of electron energy which left atom is $E_3 = E_{IF} + E_{1S} + E_{nS}$, where $E_{IF} = E_F - E_I$, E_I and E_F are energies of the nuclear states, E_{1S} and E_{nS} are the atomic electron energies ($\hbar$ = c = 1).

The radial part of the wave functions of the bounded electron ψ_{ns} has view

$$\psi_{ns}(r) = \frac{\eta_{en}^{3/2}}{\sqrt{\pi}} \frac{e^{-\eta_{en} r}}{n} L^1_{n-1}(2\eta_{en} r), \tag{2}$$

where $L^1_{n-1}(2\eta_{en} r)$ is Laggera polinom; $\eta_{en} = Z_n m\alpha / n$, Z_n is effective nuclear charge, m is electron mass; α is the fine structure constant. The wave functions of another 1s-electron which annihilates with positron has the similar view but with change $\eta_{en} \to \eta_0 = Z_0 m\alpha$, where Z_0 is effective charge for this electron. Strictly speaking the wave functions (2) are not wave functions of the atomic electrons in Coulomb field of nucleus [11]. It is because for the wave functions of the atomic electrons in Coulomb field of nucleus is used the same nuclear charge Z for all electrons instead of the effective nuclear charge Z_n. The interaction between electrons of atomic shell is approximately taken into account by means of introduction of screening potential and therefore effective charge for each electron. We use here the approximated method offered by Sleter [12]. In this approach it is expected that each electron moves in Coulomb field of the nucleus and central field of another electrons. Sleter suggested some recipe for calculation of such effective charge Z_{ef} for the electron of any shell. The more consistent approaches need the complicated numerical calculations.

We consider the ratios of probabilities of these processes for the electrons from different shells. Therefore we will neglect by influence of Coulomb field on Green function and for this function is used the next expression $S_{E_{03}}(\mathbf{r}) = 2\pi^2 B_3 \frac{e^{ib_n r}}{r}$ [8], where

$$B_3 = \beta E_{03} + m, \qquad b_n = \sqrt{E_{03}^2 - m^2}, \qquad E_{03} = E_{1S} + E_{nS} - \varepsilon. \tag{3}$$

The probability amplitude S_{fi} in this case has view:

$$S_{fi} = -\frac{ie^2 \eta_0^{3/2} \eta_{en}^{3/2}}{16\pi^4} G_V M^{\beta}_{FI} (\bar{u}_{\varepsilon} \gamma_{\mu} u_{ns})(\bar{u}_{\nu} \gamma_4 (1+\gamma_5) B_3 \gamma_{\mu} u_{1S}) I_n(\mathbf{p}_{\varepsilon}) \delta(E_3 - \varepsilon - p_{\nu}). \tag{4}$$

Here $\bar{u}_{\nu}$, $\bar{u}_{\varepsilon}$, u_{ns} are bispinors parts of wave functions of neutrino, electron leaving the atom and atomic electron accordingly. Integral $I_n(\mathbf{p}_{\varepsilon})$ in (4) has the form

$$I_n(\mathbf{p}_{\varepsilon}) = \frac{1}{n} \int \frac{d\mathbf{q}\, d\mathbf{r}_2\, d\mathbf{r}_3}{q^2 \cdot r_2} e^{i\mathbf{r}_2\mathbf{q} + (ib_n - \eta_0) r_2} e^{i\mathbf{r}_3(\mathbf{q} - \mathbf{p}_{\varepsilon}) - \eta_{en} r_3} L^1_{n-1}(2\eta_{en} r_3). \tag{5}$$

For probability $W_{\beta^+ K,n}$ may be written the expression

$$W_{\beta^+ K,n} = 2\pi \sum_{s_e, s_{\nu}} \int \frac{d\mathbf{p}_{\varepsilon}}{(2\pi)^3} \frac{d\mathbf{p}_{\nu}}{(2\pi)^3} \left| U_{fi} \right|^2 \delta(E_3 - \varepsilon - p_{\nu}), \tag{6}$$

where amplitude U_{fi} is determined from (4) using definition (7):

$$S_{fi} = 2\pi U_{fi} \delta(E_3 - \varepsilon - p_{\nu}), \tag{7}$$

After summation over all spin projections and integration over angles and energies of neutrino we obtain the final expression for the probability $W_{\beta^+ K,n}$ of K-electron-positron annihilation and following ejection of s-electron of daughter atom from the shell with number n:

$$W_{\beta^+ K,n} = \frac{4\alpha^2 (Z_0 Z_n)^3 (m\alpha)^6}{\pi^3 n^3} \left| M^{\beta}_{FI} \right|^2 I_{\beta^+ K,n}. \tag{8}$$

Integral in (8) $I_{\beta^+K,n}$ has the following view

$$I_{\beta^+K,n}=\int_m^{E_3} d\varepsilon\sqrt{\varepsilon^2-m^2}\left(\frac{E_3-\varepsilon}{(\varepsilon^2-m^2+\eta_{sn}^2)^n}\right)^2\frac{[(\varepsilon+m)(\varepsilon-3m)^2+3(\varepsilon-m)^3]\left|3\eta_0-ib_n\right|^2}{\left|(\varepsilon^2-m^2+4\eta_0^2-b_n^2-4i\eta_0 b_n)(\eta_0-ib_n)\right|^2}\varphi_n(\varepsilon)\ . \tag{9}$$

The functions $F_n(\varepsilon)$ are given below at equation (10) for the different values n:

$$\varphi_1(\varepsilon)=1,\qquad \varphi_2(\varepsilon)=(\varepsilon^2-\eta_{e2}^2-m^2)^2,\qquad \varphi_3(\varepsilon)=[(\varepsilon^2-m^2)^2-\frac{10}{3}(\varepsilon^2-m^2)\eta_{e3}^2+\eta_{e3}^4]^2\ ,$$

$$\varphi_4(\varepsilon)=[(\varepsilon^2-m^2)^3-7(\varepsilon^2-m^2)^2\eta_{e4}^2+7(\varepsilon^2-m^2)\eta_{e4}^4-\eta_{e4}^6]^2\ . \tag{10}$$

Let us find the ratio of probability $W_{\beta^+K,1}$ (8) to the probability of β^+ - decay W_{β^+}:

$$\frac{W_{\beta^+K,1}}{W_{\beta^+}}=8\alpha^2(Z_0Z_1)^3(m\alpha)^6\ \frac{I_{\beta^+K,1}}{I_{\beta^+}}\ . \tag{11}$$

Integral I_{β^+} is defined at [8]. Formula (8) for the probability of this process is general and may be applied to any atom. Let us consider β^+ -decay of nucleus $^{45}_{22}\mathrm{Ti}$ to the nucleus $^{45}_{21}\mathrm{Sc}$.

Accordingly [12] the effective charges for electrons are $Z_{ef}=Z_n=Z-a_n$, where a_n are screening constants which defined as follows. The electrons are split on the groups: (1s); (2s, 2p); (3s, 3p); (4s, 4p) and so on. Then the following rules are used:

1. All electrons which quantum numbers n, l are bigger than quantum number n, l of electron under consideration do not influence on the screening constants a_n for given electron.

2. For s- and p-electrons every electron pertaining to group with quantum number n smaller by factor 1 than considered electron increase the screening constant a_n on 0.85. Each electron from more deep groups increases the screening constant a_n on 1.

3. Each electron pertaining to the same group that considered electron increases the screening constant a_n on 0.35. Exception is 1s group where the second electron of the same group increases the screening constant a_n on 0.3.

Using this prescriptions we obtain the following effective charges of s- electrons for different n for atom $^{45}_{21}\mathrm{Sc}$:

$$Z_0=20.7,\quad Z_1=21,\quad Z_2=17.7,\quad Z_3=10.75,\quad Z_4=2.8\ . \tag{12}$$

Using Z_{ef} (12) we obtain the following estimate for the ratio of probability positron - K-electron annihilation and following ejection of the second K-electron from atom $W_{\beta^+K,1}$ to the probability of β^+ -decay W_{β^+}

$$\frac{W_{\beta^+K,1}}{W_{\beta^+}}\approx 6\cdot 10^{-6}. \tag{13}$$

Accordingly (8), the ratios of the $W_{\beta^+K,n}$ to $W_{\beta^+K,1}$ for n = 2, 3, 4 are

$$\frac{W_{\beta^+K,n}}{W_{\beta^+K,1}}=\frac{1}{n^3}\left(\frac{Z_n}{Z_1}\right)^3\frac{I_{\beta^+K,n}}{I_{\beta^+K,1}}\ . \tag{14}$$

Calculating the integrals $I_{\beta^+K,n}$ (9) we obtain the following estimates for the ratios of probabilities of different processes with taking into account the screening of nuclear charge:

$$\frac{W_{\beta^+K,2}}{W_{\beta^+K,1}}\approx 0.18\qquad \frac{W_{\beta^+K,3}}{W_{\beta^+K,1}}\approx 0.059\qquad \frac{W_{\beta^+K,4}}{W_{\beta^+K,1}}\approx 0.01 \tag{15}$$

We shall note that in a case when the screened action of the atomic electrons is not taking into account the analogously ratios of probabilities are [9]:

$$\frac{W_{\beta^+K,2}}{W_{\beta^+K,1}} \approx 0.17 \qquad \frac{W_{\beta^+K,3}}{W_{\beta^+K,1}} \approx 0.057 \qquad \frac{W_{\beta^+K,4}}{W_{\beta^+K,1}} \approx 0.024 \tag{16}$$

Thereby the screened action of atomic electron change the ratios of probabilities according results (15) and (16) very small for the shells with n = 2, 3 and decreased nearly two times only for n = 4.

For the wave function of the flying from atom electron $\bar{\psi}_{\varepsilon}(\mathbf{r}_3)$ was used the plane wave function. This approximation is not enough correct at small electron energies. The preliminary calculations show that taking into account the corrections to the Born approximation [13, 14] for the flying from of atom electron plays important role for all shells. For example the first two ratios from (15) become bigger by factor nearly two.

If we want to take into account the Coulomb field in the Green function we need use in expression for $S_{E_{03}}(\mathbf{r})$ (3) instead of plane wave the Whittaker function $W_{S,1/2}(z)$ [15]:

$$e^{ib_n r} \to \Gamma(1-s) W_{S,1/2}(-2ib_n r), \tag{17}$$

where $s = i Z_{ef} \alpha \frac{E_{03}}{b_n}$. Using this new Green function we may calculate the probability amplitude S_{if} (1) and probability $W_{\beta^+K,n}$ (8) only numerically. In this case we obtain new estimate for the ratio (13):

$$\frac{W_{\beta^+K,1}}{W_{\beta^+}} \approx 7.4 \cdot 10^{-6} \tag{18}$$

But the ratios of probabilities (15) of different processes changed very small. The preliminary estimates for these ratios are following:

$$\frac{W_{\beta^+K,2}}{W_{\beta^+K,1}} \approx 0.19 \qquad \frac{W_{\beta^+K,3}}{W_{\beta^+K,1}} \approx 0.062 \qquad \frac{W_{\beta^+K,4}}{W_{\beta^+K,1}} \approx 0.011 \tag{19}$$

Therefore the annihilation process of positron with K-electron of daughter atom and following ejection from atomic shell the second K-electron is significantly more probable than processes where the second electron is eject from L, M or N shells. It is true independently from taking into account the screening or not. Taking into account the screening is important only for electron from upper shell n = 4. For the shells with quantum numbers n = 1, 2, 3 the influence of screening is not essential. The important role plays taking into account of Coulomb field at the calculation of wave function of the ejected from the atom electron and the Green function. The last two factors will are considered more consistent in the following paper.

REFERENCES

1. *Shimizu S., Mucoyama T., Nakayama Y.* Radiationless annihilation of positron in lead // Phys. Rev. - 1968. - Vol. 173, No. 2. - P. 405 - 416.
2. *Present R., Chen S.* Nuclear desintegration by positron- K-electron annihilation // Phys. Rev. - 1952. - Vol. 85. - P. 447 - 451.
3. *Mukoyama T., Shimizu S.* Nuclear excitation by positron annihilation // Phys. Rev. - 1972. - Vol. C5. - P. 95 - 99.
4. *Vishnevskii I.N., Zheltonozhskii V.A., Svyato V.P., Trishin V.V.* Nuclear excitation by positron photonless annihilation // Lett. JETP. - 1979. - Vol. 30. - P. 394 - 401.
5. *Grechuhin D.P.*, *Soldatov A.A.* Nuclear exitation at positron annihilation // JETP. - 1978. - Vol.74. - P. 13 - 22.
6. *Borozenec G.P., Vishnevskii I.N., Zheltonozhskii V.A.* // Sov. J. Nucl. Phys. - 1983. - Vol. 43. - P.13 - 22.
7. *Kolomietz V.M., Pununskiy O.G., Fedotkin S.N.* // Bull. Rus. Acad. Scien.: Phys. - 1988. - Vol. 52, No. 1. - P. 12 - 17.
8. *Fedotkin S.N.* Annihilation of positron ejected at β^+-decay with electron of daughter ato// Nucl. Phys. At. Energy. - 2010. - Vol. 11, No. 3. - P. 233 - 238.
9. *Fedotkin S.N.* Ionization of atoms at positron annihilation at β^+-decay // Nucl. Phys. At. Energy. - 2011. - Vol. 12, No. 4. - P. 335 - 338.
10. *Mukoyama T., Shimizu S.* L-shell contributions to internal ionization accompanying elect capture // Phys. Rev. - 1974. - Vol. 9. - P. 2300 - 2306.
11. *Bete G., SolpiterE.* Quantum mechanic of atom with one or two electrons. - M.: FizMatGiz, 1960. - 562 p.
12. *Slater J.C.* // Phys. Rev. - 1930. - Vol. 36. - P. 37 - 49.
13. *Elwert G.* // Ann. d. Phys. - 1939. - Vol. 34. - P. 178 - 189.
14. *Haitler V.* Quantum theory of radiation. - M.: Inostr. Lit., 1956. - 491 p.
15. *Glauber R.J., Martin P.C.* Radiative capture of orbital electrons // Phys. Rev. - 1956. - Vol. 104. - P. 158 - 175.

RESULTS FROM KamLAND-Zen

Azusa Gando
(for the KamLAND-Zen collaboration)

Research Center for Neutrino Science, Tohoku University, Sendai, Japan

We present results of the KamLAND-Zen experiment, measurement of ^{136}Xe double-beta decay with xenon loaded liquid scintillator. Based on an exposure of 112.3 days with 125 kg of ^{136}Xe, two-neutrino double-beta decay half-life is measured precisely to be $T_{1/2} = 2.30 \pm 0.02(\text{stat}) \pm 0.12(\text{syst}) \cdot 10^{21}$ yr. For the neutrino-less double-beta decay, no signal has been observed. A lower limit of half-life is set to $T_{1/2} > 6.2 \cdot 10^{24}$ yr at 90 % C.L. and the corresponding upper limit of the effective neutrino mass is ranged to (0.26-0.54) eV depending on the adopted nuclear matrix elements. Half-lives of Majoron-emitting neutrino-less double-beta decay with spectral index n = 1, 2, 3 and 7 are also estimated. As for "ordinary" decay (n = 1), we have obtained lower limit of half-life, $T_{1/2} > 2.7 \cdot 10^{24}$ yr at 90 % C.L., corresponding to the upper limit of the effective Majoron-emitting coupling, $\langle g_{ee} \rangle < (0.8 - 1.6) \cdot 10^{-5}$ (90 % C.L.). This result is the most stringent limit on $\langle g_{ee} \rangle$ for all double-beta decay nuclei and excludes a previously unconstrained region of this parameter.

1. Introduction

Double-beta decay is a very slow nuclear transition in which a nucleus (A, Z) decays into its isobar (A, Z + 2). It has two main decay modes that two-neutrino double decay and neutrino-less double beta decay. Two-neutrino double-beta decay, which emits two electrons and two anti-neutrinos, is described by known physics and its half-life has been measured with various nuclei. In contrast, neutrino-less double-beta decay was predicted theoretically, but not yet observed (except for one claim). Some models predict decay with the emission of new boson, called Majoron. It violates the lepton number conservation, and requires two characteristic neutrino properties; neutrinos have mass and are Majorana type lepton. Although absolute masses of neutrinos are not known yet, neutrino oscillation experiments established that neutrinos have non zero mass. If neutrino-less double-beta decay is observed, we can conclude the neutrino is Majorana particle. In addition, if its decay transition mechanism is simply exchange of a light Majorana neutrino, effective neutrino mass $\langle m_{ee} \rangle$, which is proportional to square root of neutrino-less double-beta decay rate, it provides neutrino mass hierarchy and information of absolute neutrino mass scale. Allowed region of $\langle m_{ee} \rangle$ narrowed by oscillation experiments are divided into three categories: degenerated hierarchy ($m_1 \sim m_2 \sim m_3$), inverted hierarchy ($m_2 > m_1 >> m_3$) and normal hierarchy ($m_3 >> m_2 > m_1$). In addition, there is a claim of observation at a few hundred meV, a part of degenerated hierarchy, with ^{76}Ge experiment [1]. From an experimental point of view, features of double-beta decay, very long half-life ($>10^{18}$ yr) and a few-MeV Q value, require a large amount of isotopes and low background environment. Recent experiments plan to use more than 100 kg of double-beta decay isotopes with various techniques to cover the degenerated hierarchy. If extension of nucleus mass to order of ton is realized, searching for inverted hierarchy will not be impossible.

KamLAND-Zen (KamLAND ZEro Neutrino double-beta decay) experiment studies ^{136}Xe (Q value = 2.476 MeV) double-beta decay with xenon loaded liquid scintillator. The first phase was started in September 2011, with ~300 kg of ^{136}Xe to explore the degenerated hierarchy and test the claim of observation.

2. Detector

KamLAND-Zen is a modification of the existing detector KamLAND, which primary designed to observe a few MeV neutrinos and has large and clean environment such as highly purified 1,000 ton of liquid scintillator (LS). The double-beta decay source/detector is 13 tons of Xe-loaded liquid scintillator (Xe-LS) contained in a 1.54-m-radius spherical inner balloon (IB). IB is constructed from 25-μm-thick transparent clean nylon film, and is suspended at the center of the KamLAND detector by 12 film straps made of the same material as IB. The Xe-LS consists of 82 % decane and 18 % pseudocumene (1,2,4-trimethylbenzene) by volume, 2.7 g/liter of the fluor PPO (2,5-diphenyloxazole), and (2.44 ± ± 0.01) % by weight of enriched xenon gas. The isotopic abundances in the enriched xenon were measured by a residual gas analyzer, to be (90.93 ± 0.05) % ^{136}Xe, (8.89 ± 0.01) % ^{134}Xe, and the other xenon isotopes are negligible. Xe-LS is surrounded by 1 kton of LS contained in a 6.5-m-radius spherical balloon. These density difference is controlled within 0.10 % to reduce the load for IB, and LS acts as an active shield for external gamma's and as a detector for internal radiation from the Xe-LS and/or IB. Scintillation light is monitored by 1,325 of 17-inch and 554 of 20-inch photomultiplier tubes (PMTs) mounted on the 18-m-diameter spherical stainless-steel tank. Stainless-steel tank is surrounded by outer detector fulfilled with 3.2 kton of pure water and 225 of 20-inch PMTs. It works as a water Cherenkov detector to vetoes/shields cosmic ray muons, their induced fast neutrons, and external gamma rays from surrounding rock. Schematic view of the detector is shown in Fig. 1. Detail of KamLAND detector is also described in Ref. [2].

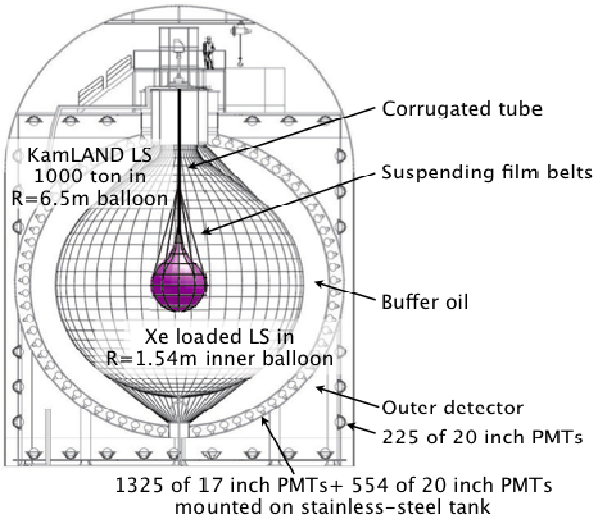

Fig. 1. Schematic view of KamLAND-Zen.

Modification of KamLAND for the double beta decay experiment was done in August 2011. The most important work, inner balloon installation, was successfully finished within 2 hours. Inner balloon was firstly inflated with "dummy-LS" which is Xe-free LS, to check its shape and to find possibility of leakage by small amount of Rn as a tracer. After that, Xe-LS filling was started to replace with dummy-LS. KamLAND (running for about 10 years) provides established DAQ and analysis tools. It is useful to monitor the detector condition during modification. Data taking for double beta decay started on September 24, 2011. After Rn decay and removal of "monitor system" consist of web cameras and LED lights, the data presented here were collected between October 12, 2011, and February 9, 2012.

3. Calibration and systematic uncertainty

KamLAND-Zen observes the summed energy of two electrons in the double-beta decay due to inseparable scintillation light of those. Event energy (visible energy) is estimated by the number of PMT hit and observed photoelectron (p.e.) after correcting various parameters such as gain, dark rate and transparency depending on the event vertices. The energy response is calibrated with three kind of sources that (1) ^{208}Tl 2.614 MeV gamma's from artificial calibration source of ThO2-W, (2) 2.225 MeV gamma's from spallation neutrons capture on protons, and (3) ^{214}Bi from ^{222}Rn (τ = 5.5 days) introduced during filling of liquid scintillator. From the energy distribution of (1) and Monte Carlo study, energy resolution is estimated to be σ = (6.6 ± 0.3) %/sqrt[E(MeV)]. The systematic variation of the energy reconstruction is monitored by (2) and it is less than 1.0 %. The detector energy response is also stable within 1.0 %. Energy nonlinearity effects caused by scintillator quenching and Cherenkov light production are constrained by 2.614 MeV peak of ^{208}Tl gamma ray and spectrum shape of ^{214}Bi, fitted well with simulation data. The vertex resolution is estimated to be σ □15 cm/ sqrt[E(MeV)] from radial vertex distribution of 1.2 < E < 2.0 MeV and 2.2 < E < 3.0 MeV window. The vertex reconstruction performance is also estimated with ^{214}Bi.

Fiducial volume (1.2-m-radius) is selected to suppress the background from IB material. Xe-LS volume in the fiducial volume is 7.24 m^3, corresponding amount of ^{136}Xe is 125 kg, and volume ratio of FV to total volume (16.51 ± ± 0.17 m^3) is 0.438 ± 0.005. Total volume was measured by a flow meter during the deployment. This volume fraction is compared with event-counting ratio of ^{214}Bi. In this calculation, IB surface background contribution is subtracted and its uncertainty is included to the event-counting ratio. The total difference of those ratios gives an estimate of the FV uncertainty (5.2 %). Other systematic uncertainties come from enrichment of ^{136}Xe (0.05 %), Xe concentration (0.34 %), detector energy scale (0.3 %), Xe-LS edge effect (0.06 %), and detection efficiency (0.2 %), and total systematic uncertainty is evaluated to 5.2 % from the quadratic sum of individual contributions.

4. Backgrounds

In the two-neutrino double-beta decay region, unexpected backgrounds, ^{134}Cs and ^{137}Cs are appeared. It is clearly seen that ^{134}Cs dominates around the IB boundary. Visible energy distribution as a function of R^3 distribution also shows the two peak of ^{134}Cs on the IB. Amount of ^{137}Cs can't be explained by the spallation of ^{136}Xe as Cs is not observed in Xe-LS. These rare artificial nucleus are brought by the fallout of Fukushima I reactor since fabrication of IB was done in Sendai (100 km far from the reactor). The ratio of observed activity of ^{134}Cs/^{137}Cs is consistent with soil sample measurements.

In the neutrino-less double-beta decay window (2.2 < E < 3.0 MeV), we also found unexpected peak (called 2.6 MeV peak). It distributes in Xe-LS uniformly and event rate is stable. This peak is fitted with neutrino-less double-beta decay spectrum firstly, but found to have ~3 % energy difference. The hypothesis that the peak is solely explained by neutrino-less double-beta decay event is excluded at more than 5σ C.L. by χ^2 test. It will be contemplated that it is well-known 2.614 MeV coming from ^{208}Tl (Q = 5.0 MeV) in ^{232}Th decay chain, however, it won't. KamLAND (or KamLAND-Zen) cannot distinguish beta and gamma rays. Then ^{208}Tl is detected with coincident beta/gamma in liquid scintillator, and its 2.614 MeV distribute in 3 - 5 MeV. There are two possibilities of the 2.6 MeV peak: long-lived radioactive impurities or cosmogenic spallation nuclei. Unfortunately, ex-situ measurements don't have enough sensitivity to determine isotopes due to its small amount. So we search all isotopes and decay path in ENSDF [3] database as the following procedure. For all tabulated decay chains in the database, the visible energy spectrum is calculated taking into account of alpha quenching, energy resolution, energy non-linearity and the time structure of the chain and pile-up in DAQ. Considering only nuclei with peak structure is in 2.4 - 2.8 visible-MeV, and has long-lived

parent whose lifetime is longer than 30 days, only 4 nuclei remains; $^{110}Ag^{m}$ (beta decay, τ = 360 day, Q = 3.01 MeV), ^{88}Y (EC decay, τ = 154 day, Q = 3.62 MeV), ^{208}Bi (EC decay, τ = 5.31 · 105 yr, Q = 2.88 MeV), and ^{60}Co (beta decay, τ = 7.61 yr, Q = 2.82 MeV) as potential background sources. 4 background candidates are all included in the fitting as free parameters since there is no clear identification of the background nor determination by an ex-situ measurement. From fitting, the presence of $^{110}Ag^{m}$ is dominated and ^{60}Co is strongly suppressed by the spectrum shape. The presence of $^{110}Ag^{m}$ may be explained by the spallation of ^{136}Xe at aboveground caused by high cosmic ray flux since Xe gas was enriched in Russia and sent to Japan by airplane. It might be a fallout product by the Fukushima I reactor accident in March 2011 since it is observed with Ge detector in the soil sample in Sendai. In contrast, the possibility of ^{208}Bi is quite difficult to explain. From Xe gas bottle and filter of Xe handling system used for making Xe-LS, ^{209}Bi, not ^{208}Bi, was detected with finite value by ICP-MS, but for Xe-LS, it was less than detection sensitivity. Calculated amount of ^{208}Bi from measured ^{209}Bi in Xe-LS cannot explain the peak in the window. If bismuth was contained in Xe-LS, the 2.3 MeV peak of ^{207}Bi should also appear, however, no clear peak found and ratio of ^{207}Bi /^{208}Bi is much smaller than expected. Short-lived nuclei with a lifetime between 100 sec and 30 days possibly supported by muon spallation is stringently constrained from the study of energy spectrum with close (A, Z) nuclei scaled with the production cross sections [4]. The estimated value from data with lifetime < 100 sec associated with muons depositing more than ~3 GeV is $6.7 \cdot 10^{-3}$ (ton·day)$^{-1}$ at 90 % C.L., where ton is a unit of the Xe-LS mass.

5. Result

We measured the half-lives of ^{136}Xe two-neutrino, neutrino-less and Majron-emitting double-beta decays from likelihood fit to the binned energy distribution between 0.5 and 4.8 MeV. The double-beta decays, and all backgrounds are fitted simultaneously. Main backgrounds contained in Xe-LS such as ^{85}Kr, ^{40}K, ^{210}Bi and the ^{238}U-^{222}Rn and ^{232}Th-^{224}Ra decay chains are unconstrained, while ^{222}Rn-^{210}Pb and ^{228}Th-^{208}Pb chains, ^{10}C, ^{11}C and contribution from IB such as ^{238}U chain, ^{232}Th chain, ^{134}Cs and ^{137}Cs are allowed to vary but constrained by the estimated rates respectively. For the possible backgrounds in Xe-LS, we also include reactor fallout which was found in the ex-situ measurement and have half-life longer than 30 days, such as ^{137}Cs, ^{134}Cs, $^{110}Ag^{m}$, $^{129}Te^{m}$, ^{95}Nb, ^{90}Y (from ^{90}Sr), and ^{89}Sr in the fit without any constraint. For the neutrino-less double-beta decay window, 4 nuclei ($^{110}Ag^{m}$, ^{208}Bi, ^{88}Y, ^{60}Co) searched from ENSDF are included in the fit as unconstrained free parameters. Calibration source ^{208}Tl and radon-induced ^{214}Bi are used for constraint of the energy scale uncertainty. The result of fit is presented in the Fig. 2. Totally 80 % of ^{136}Xe two-neutrino double-beta spectrum is in the fitting range and the best-fit number of decay is $(5.16 \pm 0.04) \cdot 10^{4}$, which correspond to an event rate of 81.3 ± 0.6 (ton·day)$^{-1}$. Combined background decay rate of $^{110}Ag^{m}$, ^{208}Bi, ^{88}Y, ^{60}Co is 0.20 ± 0.03 (ton·day)$^{-1}$. The limit of neutrino-less double-beta decay and Majron-emitting double-beta decay is calculated by floating these backgrounds. The upper limit (90 % C.L.) of neutrino-less double-beta decay is < 19 events, and corresponding event rate is < 0.03 (ton·day)$^{-1}$. For Majoron-emitting double-beta decay, half-lives for spectral index n = 1, 2, 3 and 7 are estimated. Decay rate in 1.2 < E < 2.0 MeV and 2.2 < E < 3.0 MeV are stable during the data-set.

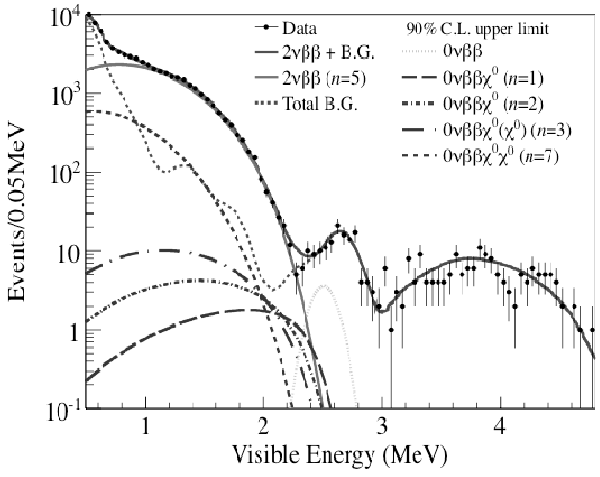

Fig. 2. Energy Spectrum of two-neutrino double-beta decay and best fit background. Limit of neutrino-less double-beta decay and Majoron-emitting double-beta decay are also shown.

From the fitting result, the measured half-life of ^{136}Xe two-neutrino double-beta decay is $T^{1/2} = 2.30 \pm \pm 0.02(stat) \pm 0.12(syst) \cdot 10^{21}$ yr. Estimated lower limit of ^{136}Xe neutrino-less double-bet decay half-life is $T^{1/2} > 6.2 \cdot 10^{24}$ yr at 90 % C.L. From this limit, corresponding upper limit of effective neutrino mass via QRPA (CCM SRC) [5] and shell model [6] is 0.24 - 0.56 eV. The half-lives of Majron-emitting double-beta decay is estimated to be $2.6 \cdot 10^{24}$, $1.0 \cdot 10^{24}$, $4.5 \cdot 10^{23}$, and $1.1 \times \times 10^{22}$ yr for spectral index n = 1, 2, 3 and 7, respectively. The most stringent upper limit on the effective Majoron-neutrino coupling is estimated from an ordinary (n = 1) decay to be $\langle g_{ee} \rangle < (0.8 - 1.6) \cdot 10^{-5}$ (90 % C.L.).

6. Summary

KamLAND-Zen measured ^{136}Xe two-neutrino double-beta decay half-life the most precisely. This result is consistent with the measurement by EXO-200 and significantly below the lower limit obtained by a previous experiment. Obtained lower limit of neutrino-less double-beta decay half-life improves slightly from KamLAND-Zen 1st result. Half-lives of Majoron-emitting neutrino-less double-beta decay with spectral index n = 1, 2, 3 and 7 are estimated, and for an ordinary (n = 1) decay, a factor of five more stringent than previous limits is obtained. Majorana coupling constant is the most stringent limit for all double-beta decay nuclei.

To improve the neutrino-less double-beta sensitivity, removal of contaminants in the Xe-LS such as distillation is planned. In the future, the largest systematic uncertainty from fiducial volume determination will be reduced by source calibration inside of the inner balloon.

REFERENCES

1. *Klapdor-Kleingrothaus H.V., Krivosheina I.V.* The evidence for the observation of $0\nu\beta\beta$ decay: the identification of $0\nu\beta\beta$ events from the full spectra // Mod. Phys. Lett. - 2006. - Vol. A21. - P.1547 - 1566.
2. *Abe S. et al.* (*KamLAND Collaboration*). Production of radioactive isotopes through cosmic muon spallation in KamLAND // Phys. Rev. - 2010. - Vol. C81. - P. 025807 (14 p.).
3. *ENSDF*, the Evaluated Nuclear Structure Data File available at // http://ie.lbl.gov/databases/ensdfserve.html (2006).
4. *Napolitani P. et al.* Measurement of the complete nuclide production and kinetic energies of the system ^{136}Xe + + hydrogen at 1 GeV per nucleon // Phys. Rev. - 2007. - Vol. C76. - P. 064609 (16 p.).
5. *Simkovic F., Faessler A., Muther H. et al.* $0\nu\beta\beta$-decay nuclear matrix elements with self-consistent short-range correlations // Phys. Rev. - 2009. - Vol. C79. - P. 055501 (10 p.).
6. *Menendez J., Poves A., Caurier E., Nowacki F.* Disassembling the nuclear matrix elements of the neutrinoless $\beta\beta$ decay // Nucl. Phys. - 2009. - Vol. A818. - P. 139 - 151.

ON THE STRUCTURE OF TRIAXIAL NUCLEI

H. G. Ganev

Joint Institute for Nuclear Research, Dubna, Moscow region, Russia

The dynamical symmetry limit of the two-fluid Interacting Vector Boson Model (IVBM), defined through the chain $Sp(12,R) \supset U(3,3) \supset U_p(3) \otimes \overline{U_n(3)} \supset SU^*(3) \supset SO(3)$, is applied for the description of nuclear collective spectra exhibiting axially asymmetric features. It is shown how stable triaxial shapes can be obtained in the IVBM by the addition of different types of perturbations to the $SU^*(3)$ model Hamiltonian. The influence of a Majorana interaction on the produced low-lying energy spectra is studied. The theoretical predictions are compared with the experimental data for two even-even nuclei assumed to be axially asymmetric. It is shown that by taking into account the full symplectic structures in the considered dynamical symmetry of the IVBM, the proper description of the low-lying energy spectra and the γ-band energy staggering of the nuclei under considerations can be achieved. The obtained results suggest a more complex and intermediate structure between the γ-rigid and γ-unstable limiting cases.

1. Introduction

It has been known for a long time that in certain mass regions nuclei with static deformation show deviations from a rigid axially symmetric picture. The possibility of static triaxial shapes for the ground state of nuclei is a long-standing problem in nuclear structure physics despite the fact that very few candidates have been found experimentally [1],[2]. In the geometrical approach the triaxial nuclear properties are usually interpreted in terms of either the γ-unstable rotor model of Wilets and Jean [3] or the rigid triaxial rotor model (RTRM) of Davydov et al. [4]. These models exploit the geometrical picture of nucleus according to the Collective Model of Bohr and Mottelson, expressed in terms of the intrinsic variables β and γ where the former specifies the ellipsoidal quadrupole deformation and the latter the degree of axial asymmetry. To describe the deviations from axial symmetry the model of Wilets and Jean assumes that the potential energy is independent of the γ-degree of freedom, while in the model of Davydov et al. one considers a harmonic oscillator potential with a minimum at finite values of γ producing a rigid triaxial shape of the nucleus.

The question of whether asymmetric atomic nuclei are γ-unstable or γ-rigid has been an ongoing and active issue in nuclear structure physics for over half a century. A number of signatures of γ-unstable and γ-rigid structures in nuclei has been discussed [1, 2, 5]. While it might be thought that the potential energy surfaces that are nearly γ-flat or which display deep minima for some value of γ would produce rather different nuclear spectra, this is in fact not the case. Indeed, the predictions for γ-unstable and γ-rigid potentials are nearly identical for most observables if the average value of γ in the first case, $\gamma_{\rm rms}$, is equal to the γ_{rigid} in the second, a situation occurring for example in the Os-Pt region. However, a clear distinction arises in the γ band, where both the γ-unstable and γ-rigid models exhibit an opposite energy staggering. The comparison of a γ-rigid rotor and a γ-unstable models yields similar ground state band energies, but the levels of γ-band are grouped as 2^+, (3^+, 4^+), (5^+, 6^+), ... in γ-unstable and as (2^+, 3^+), (4^+, 5^+), ... in γ-rigid models, respectively. Thus, obviously the structure of the γ band is crucial for the identification of the shape in the real nuclei and hence for the manifestation of the γ degrees of freedom.

In Ref. [6] a new dynamical symmetry limit of the two-fluid Interacting Vector Boson Model (IVBM) was introduced, which seems to be appropriate for the description of deformed even-even nuclei, exhibiting triaxial features. It was shown there that the addition of Majorana interaction to the $SU^*(3)$ model Hamiltonian produces a stable triaxial minimum. In this paper, we develop further our theoretical approach and focus on the γ-band properties and show how the γ-band energies (and the corresponding energy staggering) are affected by the presence of the introduced interaction. The theoretical predictions are compared with the experimental data for the two isotopes ^{192}Os and ^{112}Ru, respectively. It is shown that by taking into account the full symplectic structures in the considered dynamical symmetry of the IVBM, the proper description of the energy spectra and the γ-band energy staggering of the nuclei under considerations can be achieved.

2. The algebraic structure of the U(3,3) dynamical symmetry

It was suggested by Bargmann and Moshinsky [7] that two types of bosons are needed for the description of nuclear dynamics. It was shown there that the consideration of only two-body system consisting of two different interacting vector particles will suffice to give a complete description of N three-dimensional oscillators with a quadrupole-quadrupole interaction. The latter can be considered as the underlying basis in the algebraic construction of the *phenomenological* IVBM.

The algebraic structure of the IVBM [8] is realized in terms of creation and annihilation operators of two kinds of vector bosons $u_m^\dagger(\alpha)$, $u_m(\alpha)$ (m = 0,±1), which differ in an additional quantum number α=±1/2 (or α=p and n) -the projection of the T-spin (an analogue to the F−spin of IBM-2 or the I−spin of the particle-hole IBM). We consider the following reduction chain of the dynamical symmetry group $Sp(12,R)$ of the IVBM for studying the triaxiality in atomic nuclei:

$$Sp(12,R) \supset U(3,3) \supset U(3,3) \supset U_p(3) \otimes \overline{U_n(3)} \supset SU^*(3) \supset SO(3), \tag{1}$$
$$\nu \qquad\qquad [N_p]_3 \quad [-N_n]_3 \qquad\quad K \quad L$$

where the labels below the different subgroups are the quantum numbers corresponding to their irreducible representations (irreps). As it was shown in Ref. [6], this dynamical symmetry is appropriate for nuclei in which the one type of particles is particle-like and the other is hole-like.

All bilinear combinations of the creation and annihilation operators of the two vector bosons generate the boson representations of the non-compact symplectic group $Sp(12,R)$:

$$F_M^L(\alpha,\beta) = \sum_{k,m} C_{1k,1m}^{LM} u_k^\dagger(\alpha) u_m^\dagger(\beta), \qquad G_M^L(\alpha,\beta) = \sum_{k,m} C_{1k,1m}^{LM} u_k(\alpha) u_m(\beta) \tag{2}$$

$$A_M^L(\alpha,\beta) = \sum_{k,m} C_{1k,1m}^{LM} u_k^\dagger(\alpha) u_m(\beta), \tag{3}$$

where $C_{1k,1m}^{LM}$, which are the usual Clebsch-Gordan coefficients for $L = 0,1,2$ and $M = -L,-L+1, \ldots, L$, define the transformation properties of (2) and (3) under rotations. We also introduce the following notations $u_k^\dagger(\alpha = 1/2) = p_k^\dagger$ and $u_k^\dagger(\alpha = -1/2) = n_k^\dagger$. In terms of the p- and n-boson operators, the Weyl generators of the ladder representation of $U(3,3)$ are [6]

$$p_k^\dagger p_m, \quad p_k^\dagger n_m^\dagger, \quad -n_k p_m, \; -n_m^\dagger n_k \tag{4}$$

which are obviously a subset of symplectic generators (2, 3). The first-order Casimir operator of $U(3,3)$ is

$$C_1[U(3,3)] = \sum_k (p_k^\dagger p_k - n_k^\dagger n_k), \tag{5}$$

and does not differ essentially from the operator T_0 defined in [8] $T_0 = 1/2 C_1[U(3,3)] + 3/2$. The $U(3,3)$ irreps (ladder irreducible representations) contained in either (even) $<(1/2)^6>$ or (odd) $<(1/2)^5 3/2>$ irrep of $Sp(12,R)$ are denoted by ν, and their branching rules are given in [6]. In the present application we consider only the even irreducible representation of $Sp(12,R)$.

The direct product $U_p(3) \otimes \overline{U_n(3)}$ subalgebra is defined by the subset of the number preserving generators (4) of $U(3,3)$, namely

$$p_k^\dagger p_m, \quad -n_m^\dagger n_k \tag{6}$$

Then, the combined (particle-hole) algebra $U^*(3)$ is simply expressed by the linear combination operators $A_{km} \equiv \{p_k^\dagger p_m - n_m^\dagger n_k\}$ of (6), which can also be defined in the following way [6]

$$M = N_p - N_n, \qquad L_M = L_M^p + L_M^p, \qquad Q_M = Q_M^p - Q_M^p. \tag{7}$$

The second order Casimir operator of $U^*(3)$ is $C_2[U^*(3)] = \sum_{ij} A_{ij} A_{ji}$. The $SU^*(3)$ algebra is obtained by excluding the operator M which is the single generator of the $O(2)$ algebra, whereas the angular momentum algebra $SO(3)$ is generated by the generators L_M only.

We can label the basis states according to the chain (1) as:

$$|\nu; N_p, N_n; (\lambda,\mu); KL>, \tag{8}$$

where ν is the eigenvalue of the $U(3,3)$ first order Casimir operator, N_p and N_n label the $U_p(3) \otimes \overline{U_n(3)}$ irreps, (λ,μ) are the $SU^*(3)$ quantum numbers, K is the multiplicity index in the reduction $SU^*(3) \supset SO(3)$, and L is the angular momentum of the corresponding collective state.

Symplectic classification of the SU*(3) basis states

$N\backslash\nu$	$\cdots$	6	4	2	0	−2	−4	−6	$\cdots$
0					$(0,0)$				
2				$(2,0)$	$(1,1)$ $(0,0)$	$(0,2)$			
4			$(4,0)$	$(3,1)$ $(2,0)$	$(2,2)$ $(1,1)$ $(0,0)$	$(1,3)$ $(0,2)$	$(0,4)$		
6		$(6,0)$	$(5,1)$ $(4,0)$	$(4,2)$ $(3,1)$ $(2,0)$	$(3,3)$ $(2,2)$ $(1,1)$ $(0,0)$	$(2,4)$ $(1,3)$ $(0,2)$	$(1,5)$ $(0,4)$	$(0,6)$	
⋮		⋮	⋮	⋮	⋮	⋮	⋮	⋮	

The basis states associated with the even irreducible representation of the $Sp(12,R)$ can be constructed by the application of powers of raising generators $F_M^L(\alpha,\beta)$ of the same group on the boson vacuum state. Each raising operator will increase the number of bosons N by two. The $Sp(12,R)$ classification scheme for the $SU^*(3)$ boson representations is shown in the Table. The ladder representations of the non-compact algebra $U(3,3)$ act along the columns ("ladders") in the space of the boson representation of the $Sp(12,R)$ algebra, defined through the eigenvalues ν of the first Casimir operator M of the $U(3,3)$ algebra. There exists a connection between this ladder representation ("vertical classification") and the boson representation of $U(6)\subset Sp(12,R)$ ("horizontal classification"). Each row (fixed N) of the Table corresponds to a given irreducible representation of the $U(6)$. Note that the number of bosons $N = N_p + N_n$ is not a good quantum number along the ladder representations of $U(3,3)$.

3. The energy spectrum

The most general Hamiltonian with $SU^*(3)$ symmetry consists of the Casimir invariants of $SU^*(3)$ and its subgroup $SO(3)$

$$H = aC_2[SU^*(3)] + bC_2[SO(3)]\,, \tag{9}$$

where $C_2[SU^*(3)] = 1/6Q^2 + 1/2L^2$ and the quadrupole operator $Q_M = Q_M^p - Q_M^p$. The spectrum of this Hamiltonian is determined by

$$E = a(\lambda^2 + \mu^2 + \lambda\mu + 3\lambda + 3\mu) + bL(L+1)\,. \tag{10}$$

We point out that there are very large degeneracies in the resulting energy spectrum caused by the large values of λ and μ, which is not observed in the real nuclear spectra. In the present application we consider $Sp(12, R)$ to be the group of the dynamical symmetry of the model and make use of the following Hamiltonian:

$$H_{U(3,3)} = a_1M^2 + b(N_n^2 - N_p^2) + a_3C_2[SU^*(3)] + b_3C_2[SO(3)]\,, \tag{11}$$

expressed as a linear combination of the Casimir operators of the different subgroups in the chain (1). The Hamiltonian (11) is diagonal in the basis (8). Then its eigenvalues that yield the spectrum of the nuclear systems are:

$$E(\nu; N_p, N_n; (\lambda,\mu); L) = a_1\nu^2 + b(N_n^2 - N_p^2) + a_3(\lambda^2 + \mu^2 + \lambda\mu + 3\lambda + 3\mu) + b_3L(L+1)\,. \tag{12}$$

The energy spectrum determined by Eq.(12) will be the starting point for our further calculations.

4. Triaxial shapes in the IVBM

In Ref.[6] it has been shown that the addition of different types of perturbations to the $SU^*(3)$ energy surface, in particular the addition of a Majorana interaction and an $O(6)$ term to the $SU^*(3)$ model Hamiltonian, produces a stable triaxial minimum in the potential energy surfaces. In present work we consider only the inclusion of a Majorana interaction to the model Hamiltonian and study the influence of the latter on the produced low-lying energy spectra. We expect that many experimental properties of some deformed even-even nuclei, exhibiting axially asymmetric features, to be explained with the perturbed Hamiltonian under consideration.

We present a schematic calculations starting with the Hamiltonian H (11) to which a perturbation term is added. The Hamiltonian which contains Majorana interaction is written in the form

$$H = H_{U(3,3)} + aM_3\,, \tag{13}$$

where the Majorana operator is defined as $M_3 = 2(p^\dagger \times n^\dagger)^{(1)} \cdot (p \times n)^{(1)}$ and it is related to the $U(3)$ second order Casimir invariant $C_2[U(3)]$, defined in Ref.[8], via the relation $C_2[U(3)] = N(N+2) - 2M_3$. The Hamiltonian H contains the pure $SU^*(3)$ symmetry, when only $a_3 \neq 0$ in Eq. (11).

In our application, the most important point is the identification of the experimentally observed states with a certain subset of basis states from symplectic extension of the model (see the Table). As in our previous applications of the symplectic IVBM, we use the algebraic concept of "yrast" states, introduced in [9]. According to this concept we consider as yrast states the states with given L that minimize the energy with respect to the number of vector bosons N that build them. Since the GSB in the triaxial nuclei is supposed to belong to the $SU^*(3)$ irreps of the type ($\lambda = N_p$, $\mu = N_n$), we map the states of the GSB onto the ladder representation of $U(3,3)$ with $v = 0$ (the middle column of the Table). The presented mapping of the experimental states onto the *SU(3)* basis states, using the algebraic notion of yrast states, is a particular case of the so called "stretched" states [10], which in our case are defined as the states of the type $(\lambda,\mu) = (\lambda_0 + k, \mu_0 + k)$, where k = 0, 2, 4, ... In the symplectic extension of the IVBM the change of the number k, which is related in the applications to the angular momentum L of the states, gives rise to the collective bands. Thus, explicitly the states of the GSB are identified with the $SU^*(3)$ multiplets $(\lambda, \mu) = (k, k)$, where $k = L$. The same type of stretched states $(\lambda_0 + k, \mu_0 + k)$ are associated with the states from the γ band, where the symplectic band head structure of the considered band is determined by the initial number of phonons $N_0 = \lambda_0 + \mu_0 = 6$ $(\lambda_0 = 2, \mu_0 = 4)$. Additionally, for the γ band to each single $SU^*(3)$ irrep (λ, μ) (k-fixed) we put into correspondence two consecutive states with angular momentum L and $L + 1$, respectively. This choice allows us to reproduce the doublet structure of the γ-band. We note that the present choice of the $SU^*(3)$ multiplets associated with the states of the γ-band is quite similar to the phonon multiplet structure of the γ-band states within the framework of the IBM-1 in its $O(6)$ limit, where the states cluster in doublets differing in the $O(5)$ label τ, which corresponds to the phonon-like quantum number Λ in the γ–unstable model of Wilets and Jean [1]. The Majorana term in the Hamiltonian H (13) is not diagonal in the basis (8), and hence mix different SU(3) multiplets.

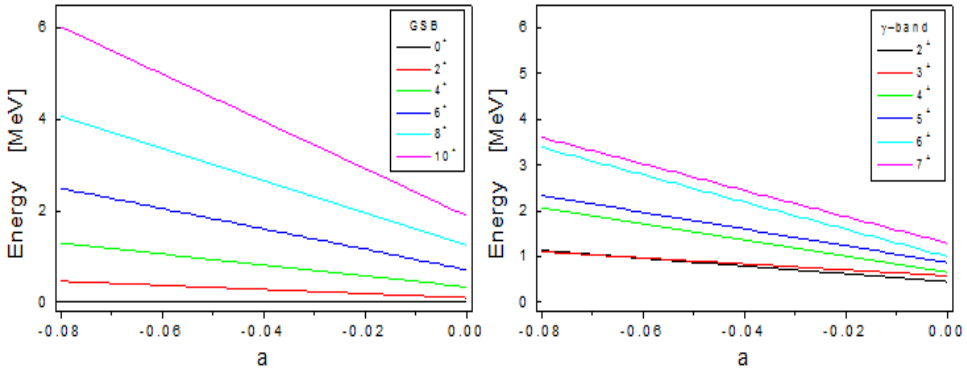

Fig. 1. Energies of the ground and γ bands as a function of the strength parameter a.

To show the influence of the Majorana interaction on the energy spectrum, we present the model calculations with the IVBM Hamiltonian (13) in which the Majorana interaction is included and diagonalyzed numerically. The evolution of the ground and γ bands as a function of the strength parameter a is shown in Fig. 1. The values of the rest model parameters are a_1=0.10343 MeV, b = −0.00274 MeV, a_3 = −0.00116 MeV and b_3= 0.02092 MeV. From the Figure one can see that the inclusion of the Majorana term does not change the level spacings of the ground state band and hence preserves its character. It can be also seen that the γ-rigid-like doublet structure of the γ-band is conserved for a wide interval of the values of the parameter a, but for a = 0 MeV (no mixing of the SU(3) irreps) one obtains the well known γ-unstable-like structure. For $a \simeq -0.005 \div -0.01$ MeV we obtain intermediate situation with more regular spacing of the energy levels.

5. Numerical results

As an example, our theoretical considerations are applied for the calculation of the excitation energies of the ground and γ bands in the two nuclei ^{192}Os and ^{112}Ru, which are assumed in the literature to possess triaxial shapes. The values of the model parameters a_1, b, a_3, b_3 and a are determined by fitting the energies of the ground and γ-bands for the corresponding isotopes to the experimental data [11], using a χ^2 -procedure. The theoretical predictions, compared with experiment, are presented in Fig. 2. From the Figure one can see that the doublet structure of the γ band, predicted by the model, is well reproduced except for the first doublet where it is more pronounced than the experimentally observed one. Nevertheless, the calculated energy levels of both ground state and γ bands agree rather well with the observed data except the first and the last collective states of the γ band.

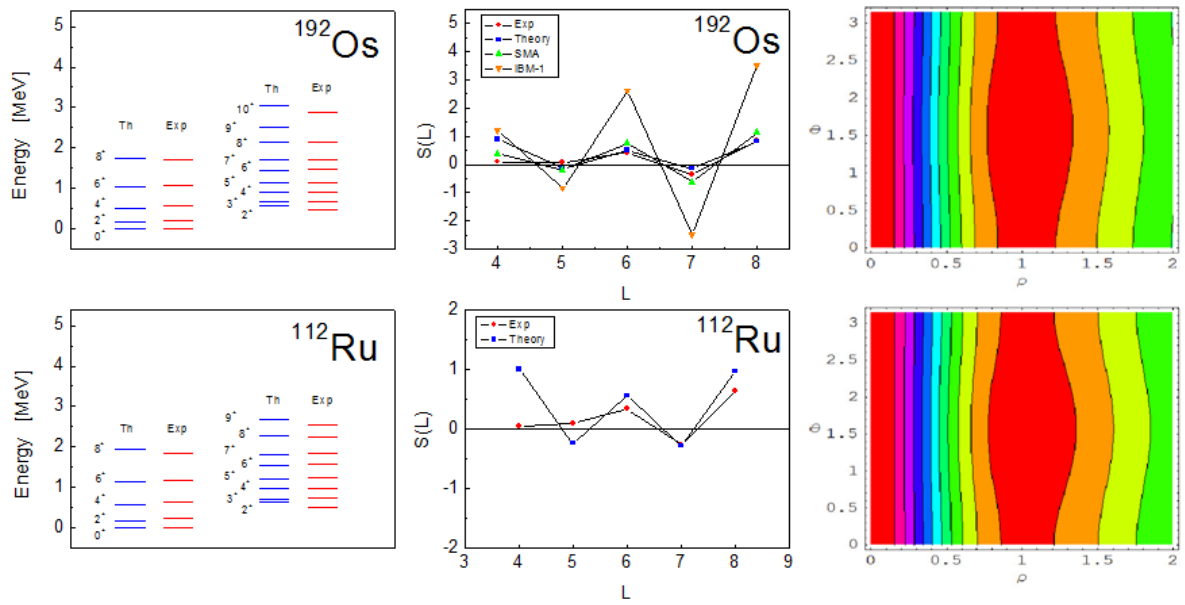

Fig. 2. The excitation energies for GSB and γ band, the calculated and experimental staggering *S(L)* of the γ band, and the scaled energy surfaces $\varepsilon(\rho, \theta)$ for ^{192}Os and ^{112}Ru, respectively. The values of the model parameters are $a_1 = 0.10343$ MeV, $b = -0.00274$ MeV, $a_3 = -0.00116$ MeV and $b_3 = 0.02092$ MeV for ^{192}Os, and $a_1 = 0.11446$ MeV, $b = -0.00561$ MeV, $a_3 = -0.00140$ MeV and $b_3 = 0.02126$ MeV for ^{112}Ru, respectively.

There is a long-standing debate about the nature of the spectra of *Os* and *Pt* isotopes. Some groups consider these nuclei as being γ-unstable [12 - 14], while other as asymmetric rotor [4], which assumes rigidity in the γ degrees of freedom. The Os and Pt isotopes have been treated in terms of the IBM in the transition region from the rotor to the γ–unstable limit [15]. In Ref. [16], these isotopes are considered as a text-book example of this transition. In Ref. [17] it was shown that the empirical deviations from the *O*(6) limit of the IBM, in the Os-Pt region, can be interpreted by introducing explicitly triaxial degrees of freedom, suggesting a more complex and possibly intermediate situation between γ-rigid and γ-unstable properties. Indeed, as it can be seen from the presented examples, the experimentally observed level spacings in the γ band are more regular. In terms of the potentials, this means that the true potentials are γ-dependent.

A number of signatures of γ-unstable and γ-rigid structures in nuclei has been discussed [1, 2, 5]. Many authors investigated the transition from the γ-unstable regime to a triaxial behavior. The two nuclear phases, as it was mentioned, are characterized by different doublet structures in the γ band. A useful quantity that distinguishes these two cases is the energy staggering signature [1, 2]: $S(L) = [E(L) - E(L-1)] - [E(L-1) - E(L-2)] / E(2_g^+)$, where $E(L)$ stands for the energy of the state L^+ belonging to the γ band. Analysis of the experimental staggering in different isotopic chains reveals several different patterns [2] that can be categorized based on the standard limits discussed in the IBM. Just to mention few cases, the *Xe*, *Ba* and *Ce* nuclei are well-known examples [17 - 19] of the transition between vibrational and γ-unstable structures that show strong staggering with negative *S*(*L*) values at even-*L* and positive *S*(*L*) values at odd-*L* spins. The heavy rare-earth nuclei ($N > 82$), known to display an axially symmetric behavior, show a similar staggering pattern with a smaller overall magnitude than that observed in the *Xe*, *Ba* and *Ce* isotopes. Nuclei that display staggering patterns very different from those described above are scarce and include, for example, ^{190}Os, ^{192}Pt, and ^{112}Ru. These nuclei develop a staggering pattern where *S*(*L*) is positive for even-*L* and negative for odd-*L* values, i.e. with the opposite phasing than in the other two cases mentioned above. As shown in Ref. [2] the geometrical models and the IBM-based models can describe the basic trends observed in the experimental staggering. It is shown that the geometrical models that incorporate rigid triaxiality are characterized by strong staggering with positive values for even-*L* and negative values for odd-*L* spins. The staggering is largest for the RTRM where it increases linearly with *L* and smallest for the models that use a harmonic oscillator β^2 potential. Similarly, the IBM shows a jump over to the triaxial region along the transition from *U*(5) to *SU*(3), characterized by the same staggering pattern as the one found in the geometrical models but with a smaller overall magnitude.

To see whether this signature is captured by the present approach, we plotted the function *S*(*L*) within the framework of the IVBM for the two nuclei under consideration in Fig. 2, compared with the experimental data. For ^{192}Os, the predictions of the IBM-1 with a term quadratic in $(Q \otimes Q \otimes Q)_0$ [20] and sextic and Mathieu approach (SMA) [21] that incorporate a γ-rigid structures are also shown. As it can be seen from the Figure, the present approach predicts a staggering pattern for ^{192}Os and ^{112}Ru similar to the one observed in the geometrical models and the IBM that incorporate triaxiality. In both cases, the overall magnitude of the theoretical staggering is similar or slightly larger than the magnitude of the staggering observed in the considered axially asymmetric nuclei. The γ-rigid staggering is well developed in the region $L \geq 5$ where also its magnitude increase with the spin. The latter suggests that the triaxiality

evolves together with the collectivity.

The geometry associated with a given Hamiltonian can be obtained by the coherent state method. The standard approach to obtain the geometrical properties of the system is to express the collective variables in the intrinsic (body-fixed) frame of reference. Then the ground-state energy surface is obtained by calculating the expectation value of the boson Hamiltonian (13) with respect to the corresponding coherent states. In the case of IVBM, the (scaled) energy surfaces $\varepsilon(\rho,\theta)$ depend on two coherent state parameters ρ and θ, determining the "shape" of the nucleus [6, 8]. The latter are related to the standard collective model "shape" parameters β and γ. For more details we refer the reader to the Refs.[6],[8]. We plot the ground state energy surfaces for ^{192}Os and ^{112}Ru with the model parameters obtained in the fitting procedure in the form of contour plots in Fig. 2. From the Figure one sees a nearly γ-flat potentials with an extremely shallow ($\sim$ 4 - 6 keV) triaxial minima for the ground state in the two nuclei under consideration. The triaxial minima are obtained at $\rho_0 = 1$ and $\theta_0 = 90^0$ which correspond to $\gamma_{eff} = 30^0$ [6]. In other words, the potentials obtained in the present approach are indeed γ-dependent, representing the case of mixing of γ-flat and γ-rigid structures.

6. Summary

In the present work, we apply one of the dynamical symmetry limits of the two-fluid Interacting Vector Boson Model, defined through the chain $Sp(12,R) \supset U(3,3) \supset \quad U_p(3) \otimes \overline{U_n(3)} \supset SU^*(3) \supset SO(3)$, for the description of two even-even nuclei, possessing axial asymmetry. We have investigated the effect of the introduction of a Majorana interaction to the $SU^*(3)$ model Hamiltonian. It is shown that the latter introduces a potential which has a minimum at $\gamma = 30^0$ and change the γ-band doublet structure from that of γ-unstable to that of γ-rigid type. This allows for the description of these two limiting cases, as well as the situation in between, which is characterized by more uniform energy level spacings in the γ-band, and described actually by γ-dependent potentials.

The theoretical predictions are compared with the experimental data for the two isotopes ^{192}Os and ^{112}Ru. It is shown that by taking into account the full symplectic structures in the considered dynamical symmetry of the IVBM, the proper description of the energy spectra and the γ-band energy staggering of the nuclei under considerations can be achieved. The obtained results show that the potential energy surfaces for ^{192}Os and ^{112}Ru, possess almost γ-flat potentials with extremely shallow triaxial minima, suggesting a more complex and intermediate situation between γ–rigid and γ-unstable structures.

REFERENCES

1. *Zamfir N.V., Casten R.F.* // Phys. Lett. – 1991. – Vol. B260. – P. 265.
2. *McCutchan E.A., Bonatsos D., Zamfir N.V., Casten R.F.* // Phys. Rev. – 2007. – Vol. C76. – P. 024306.
3. *Wilets L., Jean M.* // Phys. Rev. –1956.– Vol. 102. – P. 788.
4. *Davydov A.S., Filippov G.F.* // Nucl. Phys. – 1958. – Vol. 8. – P. 237.
5. *Liao Ji-zhi* // Phys. Rev. – 1995. – Vol. C51. – P. 141; *Bihari C. et al.* // Phys. Scr. – 2008. – Vol. 77. – P.055201; *Bihari C. et al.* // Phys. Scr. – 2008. – Vol. 78. – P. 045201; *Mani Varshney* // Phys. Scr. – 2011. – Vol. 83. – P. 015201.
6. *Ganev H.G.* // Phys. Rev. – 2011. – Vol.C84. – P. 054318.
7. *Bargmann V., Moshynsky M.* // Nucl. Phys. – 1960. – Vol. 18. – P. 697; *Bargmann V., Moshynsky M.* // Nucl. Phys. – 1961. – Vol. 23. – P. 177.
8. *Ganev H.G.* // Phys. Rev. – 2011. – Vol. C83. – P. 034307.
9. *Ganev H., Garistov V.P., Georgieva A.I.* // Phys. Rev. – 2004. – Vol. C69. – P. 014305.
10. *Rowe D.J.* // Rep. Prog. Phys. – 1985. – Vol. 48. – P.1419.
11. *Evaluated* Nuclear Structure Data File (ENSDF), http://ie.lbl.gov/databases/ensdfserve.html
12. *Kumar K., Baranger M.* // Nucl. Phys. – 1968. – Vol. A122. – P.273.
13. *Leander G.* // Nucl. Phys. – 1976. – Vol. A273. – P. 286.
14. *Seiwert M., Hess P., Maruhn J., Greiner W.* // Phys. Rev. – 1981. – Vol. C23. – P. 2335; *Hess P., Maruhn J., Greiner W.* // J. Phys. G. – 1981. – Vol. 7. – P. 737.
15. *Casten R. F., Cizewski J.A.* // Nucl. Phys. – 1978. – Vol. A309. – P. 477.
16. *Casten R.F.* Nuclear Structure from a Simple Perspective. – Oxford: Oxford University, 1990.
17. *Casten R.F., Von Brentano P., Heyde K. et al.* // Nucl. Phys. – 1985. – Vol. A439. – P. 289.
18. *Puddu G., Scholten O., Otsuka T.* // Nucl. Phys. – 1980. – Vol. A348. – P. 109.
19. *Zamfir N.V., Casten R.F.* // Phys. Lett. – 1985. – Vol. B152. – P. 22.
20. *Thiamova G.* // Eur. J. Phys. – 2010. – Vol. A45. – P. 81.
21. *Raduta A.A., Buganu P.* // Phys. Rev. – 2011. – Vol. C83. – P. 034313.

NEW OBSERVATIONS FOR THE TRIGGERING OF ^{178m2}Hf ISOMER EMBEDDED IN Ta MATRIX BY 25 keV ELECTRONS

V. I. Kirischuk, N. V. Strilchuk

Institute for Nuclear Research, National Academy of Sciences of Ukraine, Kyiv, Ukraine

^{178m2}Hf isomer triggering has been studied using new experimental setup developed at Kharkov National University and installed at Kyiv Institute for Nuclear Research. The target presenting a single Ta foil of 100 μm thickness with ^{178m2}Hf isomeric activity of 5 Bq has been irradiated by 25 keV electron beam. The enhanced counting rates of all the ground-state band transitions, just as γ89 keV isomeric and γ216 keV 8^--state band transitions have been observed. Our data are consistent with an estimate for the triggering effect of 2.8 ± 0.8 % and corresponding triggering cross-section can qualitatively be estimated as $\sigma_{trig} = 5.4 \cdot 10^{-27}$ cm^2.

1. Background and introduction

The 16^+ four-quasiparticle state of the nucleus ^{178}Hf, a K isomer with the excitation energy E_e = 2.4474 MeV and half-life $T_{½}$ = 31 years, is considered as the most promising on the way to create gamma-ray sources controlled by low energy photons. Consequently, this isomer has become the subject of intense experimental study for possible mechanisms that could trigger its decay. Since 1998 a number of experiments have been performed, nevertheless the obtained positive results completely exclude the negative results and vice versa yet [1, 2].

The depopulation of ^{180m}Ta isomer [3] with high-energy bremsstrahlung radiation has shown that the energy stored in isomeric levels can be triggered by photons. The experiments have reliably demonstrated that the intermediate states through which the triggering occurs can be found at the excitation energies about 2.8 MeV. It has been quite straightforward to suppose that if instead of the ground or low excited state of a nucleus some highly excited nuclear state is used then the analogous triggering effect could be reached using photons with much lower energy. Thus, photons with the energy of around 300 keV can be enough to observe ^{178m2}Hf isomer triggering.

2. Target and experimental setup

The uniqueness of ^{178m2}Hf isomer has several very essential disadvantages. First, the production of this isomer is extremely difficult task. Second, the more productive nuclear reaction is chosen for it, the longer (in most cases from 6 to 20 years) cooling time for the by-products activity reduction is required.

Such situation forced the intense search all over the world for any Ta targets irradiated by high energy projectiles many years ago. A set of Ta foils with ^{178m2}Hf isomer activity has recently been found at Kyiv Institute for Nuclear Research as well. All these foils of 100 μm thickness were used as the partial energy absorbers in nuclear experiments with 100 MeV α-particles many years ago. At such energies of α-particles the original contaminant production is not very high and the most undesirable by-product ^{172}Hf, presented in significant quantities in all ^{178m2}Hf isomeric targets available yet, has not been produced at all. Now the most part of contaminants decayed completely and the total activity of the foils is presented only by ^{178m2}Hf isomer and ^{179}Ta ($T_{1/2}$ = 664.5 d). ^{179}Ta decays exclusively by electron capture to ^{179}Hf ground state and there are no γ-rays in its spectrum that can be recorded by HPGe detector save for Hf characteristic x-rays. Thus ^{179}Ta, while it can be removed by subsequent chemical processing and extraction of Hf fraction, is a minor problem for ^{178m2}Hf isomer triggering experiments.

On the other hand, Hf characteristic x-rays can be used as the base lines in the triggering measurements ensuring the reliable control for the stability of measurement geometry during the irradiations as well. The measured decay rates of ^{178m2}Hf isomer and ^{179}Ta in a single foil are about 5 Bq and 420 Bq, correspondingly. Therefore, even taking into account that the yields of K_α(Hf) in the decay of ^{178m2}Hf isomer are approximately twice higher than in the decay of ^{179}Ta [4], the contribution of ^{178m2}Hf isomer in the total acquisition rate of K_α(Hf) lines does not exceed 3 %. Thus, any triggering effect at the level of several percent cannot surely be detected in the recorded K_α(Hf) lines.

Taking into account all the experience acquired during the initial ^{178m2}Hf isomer triggering experiments with dental x-ray machine, a new experimental setup has been developed at Kharkov National University and installed at Kyiv Institute for Nuclear Research allowing the irradiation of isomeric targets directly by electrons (or by x-rays when corresponding converters are used) with the energies of 1 - 25 keV and currents 0 - 150 μA.

The given ^{178m2}Hf isomer triggering experiments have been conducted using as a target the single Ta foil with about 5 Bq isomeric activity. Such target has at least two-fold advantage. First, it can be irradiated directly by electrons at maximal currents without any risk to be overheated and evaporated into vacuum. Secondly, while the isomer is embedded in Ta matrix the efficiency of the bremsstrahlung radiation and characteristic x-rays is maximal.

Low energy bremsstrahlung radiation has essentially been absorbed by the experimental setup wall to quite acceptable levels without noticeable decrease of ^{178m2}Hf isomer γ-rays, even the lowest energy ones. Additionally, the target unit of the experimental setup has been heavily and rather effectively shielded against natural γ-ray background by more than 10 cm of Pb. Therefore, according to our estimates the sensitivity of ^{178m2}Hf isomer triggering experiments must be orders of magnitude higher than in the case of the initial experiments with dental x-ray machine.

3. Experiment details and results

In the present measurements 25 keV electron beam at the maximal current of 150 μA has been used. The diameter of the beam spot at the target was about 8 mm – about the same size as a spot of ^{178m2}Hf isomer activity in the target. The γ-ray spectra have been acquired using HPGe coaxial detector mounted on the opposite side of the target in the horizontal plane and at 180° to the horizontally incident electron beam. In our experiment GC 2018 (CANBERRA) detector with the efficiency 20 % and energy resolution at γ1332 keV peak of ^{60}Co better than 1.8 keV and the standard acquisition system based on CANBERRA InSpector 2000 unit have been used. The distance from the detector front face to the target taking into account the thickness of the experimental setup wall was less than 5 mm. The acquisition rate in γ213 keV peak of ^{178m2}Hf isomer taking into consideration its essential absorption in Ta and additional absorption in rather thin Al wall of experimental setup and Al detector cap was around 0.2 count/s, moreover the dead time of the γ-ray spectrometer was less than 0.1 % even during the irradiations.

L_x lines of Hf cannot be detected in our experiments, consequently the bremsstruhlung radiation with the endpoint energy of 25 keV has been used as the beam-on monitor of electron currents on the target material in all runs of measurements ensuring that the experimental luminosity remain at the expected values. At the same time, the bremsstruhlung radiation rate registered by the detector was low enough for x-ray coincidence detection.

The overall series of measurements have involved a number of runs of beam-on measurements in the same measurement geometry and the total acquisition period of about 8 hours – the average life time of the cathode during which the stable beam spot at the target is guaranteed. In order to monitor the stability of measurement geometry, several runs of beam-off measurements have been conducted before and after the irradiations, just as between the separate beam-on measurements each accumulating data over the periods from a few hours to around 3 days.

The enhanced beam-on counts of ground state band (GSB) transitions and γ216 keV transition of 8^- band compared to the beam-off counts acquired for the same time have been recorded. Corresponding triggering effects observed in GSB, 8^- band (to be correct absolutely the γ93 keV transition and γ88 keV isomeric transition have been included into the estimates of triggering effect for the GSB and 8^- band, respectively, though in fact no enhanced counts were recorded in these transitions within obtained uncertainties) and total triggering effect in all mentioned above transitions have been calculated as 2.9 ± 1.0 %, 2.6 ± 1.4 % and 2.8 ± 0.8 %, correspondingly.

It is rather remarkable that the recorded triggering effects turned out to be practically the same for the GSB and 8^- band, while in the GSB case the uncertainty is obviously lower due the better statistics of the GSB transitions. While the triggering mechanism is unknown we can only claim the total triggering effect of 2.8 % for all above-mentioned transitions.

At the same time, the counting rates of $K_{\alpha 1}$ and $K_{\alpha 2}$ lines of Hf have been recorded at the levels 4.170 ± 0.015 and 1.953 ± 0.012 decays per second for the beam-on and 4.185 ± 0.009 and 1.974 ± 0.006 decays per second for beam-off spectra, correspondingly, thus no enhancement in $K_{\alpha 1}$ and $K_{\alpha 2}$ lines has been observed guarantying that the measurement geometry is keeping stable during all the beam-on and beam-off runs.

The relevant portions of difference spectrum in the energy range from 208 to 222 keV (left) and from 318 to 334 keV (right), accordingly for the total beam-on and beam-off spectra normalized to the same period of time are presented in Figs. 1, *a*. The channel widths are 151.42 eV/channel. The differences, with the points summed over an energy interval corresponding to the detector resolution, reflect the excess in de-excitation of the isomer and are consistent with the triggering effect of about 2.8 %. Along with the difference spectra the beam-off spectra normalized to the same period of time and 2.8 % enhancement factor are plotted as well (Figs. 1, *b*). Quite different pictures are observed for the same portions of the difference spectrum for separate beam-off (Figs. 1, *c*) and beam-on (Figs. 1, *d*) spectra normalized to the same period of time. Additionally, Figs. 1, *d* demonstrate that the observed triggering effect is quite stable for different runs of beam-on experiments.

Some differentiation observed in Figs. 1, *a* is due to the slight shift of energy calibration (in the case of γ213 keV the shift is 27 ± 8 eV or 0.178 ± 0.053 channels) in the beam-on spectra compared to the beam-off spectra. All the reasons for the differentiation are shown in Fig. 2. Consequently, the positive waves of the differences have quite expectedly been shifted to higher energies by about half-width (FWHM) of corresponding γ-ray peaks and such shifts are clearly visible in Figs. 1, *a*.

Additionally to the shift of energy calibration to the higher energies the line width broadening has been detected in the beam-on spectra as well. In the event of γ216 keV peak the half-width is 5.97 ± 0.02 and 6.07 ± 0.08 channels for the beam-off and beam-on spectra respectively, thus the broadening is about 0.10 ± 0.09 channels or 15 ± 14 eV and such broadening though being very small turns out to be quite clearly seen in Fig. 2. No differentiations have naturally been registered in Figs. 1, *c* and only partly registered in Figs. 1, *d* due to a little higher current in the final runs of beam-on measurements when the cathode used to work more effectively. At the same time, the triggering effect is also clearly visible in Fig. 2 since γ216 keV peak in the beam-on spectrum not only higher than in the beam-off spectrum, but wider as well.

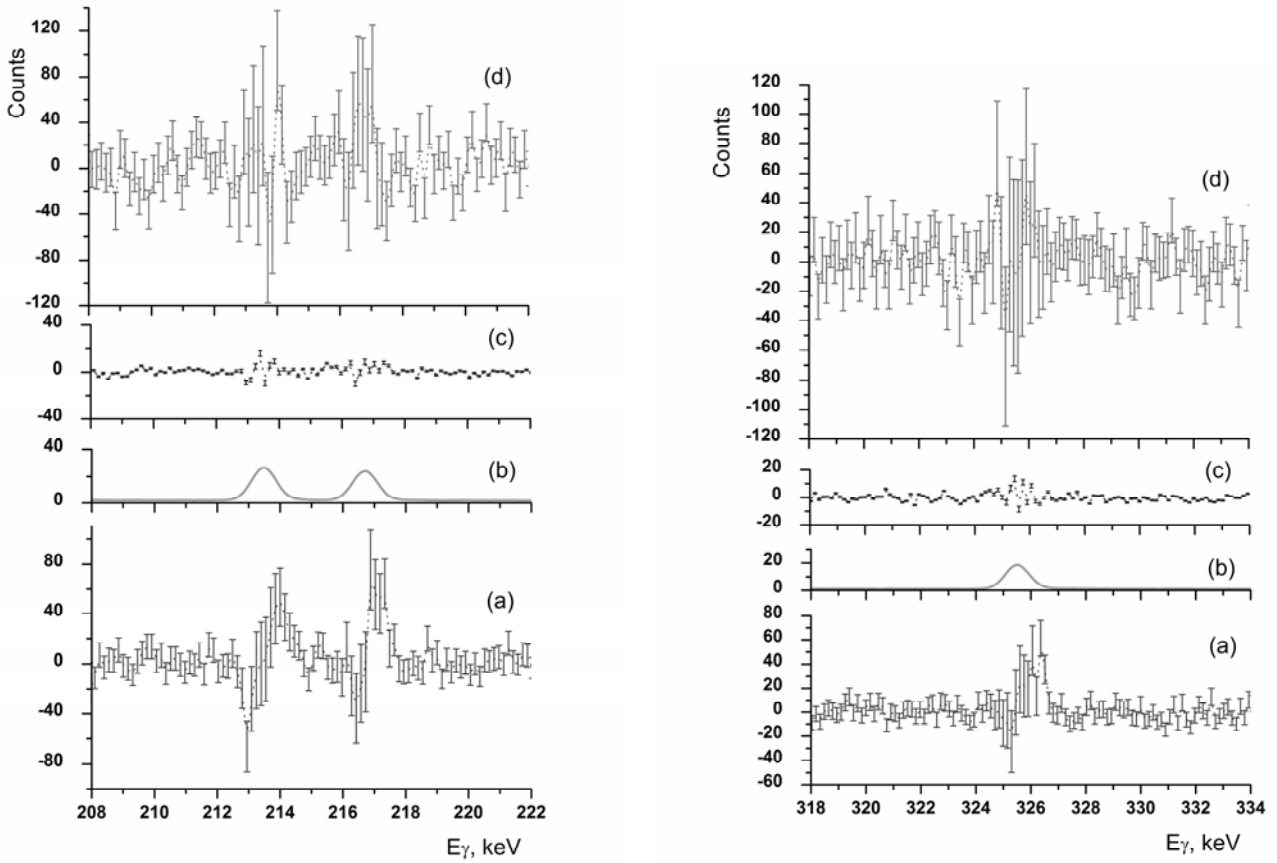

Fig. 1. The points with error bars show the difference gamma-ray spectra for the beam-on and beam-off spectra (*a*); different beam-off spectra (*c*) and different beam-on spectra (*d*) acquired in the energy region from 208 to 222 keV (left) and 318 to 334 keV (right), respectively and normalized to the same period of time. For the reference the beam-off spectra normalized to the same period of time and 2.8 % enhancement factor (*b*) are plotted as well.

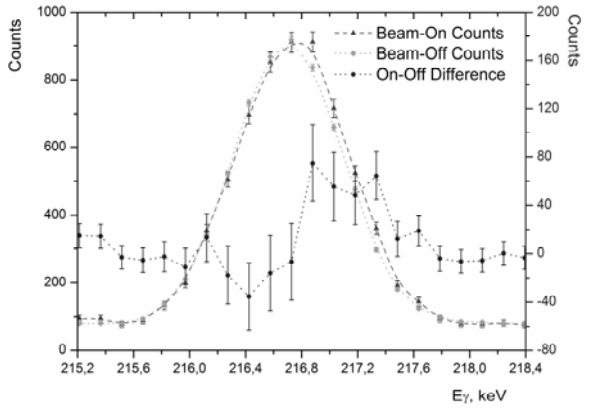

Fig. 2. Shifted energy calibration and broadened line widths recorded in the beam-on spectra compared to the beam-off spectra are a reason why the differentiation is clearly observed in the difference spectra shown in Figs. 1, *a*.

4. Discussions

In the same manner to that used in the previous works we can estimate (at least qualitatively) the triggering cross-section as well. The enhancement factor S can be expressed through the triggering cross-section according to the relation

$$S\,(N/\tau) = (N/A)\,F\,\sigma_{trig}\,, \qquad (1)$$

where N is the number of isomeric states in the target, τ is the lifetime of the isomeric state ($1.4 \cdot 10^9$ s), A is the area of the target, F is the number of incident electrons, and σ_{trig} is the triggering cross-section for the isomer de-excitation. N/τ is the normal decay rate of the isomeric nuclei in the target. This then gives

$$\sigma_{trig} = S\,[A/(\tau \cdot F)], \qquad (2)$$

As a result, with the values of A = 0.8 cm^2 and F = $3 \cdot 10^{15}$ e/c (~150 μA), the triggering cross-section estimate $\sigma_{trig} = 5.4 \cdot 10^{-27}$ cm^2 can be deduced.

While nothing is known about the triggering mechanisms and what part of the irradiation beam (electrons or x-rays) is involved in the triggering process, the triggering cross-section can be orders of magnitude as lower, if for instant any multiplication processes are involved, as higher, than we have estimated.

5. Conclusions

In summary, we have repeated the initial ^{178m2}Hf isomer triggering experiments using the new experimental setup and the isomeric source not used before. The evidence for the triggering of ^{178m2}Hf isomer as the enhanced counting rates of all ground-state band transitions, just as γ89 keV isomeric and γ216 keV 8$^-$-state band transitions has been

observed. Our data are consistent with an estimate for the triggering effect of 2.8 ± 0.8 % and corresponding triggering cross-section can qualitatively be estimated as $\sigma_{trig} = 5.4 \cdot 10^{-27}$ cm^2.

Additionally, it has been demonstrated that even using very weak isomeric source the sensitivity of our ^{178m2}Hf isomer triggering experiments is much higher than in the initial triggering experiments with dental x-ray machine. More detailed conclusions can be made when much stronger isomeric source will be prepared and ready for use. In this case the increased emission of γ-rays could be detected in every separate transition supplying exclusively valuable information about possible scenarios and mechanisms of the induced decay of ^{178m2}Hf isomer. It would allow to conduct the coincidence measurements as well.

ACKNOWLEDGMENTS

We are indebted to Prof. Valentine V. Chorny and his colleagues for their help in the development of new experimental setup and to Prof. Aleksey I. Feoktistov and Dr. Vladimir T. Kupryashkin for their help in various aspects of these measurements. Special thanks to Prof. Victor A. Zheltonozhskiy, Dr. Anatoly P. Lashko, Dr. Leonid P. Sidorenko and Dr. Andrey N. Savrasov for their encouragement of this investigation.

REFERENCES

1. *Kirischuk V.I., McDaniel P., Collins C.B. et al.* Status and perspectives for the experimental investigation of ^{178m2}Hf isomer triggering by low-energy photons // Proc. of the 7th AFOSR Workshop “Isomers and Quantum Nucleonics” (June 26 - July 1, 2005, Dubna, Russia) / Ed. by S.A. Karamian, J.J. Carroll and E.A. Cherepanov. - JINR, Dubna, 2006. - P. 99 - 103. See also the references to our earlier papers in *Collins C.B., Zoita N.C., Rusu A.C. et al*. Accelerated decay of the 31-yr isomer of Hf-178 induced by low-energy photons and electrons // Laser Physics. - 2004. - Vol. 14. - No. 2. - P. 154 - 165.
2. *Ahmad I., Banar J.C., Becher J.A. et al.* Search for x-ray induced decay of the 31-yr isomer of ^{178}Hf using synchrotron radiation // Phys. Rev. C. - 2005. - Vol. 71. - P. 024311 - 024326. See all the references to the previous papers inside as well.
3. *Collins C.B., Eberhard C.D., Glesener J.W., Anderson J.A.* Depopulation of the isomeric state ^{180}Ta^m by the reaction ^{180}Ta$^m(\gamma, \gamma')^{180}$Ta // Phys. Rev. C. - 1988. - Vol. 37. - P. 2267 - 2269.
4. *Browne E., Firestone R.B.* Table of Radioactive Isotopes / Ed. by V.S. Shirlay. - New York: John Wiley & Sons Inc., 1986.

OPTIMIZATION OF LIGHT COLLECTION FROM CRYSTAL SCINTILLATORS FOR CRYOGENIC EXPERIMENTS

V. M. Mokina[1], F. A. Danevich[1], V. V. Kobychev[1], H. Kraus[2], V. B. Mikhailik[2], L. L. Nagornaya[3]

[1] Institute for Nuclear Research, National Academy of Sciences of Ukraine, Kyiv, Ukraine
[2]Department of Physics, University of Oxford, Oxford, United Kingdom
[3] Institute for Scintillation Materials, Kharkiv, Ukraine

Cryogenic scintillation bolometers are a promising technique to search for dark matter and neutrinoless double β decay. Improvement of light collection and energy resolution are important requirements in such experiments. Energy resolutions and relative pulse amplitudes of scintillation detectors using $ZnWO_4$ scintillation crystals of different shapes (cylinder $\varnothing 20 \times 20$ mm and hexagonal prism with diagonal 20 mm and height 20 mm), reflector materials and shapes, optical contact and surface properties (polished and diffused) were measured. The crystal scintillator of hexagonal shape shows the better energy resolution and pulse amplitude. The best energy resolution (FWHM = 9.3 % for 662 keV γ quanta of ^{137}Cs) was obtained with a hexagonal scintillator with all surfaces diffuse, in optical contact with a PMT and surrounded by a reflector (3M) of size $\varnothing 26 \times 25$ mm. In the geometry "without optical contact" representing the conditions of light collection for a cryogenic scintillating bolometer the best energy resolution and relative pulse amplitude was obtained for a hexagonal shape scintillator with diffuse side and polished face surfaces, surrounded by a reflector with a gap between the scintillator and the reflector.

1. Introduction

Cryogenic scintillators are a promising technique to search for dark matter and neutrinoless double β decay due to excellent energy resolution, particle discrimination ability, and low energy threshold. They also offer the important possibility to use compounds with nuclei of interest. For instance, the CRESST collaboration already uses low-temperature $CaWO_4$ scintillating bolometers to search for weakly interacting massive particles (WIMP) [1], while several experiments are in preparation to search for dark matter and double β decay. In particular the EURECA project [2] aims to build a ton scale cryogenic detector to achieve sensitivity to WIMP-nucleon scattering cross sections on the level of 10^{-10} - 10^{-11} pb. A couple of R&D projects are progressing towards building double β decay experiments for the exploration of neutrino mass hierarchy scenarios using $CaMoO_4$ [3], ZnSe [4, 5], $CdWO_4$ [6], or $ZnMoO_4$ [7] crystal scintillators. Light collection plays an important role in dark matter experiments where a low energy threshold is essential, while in 2β experiments the light collection is crucial to achieve effective pulse-shape discrimination, in particular of random coincidence events which was recently recognized as one of the problematic sources of background in bolometric detectors [8]. Therefore it is essential to optimize light collection from crystal scintillators in cryogenic scintillating bolometers.

Zinc tungstate ($ZnWO_4$) crystals have optical properties rather similar to that of $CaWO_4$, $CdWO_4$, $CaMoO_4$, $ZnMoO_4$, ZnSe and some other oxide crystal scintillators. All these are promising targets for dark matter and/or double β decay experiments. Therefore one could use this material to find optimal light collection conditions for a wide range of scintillators in cryogenic scintillating bolometers. It should be stressed that $ZnWO_4$ crystal scintillators are promising detectors to search for dark matter and double β decay owing to the presence of zinc and tungsten (elements containing potentially double β active isotopes), high light output and very low level of radioactive contamination [9 - 14]. The purpose of this work was to study the dependence of energy resolution and relative pulse amplitude of $ZnWO_4$ scintillation detectors on crystal shape (hexagonal and cylindrical), design and material of the reflector, optical contact, and optical condition of the crystal scintillator surface (polished and diffuse).

2. Measurements and results

To ensure as much as possible identical optical properties two $ZnWO_4$ crystal scintillators were produced from one $ZnWO_4$ crystal ingot in the Institute of Scintillation Materials (Kharkiv, Ukraine). One crystal was of cylindrical shape with dimensions $\varnothing$ 20×20 mm (C), another was in the form of a hexagonal prism with diagonal 20 mm and height 20 mm (H).

The similarity of the two crystals' optical properties was verified by measurements of transmission using a spectrophotometer (Shimadzu, UV-3600). Results of the measurements presented in Fig. 1 evidence that both samples have very similar absorption properties.

Measurements of energy resolution and relative pulse amplitude with γ-sources were carried out for the following conditions (Fig. 2):

A) $ZnWO_4$ crystal wrapped in 3 layers of PTFE tape and optically connected to the PMT;

B) $ZnWO_4$ crystal surrounded by cylindrical reflector (3M) $\varnothing 26 \times 25$ mm and optically connected to the PMT;

C) $ZnWO_4$ crystal surrounded by cylindrical 3M reflector $\varnothing 26 \times 25$ mm and placed on small plexiglas supports (3 cubes with dimensions $2 \times 2 \times 2$ mm), without optical contact between the crystals and the PMT.

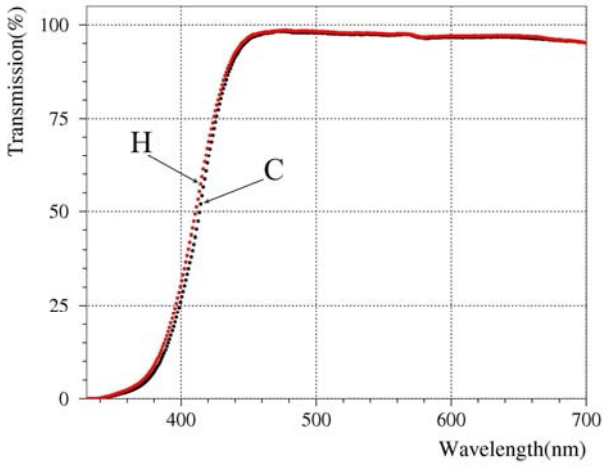

Fig. 1. The optical transmission spectra of cylindrical (C) and hexagonal (H) $ZnWO_4$ crystals. The spectra were measured with a 2 mm sample in the reference beam to account for reflections.

The optical contact in geometries "A" and "B" was provided by Dow Corning Q2-3067 optical gel. Geometry "C" represents, to some extent, the conditions of light collection in a cryogenic scintillating detector.

The measurements were carried out for four conditions of the crystals' surfaces:

1)all surfaces of the $ZnWO_4$ crystal scintillator were polished;

2)the side surfaces of the crystals were diffuse, the face surfaces polished;

3)the side surfaces and top face of the crystals were diffuse, the face viewed by the PMT was polished;

4)all surfaces of the crystals were diffuse.

Grinding the surfaces was done with sanding paper P1000 (KWH Mirka Ltd) with grain size 18 ± 1 microns. The average roughness of the diffuse surface was estimated to be at the level of ≈ 10 microns by using an optical microscope. The roughness of the polished surfaces is ≈ 0.2 micron.

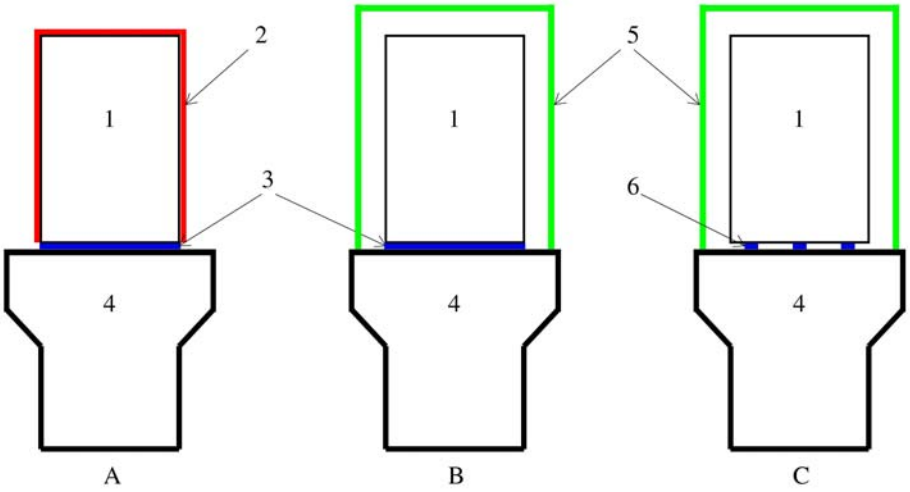

Fig. 2. Conditions of measurements with $ZnWO_4$ crystal scintillators
(*1* – crystal; *2* – 3 layers of PTFE tape; *3* – optical contact; *4* – PMT; *5* – 3M reflector; *6* – Plexiglas support).

To measure the scintillation properties, crystals were viewed by a 3" photomultiplier (PMT) Philips XP2412.

The positions of the γ sources (^{137}Cs and ^{207}Bi) were chosen to provide a counting rate less than 250 counts/s. The energy spectra were accumulated over 30 minutes in case of the ^{207}Bi source and for 40 min with the ^{137}Cs source, from 30 minutes after switching on the high voltage for the PMT.

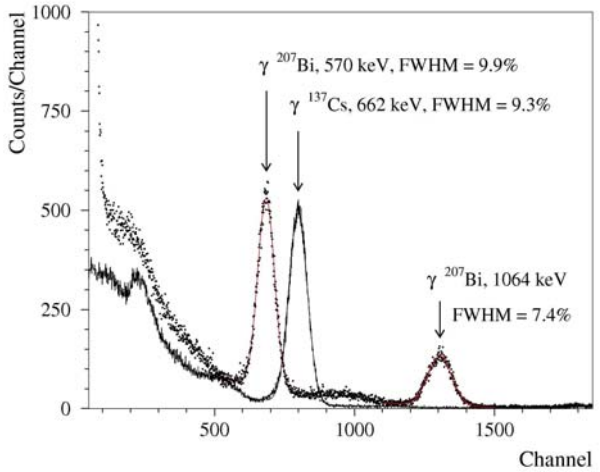

Fig. 3. Energy spectra of ^{137}Cs and ^{207}Bi γ rays measured for the $ZnWO_4$ crystal of hexagonal shape with all surface diffuse, in geometry "B" (see text and Fig. 2).

The temperature during the measurements was in the range of 21 - 26 °C. Variation of the $ZnWO_4$ light output on temperature was estimated to be in the range of ≈ 3 % in this temperature interval. To check the stability of the spectrometer a $ZnWO_4$ crystal scintillator 10 × 10 × 5 mm was periodically installed on the PMT and irradiated by γ quanta from a ^{137}Cs source. All the data were corrected offline, taking into account the position of the ^{137}Cs peak measured with the 10 × 10 × 5 mm scintillator.

The energy spectra of ^{137}Cs and ^{207}Bi γ quanta, exhibiting the best energy resolutions are presented in Fig. 3. These were accumulated with the hexagonal $ZnWO_4$ crystal scintillator in optical contact with the PMT, surrounded by the 3M reflector, with all surfaces diffuse.

The measurements for surface configurations *1* - *3* were repeated three times and that for configuration *4* was carried out once.

Average data on the energy resolution and relative pulse amplitude measured with 662 keV γ quanta of ^{137}Cs for the different conditions of measurements are presented in Figs. 4, 5 and 6.

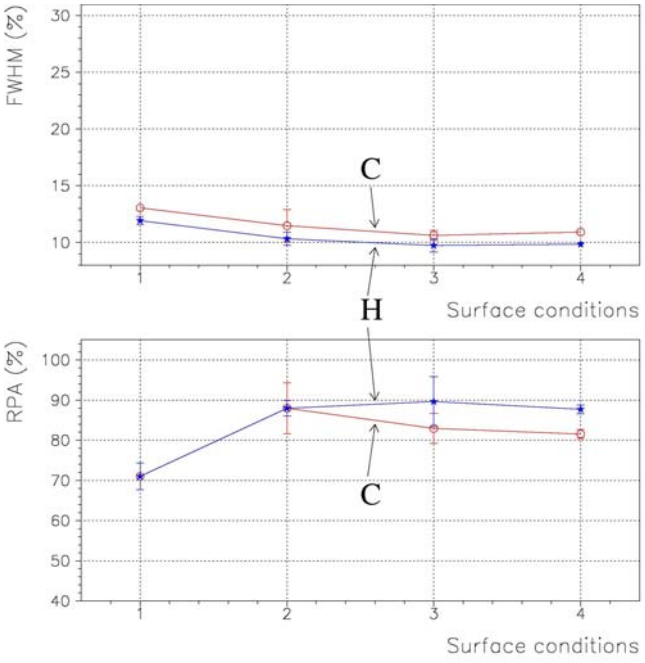

Fig. 4. Energy resolution and relative pulse amplitude (RPA) for hexagonal (H) and cylindrical (C) $ZnWO_4$ scintillator crystals for geometry "A" (see Fig. 2) measured with a ^{137}Cs source for different crystal surface conditions (*1* – polished; *2* – diffuse side; *3* – diffuse side and top face; *4* – all surface diffuse).

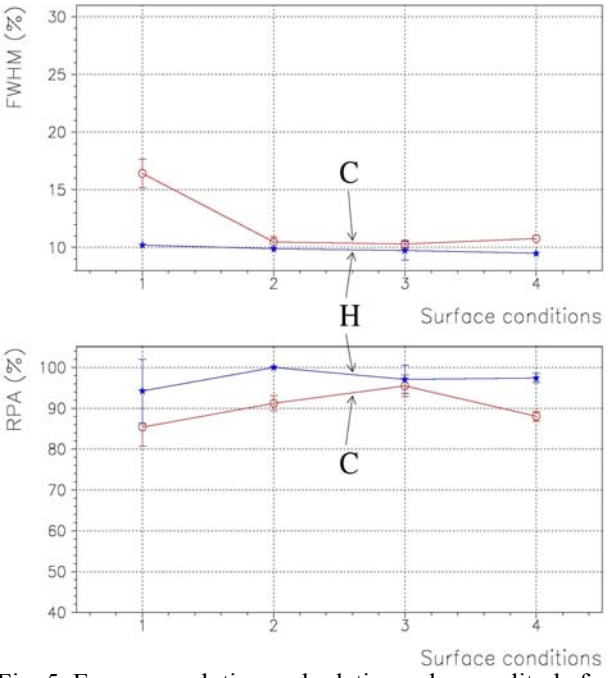

Fig. 5. Energy resolution and relative pulse amplitude for hexagonal (H) and cylindrical (C) $ZnWO_4$ scintillator crystals for geometry "B" (see Fig. 2) measured with a ^{137}Cs source for different crystal surface conditions (*1* – polished; *2* – diffuse side; *3* – diffuse side and top face; *4* – all surface diffuse).

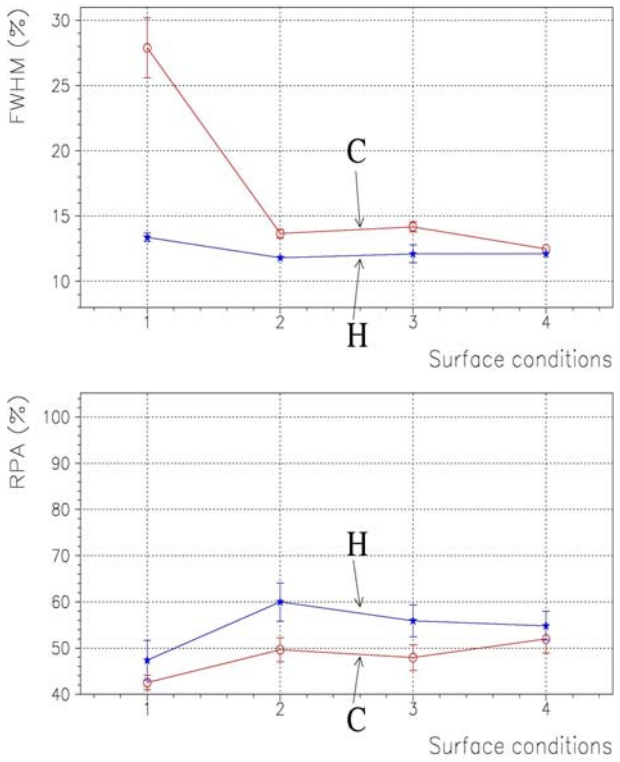

Fig. 6. Energy resolution and relative pulse amplitude for hexagonal (H) and cylindrical (C) $ZnWO_4$ scintillator crystals for geometry "C" (see Fig. 2) measured with a ^{137}Cs source for different crystal surface conditions (*1* – polished; *2* – diffuse side; *3* – diffuse side and top face; *4* – all surface diffuse).

3. Conclusions

Effects of crystal scintillator shape, reflector material and shape, optical contact and surface treatment were tested with two $ZnWO_4$ crystal scintillators: a hexagonal prism (height 20 mm, diagonal 20 mm) and a cylinder (height 20 mm, diameter 20 mm) produced from the same crystal boule. That the optical properties of the samples were the same within errors was confirmed through transmittance measurements.

The hexagonal crystal shows better energy resolution and relative pulse amplitude for all tested measurement conditions. The best energy resolution (FWHM = 9.3 % for 662 keV γ quanta of ^{137}Cs) was obtained with the hexagonal scintillator with all surfaces diffuse, in optical contact with the PMT, and surrounded by a cylindrical reflector (3M). The maximal light output was measured with the hexagonal scintillator with side surfaces diffuse and polished end faces, in optical contact with the PMT and surrounded by a cylindrical reflector (3M) with a ≈5 mm gap between the scintillator and the reflector.

In the geometry "without optical contact" representing the conditions applicable for light collection in a cryogenic scintillating bolometer the light collection efficiency is reduced by almost a factor of two when compared with the two other experimental geometries. This is due to substantial reflection losses at the boundaries of the crystal-gap and air-PMT interfaces. The energy resolution of the detector, though degraded, remains useful for practical applications. The best relative pulse amplitude and energy resolution

(FWHM = 11.8 % for 662 keV γ quanta of ^{137}Cs) were obtained for the hexagonal shape scintillator with diffuse side surfaces and polished end faces, surrounded by a cylindrical reflector with a gap between the scintillator and the reflector.

REFERENCES

1. *Angloher G. et al.* Results from 730 kg days of the CRESST-II Dark Matter Search // Eur. Phys. J. - 2012. - Vol. C72. - P. 1971.
2. *Kraus H. et al.* EURECA - The Future of Cryogenic Dark Matter Detection in Europe // Proc. of Science: PoS - idm2008 - P. 013 - 7.
3. *Lee J. et al.* The development of a cryogenic detector with $CaMoO_4$ crystals for neutrinoless double beta decay search // Astropart. Phys. - 2011. - Vol. 34. - P. 732.
4. *Giuliani A. et al,* Proc. of the Fifth International Conference - Beyond 2010 / Ed. by H.V. Klapdor-Kleingrothaus, I.V. Krivosheina and R. Viollier. - World Scientific, 2011. - P. 256.
5. *Arnaboldi C. et al.* Characterization of ZnSe scintillating bolometers for Double Beta Decay // Astropart. Phys. - 2011. - Vol. 34. - P. 344.
6. *Gironi L. et al.* $CdWO_4$ bolometers for double beta decay search // Opt. Mater. - 2009. - Vol. 31. - P. 1388.
7. *Beeman J.W. et al.* $ZnMoO_4$: A promising bolometer for neutrinoless double beta decays searches // Astropart. Phys. - 2012. - Vol. 35. - P. 813; *Beeman J. W. et al.* A next-generation neutrinoless double beta decay experiment based on $ZnMoO_4$ scintillating bolometers // Phys. Lett. - 2012. - Vol. B710. - P. 318.
8. *Chernyak D.M. et al.* Random coincidence of $2\nu2\beta$ decay events as a background source in bolometric $0\nu2\beta$ decay experiments // Eur. Phys. J. - 2012. - Vol. C72. - P. 1989.
9. *Danevich F.A. et al.* $ZnWO_4$ crystals as detectors for 2β decay and dark matter experiments // Nucl. Instr. Meth. - 2005. - Vol. A544. - P. 553.
10. *Kraus H. et al.* Feasibility study of a $ZnWO_4$ scintillator for exploiting materials signature in cryogenic WIMP dark matter searches // Phys. Lett. - 2005. - Vol. B610. - P. 37.
11. *Mikhailik V., Kraus H.* Cryogenic scintillators in searches for extremely rare events // J. Phys. D: Appl. Phys. - 2006. - Vol. 39. - P. 1181.
12. *Belli P. et al.* Radioactive contamination of $ZnWO_4$ crystal scintillators // Nucl. Instr. Meth. - 2010. - Vol. A626 - 627. - P. 31.
13. *Belli P. et al.* Final results of an experiment to search for 2β processes in zinc and tungsten with the help of radiopure $ZnWO_4$ crystal scintillators // J. Phys. G: Nucl. Part. Phys. - 2011. - Vol. 38. - P. 115107 (15 p.).
14. *Cappella F. et al.* On the potentiality of the $ZnWO_4$ anisotropic detectors to measure the directionality of Dark Matter, submitted in Eur. Phys. J. C.

THE BOLOMETRIC WAY TOWARDS THE DIRECT DARK MATTER DETECTION: THE EDELWEISS EXPERIMENT AND THE EURECA PROSPECT

C. Nones
(on behalf of the EDELWEISS collaboration)

CEA Saclay, DSM/IRFU/SPhN, Gif-sur-Yvette, France

Within the current cosmological concordance model, a large fraction of the mass in the universe is made of dark matter. One tool to detect dark matter in the form of WIMPs is given by the direct detection. The EDELWEISS experiment, operated in the Frejus laboratory in a low-background environment, uses cryogenic germanium detectors to look for a direct search of WIMPs. These detectors are subject to constant improvement with respect to the rejection capabilities against non WIMP interactions. We present here the results of a WIMP search carried out with ten so-called InterDigit detectors, technology that enables a high level of gamma radioactivity rejection within a controlled fiducial volume. A cross-section of $4.4 \cdot 10^{-8}$ pb could be excluded for a WIMP mass of 85 GeV. We also report the search for low-energy WIMP-induced nuclear recoils for an exposure of 113 kg.d. The status of the EDELWEISS-III project, which will operate 40 newly-designed FID detectors in an upgraded installation, will be given as well as a short presentation of the EURECA project aiming to a cross-section of 10^{-10} - 10^{-11} pb.

1. Introduction

One of the key ingredients for the current cosmological concordance model is the existence of a dark, matter-like fluid ruling the dynamics of structures from the current galactic scales to the largest scales at early cosmic times. Weakly Interacting Massive Particles (WIMPs) are a generic class of dark matter particles with particularly appealing features. They appear in several extensions of the current Standard Model of particle physics, where thermal production mechanisms for such particles in the Big Bang naturally yield the order of magnitude for the observed cosmic abundance [1]. A vast effort is currently dedicated to the direct detection of WIMPs from the Milky Way halo through the coherent elastic scattering on nuclei constituting a terrestrial detector. A roughly exponential nuclear recoil spectrum is expected with typical energies of a few tens of keV. Theoretical models predict a wide range of WIMP-nucleon scattering cross sections. Current searches are approaching sensitivities for rates of a few 10^{-3} evts/kg/day, corresponding to cross sections for spin-independent interactions at the level of a few 10^{-8} pb. Since we are dealing with very rare event searches, the dedicated detectors must therefore achieve a low energy threshold combined with high background rejection capabilities.

Although several constrained WIMP models point out to WIMP masses $M\chi$ ~100 GeV, lighter fermions with masses down to ~2 GeV are possible [2, 3].

2. The bolometric technique and the EDELWEISS experiment

Bolometers are calorimeters working at low temperatures in which the energy of particle interactions is converted into phonons and measured via a temperature variation. These thermal detectors measure the portion of the deposited energy converted into phonons and guarantee a better intrinsic energy resolution. Nevertheless they are slow detectors so that they are suitable only for experiments working at low rates. Bolometers consist of two main components: an energy absorber, where particles deposit their energy and a sensor, which converts the excess phonons produced by the particle into a signal.

The EDELWEISS experiment [4] is a direct WIMP search experiment, where nuclear recoils induced by collisions with WIMPs from the galactic halo are detected using germanium bolometers working at very low temperatures (20 mK) with the simultaneous measurement of ionization and phonon signals. The comparison of the two signals makes possible to separate on an event-by-event basis the nuclear recoils from the electron recoils induced by β and γ radioactivity that constitute the major source of background in most present-day direct WIMP searches. Detectors are operated at the Underground Laboratory of Modane in the Frejus Tunnel under the French-Italian Alps. The 1780 rock overburden (4800 m water equivalent) results in a muon flux of about 5 μ/m^2/day in the experimental hall and the neutron flux above 1 MeV is 10^{-6} n/cm^2/s. [5].

In the next two sub-sections detectors and their improvement in time will be given.

2.1. EDELWEISS-II: ID detectors

Given the experience acquired with EDELWEISS-I, a new design for the detector was required. The new-generation detectors called ID (InterDigit) are essentially a variation of the coplanar grid technique, in which interleaved concentric strips are substituted for the classical disk-shaped collection electrodes. The depth of an event relative to the surfaces can be inferred from a comparison of the ionization signals on the different strips, making possible a rejection of energy deposits at the detector surfaces [6]. The EDELWEISS-II phase consisted of ten hyperpure germanium crystals of cylindrical shapes with a diameter of 70 mm and a height of 20 mm with a mass in the range 360 - 410 g the phonon signal. The detectors are in individual copper casings, stacked in towers of two to three ID detectors. During the entire

data-taking periods, the dilution refrigerator maintains the detectors at a stabilized temperature of 18 mK. A total effective exposure of 384 kg·d has been achieved and results on WIMP search will be given in Section 4.

2.2. EDELWEISS-III: FID800 detectors

To go beyond the EDELWEISS-II sensitivity and to be competitive with other experiments, a third phase of this experiment is foreseen. The EDELWEISS-III project consists in an upgrade of both the current EDELWEISS setup and detectors. The main goal is to reach sensitivity to WIMP-nucleon cross-section of the order of $5 \cdot 10^{-9}$ pb in a short term requiring an exposure of 3000 kg.d. For the reduction of the β and γ backgrounds, the development of an improved detector design, named Full InterDigit (FID) has been pursued. 800 g crystals are equipped with two NTD heat sensors and are covered by interleaved electrodes on all their surface. There is therefore no guard region anymore inside the crystal volume. Both the increase of crystal mass and the removal of guard regions increase strongly the fiducial mass for each individual detector. In addition, simulations have shown that Compton interactions spanning the fiducial and low- field guard regions may induce fake WIMP candidates. Large-statistics gamma-ray calibration of the first FID detectors have indeed shown improved rejection performances relative to ID detectors. The plan is to install 40 FID800 detectors in 2013. Infrastructure upgrades (cabling, cold electronics, cryogenics and acquisition) are necessary to host these new detectors, to reduce microphonic noise and hence the analysis threshold, and will also reduce the neutron budget within the cryostat. In addition, an inner polyethylene shield will be installed to reduce the flux of fast neutrons coming from outside the cryostat. Fig. 1 (*left*) shows a picture of a FID detector: interleaved electrodes are visible on all its surface and also the NTD sensor is appreciable on the top surface. Fig. 1 (*right*) represents a sketch of the electric field lines inside the crystal resulting in a 75 % of fiducial volume (~ 640g).

Fig. 1. *Left*: picture of a FID detector of 800 g in its copper holder. Interleaved electrodes are visible on all its surface and also the NTD sensor is appreciable on the top surface. *Right*: sketch of the electric field lines inside the crystal.

3. Final results of the EDELWEISS-II WIMP search

A WIMP search was carried out between April 2009 and May 2010 with the ten ID 400-g detectors described in Section 2.1. While all heat sensors were working correctly, a few veto or guard electrodes were malfunctioning, but the redundancy between channels prevented the loss of detectors for physics. The EDELWEISS-II setup provided a remarkably stable cryogenic environment at 18 mK during all this run. For each detector, an online trigger was applied on the heat sensor timelines and the recorded pulses have been then processed offline using optimal filters. Noisy periods have been rejected using the measured FWHM baselines, and requiring them to be below 2 keV for fiducial ionization and 2.5 keV for heat and guard ionization. These cuts have implied a 17 % exposure loss. The WIMP search cuts are then simply: fiducial volume selection; coincidence rejection (coincidences between detectors as well as with the muon veto); and finally selection of recoil energies between 20 and 200 keV, and ionization yields within the 90 % NR region and outside the 99.99 % gamma region. This results in a 384 kg.days net exposure [7].

The expected backgrounds are gamma and beta radioactivities, and fast neutron interactions. Summing all these background upper limits gives an estimation of 5.1 background events in the NR region for the WIMP search [8 - 9]. The observed distribution shows five events in the WIMP-search region (Fig. 2, *left*), one at 172 keV and the other ones between 20 and 23.2 keV. Given the abovementioned backgrounds, there is no clear evidence for WIMPs.

Applying the standard procedure in the field to set an upper limit in the presence of a weak, poorly constrained background, we obtain a limit on the spin-independent WIMP-nucleon cross-section of $4.4 \cdot 10^{-8}$ pb for a WIMP mass of 85 GeV. The 90 % limit as a function of WIMP mass is presented in Fig. 2, *right*. This limit is degraded by the presence of the observed events at low energy.

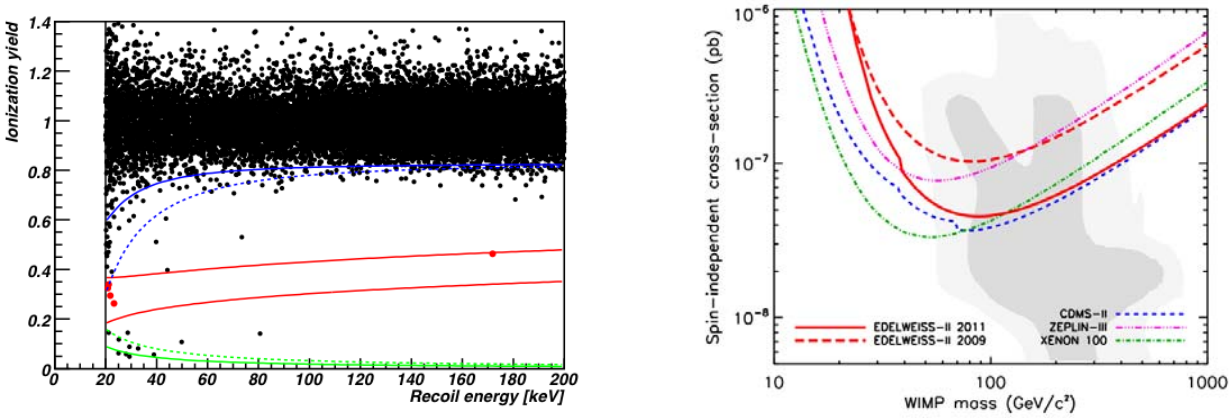

Fig. 2. *Left*: Ionization yield vs recoil energy of fiducial events recorded by EDELWEISS-II in an exposure of 427 kg·d. The WIMP search region is defined by recoil energies between 20 and 200 keV, and an ionization yield inside the 90 % acceptance band (full red lines, corresponding to an effective exposure of 384 kg·d). WIMP candidates are highlighted in red. The average (resp. worst) one-sided 99.99 % rejection limits for electron recoils are represented with a continuous (resp. dashed) blue line. The average (resp. worst) ionization thresholds are represented with a continuous (resp. dashed) green line. *Right*: Limits on the cross-section for spin-independent scattering of WIMPs on the nucleon as a function of WIMP mass, derived from the present work, together with the limits from CDMS, ZEPLIN and XENON100. The shaded area corresponds to the 68 % and 95 % probability regions of the cMSSM.

4. Results for low-mass WIMPs with the EDELWEISS-II detectors

We present here a search for low-mass WIMPs using data collected by the EDELWEISS-II detectors in 2009 - 2010 [10]. The analysis optimized for WIMP masses above 50 GeV with a threshold set at recoil energy of 20 keV has already been presented in the previous section. This strategy, however, is not adequate for a search dedicated to models in which the WIMP mass is of the order of 10 GeV, for which the highest expected recoil energy is of the order of 10 keV. At this purpose we use a restricted dataset, selected on the basis of detector thresholds and backgrounds, for which low-background sensitivity to nuclear recoils down to 5 keV could be achieved. With a total exposure of 113 kg·d we find no evidence for an exponential distribution of low-energy nuclear recoils that could be attributed to WIMP elastic scattering. For WIMPs of mass 10 GeV, the observation of one event in the WIMP search region results in a 90 % CL limit of 1.0×10^{-5} pb on the spin-independent WIMP-nucleon scattering cross-section, which constrains the parameter space associated with the findings reported by the CoGeNT, DAMA and CRESST experiments. Further improvements in the resolution of individual channels, and in particular ionization channels, are ongoing and should allow significant progress towards background-free, low mass WIMP searches.

5. EURECA and future perspectives

EURECA (European Underground Rare Event Calorimeter Array) will aim to merge mainly the EDELWEISS and the CRESST collaborations to build a facility to house up to 1000 kg of detectors which will allow an increase of sensitivity by two orders of magnitude in the WIMP-nucleon cross section [11]. With a shield consisting of a large water tank in which will be immersed the 1 m^3 cryostat housing the detectors, with innovative cryogenics which will rely on European expertise in the field, with adaptable cabling and electronics options, the EURECA infrastructure will be an essential tool for the community interested in the use of cryogenic detectors for dark matter searches but also for other rare event searches (Fig. 3).

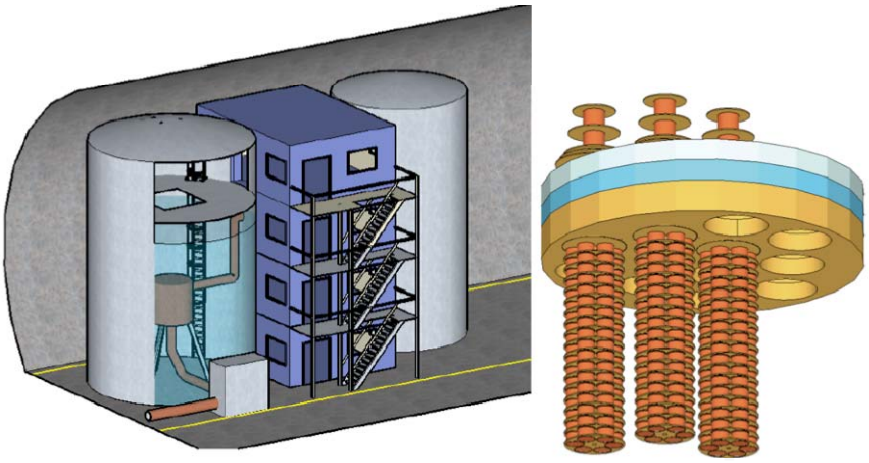

Fig. 3. Sketch of the EURECA cryostat inside a shield consisting of a large water tank. The 1 m^3 cryostat will house the detectors arranged in towers.

Beyond European detectors, it will be designed to host any type of detector, including the ones currently studied by SuperCDMS teams, following the current collaborative work performed by the two collaborations.

EURECA will have two stages. The first phase will involve building the infrastructure, cryostat and shielding, and operating 150 kg of detectors while the second phase will be completed with 850 kg of additional detectors, the weight between the different detectors being agreed within the collaboration according to the physics reach. Thanks to a site-independent design, this infrastructure can be hosted in different locations. Such a unique facility, planned to operate over a long term, will be designed to ensure an exceptionally clean radioactive environment in order to provide the highest sensitivity in the field. A conceptual design report has been written and it should be considered as the first step towards construction and exploitation of that facility.

6. Conclusions

Important progresses have been done with cryogenic Ge detectors in the EDELWEISS experiment during last years. There is still a comfortable space for detector improvements including also larger masses. In addition, thanks to the big versatility of these detectors, they can be adapted to lower thresholds; at this purpose the collaboration is working on the heat channel with the development of new innovative heat sensors, called ”NbSi superconductive resistive meanders”, that have the potentiality to decrease the threshold improving also the energy resolution.

For the near future, new data in the coming year will contribute to clarify the present situation especially at low mass, a hot topic still at nowadays. In the next future, EURECA [7], a Ton scale Dark matter experiment, will search for WIMP interactions down to $\sigma \sim 10^{-10}$ pb corresponding to a rate of ~1 event/ton/year. It is clear that to achieve this further step different present limitations should be overcome.

ACKNOWLEDGMENTS

This project is supported in part by the Agence Nationale pour la Recherche under contract ANR-06-BLAN-0376-01 and partly by the CEA - EUROTALENTS Programme (COW project) within the 7th European Community Framework Programme.

REFERENCES

1. *Bertone G., Hooper D., Silk J.* Particle Dark Matter: Evidence, Candidates and Constraints // Phys. Rep. - 2005. - Vol. 405. - P. 279 - 390.
2. *Lee B., Weinberg S.* Cosmological Lower Bound on Heavy-Neutrino Masses // Phys. Rev. Lett. - 1977. - Vol. 39. - P. 165 - 168.
3. *Bottino A. et al.* Light Neutralinos and WIMP direct searches // Phys. Rev. Dю - 2004. - Vol. 69. - P. 037302 - 037302-4.
4. http://edelweiss.in2p3.fr/
5. *Sanglard V. et al.* Final results of the EDELWEISS-I dark matter search with cryogenic heat-and-ionization Ge detectors // Phys. Rev. D. - 2005. - Vol. 71. - P. 122002 - 122002-16.
6. *Broniatowski A. et al.* A new high-background-rejection dark matter Ge cryogenic detector // J. Phys. Lett. B. - 2009. - Vol. 681. - P. 305 - 309.
7. *Armengaud E. et al.* Final results of the EDELWEISS-II WIMP search using a 4-kg array of cryogenic germanium detectors with interleaved electrodes // Phys. Lett. B. - 2011. - Vol. 702. - P. 329 - 335.
8. *Armengaud E. et al.* Background studies for the EDELWEISS dark matter experiment // Submitted to Astroparticle Physics.
9. *Schmidt B. et al.* Muon-induced background in the EDELWEISS dark matter search // Submitted to Astroparticle Physics.
10. *Armengaud E. et al.* A search for low-mass WIMPs with the EDELWEISS heat-and-ionization detectors // Phys. Rev. D. - 2012. - Vol. 86. - P. 051701(R) - 051701-6.
11. *Kraus H. et al.* EURECA - the European future of dark matter searches with cryogenic detectors // Nucl. Phys. B. - 2007. - Vol. 173. - P.168 - 171.

NEW DETECTORS IN INVESTIGATIONS OF 2β DECAY

N. I. Rukhadze[1], Ch. Briançon[2], V. B. Brudanin[1], J. Čermák[3], P. Čermák[3], J. M. Jose[3], A. A. Klimenko[1], P. Loaiza[4], F. Piquemal[4], E. N. Rukhadze[3], I. Štekl[3], Yu. A. Shitov[1], J. Vlášek[3], G. Warot[4], E. A. Yakushev[1]

[1] Joint Institute for Nuclear Research, Dubna, Moscow region, Russia
[2] Centre de Spectrométrie Nucléaire et de Spectrométrie de Masse, Orsay, France
[3] Institute of Experimental and Applied Physics, Czech Technical University, Prague, Czech Republic
[4] Laboratoire Souterrain de Modane, Modane, France

A search for EC/EC decay of ^{106}Cd performed by the TGV-2 experiment will be expanded by using of a new type of spectrometers. Silicon Pixel Detectors (SPD) will be used to search for 2νEC/EC decay as they have a high efficiency to detect two correlated low energy X-rays emitting in this decay. Low background HPGe detector with the sensitive volume of 600 cm^3 has a high efficiency to detect γ-rays and will be used for investigations of a resonant 0νEC/EC decay of ^{106}Cd and $2\beta^-$ decay to the excited states of daughter nuclei.

1. Introduction

The double beta decay processes ($\beta^-\beta^-$, β^+ β^+, β^+/EC, EC/EC) are of major importance for particle and nuclear physics as powerful tools for the study of lepton number conservation and neutrino properties [1]. Two-neutrino mode of $\beta^-\beta^-$-decay has been experimentally measured for several isotopes [2], while other double beta decay processes have never been observed in direct experiments. The claim of a positive 2νEC/EC signal for Barium isotopes using a geochemical technique [3] has to be confirmed by direct measurements as the robustness of this implicit experimental method is debatable. The ^{106}Cd ($Q_{EC/EC}$ = 2775.39 ± 0.10 keV) isotope is one of the most favorable candidates for studying EC/EC-decay due to the high decay energy. The 2νEC/EC decay of ^{106}Cd with a transition to the ground state of ^{106}Pd ($0^+ \rightarrow 0^+$, g.s.) is characterized by emission of two Palladium (Pd) X–rays each with an energy of ~21 keV. The best experimental limit on 2νEC/EC decay of ^{106}Cd was obtained in the TGV-2 [4, 5] experiment - $T_{1/2} > 4.2 \cdot 10^{20}$ yr (at 90 % C.L.) [6, 7]. The TGV-2 experiment showed an increased number of KX-KX coincidences events in the region of ~21 keV, which might be the 2νEC/EC decay of ^{106}Cd. But the statistics was not enough to make any significant claim about the presence of the process searched. A larger statistics of KX-KX events should be accumulated with a higher mass of enriched ^{106}Cd and increased number of detectors used. The quantity of detectors will be increased by using a new additional spectrometer – Telescope of Silicon Pixel Detectors [8]. Using Silicon Pixel Detectors (SPD) one can achieve good energy resolution, pixelization with the pitch at the level of tens of micrometers together with information on energy deposited in each pixel provide excellent tool for particle identification.

Investigation of resonant neutrino-less double electron capture decay (0νEC/EC) of ^{106}Cd was also performed by using the TGV-2 spectrometer [6, 7]. According to information of [9] it was based on analyzing of KX-γ coincidences to obtain the possible KL-capture resonant transition to the excited 2741 keV state of ^{106}Pd or by KK-capture to the excited 2718 keV state of ^{106}Pd. The populated levels (2741 keV and 2718 keV) de-excite by emission of 2741 keV γ-ray or by 2229 keV and 512 keV γ-quanta cascade and 1160 keV, 1046 keV and 512 keV γ-quanta cascade. Recalculation of the level scheme of ^{106}Pd made in [10] had disfavored the processes of interest and increased uncertainties of the levels characteristics, especially for the levels suitable for 0νEC/EC resonant transitions (see details in [6]). But ^{106}Cd is still the main candidate for the searching for 0νEC/EC resonant decay [11]. It means that the only way of search for the 0νEC/EC resonant decay of ^{106}Cd is to measure all γ-rays emitting in the EC/EC decay of ^{106}Cd. The best set-up for this measurement is the low-background high-efficiency HPGe spectrometer. Such spectrometer was installed at the Modane underground laboratory (LSM, France, 4800 m w.e.). It will be also used for the investigations of $\beta^-\beta^-$-decay to the exited states of daughter nuclei.

2. Silicon Pixel Telescope

The new detector intended for the search for EC/EC decay of ^{106}Cd - Silicon Pixel Telescope (SPT) will be based on hybrid pixel devices Timepix [8] developed in CERN by Medipix collaboration [12]. Silicon Pixel Detector (SPD) consists of the silicon sensor (256 × 256 pixel matrix, 55 μm pitch, size 1.4 cm × 1.4 cm, thickness 300 μm) bump-bonded to the Timepix readout chip. An analog circuitry and a digital counter are integrated with each pixel of this detector. The Timepix device, operated in Time Over Threshold (TOT) mode, can use the counter as a Wilkinson type ADC providing spectroscopic capabilities in each individual pixel. For data acquisition the SPD was connected to PC via USB readout interface (Fig. 1). Data from the SPD were recorded frame by frame with the shutter time of 0.1 s and the dead time of 20 ms. Energy calibration of the SPD was performed for each separate pixel by using radioactive sources of ^{55}Fe,^{241}Am, and X-rays of Cd, Cu, Zr and In. The ability of the SPD to identify α,β,μ particles [6] and localize them precisely leads to effective background discrimination and improving of signal-to background ratio (S/B).

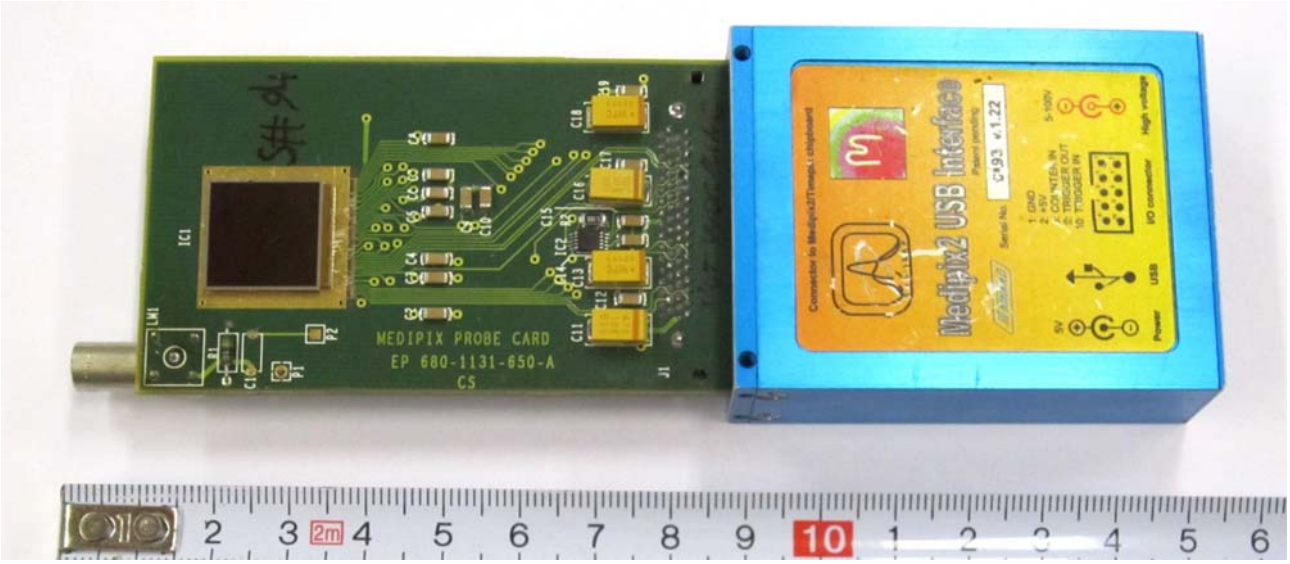

Fig. 1. The module of Timepix SPD connected to USB readout interface.

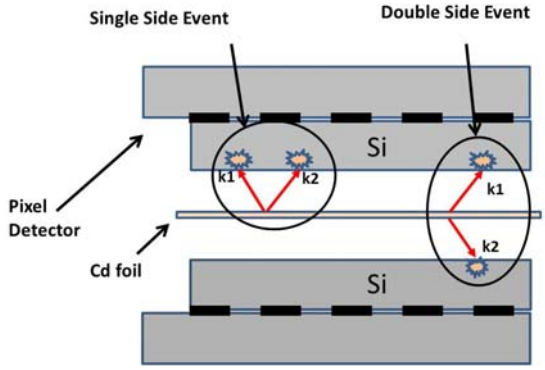

Fig. 2. The scheme of detection of two Pd X-rays using a pair of SPD and a foil of ^{106}Cd.

The SPD works at room temperature and has a high efficiency for registration of low energy X-rays (15 - 25 keV) – up to ~ 17 % for the detector thickness of 300 µm, and up to ~44 % for the detector thickness of 2 mm. Good geometrical acceptance of the SPT provides a possibility of increasing the efficiency to detect two correlated Pd X-rays, emitted in EC/EC decay of ^{106}Cd, by registration of not only double side events (DSE), as in the TGV-2 spectrometer, but also single side events (SSE) (Fig. 2).

The Timepix technology was not tuned for ultra-low background measurements. It was confirmed by measurements of the SPD background. Parts of the SPD were measured by using of a low background HPGe detector located in LSM in order to find the source of background. The obtained results [8, 13] showed that the main source of the internal background was Printed Circuit Board (PCB) which was necessary to be replaced by clean analog. New PCB were produced from the CuFlon material (Teflon plated by copper), which was found to have the least radioactive contaminations among materials used for the PCB. A prototype of the SPT was produced from a pair of the SPD (face-to-face detectors) with the CuFlon PCB. The distance between the sensors was 5 mm. It could be reduced to 1 mm by using flexible PCB design. For the measurements of background the SPT was surrounded by a lead shielding with a thickness of 5 cm. These measurements were performed at LSM underground laboratory and at surface. The results obtained were compared to the results obtained in measurements of single SPD with the "standard" PCB (Fig. 3).

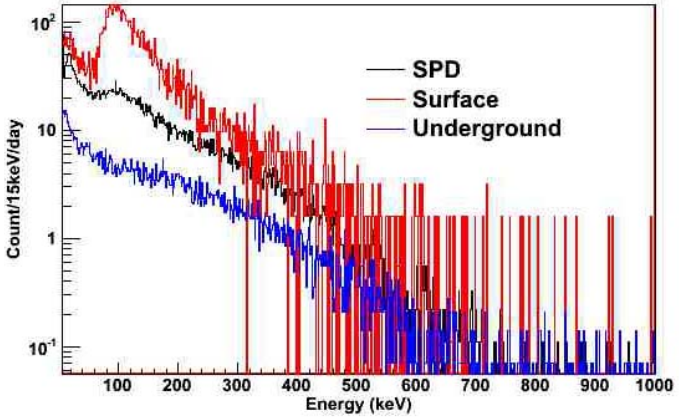

Fig. 3. Comparison of background spectra obtained in measurements with the SPD (underground) and the SPT (surface and underground), surrounded by a lead shielding with a thickness of 5 cm. Spectra are normalized to counts/15 keV/day.

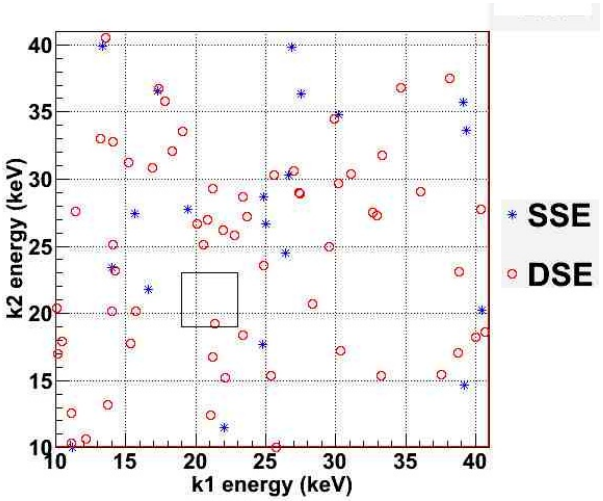

Fig. 4. Scatter plot of SSE and DSE obtained during 320 hours background measurement in LSM.

The background of the SPT with Cuflon PCB was suppressed by a factor of 3 in comparison to the SPD on standard PCB. Suppression factor of ~40 in total counting rate (CR) was achieved using methods of passive shielding (lead shielding, location in underground laboratory). Thus the total number of the SSE was suppressed in ~80 times, and the DSE in ~ 30 times. The measurement of the SPT background in LSM was performed during 320 hours. Fig. 4 shows a scatter plot of the SSE and the DSE of this measurement in low energy region. Region of interest (19 - 23 keV) for the search for 2νEC/EC decay of ^{106}Cd was pointed.

The passive shielding will be increased by additional layers of lead, copper and polyethylene for further suppression of radioactive background. Readout electronics is planned to be separated from the sensor by using the flexible PCB. We also try to reduce the current dead time of reading data as much as possible. The measurement of background with Cd foil installed between the SPD will show the suppression of the DSE. We are studying the possibility of using pixel detectors on the base of GaAs as their efficiency for registration of Pd X-rays seems to be approximately twice higher at approximately the same level of radioactive contaminations. Using the SPT spectrometer together with TGV-2 we hope to increase the sensitivity of the search for 2νEC/EC decay of ^{106}Cd up to $T_{1/2} \sim (0.8 - 1.0) \cdot 10^{21}$ yr.

3. HPGe spectrometer

The low background HPGe detector produced by Canberra is based on P-type crystal with the sensitive volume of 600 cm^3 and efficiency of 160 %. The crystal was mounted in ultra low background U-type cryostat with cooled FET. The energy resolution of detector is ~1.2 keV at 122 keV (^{57}Co) and ~2 keV at 1332 keV (^{60}Co). Constructive details of inner part of cryostat are produced from materials with ultra low radioactive contaminations and are separated from crystal by additional shielding from archeological lead. The distance from the crystal to the end cap is 4 mm. The detector part of cryostat is surrounded by several layers of archeological lead (~12cm) and low active lead (~20 cm) which are made in a ring shape and placed inside tightly closed stainless steel cover (Fig. 5). Two internal layers of archeological lead with the thickness of ~7 cm can be removed to measure of big samples in Marinelli beakers and bobbins. The internal part of the passive shielding is blown by the air without Radon. The electronic part of the spectrometer is based on NIM electronic modules produced by Canberra – High Voltage Power Supply 3106D, Spectroscopy Amplifier 2022, ADC Multiport II (16384 channels). The first part of measurements was performed by using a Digital Signal Analyzer Lynx. The software of Genie 2000 version 3.2.1 is used for data taking and analysis of spectra. Spectrometer is installed in Modane underground laboratory, LSM, France (4800 m w.e.), which provides the suppression of muons flux in ~$2 \cdot 10^6$ times and fast neutrons in ~10^3 times.

Fig. 5. The HPGe detector in passive shielding (left part) and the inner part of passive shielding (right part).

The sensitivity of measurements depends on the level of spectrometer background, the mass and shape of samples, and the geometry of measurements (efficiency). The background is the object of permanent control to avoid of any contaminations of the detector and the passive shielding. The detector was produced recently and its background (Fig. 6) consists of not only natural activity of ^{40}K, and isotopes of U and Th rows, but also of some cosmogenic

isotopes, such as ^{57}Co ($T_{1/2}$ = 271.79d), ^{54}Mn ($T_{1/2}$ = 312.3d), ^{65}Zn ($T_{1/2}$ = 244.26d), produced in Ge crystal during its location on the surface. Starting of the time when detector was located in underground laboratory (November 2010) the level of mentioned isotopes permanently decreases and in few years the traces of these isotopes will not be observed in the background spectra. Energy calibration of spectrometer was performed by using ^{152}Eu and ^{133}Ba. To calibrate spectrometer by efficiency, except already named pointed sources, the special samples prepared from powder of La_2O_3 are used. Using of this powder is based on the fact that natural La consists of 0.0902 % of ^{138}La ($T_{1/2} = 1.05 \cdot 10^{11}$ yr) which characterized by emission of γ-rays with energies of 788.7 keV and 1435.8 keV, and low energy KX-rays of Ba and Ce with energies in the region of 31.45 - 40.33 keV. The activity of such sample may be easily calculated by the mass of La_2O_3 and it is possible to obtain the efficiency for the measurement of samples in Marinelli beakers or bobbins.

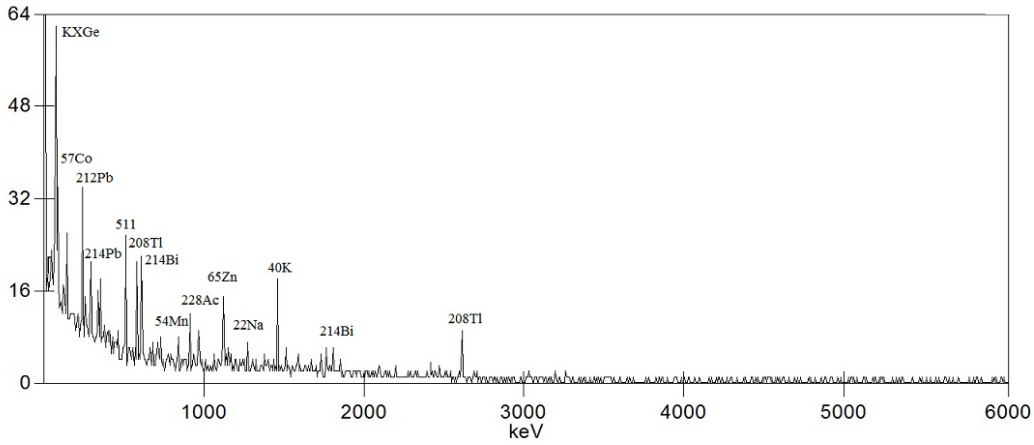

Fig. 6. Spectrum of the detector background measured during 40 days.

The main goal of the spectrometer is the measurement of double beta decay processes to the excited states of daughter nuclei, when the objects to detect are γ-rays, emitting in depopulation of excited states. We plan to perform the investigation of 0νEC/EC resonant decay of ^{106}Cd with ~10 g of ^{106}Cd (enrichment of 98.4 %). The sensitivity of 1 year measurement will be on the level of $T_{1/2} \sim 10^{21}$ yr. In our further plans are measurements of $2\nu\beta^-\beta^-$ - decays of ^{82}Se, ^{100}Mo, ^{150}Nd to the excited states of daughter nuclei with the mass of investigated isotopes from one to several kilograms. The sensitivity of such measurements will be on the level of higher than $T_{1/2} \sim 10^{21}$ yr.

ACKNOWLEDGEMENTS

This work was performed under collaboration agreement No.04-66 between IN2P3 and JINR and partly supported by grants MSM6840770029, RI LSM/ULISSE, LG11030 and by Russian Foundation for Basic Research under grant No.11-02-00813. We are grateful to the LSM laboratory that provided service for work underground and highly valuable technical assistance.

REFERENCES

1. *Haxton W.C., Stephenson G.S.* Double beta decay // Prog. Part. Nucl. Phys. - 1984. - Vol. 12. - P. 409 - 479.
2. *Tretyak V.I., Zdesenko Yu.G.* Tables of double beta decay - an update // At. Data and Nucl. Data Tables. - 2002. - Vol. 80. - P. 83 - 116.
3. *Meshik A.P. et al.* Weak decay of 130Ba and 132Ba: Geochemical measurements // Phys. Rev. - 2001. - Vol. C64. - P. 035205 (6 p.).
4. *Beneš P. et al.* The low background spectrometer TGV II for double beta decay measurements // Nucl. Instr. Meth. - 2006. - Vol. A569. - P. 737 - 742.
5. *Rukhadze N.I. et al.* New limits on double beta decay of ^{106}Cd // Nucl. Phys. - 2011. - Vol. A852. - P. 197 - 206.
6. *Rukhadze N.I. et al.* Search for double beta decay of ^{106}Cd // Bulletin of the Russian Academy of Sciences: Physics. - 2011. - Vol. 75. - P. 879 - 882.
7. *Rukhadze N.I. et al.* Experiment TGV-2. Search for double beta decay of ^{106}Cd // J. of Physics: Conference Series. - 2012. - Vol. 375. - P. 042020 (4 p.).
8. *Cermak P et al.* Use of silicon pixel detectors in double electron capture experiments // JINST. - 2011. - Vol. 6. - P. C01057 (10 p.).
9. *Firestone R.B., Shirley V.S.* Table of isotopes / 8th ed.:1998 update. - New York: John Wiley & Sons, Inc., 1996.
10. *De Frenne D., Negret A.* Nuclear Data Sheets for A = 106 // Nuclear Data Sheets-2008. - Vol. 109. - P. 943 - 1102.
11. *Krivoruchenko M.I. et al.* Resonance enhancement of neutrinoless double electron capture // Nucl. Phys. - 2011. - Vol. A859. - P. 140 - 171.
12. http://medipix.web.cern.ch/medipix/index.php
13. *Brudanin V.B. et al.* Summary of the TGV experiment and future plans // Proc. of the Workshop on Calculation of Double-Beta-Decay Matrix Elements (Medex'11) / Ed. by O. Civitarese, I. Stekl, J.Suhonen. - New York, AIP, 2011. - P. 110 - 114.

INTEGRATED PC-BASED SYSTEM FOR DETECTING AND PARAMETER MONOTORING AT THE DUBNA GAS FILLED RECOIL SEPARATOR

Yu. S. Tsyganov, A. N. Polyakov, A. M. Sukhov

Flerov Laboratory of Nuclear Reactions, Joint Institute for Nuclear Research, Dubna, Moscow region, Russia

New detection system of the Dubna Gas Filled Recoil Separator [1 - 3] (DGFRS) was put into operation in May 2012. It includes 32-strip position sensitive PIPS detector manufactured by CANBERRA NV, 24-strip back side PIPS detector, 8-strip "VETO" PIPS detector, time-of-flight low pressure (~1.7 Torr) pentane-filled gaseous detector, CAMAC fast ADC's with 5 μs dead time per three signals (energy, top position, bottom position), modified CC012 crate controller and PC-based C++ Builder code for spectrometry data acquisition. New parameter monitoring system (project) is reported too together with the brief review of the present system. It is planned to put into operation with this system during 2013-2014. Examples of applications in the long-term experiments aimed at the synthesis of superheavy elements in ^{48}Ca induced complete fusion nuclear reactions are also presented. Namely with the DGFRS facility 45 new isotopes of superheavy nuclei were synthesized since 2001.

1. Introduction

From the viewpoint of detection system the experiment on synthesis and study of the properties of superheavy nuclei is one of the most difficult tasks. In fact, these experiments can be considered extreme in many cases:

- extremely low formation cross sections of the products under investigation;
- extremely high heavy ion beam intensities;
- high radioactivity of actinide targets, which are used in the experiments aimed at the synthesis of superheavy nuclei;
- extremely long duration of the experiment;
- extremely low yield of the products under investigation;
- very high required sensitivity of the detection system and
- radical suppression of the background products (method of "active correlations");
- high reliability level of monitoring system.

Three last points are the subject of the present paper in a wide sense as well as the examples of applications of the mentioned systems and methods. Deeply modified method of "active correlation" is one of them.

2. New the DGFRS detection system

New DGFRS detecting module consists of 32 strip (Fig. 1) position sensitive PIPS detector (size 12 × 6 cm^2), 24 strip side PIPS detector and 8 strip "VETO" PIPS detector. The EVRs recoiling from the target were separated in flight from ^{48}Ca beam ions, scattered particles, and transfer reaction products by the DGFRS. EVRs passed through a time-of-flight (TOF) detector and were implanted in focal plane PIPS detector. Namely, detecting TOF signal provides discrimination of charge particles coming from cyclotron with respect to decay signals of implanted nuclei. The position-averaged detection efficiency for α-decay of implanted nuclei was about 87 % of 4π.

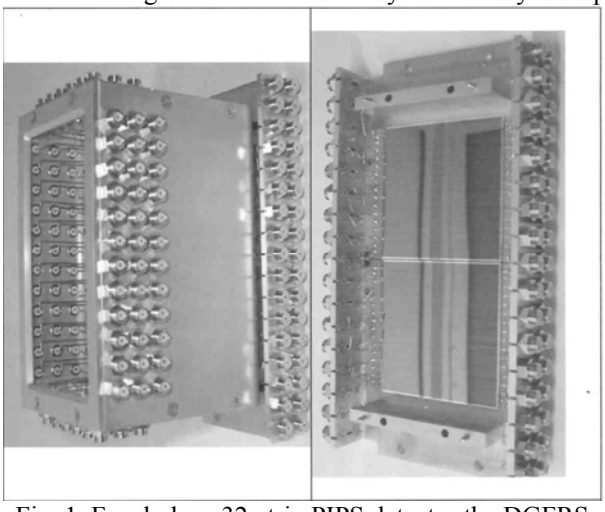

Fig. 1. Focal plane 32-strip PIPS detector the DGFRS.

To measure a vertical position we use both two signals – "top" signal and "bottom" signal. For operation with α-particle range signals (~0.6 to 20 MeV) we apply fast ADC PA3n (design by "Tekhinves", special economy zone "Dubna"). It allow to detect event by event signals with minimum (firs) dead time of 4.9 μs (Fig. 2) and regular dead time from 12 to 40 μs. It means that "minimum" signal sequence which can be detected by the system is approximately this: 5-40-5-40-5-40 or 5-12-5-12-5-12 … microseconds. The algorithm to search for EVR-alpha correlation sequence in a real-time mode is based on a simple idea. It consists in searching the time-energy –position EVR (evaporation residue) – alpha links using the discrete representation of the resistive layer of PIPS focal plane detector separately for "EVR", "alpha" signals. Thus, the real PIPS detector is represented in the PC RAM in the form of four matrices: two for recoils (EVR, static top/bottom), another two for alphas (top/bottom, dynamic-no storage elements except for the given cells). Those matrices are filled with the values of elapsed times obtained from CAMAC "Tekhinvest" module. The second index of the matrix element is defined by event vertical position, whereas the first index is in fact the strip number (1 to 32). In a case of alpha signal detection, a comparison with recoil matrix is made, involving neighbor elements (± 4). If the minimum "top" or "bottom" is less or

equal to the setting time (or calculated from any formulae with incoming energy dependence) the system turns on the beam chopper which deflects the heavy ion beam in the injection line of the cyclotron for one minute. At the next step PC code (Builder C++) ignores the vertical position of the alpha signal during beam-off interval. If such a decay takes place in the same strip that generated the pause, the duration of the beam-off interval is prolonged up to ten minutes (experiment $^{48}Ca+^{249}Bk \rightarrow 117+3,4n$; 2012).

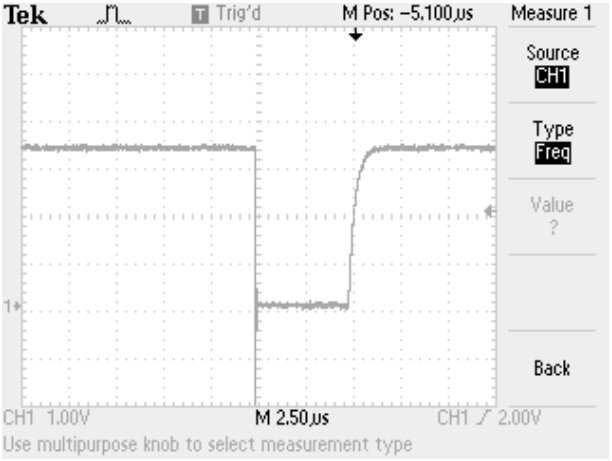

Fig. 2, *a*. Signal "dead time" of ADC PA3n.

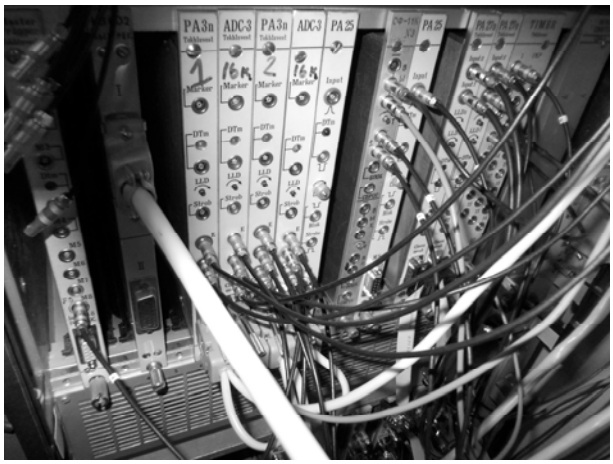

Fig. 2, *b*. CAMAC crate containing two Pa3n ADC units.

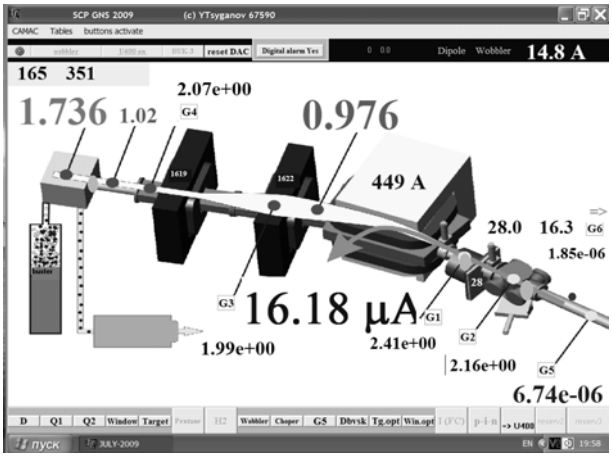

Fig. 3. The protection system user interface main form.

Of course, in the real experiment, in order to apply the mentioned above algorithm, calibrations procedures are strongly required. Calibration parameters are extracted from test reaction $^{nat}Yt+^{48}Ca \rightarrow ^{217}Th$ + 3n. It takes about 200 calibration parameters to provide the real-time search for EVR- α chains. Note, that the DGFRS detection system operates together with PC-based parameter monitoring and protection system which is described in detail in the Ref. [4 - 8]. In the Fig. 3 one can see main user interface form.

In the Fig. 3 the main parameters are: 1.736- pentane pressure in the TOF module (Torr), 16.18 µA- beam current at the DGFRS Faraday cup, 28.0- target wheel rotation speed (1/s), 0.976- hydrogen pressure in the separator, 449 A – dipole magnet current value, 165 – rate of events (1/s), 6.74e-06 – vacuum value before the separator, 14.8 A – beam wobbling winding current value. The main goal of that system application is to provide quick deflection of the cyclotron beam in the case of the system detected any "alarm" situation (e.g. associated with rotation of the actinide target wheel, vakuum line, hydrogen or pentane pressure, etc.)

2.1. Examples of application

As an example of application of the reported system in the Bk+Ca → 117 +3n experiment, one can see in the Fig. 4 multi-decay chain of Z = 117 nucleus. In that Figure: ER energy is 13.1 MeV, α_1 to α_6 10.97, 9.78, 9.75, 9.04, 9.38 and 8.69 MeV, respectively. Correlation time for ER-α_1 chain is 3.986 ms. Energies for fission fragments are 179.8 and 16.1 Mev (in focal plane detector and side detector.

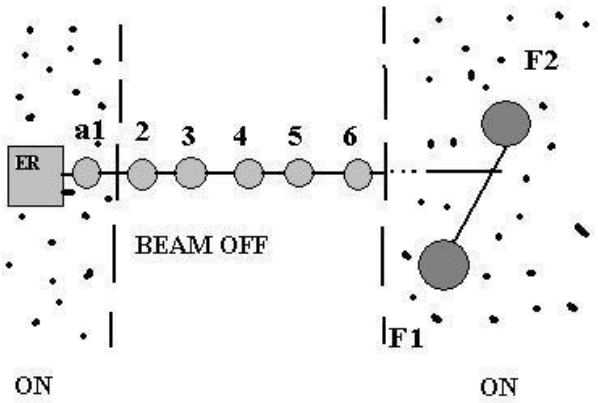

Fig. 4. Schematic of Z = 117 decay detected with the reported technique. Five alpha particles were detected in background free mode. Sequence ER –α-α-α-α-α-α-SF. Frequency of background signals are shown symbolically by points. Chain ER-α provided Beam Off interval, and the next alpha signal provided prolongation of the pause

Summary

New DGFRS detection and parameter monitoring system has been designed and successfully applied in the $^{249}Bk+^{48}Ca \rightarrow 117+3,4n$. Namely with radical background suppression due to that application, it has became possible to provide clear identification of decaying products. In a nearest future we plan to parallelize that system with ORNL design digital system [9].

Authors are indebted to Drs. V. Utyonkov, A. Voinov and V. Zhuchko for their help in putting the system into operation.

REFERENCES

1. *Tsyganov Yu.* Pulse amplitude analysis of rare events measured in heavy-ion-induced nuclear reactions // Nucl. Instrum. and Meth. in Phys. Res. - 2007. - Vol. A582/2. - P. 696 - 700.
2. *Tsyganov Yu., Polyakov A., Sukhov A.* An improved real-time PC-based algorithm for extraction of recoil-alpha sequences in heavy-ion induced nuclear reactions // Nucl. Instrum and Meth. in Phys. Res. - 2003. - Vol. A513. - P. 413 - 416.
3. *Tsyganov Yu.* The Dubna gas-filled recoil separator: status and developments // J. Phys. G: Nucl. Part. Phys. - 1999. - Vol. 25. - P. 937 - 940.
4. *Sukhov A.*, *Polyakov A., Tsyganov Yu*. Parameter monitoring and Control System of Dubna Gas Filled Recoil Separator // Phys. of Part. and Nuclei Lett. - 2010. - Vol. 7, No. 5. - P. 603 - 615.
5. *Tsyganov Yu.*S., *Polyakov A.N., Sukhov A.M.* Method of active correlations: present status.// Proc. of the 3-rd Int. Conf. “Current Problems in Nuclear Physics and Atomic Energy” (Kyiv, June 7 - 12, 2010). - Kyiv, 2011. - P. 379 - 381.
6. *Tsyganov Yu.*S. Detection of highly ionized particles: basic nonlinear near surface phenomena in silicon radiation detectors // ECHAYA.-2012 (in print).
7. *Tsyganov Yu.*, *Polyakov A., Sukhov A. et al.* Automation of the experiments aimed to the synthesis of superheavy elements // Proc. of the XXIII Int. Symp. NEC’2011 (Varna, Bulgaria, Sept. 12 - 19, 2011). - P. 281 - 285.
8. *Tsyganov Yu.*, *Polyakov A., Sukhov A. et al.* Method of active correlations: present status. // Proc. of RT-2010 IEEE-NPSS Conf. (Lisbon, Portugal, May 24 - 28, 2010). - P. PDAQ-4.
9. *Miernik K., Miller D.* (ORNL) Private communication.

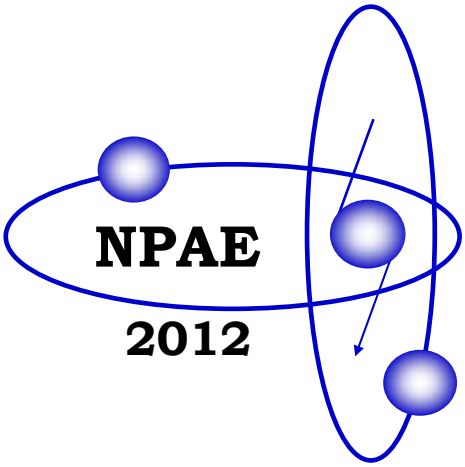

Section 5

Neutron and Reactor Physics, Nuclear Data

NEUTRON CONTROL OF WELL DEBIT INCREASING BY ACOUSTIC INFLUENCE ON OIL FORMATION

B. Yu. Bogdanovich[1], A. V. Nesterovich[1], D. R. Khasaya[1], A. E. Shikanov[1], E. A. Shikanov[2], A. V. Il'inskiy[3], L. V. Mihailov[4], N. F. Kolomiets[4]

[1] *National Research Nuclear University "MEPhI", Moscow, Russia*
[2] *Closed Joint Stock Company "SPECTR KSK", Moscow, Russia*
[3] *Institute for Geophysics and Radiation Technologies of the International Higher Education Academy of Sciences* (*IGRT IHEAS*), *Moscow, Russia*
[4] *Institute for Nuclear Research, National Academy of Sciences of Ukraine, Kyiv, Ukraine*

The fall in oil production rate wells is due to the deterioration of the permeability of the productive zone of extraction fluid, and is very common negative phenomenon, arising in the design field. This effect is almost inevitable, since the extraction of the productive layer of fluid acts as a filter, trapping and accumulating in the operation of the well all sorts of impurities in their pores or cracks.

One of the most effective methods of cleaning fluid productive zone recovery is the acoustic effect (AE) in her longitudinal ultrasonic wave pressure. At the same time in the pores of the reservoir, fluid-filled productive, there are transient oscillatory micro streams. With sufficient intensity ultrasound waves are micro steams help clean extraction of the productive zone of the fluid from the above pollutants [1].

The effectiveness of the AE direction in oil reservoirs can be improved by controlling the parameters of the processes occurring before and after AE in oil reservoirs, followed by a choice of intervals stimulation of oil. Measurements of changes in these processes in the reservoir are made remotely via a metal pipe casing that requires the use of transparent methods of control.

The most effective is reagent pulsed neutron method. It allows you to monitor changes in fluid layers chlorine in the process of displacement of injected reagent containing solution. The specified control is performed pulsed neutron method based on measurement of the lifetime of thermal neutrons in the reservoir, depending on the composition of the substance contained in the pores. This structure defines the process of forming a hole in the reservoir and as a result of slowing down, thermalization, and diffusion of the field of thermal neutrons, Falling in time exponentially.

Decrement of the thermal neutron density decline characterizes the content of chlorine in the reservoir due to its anomalously high radiative capture cross section. This allows us to solve the problem of determining water contact because of lack of chlorine in the oil-rich part of the reservoir and the presence of excess reagent in a solution in water due to its mineralization. The absence of formation water and hydrocarbon in the reservoir also affects the decrement of the decay of the neutron density, which is proportional to the total cross section of neutron absorption.

In implementing the method of pulse neutron-neutron logging (PNNL) in the study area provide periodic field impulse of fast neutrons emitted by the accelerating tube (AT), resulting in leakage to its target nuclear reaction T (d, n) 4He. After slowing down the neutrons to thermal velocities begins the process of decay of the neutron density. In this recession the spatial density of neutrons occurs exponentially with a decrement proportional to the total cross section of neutron absorption [2]. Measurement of decay of the neutron density is filled with 3He detectors, which proceeds in the amount of nuclear reaction 3He (n, p) T, with subsequent analysis of the temporal spectrum of the known methods used in experimental nuclear physics [3].

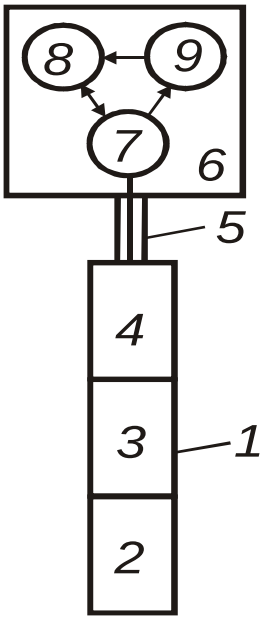

Fig. 1. Schematic diagram of the apparatus of the complex Indian National Congress. *1* – downhole pressure resistance in the guard body for pressures up to 10 Pa; *2* – neutron emitter based on AT; *3* – detection system; *4* – hole, executive and telemetry system with a time analyzer; *5* – Carrying logging cable; *6* – complex ground equipment (logging station); *7* – ground control units and telemetry; *8* – board computer; *9* – depth downhole tool into the well indicator.

The measurements were carried out using hardware-methodical complex AIOC-43 (development VNIIA named by N. L. Duhov) [4] on the basis of compact pulsed neutron generator [5] and multi-channel time analyzer [3].

Fig. 1 shows the general block diagram of hardware-methodical complex set of PNNL to be used for monitoring the effectiveness of AE.

On command from the ground control unit through the executive system is launched neutron emitter in the repetitively pulsed mode. As a result of the interaction of fast neutrons generated in the target vacuum AT, in the studied environment geophysical field is formed by thermal neutrons.

Detection system is designed to convert the field into analog electrical signals, which in a borehole telemetry system are converted into digital information that is sent to the logging cable in the ground-based geophysical telemetry unit. In this unit, this information is decoded and formatted as a series of files that are coming to the PC. The computer is processing the information on the two-component processing algorithms logging signal [3, 6]. The result is a dependence of the decrement thermal neutron density λ of the depth of the reservoir under study.

If the acoustic effects of the inflow of hydrocarbon fluid, it will be recorded a significant decrease in the decrement of decay of the density of thermal neutrons, as this decreases the concentration of nuclides detected by the detector. In the event of failure of the process of acoustic feedback or fill water reservoir effect of the change of the decrement will be less significant.

Fig. 2 shows the general scheme of the complex AE in conjunction with EMC PNNL used in the experiment.

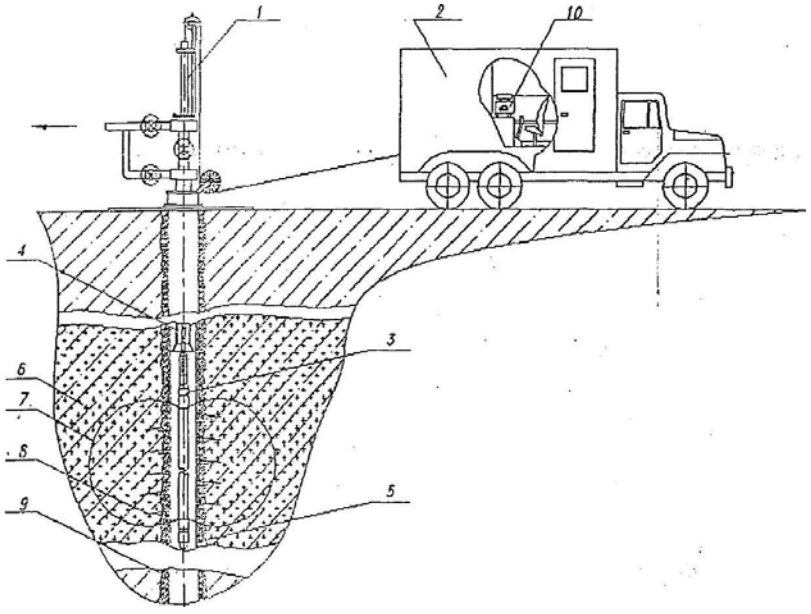

Fig. 2. Scheme of the experimental complex AE-PNNL for the stimulation of oil: *1* – fitting well; *2* – Geophysical Station; *3* – geophysical instrument; *4* – Tube Pumps, Compressor; *5* – Casing; *6* – oil reservoir; *7* – loop orientation of the neutron flux in the well; *8* – perforations; *9* – cement ring 10 ground geophysical equipment (PNNL, AE).

The complex consists of a ground control unit (geophysical station), which manages removable geophysical instruments (instrument pulsed neutron generator and the unit of acoustic effects) depending on the work performed. Replacement geophysical instruments lowered into the well through the valve on the tubing to the oil reservoir. Geophysical surveys were conducted at the perforations layers.

Measurements were carried out by the method of PNNL, first after the injection of the labeled solution, then after 8 hours of recovery (recovery of productive hydrocarbons), and finally, after an interval AE in the analyzed section of the reservoir. Record PNNL executed at a rate of rise of 40 m/h The main interpretative the-damping rate of the thermal neutron density λ was calculated from measurements PNNL using a special two-component signal processing logging. The working solution used a standard technical solution of NaCl with a density of 1180 kg/m3.

During the experiment in a well on the above procedure were performed as follows:

a) Background recording PNNL followed by treatment with a logging signal in the test interval;

b) Injection into the well of the solution, the subsequent recording and signal processing PNNL;

c) a record PNNL after 8 hours of recovery;

d) aimed at the AE layers and the subsequent recording and processing of PNNL

Fig. 3 (third fragment) are obtained as a result of the experiment well logs.

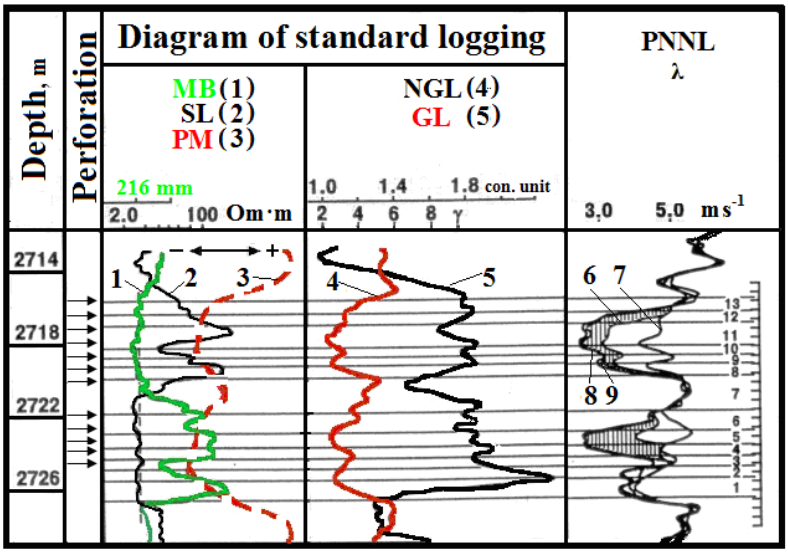

Fig. 3. Diagrams of the experimental results in the well by the method of neutron-"labeled" substance and directional acoustic stimulation (right vertical scale shows the number of layers).

For better reliability of their interpretation of the first two fragments of the same Figure shows the standard geophysical logging diagrams describing the study section: MB - measurement of borehole diameter (caliper), SL-side logging (logging type of resistivity recovery wells), PM-potential measurement spontaneous polarization, depending on the lithology of the borehole that is logged on the potential difference between two spaced electrodes (probes) NGL - neutron-gamma logging (measurement of the intensity of the secondary γ-radiation produced by irradiation of rock neutron source rocks in the well-GC γ-ray logging (recording the intensity of natural γ-radioactivity of rocks in the well).

PNNL Charts presented at the third passage the Figure illustrate the change in control of the damping rates of the density of thermal neutrons in the process of carrying out work in a well to intensify the flow of oil.

The test section is divided into 12 different oil reservoirs filtration properties of the reservoir with the numbers n = (1 ÷ 12). Numbering decreases with the depth of their location.

Each individual layer is characterized by different dynamics, the degree of absorption and impact of the labeled solution. A comparison of background diagrams and control charts in each cycle of measurement established that the error of determination are usually random in nature and can reach 2 % in layers of thickness 1 m. When comparing the results of measurements in different cycles are observed are small (5 %) differences of values of the damping decrement of thermal neutrons due to the different filling of the hole. This distortion is easily eliminated by comparing the diagrams in the supporting layers - nekollektornyh with a known unchanging properties of the damping decrement of thermal neutrons. The data obtained were evaluated λ changes of reservoir properties of the layers.

The absence or weak change in the λ layers 1, 2, 3, after injection of NaCl solution, and eight of their development shows that there is no hydrodynamic connection with the well layer.

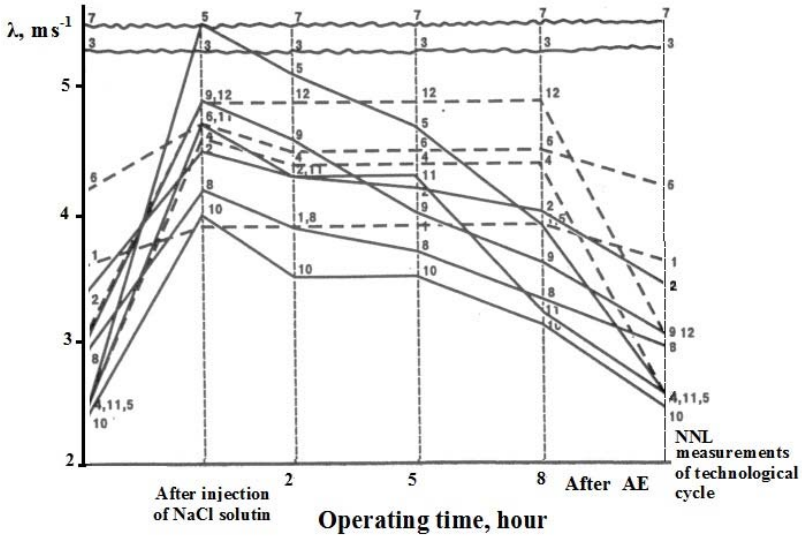

Fig. 4. Temporary change in the decrement of λ strata in the process of technological cycle of measurements Congress on the well.

A significant change in λ in layers 4, 5, 6, 8, 9, 10, 11, 12 indicates the presence of hydrodynamic connection with the well layer. Significant changes in λ in these layers after the directional acoustic effects suggests that the layers have also increased capacitive properties.

Fig. 4 shows graphs comparing the change in the decrement of λ in different layers in the time domain work on the well. The ordinate values of the decrement of the recession delayed thermal neutron density λ for different intervals of measurement technology cycles, pulsed neutron-reagent method (horizontal axis). At the same time with different layers have different numbering of reservoir properties.

The results of correlation comparing the measured values of λ before and after directional acoustic effects with the use of the reagent solution with NaCl showed purification processes petroleum reservoir formations. This is a group with lower reservoir properties - layers 4, 5, 8, and to the development of layers 9,10,11.

The data obtained with the use of the AE reagent indicate that intensification of treatment reservoirs containing oil. This is a group with lower - fluid properties (layers 4, 5, 6, 9, 10, 12), which were not doosvoeny 8 hours working out well.

Factor increasing the adaptability of this technique is the possibility of combining it with traditional activities at the wells, requiring the use of chlorine-containing substances. For example, the jamming hole solutions NaCl, CaCl during repair work, hydrochloric acid treatment beds etc.

In order to solve the complex problems of the intensification of the tributaries of the cut and detailing of the inhomogeneous oil reservoir on the dynamics of the displacement processes of filtration and connection to the work of the oil reservoir (thickness h> 0,2 m) with a variety of reservoir properties.

REFERENCES

1. *Kuznetsov O.L., Efimova S.A.* The use of ultrasound in the oil industry. - Moscow: Nedra, 1983.
2. *Shimelevich Ys., Cantor S., Shkolnikov A. S. et al.* Physical basis of pulsed neutron techniques for wells // Nedra. - 1976. - P. 122 - 130.
3. *Bogdanovich B.Y., Nesterovich A.V., Shikanov A. E. et al.* Remote radiation control with linear accelerators. Vol. 2. Radiation monitoring systems. - M.: Mechanical Engineering, 2012. - 284 p.
4. *Amur A. G., Kurdyumov I. G., Titov I. A. et al.* Apparatus pulsed neutron-neutron logging for use in modern technology for wells. Sat Materials of the Int. Scie. Conf. "Portable neutron generators and technologies based on them". - Moscow, VNIIA them. NL Spirit, 2005. - P. 253 - 255.
5. *Bessarabian J. G., Bogolyubov E. P., Kurdyumov I. G. et al.* Downhole neutron emitter // Instruments and Experimental Techniques. - 1994. - No. 5.
6. *Startsev A. A., Fedyna E. A., Shikanov A. E.* // Appl. Radiat. Isot. - 1997. - Vol. 48, No. 10 - 12. - P. 1329 - 1330.

BENCHMARK ON TRAVELING WAVE FAST REACTOR WITH NEGATIVE REACTIVITY FEEDBACK OBTAINED WITH MCNPX CODE

V. V. Gann, A. V. Gann

National Scientific Centre "Kharkiv Institute of Physics and Technology", Kharkiv, Ukraine

This paper presents results of computer simulations of traveling wave fast reactor with negative reactivity feedback. The results were obtained using MCNPX code combined with CINDER90 subroutine for depletion calculations. We considered 1-D model of TWR containing 4 m long core made of mixture of 66 at. % ^{238}U and 34 at. % ^{10}B. Ignitor made of ^{235}U was located in the center of the core. Boron was included as imitator of structural in-core materials and coolant. Negative reactivity feedback was adjusted to reactor power of 500 MW. In this case two burning waves originated from the igniter and travel to the ends of the core during the following 40 years; coefficient of utilization of ^{238}U reached 80 %. Distribution of specific power in traveling wave, isotope concentration of fission products and actinides, neutron flux, fast neutron spectrum, specific activity were calculated. Data of the computer simulation is in qualitative agreement with theoretical results obtained in slow burning wave approximation.

1. Introduction

Concept of the Traveling Wave Reactor (TWR) is one of the brilliant ideas of 20-th century that suggests using depleted U or Th as fuel and promises to supply inexhaustible source of energy worldwide. This idea was developed in many articles [1 - 6]. Two types of TWR were considered: self-regulating nuclear burning wave by L. Feoktistov [1] – reactor with fixed power, and TWR with negative reactivity feedback by E. Teller [2] – reactor that supplies "power on demand".

Nuclear burning begins in ignition part of the core containing enriched U; when concentration of ^{239}Pu in ^{238}U becomes high enough due to $^{238}U + n = {}^{239}U \rightarrow {}^{239}Np \rightarrow {}^{239}Pu$ breeding process, two burning waves appear from both sides of the ignition zone, detach from it and propagate to the ends of the core during following 30 - 40 years.

This paper presents results of Monte Carlo simulation of traveling wave fast reactor with negative reactivity feedback. Computer simulation was generated by MCNPX code combined with CINDER90 subroutine for depletion calculations using ENDF/B-VII neutron data library. We considered 1-D model of TWR containing the core 60 cm in diameter and 4 m in length. The core is made of mixture of 66 at. % ^{238}U + 34 at. % ^{10}B; enriched uranium igniter 50 cm length is located in the center of the core. Boron was included as an imitator of structural in-core materials and coolant. Negative reactivity feedback was adjusted to reactor power of 500 MW. Operational life was determined to be ~ 40 years with coefficient of utilization of ^{238}U reaching 80 %. Distribution of specific power, isotope concentration of fission products and actinides, neutron flux, neutron spectrum and specific activity in traveling wave were calculated.

Theory of TWR with negative reactivity feedback was developed in slow burning wave approximation. Based on this theory, simple approximation formulas describing computer simulation results were obtained.

2. Computer model of TWR

Table 1. **Parameters of TWR model**

Composition of material	66 at. % ^{238}U, 34 at. % ^{10}B
Composition of igniter	66 at. % ^{235}U, 34 at. % ^{10}B
Density, g/cm^3	10
Length of igniter, cm	50
Total length, cm	400
Diameter, cm	60
Boundary conditions	Mirror
Temperature, C	700
Power, MW	500

TWR model consists of cylinder R = 30 cm made of mixture of ^{238}U and ^{10}B. Igniter of burning waves is made of ^{235}U shaped as a flat disk 50 cm thick that is located in the center of the core. Boron is added to compensate for excess reactivity that could reach $\rho \approx 0.2$ without it. The core is divided into cylindrical cells that are 5 cm long; total length of the core is 400 cm (Table 1). Mirror boundary conditions are used on the side of cylinder. Burning wave ignition process takes approximately 20 years. When sufficient amount of ^{239}Pu is generated near the igniter, two burning waves brake away from ignition zone and propagate to the ends of the core (Fig. 1). The time-step interval of computer simulation is approximately 1000 days.

Fig. 2 shows relationship between multiplication constant k_{eff} and time that would occur in the system without negative reactivity feedback. The system reaches stationary state after ~20 years, which is followed by the period of stationary burning for ~24 years. During stationary burning period value of k_{eff} remains practically constant until the waves reach the ends of the core. Negative reactivity feedback maintains reactor power at a set level of 500 MW and ensures criticality of the reactor during its operational time.

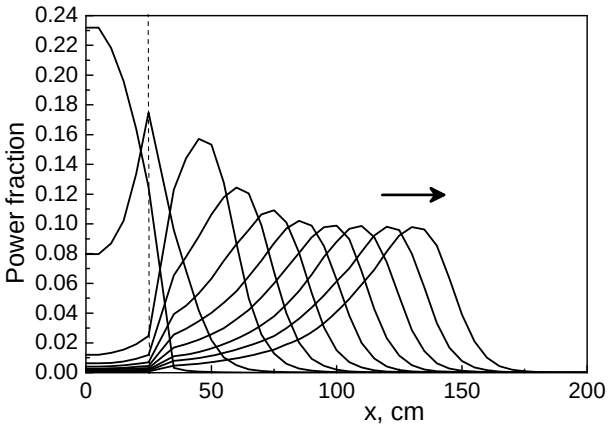

Fig. 1. Traveling wave dynamics (right half of core).

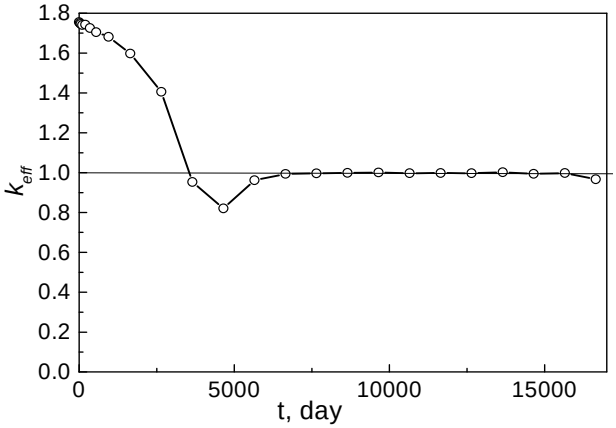

Fig. 2. k_{eff} depending on time.

3. Computer simulation results

Table 2. **Parameters of traveling wave**

Velocity of wave	4.3 cm/year
Specific power	1.7 KW/cm^3
^{239}Pu concentration (max)	7.2 at. %
Fluence of neutrons	7.8 10^{24} n/cm^2
Fuel burnup	650 MWd/MTU
^{238}U utilization coefficient	80 %
^{239}Pu concentration in corium	2 at. %
Specific activity, residual	7 C/g
Average ν	2.93

Table 2 shows basic parameters of traveling burning wave, that were obtained using MCNPX v. 2.6 code for computer simulation. Figs. 3 - 6 provide profiles of specific power, neutron flux and spectrum, concentration of ^{239}Pu and ^{8}U, activity distribution along the reactor core at time $t = 11400$ days. Following from Fig. 4, maximum concentration of ^{239}Pu precedes maximum power in the wave.

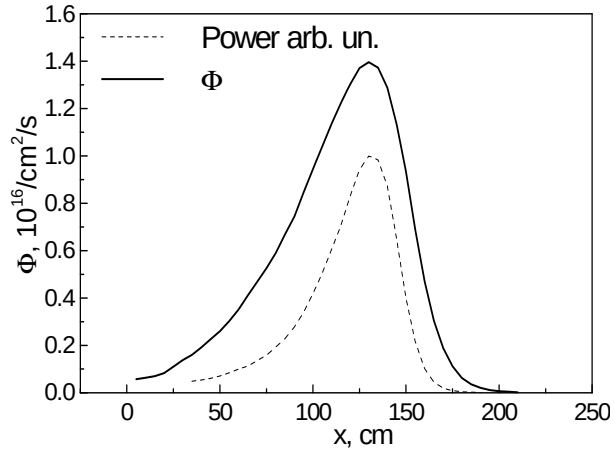

Fig. 3. Profiles of neutron flux and specific power.

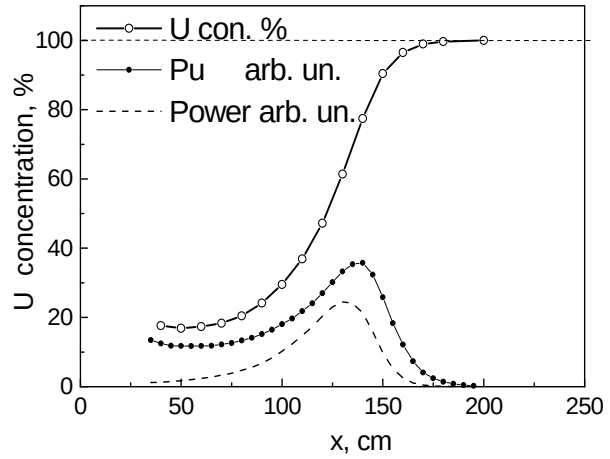

Fig. 4. Profiles of ^{238}U and ^{239}Pu concentration.

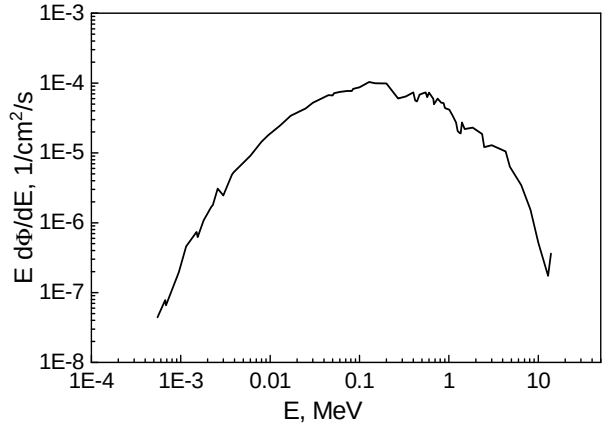

Fig. 5. Neutron spectrum.

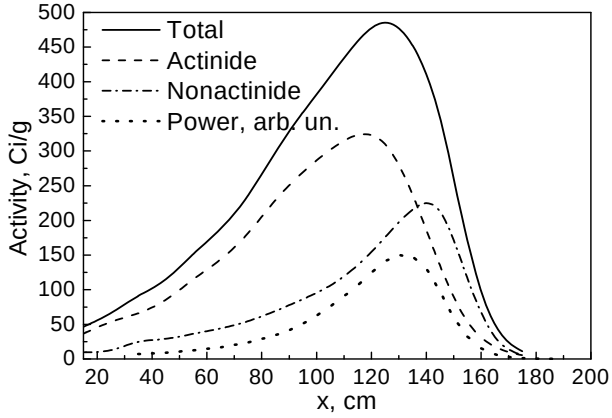

Fig. 6. Activity distribution in wave.

Speed of the traveling wave is 4.3 cm/year, maximum specific power is 170 W/g; ^{238}U utilization coefficient reaches 80 % with ^{239}Pu maximum concentration amounting to 7.2 at. %. ^{239}Pu concentration in burnt-up material is 2 %, residual specific activity behind the wave amounts to 7 Ci/g. Fluence of neutrons in burnt-up material approaches 7.8 10^{24} n/cm^2.

Actinides ^{239}U and ^{239}Np as well as fission products Xe, Cs, I and Ru are responsible for the most of the total activity.

4. Theory of slow traveling wave

Slow wave [6] of ^{239}Pu breeding and burning can be described by the following set of equations:

$$D\frac{\partial^2\Phi}{\partial x^2}+(\nu\Sigma_f-\Sigma_a)+S=0\,,\quad \Sigma_f=\sigma_f n_9\,,\ \Sigma_a=\sigma_a(n_8+n_9)+\sigma_c n_c\,, \tag{1}$$

$$\frac{\partial n_8}{\partial t}=-n_8\sigma_a\Phi\,,\quad \frac{\partial n_9}{\partial t}=(\sigma_{89}n_8-\sigma_a n_9)\Phi\,,\ \frac{\partial n_c}{\partial t}=2\sigma_f n_9\Phi\,, \tag{2}$$

where Φ is neutron flux; n_8 and n_9 are concentration of ^{238}U and ^{239}Pu respectively; n_c is fission product concentration; D is neutron diffusion coefficient; σ_{89} is ^{238}U → ^{239}Pu transmutation cross-section; $\tau_{89}\approx 2.3$ days is $^{239}U \rightarrow {}^{239}Np \rightarrow {}^{239}Pu$ decay time; σ_f is ^{239}Pu fission cross-section; ν is neutron multiplicity; σ_c and $\sigma_a\approx\sigma_{a8}\approx\sigma_{a9}$ are microscopic cross-sections of neutron absorption by the fission products and by ^{238}U and ^{239}Pu nuclei; Q is Q-value for ^{239}Pu; P is reactor power; S is the term describing negative reactivity feedback and operation control devices. Standard form of the term S is: $S=-\rho\nu\Sigma_f\Phi$, where $\rho=(k_{eff}-1)/k_{eff}$ is instantaneous value of reactivity without feedback. Slow wave approximation is valid if speed v meets the requirement: $v\tau_{89}\sqrt{\sigma_a n_8(0)/D}<<\chi$.

Let us find a solution of Eqs. (1) and (2) in the traveling wave form $\Phi(x,t)=\Phi(t-x/v)$ and replace time t with a new variable $\varphi=\sigma_a F$, that is proportional to fluence F and varies from 0 to maximum value $\chi=\sigma_a F_{\max}$:

Eqs. (1) and (2) take the following form:

$$\frac{D\sigma_a^2}{2v^2}\frac{d^2\Phi^2}{d\varphi^2}+\nu(1-\rho)\Sigma_f-\Sigma_a=0\,, \tag{3}$$

$$\frac{dn_8}{d\varphi}=-n_8\,,\ \frac{dn_9}{d\varphi}=n_8\sigma_{89}/\sigma_a-n_9\,,\ \frac{dn_c}{d\varphi}=2n_9\sigma_f/\sigma_a\,, \tag{4}$$

$$P=vQ/\sigma_a\int_0^{\chi}\Sigma_f d\varphi\,;\quad \varphi=\sigma_a\int_{-\infty}^{t}\Phi(t')dt'\,. \tag{5}$$

For existence of the stationary solution, function $\Phi(\phi)$ must meet the following boundary conditions: $\Phi(0)=0$, $\Phi(\chi)=0$, $\Phi'(0)=0$, $\Phi'(\chi)=0$.

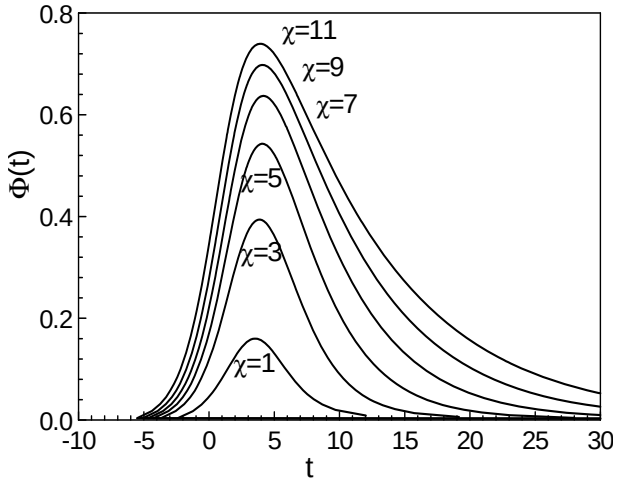

Fig. 7. Flux depending on time for different values of χ.

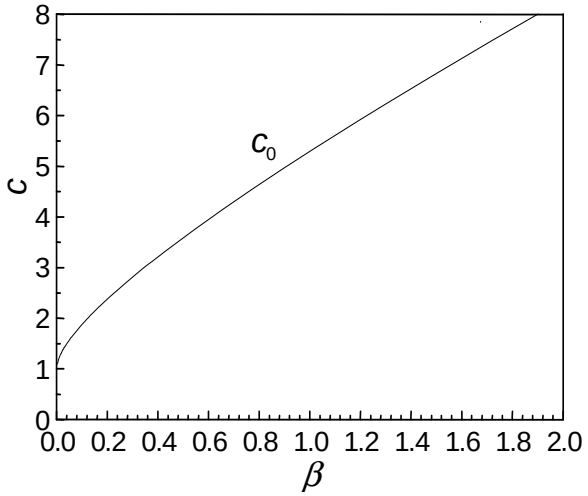

Fig. 8. Solution (7) existence domain: $c>c_0$.

Integrating Eqs. (3) and (4) we have:

$$\Phi^2 = \frac{2n_8(0)v^2}{D\sigma_a} f(\varphi,q)\,; \quad f(\varphi,q) = \beta\varphi^2 + (1-2\beta-q)\varphi + (1-2\beta-2q)(e^{-\varphi}-1) - q\varphi e^{-\varphi}], \tag{6}$$

where $\beta = \frac{\sigma_c\sigma_f\sigma_{89}}{\sigma_a^3}$, $q = \frac{2\beta\chi - (1-2\beta)(e^{-\chi}-1)}{1-(1+\chi)e^{-\chi}}$, $c = \frac{\sigma_{89}}{\sigma_a}\left(\frac{\nu\sigma_f}{\sigma_a} - 1\right)$, $c_0 = q - 2\beta$.

Then, we obtain an implicit solution for the function $\varphi(t)$ (Fig. 7):

$$(t - x/v)\sigma_a = \int_{\chi/2}^{\varphi} \frac{d\varphi'}{\Phi(\varphi',\chi)}\,, \tag{7}$$

where speed of wave v can be obtained from Eq. (5) for a set value of reactor power:

$$P = vQ\,n_8(0)(1 - e^{-\chi} - \chi e^{-\chi})\sigma_f\sigma_{89}/\sigma_a^2\,. \tag{8}$$

Solution (7) is valid above the line c_0 in Fig. 8; the wave does not propagate below the line c_0 because of the large absorption of neutrons.

5. Analytical approximation of the computer simulation results

Following from Eq. (6) (see also [3]), function $1/\Phi(F)$ is analytical function of F with simple poles at the ends of the interval $0 \le F \le F_{max}$: $1/\Phi(F) = R(F)\left[1/F + 1/(F_{max} - F)\right]$. Here, F_{max} is the fluence in fuel behind the wave and $R(F)$ is a smooth function. The simplest function of this type is: $1/\Phi(F) = B\left[A/F + 1/(F_{max} - F)\right]$. When substituted into Eq. (7), this function gives an analytical solution with adjustable parameters A, B, F_{max} and v:

$$t - x/v = B\ln\left(\frac{F^A}{F_{max} - F}\right). \tag{9}$$

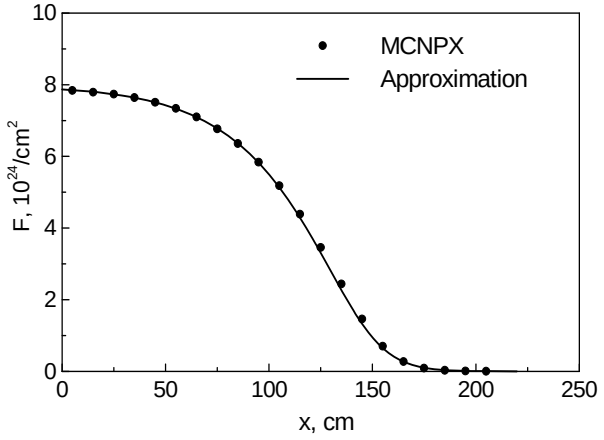

Fig. 9. Analytical approximation of fluence.

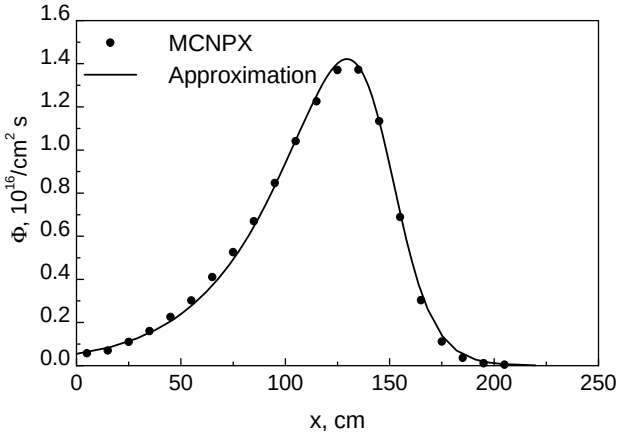

Fig. 10. Analytical approximation of flux.

Figs. 9 - 12 show analytical approximation of flux (in 10^{16} n/cm^{2}s), fluence (in 10^{24} n/cm^2) and concentration of ^{238}U and ^{239}Pu (in at. %), obtained by fitting Eq. (9) to the results of the computer simulation:

$$\Phi(x) = 0.43\Big/\left(\frac{0.3}{F} + \frac{1}{8-F}\right);\; x = 87 - 32\,\ln\left(\frac{F^{0.3}}{8-F}\right);\; n_8(x) = 100e^{-0.25F}\;;\; n_9(x) = 10\,F\,e^{-0.5F}\,. \tag{10}$$

As Figs. 9 - 12 show, simple analytical approximation (10) offers good description of computer simulation results obtained using MCNPX code.

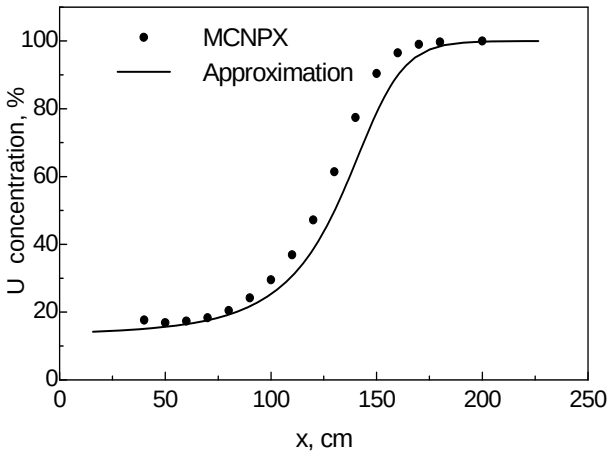

Fig. 11. Approximation of ^{238}U concentration.

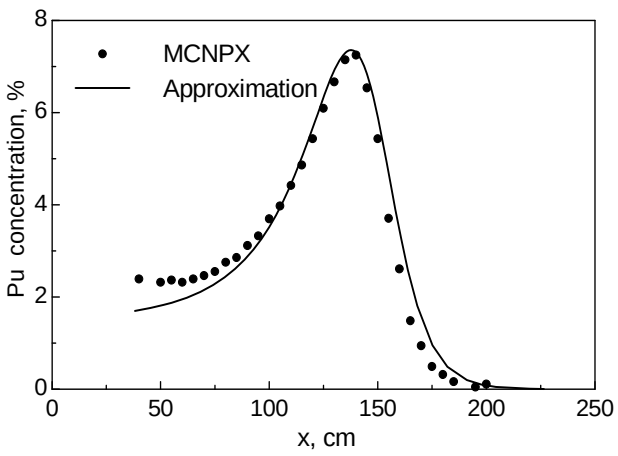

Fig. 12. Approximation of ^{239}Pu concentration.

6. Traveling wave stability

Numerical solution of nonstationary Eqs. (1) and (2) for collision of burning wave with 7 % ^{239}Pu block is plotted in Fig. 13 (right). Due to negative reactivity feedback, neutron flux and ^{239}Pu production rate decrease but the reactor power remains constant. After burning extra ^{239}Pu neutron flux profile recovers.

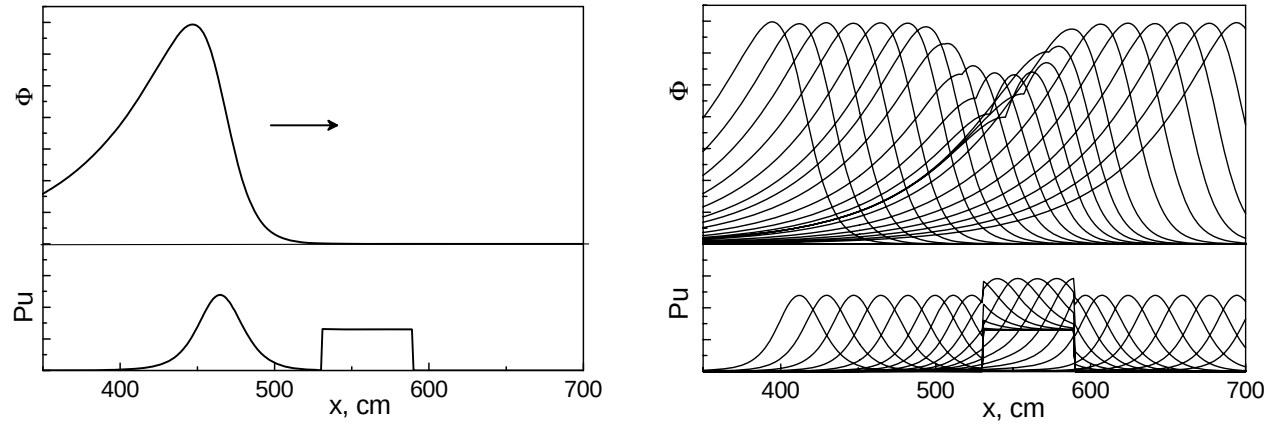

Fig. 13. Collision of burning wave with 7 % ^{239}Pu block: $\Phi(x)$ – top, $n_{Pu}(x)$ – bottom.

Therefore, solution (7) is stable against disturbances of traveling wave parameters with relaxation time of about one year.

7. Summary

Stable nuclear burning wave can propagate in TWR with negative reactivity feedback at set power [7]. Wave profile does not depend on speed of the wave. In the case of adiabatic variation of power, solution (7) remains valid if value P is replaced by $P(t)$. This allows for stopping and resuming reactor operation as well as varying reactor power without changing the geometry or fuel composition in the core ("power on demand" [2]).

Data of the computer simulation of TWR obtained using MCNPX code is in qualitative agreement with the theoretical results. Obtained analytical approximation offers us quantitative description of the traveling burning wave.

These results can be used for validation of other codes or for comparison with theoretical calculations of traveling nuclear burning wave with negative reactivity feedback.

REFERENCES

1. *Feoktistov L.P.* Neutron-fissioning wave // Dokl. Akad. Nauk SSSR. - 1989. - Vol. 309. - P. 864 - 867 (in Russian).
2. *Teller E.* Nuclear Energy for the Third Millenium // Preprint UCRL-JC-129547, LLNL. - 1997.
3. *Van Dam H.* Self-stabilizing criticality waves // An. Nucl. Energy - 2000. - Vol. 27. - P. 1505 - 1521.
4. *Sekimoto H. et al.* A new burnup strategy CANDLE // Nucl. Sci. Eng. - 2001. - Vol. 139. - P. 306 - 317.
5. *Fomin S., Mel'nik Yu., Pilipenko V., Shul'ga N.* Investigation of Self-Organization of the Non-Linear Nuclear Burning Regime in Fast Neutron Reactors // An. Nucl. Energy - 2005. -Vol. 32. - P. 1435 - 1456.
6. *Pavlovich V.M., Rusov V.D., Khotyayintsev V.M. et al.* Slow Nuclear Fission Wave Reactor // Atomic Energy - 2007. - Vol. 102. - P. 151 - 158.
7. *Gann V.V., Abdullaev A.M., Gann A.V.* Comparison of Breeding Properties of U and Th by using the code MCNPX // Proc. of XIX Int. Conf. on Physics of Radiation Phenomena and Radiation Material Science, Alushta. - 2010. - P. 268 - 269.

DEVELOPMENT OF THE CODE FOR FILTER CALCULATION

O. O. Gritzay, M. M. Vakulenko

Neutron Physics Department, Institute for Nuclear Research, National Academy of Sciences of Ukraine, Kyiv, Ukraine

This paper describes a calculation method, which commonly used in the Neutron Physics Department to develop a new neutron filter or to improve the existing neutron filter. This calculation is the first step of the traditional filter development procedure. It allows easy selection of the qualitative and quantitative contents of a composite filter in order to receive the filtered neutron beam with given parameters.

1. Introduction

A neutron filtered beam technique (NFBT) was launched at the Kyiv Research Reactor (KRR) for more than 30 years. The most significant advantage of this method is its suitability to produce high-intensity neutron lines in the keV energy region. More than ten quasi-mono-energetic neutron lines were created in the energy region from thermal energy to 150 keV instead reactor neutron spectrum using the composite neutron filters. These beams were used and continue to use in fundamental scientific, namely for determination of the neutron cross sections with high accuracy. New tasks require availability of new neutron beams with different characteristics, so development of the new neutron filters is in progress.

2. Formulation of problem

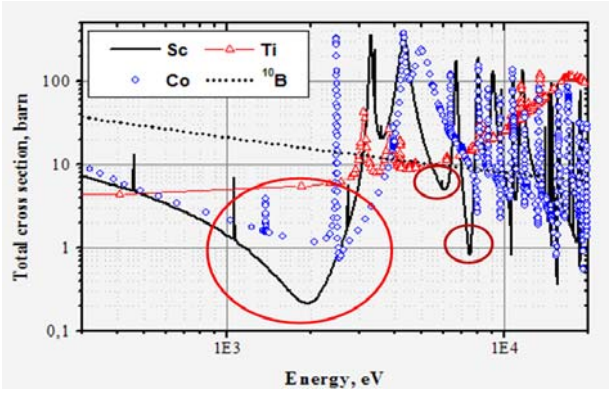

Fig.1. The energy dependence of the neutron total cross section of Sc, Co, Ti, ^{10}B.

The idea of filtering reactor neutrons possessing a continuous spectrum by means of materials, whose total neutron cross sections possess deep interference, was first suggested by O.D. Simpson and L.G. Miller in 1968. If we transmit a "white" reactor spectrum through thick layer of this material, we obtain the quasi-mono-energetic neutron line with the average energy, coincident with this deep interference minimum. For example, an energy dependence of the scandium neutron total cross section is presented in Fig. 1. It can see a deep interference minimum at the energy close to 2 keV (marked by large oval in Fig.1). However, interference minima occur at another's energies (two of them are marked by small ovals in Fig.1). So, to obtain only one quasi-mono-energetic neutron line, it is necessary to remove the lines caused by these minima. It is possible to do if we add materials, for which resonance maxima coincide with the interference minima for the main filter material with the exception of the deepest interference minimum. The energy dependence of the neutron total cross section of some appropriate materials is presented in Fig.1.

There are two ways of a filter component selection.

- Experimental way:

Different materials are putting on the reactor neutron beam, neutron beam passed through them is measured and step by step an optimal composition of filter is selected. It is universal way, but very long and difficult. Usually it was used for the filter creation 30 - 40 years ago.

- "Calculation" way:

Model calculation of the neutron filtered spectra is provided using information from the ENDF/B libraries. Then, a filter with the components chosen by this calculation is made, and an experimental testing of the created filter is carried out.

It is short and easy way, it is only limited by the ENDF/B information. Today usually this way is used for the filter creation.

This work was intended to generation of software tools for the model calculation of the neutron filtered spectra at the KRR.

3. The package FILTER

In order to receive the filtered neutron beam with given parameters, the package FILTER was developed. It allows

- calculation of the filtered neutron spectra and
- selection of a qualitative and quantitative content of the composite filter.

This package contains of

- Special data libraries;
- Computer code Filter-7.1 (using Compaq Visual Fortran Version 6.1).

3.1. Special data libraries

The package FILTER includes tree special data libraries.

1st library. The files with the total neutron cross sections for a set of materials in the point-wise format and with the linear-linear interpolation low. The total list of these files now contains 133 units.

These cross sections were calculated using the code packages PREPRO/NJOY together with the most updated Libraries of Evaluated Nuclear Data. An accuracy of the linearization procedure was taken as 0.1 %, the temperature of materials as 300K.

In necessary cases this list may be added with a new cross section file.

Table 1. **A part of a list of the total neutron cross section files**

#	Isotope	Name of file	Library
1	1H1	1H1.jn2	JENDL-3.2
2	1H1	1H1.jn4	JENDL-4.0
3	3Li6	3LI6.jn2	JENDL-3.2
…	…	…	…
133	92U238	92U238.jn2	JENDL-3.2

2nd library. File DENSITY.dat is a density of material (in g/cm^3).

This file is used when the filter components are specified in cm (length). Today the total list of material density includes 55 items. A part of this list is presented in Table 2.

Table 2. **A part of a list of the material densities**

#	Material	Density (g/cm^3)
1	3Li6	0.5340
…	…	…
53	92U238	19.0400
54	FLUENTAL	3.0000
55	PE	0.9180

3rd library. Files HE3_NP and H1_NEL.

Files HE3_NP includes the energy dependent cross section for reaction 3He (n, p). Files H1_NEL includes the energy dependent cross section for reaction of neutron elastic scattering at hydrogen. Both cross sections were calculated with the use of JENDL-3.3 library.

This information is required to take into account the energy-dependent efficiency in the case, when He-3 or proton recoil counter is used for neutron registration.

3.2. Computer code Filter-7.1

The code uses a simple expression for calculation of the filtered neutron spectra F(E):

$$F(E) = \exp[-\sum n_i \cdot \sigma_i(E)] \cdot \Phi(E)\,, \qquad (1)$$

where n_i – nuclear thickness of the *i*-th filter component; $\sigma_i(E)$ – total neutron cross section of the *i*-th nuclide; $\Phi(E)$ – the incident reactor neutron spectrum.

To take into account an efficiency of the used neutron detector, the function $F_d(E)$ is also calculated:

$$F_d(E) = \exp[-\sum n_i \cdot \sigma_i(E)] \cdot \Phi(E) \cdot \sigma_{reac}(E)\,, \qquad (2)$$

$\sigma_{reac}(E)$ – cross-section of the reaction, which used for neutron detection.

The correctness of this approach was tested comparing the results obtained in the exact simulation of the KINR experimental set-up using the MCNP4C code.

Peak retrieval in the filtered neutron spectra is realized automatically. This automatic peak search algorithm consists of 3 steps.

1-st step The search of maximum value F_{max} of the F(E) function.

2-nd step The search of peaks whose value exceeds the threshold AK*F_{max}

Parameter AK is set by the user in the task input file, on default AK=0.0001. Using this parameter, very small peaks remove from consideration (Fig. 2). Peaks, that are lower than line, aren't taken into consideration. Correctness of the given value AK is tested by calculation how much the sum of the area under all founded peaks differs from the area

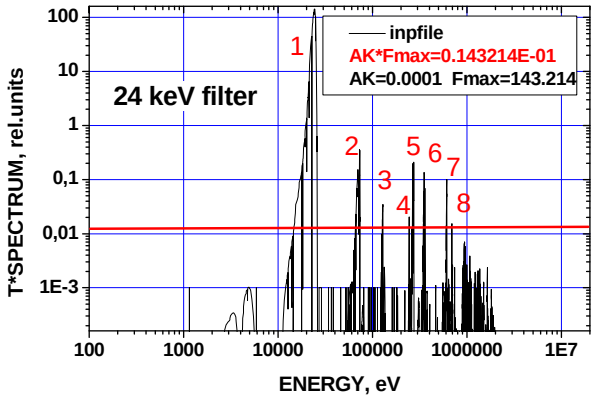

Fig. 2. Explanation of choice of the AK value.

under the entire function F(E). If this difference is above 1 %, a warning appears in the output.

3-rd step Assembly of the closely spaced peaks (found in step 2) in one peak,

$$\text{if } \frac{E_i^{left} - E_{i-1}^{right}}{E_i^{left}} < AKE,$$

where E_{i-1}^{right} – the extreme right value of energy for (*i-1)*-th peak; E_i^{left} – the extreme left value of energy for *i*-th peak (Fig. 3).

The total neutron cross sections of the filter materials may have very narrow resonances. They become apparent in the calculated filtered neutron spectra as very narrow deeps. Of course they cannot be shown in experimental spectrum through the energy resolution of spectrometer. The code considered them as the separate peaks, therefore the closely spaced peaks have to be combined in one peak.

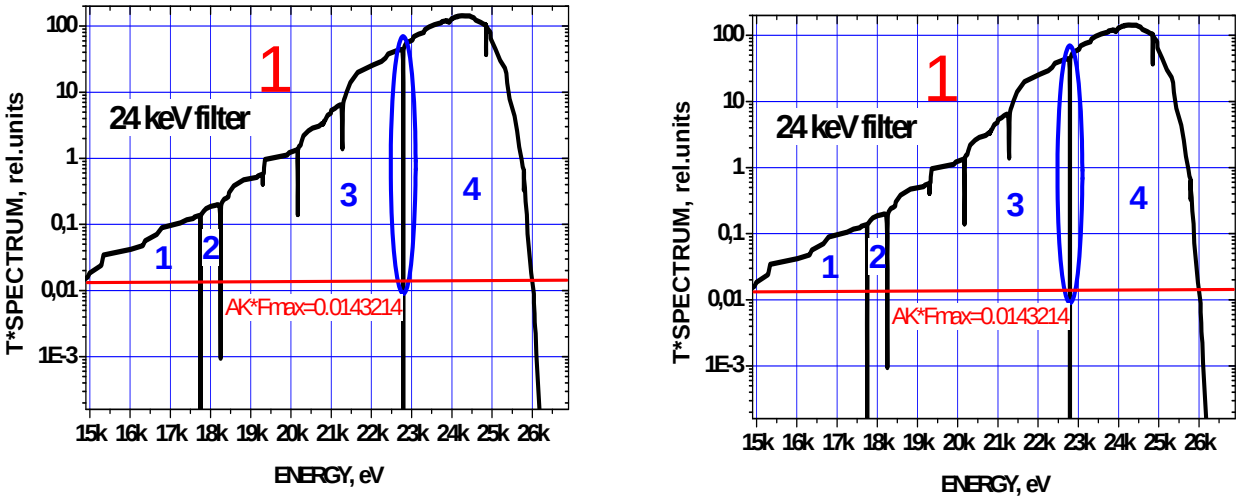

Fig. 3. Explanation of choice of the AKE value.

It is very easy to see in Fig. 3, where the energy region, marked in Fig. 2 as 1, is presented. Four peaks (1, 2, 3, 4) were found in the energy region 1. As the above noted condition is satisfied for all these peaks (see example for 3 and 4), only one peak will be found in the energy region 1.

Parameter AKE is set by the user in the task input file, on default AKE = 0.012.

After running the code generates the result output files. There are four types of the output files. Two of them are mandatory, another one are created on user request.

INPname.dat – a file, which includes the calculated filtered neutron spectra.

INPname.LST – a report, which includes input information (nuclides, thicknesses, AK, AKE) and tables of the found peaks with their characteristics.

INPname.CMP – a file, which includes the computer readable information about the found peaks. It is useful for the comparison procedure.

INPname.Gxx – files, which include the computer readable information for xx spectrum line in GROUPIE format (xx – the number of line in the calculated spectrum).

Number and type of the output files is specified by the user in the task input file INPname.

A manual with detailed information concerning input and output parameters, the executable code Filter-7.1 and all special data libraries are on the site http://ukrndc.kinr.kiev.ua/FILTER-7.html

In order to facilitate a preparation of the task input file for the code Filter-7.1, graphical user shell was created using scripting language Lua and cross-platform graphics library IUP. This also makes easy the adaption of the code to operating systems other than MS Windows. One of the windows, created by this graphical shell, is presented in Fig. 4.

This graphical user shell will be located on the UkrNDC site, too.

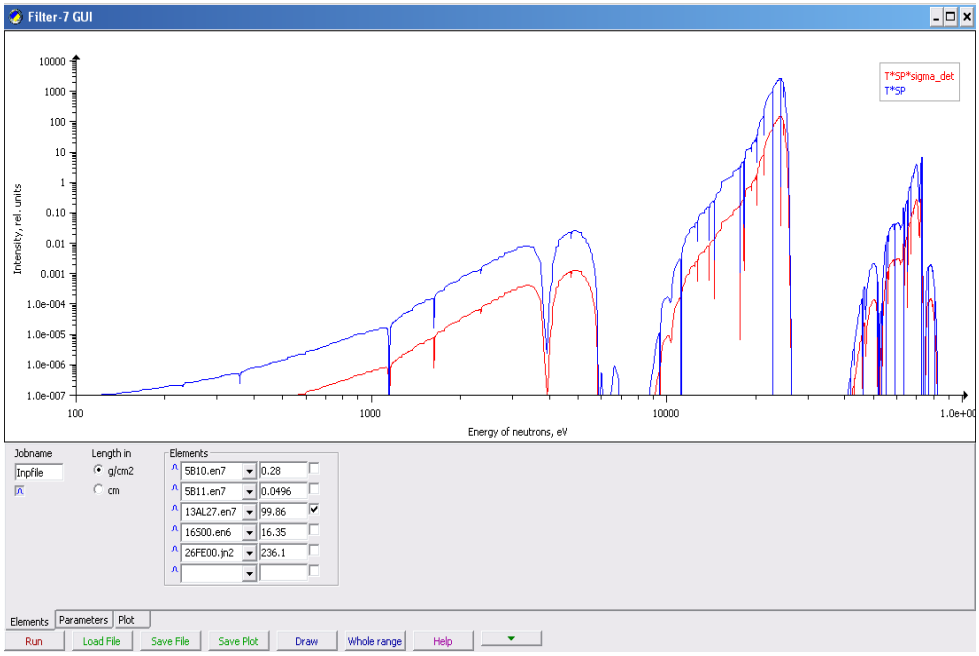

Conclusions

The package for filter calculation is developed.
It allows

- Simulation of the filtered quasi-mono-energetic neutron spectrum with necessary parameters.
- Putting into calculation practically any material and isotope combination.
- Getting information about parameters of the calculated filtered spectrum:
- Energies of the main line and additional lines
- Relative intensities of all lines, i.e. purity of the neutron filtered beam.
- Width of the main line.
- Easy and shortly creation of the neutron filters. Owing to the used algorithm, the calculation time is very short.

The graphical user shell makes easy

- Input data preparation for the code
- Adaption of the code to operating systems other than MS Windows.

The package Filter is free and it is available using the UkrNDC site.

DETERMINATION OF TOTAL NEUTRON CROSS SECTION OF ^{52}CR WITH USING AVERAGE ENERGY SHIFT METHOD FOR FILTERED NEUTRON BEAM

O. O. Gritzay[1], A. K. Grymalo[1], V. V. Kolotyi[1], V. A. Pshenychnyi[2], V. P. Shakhov[1], V. M. Venedyktov[1]

[1] *Institute for Nuclear Research, National Academy of Sciences of Ukraine, Kyiv, Ukraine*
[2] *State Scientific-Engineering Center for Control and Emergency Response, Kyiv, Ukraine*

The measurements of the total neutron cross section of ^{52}Cr, obtained for the neutron energies from 58.6 keV to 48.4 keV, were carried out on the horizontal experimental channel HEC-8 of the WWR-M10 reactor. The multipurpose automatized Installation for Angle Scattering Distribution (IASD-3) was used. The transmission method was applied. The composite neutron filter with the average energy 59 keV was used. The shift of the filter energy is realized using the neutron energy dependence on scattering angle. The scattering samples carbon and polyethylene were used. The obtained experimental results were compared with the total neutron cross sections from the evaluated nuclear data libraries ENDF/B-VII, JENDL-4.0, JEFF-3.1, CENDL-3.1, BROND-2.2, ROSFOND-2010.

1. Introduction

The ^{52}Cr isotope was used as an object of our experimental investigation. The averaged total neutron cross section of this isotope was measured by us in the energy region 50.7-60.4 keV in 2004 [1], and the obtained result shown a good agreement with the ENDF libraries, except BROND-2 and CENDL-2. One wide s-wave resonance at the energy near 50 keV and two narrow p-wave resonances at the energies near 48 and 58 keV are presented for the ^{52}Cr total neutron cross section in all ENDF libraries (see, for example, Fig. 1), but parameters of these resonances are different.

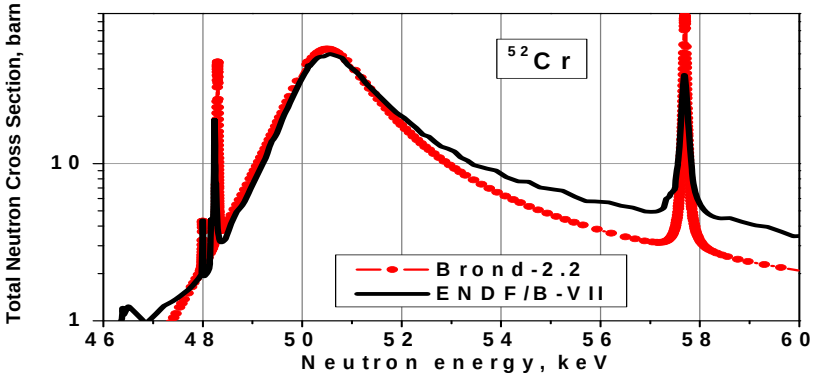

Fig. 1. Total neutron cross section of the ^{52}Cr from libraries BROND-2.2 та ENDF/B-VII.

Determination of the resonance parameters is not possible if the average neutron cross section is measured only in one energy region. A set of these values, measured in the shifted energy regions, makes it possible to determine the parameters of resonance in the energy range of coverage. The measurement of the total neutron cross section of ^{52}Cr at the neutron energies 48.4, 52, 55, 58, 58.3 and 58.6 keV is the first step to solve this task.

2. Experimental set-up

The experimental investigations of the total neutron cross sections for ^{52}Cr were carried out at the 8-th horizontal experimental channel (HEC-8) at the Kyiv Research Reactor WWR-M10. The composite neutron filter with the average energy 59 keV was used. The components of the filter take place in the first three disks of shutter and in the outside collimator. A scheme of the experimental installation on the HEC-8 is shown in Fig. 2.

The multipurpose automatized IASD-3 was used to receive a set of the total neutron cross sections for the energies 48.4, 52, 55, 58, 58.3 and 58.6 keV. The detailed description of this installation was published in [2]. A scheme of the IASD-3 is shown in Fig. 3.

The proton recoil detector LND-281 (Gas Filling H+CH^4+N_2, diameter – 38.1 mm, length – 254.0 mm, gas pressure – 3240 torr), electronic blocks: preamplifier, CAMAC blocks, personal computer and communication lines were used for neutron registration.

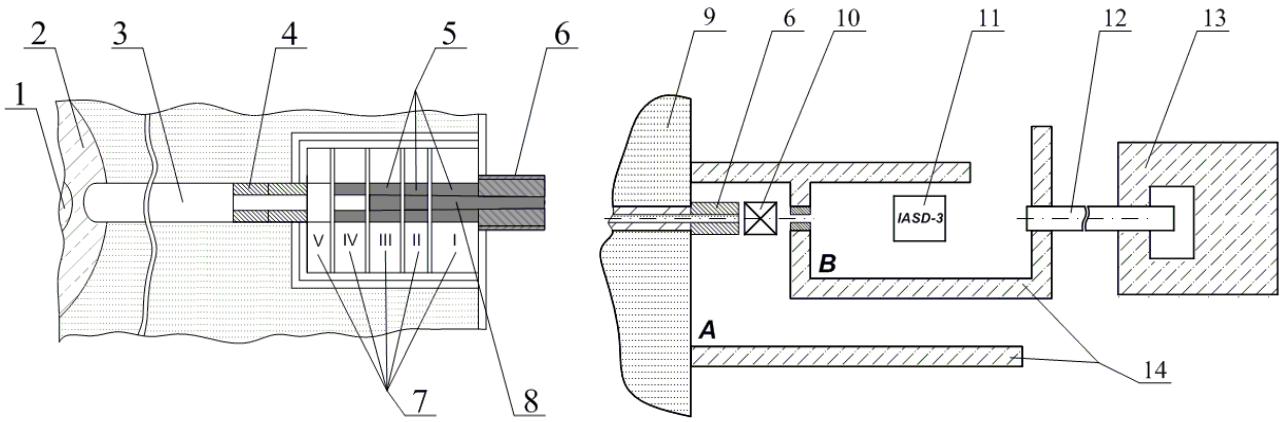

Fig. 2. A scheme of the experimental installation on the HEC-8:
1 – reactor core; *2* – beryllium reflector; *3* – horizontal channel; *4* – preliminary collimators; *5* – elements for forming of the beam; *6* – outside collimator; *7* – shutter disks; *8* – filter components; *9* – biological shielding; *10* – device for sample removing; *11* – Installation for Angle Scattering Distribution (IASD-3); *12* – tube to conduct of beam to neutron catching; *13* – neutron beam catching; *14* – radiation shielding of installation.

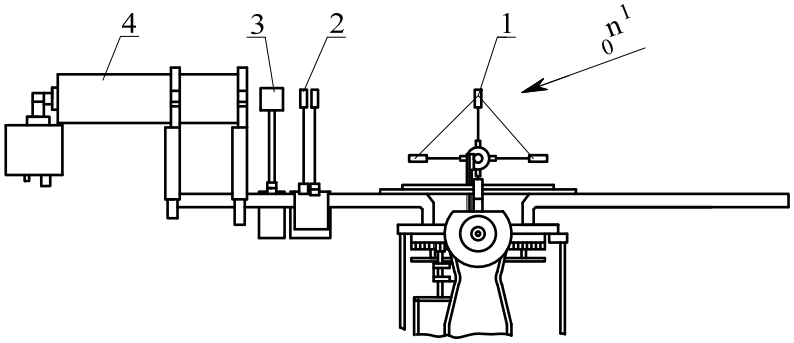

Fig. 3. Version of the IASD-3 configuration for measurements of the total neutron cross sections using the shift average energy method: *1* – scattering-samples; *2* – investigated sample; *3* – device to overlap a neutron beam by polyethylene (background measurement); *4* – detector.

3. Experimental details: filter, scattering sample, investigated sample

Table 1. **The 59 keV filter components**

Elements	S	^{58}Ni	V	Al	^{10}B
Thickness, g/cm^2	116.53	81.42	24.44	5.4	0.5

The filter with the average neutron energy 59 keV was used in the experimental investigations [1, 3 - 5]. Now this filter was recalculated and complemented by the new components. These calculations were done by the Filter-7 code using the CENDL-2 and JENDL-3.3 libraries. The components of this filter are presented in Table. 1. The calculated neutron spectrum after this filter is presented in Fig. 4.

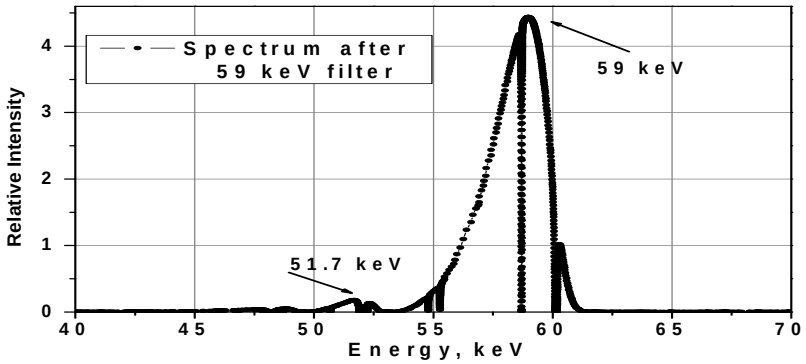

Fig 4. Calculated neutron spectrum after the 59 keV filter.

The purity of the filter was about 99.7 %. Other additions to the main neutron line were negligible: a line with the energy 36.1 keV was about 0.1 %, two groups of the energy lines 230 - 280 keV and 325 – 368 keV were about 0.15 % and 0.62 %, respectively. The contribution of the lines above 540 keV was 0.4 %. The calculated energy and width of the neutron line (95 % response function) after this filter are: $59 \pm^{1.2}_{6.7}$ keV.

To provide appreciable shift of the initial average energy 59 keV, a number of elements and compounds were considered by us as a scattering-sample. More detailed information about choosing of the scattering-samples is presented in [2]. As it is well known, the largest shift of the initial energy is provided by scattering on hydrogen. As hydrogen cannot be used as a sample (because it is gas), polyethylene sample was decided to apply as a scatter. As the scattered neutron spectrum after the CH_2 scattering-sample consists of two energy lines – neutrons scattered on H and neutrons scattered on C, the measurements with the scattering-sample C were carried out to make correction on a contribution of the neutrons scattered on carbon. The initial neutron line with the average energy 59 at keV produces at the scattering angles 15^0, 20^0 and 25^0 the scattered neutron lines with the average energies 55, 52, 48.4 keV and 58.6, 58.3, 58 keV if neutrons are scattered by hydrogen and carbon, respectively (Fig. 5).

Thickness of the used scattering-samples C and CH_2 was 10.02 ± 0.01 and 4.52 ± 0.01 mm.

The investigated ^{52}Cr sample was made of a metal powder, loaded into aluminum container. A thickness of the ^{52}Cr sample was 0.0173 ± 0.0002 nucl/barn.

Fig. 5. The calculated scattered neutron spectra at the angles 15^0, 20^0 and 25^0 on the scattering-samples CH_2 and C.

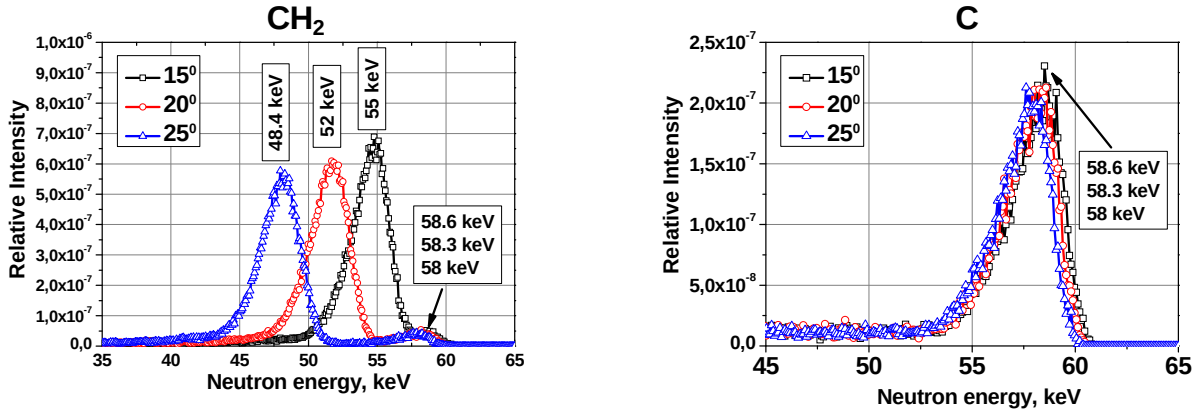

Fig. 5. The calculated scattered neutron spectra at the angles 15, 20 and 25° on the scattering-samples CH_2 and C.

4. The experimental and calculated results

Two series of measurements were carried out. Eight types of measurements (four for the scattering-sample C and four for the scattering-sample CH_2) were done in each run:

1) the investigated ^{52}Cr sample on the scattered neutron beam (position 2 in Fig. 3);
2) the ^{52}Cr sample on the beam with the polyethylene sample (position 3 in Fig. 3);
3) aluminum container on the scattered neutron beam (position 3 in Fig. 3, so called "direct" beam);
4) aluminum container on the beam with the polyethylene sample (position 2 in Fig. 3).

Duration of one measurement run was 2-4 hours. To remove the influence of instability factors, the samples at the neutron beam were replaced every minute. The total measured time in the first series amounts to 15, 26, 22 hours at the scattering angles 15^0, 20^0 and 25^0, this time in the second series was about 23, 20, 22 hours.

After careful examination, the measured spectra of the same type were summed for each series of measurements. A transmission of the ^{52}Cr sample was calculated with using the formula:

$$T = \frac{\sum_{i=I1}^{I2} N_{iSMP} - \sum_{i=I1}^{I2} N_{iSMP+PE}}{\sum_{i=I1}^{I2} N_{iDB} - \sum_{i=I1}^{I2} N_{iDB+PE}}, \qquad (1)$$

where N_{iSMP} – the number of counts in the i-th channel of the spectrum beam after sample; $N_{iSMP+PE}$ - the same, but after sample + polyethylene; N_{iDB} - the number of counts in the i-th channel of the "direct" beam spectrum; N_{iDB+PE} - the same, but "direct" beam + polyethylene. The channel numbers I1 and I2 have been chosen in the region of the proton-recoil plateau. The spectra after polyethylene were corrected on gamma-attenuation in the used polyethylene sample. The transmission values T_γ were calculated by the MCNP 4C code. They are a little different for each angle and equal to 0.81 ± 0.08, 0.81 ± 0.07 and 0.80 ± 0.07 for the angles 15^0, 20^0 and 25^0, respectively.

The observed total neutron cross section was calculated by the next formula:

$$\sigma_{obs} = -\frac{1}{n}\ln T, \qquad \Delta\sigma_{obs} = -\frac{1}{n}\sqrt{\left(\frac{dT}{T}\right)^2 + (\sigma_{obs}dn)^2}, \qquad (2)$$

where n – thickness of the ^{52}Cr sample in nucl/barn.

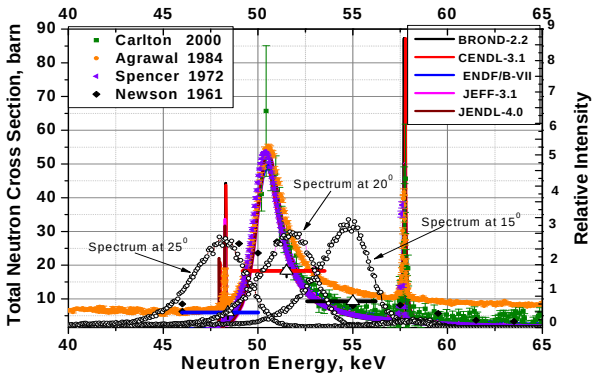

Fig. 6. The measured total cross sections and data from the EXFOR and ENDF/B libraries.

To determine the total neutron cross section ^{52}Cr for the average energies 55, 52 and 48.4 keV, the observed total neutron cross section was corrected. This correction is connected with existence in the neutron scattered spectrum on CH_2 neutrons scattered on carbon. It was introduced by a design-experimental approach. The ^{52}Cr total cross section at the neutron energies 58, 58.3, 58.6 keV was given from this experiment. On account of these energies are very near in value, it is assumed that these cross sections are equal in value, too. So, the experimental spectra, measured with the carbon-scatter at the angles 15^0, 20^0 and 25^0, were respectively summed. Its value was determined equal to 2.97 ± 1.22 barn. The proportions of the scattered neutron lines were given from the calculated scattered spectra (see Fig. 5) obtained by the MCNP 4C code.

The measured total cross sections are presented in Fig. 6 together with the data from the EXFOR and ENDF/B libraries.

For compare our experimental results with the evaluated data, the point-wise total neutron cross section of ^{52}Cr from the ENDF/B libraries was averaged on the calculated spectrum of the scattered neutrons. In this procedure the next energy limits were taken: 48.4 ÷ 57.6, 45.9 ÷ 55.1 and 42.0 ÷ 52.0keV at the scattering angles 15^0, 20^0 and 25^0, respectively. The obtained values are presented in Table 2.

Table 2. **Our experimental results and the averaged total cross sections of ^{52}Cr from the ENDF/B libraries**

	Average energy, keV	ENDF/B-VII	JEFF-3.1 ROSFOND	JENDL-4.0	CENDL-3.1	BROND-2	Our exp. results n = 0.0173 nucl/barn
Scatter-sample H							
15^0	55	10.51	10.05	9.62	8.22	8.62	9.27 ± 0. 51 (6 %)
20^0	52	23.21	23.36	23.10	20.87	22.91	18.29 ± 0.89 (5 %)
25^0	48.4	6.57	5.75	6.06	6.62	6.99	5.94 ± 0.49 (8 %)

In Table 2 it is seen, the changes of our experimental results with changes of the angles reproduce a trend of changes of the cross sections from the ENDF/B libraries. Unfortunately, for today we cannot say which library provides more reliable results, because at present time just one sample of ^{52}Cr was used in our experiment, so a correction on the self-shielded effect was not be done for the measured values of the total cross sections of ^{52}Cr. The rough estimation, done by the MCNP 4C code calculations, shown that the difference between the total cross sections at these energies and these observed self-shielded cross sections may rich 2-6 %. The measurements of the different ^{52}Cr samples are planned in the future.

Conclusions

A set of the total neutron cross sections of ^{52}Cr for energies 55, 52 and 48.4 keV were obtained. These values are preliminary data, as the self-shielded effect was not being taken into account.

Changes of our experimental results with changes of angles (15^0, 20^0 and 25^0) reproduce a trend of changes for the cross section from the evaluated nuclear data libraries.

Our results shown, that evaluation of the parameters of the investigated resonance is possible. Measurements of the different samples of ^{52}Cr and at the different angles are necessary for it.

REFERENCES

1. *Gritzay O.O., Kolotyi V.V., Klimova N.A.et al.* Total Cross Section and Self-Shielding Effects of Cr-52 Isotope Measured at Kyiv Research Reactor Neutron Filtered Beams // Proc. of the ND2004, Santa Fe, USA, 2004.
2. *Gritzay O.O., Grymalo A.K., Kolotyi V.V. et al.* Research of Isolated Resonances Using the Average Energy Shift Method for Filtered Neutron Beam // Proc. of the 3-rd Int. Conf. “Current Problems in Nuclear Physics and Atomic Energy” (Kyiv, Ukraine, 7 - 12 June, 2010). - Kuiv, 2011. - P. 483.
3. *Gritzay, O.O., Kolotyi, V.V., Klimova, N.A. et al.* Precision Neutron Total Cross Section Measurements for Natural Carbon at Reactor Neutron Filtered Beams // Proc. of the ISRD12, Gatlinburg, USA, 2005.
4. *Libman V.A., Gritzay O.O., Razbudey V.F.* Average Resonant Capture Cross Section of 181Ta at 59 keV Filtered Neutron Beam // Proc. of the 2-rd Int. Conf. “Current Problems in Nuclear Physics and Atomic Energy” (Kyiv, Ukraine, 9 - 15 June, 2008). - Kyiv, 2009. - P. 548.
5. *Грицай О.О., Гримало А.К., Колотий В.В. та ін.* Дослідження повного нейтронного перерізу гафнію на фільтрованому пучку нейтронів з енергією 59 кеВ // Науковий вісник Ужгородського університету. Серія “Фізика” - 2011. - Т. 30. - P. 142 - 147.

BASED ON MANGANESE FILTERED NEUTRON BEAM AT THE KYIV RESEARCH REACTOR

O. O. Gritzay, V. A. Libman, S. P. Volkovetskyi

Institute for Nuclear Research, National Academy of Sciences of Ukraine, Kyiv, Ukraine

The history and processing of based on manganese filtered neutron beam construction described. The fractional step method was used to compose new filter. The neutron spectrometer with hydrogen proportional counter was employed to measuring neutron spectra. There is present the composition of filtered neutron beam with average energy 275 keV.

1. Some history

For the beginning, there is some history. Approximately 40 years ago, our department began to work with the filtered neutron beams (FNB). At first, we used only traditional filters, i.e. filters based on scandium, iron, and silicon. These filters separate the quasi-mono-energetic lines with the average energies about 2, 24, 54 and 148 keV from reactor spectrum.

However, by the end of 1970ies, this energy scale has become insufficient for us, and we undertook attempts to create new filters. The main "tools" for selection of components for new filters were:

- the atlas BNL with the diagrams of neutron cross sections of elements;
- neutron spectrometer based on the proportional hydrogen counter CHM-38 and
- experience and intuition of the researcher.

Attempt to create the FNB with the energy near 18 keV led us to manganese, which, according to the BNL atlas, has a deep minimum at this energy. The experimental spectrum of neutrons, passed through manganese, has shown the expected 18 keV line as well as a quite intensive line at the energy about 275 keV. It was an incitement for creation of the filtered neutron beam with this energy.

2. Further development

At the beginning of the 21-st century, the constructing of FNB is essentially simplified, because the evaluated nuclear data libraries (ENDLs) are available as well as the computer codes for the filter calculations. One of such codes was created in our department [1]. This code allows simulation of the future filter, being based on information from the ENDLs. Based on the obtained calculation results, one can estimate such its parameters, as a middle energy, a width of neutron line, a relative «cleanness» of this line and an expected flux at the filter outgoing. Now different variants of future filter may be simulated, and then only the acceptable compositions are checked out experimentally. This method essentially economizes as a measuring time at reactor beam, as materials components of the future filter.

However, the data about a structure of the total neutron cross sections in the energy range 100 - 500 keV are missed in the ENDLs for some materials. Unfortunately, it appears that manganese belongs to such materials (see for example Fig. 1). Similar situation is for some other materials, which we planned to use, as supplementary filter components (for example, zinc, copper). Therefore, we had to go back to old use-proven method, described above, i.e. experimental method.

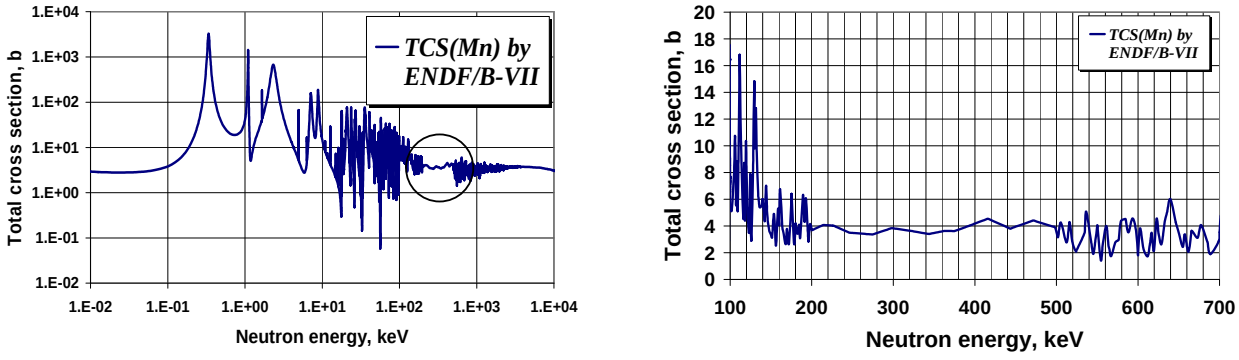

a *b*

Fig. 1. Total cross section of manganese (*a*) and its fragment (*b*) by ENDF/B-VII.

The attempt to use the existing experimental data for the manganese total cross section did not bring a success too. The next Figure (Fig. 2) shows experimental data about manganese total cross section structure received by three groups of authors. Unfortunately, the Pineo's group data [2] is not enough detail; the Garg's group data [3] terminate near 200 keV, and the Rohr's group data [4] terminate at 257 keV that is slightly less than the region of our interest.

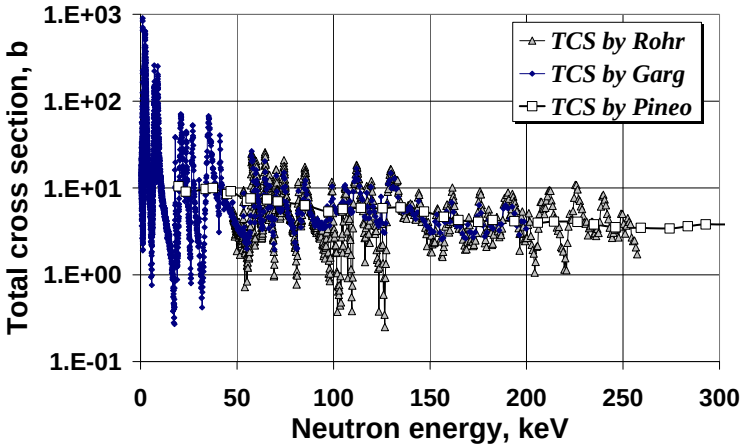

Fig. 2. Total cross section structure of manganese by experimental data.

3. Experiment

The experimental scheme is shown in Fig. 3. The neutron beam, passed through approximately 50 cm of manganese powder, was collimated by the borated polyethylene and lead collimators. Then it was directed through the additional component samples and through the next collimators into the proportional counter. The sample changes are carried out strictly in accordance with the program specified by researcher.

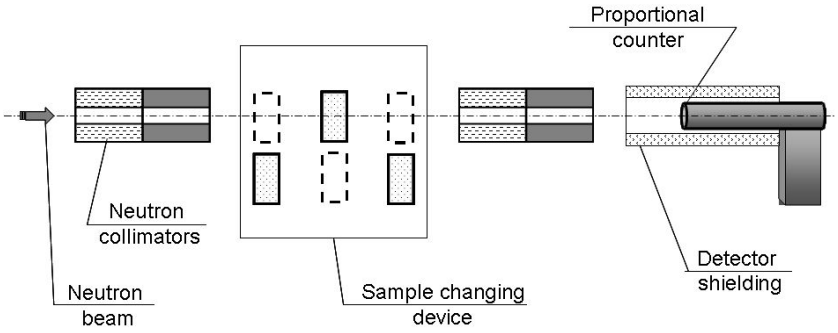

Fig. 3. Scheme of experiment.

The measuring carried out cyclically: direct beam, beam overlapped by 1st sample, 2nd sample, etc. Each position was measured during 1 minute in one cycle and then cycle repeated. Number of cycle specifies in research program. This measuring system makes possible to refuse a beam monitoring.

3.1. Spectrometer

For measuring of neutron spectra such configuration of neutron spectrometer was used:

- proportional hydrogen counter CHM-38;
- height analyzer based on ADC 712;
- sample changing device which changes the sample position at the neutron beam in accordance with desired program.

The spectrometer parameters are:

- measuring energy range of neutrons – 10 700 keV;
- energy resolution – 7 % at neutron energy 764 keV;
- cyclic measuring regime, that allows to dispense with neutron beam monitor during the measurement.

3.2. Measurements

The reactor neutron beam, passed through approximately 50 cm of manganese powder (called further as direct beam), was measured by this spectrometer Nine neutron lines with the energies 18, 26, 33, 56, 76, 86, 110, 133 and 275 keV were found in this spectrum (Fig. 4). We had to find also the lines with energies 1.2 and 5.9 keV in accordance with ENDLs (for example, ENDF/B VII), but they are out-of-range our spectrometer.

To obtain the «almost clean» neutron beam with the average energy 275 keV it is necessary to reject the «admixture» neutron lines with energies 18, 26, 33, 56, 73, 86, 110 and 133 keV. We should to choose materials, which reject or at least decrease these perturbing lines, but herewith distort the base line at 275 keV as little as possible. The

copper, zinc, aluminum, vanadium, cobalt, sulfur, iron-56 and nickel-58 isotopes were tested as these supplementary components. We transmitted the direct beam through these supplementary materials and determined their neutron transmissions for all neutron lines.

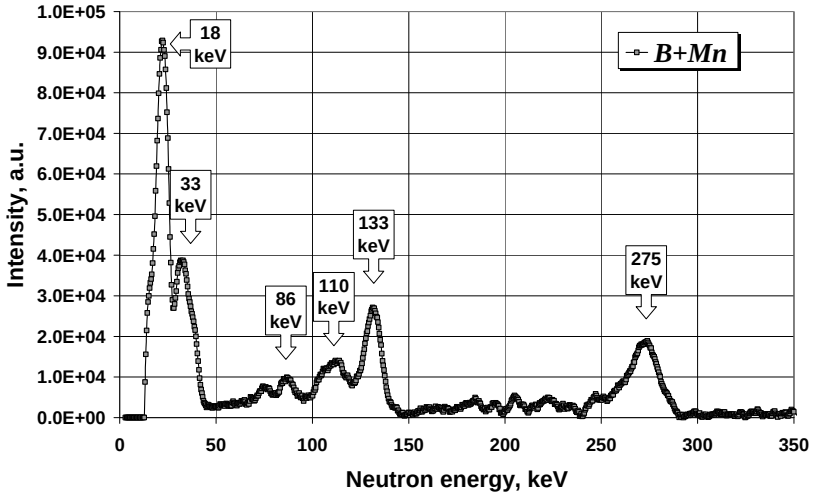

Fig. 4. Neutron spectrum after 258 g/cm^2 of manganese.

4. Processing of measured spectrums

4.1. Response function and recovering neutron spectra

As known, response function of hydrogen counter for mono energetic neutron line is a rectangular stair. Then on a set of quasi-mono energetic neutron lines, a counter «reacts» as a set of such stairs. A dip centre of each stair will correspond to the neutron energy and area under stair will correspond to its intensity. The Fig. 5 shows a fragment of the proton recoil spectrum.

The reconstruction of the neutron spectrum from the apparatus proton recoil spectrum was made using the formula (1), starting from the last channel.

$$y_i^n = (y_i^p - y_{i+1}^p) \cdot x_i \; ; \tag{1}$$

where y_i^n – the number of counts in i-th channel of the recovered neutron spectrum; y_i^p – the number of counts in i-th channel of the apparatus proton recoil spectrum; x_i – channel number.

An example of recovered neutron spectrum also is shown in the Fig. 5.

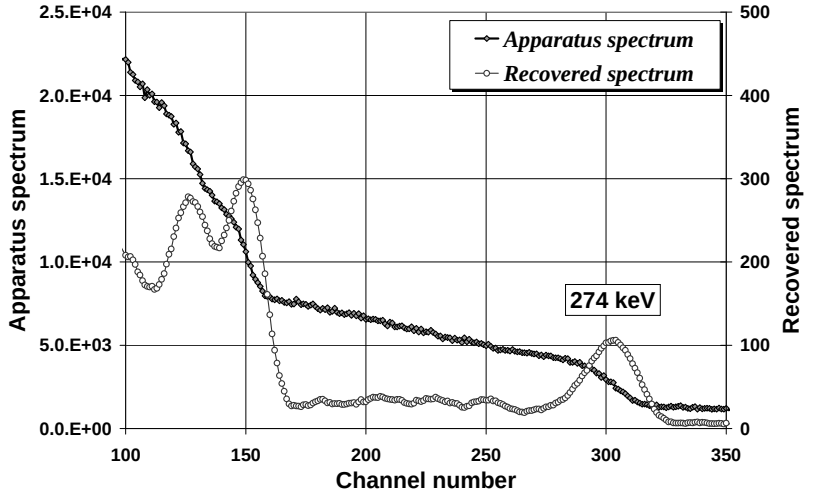

Fig. 5. Fragment of apparatus (proton recoil) and recovered (neutron) spectra.

The recovered neutron spectra were calibrated and then they were corrected for the scattering neutron cross section in hydrogen.

4.2. Spectrometer calibration

The precise pulse generator NZ 635/B we used for energy calibration of neutron spectra. We put its pulse with 7.64 V amplitude to the centre of the 764 keV peak from the ^{3}He(n, p) reaction, which takes place in the counter CHM-38 due to the presence of small amount of helium-3 in it. Thereby we link up the generator amplitude with the neutron energy and get ability to mark obtained spectra irrespective of the amplifier gain. The Fig. 6 shows an example of marked apparatus spectrum.

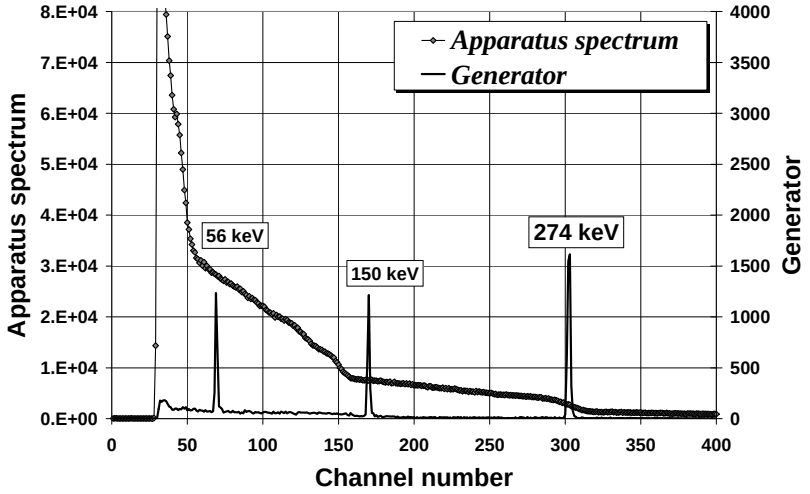

Fig. 6. Fragment of marked apparatus spectrum.

Since the cross section of the ^{3}He(n,p) reaction increases with the neutron energy decreasing, we reduce neutron energy using the paraffin cover and get the 764 keV peak for generator binding.

4.3. Optimization procedure

Using the measured spectra, the transmissions were calculated for each additional component and for every neutron lines. And then these values were reduced to the transmission for 1 cm thickness of each component. The obtained values are shown in the Table.

Experimentally obtained transmission of 1 cm of materials for all observed neutron lines

En, keV	Mn	Co	V	^{56}Fe	Zn	Cu	Al
18	0.96			0.83			0.94
26		0.54	0.52	0.75			0.97
33	0.87	0.40	0.53				0.76
56	0.85		0.55	0.97	0.81		
73	0.91	0.91		0.90	0.61	0.76	
83	0.95	0.70	0.73	0.97	0.79	0.59	0.82
111	0.90	0.67	0.83	0.80	0.75	0.62	0.94
131	0.99	0.33		0.97	0.65	0.74	0.83
274	**0.89**	**0.64**	**0.88**	**0.87**	**0.67**	**0.63**	**0.82**

In order to choose the optimal filter composition, comparison of these values for the perturbing neutron lines with ones for the main (275 keV) neutron line was done. A material, for which this transmission for the 275 keV line is greater than for the perturbing neutron lines, may be suitable for the components of the 275 keV filter. As it can see from table, these conditions come true for vanadium (lines 26, 33, 56, 83 and 111 keV), aluminum (33 keV), and iron-56 (26 and 111 keV). Therefore, just these materials were chosen to compose the filter. We selected such thickness of these materials, which decrease the main filter line (275 keV) at most 3 times.

5. Conclusions

For today the latest composition of 275 keV filter is: ^{10}B – 0.3 g/cm^2; ^{11}B – 0.05 g/cm^2; Mn – 258 g/cm^2; V – 24 g/cm^2; ^{56}Fe – 55 g/cm^2; Al – 3 g/cm^2 (Fig. 7).

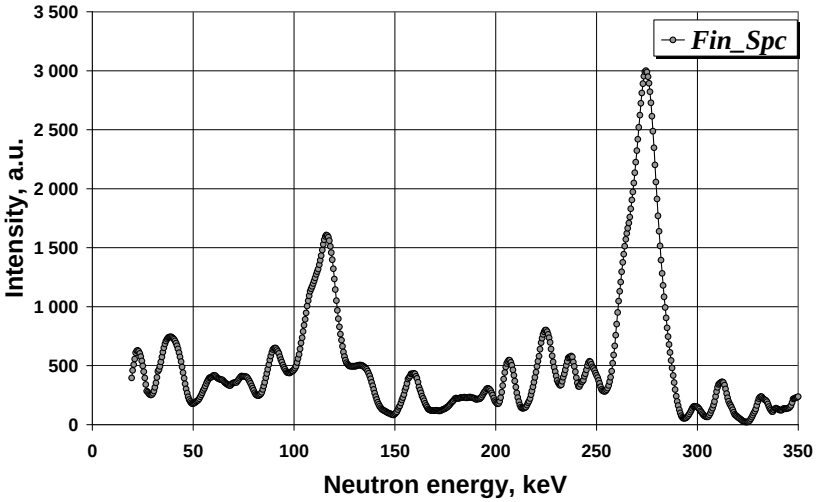

Fig. 7. Spectrum of filter based on manganese.

We cannot assert that this is a final variant of this filter because the main characteristics (average energy of the main line, its energy width, its "purity", and flux) are not yet determined by experiment. In Fig. 7 it is shown "semi calculated" variant of the filter based on the experimentally obtained transmissions of the supplemental components. We plan to check real filter parameters in future. It is assumed that a "purity" of this filter will be also improved.

Also, we plan to determine the manganese neutron total cross section in minima as well as the total neutron cross section of natural copper, zinc and scandium using the neutron beam passed through this filter.

REFERENCES

1. http://ukrndc.kinr.kiev.ua/FILTER-7.html
2. *Pineo W.F.E., Divadeenam M., Bilpuch E.G. et al.* Neutron Strength Functions and Average Total Cross Sections: The Behavior of the Average Cross Sections and S-Wave Scattering Lengths // Annals of Physics. - 1974. - Vol. 84. - P. 165.
3. *Garg J.B., Rainwater J., Havens W.W.* (*Jr.*). Neutron Resonance Spectroscopy in Vanadium, Manganese, and Cobalt // Nuclear Science and Engineering. - 1978. - Vol. 65. - P. 76.
4. *Rohr G., Friedland E.* A Study of Neutron Resonances of Vanadium and Manganese // Nuclear Physics A. - 1967. - Vol. 104. - P. 1.

THE AVERAGED CROSS SECTIONS OF NATURAL CARBON IN THE ENERGY REGION 90 - 160 keV

O. O. Gritzay, S. P. Volkovetskyi, V. A. Libman

Neutron Physics Department, Institute for Nuclear Research, National Academy of Sciences of Ukraine, Kyiv, Ukraine

This paper presents the results of measurements of the total cross-section of carbon in the energy region 90 - 160 keV. These results were obtained using a method of the modified filtered beams, developed in the Neutron Physics Department and implemented in the horizontal experimental channel HEC-9 at the Kyiv research reactor. The experiment was carried out using 5 modified filters. Ten values of the averaged cross-sections of carbon were obtained.

1. Rationale for measuring total cross section of carbon

As it is well known, carbon is widely used as a reactor structural material and as a scattering standard, especially at the energies below 2 MeV, where the neutron total cross-section and elastic scattering cross-section are almost identical. The total neutron cross-sections of carbon were measured in 145 experimental works during 1935 - 2007, but only a small part of them was dedicated to these investigations in the energy range 1 - 500 keV. The measurements of the total neutron cross-section of carbon were done in our department, too [1]. A strong dependence on the sample thickness of the effective cross-section of natural carbon was observed by us at the energy region 119 - 157 keV. The total cross-section of natural carbon, obtained by extrapolation of the observed cross-sections to zero sample thickness, was determined as equal to 4.63 barns. This value is much more than the EXFOR and ENDF/B library values as shown in Fig. 1, *a*. The majority of the presented in EXFOR measurements were carried out with one carbon sample, so the cross-section dependence on the sample thickness could not be detected in these works. Our measurements [1] were done with ten samples of natural carbon. The observed dependence may be due to the fact that the strong resonance exists in this energy region. Really, in compliance with [2] a p-wave resonance is present at the energy 152.4 keV for ^{13}C+n reaction. But the natural abundance of the ^{13}C isotope is 1.1%, so the observed dependence cannot be explained by presence of this resonance (see Fig. 1, *b*).

Simultaneously with release of our work [1], the theoretical work [3] was published. The strong resonance for ^{12}C+n reaction was predicted by these authors near 0.1 MeV. Therefore, an experimental investigation of the total cross-section of natural carbon in this region was continued [4, 5] and is continued now. The main purpose of these researches is to identify this resonance in experiment and determine its parameters (if it exists).

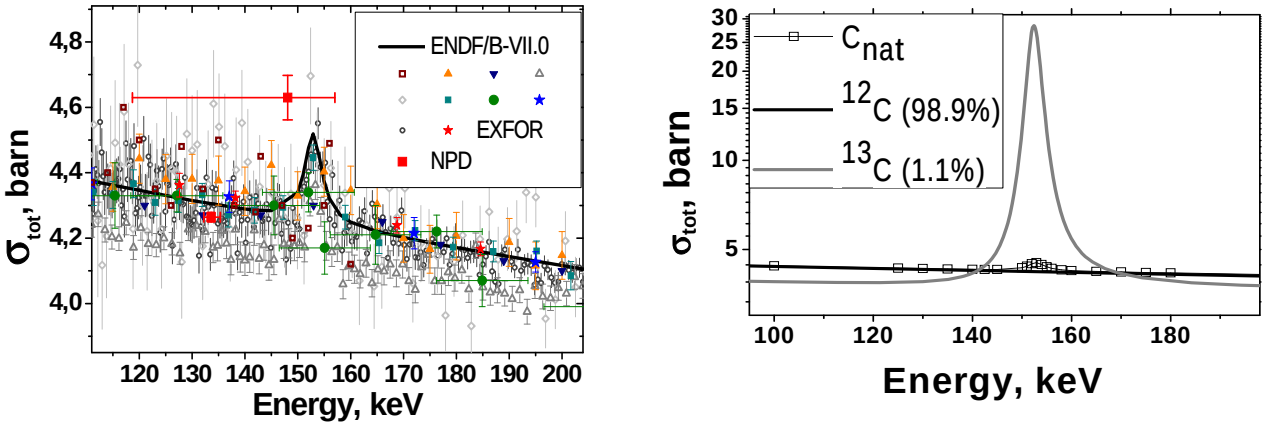

a *b*

Fig. 1. *a* - the ENDF/B and EXFOR data for the total neutron cross-section of natural carbon an; *b* - the total neutron cross-section of natural carbon, ^{12}C and ^{13}C isotopes from the ENDF/B library.

2. The method's idea of the modified filtered beams

Identification of the resonance is not possible if only one value of the average total cross section of carbon is obtained in the energy region near 150 keV. A set of the average values is necessary in the investigated energy interval to provide information for a resonance. Traditional method of the filtered neutron beams does not allow implementation of this task using a standard set of the filters. Therefore, this technique has been improved by means of development of the method of the modified filtered beams (MMFB).

The main idea of the MMFB is to divide the primary neutron line after the silicon filter (average energy of 144 keV) into the narrower lines by addition of a modifying component. The modifying components are chosen from the materials, the total neutron cross sections of which have the minimums and maximums in the energy range of this primary neutron line. For example, the total neutron cross sections of the main component (silicon) and ^{54}Fe (modifying component) are

presented in Fig. 2, *a*. As it is seen in Fig. 2, *a*, three minimums in $\sigma_{tot}^{^{54}Fe}(E)$ are located in the energy region of the interference minimum of the basic component. By means of an optimization of the modifying component thickness, we can obtain three neutron lines after this modified filter. The result of this modification is shown in Fig. 2, *b*.

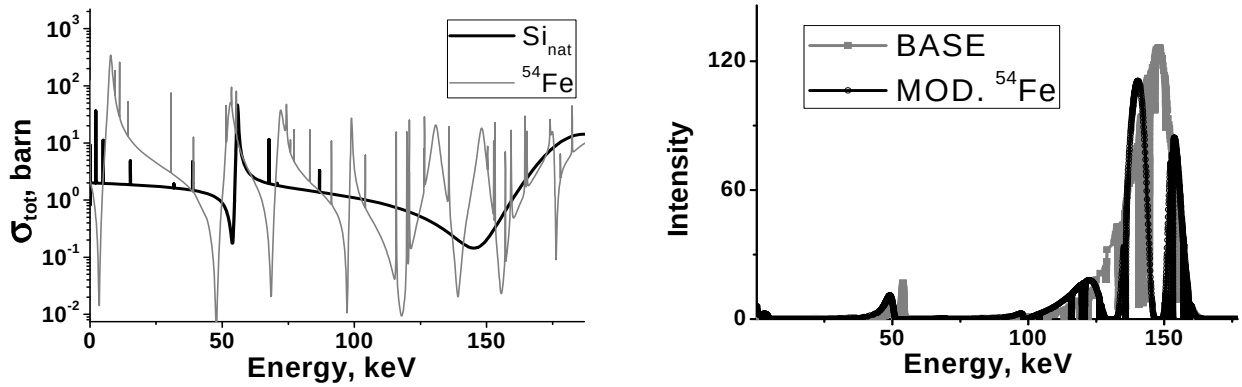

a *b*

Fig. 2. *a* – the total neutron cross-section of Si and ^{54}Fe;
b – calculated neutron spectra after the base and modified by ^{54}Fe filters.

3. The experimental set-up and measuring

Measurements were carried out on the horizontal experimental channel HEC-9 at the Kyiv Research Reactor using the MMFB. The experimental installation is shown in Fig. 3. A composition of the filter assemblies used in this experiment is presented in Table 1.

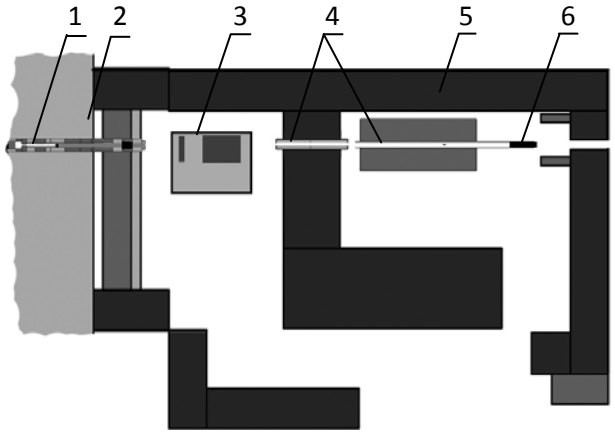

Fig. 3. Scheme of the experimental installation mounted on HEC-9: *1* – filter assembly; *2* – biological protection of reactor; *3* – system of the sample movement; *4* – collimators; *5* – protection of the channel; *6* – neutron detector.

Table 1. **A composition of the used filtered assemblies**

Name of filter	Number of lines	Components, g/cm^2						
		^{10}B	Si_{nat}	Ti_{nat}	V_{nat}	^{58}Ni	^{54}Fe	Al
Base	1	0.2	213.43	11.49	-	-	-	-
Mod. V	3	0.2	184.07	7.66	24.44	-	-	-
Mod. Ni	2	0.2	184.07	7.66	-	20.49	-	-
Mod. Fe	3	0.2	184.07	-	-	-	77.45	-
Mod. Al	1	0.2	213.43	-	-	-	-	10.00

Two types of the carbon samples were used in these measurements: 1) solid samples from a reactor graphite (C 99.9%); 2) carbon discs, each of them has thickness 1 mm (C 99.997 %). The characteristics of the used samples are presented in Table 2. The measurements were carried out using at least 3 samples for each filter modification.

Table 2. **Characteristics of the used carbon samples**

Mod. Fe-54, Mod. Al				
Massa, g	Diameter, mm	Thickness		
		mm	10^{-3} nuclear/barn	Type
1.2800	30.40	1.00	8.842±0.029	1
2.5620	30.40	2.00	17.697±0.058	1
3.8495	30.40	3.00	26.591±0.088	1

Continuation of Table 2

Mod. Fe-54, Mod. Al				
Massa, g	Diameter, mm	Thickness		
		mm	10^{-3} nuclear/barn	Type
5.0650	29.95	4.16	36.047±0.120	2
8.1635	29.90	6.76	58.293±0.195	2
13.2350	29.90	10.94	94.506±0.316	2
15.3650	29.90	12.91	109.716±0.367	2
21.2325	29.90	17.74	151.614±0.507	2
25.6870	29.95	21.27	182.810±0.610	2
Base, Mod. V, Mod. Ni-58				
Massa, g	Diameter, mm	Thickness		
		mm	10^{-3} nuclear/barn	Type
1.2870	30.04	1.00	8.898±0.006	1
2.5657	30.04	2.00	11.774±0.012	1
3.8494	30.04	3.00	26.614±0.018	1
5.0720	29.90	4.16	36.024±0.024	2
6.2886	29.90	5.15	46.646±0.030	2

4. Algorithm for treatment of experimental spectra

Algorithm for treatment of experimental spectra is divided into two stages:

- Initial processing of the proton recoil spectra and reconstruction of the neutron spectra;
- Getting the parameters of the neutron lines, determination of the total neutron cross-section.

The first stage contains of the following procedures: dead time correction, background corrections, summation of the similar spectra, smoothing the summed spectra, differentiation of the smoothed proton recoil spectra to obtain the non-adjusted neutron spectra. These procedures were described in [5]. It was assumed that this differentiation could recover the neutron spectrum. However, the subsequent analysis showed that this recovery is not complete, and the differentiated spectra have to be adjusted.

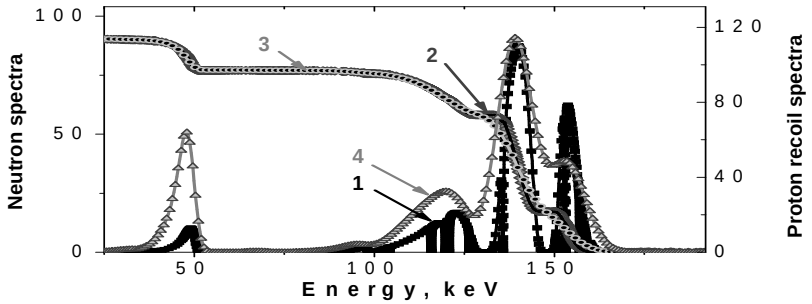

Fig. 4. Output calculated spectra: *1* – neutron spectrum; *2* – reconstructed proton recoil spectrum; *3* – blurred proton recoil spectrum; *4* – differentiated proton recoil spectrum, i.e. reconstructed neutron spectrum.

So, a new approach is being developed to do this adjustment. It consists of the following steps. Output results after each step are presented in Fig. 4.

- Calculation of a neutron spectrum after the given modified filter (1 in Fig. 4). This calculation is performed by the FILTER-7.1 code [6] using the ENDF/B libraries. A thickness of the filter components are taken just the same as in reality.
- Reconstruction of the proton recoil spectrum from the calculated neutron spectrum (2 in Fig. 4). It is performed by formula:

$$Q_i = \sum_{j=i}^{N-1} \frac{(I_{j+1} + I_j) \cdot (E_{j+1} - E_j)}{(E_{j+1} + E_j)}, \quad (1)$$

where Q_i – number of counts in i-th channel (energy of this channel is E_i) in the proton recoil spectrum; I_{j+1}, I_j – number of counts (j + 1)-th and j-th channels in the calculated neutron spectrum at the relevant energies E_{j+1} and E_j.

- Blurring the reconstructed spectrum to take into account the energy resolution of the detector system (3 in Fig. 4). It is performed by formula:

$$R_i = \sum_{j=1}^{N} Q_j \cdot \frac{\exp\left(-\frac{(E_i + E_j)^2}{2\sigma^2}\right)}{\sigma\sqrt{2\pi}}, \qquad (2)$$

where R_i – number of counts in i-th channel (energy of this channel E_i) in the blurred proton recoil spectrum; Q_j – number of counts in i-th channel (energy of this channel E_j) in the reconstructed proton recoil spectrum; σ – an energy-dependent resolution parameter. It was estimated from experiment and was taken σ = 0,075·E.

- Differentiation of the blurred spectrum (4 in Fig. 4).

Then, this reconstructed neutron spectrum 4 was fitted by the function

$$F(x) = \sum_{i=1}^{M} A_i \frac{1}{1 + e^{-\frac{x - Xc_i + \frac{W_{1i}}{2}}{W_{2i}}}} \left(1 - \frac{1}{1 + e^{-\frac{x - Xc_i - W_{1i}/2}{W_{3i}}}}\right) + \sum_{j=1}^{N} \frac{A_j}{W_j\sqrt{\frac{\pi}{2}}} e^{-2\frac{(x - Xc_j)^2}{W_j^2}}, \qquad (3)$$

where the first sum describes non-symmetrical lines, the second one describes symmetrical lines (A_i, A_j – amplitudes; Xc_i, Xc_j – energy parameters, which correspond to coordinate position of maximum for *i*-th and *j*-th lines; W_{1i}, W_{2i}, W_{3i}, W_j – width parameters; M – number of non-symmetrical lines; N – number of symmetrical lines). This fitting was carried out using the OriginLab OriginPro ver.8 software. A result of this procedure is presented in Fig. 5, *a*. Similar procedure was performed with the non-adjusted neutron spectrum (see description of the treatment of experimental spectra in the beginning of this paragraph). The output results after the last two procedures are compared and the corresponding energy calibration corrections are brought in the non-adjusted neutron spectrum (see Fig. 5, *b*). These corrections are also introduced in the obtained spectra, when the carbon samples are on the beam. All spectra ("direct beam" and after samples) are fitted by the same chosen function with keeping energies and widths of the lines. The areas under the approximated lines are used for calculation of the sample transmission.

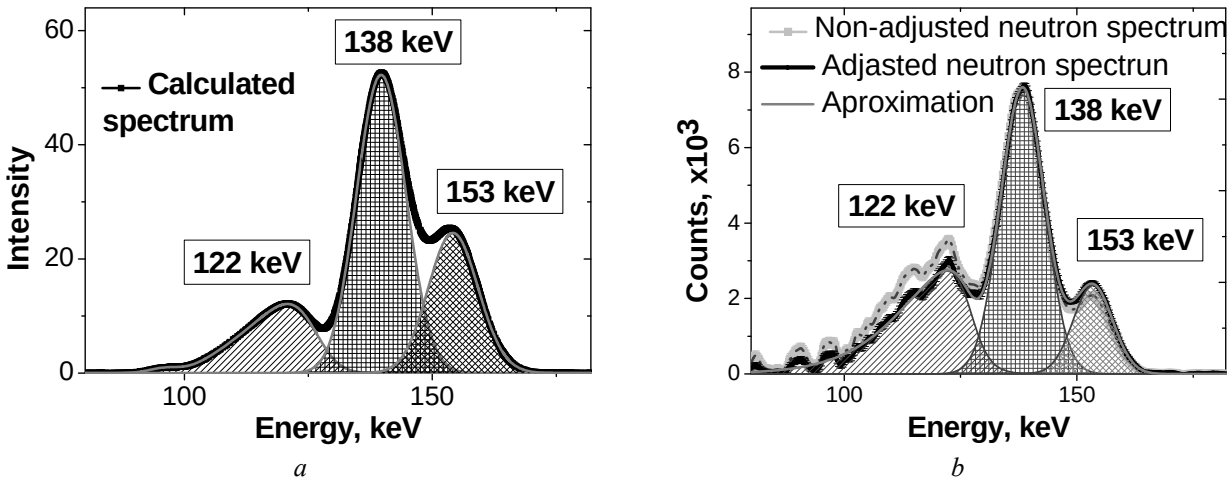

a *b*

Fig. 5. Fragments of the differentiated spectra and the separate line approximations:
a - for the calculated spectrum; *b* - for the experimental spectrum.

6. Results

The modified filters allowed determination of 10 values of the averaged total neutron cross-sections of natural carbon in the energy region 90-160 keV. The cross-section dependence on the sample thickness was not observed in these measurements, so the final total neutron cross-sections were determined as mean values of the data obtained for the different samples. These final values are presented in Table 3. A visual comparison of these values with the ENDF/B data is shown in Fig. 6, *a*.

Simultaneously with creation of the neutron lines in the energy region 90-160 keV, the filters, modified by ^{58}Ni, V and Al, create in the filtered neutron spectra a line with the average energy close to 54 keV. The averaged total neutron cross-sections of natural carbon were also determined at this energy, using this new processing approach. As the total neutron cross section of natural carbon is very well known in the energy region near 54 keV, the determined values may be used as the reference data. These determined values are presented in Fig. 6, *b*. As it can see in Fig. 6, *b*, a good agreement is observed between the ENDF/B data and our results. It is a good confirmation test of the chosen processing approach.

Table 3. **The measured averaged total neutron cross-section of natural carbon**

Filter name	E_c, keV	E_{min}, keV	E_{max}, keV	σ, barn	Δσ, barn	Δσ/σ · 100 %
Base	146.5	90.9	171.2	4.27	0.21	4.9
Mod. V	107.3	87.0	127.5	4.34	0.79	18.2
	131.6	123.2	140.1	4.24	0.29	6.7
	147.5	135.7	159.2	4.38	0.12	2.7
Mod. Ni	132.7	88.1	148.8	4.24	0.26	6.1
	150.9	139.6	162.2	4.18	0.26	6.3
Mod. Fe	122.1	75.3	136.2	4.43	0.73	16.4
	138.3	128.8	147.8	4.30	0.05	1.2
	153.5	145.0	161.9	4.40	0.05	1.1
Mod. Al	131.8	91.7	166.2	4.35	0.11	2.5

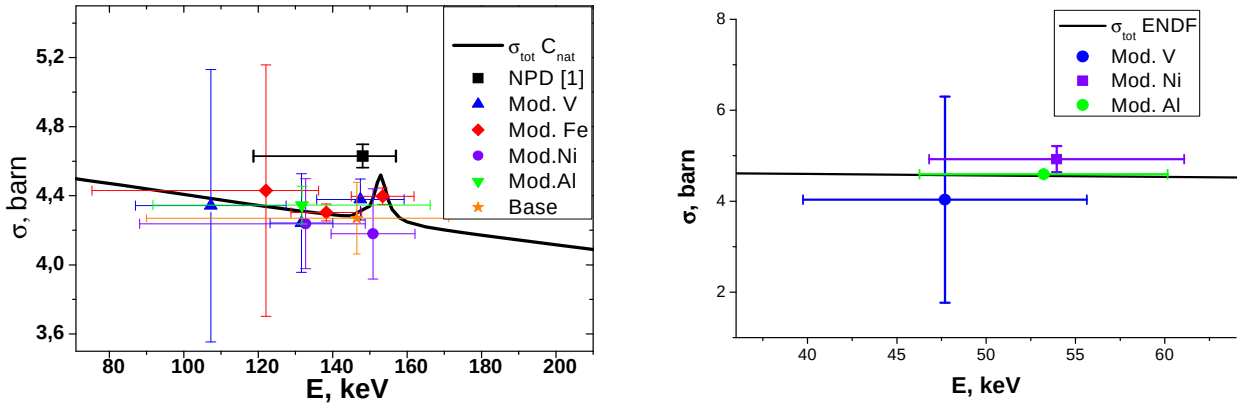

a *b*

Fig. 6. Comparison of the experimental σ_{tot} of carbon with the ENDF/B data.

Now we are developing algorithm to recover the energy dependence of the neutron cross-section in the energy region 90 - 160 keV, using the measured average values. To do the recovery in this region, we also plan to carry out additional measurement to get better accuracy. Analysis of these measured average total neutron cross-section of natural gives grounds to assume that a strong resonance for ^{12}C + n reaction, predicted in [3], is absent in energy region 130 - 160 keV.

REFERENCES

1. *Gritzay O.O., Kolotyi V.V., Kalchenko O.I. et al.* The Total Neutron Cross Section for Natural Carbon in the Energy Range 2 to 148 keV // Proc. of the ND2007 (Nice, France, April 22 – 27). - P. 543.
2. *Mughabghab S.F.* Atlas of Neutron Resonances, Resonance Parameters and Thermal Cross Sections / 5-th Ed. - NNDC BNL Upton, USA.
3. *Canton L., Amos K., Karataglidis S. et al.* Particle-unstable light nuclei with a Sturmian approach that preserves the Pauli principle // Nucl. Phys. - 2007. -Vol. A790. - P. 251 - 256.
4. *Gritzay O.O., Kolotyi V.V., Volkovetskyi S.P.* Analysis possibility of using of neutron filtered beam technique at reactor for determination of carbon resonance parameters in the 150 keV region // Nuclear Physics and Atomic Energy. - 2009. - Vol. 10, No. 4. - P. 418 - 423.
5. *Gritzay O.O., Kolotyi V.V., Volkovetskyi S.P. et al.* Using of neutron filtered beam technique at reactor for determination of carbon resonance parameters in the 150 keV region // Proc. of the 3-rd Int. Conf. “Current Problems in Nuclear Physics and Atomic Energy” (Kyiv, Ukraine, June 7 - 12, 2010). - Kyiv, 2011. - P. 468 - 472.
6. http://ukrndc.kinr.kiev.ua/FILTER-7.html

CROSS SECTIONS OF (n, α) REACTIONS ON RARE-EARTH ELEMENTS FROM Tb THROUGH Lu AT En~14 MeV

A. O. Kadenko[1], N. R. Dzysiuk[2], O. M. Gorbachenko[1], I. M. Kadenko[1,2], V. A. Plujko[1,3], G. I. Primenko[1]

Nuclear Physics Department, Taras Shevchenko National University, Kyiv, Ukraine
[2] International Nuclear Safety Center of Ukraine, Kyiv, Ukraine
[3] Institute for Nuclear Research, National Academy of Sciences of Ukraine, Kyiv, Ukraine

The cross sections of the neutron reactions at E_n = 14.6 MeV on the isotopes of Tb-159, Dy-164, Er-168, Er-170, Yb-174, Yb-176, Lu-175, and Lu-176 with alpha-particle emission were studied by the use of new experimental data and different theoretical approaches. New and improved experimental data were obtained with the neutron-activation technique. The samples of natural composition of rare earth elements were irradiated with d-t neutrons from the neutron generator NG-300. Gamma-ray spectra of the induced activities of irradiated samples were measured with HPGe spectrometer. The uncertainties of the experimental cross sections were thoroughly estimated. Available experimental results and evaluated nuclear data from the EXFOR, TENDL, ENDF data libraries were compared with different systematics and calculations with the EMPIRE 3.0 and TALYS 1.2 codes. Contribution of pre-equilibrium decay was analyzed. Different systematics for estimations of the investigated cross-sections have been tested.

1. Introduction

Neutron activation cross sections for energies around 14 MeV are basic data required for design calculations in nuclear technologies that involve neutrons. Indeed, the amount of their various applications is increasing rapidly. Nuclear data are one of the main tools for extracting an important information about the nuclear structure, excited states, reaction mechanisms, and useful to confirm predictions of nuclear reaction theory [1, 2]. Certainly, up to now, many works dealing with cross section data measurements have been reported and much effort was paid to compilations and their evaluations. That proves a number of evaluated data libraries including general purpose and specialized ones. Unfortunately, in the energy and mass region of mentioned elements the experimental data are scarce and inconsistent [3]. Moreover, the (n, α) cross section data are of a great interest, since they are crucial in the domain of nuclear fusion technology. Also, Dy, Er and Yb belong to the category of fission products are used as a burnable poison in nuclear reactor control rods because of its high neutron absorption cross section and high melting point. The present study is motivated by necessity to measure accurate cross section data and performing based on them evaluations. Considered elements belong to the group of rare-earth (lanthanides) and are characterized by very specific nuclear properties, which impact the search for nuclear limits of stability, proton radioactivity as well as new reaction channels.

The cross sections of the neutron reactions at E_n = 14.6 MeV on the isotopes of Tb-159, Dy-164, Er-168, Er-170, Yb-174, Yb-176, Lu-175, and Lu-176 with alpha-particle emission were studied by the use of new experimental data and different theoretical approaches.

2. Experimental technique and measurement

Using the well operated intense neutron source at the Department of Nuclear Physics, Taras Shevchenko National University of Kyiv [4], cross sections for the ^{175,176}Lu(n,α)^{172,173}Tm, ^{174}Yb(n,α)^{171}Er, ^{176}Yb(n,α)^{173}Er, ^{159}Tb(n,α)^{156}Er at 14.6 MeV neutron energy were measured. Cross section measurements were performed with the neutron activation technique [5]. Neutron generator NG-300 was used as a source of neutrons with a maximum neutron flux density of (d,t) neutrons ~ $5.2 \cdot 10^8$ (1/cm^2·s) which was determined experimentally. The 14 MeV neutrons were produced via the T(d,n)^{4}He reaction by bombarding a T-Ti target mounted on a target assembly. The target consisted of 25 Ci of tritium absorber on a Titanium substrate. The maximum current of the Deuterium ion beam was 1.0 mA. Mixed ion beam component (D+-D2+) with maximum energy ~ 225 keV was used for the neutron generation. In order to avoid any considerable distortion factors due to neutrons generation the corresponding neutron spectrum incident at specimen was modelled previously. The samples of Tb, Lu, Dy, Er, and Yb of natural composition were used. Two Dy samples in the shape of disc foil with Ø 15.4×0.07 mm dimensions and 132 mg mass each were irradiated at 0˚ degree angle toward to a primer deuteron beam. The Lu samples were irradiated under 0°, 65°, 135° with the purpose to measuring the excitation function. Before irradiation the dysprosium samples were studied for presence of impurities, among them the following were reported: Gd – 1.21 %, Sc – 0.039 %, Cu – 0.017 %. The Erbium specimen had a shape of parallelepiped with 8.5 × 7.3 × 2.1 mm dimensions and 1.022 g mass and was irradiated at the same geometry conditions (0˚). Lu specimens were in the shape of disk foil with 1.3 mm thickness and 6.3 g mass. Tb specimen was in the shape of disk foil with 2 mm thickness and 1.9 g mass. The γ-ray spectra of the specimens with induced activity were measured with a lead-shielded high-purity germanium (HPGe) spectrometer (coaxial-type detector, volume ~ 110 cm^3). The energy resolution was 2.0 keV for gamma rays with energy 1332 keV corresponding to 60Co decay and 0.9 keV for gamma rays with energy 122 keV, accompanying a decay of ^{57}Co. Obviously, to prepare more intense activities and to reach higher nuclear reaction yield, it is necessary to irradiate specimens at the closest position from the neutron source. Such geometry corresponds to 0˚ degree angle and specimen location directly over the target (4 mm from the titanium layer), however, the irradiation angle comes to have a broad distribution, and thus the D-T neutron

peak energies change depending on the distances between the source and the specimen. Unfortunately this energy straggling cannot be avoided and demands a correct determination the average neutron energy over specimen with following accounting the exact spread limits. For this reason the Monte Carlo simulation [6] as well as a kinematical approach with DROSG code was utilized. The neutron fluence rate at the irradiated position was measured using the $^{27}Al(n, \alpha)^{24}Na$ ($T_{1/2}$ = 14.959 h) reaction as well as the value of cross sections were determined respect to the same standard reaction $^{27}Al(n,\alpha)^{24}Na$ [7]. During irradiation the neutron flux deviation was kept within ± 5 %. The full energy peak efficiencies at the standard position were calibrated with the standard γ-ray sources of ^{241}Am, ^{137}Cs, ^{60}Co, and ^{152}Eu in the energy range between 50 - 1400 keV.

3. Data analysis

A detailed analysis of the literature and databases indicated that the cross section data in the considered energy range for rare-earth elements are very scarce and inconsistent. Moreover, mostly all prior reported data have been obtained with activation technique by using absolute beta counting for the determination of the activities. It may be one of the reasons of essential uncertainties. It should be emphasized that the biggest problem in working with all the aforementioned elements is the presence of several isotopes in the natural composition, the only exclusion is terbium. As a consequence, the strong interference of nuclear reaction products may take place, what reduces essentially the list of possible reaction channels for measurement with the activation technique applied.

Theoretical predictions for the nuclear reactions may help us to understand the nuclear reaction mechanisms and in general nucleon-nuclear interactions. Currently, the cross sections were calculated with the EMPIRE-3.0 [8] and TALYS-1.2 [9] codes in order to perform a comparison. These codes were chosen since they contain a wide spectrum of nuclear reaction models that provides the quantitative calculations. In this paper, nuclear reaction calculations have been performed largely with input parameters and models by default. Results of calculations have been compared to the data taken from the EXFOR database [10] and the latest versions of evaluated nuclear data libraries: ENDF/B-VII, TENDL-2010, JENDL-4.0.

A literature survey revealed several papers detailing experiments on the cross section of the $^{159}Tb(n, \alpha)^{156}Eu$ reactions at 14.7 MeV neutron energy. Below there is a plot of excitation function for the reaction $^{159}Tb(n, \alpha)^{156}Eu$, more details are presented in ref [11]. The cross section value obtained in this paper is in rather good agreement (see Fig. 1) with work of [15 - 17]. Such consistency could be considered as an independent confirmation of the correctness of our application of the activation techinque.

The (n, α) reaction cross section for the terbium was calculated with utilization the systematics of Konobeyev [12] and Kadem [13]. The result of comparison between calculations with the EMPIRE 3.0, TALYS-1.2 codes and evaluated data from the ENDF/B-VII is given in Fig. 1. The calculations with the EMPIRE 3.0 code was made with taking into account pre-equilibrium processes by exciton model (PCROSS = 1.5) and without ones (PCROSS = 0). The calculations with the TALYS-1.2 code were made with the default input parameter values.

Similar to the theoretical calculation procedure, which employed the utilization of the different codes and data taken from databases, a set of curves was also obtained for the Dy isotopes. The dependence of (n, α) cross section versus number of neutrons is presented in Fig. 2.

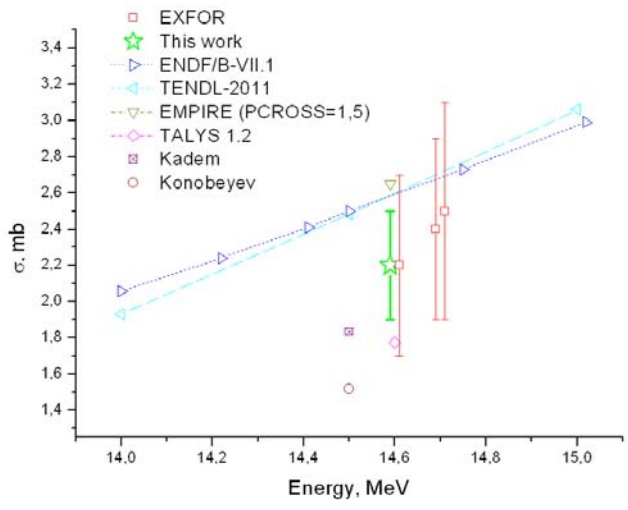

Fig. 1. Excitation function for the reaction $^{159}Tb(n,\alpha)^{156}Eu$.

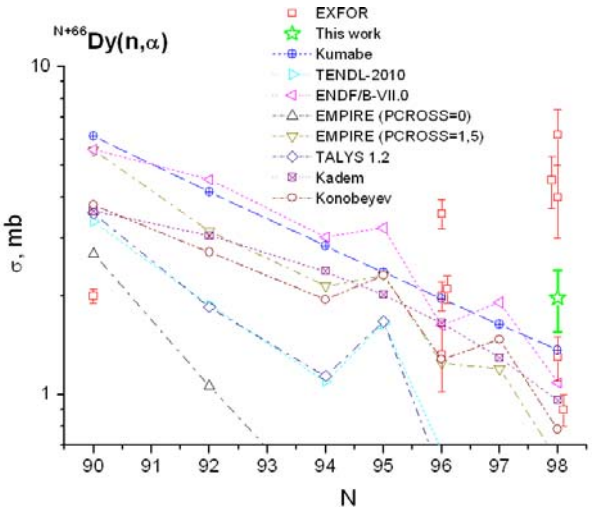

Fig. 2. The cross section dependence of the (n, α) nuclear reaction on neutron number in dysprosium mother nucleus.

The (n, α) reaction cross section at the incident neutron energy of 14.6 MeV for the dysprosium isotopes have been calculated with the systematics of Konobeyev [12], Kadem [13], Kumabe [14], as well as the EMPIRE-3.0 and TALYS-1.2 codes. The corresponding plot with the comparison of the results is shown in Fig. 2. In addition, data have been taken from the EXFOR, ENDF/B-VII.0, and TENDL-2010 databases. For the reaction (n α), analogically to (n, p), the pre-equilibrium processes are the most probable, and a contribution of α-particle emission at this stage increases

essentially the final cross section value. As could be seen from the Fig.2 the cross section for the (n, α) reaction is quite considerably decreasing with increasing the neutron number in the mother nucleus of dysprosium.

Following a similar procedure as described above, the (n, α) reaction cross sections were analyzed and the predictions of these cross sections were performed by means of the expressions suggested by Konobeyev [12], Kadem [13] and Kumabe [14]. Fig. 3 shows a comparison between theoretical calculations with the EMPIRE3.0 and TALYS-1.2 codes, data measured in the present paper and experimental cross section values from earlier work. Evaluated data have been taken from the ENDF/B-VII.0 and TENDL-2010 databases. The behavior of this cross section does resemble to the dependence observed for dysprosium.

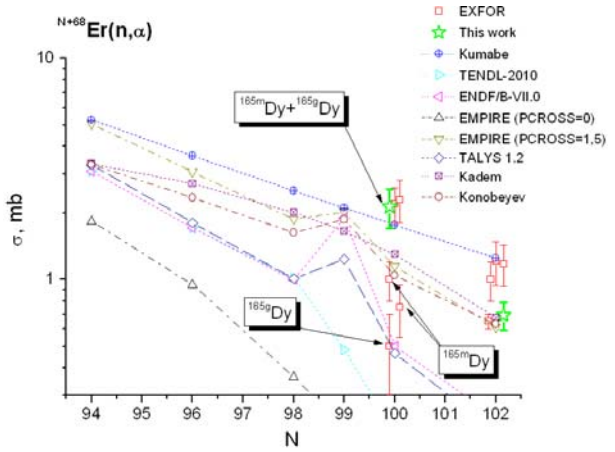

Fig. 3. The cross section dependence of the (n, α) nuclear reaction on neutron number in erbium mother nucleus.

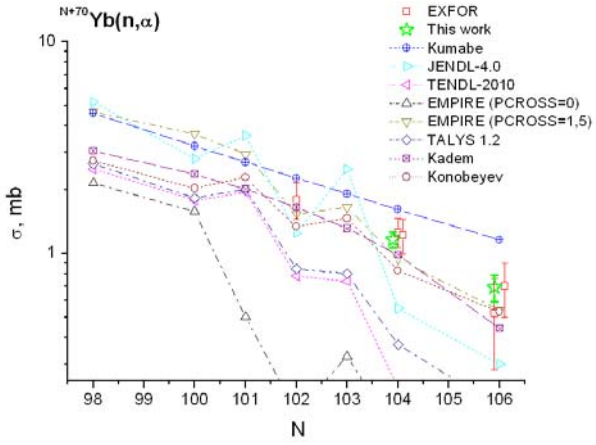

Fig. 4. The cross section dependence of the (n, α) nuclear reaction on neutron number in ytterbium mother nucleus.

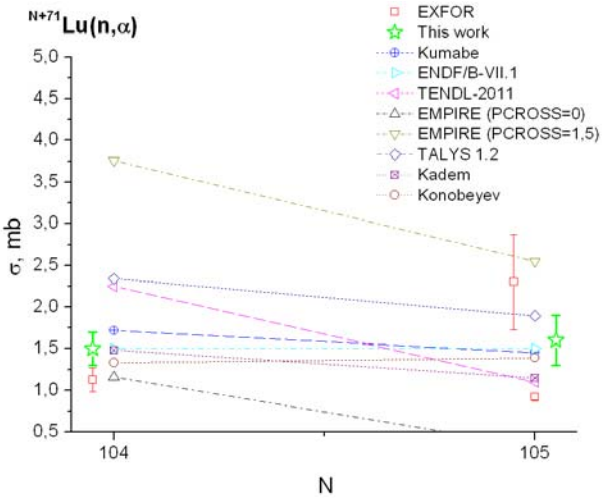

Fig. 5. The cross section dependence of the (n, α) nuclear reaction on neutron number in lutetium mother nucleus.

The (n, α) reaction cross section at the incident neutron energy of 14.6 MeV for the ytterbium isotopes have been calculated with the systematics of Konobeyev [12], Kadem [13], Kumabe [14], with the EMPIRE-3.0 and TALYS-1.2 codes as well as retrieved from the experimental EXFOR and evaluated ENDF/B-VII.0, TENDL-2010 databases. The result of comparison is presented in Fig.4. This analysis of (n, α) cross section dependence on number of neutrons confirms a straight line trend (see Figs. 2 - 5) and indicates this was a correct approach to this study, and demonstrated the reliability of our measured data.

Indeed, there have been many systematic experimental studies in the 14 - 15 MeV energy range for cross sections, such as (n, α). These studies indicate essential disagreements which should be excluded by means of involving the reliable experimental data. Moreover, the analysis of nuclear data in these particular mass and energy ranges showed that they were mostly obtained a long time ago and referred to the problems with insufficient, and sometimes even incorrect, nuclear structure information. That is why the main aim must be an obtaining new and more accurate experimental data for thorough analysis of prior systematics and improving the theoretical approaches.

The (n, α) reaction cross section for both lutetium isotopes have been measured at the incident neutron energy of 14.6 MeV. Similarly to the procedure mentioned above, these cross sections have been calculated with the systematics of Konobeyev [12], Kadem [13] and Kumabe [14] as well as with the EMPIRE-3.0 and TALYS-1.2 codes. Experimental data have been obtained from the experimental EXFOR and evaluated ENDF/B-VII.1, TENDL-2011 databases.

4. Summary

The cross section of the nuclear reaction (n, α) was measured on isotopes of terbium, dysprosium, erbium, ytterbium, and lutetium at the incident neutron energy 14.6 ± 0.2 MeV. Obtained results were compared with available experimental data, evaluated nuclear data and the results of theoretical calculations. In major cases measured results are in rather good agreement within uncertainties with available experimental data. Calculated values of the cross sections with the EMPIRE 3.0 code with taking into account pre-equilibrium processes much better describes experimental data than the TALYS-1.2 code with parameters by default. Accounting the pre-equilibrium component increases essentially the value of (n, α). These results could be used for nuclear reaction models and for testing current knowledge about nuclear reaction theory. The obtained cross section values can be considered as additional data for nuclear data

evaluation, as we think they provide a more reliable assessment of cross section values for these reactions. The analysis of (n, α) cross section dependence on number of neutrons confirmed a straight line trend. It could be concluded that among so many proposed systematics, it is hard to select the right one because of a lack of sufficient experimental data. It seems most probably that the idea of selecting or deriving the systematics to cover a wide range on nuclides, is not fully worthwhile. The present results can be used for the evaluation of the nuclear data libraries. EMPIRE 3.0 code calculated values of the reaction cross sections with pre-equilibrium processes consideration are in good agreement with experimental data. At the same time the cross section calculations using the TALYS 1.2 code with parameters by default, are not so close to experimental data. Konobeyev systematics is the most acceptable to fit available experimental data and is recommended for further utilization. Presented results can be utilized in the field of nuclear energy applications as well as in a testing of nuclear reaction models.

REFERENCES

1. *Koning A.J, Blomgren J.* Nuclear data for sustainable nuclear energy // JRC Scientific and Tech. Rep. - 2009. - Vol. EUR23977EN
2. *Capote R., Herman M., Obložinský P. et al.* RIPL - Reference Input Parameter Library for Calculation of Nuclear Reactions and Nuclear Data Evaluations // Nuclear Data Sheets. - 2009. - Vol. 110. - P. 3107 - 3214; see RIPL-3 web site at http://www-nds.iaea.org/ripl3/.
3. *Forrest R.A.* Data requirements for neutron activation Part I: Decay data // Fusion Engineering and Design. - 2006. - Vol. 81. - P. 2143 - 2156.
4. *Primenko G.I., Maidanyuk V.K, Neplyuev V.M.* Devices and Technique of experiment. - 1989. - No. 6. - P. 39.
5. *Kuznetsov R.A.* Activation analysis. - M.: Atomizdat, 1974. - 344 p. (In Russian).
6. *Briesmeister J.F.* MCNP - a general Monte Carlo N-particle transport code: Los Alamos National Laboratory Report, 1997. Vol. LA-12625-M.
7. *Filatenkov A.A., Chuvaev S.V.* // Khlopin Radiev. Inst. Leningrad Reports. - 2001. - No. 258.
8. *Herman M., Capote R., Carlson B.V. et al.* EMPIRE 3.0: Nuclear Reaction Model Code System for Data Evaluation // Nuclear Data Sheets. - 2007. - Vol. 108. - P. 2655 - 2715. http://www.nndc.bnl.gov/empire/
9. *Koning A.J., Hilaire S., Duijvestijn M.C.* TALYS-1.0 // Proc. of the Int. Conf. on Nucl. Data for Science and Technology - ND2007 (Nice, France, April 22 - 27, 2007) / Eds. O. Bersillon, F. Gunsing, E. Bauge, R. Jacqmin, S. Leray. - EDP Sciences, 2008. - P. 211 - 214. http://www.talys.eu/home/
10. Cross section information storage and retrieval system (EXFOR) // National Nuclear Data Center (NNDC), Brookhaven National Laboratory, USA. http://www.nndc.bnl.gov/index.jsp (online).
11. *Dzysiuk N., Kadenko I., Koning A.J., Yermolenko R.* Cross sections for fast-neutron interaction with Lu, Tb and Ta isotopes // Physical Review. - 2010. - Vol. C81. - P. 014610.
12. *Konobeyev A.Yu., Fisher U., Broeders C.H.M.* Improved systematic of (n, α) reaction cross-section at 14.5 MeV // Applied Radiation and Isotopes. - 2009. - Vol. 67. - P. 357 - 361.
13. *Kadem F., Belgaid M., Amokrane M.* Systematic studies of (n, α) reaction cross-section at 14.5 MeV // Nuclear Instruments and Methods in Physics Research. - 2008. - Vol. B 266. - P. 3213 - 3220.
14. *Fujino Y., Hyakutake M., Kumabe I.* Activation cross section of zirconium and Molybdenum isotopes for 14.6 MeV neutrons // Bull. Inst. Chem. Res. - 1982. -Vol. 60, No. 2. - P. 205 - 207.
15. *Xiangzhong Kong, Vongchang Wang, Jingkang Yang* Cross Sections for (n, 2n), (n, p) and (n, a) Reactions on Rare-earth Isotopes at 14.7 MeV // Applied Radiation and Isotopes. - 1998. - Vol. 49, Issue 12. - P. 1529.
16. *Qaim S.M.* Activation cross sections of (n, alpha) reactions at 14.7 mev in the region of rare earths // Radiochimica Acta. - 1984. - Vol. 35. - P. 9.
17. *Kulisic P., Cindro N., Strohal P., Lalovic B*. Direct processes in (n, a) reactions // Nuclear Physics. - 1965. - Vol. 73. - P. 548.

INFLUENCE OF CORE MODEL PARAMETERS ON THE CHARACTERISTICS OF NEUTRON BEAMS OF THE RESEARCH REACTOR

N. A. Khafizova, V. K. Sakharov, M. V. Shchurovskaya

National Research Nuclear University «MEPhI», Moscow, Russia

IRT MEPhI reactor is equipped with a number of facilities at horizontal experimental channels (HEC). Knowing of parameters influencing spatio-angular distribution of irradiation fields is essential for every application area. The research was made for neutron capture therapy (NCT) facility at HEC of the reactor. Calculation methods have been used to estimate how the reactor core parameters influence neutron beam characteristics at the HEC output. An impact of neutron source model in Monte Carlo calculations by MCNP code on parameters of neutron and secondary photon field at the outlet of irradiation beam tubes of research reactor is estimated. The study shows that specifying neutron source with fission reaction rate distribution in SDEF option gives almost the same results as criticality calculation considered as the most accurate. Our calculations show that changes of the core operational parameters have insignificant influence on characteristics of neutron beams at the HEC output.

1. Introduction

Every research reactor is a unique nuclear facility designed for carrying out nuclear physics experiments in both reactor physics and many applied problems. In the last case there are horizontal and vertical channels at which output neutron beams are formed with specified spectral and angular radiation distribution. Having the core as an initial neutron source we can form neutron spectrum at the reactor channel output with either making changes in the core and the reflector or selecting peripheral equipment impacting the way neutrons pass through the core to the channel output. As usual the first method is extremely rare for a functioning reactor and the problem is solved by modifying peripheral equipment. This becomes exceptionally important if an experimental task for a reactor changes. Recently many studies on NCT-facilities constructions are held at research reactor (for example at Kiev Research Reactor (10 MW) and at Research Reactor in Tashkent (10 MW)). How changes in construction and operational parameters of the reactor core influence neutron beam characteristics is essential for estimations of experimental results errors as a physicist has only beam monitoring but no information on how its characteristics are influenced by the changes in the core.

Monte Carlo full-sized three dimensional modeling of neutron spectrums forming at outputs of research reactor channels requires estimation of errors caused by inaccuracies in specifications of source parameters. Knowing of these errors helps to reduce calculation times without losing accuracy results in multivariate tasks.

In the presented computational research issues of sensibility of neutron beam characteristics at horizontal reactor channel to the core modifications are considered for NCT-facilities at the IRT MEPhI. All the calculations are made with MCNP-4c2 [1].

2. Description of experimental devices for NCT at the reactor

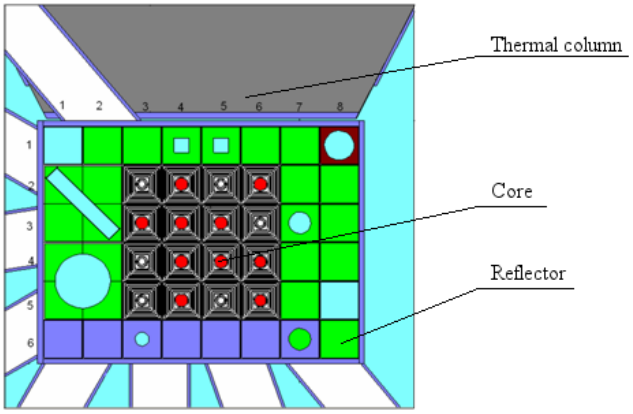

Fig. 1. General view of reactor IRT MEPhI and the core.

IRT MEPhI Research Reactor is a 2,5 MW pool-type reactor currently uses IRT-3M fuel assemblies (FA) with high-enriched (90 %) fuel. IRT MEPhI Reactor was opened in May 1967. Different studies are carried out at a graphite thermal column, 10 horizontal experimental channels and vertical channels in the reflector of this reactor. General view of reactor IRT MEPhI and the core is shown in Fig.1.

Experimental irradiation facility for pre-clinical NCT-studies has already been created at the IRT MEPhI. Radiobiology channel HEC-4 was started to operate for NCT [2]. It was decided to create a new facility at HEC-1 for more opportunities of the reactor using for NCT. Project of clinical channel HEC-1 at the thermal column of IRT MEPhI Reactor was developed for NCT with thermal and epithermal neutrons.

Calculational MCNP model for NCT studies describing in details real three-dimensional geometry of irradiation facilities at the HEC-1 and HEC-4 was developed. Design of the facilities at the HEC-4 [2] and HEC-1 [3] based on various calculations of neutron and contamination photon fields characteristics at these channels and satisfying NCT requirements was suggested and partially realized.

3. Problem statement

Characteristics of neutron beam used for experimental studies depend on both parameters of facility (geometry and material composition) at the HEC and parameters of the reactor core being a neutron source. Facility parameters at the channel are studied and selected at a design stage. Parameters of the reactor core usually come from general reactor design aspects and are not specialized for experimental needs.

We investigated influence of both the core parameters and their ways of specifying within the calculation model on the results of horizontal beams characteristics calculations. The parameters are: number of fuel assemblies (FA) in the core, material composition of fuel, material composition of non-fuel components of the core, geometry of the fuel assemblies, reflector geometry. The research was made for NCT-facility at HEC-1 of the reactor IRT MEPhI.
The geometry of NCT-facility at HEC-1 is shown in Fig. 2.

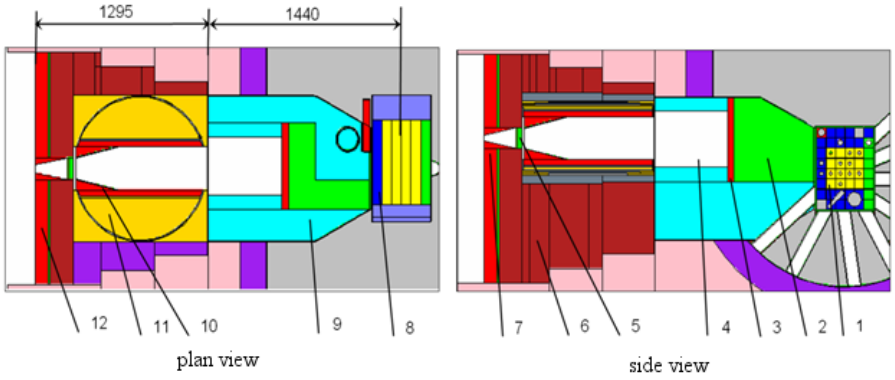

Fig. 2. Design of NCT-facility at the HEC-1. Designation: *1* – core; *2* – aluminum; *3* – lead shielding; *4* – cavity; *5* – Al + Bi filter; *6* - heavy concrete; *7* – second lead collimator; *8* – beryllium reflector; *9* – thermal column graphite; *10* – first lead collimator; *11* – heavy concrete shutter; *12* – lead wall.

We used local estimation to calculate different energies neurons fluxes: thermal (E < 0.5 eV), epithermal (0.5 eV < < E < 10 keV), fast (E > 10 keV) and photon kerma (tally F5) at the beam outlet.

4. Calculations methods to define the core as a neutron source

We used two ways of core modeling as neutron source in MCNP calculations:

To carry out the criticality calculation (KCODE). In this case a spatio-energy distribution of the neutron source is obtained by MCNP calculations of K_{eff}.

To set a known spatial distribution of the neutron source with the SDEF option. Fission rate distribution resulting from neutronic calculations using diffusion or Monte Carlo code can be used as the spatial distribution of the source.

The first option was considered the most accurate. The variant with criticality calculation requires accurate and detailed setting of the parameters of the core and the nearest to it reflector. In this option the geometric model for calculating the parameters of neutron horizontal beams was combined with a detailed geometric core model that was used for calculating operational neutron-physical parameters of the core. In the reference criticality calculated variant parameters are highly close to the reality. We considered the real geometry of FA, burnup distribution and absorbing rods location that were actual for summer of 2009.

Using this combined model is not always reasonable. In this study we use this model as the reference but it is possible to make a faster and less detailed model using SDEF option while accuracy remains the same.

In variants calculated with SDEF option FA are represented as homogeneous mixture of fuel, aluminum claddings of fuel elements (FE) and water. The central channel which can contain either water or an absorbing rod (B_4C) is considered as a special zone.

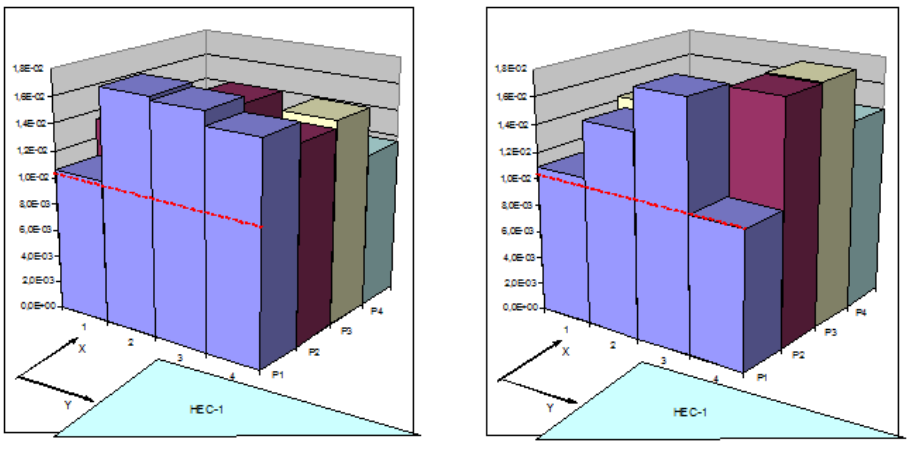

Load №1 of the core Load №2 of the core

Fig. 3. Fission reaction rate distribution in FA of the core at the high level in front of HEC-1. P1 is the nearest to the thermal column. Dash line is a uniform fission rate distribution.

The source distribution is given in proportion to the fission reaction rate in nine levels of different height and calculated with diffusion program. Distributions for two real loads of IRT MEPhI reactor core are shown in Fig. 3.

Results of calculation of beam parameters at HEC-1 with different spatial source distribution are given in Table 1. They are a mentioned above variant with the distribution proportional to the fission rate distribution («real» distribution for the load №1 of the reactor core – SDEF-1), a variant with the uniform distribution (SDEF-2) and a variant with cosine distribution (SDEF-3). As shown in Fig. 3 the «real» distribution in high level in front of HEC-1 is 1.5 higher than the uniform one.

Table 1. **Characteristics of neutron beam at HEC-1 with different spatial source distribution**

Characteristic	SDEF-1	SDEF-2	SDEF-3	KCODE
Neutron flux, $s^{-1}cm^{-2}$				
Thermal	$2{,}05 \cdot 10^{9} \pm 0{,}012$	$1{,}81 \cdot 10^{9} \pm 0{,}02$	$1{,}77 \cdot 10^{9} \pm 0{,}03$	$2{,}06 \cdot 10^{9} \pm 0{,}017$
Epithermal	$1{,}19 \cdot 10^{9} \pm 0{,}023$	$1{,}02 \cdot 10^{9} \pm 0{,}04$	$8{,}75 \cdot 10^{8} \pm 0{,}06$	$1{,}12 \cdot 10^{8} \pm 0{,}032$
Fast	$2{,}6 \cdot 10^{8} \pm 0{,}05$	$2{,}2 \cdot 10^{8} \pm 0{,}09$	$2{,}35 \cdot 10^{8} \pm 0{,}13$	$2{,}3 \cdot 10^{8} \pm 0{,}046$
Kerma of photons, Gy/s	$2{,}57 \cdot V10^{-3} \pm 0{,}029$	$1{,}57 \cdot 10^{-3} \pm 0{,}11$	$1{,}81 \cdot 10^{-3} \pm 0{,}20$	$2{,}76 \cdot 10^{-3} \pm 0{,}041$

The presented results show that thermal and epithermal neutron flux in the variant with the uniform source distribution (SDEF-2) is fewer by 12 - 15 % than in SDEF-1 variant. The difference reaches 25 % in SDEF-3 variant. This difference is caused by the fact that neutron source in FA adjacent to thermal column is lower than «real» for the uniform and the cosine distributions. This FA contribution in the neutron flux is higher than others'.

The presented results also show that variant with homogeneous core and the specified source distribution (SDEF-1) gives almost the same results as the variant with detailed core model and the criticality calculation (KCODE).

We considered variants of calculation where source distribution was specified in the same way (SDEF-1) but material composition of the core was given with different levels of details. In the first variant FA are represented as homogeneous mixture of fuel, aluminum claddings of FE and water, absorbing rods are placed at the real depth, isotopic fuel composition is the same for all FA and corresponds to the 30 % of burnup (SDEF-1, Table 1).

The second variant differs from the first only in the isotopic fuel composition corresponding to the 0 % of burnup (fresh core). In the third variant FA are also represented as homogeneous mixture, absorbing rods are replaced by water, isotopic fuel composition is the same for all FA and corresponds to the 0 % of burnup. The fourth variant differs from the first one in that the hydrogen concentrations of FA materials are increased by 1.2 times.

Calculation results for these variants are presented in Table 2.

Table 2. **The HEC-1 parameters for different variants of material composition of the core**

Parameter	Variant							
	1		2		3		4	
Neutron flux, $10^{9}\ s^{-1}cm^{-2}$								
Thermal	2,05	(±0,012)	2,03	(±0,012)	2,07	(±0,017)	2,00	(±0,017)
Epithermal	1,19	(±0,023)	1,15	(±0,02)	1,19	(±0,03)	1,10	(±0,03)
Fast	0,26	(±0,05)	0,21	(±0,04)	0,22	(±0,06)	0,21	(±0,06)

Detalization of material components definition influences only the results of fast neutron flux calculation.

The presented results show that if the spatial source distribution is fixed then specifying parameters such as a heterogeneous structure of FA, a fuel burnup, control rods (CR) location are not needed in details. This is caused by the fact that only those neutrons reach HEC-1 output which have not slowed down in the core. An absolute number and a spatial distribution of produced fast neutrons are fixed in SDEF option. Some of fast neutrons slow down in the core and at the nearest reflector after producing; others become a neutron source of the horizontal channel. Above-mentioned parameters have a little effect on fast neutrons moderating in the core, they basically influence on absorbing of thermal neutrons. Since a fission process is not considered in SDEF option, the inaccuracy of rate calculation of thermal neutron absorbing in the core has no effect on fast neutron source of horizontal channel.

Specifying of spatial source distribution known from preliminary reactor calculation allows to make significantly easier core model for horizontal beams calculation. It should be noticed that for criticality calculation such parameters as FA heterogeneous structure, fuel burnup, CR location are needed to specify in details because in this case the source forms on basis of real thermal and fast neutron balance in the core. It should be noted also that criticality calculation time is higher than time of calculation with SDEF option by 2 times. Thus it is important to specify spatial source distribution for calculation with SDEF option as close to real as it possible.

5. Influence of core operation parameters

One of main reactor parameters influencing on neutron source distribution is a number of FA in the core. Calculation results for one of the facility constructions at HEC-1 with the reactor core contains 16 or 12 FA are presented in Table 3.

Table 3. **HEC-1 parameters for IRT MEPhI Reactor core contains 16 and 12 FA**

Parameter	16 FA	12 FA
Neutron flux, 10^9 $s^{-1}cm^{-2}$		
Thermal	0,76 (±0,021)	0,60 (±0,016)
Epithermal	1,2 (±0,025)	0,90 (±0,02)
Fast	0,44 (±0,038)	0,34 (±0,033)
Kerma of photons, 10^{-3} Gy/s	1,6	1,4

The spatial source distribution in SDEF option is different for the core loads with 16 and 12 FA and is specified in accordance to fission reaction rate distribution of these loads.

Within the same reactor power neutron flux per FA is higher for the load with a smaller amount of FA, thermal and epithermal neutron fluxes at the HEC-1 output are also higher by 25 - 30 % in this case. It should be noticed that FA number in the core usually stays the same, except changing fuel type in the reactor, such as conversion from high-enriched fuel to low-enriched.

Influence of fuel burnup distribution in the core and absorbing rods location on neutron beam characteristics at the HEC-1 was investigated. Two real loads of IRT MEPhI Reactor containing 16 FA at different levels of burnup were considered.

Fission reaction rate distributions in FA of the core at the high level in front of HEC-1 for loads №1 and №2 are shown in Fig. 3. Insertion depth of absorbing rods for load № 1: AR = 250 mm, CR - 1, 2 = 0, CR - 3 = 344 mm; for load №2 : AR = 200 mm, CR - 1 = 0, CR - 2 = 219, CR - 3 = 580 mm (580 mm – rod is fully inserted). AR rod is located in cell 6 - 2, CR - 2 rods are located in cells 4 - 2 and 4 - 5, CR - 3 rods – in cells 3 - 3 and 4 - 3 (cell numbering is shown in Fig. 1, the first number is pattern column, the second number is pattern raw).

Table 4. **HEC-1 parameters for two different loads of the core containing 16 FA**

Parameter	Load № 1	Load № 2
Neutron flux, 10^9 $s^{-1}cm^{-2}$		
Thermal	2,05 (±0,012)	1,92 (±0,012)
Epithermal	1,19 (±0,023)	1,06 (±0,023)
Fast	0,26 (±0,05)	0,199 (±0,046)

The represented results show that thermal, epithermal and fast neutron fluxes for load № 2 are less than for load № 1 by ~5, ~10 and ~20 % respectively. So above mentioned HEC parameter changes can be seen in transition from one load of the core to another during routine reactor operation.

Both changing of loading pattern and changing of control rods insertion depth influence parameters of HEC. Two calculations of load №1 were held to estimate possible changes of these parameters within the entire campaign: at the beginning of the cycle when CR insertion depth was AR = 250 mm, CR - 1, 2 = 0 mm, CR - 3 = 344 mm; and at the end of the cycle when CR insertion depth was AR = 250 mm, CR - 1, 2, 3 = 0 mm. The first variant is KCODE variant from Table 1. The second variant is also obtained from criticality calculation of load №1 but with another rods location as shown above (Table 5).

Table 5. **HEC-1 parameters for load №1 of IRT MEPhI core with different locations of absorbing rods**

Parameter	AR=250 mm, CR - 3 = 344 mm		AR = 250 mm, CR - 3 = 0 mm	
Neutron flux, 10^9 $s^{-1}cm^{-2}$				
Thermal	2,06	(±0,017)	2,00	(±0,017)
Epithermal	1,12	(±0,032)	1,09	(±0,031)
Fast	0,23	(±0,046)	0,24	(±0,06)

Changing of the absorbing rods location during the campaign has insignificant effect on HEC-1 parameters. It should be noticed that this conclusion is applicable only for mutual location of absorbing rods and the horizontal channel at IRT MEPhI.

6. Conclusions

The studies shows that it is unreasonable to use highly detailed model of the core and horizontal beams for calculations of neutron beams parameters especially with criticality calculation. It is more reasonable for operational neutron-physical calculation to have a special detailed model of the core and the nearest reflector. Within this model a spatial distribution of fission reaction rate is determined by criticality calculation. For calculations of horizontal neutron beams parameters it is suggested to use a model with simplified presentation of the core and with setting of neutron source distribution in SDEF option according to mentioned above fission rate distribution.

The model with a homogeneous core and the specified source distribution (SDEF) gives almost the same results as

the variant with detailed core model and the criticality calculation (KCODE). Changes in the core (burnup, fuel reloads, CR position) with the same FA number can cause changes of thermal and epithermal neutron fluxes by ~10 %. The change in fast neutron flux is ~20 %. If FA number changes dramatically, change of neutron flux reaches 30 %.

REFERENCES

1. *Briesmeister J.F.* (*Ed.*) MCNP - A General Monte Carlo N-Particle Transport Code. Version 4C". - LA-13709-M, 2000.
2. *Zaytsev K.N., Portnov A.A., Sakharov V.K. et al.* Optimization of beam parameters for neutron capture therapy at IRT MEPHI // Medical physics. - 2011. - No. 4 (52). - P. 28
3. *Khoklov V.F., Portnov A.A., Zaytsev K.N. et al.* Making the first Russian database for experimental research in neutron capture therapy of cancer at HEC-4 of nuclear reactor IRT MEPHI. // Russian research and practice conference "Russian antitumor drugs" (Moscow, March, 16 - 18, 2005) // Russian biotherapy journal. - 2005. - Vol. 4, No. 1. - P. P. 5 - 10.

INVESTIGATION OF THE POSSIBILITIES OF OBSERVING THE EFFECTS OF THE PARITY VIOLATION IN NEUTRON DIFFRACTION

V. L. Kuznetsov, E. V. Kuznetsova

Institute for Nuclear Research, Russian Academy of Sciences, Moscow, Russia

The parity violation in neutron diffraction in perfect single crystal of KBr was investigated. The neutron spectrum was approximated by the function 1/E. The neutron detection efficiency and angular divergence of the neutron beam falling on the crystal were taken into account. The enhancement the effects of parity violation in neutron diffraction was detected both in reflected and in transmitted neutron beam. An entirely new method (compensation-diffraction method) was proposed to search for the effects of parity violation in neutron diffraction. Sensitivity of the method, according to the calculations, increases 5.6 times. In this case the parasitic P - odd dichroism in the total cross section is suppressed in ~ 800 times. The influence of the divergence of the neutron beam by the value of parity violation in neutron diffraction was investigated. The calculations were performed to optimize the specific experimental studies.

1. Introduction

In [1 - 4] it was shown that in the case of dynamical diffraction of neutrons by Laue, can be a significant increase in the magnitude of the parity violation. The importance of the study of spatial parity violation in neutron diffraction has been described in [5]. In [6] does not taken into account features of dynamical diffraction, and the result opposite [1 - 4] was obtained.

The spin rotation of transversely polarized neutrons was first discovered at the Institute Laue Langevin [7]. This phenomenon is due to the coherent scattering amplitude that violates spatial parity. In [8, 9] was investigated the rotation of the transverse spin polarized neutron and dichroism in the vicinity of the p-resonance of lanthanum. Both P-odd effects are in good agreement with theory [10 - 12] and have a very large value of ~ 0.1 relative to the cross section of p-resonance.

We calculated the P-odd effects in neutron diffraction in the symmetric Laue geometry, depending on the divergence of the incident neutron beam, the thickness of the crystal and taking into account the boundary conditions. Just as in [1] we considered the P-odd effect in the dynamical diffraction of longitudinally polarized neutrons by a single crystal. In this case, there is no spin-orbit interaction because the neutron spin lies in the scattering plane. Schwinger interaction was not taken into account. All calculations were performed for the wavelength range of neutrons ~ 0.3 Å, because here the amplitude of the weak interaction has the greatest value and this area is available for pulsed neutron sources, neutron complex of INR RAS, and the IBR-2 reactor of JINR LNP.

It should be noted that the neutron interact with all nuclei of the crystal and nuclear resonance parameters can be changed in the diffraction [13].

Amplitudes

The amplitude of the interaction of neutrons with the nucleus, taking into account the weak interaction can be represented as:

$$f = f_0 + f_{ss} + f_{pp} + f_{sp}, \tag{1}$$

here f_0 - the amplitude of potential scattering, f_{ss}; f_{pp} - scattering amplitudes of the s-and p-wave resonance, respectively; f_{sp} - scattering amplitude associated with the mixing of states of different parity by the weak interaction.

The sum of the amplitudes of the f_0 and f_{ss} away from the s-resonance is a constant:

$$f = (f_0 + f_{ss}). \tag{2}$$

The contribution of the amplitude f_{pp} can be neglected, since $(f_0 + f_{ss}) >> f_{pp}$.

The f_{sp} amplitude is:

$$f_{sp} = f_{PV}\cdot\mathbf{s}(\mathbf{p} + \mathbf{p}') + f_{(PT)V}\cdot\mathbf{s}(\mathbf{p}' - \mathbf{p}), \tag{3}$$

here f_{PV}, $f_{(PT)V}$ - amplitude of the weak neutron-nuclear interactions that violate the spatial parity and the spatial parity and time reversal, respectively; s - spin of the neutron; p, p′ - the unit vectors corresponding to the direction of the momentum of the incident and scattered neutrons. The second term in (3) violates spatial parity and time reversal, and therefore will be much smaller than the first, according to [14]. In the case where the angle between the vectors p and p′ small (this is true in the vicinity of the p-resonance) f_{sp} amplitude becomes:

$$f_{sp} = \pm 2f_{PV}. \tag{4}$$

The sign of the amplitude depends on the "helicity" of the neutron and on the sign of the weak interaction matrix

element, and the factor 2 takes into account the possibility of capture of s - wave neutron and of emission the p - wave neutron and vice versa. In addition, the amplitude of the f_{sp} depends on the momentum of the neutron. Finally, the scattering amplitude, taking into account the weak interaction has the form:

$$f(k) = (f \pm f_{sp}(k)) = f\cdot(1 \pm (f_{sp}(k)/f)), \quad (5)$$

where $k = 2\pi/\lambda$ is wave vector of the neutron, and λ - wavelength of the neutron.

The amplitude of the f_{sp} depends on k and is given by [1]:

$$f_{sp}(k) = \mathcal{P}\cdot \sigma_p(E) \cdot (E - E_p)/((E - E_s)\,\Gamma_p) \cdot k/4\pi, \quad (6)$$

here $\mathcal{P} = \Delta\sigma/(2\cdot\sigma_p(E_p))$ − the value of the P-odd asymmetry in the total cross section in the p-resonance; $\sigma_p(E)$ – total p-resonance cross section; E – energy of incident neutrons; E_p, E_s – energy p-and s-resonances; Γ_p – full width of the p-resonance; k – wave number of the neutron. It is evident that the suppression of the amplitude of $f_{sp}(k)$ is mainly due to the factor 1 / (E - Es).

Diffraction

When calculating the space-odd effects in neutron diffraction was considered symmetrical diffraction in Laue geometry in a two-wave approximation of dynamical diffraction of neutrons [16, 17].

The intensity distribution of the neutron beam as a function of the angle of incidence θ was approximated as:

$$J^{\pm}(\theta) = J_0\cdot\exp(-((\theta_B - \theta)/\Delta\theta_n)^2), \quad (9)$$

where θ_B-Bragg angle; $\Delta\theta_n = ((\delta\theta_n)^2 + (\theta_m)^2)^{0.5}$; $\delta\theta_n$ – the half-width of the angular distribution of incident neutrons; θ_m – a mosaic crystal, $J_0 = 1$.

The asymmetry of the reflected neutrons as a result of diffraction was determined as:

$$P_{PVD}\cdot P_n = \int(R^+\cdot J^+ - R^-\cdot J^-)d\theta/\int(J^+ + J^-)d\theta. \quad (10)$$

Here J^+, J^- – the intensity of the incident neutron beam of positive and negative helicity dependent on the angle of refraction of neutrons in a crystal, due to boundary conditions. The polarization of the incident neutrons was considered 100 %, ie, $P_n = 1$.

The intensity of the reflected beam of neutrons is of the form:

$$P_{ref}(y) = (\sin(\pi t/\Delta_0\cdot(1 + y^2)^{0.5})^2)/(1 + y^2), \quad (11)$$

and the intensity of the diffracted transmitted beam of neutrons is of the form:

$$P_{tr}(y) = 1 - P_{ref}(y). \quad (12).$$

Here y – angular variable, which takes into account the deviation of the reflected neutron from the Bragg angle; t – thickness of the crystal in centimeters; Δ_0 – length of extinction; $(\pi t/\Delta_0)$ – the reduced thickness of the crystal.

The length of the extinction is the form:

$$\Delta_0 = \pi\cdot v_c\cdot\cos(\theta_B)/(\lambda_n\cdot|f(k)|\cdot F_{200}\cdot e^{-2W}), \quad (13)$$

here v_c – unit-cell volume; F_{200} – a geometrical structure factor of neutron reflection from the plane (200) single crystal of KBr. e^{-2W} – Debye - Waller believed to be 1, while according to [18] it is equal to 0.955. The amplitude f (k) takes into account the violation of spatial parity (5). Functions P_{ref} (y), P_{tr} (y) are oscillatory in nature, and the distance between adjacent peaks of a few hundredths of a second of arc, as the $(\theta - \theta_B) \approx y\cdot 10^{-5}$. Neutrons with a beam divergence will be almost no. Potassium bromide single crystals have a mosaic about 40" or less [19].

Therefore, to search for the parity violation in the diffraction it is necessary to consider the integral neutron reflection diffraction.

It is defined as follows:

$$R_{ref} = R^{\pm} = \int_{-\infty}^{\infty} P_{ref}(y)\cdot dy = \pi/2 \int_0^{2\pi t/\Delta} J_0(x)\cdot dx, \quad (14)$$

$$R_{tr} = \int_{-\infty}^{\infty} (1 - P_{ref}(y))\cdot dy\,. \quad (15)$$

The integral (14) was calculated by trapezoidal rule, the numerically. The integration step was equal $5 \cdot 10^{-5}$. The integration limits are actually a geometric mean of the angular divergence of the beam of incident neutrons θ_n, and a mosaic crystal θ_m. That is, the deviation from the Bragg angle $(y - y_B) \approx 2 \cdot (\theta_n - \theta_B) \cdot \sin(2\theta_B) \cdot 10^5$, θ_n are the angles in radians. The angle $\theta_n = ((\delta\theta_n)^2 + (\theta_m)^2)^{0.5}$.

For crystals with reduced thickness $\pi t/\Delta_0 > 5$ the formula for the integral reflection (14) has an approximate form [17]:

$$R_{ref} = R^{\pm} = \pi/2\{1 - 0.798\cos(2\pi t/\Delta_0 + \pi/4)/(2\pi t/\Delta_0)^{0.5}\}. \quad (16)$$

In the case of symmetrical Laue diffraction (16) can be written as [20]:

$$R^{\pm} = \pi/2\{1–0.798\ \cos(2B \cdot \mathrm{tg}(\theta_B) + \pi/4)/(2B \cdot \mathrm{tg}(\theta_B))^{0.5}\}, \quad (17)$$

where θ_B - Bragg angle; $B = 2 \cdot d_{200} \cdot N_c \cdot t \cdot |f(k)| \cdot F_{200} \cdot e^{-2W}$; $2 \cdot d_{200} = 6.59$ Å, $N_c = 3.478 \cdot 10^{21}$ – the number of cells per cm^3; F_{200} - the geometric structural factor; t - thickness of the crystal in cm.

In the calculations we used the neutron spectrum ~ $1/E_n$, and the efficiency of neutron detection $\varepsilon_{eff} = (1 - \exp(-3 \cdot \lambda))$.

Thus, using the above formulas can investigate the dependence P_{PVD} on the thickness of single crystal on the Bragg angle on the angular divergence of the neutron beam.

Results

Fig. 1 shows the results of calculations P_{PVD}, depending on the reduced thickness of the crystal $\pi \cdot t/\Delta_0$ for $(f_{sp}(k)/f) = 5 \cdot 10^{-5}$. Red circles - results of the numerical integration of (11) in the range of integration in (-5, 5) with step $\Delta y = 5 \cdot 10^{-4}$. The black squares - the results of calculations by formulas (10) and (17) with an angular divergence of the incident neutron beam $\Delta\theta_n = 10 - 6$. Green line - calculations by formula (24) [1] multiplied by factor ½.

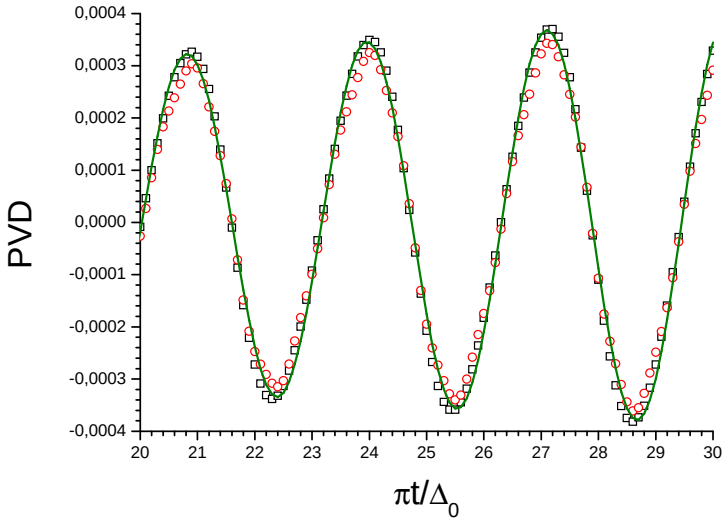

Fig. 1 shows the results of calculations P_{PVD}, depending on the reduced thickness of the crystal $\pi \cdot t/\Delta_0$ for $(f_{sp}(k)/f) = 5 \cdot 10^{-5}$. Circles - results of the numerical integration of (11) in the range of integration in (-5, 5) with step $\Delta y = 5 \cdot 10^{-4}$. Squares - the results of calculations by formulas (10) and (17) with an angular divergence of the incident neutron beam $\Delta\theta_n = 10^{-6}$. Line - calculations by formula (24) [1] multiplied by factor ½.

The results of numerical integration and calculation of the formula (16) agree within 10 %, a slight discrepancy may be due to the finite limits of integration and sufficiently large value of the integration step.

It is seen that even at a constant value (f_{sp}/f), P-odd asymmetry in the neutron diffraction, although it has increased, but oscillates strongly as a function of the reduced thickness of the crystal. Therefore, to obtain a result, we have to choose the reduced thickness of the crystal exactly. Measurement of P-odd asymmetry in the neutron diffraction may be done on the installation "KOLKHIDA" at the IBR-2.

The magnitude of the angular divergence of the incident neutron beam at this installation is equal to $\sim 3 \cdot 10^{-3}$ [21]. Using (10) and (17) were calculated magnitude of parity violation, depending on the reduced thickness of a single crystal of potassium bromide for two values of the angular divergence of the incident neutron beam. In these calculations, the value $(f_{sp}/f) = 1 \cdot 10^{-4}$ was constant. The results are shown in Fig. 2.

It is evident that the use of thick crystals does not increase the gain. Moreover, the use of thin crystals reduces the contribution of the P-odd dichroism. This increases the reliability of measurement PVD, although is not essential. The magnitude of the P-odd dichroism can be measured simultaneously with PVD with much better accuracy. Note that the crystal thickness 1 cm corresponds to the reduced thickness of ~ 25.

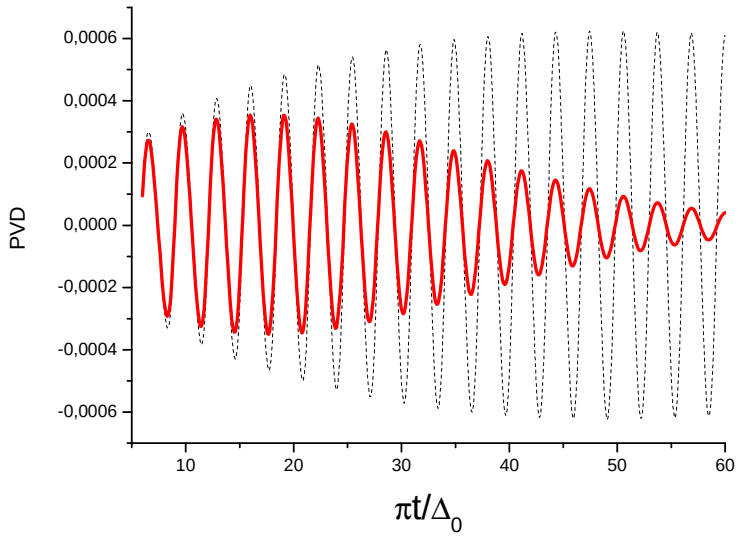

Fig. 2 shows dependence PVD on reduced thickness of the single crystal for the divergence of the neutron beam $1 \cdot 10^{-3}$ – dash curve and for the divergence of the neutron beam $3 \cdot 10^{-3}$ – thick solid curve.

Fig. 3 shows the calculation of PVD, depending on the Bragg angle, for KBr crystal thickness of 1 cm and a maximum value of the amplitude $(f_{sp}/f) = 1 \cdot 10^{-4}$. Calculations were made both with the boundary conditions (the dependence of the refractive index of the neutron wave from the direction of the neutron spin) and without taking into account the boundary conditions. It is seen that taking into account the boundary conditions, PVD significantly changes the magnitude and character of the dependence. PVD magnitude increases and has maximum in the resonance.

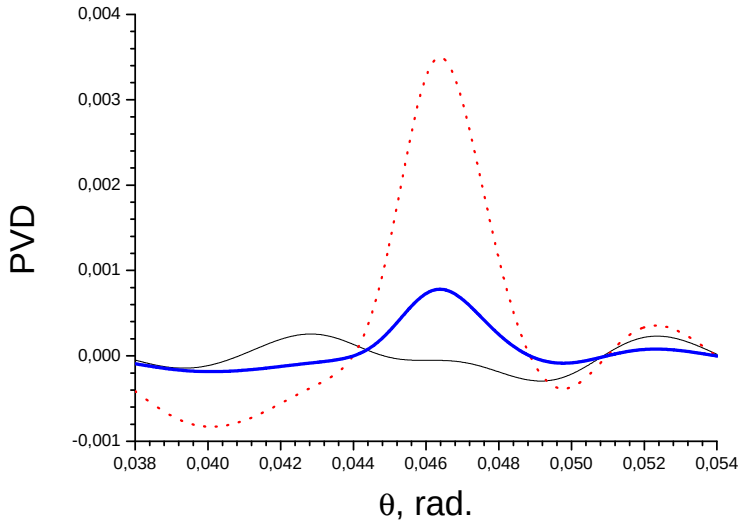

Fig. 3. Parity violation depends on the Bragg angle for a single crystal of potassium bromide thickness of 1 centimeter. The thing line - the calculation is made without taking into account the boundary conditions and angular divergence of the neutron beam $3 \cdot 10^{-3}$, the thick line - the boundary conditions are taken into acount, the divergence of the neutron beam $3 \cdot 10^{-3}$, the dot line - the boundary conditions are taken into account, and the divergence of the neutron beam $1 \cdot 10^{-3}$.

Now we can evaluate the possibility of measuring the P-odd effects in longitudinally polarized neutron diffraction.

In [21] were performed measuring the polarization of the neutron beam of the installation “KOLKHIDA”. The polarizer and analyzer of the polarization of the neutron beam used single crystals of the alloy Co (92 %) Fe (8 %). The counting rate of neutrons reflected the analyzer was about 2 n/sec. PVD magnitude is $7.8 \cdot 10^{-4}$ for the divergence of neutron beam $3 \cdot 10^{-3}$. Assuming that the measurement PVD count rate will be the same the PVD magnitude can be measured on the neutron beam of the installation “KOLKHIDA” at the IBR-2 LNP JINR during of 35 days.

Using (14), (15) we calculated PVD for the neutron beam with a small angular divergence. It turned out that the PVD in reflected and transmitted beams of neutron diffraction is almost equal in magnitude but opposite in sign. This result allows us realise a unique diffraction-compensation method of measurements. This method is similar to the method proposed in [22] for measuring the P-odd asymmetry in the transmission of longitudinally polarized neutrons with high-aperture polarimeter where the test sample was neutron polarizer. The proposed method was successfully implemented in [23, 24] when working with thermal neutrons, and in [25] - in the resonance neutron energy.

Subtracting PVD_{tr} of PVD_{ref} get twice the PVD. Neutron counting while also doubled. Thus the sensitivity of the installation is increased by 5.6 times.

The proposed method solves the problem of compensation for fluctuations in the neutron field in time and space, since the test crystal sees the same bright spot, and measurements of polarization are carried out simultaneously. The second advantage of this method - it is actually the complete destruction of the contribution of the P-odd dichroism in transmission. Bloch waves pass through the crystal the same way, have the same magnitude of the polarization caused P-odd dichroism, and this polarization disappears after the subtraction.

Conclusions

The calculations confirmed the results of [1 - 4]. It is shown that allowance for the boundary conditions (birefringence) significantly increases the magnitude of parity violation. Furthermore the effect changes the dependence on the Bragg angle.

The effect of spatial parity violation in the transmission of diffracted neutron beam was first calculated. Proposed an entirely new compensation-diffraction method for measuring the effects of parity violation in neutron diffraction, allowing to increase the sensitivity setting of 5.6 times.

The authors are grateful to E. A. Koptelov, V. N. Shvetsov, P. V. Sedyshev, L. B. Pikelner, V. V. Novitsky, V. V. Fedorov, V. V. Voronin for useful discussions and support the work.

This work was supported by the Russian Foundation for Basic Research, grant 10-02-01113-a.

REFERENCES

1. *Zaretsky D.F., Sirotkin V.K.* // Physics of Atomic Nuclei. - 1984. - Vol. 40. - .P.1256.
2. *Baryshevsky V.G., Tile S.* // Bulletin of the Belarusian University. - 1986. - Ser. 1 (1). - P. 3.
3. *Baryshevsky V.G.* // Physics of Atomic Nuclei. - 1995. - Vol. 58. - P. 1558.
4. *Baryshevsky V.G.* // J. Phys. G: Nucl. Part. Phys. - 1997. - Vol. 23. - P. 509.
5. *Abov Yu.G.* // UFN. - 1996. - Vol. 166. - P. 949.
6. *Petukhov A.K.* // Physica. - 1999. - Vol. B267 - 268. - P. 294.
7. *Forte M. et al.* // Phys. Rev. Lett. - 1980. - Vol. 45. - P. 2088.
8. *Serebrov A.P., Petuhov A.K.,.Valsky G.V. et al.* // JETP Letters. - 1995. - Vol. 62. - P. 529.
9. *Heil W., Humblot H., Krasnoschekova I. et al.* // Physica. - 1999. - Vol. B 267 - 268. - P. 289.
10. *Karmanov V.A., Lobov G.A.* // JETP Letters. - 1969. - Vol. 10. - P. 332.
11. *Sushkov O.P., Flambaum V.V.* // UFN. - 1982. - Vol. 136. - P. 3.
12. *Bunakov V.E., Gudkov V.P.* // Zs. Phys. - 1981. - Bd. 303. - P. 285.
13. *Kagan Yu., Afanasyev A.M.* // JETP. - 1965. - Vol. 49. - P. 1504; Ibid. - 1966. - Vol. 50. - P. 271.
14. *Barabanov A.L., Kuznetsov V.L.* // Phys. Letters. - 1989. - Vol. B232. - P. 151.
15. *Alfimenkov V.P.* // UFN. - 1984. - Vol. 144. - P. 361.
16. *Abov Yu.G., Elyutin N.O., Tyulyusov A.N.* // Phys. of Atomic Nuclei. - 2002. - Vol. 65. - P. 1989.
17. *Pinsker Z.G.* X-ray crystal optics. - Moscow: Nauka, 1982.
18. *Basar Khairul et al.* Diffuse Neutron Scattering of KBr at Room Temperature and Its Application as Background Function in Rietveld Analysis // ITB J. Sci. - 2009. - Vol. 41 A, No. 1. - P. 50 - 58.
19. *Kuznetsov V.L., Berlev A., Kuznetsova E.V.* Tests of a prototype plant for the study of effects of parity nonconservation in neutron diffraction on single crystals of potassium bromide (KBr), 1299.2011. - Moscow, 2011. - (Prepr. / INR RAS).
20. *Alexandrov Yu.A., Chalupa B., Eichhorn F. et al.* Neutron optical experiments at the IBR-2 pulsed reactor // Physica. - 1988. - Vol. B151. - P. 108 - 112.
21. *Abov Yu.G., Alfimenkov V.P., Lason L. et al.* An "KOLKHIDA" for experimental studies of the interactions of neutrons with polarized nuclei. - Dubna, 2008. - (Prep. / JINR; P13-2008-69).
22. *Kuznetsov V.L.* A method for measuring the P-odd asymmetry of transmission of longitudinally polarized neutrons with high-aperture polarimeter. - Moscow, 1984. - (Prep. / IAE-4057/2).
23. *Bondarenko L.N., Zhukov S.V., Kuznetsov V.L.* // JETP Letters. - 1987. - Vol. 45. - P. 515.
24. *Bondarenko L.N., Zhukov S.V, Kuznetsov V.L.* // JETP Letters. - 1987. - Vol. 46. - P. 222.
25. *Biryukov A.S., Bondarenko L.N., Zakharov Yu. et al.* // Yad. Fis. - 1987. - Vol. 45. - P. 1511.

THE STUDY OF THE POSSIBILITY FOR MEASURING OF THE PARITY VIOLATION IN NEUTRON DIFFRACTION ON THE FIRST CHANNEL OF THE IBR-2

V. L. Kuznetsov[1], E. V. Kuznetsova[1], P. V. Sedyshev[2], V. N. Shvetsov[2], A. V. Churakov[2]

[1] *Institute for Nuclear Research, Russian Academy of Sciences, Moscow, Russia*
[2] *Joint Institute for Nuclear Research, Dubna, Moscow region, Russia*

The experiment was performed at a 30-meter time of flight path of the channel N1 of the IBR-2 reactor. The system of registration and storage of information were tested. The parameters of the neutron beam are determined. An indication on the pendellösung effect was observed, that is evidence of a good quality of the potassium bromide single crystal as well as the low divergence of neutron beam. Using these results we have estimated the time for detecting the effect of parity violation in the diffraction of neutron with the statistical accuracy of 10^{-4}.

Introduction

In papers [1 - 4] it was shown that in the case of Laue dynamical diffraction of neutrons, a significant increase of the effects of parity violation can be seen.

Strengthening of P-odd effects in neutron diffraction is due to the oscillatory dependence of the integrated intensity of the reflected beam of neutrons from the reduced thickness of the crystal. In paper [1] was obtained an expression for the asymmetry in the neutron diffraction as a function of the reduced thickness of the single crystal in the form of:

$$A_{dif} = (f_{sp}/2) \cdot (\pi \cdot t/\Delta_0)^{0,5} \cdot \cos((\pi \cdot t/\Delta_0) - \pi/4), \quad (1)$$

here $(f_{sp}/2)$ – the coherent amplitude of the weak nuclear interaction of neutrons; $(\pi \cdot t/\Delta_0)$ - the reduced thickness of the crystal; Δ_0 – extinction length; t – the thickness of the crystal.

In [5] the expression for the integrated intensity of the reflected beam of neutrons in the conditions of dynamic diffraction was given:

$$R_{ref} = \pi/2\{1 - 0.798 \cdot \cos(2\pi t/\Delta_0 + \pi/4)/(2\pi t/\Delta_0)^{0.5}\}. \quad (2)$$

When comparing the expression (1) to (2), it is clear that the observation of the oscillations of the integrated intensity of the reflected beam of neutrons is a prerequisite for the detection of P-odd asymmetry in the neutron diffraction.

During the power cycle, two days of beam time were given for testing a prototype setup to search for spatial parity violation in neutron diffraction (PVND) on the 30-meter base of the first channel IBR-2M.

Objectives of the study were as follows:

1. determination of the neutron flux density in the vicinity of the p-resonance of potassium bromide (E = 0.88 eV);
2. determination of the number of neutrons reflected from a single crystal of potassium bromide;
3. determining the background conditions.

Experiment and results

The neutron flux density was measured by means of a fission ionization chamber on the 12-m flight base of the 1st channel and had a magnitude of ~ $3 \cdot 10^4$ n/ ($cm^2 \cdot s \cdot eV$).

In the bunker of the 30 meter base of the first channel a prototype installation PVND – goniometer was set up, on which a single potassium bromide crystal was mounted, and at a distance of 2.4 m from the single-crystal a neutron detector was installed which is an assembly of the four counters SNM-17. The neutron detection efficiency is approximately equal to 0.3. The detector was set up at an angle $2\theta_B = 0.1$ radian to the beam axis of the incident neutrons. Preliminary measurements associated with the alignment of the single crystal and neutron detector have been taken. The axis of the neutron beam was defined using a coordinate-sensitive detector (Fig. 1).

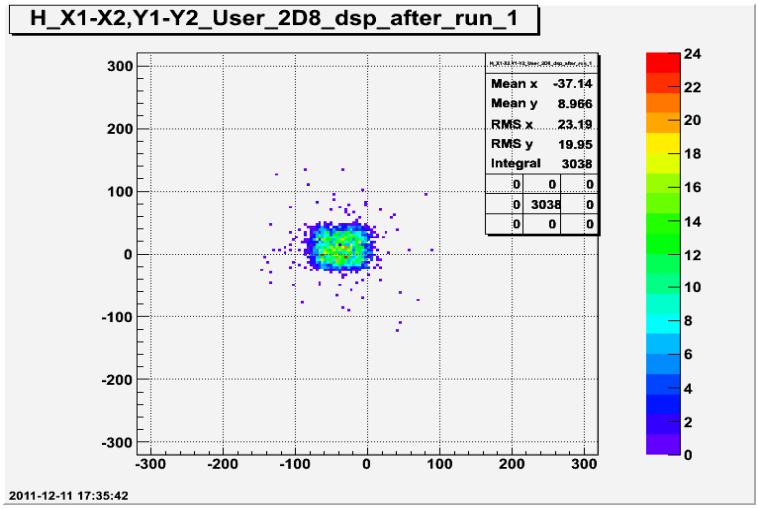

Fig. 1. The position and shape of the neutron beam defined by using a position-sensitive detector. The area of the neutron beam is 4 cm^2.

To determine the flight path and the time of a power pulse to the signal "Start" was measured TOF spectrum of neutrons diffraction from polycrystalline iron, shown in Fig. 2.

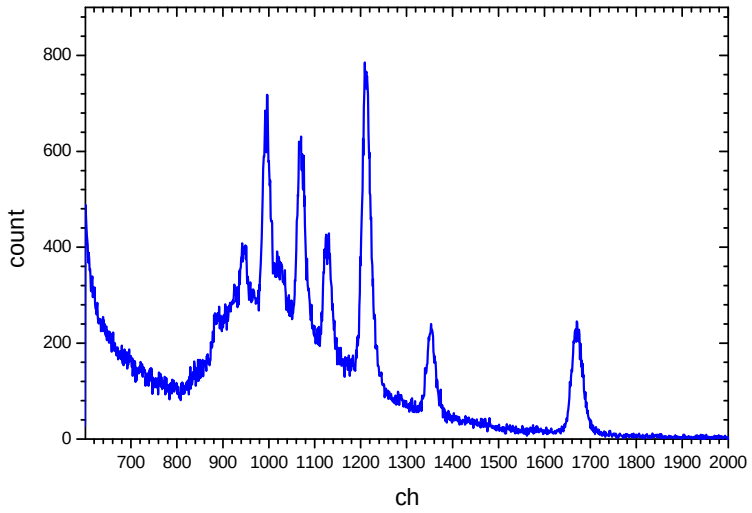

Fig. 2. TOF spectrum of neutrons diffraction from polycrystalline iron.

Neutron diffraction angle $2\theta_B = \pi/2$ were measured. Log detector was turned perpendicular to the axis of the beam, which was installed iron sample. From the known interplanar distances polycrystalline iron was determined flight path (28.32 ± 0.09) m and the burst.

Using these parameters, TOF spectra were constructed depending on the wavelength. Fig. 3 shows the spectrum of the neutron diffraction from the reflection plane (200) single crystal KBr, depending on the wavelength of the neutrons. Time to spectrum is 85 minutes.

After subtraction of background substrate neutron count in the first order of reflection is 28 neutrons per second.

Our calculations show that, as the oscillations of the integrated intensity of the reflected beam of neutrons, and the magnitude of the P-odd effects in the diffraction depended on the mosaic single crystal and the angular divergence of the neutron beam incident on the crystal. We tried to find the oscillations of the integrated intensity of the reflected beam of neutrons, turning the crystal around an axis perpendicular to the reflecting planes. The thickness of the crystal changes as a function $t = t_0/\cos(\varphi)$, where $t_0 = 1$ cm, φ - angle of rotation of the crystal. The measurements were carried out at equal angles $\varphi = 0^o$, 3 ° 25 ', 6 ° 50'.

Fig. 4 shows a comparison of the intensity of the reflected beam of neutrons from a single crystal of potassium bromide with a curve calculated according to the theory of dynamical diffraction of neutrons [5, 6] for the case of symmetric reflection in the Laue geometry. The experimental values of the integrated intensity of the neutron reflection (points) were normalized so that one point got on the calculated curve, reflect the neutron diffraction. The thickness of the crystal is expressed in terms of the reduced thickness t/Δ_0, where Δ_0 – extinction length of neutrons in a single crystal of potassium bromide to the reflection plane (200).

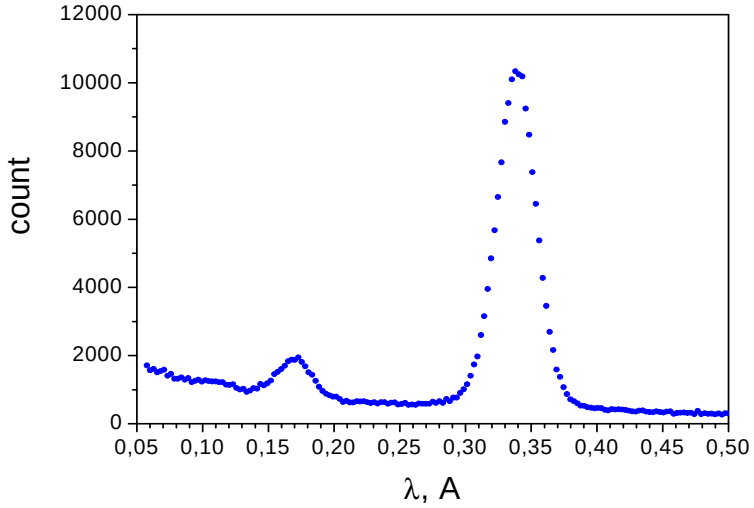

Fig. 3. The spectra of neutrons diffracted on KBr single crystal obtained
from TOF spectra using parameters defined from TOF spectra of neutrons diffracted on iron.

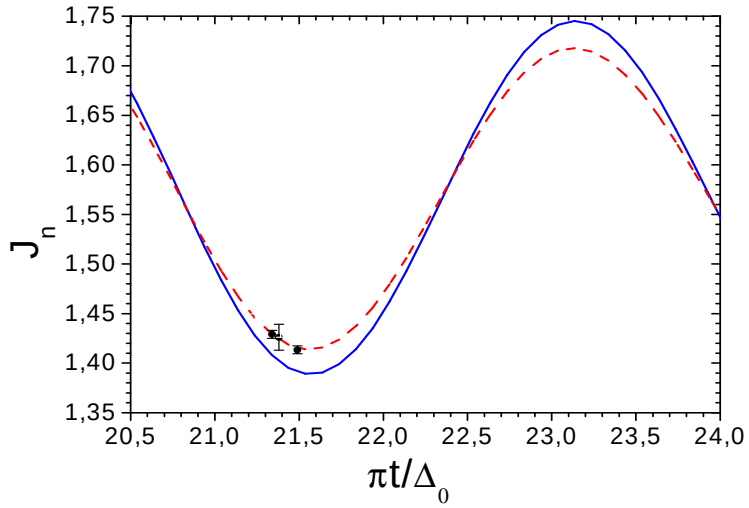

Fig. 4. The integrated intensity of the beam reflected neutrons as a function of the reduced thickness of the crystal. Black circles - experimental data, solid line - calculated intensity, reflect an angular divergence of the incident neutron beam $1 \cdot 10^{-3}$; dashed line - calculated intensity, reflect an angular divergence of the incident neutron beam $2 \cdot 10^{-3}$.

A satisfactory agreement between the calculated and experimentally measured intensities of the integral neutron diffraction reflections can be an indication of the existence of the oscillation behavior of the intensity of the reflected neutrons. This indicates a good quality of the neutron beam and a good quality of the single crystal.

Given that all the neutrons, which satisfy the conditions of diffraction and have experienced total reflection, we can estimate the time required to detect parity violation in diffraction. With an increase in detection efficiency is 2 times require about 30 days of beam time to identify the effect on the level of statistical accuracy of $3 \cdot 10^{-4}$.

Conclusions

As a result of this work were as follows:

1) we measured the parameters of the neutron beam;

2) we measured the amount of reflected diffraction neutrons;

3) we found an evidence for the pendulum behavior of the intensity of the reflected diffraction neutrons, indicating a good quality of the single crystal and neutron beam;

4) we estimated the time needed to detect the effect of spatial parity violation in diffraction at the level of statistical accuracy of 10^{-4}. It is equal to 30 days of beam time.

ACKNOWLEDGMENTS

The work was supported by the Russian Fund for Basic Research, grant 10-02-01113-a.

The authors are grateful to E. A. Koptelov, R. A. Sadycov, V. S. Litvin (INR), L. B. Pikelner, V. V. Novitsky (LNP JINR) for their support, helpful discussions and assistance.

REFERENCES

1. *Zaretsky D.F., Sirotkin V.K.* //Yad. Fis. - 1984. - Vol. 40. - P. 1256.
2. *Baryshevsky V.G., Cherepitsa S.V. //* Bulletin of the Belar. Univ. Ser. 1 (1). - 1986. - P. 3.
3. *Baryshevsky V.G.* // Yad. Fis. - 1984. - Vol. 58. - P. 1558.
4. *Baryshevsky V.G.* // J. Phys. G: Nucl. Part. Phys. 1997. - Vol. 23. - P. 509.
5. *Abov Yu.G. et al*. // Yad. Fis. - 2002. - Vol. 65. - P. 1989.
6. *Pinsker Z.G.* // X-ray crystal optics. - M., 1982.

NEUTRON SOURCES FOR NEUTRINO INVESTIGATIONS WITH THE LITHIUM CONVERTER

V. I. Lyashuk[1,2], Yu. S. Lutostansky[1]

[1] *National Research Centre "Kurchatov Institute" Moscow, Russia*
[2] *Institute for Nuclear Research, Russian Academy of Sciences, Moscow, Russia*

Creation of the powerful antineutrino source with a hard spectrum ($E_{\tilde{\nu}}^{max}$ = 13 MeV, $< E_{\tilde{\nu}} >$ = 6.5 MeV) is possible on the base of β^--decay of the short lived ^{8}Li ($T_{1/2}$ = 0.84 s) isotope formed in the reaction ^{7}Li(n, γ) ^{8}Li. The ^{8}Li. isotope is a prime perspective antineutrino source taking into account that neutrino cross section depends as $\sigma \sim E_\nu^2$. at the considered energy. The creation of this type powerful neutrino source (neutrino factory) is possible by (n,γ)-activation of high-purified ^{7}Li isotope under intensive neutron flux. As a neutron source for this purpose can be used the nuclear reactors (of steady-state flux and pulsed one), neutron sources on the base of accelerators and neutron generating targets, beam-dumps of large accelerators. The capabilities and perspectives of neutron sources are considered for the purpose of creation of the neutrino factory. Different realizations of lithium antineutrino sources (lithium converter on the base of high purified ^{7}Li isotope) are discussed: static regime (i.e., without transport of ^{8}Li isotope to the detector); dynamic regime (pumping of activated lithium to a remote detector in a closed cycle); lithium converter on the base of (a) a pulse reactors and (b) constructed as tandem of an antineutrino source and accelerator with a neutron-producing target. Heavy water solution of LiOD is proposed as a substance for the lithium converter. The expressions for neutrino fluxes in the detector position are obtained.

1. Introduction

The difficulties on research of neutrino interaction with substance are stipulated extremely by small cross sections of the reactions. So, for the artificial neutrino source such characteristics as flux and spectrum are the most important. The smallness of cross sections extremely complicates separation of neutrino effect from background. In this case a high neutrino flux can be a decisive factor for obtaining of reliable results. On the other hand, the probability of registration strongly depends on neutrino energy. For the energy spectrum discussed in this work the dependence of the neutrino cross section is the square-law: $\sigma_\nu \sim E_\nu^2$.

In earthly conditions the Sun, nuclear reactors and accelerators are exceptional on intensive neutrino fluxes [1 - 3]. The solar $\tilde{\nu}_e$ -neutrinos fluxes are estimated as $\approx 6.6 \cdot 10^{10}$ cm$^{-2} \cdot$ s^{-1}. However, the energy of ~98 % of all solar neutrinos does not exceed 0.86 MeV. In experiments with artificial neutrino sources there is a certain freedom in specification of an energy and neutrino fluxes. The density of $\tilde{\nu}_e$ -flux from a nuclear reactor [3] is determined by its power *P* and for distance *R* is:

$$F[\text{cm}^{-2} \cdot s^{-1}] \cong \bar{n}\, P / 4\pi R^2 E = 1.5 \cdot 10^{12} P[MW] / R^2[m], \quad (1)$$

where $\bar{n} \cong 6$ - mean number of β^--decays for both fission fragments of ^{235}U, $\overline{E} \cong 200$ MeV - mean energy released at ^{235}U-fission. Then, at the power *P* = 2800 MW (the Bugeu reactor, France) and distance *R* ≅ 18 m (as in the realized reactor experiments on search of neutrino oscillations [4, 5]) the flux is $F \cong 1.3 \cdot 10^{13}$ cm$^{-2} \cdot$ c^{-1}. Antineutrinos $\tilde{\nu}_e$ emitted at β^--decay of fission fragments in a nuclear reactor have energy $E_{\bar{\nu}} \le 10$ MeV and cross sections of the interaction with protons, electrons and deuterons are in the interval 10^{-46} -10^{-43} cm^2. The interaction of neutrinos ν_μ and $\tilde{\nu}_\mu$ is studied at meson factories and at high energy accelerators. The cross sections strongly grow at these energies, but the neutrino fluxes are on many fewer orders than in reactor experiments.

2. Physical basis for creation of the antineutrino sources

Alongside with the obvious advantage on a neutrino flux the nuclear reactor has a disadvantage too-small hardness of $\tilde{\nu}_e$ -spectrum. This disadvantage can be filled having realized the idea to use a high-purified ^{7}Li isotope for engineering of a reactor neutrons-to-antineutrino converter, which is located close by the active zone of a reactor. In a reactor neutrons flux a short-lived isotope ^{8}Li ($T_{1/2}$ = 0.84 s) is created in the reaction ^{7}Li(n, γ)^{8}Li and at β^--decay emits hard antineutrinos of a well determined spectrum with the maximum energy $E_{\tilde{\nu}}^{max}$ =13.0 MeV and mean energy $\overline{E}_{\tilde{\nu}}$ = = 6.5 MeV. As a result the summary $\tilde{\nu}_e$ -spectrum from the active zone of a reactor and from decays of ^{8}Li isotope becomes considerably harder in comparison with the purely reactor spectrum (Fig. 1). The converter constructed according this idea will realize the static regime of operation.

The idea of a neutrino source, based on ^{8}Li decay was discussed firstly in [6] and for pulse reactor in [7]. The

questions of constructing the intensive neutrino sources with a hard spectrum, different types of lithium converters for reactors working in a stationary and pulse mode, applications of converters for neutrino researches are considered in Ref. [8 - 10].

The simple schema of spherical construction of multi-layer converter in a static regime is presented in the Fig. 2 as geometry ***A*** and ***B***. The active zone radius R = 23 cm corresponds to a 51.0-liter volume to that of the high-flux PIK reactor [10, 11].

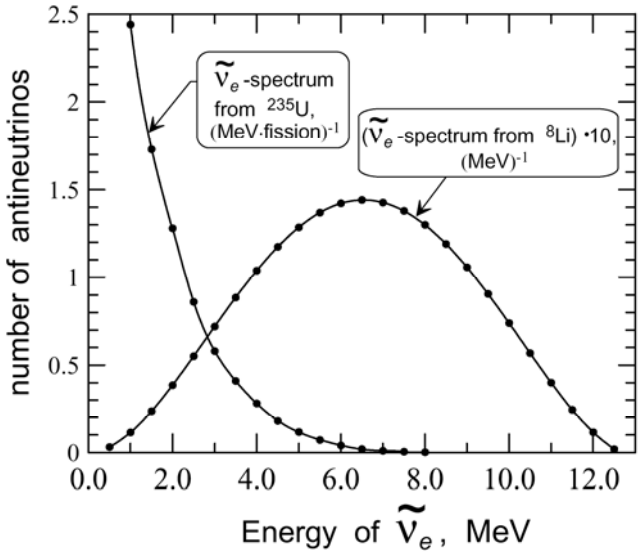

Fig. 1. $\tilde{\nu}_e$ - spectra from ^{235}U and β-decay of ^{8}Li.

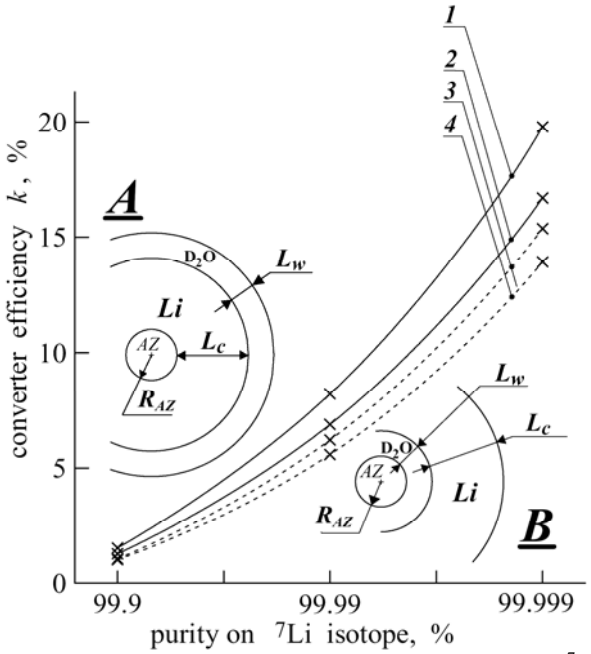

Fig. 2. Dependence of converter efficiency ***k*** on ^{7}Li isotope purity (with admixture of ^{6}Li) in the geometry ***A*** and ***B*** for lithium thickness L_C, heavy water layer L_w and reactor active zone radius R_{AZ} = 23 cm.

To compare these two types of geometry the calculations were performed (using MAMONT code [10, 11]) for three converter thicknesses: L_C = 130, 150 and 170 cm. The thickness of iron shells was 1 cm. The D_2O acts as a reflector in geometry ***A*** and as an effective moderator in geometry ***B.*** The D_2O thickness of L_W = 30 and 15 cm are sufficient for the reflector in geometry ***A*** and nearly optimal for the moderator in geometry ***B.*** In the calculations it was assumed that one neutron with the fission spectrum escaped from the active zone per one fission. So, according to our calculations, the geometry ***A*** gives better results for the converter efficiency- ***k***, where ***k*** is equal to the number of ^{8}Li isotopes created per one neutron escaping from the active zone. The spectrum hardness of combined active zone plus converter $\tilde{\nu}_e$-spectrum increases considerably at ***k*** ≥ 20 %. This positive effect let to increases the cross section σ_ν for many times due to $\sigma_\nu \sim E_\nu^2$ dependence.

The main problem is to increase the efficiency of converter and in so way to increase the hardness of the summary $\tilde{\nu}_e$-spectrum. This may be done in some ways: 1) to increase the ^{7}Li isotopic purity up to about 99.999 % in order to reduce the strong parasitic absorption on the ^{6}Li isotope; 2) not to use ^{7}Li isotope in the metallic state, but its chemical combinations (see below); 3) to use the reactor-converter system in the dynamic regime of exploitation (see below); 4) to realize the pulse reactor-converter system [7, 8].

3. Choice of the converter matter

To increase the efficiency of converter purifying the significant mass of ^{7}Li isotope up to the 99.999% grade is difficult. The constructive way may be to use ^{7}Li isotope with realistic grade of purification (about 99.99%), but in chemical compositions instead of lithium in metallic state. The perspective candidates for use as substance in a converter can be a heavy water solution of lithium hydroxides (LiOD, $LiOD \cdot D_2O$) and lithium deuteride - LiD [12, 13].

The most perspective was considered LiOD heavy water solution. Thus, using it permits to reduce the layer thickness L_C up to ≈1 m and sharply to reduce a required mass of a high-purified lithium: for example, for ^{7}Li purification grade 99.99 % in order to ensure the efficiency level κ = 0.075 (at LiOD concentration of 9.46 % in heavy water solution) it will be necessary the lithium mass in ~350 times less compare to the converter with ^{7}Li in metallic state only. Other considered chemical compositions like Li_2C_2, Li_2CO_3, Li_2O, $LiDCO_3$, LiF, $LiDF_2$ are not so perspective.

The choice of converter matter can be considered as the task of optimization for set of parameters: matter and converter geometry, lithium purity on ^{7}Li isotope, mass of lithium m_{Li} in the converter. Choosing the perspective type of

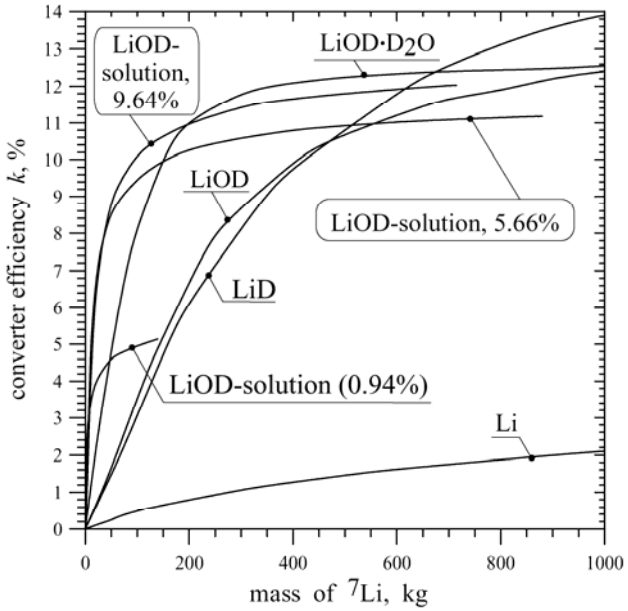

Fig. 3. Dependence of converter efficiency $\boldsymbol{k}$ on lithium mass m_{Li} for different chemical compositions and heavy water solution of LiOD (with LiOD concentration 0.94, 5.66 and 9.64 %).

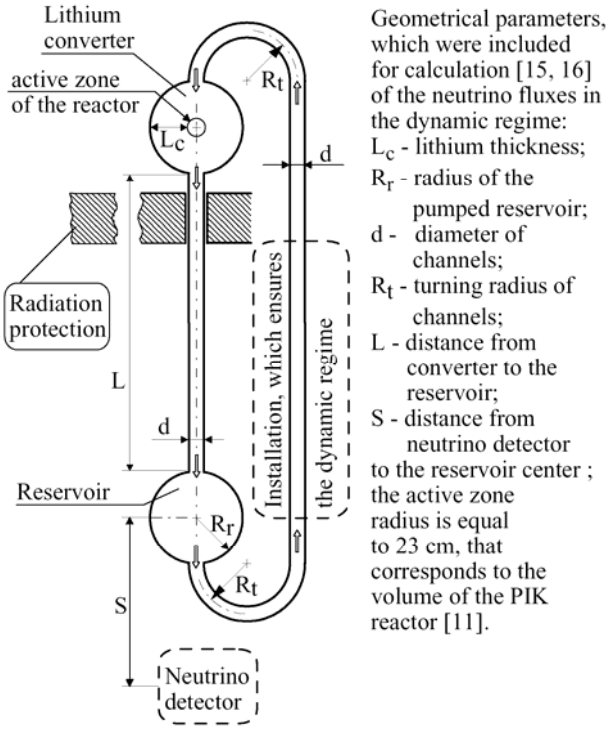

Fig. 4. Dynamic regime of the lithium antineutrino source on the basis of the nuclear reactor.

converter matter, geometry and fixing the lithium purity we can consider dependence of efficiency on mass of lithium: $\kappa(m_{Li})$. The converter efficiencies κ(in persents) as function of the lithium mass m_{Li} for different chemical compositions and heavy water solution of LiOD are presented in the Fig.3. The results were obtained in the geometry $\boldsymbol{A}$ for ^{7}Li purification – 99.99 %.

Later it was considered the boron as an alternative material for antineutrino converter on the base of $^{11}B(n,\gamma)^{12}B$ reaction [14]. But at thermal energy the cross-section ratio of parasitic absorption on ^{10}B to the beneficial one on the ^{11}B starting isotope $[\sigma_a(^{10}B)/\sigma_{n\gamma}(^{11}B) = 3837/0.0055]$ is considerably worse than for lithium $[\sigma_a(^{6}Li)/\sigma_{n\gamma}(^{7}Li) = 937/0.045]$ ratio. When for the same converter efficiencies the grade of purity required for manufacture of boron neutrino source should be ≅ 99.9997 % on ^{11}B isotope compared with technologically producible 99.99% purity of ^{7}Li in a lithium neutrino source.

4. Dynamic regime of the antineutrino source

It is possible to supply powerful neutrino fluxes with considerably greater hardness in a facility with a dynamic mode of operation [15 - 17]: liquid lithium is pumped over in a closed cycle through a converter and further in a direction to a remote neutrino detector (Fig. 4). For increasing of a part of hard lithium antineutrinos a being pumped reservoir is constructed near the $\tilde{\nu}_e$-detector. Such type of the facility will ensure not only more hard spectrum in the location of a detector but also an opportunity to investigate $\tilde{\nu}_e$-interaction at different spectrum hardness varying a rate of lithium pumping over.

However, the development of such a facility with lithium in metallic state comes across serious problems connected with necessity of a temperature regime maintenance ($t_{melting}$(Li) = 180.5 °C) and requirement in a large mass of a high-purified lithium. So, for fillup of the converter with thickness L_C = 1.5 m the required mass of lithium reaches 11.9 t. For realization of a dynamic mode the required lithium mass is increased in about 2 - 4 times [15].

For a facility with a dynamic mode of operation the heavy water solution of lithium hydroxide LiOD is look as the most perspective for converter substance, taking into account the price of high-purified lithium and questions of safety (lithium in metallic state is inflammable).

For rapid pumping over of a converter and to provide the lithium delivery (on the distance $L \approx 15 \div 25$ m in the time $t_d \leq 1$ s) it will be necessary to ensure a very significant flow rate w and linear speed $\boldsymbol{V}$ of moving in the channel. Examples of rapid pumping of the cooler (up to 5.65 m^3/s at linear speed 19.8 m/s) we can see at the reactors [18]: ATR, SRHFD (USA), GHFR (France).

5. Idea of the tandem: lithium converter plus accelerator

The conception of antineutrino source can be realized in another effective way if the neutron source will be constructed on the base of proton accelerator and target for neutron production [19, 20]. Such neutron sources exist in Russia, USA, Europe, Japan and are developing: IREN, IFMIF, JSNS/J-Park (Japan), ESS, CSNS (Table); project of electronuclear installation "Energy amplifier" by Rubbia C. [20, 21] et al. The targets are manufactured from lead,

tantalum, tungsten, uranium, mercury and also beryllium (as reflector and neutron multiplicator). Lithium (or heavy water solution of LiOD) blanket placed around such neutron generating target will be the powerful source of hard antineutrino. Realization of the dynamic regime will allow to transport the decaying ^{8}Li isotope more close to the neutrino detector [19].

Neutron sources on the base of accelerator and neutron producing target

Facility (Country, site, laboratory)	Beam parameters: particles, energy, current, frequency, Hz	Neutron yield, flux	Target; status of the facility
IN-6 (Russia, Troitsk, INR RAS)	protons, 600 MeV, 0.5 mA (average), 100 Hz (project parameters)	~$1 \cdot 10^{16}$ s^{-1}	tungsten (target in the block 1). first run in 1998 year
IREN (Russia, Dubna, JINR)	electrons, 200 MeV, 3 A (in the pulse), 150 Hz	$1 \cdot 10^{15}$ s^{-1}	plutonium (K_{eff} <0.98); under construction: (tungsten-target at 1st stage)
SNS (USA), ORNL	protons, 1 GeV, 1.4 mA (average), 60 Hz	$(1.8 - 2.7) \cdot 10^{17}$ s^{-1}	mercury; work since 2006 year
SINQ Swisserland, Paul Scherrer institute	protons, 590 MeV, 1.8 mA, steady-state flux	$1 \cdot 10^{14}$ $cm^{-2}s^{-1}$	lead; work since 1998 year
n-TOF Switzerland, Geneva, CERN	protons, 20 GeV, 4 Hz	$0.4 \cdot 10^{15}$ s^{-1}; at the distance 185 m from the target : $4 \cdot 10^{5}$ $cm^{-2}s^{-1}$	lead; work since 2000 year
IFMIF Italy, Frascati	deuterons, 40 MeV, 125 mA, steady-state flux	$(4.5 \div 10) \cdot 10^{17}$ $m^{-2}s^{-1}$	Moltem ^{7}Li; under construction
LANSCE USA, Los-Alamos	protons, 100-800 MeV, up to 1mA; 20 Hz	$1 \cdot 10^{16}$ s^{-1}; for MTS(material test facility): $2 \cdot 10^{15}$ $cm^{-2}s^{-1}$ (2012 year plan)	tungsten; work since 1985 year
KENS (Japan, Tsukuba, KEK)	protons, 500 MeV 10 μA, 20 Hz	$3 \cdot 10^{14}$ $cm^{-2}s^{-1}$	tungsten (tantalum clad); work since 1980 year
ESS Sweden, Lund	protons, 2.5 GeV, 14 Hz	$40 \cdot 10^{15}$ $cm^{-2}s^{-1}$ (peak flux);	tungsten; normal operation in 2019; 44 neutron instruments in 2025 year
CSNS China, Dongguan	protons, 1.6 GeV, 62.5 μA, 25 Hz; $1.63 \cdot 10^{13}$ proton/pulse (according to Project phase 1)	~ $5 \cdot 10^{15}$ $cm^{-2}s^{-1}$	tungsten; normal operation in 2018 year

At the end of 1970-th years Yu.Ya. Stavissky [22] proposed to utilize dump of TeV-energy protons for generation of short giant neutron pulse and suggested to develop the neutron source at Large Hadron Collider (LHC) complex in CERN. The feature of the protons accumulation in the accelerator ring is accumulation of beam defects due to loss of focusing. So, in LHC all these accumulated protons are dumped presumably every ten hours into the beam dump (which is a graphite cylinder ~ (1 · 15) m). In order to create the neutron source it was proposed the idea to install the neutron generating target at the graphite beam dump. The suggested target can be manufactured from tungsten and titanium elements. According to the simulation [22] the flux of thermal neutrons in the moderator cavity can be up to $6 \cdot 10^{19}$ neutron/(cm^2s) and about 10^{20} neutron/(cm^2s) on the neutron channel surface; specific duration of the thermal pulse - ~100 μs. If to cover the beam dump of LHC with the lithium blanket we will have an intense antineutrino source with hard spectrum. If the converter efficiency is about 20 - 30 %, then in the beam dump for neutron yield per pulse as $6 \cdot 10^{18}$ the lithium antineutrino flux will reaches ~$(1 - 2) \cdot 10^{18}$ per pulse. The possible scheme of the proposed installation is given in the Ref. [20, 23].

6. Conclusions

The work is dedicated to the development of the powerful antineutrino source with a hard spectrum on the base of lithium converter and intensive neutron source. This problem can be solved in a dynamic system where the high-purified ^{7}Li isotope (or lithium compounds) is pumped cyclically through a converter close by the active zone of a reactor and further over a channel to a remote voluminous reservoir near to the $\tilde{\nu}_e$-detector. The dynamic system allows to locate β-decays of ^{8}Li isotope near to a detector and it is basic difference and advantage (the possibility to investigate neutrino interactions at different hardness of the spectrum) in comparison with a lithium converter operating in a static mode.

The other very important advantage of a dynamic regime of operating is a possibility to modify a spectrum shape and investigate neutrino reactions at different hardness of the summary $\tilde{\nu}_e$ - spectrum varying flow rate *w* from a zero up to maximum. It was obtained the expressions for lithium antineutrino fluxes from different parts of the facility operating in the dynamic regime [15 - 17].

The dynamic scheme allows to increase cross sections of ($\tilde{\nu}_e$, *d*)-reaction in the (*n, n*)-channel in tens times and in the (*n,p*)-channel – up to two orders in comparison with cross sections in the purely reactor $\tilde{\nu}_e$-spectrum [16, 17]. The extremally powerful source with pure lithium $\tilde{\nu}_e$-spectrum can be created in case of neutron flux from an experimental nuclear explosion. In reality to construct the powerful neutrino source with pure lithium $\tilde{\nu}_e$ - spectrum is possible if to base on intensive neutron sources as pulse nuclear reactors, the tandem of accelerator with neutron producing target and (above discussed) beam dumps of large accelerators.

The work was supported by the Russian Foundation for the Basic Research Grants no. 11-02-00882, 12-02-00955 and 12-02-12114.

REFERENCES

1. *Bahcall J. N.* Neutrino Astrophysics. - Cambridge: Cambridge University Press, 1989. - 624 p.
2. *Boehm F., Vogel P.* Physics of massive neutrinos. - Cambridge: Cambridge University Press, 1987. - 303 p.
3. *Borovoi A.A., Hakimov S.Kh*. Neutrino experiments at nuclear reactors. - Moscow: Energoatomizdat, 1990. - 152 p.
4. *Cavaignac J.F., Hoummada A., Koang D.H. et al.* Indication for neutrino oscillation from a high statistics experiment at the Bugey reactor // Phys. Lett. - 1984. - Vol. 148B. - P. 387 - 394.
5. *Afonin A.I., Bogatov S.A., Borovoi A.A.* Comparison of $\tilde{\nu}_e$-intensity at two distances from Rovenskaya NPP // Pis'ma Zh. Eksp. Teor. Fiz. - 1986. - Vol. 44. - P. 111 - 114.
6. *Mikaelian L.A., Spivak P.E., Tsinoev V.G.* A proposal for experiments in low-energy antineutrino physics // Nucl. Phys. - 1965. - Vol. 70. - P. 574 - 576.
7. *Feinberg S.M., Shevelev Y.V*. Potentialities of Pulsed Reactors for Neutrino Investigations // Proc. Int. Conf. Peaceful Uses of Atomic Energy. - New York: United Nations, 1965. - Vol. 7. - P. 455 - 457.
8. *Lyutostansky Yu.S., Lyashuk V.I.* About a possibility of the neutron convereter applocation in neutrino experiments // Proc. Int. Conf. Neutron Physics (Kiev, USSR, Sept. 14 - 18, 1987). - Moscow: Atominform, 1988. - Vol. 4. - P. 182 - 186.
9. *Mikaelian L.A., Tolokonnikov S.V.* Possible Qualitative Tests Of Electroweak Interactions In Nuclear Reactor Experimental Studies // Sov. J. Nucl. Phys. - 1989. - Vol. 50. - P. 70 - 72.
10. *Lyutostansky Yu.S., Lyashuk V.I.* Powerful Hard-Spectrum Neutrino Source Based on Lithium Converter of Reactor Neutrons to Antineutrino // Nucl. Sci. Eng. - 1994. - Vol. 117. - P. 77 - 87.
11. *Lyutostansky Yu.S., Lyashuk V.I.* Lithium converter of the reactor neutrons to antineutrino. I. The static regime of the operation. - Moscow, 1989. - (Prepr. / ITEP No. 66).
12. *Lyutostansky Yu.S., Lyashuk V.I.* Lithium converter of the reactor neutrons to antineutrino. III. The converter on the basis of lithium - deuterium solutions and compounds. - Moscow, 1989. - Prepr. / ITEP No. 147).
13. *Lyutostansky Yu.S., Lyashuk V.I.* Reactor neutrino-antineutrino converter on the basis of lithium compounds and their solutions // Sov. J. At. Energy. - 1990. - Vol. 69. - P. 696 - 699.
14. *Basov N.G., Rozanov V.V.* Possibility of developing an intense neutrino source // Pis`ma Zh. Eksp. Teor. Fiz. - 1985. - Vol. 42. - P. 350 - 352.
15. *Lyutostansky Yu.S., Lyashuk V.I.* Lithium converter of the reactor neutrons to antineutrino. II. The dynamic regime of the operating. - Moscow, 1989. - (Prepr. / ITEP No. 82).
16. *Lyashuk V.I., Lyutostansky Yu.S.* The conception of the powerful dynamic neutrino source with modifiable hard spectrum. - Moscow, 1997. - (Prepr. / ITEP No. 38).
17. *Lyutostansky Yu.S., Lyashuk V.I.* Powerful dynamical neutrino source with a hard spectrum // Yad. Fiz. - 2000. - Vol. 63. - P. 1361 - 1364.
18. *Bat G.A., Kochenov A.S., Kabanov L.P.* Research Nuclear Reactors [in Russian - Issledovatel'skie yadernie reaktory]. - Moscow: Energoatomizdat, 1985.
19. *Lyutostansky Yu.S., Lyashuk V.I.* Antineutrino spectrum from powerful reactor and neutrino converter system // Physics of Elementary Particles and Atomic Nucl., Lett. - 2005. - Vol. 2. - P. 60 - 65.
20. *Lyashuk V.I., Lyutostansky Yu.S.* The possible neutron sources for neutrino factory (review). - Moscow, 2007. - (Prepr. / ITEP No. 12).
21. *Revol J.-P.* An accelerator-driven system for the destruction of nuclear waste // Uspekhi Fizicheskikh Nauk. - 2003. - Vol. 173. - P. 747 - 755.
22. *Stavissky Yu.Ya.* Giant pulses of thermal neutrons in large accelerator beam dumps. Possibilities for experiments // Uspekhi Fizicheskikh Nauk. - 2006. - Vol. 176. - P. 1283 - 1292.
23. *Lyutostansky Yu.S., Lyashuk V.I.* The Concept of a Powerful Antineutrino Source // Izvestiya Rossiiskoi Akademii Nauk. Seriya Fizicheskaya. - 2011. - Vol. 75. - P. 504 - 509.

STATISTICAL NATURE OF NEUTRON ACTIVITY IN THE FISSION OF HEAVY NUCLEI

V. T. Maslyuk, O. A. Parlag, O. I. Lendyel, T. I. Marynets, M. I. Romanyuk

Institute of Electron Physics, National Academy of Sciences of Ukraine, Uzhgorod, Ukraine

It is shown that some characteristics of the neutron emission can be explained in the framework of statistical theory, which studies the stability of the ensemble of nuclear fragments and fission neutrons. The theory able to reproduce the known experimental "sawtooth"-curve of the neutron multiplicity $n(A)$ and allows one to set the total neutron multiplicity as a function of (A, Z) and the excitation energy of the initial nucleus.

1. Introduction

Studies of the neutron emission's nature under the different schemes of nuclei fission are very important for the understanding of nuclear matter's stability origin and for many practical applications, such as nuclear power. Thus, the choice of optimal material collections that include heavy and medium-heavy isotopes of metals is particularly important for a new generation of nuclear power reactors, which are more versatile on components of nuclear fuel. This requires the development of a unified approach for using the generally schemes parameterizations of neutron activity for arbitrary nucleus (A, Z) and various sorts of fission reaction as (γ, f), (α, f), (f, f'), (n, f) or (p, f).

In this work we present the abilities of the new statistical approach, proposed in [1, 2] that based on two-fragment fission scheme, takes into account the neutron emission and studies the thermodynamic ordering post-fission fragments and neutrons. The theory permits one to calculate the number of equilibrium neutrons as a function of the initial fragment mass $\nu(A)$ and the total neutron multiplicity $\overline{n}$. These functions are very important for neutron physics and numerous applications of neutron fluxes.

2. Theory

The main assumptions of the theory described in [1, 2]. We considered the scheme of the two-fragment fission and all possible nucleons distribution of initial nucleus with parameters A_0, Z_0 by two fission fragments with their different atomic masses, the protons/neutrons ratio and n_i as fission neutrons. Each such distribution creates the *i*-th two-fragment cluster contains $Z_{j,i}$ protons and $A_{j,i} - Z_{j,i}$ neutrons in the *j*-th fragment, where $j = 1, 2$, as well as n_i fission neutrons. The set of clusters of the fission fragments and neutrons forms a statistical ensemble, so it is important to study its stability.

This is by way of finding the probability of realization of such clusters for given thermodynamic parameters of ensemble such as temperature T, pressure P and *U*, initial or total energy consist of two major components: kinetic and potential energy. Kinetic energy is coming from the motion of the system's particles and is constant in our case because of constant temperature, T. Potential energy is associated with the static constituents of matter and is determined for condensed nuclear matter as a nucleolus, *U* by binding energy of the two-fragment cluster.

In the proposed statistical method, the isobaric term *PV* of ensemble was chosen in the form:

$$PV = P(V_0 - v_0 n),$$

where V_0 is the initial nucleus volume, P is the nucleon "gas" pressure and v_0 is the average volume related to a single fission neutron with total number of n. The isobaric constant Pv_0 value was estimated within 4 - 5 MeV and evaluated from the condition that the total fission neutron number $\overline{n}$ does not exceed 3 neutrons per fission (at T~0.5 MeV).

The next step is to find the distribution function $F(A_1)$ of a single fission fragment with mass A_1, or the same, $F(Z_1)$, with charge Z_1 that can be achieved by a following procedure [2]:

- forming the whole ensemble of post-scission fragment clusters, using for nucleons conservation conditions: $A_{1,i} + A_{2,i} + n_i = A_0$, $Z_{1,i} + Z_{2,i} = Z_0$;
- the initial (not normalized) values $F(A_1)$ are obtained as the sum of probabilities realization of two-fragment cluster, containing the fission fragment with the mass A_1. This procedure is similar to the method of histograms and must includes cumulative chains;
- the same procedure is valid for the initial values' determination of $F(Z_1)$;
- the Monte Carlo procedure should be applied to simulate the statistical fluctuations of the thermodynamical parameters of the fission fragments ensemble, see [3];
- next step includes the normalization procedure and determination of the final values of $F(A_1)$ and $F(Z_1)$. These functions must satisfy the following normalization equations: $\sum_{<A_1>} F(A_1) = \sum_{<Z_1>} F(Z_1) = 200\,\%$, where summation is taken over the all clusters containing the fission fragment with the mass A_1;
- the neutron emission function, $\nu(A)$, and total neutron emission number, $\overline{n}$, are very important for neutron physics and numerous applications of neutron fluxes. Among the factors that determine $\nu(A)$ and $\overline{n}$, the isotopic

composition of the initial nucleus and its excitation energy or temperature *T* are the most important [4, 5]. The emission of neutrons from fission fragments change either total binding energy of a two-fragment cluster or its entropic term.

The method of the ν(*A*) function calculation based on the probability of determining of the two-fragment cluster's realization (yield) that contains a preneutron fragment with mass *A* and the equilibrium number of neutrons *n*. Considering that cumulative yield of the fission fragments, $\bar{\nu}(A)$ is equal to value for all clusters containing the fragment with mass A from the cumulative chain:

$$\bar{\nu}(A) = 1/m \sum_{j=1}^{m} \nu_j(A) ,$$

where m is the length of the cumulative chain that forms the yields of the fragments with the mass A. The total number of neutrons emitted in the act of nucleus fission $\bar{n}$ is calculated in a following way (normalization to 200 % is used):

$$\bar{n} = 1/200 \sum_{A_i=1}^{A_i=A_0} \nu(A_i) F(A_i) .$$

3. Results and discussion

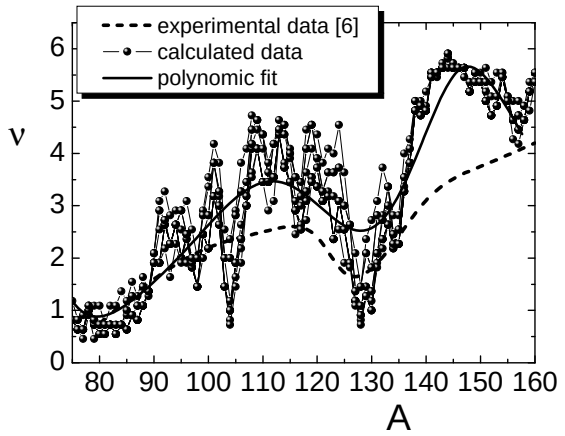

Fig. 1. The fission neutron yield is given as a function of the fusion fragment mass of ^{236}U: dashed line corresponds to the experimental data [6], circles with line present the calculated data and the solid line is the polynomial fit of our data (see more detail in the text).

In Fig. 1, the calculated and experimental [6] neutron emission functions for fission fragments of ^{236}U are shown. The cumulative chain length was *m* = 10, T = 0.5 MeV, the isobaric constant [2] Pv_0 is equal to 4.5 MeV, the fluctuation range was up to 15 % for all ΔT, Δ(Pv_0) and for the neutron emission number Δ(n_j).

As one can see, the theoretical data agree well with the experiment. Moreover, the 9th order polynomial fit of obtained data (solid line in Fig. 1) reproduces the known experimental "sawtooth"-curve of the neutron multiplicity, namely the peak about 115, minimum in vicinity of 128, the further growth in the range of 145 and decreasing up to 160. In addition, the proposed statistical method allows one to obtain the fine structure of ν*(A)*, like local minima at 98, 104, 117, 121, 128, 134, 158 and local maxima at 92, 101, 109, 114, 119, 124, 133, 144, 154.

It should be noted that experimental dependences ν*(A)* provide no data on such fine structure [7 - 9]. The fine structure might be caused by many factors, such as presence of light and heavy fragments with the magic and near-magic numbers in the cluster; the optimal proton/neutron ratio in the fragments or influence of the odd/even effects, etc.

Proposed theory allows one to calculate for neutron-induced fission of heavy nuclei the total neutron multiplicity $\nu_{A,Z}$ of the nucleus with (A, Z) as a function on the energy E_n for incident neutron. This dependence can be represented as:

$$\nu_{A,Z} = a_{A,Z} + b_{A,Z} E_n, \quad (1)$$

where the $a_{A,Z}$ ($b_{A,Z}$) values can be obtained during the processing or fitting of the databases of nuclear-physical constants. The same dependence for the temperature T under the neutron-induced fission of nucleus (A, Z) must have the following form:

$$\nu_{A,Z} = c_{A,Z} T_{A,Z}, \quad (2)$$

which allows to get initial value of nucleus temperature $T_{A,Z}^{(o)}$ at $E_n = 0$ and calorimetric dependency in form:

$$T_{A,Z} = T_{A,Z}^{(o)} + l_{A,Z} E_n. \quad (3)$$

In Fig. 2 presents the dependence $\nu_{A,Z} = \nu_{A,Z}(T)$ plotted for different parameters of model as isobaric constant and interval of statistical fluctuation. Line 1 presents dependency ν = 5.0243 T -0.7326 if Pv_0 = 3.5 MeV and line 2, respectively, ν = 4,2108 T + 1,0211. A number of statistical testing was chosen equal to 100 and such parameters were considered as true that leads to $\nu_{A,Z} = 0$ when T = 0.

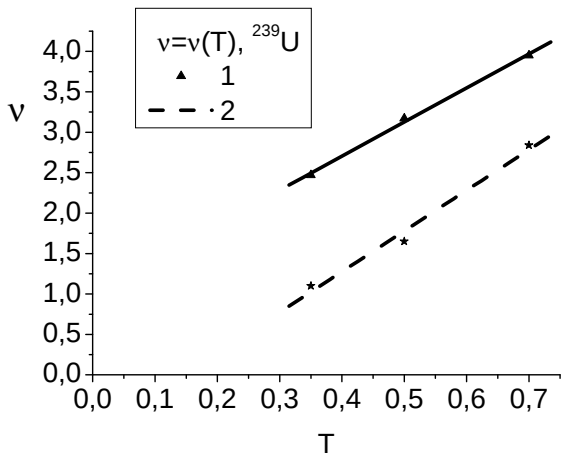

Fig. 2. The $\nu_{A,Z} = \nu_{A,Z}(T)$ dependencies for the isotope ^{239}U calculated within the statistical approach for different Pv_0 values and a number of statistical testing.

The results of the dependencies calculations both as $\overline{n} = \overline{n}(T)$ and $T = T(E_n)$, where E_n is the energy of the incident neutron for subcritical assemblies nuclei: ^{235}U, ^{238}U, ^{239}Pu, ^{237}Np, ^{243}Cm, ^{246}Cm, ^{248}Cm in the Table. There statistical fluctuations of the models parameters within 15 % were taking into account.

The data of the calculation dependencies $\overline{n} = \overline{n}(T)$ and $T = T(E_n)$ for neutron-induced fission for the typical nuclei of subcritical collections of nuclear fuel

$^{235}U + n$	$\nu = 4.41T$	$T = 0.534 + 0.0321E_n$
$^{238}U + n$	$\nu = 4.19T$	$T = 0.562 + 0.0347E_n$
$^{239}Pu + n$	$\nu = 4.35T$	$T = 0.667 + 0.0338E_n$
$^{237}Np + n$	$\nu = 4.83T$	$T = 0.552 + 0.03E_n$
$^{243}Cm + n$	$\nu = 4.61T$	$T = 0.748 + 0.033E_n$
$^{246}Cm + n$	$\nu = 4.375T$	$T = 0.784 + 0.035E_n$
$^{248}Cm + n$	$\nu = 4.577T$	$T = 0.749 + 0.035E_n$

Thus, the statistical approach allows us to offer a unique method for explaining features both the fission fragments yields (charge, mass) and fission neutron emissions. Thermodynamic parameters that characterize the stability of the initial nucleus and its fission fragments could be obtained by experiment data.

The authors are grateful to O. Grytzay for fruitful discussions. This work was carried out within the framework of the Project X-5-7 of the National Academy of Sciences of Ukraine.

REFERENCES

1. *Maslyuk V.* New Statistical Approach to the Systematization of Heavy-Nuclei Fission Fragment // Int. J. of Physics. - 2000. - Vol. 6, No. 1 - 2. - P. 1 - 8.
2. *Maslyuk V.T. et al.* New Statistical Methods for Systematizing the Nuclei Fission Fragments: Post-Scission Approach. - http://arxiv.org/abs/1202.0878
3. *Kolomietz V.M.* Stochastic aspects of nuclear large amplitude motion // Physical Review C (Nuclear Physics). - 1995. - Vol. 52, No. 2. - P. 697 - 703.
4. *Kibkalo Yu.V.* Phenomenological model for fragment mass and charge distribution in actinide nuclei fission // Fission Product Yield Data for the Transmutation of Minor Actinide Nuclear Waste. - Vienna: IAEA, 2008. - P. 157 - 182.
5. *Madland D.G.* he Los Alamos Model of Neutron Emission in Fission // Acta Physica Hungarica A. - 2000. - Vol. 10, No. 2 - 3. - P. 231 - 240. - http://www-nds.iaea.org/publications/tecdocs/sti-pub-1286.pdf
6. *Nethaway D.R., Levy H.B.* Effect of Increasing Excitation Energy on Nuclear Charge Distribution in Fission // Physical Review B. - 1965. - Vol. 139, No. 6, - P. 1505 - 1513. http://link.aps.org/doi/10.1103/PhysRev.139.B1505 DOI: 10.1103/PhysRev.139.B1505
7. *Yong-Jing Chen, Ting-Jin Liu.* Prompt neutron multiplicity distribution for $^{235}U(n, f)$ at incident energies up to 20 MeV // Chinese Physics C. - 2011ю - Vol. 35, No. 4. - P. 343 - 348.
8. *Manea V., Tudora A*. Proceedings Scientific Workshop on Nuclear Fission Dynamics and the Emission of Prompt Neutrons and Gamma Rays (Sinaia, Romania, 2010) / Ed. by F.-J. Hambsch and N. Carjan. - P. 49.
9. *Talou P., Kawano T., Lynn J.E. et al.* Recent Advances in Nuclear Fission Theory: Pre- and Post-scission Physics // Journal of the Korean Physical Society. - 2011. - Vol. 59, No. 2. - P. 797 - 802. - http://www.kps.or.kr/jkps/downloadPdf.asp?articleuid={0BBAA8C1-0150-4487-9E5C-59E3A0C1850A} DOI: 10.3938/jkps.59.797

NUCLEAR ENERGY AND ASTROPHYSICS APPLICATIONS OF ENDF/B-VII.1 EVALUATED NUCLEAR LIBRARY

Boris Pritychenko

National Nuclear Data Center, Brookhaven National Laboratory, Upton, NY, USA

Recently released ENDF/B-VII.1 evaluated nuclear library contains the most up-to-date evaluated neutron cross section and covariance data. These data provide new opportunities for nuclear science and astrophysics application development. The improvements in neutron cross section evaluations and more extensive utilization of covariance files, by the Cross Section Evaluation Working Group (CSEWG) collaboration, allowed users to produce neutron thermal cross sections, Westcott factors, resonance integrals, Maxwellian-averaged cross sections and astrophysical reaction rates, and provide additional insights on the currently available neutron-induced reaction data. Nuclear reaction calculations using the ENDF/B-VII.1 library and current computer technologies will be discussed and new results will be presented.

1. Introduction

The value of compilation, evaluation and computer storage of neutron cross sections was first recognized in the early 50's [1] prompted by the urgent needs of nuclear industry. These cross sections were first summarized in the BNL-325 report and Evaluated Nuclear Data File (ENDF) library [2 - 4]. In present days, evaluation and dissemination of nuclear reaction data are coordinated by the CSEWG and the U.S. Nuclear Data Program in USA and by the Working Party on International Nuclear Data Evaluation Cooperation worldwide. Over the years, the nuclear data activities were extended to all low- and intermediate-energy nuclear physics.

The rapid access to the latest data is based on the database storage and worldwide dissemination that relies on the presently available technologies [5] and data formats. Nowadays, size and representation of nuclear data files are no longer limited by the computer hardware and software and a collaborative effort is underway to convert nuclear data from the historic 80-character-long records to XML format.

For years, nuclear data field improvements were driven by nuclear science and technology applications. These activities evolved over the years and lead to the release of the ENDF/B-VII.1 evaluated library in December of 2011 [4]. The overall nuclear data maturation and modern computer technologies created many new opportunities for nuclear reaction calculations, data mining and analysis. In this work, I will concentrate on selected nuclear reactor operation and astrophysics integral quantities that can be extracted from the ENDF/B-VII.1 library.

2. Evaluated Nuclear Reaction Data Libraries

Increasing energy demand, concerns over climate change and dependence on overseas supplies of fossil fuels are coinciding to make the strong case for increasing use of nuclear power. Presently, ~20 % of U.S. electrical power is generated by 104 nuclear power plants. These plants provide ~75 % of non-emission generated electricity in the country. Ongoing construction and design of the new power units, 55 worldwide and 6 in the USA, require constant improvements of evaluated nuclear reaction data that are absolutely essential for reactor operations.

All evaluated nuclear reaction data files are assembled using the internationally adopted ENDF-6 format [6]. This format, maintained by CSEWG, provides the foundation for ENDF libraries. ENDF is a core nuclear reaction library containing evaluated (recommended) cross sections, neutron spectra, angular distributions, fission product yields, thermal neutron scattering, photo-atomic and other data, with emphasis on neutron-induced reactions.

In the present work, the author considers neutron elastic scattering (n,n), capture (n, γ) and fission (n, f) reactions and several integral values that are of importance for nuclear science and technology applications. Integral values of thermal neutron cross sections (σ^{2200}), Westcott factors (g^{w}), resonance integrals (RI), Maxwellian-averaged cross sections (σ^{Maxw}) and astrophysical reaction rates ($R(T9)$) were calculated in a systematic approach for Z = 1 - 100 nuclei (materials) using the nuclear reaction data, Doppler broadened at multiple temperatures. Finally, I will use these values for benchmarking and validation of the ENDF/B-VII.1 library.

2. Thermal Neutron Cross Sections, Westcott Factors, Resonance Integrals, Maxwellian-Averaged Cross Sections and Astrophysical Reaction Rates

Calculations of Westcott factors, resonance integrals, Maxwellian-averaged cross sections and reaction rates using the evaluated neutron library data have been performed. Since neutron thermal cross sections in the lab reference system are tabulated in Doppler-broadened ENDF evaluations, the author simply extracted these values from the ENDF/B-VII.1 library.

Westcott g-factor is the ratio of Maxwellian-averaged cross section to the 2200 m/s (thermal) cross section

$$g^{w} = \sigma^{Maxw}/\sigma^{2200}. \quad (1)$$

The epicadmium dilute resonance integral (RI) for a particular reaction σ(E) in 1/E spectrum is expressed by

$$RI = \int \sigma(E)/E \, dE, \tag{2}$$

where the lower integration limit E_c is determined by cadmium cutoff energy (E_c = 0.5 eV) and the upper limit is often chosen as ∞ [2].

Average cross sections for Maxwellian spectrum temperature (*kT*) [7] are defined as

$$\sigma^{Maxw}(kT) = <\sigma v>/v_T, \tag{3}$$

where v is the relative velocity of neutrons and a target nuclide and v_T is the mean thermal velocity given by v_T = = $\sqrt{2\,kT/\mu}$, where μ is the reduced mass.

The astrophysical reaction rate, R, is defined as

$$R = N_A<\sigma v>, \tag{4}$$

where N_A is the Avogadro number. To express reaction rates in [cm3/mole s] units, an additional factor of 10^{-24} can be introduced. Temperature (*kT*) , in units of energy (*e.g.* MeV) is related to that in Kelvin (*e.g.* 10^9 K) as T_9 = 11.6045 *kT*. These equations were used to calculate integral values using the original evaluated neutron data from the ENDF/B-VII.1 library within the typical range of energies.

3. Results and Discussion

Due to space limitations, only selected data sets are discussed in the current proceedings. The complete sets of ENDF/B-VII.1 thermal neutron cross sections, Westcott factors, resonance integrals, Maxwellian-averaged cross sections and astrophysical reaction rates are available in the Brookhaven report [8].

3.1. Neutron Thermal Cross Sections

ENDF/B-VII.1 thermal cross section ratio for neutron fission are shown in Fig. 1. Using the method of visual inspection one can notice deviations for light and medium nuclei and minor actinides evaluations. In the minor actinide region, deviations are actually in the JENDL-4.0 evaluations, since these were adopted by ENDF/B-VII.1 library.

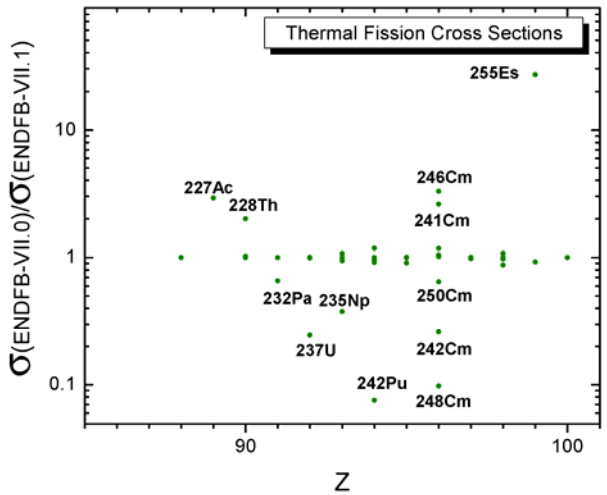

Fig. 1. Ratio of thermal neutron fission cross sections for ENDF/B-VII.0 to ENDF/B-VII.1 [3, 4]. Where discrepancies are evident, ENDF/B-VII.1 values are thought to be more accurate.

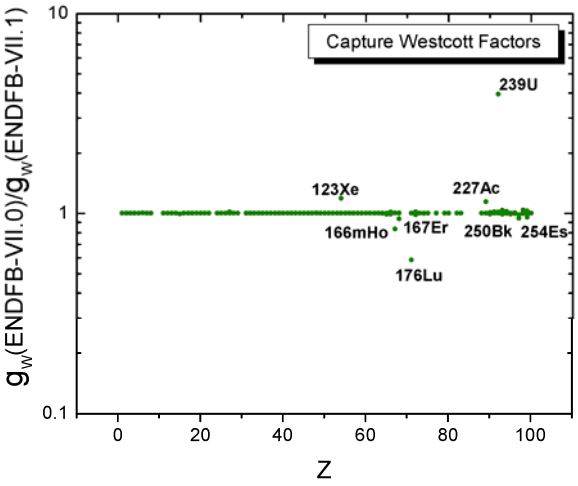

Fig. 2. Ratio of thermal neutron capture Westcott factors for ENDF/B-VII.0 to ENDF/B-VII.1 libraries [3, 4].

3.2. Westcott Factors

Complete calculation of capture and fission Westcott factors reveals that most of them are close to 1 with an exception of non-1/v σ(n, γ) nuclei: ^{113}Cd, ^{135}Xe, ^{149}Sm,^{151}Eu, ^{176}Lu, ^{182}Ta, ^{239}Pu, ^{243}Am [2]. The ENDF/B VII.0/VII.1 capture Westcott factors ratio is shown in Fig. 2.

3.3. Resonance Integrals

The ratio of Atlas of Neutron Resonances recommended neutron capture resonance integrals [2] to ENDF/B-VII.1 calculated values within the 0.5 eV - 20 MeV range of energies is shown in Fig. 3. Several data outliers in this case

could be traced to the lack of measurements and incomplete overlap of experimental and theoretical data for ^{17}O,^{166m}Ho and ^{46}Ca, ^{204}Hg, respectively. However, there are neutron capture cross section deficiencies in the minor actinide evaluations of the ^{233}Th, ^{251,253}Cf and ^{254,254m}Es.

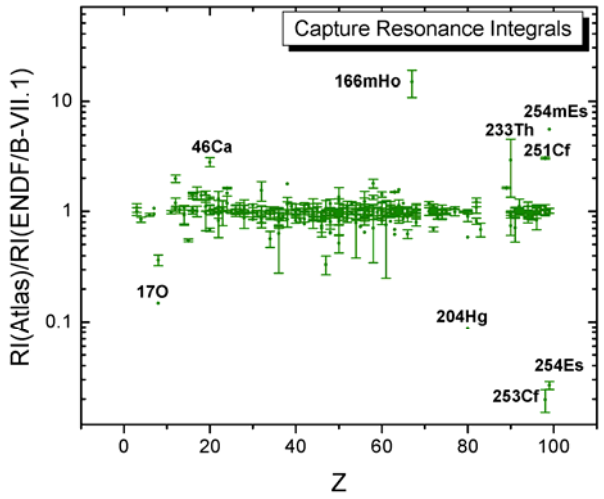

Fig. 3. Ratio of neutron capture resonance integrals for Atlas of Neutron Resonances [2] to ENDF/B-VII.1 [4].

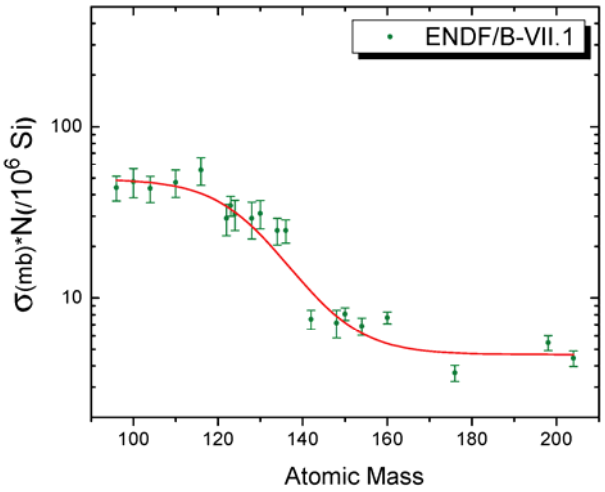

Fig. 4. ENDF/B-VII.1 library product of neutron-capture cross section (at 30 keV in mb) times solar system abundances (relative to Si = 10^6) as a function of atomic mass for nuclei produced only in the *s*-process.

3.3. Maxwellian-averaged Cross Sections and Astrophysical Reaction Rates

The slow-neutron capture (*s*-process) is responsible for creation of ~50 % of the elements beyond iron. In this region, neutron capture becomes dominant because of the increasing Coulomb barrier and decreasing binding energies. This *s*-process takes place in the Red Giants and Asymptotic Giant Branch stars, where neutron temperature (*kT*) varies from 8 to 90 keV.

It is commonly known that for the equilibrium *s*-process-only nuclei product of $\sigma^{Maxw}(kT)$ and solar-system abundances (n_A) is preserved

$$\sigma_A\, n_A = \sigma_{A-1}\, n_{A-1} = constant. \quad (5)$$

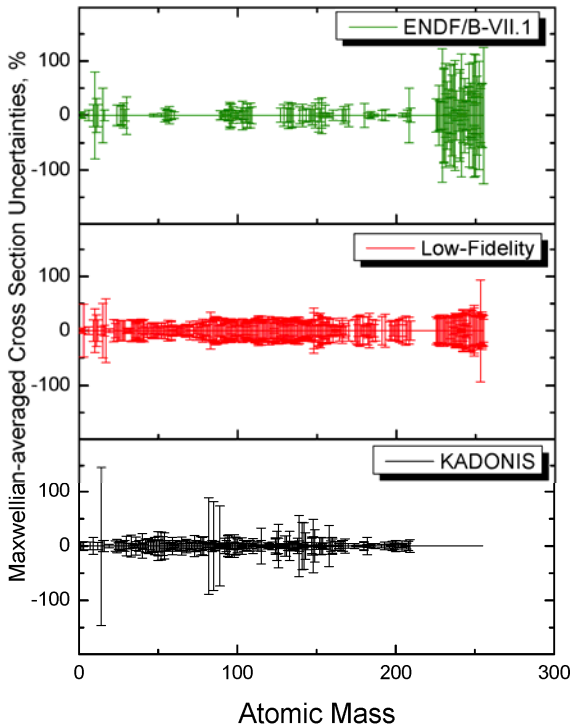

Fig. 5 Maxwellian-averaged Neutron Capture Cross Section Uncertainties for ENDF/B-VII.1 library, Low-Fidelity project and KADONIS database [4, 9, 10].

To verify this phenomenon, the calculated σ^{Maxw}(30keV) from the ENDF/B-VII.1 library were multiplied by solar abundances and plotted in Fig. 4. Visual inspection of the Fig. 4 indicates two local equilibrium and ledge-precipice break at A ~ 138 for the ENDF/B-VII.1 fit and relatively high value for ^{116}Sn. This phenomenon is due to the fact that ^{116}Sn solar abundance has *r*-process contribution. Astrophysical reaction rates and their uncertainties for the whole range of ENDF nuclei have been calculated and listed in the BNL report [8].

Additional *s*-process nucleosynthesis data could be interactively calculated and downloaded from the NucRates Web application *http://www.nndc.bnl.gov/astro*. These complimentary data sets demonstrate a strong correlation between nuclear astrophysics and nuclear industry data needs the large nuclear astrophysics potential of ENDF libraries, and a perspective beneficial relationship between both fields.

3.4. Cross Section Uncertainties

To gain better understanding of ENDF/B-VII.1 library integral values and their uncertainties, the Low-Fidelity covariances [9] were investigated. These results together with KADONIS data [10] are shown in Fig. 5.

4. Conclusion & Outlook

Increasing demands for development of new nuclear energy and astrophysics applications provided a strong motivation for this work. A complete calculation of Westcott factors, resonance integrals, Maxwellian-averaged cross sections, astrophysical reaction rates and their uncertainties has been performed. Neutron thermal cross section data were extracted from the ENDF libraries. Present data were analyzed using benchmarks, where available.

Data analysis indicates substantial progress in the improvements in the ENDF/B-VII.1 library's quality and its importance for a wide variety of applications.

ACKNOWLEDGMENTS

The author is indebted to Dr. M. W. Herman (BNL) for the constant help and support during this project and Dr. S. F. Mughabghab (BNL) for useful discussions. He is also grateful to M. Blennau (BNL) for a careful reading of the manuscript. This work was funded by the Office of Nuclear Physics, Office of Science of the U.S. Department of Energy, under Contract No. DE-AC02-98CH10886 with Brookhaven Science Associates, LC.

REFERENCES

1. *Pearlstein S.* The NNCSC: its history and functions // Nuclear News. - 1970. - P. 73 - 76.
2. *Mughabghab S.F.* Atlas of Neutron Resonances, Resonance Parameters and Neutron Cross Sections Z = 1 - 100. - Elsevier, 2006.
3. *Chadwick M.B., Obložinský P., Herman M. et al*. ENDF/B-VII.0: Next Generation Evaluated Nuclear Data Library for Nuclear Science and Technology // Nucl. Data Sheets. - 2006. -Vol. 107. - P. 2931 - 3060.
4. *Chadwick M.B., Herman M., Obložinský P. et al*. ENDF/B-VII.1 Nuclear Data for Science and Technology: Cross Sections, Covariances, Fission Product Yields and Decay Data // Nucl. Data Sheets. - 2011. - Vol. 112. - P. 2887 - 2996.
5. *Pritychenko B., Sonzogni A.A., Winchell D.F. et al.* Nuclear Reaction and Structure Data Services of the National Nuclear Data Center // Annals of Nuclear Energy. - 2006. - Vol. 33. - P. 390 - 399.
6. *Trkov A., Herman M., Brown D.A.* ENDF-6 Formats Manual: Data Formats and Procedures for the Evaluated Nuclear Data File ENDF/B-VI and ENDF/B-VII // Brookhaven National Laboratory Report BNL-90365-2009 Rev.2 CSEWG Document ENDF-102 - December 2011.
7. *Pritychenko B., Mughabghab S.F., Sonzogni A.A.* Calculations of Maxwellian-averaged Cross Sections and Astrophysical Reaction Rates Using the ENDF/B-VII.0, JEFF-3.1, JENDL-3.3 and ENDF/B-VI.8 Evaluated Nuclear Reaction Data Libraries // Atomic Data and Nuclear Data Tables. - 2010. - Vol. 96. - P. 645 - 748.
8. *Pritychenko B., Mughabghab S.F.* Neutron Thermal Cross Sections, Westcott Factors, Resonance Integrals, Maxwellian Averaged Cross Sections and Astrophysical Reaction Rates Calculated from the ENDF/B-VII.1, JEFF-3.1.2, JENDL-4.0, ROSFOND-2010, CENDL-3.1 and EAF-2010 Evaluated Data Libraries // Brookhaven National Laboratory Report BNL-98403-2012-JA (2012).
9. *Little R.C., Kawano T., Hale G.D. et al.,* Low-fidelity Covariance Project // Nuclear Data Sheets. - 2008. - Vol. 109. - P. 2828 - 2833.
10. *Dillmann I., Heil M., Kappeler F. et al.,* KADoNiS - The Karlsruhe Astrophysical Database of Nucleosynthesis in Stars // AIP Conf. Proc. - 2006 - Vol. 819. - P. 123.

NEUTRON SPECTRA AND FLUXES IN HORIZONTAL CHANNELS OF RESEARCH REACTOR WWR-M WHILE CONVERSION ON LOW ENRICHED FUEL

V. F. Razbudey

Institute for Nuclear Research, National Academy of Sciences of Ukraine, Kyiv, Ukraine

Neutron fluxes and spectra in the horizontal experimental channels of reactor WWR-M of the Kiev Institute for Nuclear research have been calculated using neutron transport Monte Carlo model with fuel enriched in ^{235}U both to 36 % and 19.7 %.

It is shown that at the very beginning operating with low-enriched fuel, when the reactor core is 28 % filled with "fresh" fuel assemblies, and the remaining cells are filled with beryllium displacers, there is a significant change in the parameters of neutron beams. However, after the reactor will begin to operate at its usual mode, that will be after completing all or most part of the core with fuel assemblies partially burnt out, spectra and fluxes in channels will restore mainly their previous values. Some differences are mainly due to changes in composition of the core - the removal of two voluminous vertical water channels located within the core.

The work can be helpful to experimenters working with extracted beams at this reactor and so at other reactors that have been converted to low-enriched fuel.

1. Introduction

Kiev research reactor of the Institute for Nuclear Research WWR-M is a basin type thermal reactor with beryllium reflector and with water both as a moderator and a coolant. Its core has a hexagonal prism shape and consists of 271 cells, in 6 of which rods of the reactor power control are placed, in 3 cells – all-stop channels. The core is formed of the fuel assemblies (FA) M2, each of which consists of three concentric tubular fuel elements (FE). Nuclear fuel in FE is uranium dioxide, enriched in ^{235}U, in an aluminum matrix. Mass of ^{235}U in a single FA is 37 g.

The reactor has 17 vertical channels for irradiation of materials, 13 of them located in the reflector and 4 in the thermal column (TC). Also, there are 10 radial horizontal channels (HEC) for experiments with extracted beams. 3 of them (HEC-6, 7 and 8) have an inner diameter of 60 mm, 1 – (HEC in thermal column) 120 mm, the other six – 100 mm.

Fuel assemblies used until 2011 had enrichment of 36 %. In 2011, in connection with the obligations taken by Ukraine, the reactor was converted to low-enriched fuel – 19.7 %.

This work aims to study the fluxes and spectra of neutrons at the outlets of horizontal channels after conversion to low-enriched reactor fuel.

2. Research method

Neutron spectra and fluxes were determined by calculating with method of statistical testing (Monte Carlo) using the program MCNP [1] and a mathematical model of the Kiev research reactor [2] which took into account its structure in detail according to technical documentation: FAs, Beryllium reflector, horizontal and vertical experimental channels, the pool, thermal column and so on. All FAs actually had different burn-up of ^{235}U, but in the calculations the burn-up was assumed to be the same. Also it was taken into account accumulation of ^{3}He and ^{6}Li in the Beryllium reflector due to reactions under action of neutrons during previous work of the reactor.

Density of neutron fluxes and spectra in the horizontal channels of the reactor depends mainly on the following factors.

1. Channel diameter. Flux density is proportional to the square of the diameter.

2. The location of the bottom of a channel with respect to Be reflector: channels can penetrate through the entire reflector (HEC-2, 4, 7, 9), only through a portion of its thickness (HEC-1, 3, 5, 6, 8) or start from the outer surface of the reflector (horizontal channel in the thermal column). General rule is: the deeper the channel penetrates through the reflector, the higher the portion of fast neutrons.

3. Initial fuel enrichment in ^{235}U and the degree of burnout.

4. The presence or absence of irradiation channels in the core.

5. Filling the core with fuel assemblies, i.e. the ratio between the number of fuel assemblies and beryllium displacers.

It was supposed that all horizontal channels are empty: no collimators, filters and mechanisms inside them.

3. Results

In this work the beam parameters at 3 compositions of the core are investigated.

Neutron spectra and fluxes have been calculated at the outlets of all HECs on axes of beams 5 cm from the biological shielding of the reactor at the compositions A, B and C (Fig. 1).

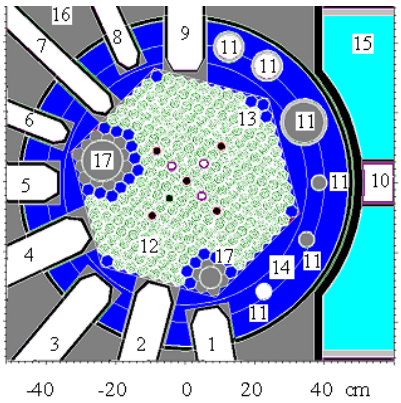

A

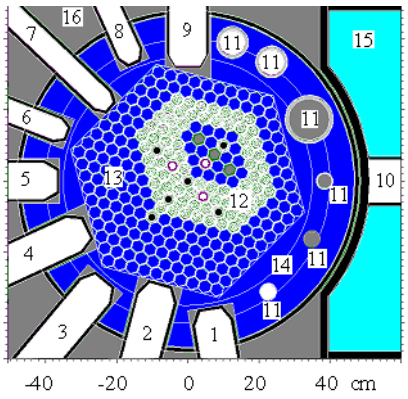

B

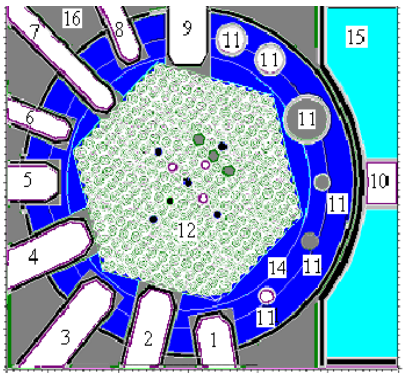

C

Fig. 1. Compositions of the core (computer model): *A* – before converting the reactor on low-enriched fuel, initial enrichment is 36 %, burn-up 39.7 %; *B* – the core after conversion on low-enriched fuel, initial enrichment 19.7 %, burn-up 0 %; *C* – after replacing all beryllium displacers with fuel assemblies, initial enrichment 19.7 %, burn-up 50 %. *1* ÷ *9* – horizontal channels HEC-1 ÷ HEC-9; *10* – horizontal channel in thermal column; *11* – vertical channels; *12* – fuel assemblies; *13* – beryllium displacers; *14* –berillyum reflector; *15* – graphite of thermal column; *16* – water in the reactor pool; *17* – vertical irradiation channels; – control rods; – all-stop channels; – cells for vertical channels inside the core.

We can see that spectra in all channels at all compositions consist of three parts (Fig. 2, *a* - *j*): a low-energy peak from 0.001 eV to 0.5 eV (thermal spectrum with the Maxwell distribution), high-energy peak from 56 keV to 20 MeV (fission neutron spectrum, partially deformed by moderation) and a horizontal section between the peaks (moderation spectrum 1/E). Shapes of the spectra are similar one to another and are typical for thermal reactors. The differences lie in the ratios between flux densities at each of the three parts (see the Table and Fig. 2, *a* - *j*) which are due to the above factors 1 - 5. We consider the peculiarities in each of these three compositions separately.

Composition A – it existed before conversion to a new fuel (Fig. 1, A). Initial enrichment of FEs is 36 %. The burn-up in the calculations was assumed to be 39.7 % (this value was obtained by calculations from the condition $K_{eff} = 1$ when the lower ends of the control rods are set at the height of the core center). Besides, six beryllium displacers and two vertical irradiation channels filled with water and screened off from FAs with 18 beryllium displacers are placed in the core.

Fluxes, especially epithermal, in HEC-1 and HEC-6 are relatively low (Fig. 3, *A*, Table). Explanation: the channels are separated from the FAs with two vertical irradiation water channels (Fig. 1, *A*). Besides, HEC-6 has a smaller diameter.

To a lesser degree, these factors become apparent in HEC-5 and HEC-7.

Most hard spectra (highest percentage of fast neutrons) are in channels that "look" immediately into the core: HEC-2, 4, 7, 9. Softest spectrum is in the horizontal channel of the thermal column.

Composition B – this loading corresponds to the beginning of operation on low-enriched fuel (Fig. 1, *B*). FAs have enrichment 19.7 %, all of them are "fresh" (burn-up 0 %). Both irradiation channels were extracted from the core. 72 fuel assemblies (in terms of single ones) were placed in the core. The remaining 187 cells are filled with beryllium displacers to compensate excess reactivity.

Total fluxes in channels HEC-1 – 4 and TC fell 1.5 – 4 times in comparison with composition A. At the same time, total fluxes in channels HEC-5 and 8 have not changed and in HEC-6, 7 and 9 increased, respectively, by 1.7, 1.4 and 1.15 times. In the most of horizontal channels fluxes of epi-thermal and fast neutrons slumped (respectively, HEC-1 – 2.5 and 3, HEC-2 – 6 and 9, HEC-3 – 11 and 14, HEC-4 – 6 and 9, HEC-5 – 2, HEC-8 – 1.4 and 2 times, HEC-TC - twice). Such changes can be mainly attributed to two factors: (a) – asymmetry placing FAs in the core (Fig. 1, *B*) – of all horizontal channels only HEC-9 is separated from FAs with two layers of beryllium displacers, HEC-7 and 8 – with three layers, HEC-6 – from four to six, the others – six layers; (b) – removal of both vertical irradiation channels.

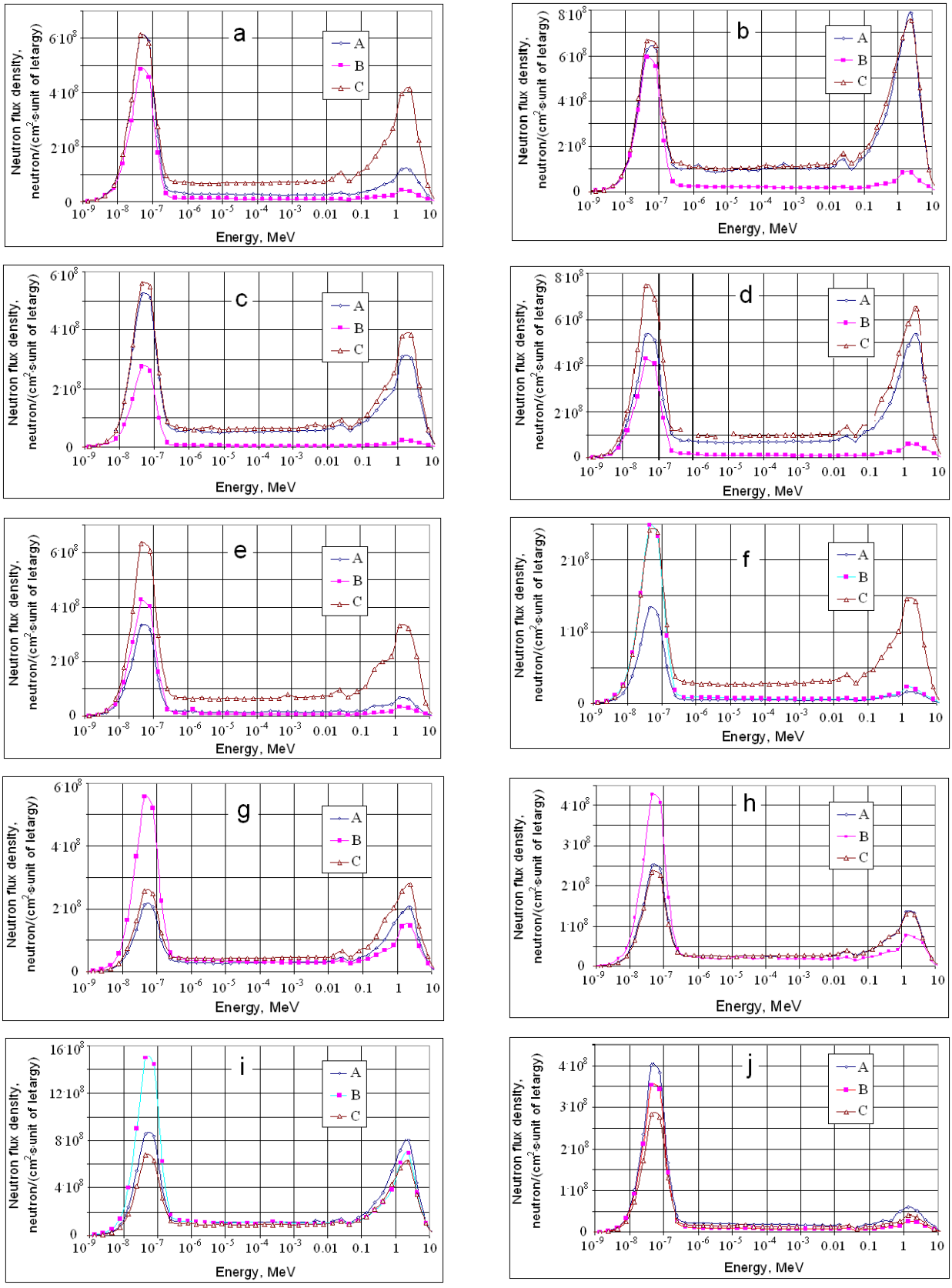

Fig. 2. Neutron spectra at outlets of horizontal channels: *a* – HEC-1; *b* – HEC-2; *c* – HEC-3; *d* – HEC-4; *e* – HEC-5; *f* – HEC-6; *g* – HEC-7; *h* – HEC-8; *i* – HEC-9; *j* – HEC-TC. Compositions of the core: *A* – before converting the reactor on low-enriched fuel, initial enrichment is 36 %, burn-up 39.7 %; *B* – after conversion on low-enriched fuel, initial enrichment 19.7 %, burn-up 0 %; *C* – after replacing all beryllium displacers with fuel assemblies, initial enrichment 19.7 %, burn-up 50 %.

Neutron flux densities and their components at three compositions of the reactor core

Horizontal experimental channel	Loading the core (composition)	Total neutron flux density, neutron/cm^2 · s	Thermal neutron flux density (< 0.5 eV), neutron/cm^2·s	Epi-thermal neutron flux density (0.5 eV - 0.05 MeV), neutron/cm^2 · s	Fast neutron flux density, (0.05 MeV - 20 MeV), neutron/cm^2 · s
HEC-1	A	1.85E+09	1.22E+09	2.98E+08	3.29E+08
	B	1.18E+09	9.47E+08	1.21E+08	1.14E+08
	C	3.20E+09	1.28E+09	8.11E+08	1.11E+09
HEC-2	A	4.43E+09	1.36E+09	1.16E+09	1.90E+09
	B	1.56E+09	1.15E+09	1.96E+08	2.13E+08
	C	4.73E+09	1.45E+09	1.28E+09	2.00E+09
HEC-3	A	2.58E+09	1.11E+09	6.32E+08	8.37E+08
	B	6.48E+08	5.29E+08	5.84E+07	6.10E+07
	C	2.97E+09	1.18E+09	1.07E+09	7.22E+08
HEC-4	A	3.31E+09	1.15E+09	7.99E+08	1.37E+09
	B	1.12E+09	8.39E+08	1.29E+08	1.53E+08
	C	4.47E+09	1.63E+09	1.16E+09	1.69E+09
HEC-5	A	1.06E+09	6.71E+08	1.94E+08	1.93E+08
	B	1.03E+09	8.37E+08	1.05E+08	8.91E+07
	C	3.06E+09	1.32E+09	7.79E+08	9.60E+08
HEC-6	A	3.60E+08	2.62E+08	5.14E+07	4.69E+07
	B	6.17E+08	4.85E+08	7.17E+07	6.01E+07
	C	1.24E+09	5.12E+08	3.22E+08	4.06E+08
HEC -7	A	1.33E+09	4.58E+08	3.40E+08	5.35E+08
	B	1.87E+09	1.13E+09	3.54E+08	3.82E+08
	C	1.82E+09	5.59E+08	4.98E+08	7.59E+08
HEC-8	A	1.20E+09	5.28E+08	3.02E+08	3.68E+08
	B	1.24E+09	8.34E+08	2.12E+08	1.91E+08
	C	1.16E+09	4.91E+08	3.03E+08	3.61E+08
HEC-9	A	5.15E+09	1.84E+09	1.28E+09	2.03E+09
	B	5.90E+09	3.02E+09	1.24E+09	1.65E+09
	C	4.05E+09	1.42E+09	1.02E+09	1.61E+09
HEC-TC	A	1.17E+09	7.88E+08	2.14E+08	1.71E+08
	B	8.63E+08	6.87E+08	1.05E+08	7.17E+07
	C	8.76E+08	5.72E+08	1.90E+08	1.13E+08

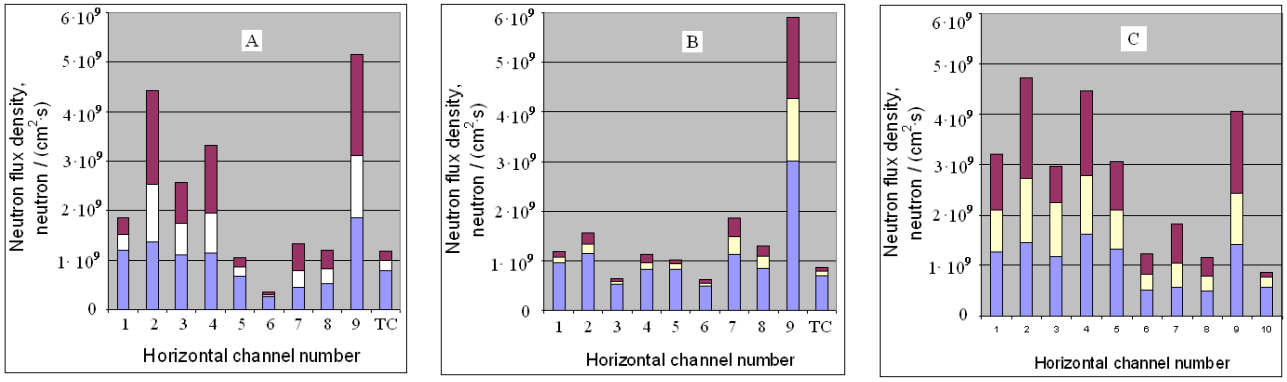

Fig. 3. Neutron flux densities and their constituents at the outlets of horizontal channels for the core compositions *A*, *B* and *C*: ■ – thermal flux density, □ – epy-thermal, ■ – fast.

Composition C – this loading corresponds to the state of the core after gradual replacement of beryllium displacers by fuel assemblies with initial enrichment of 19.7 % and burn-up of 50 % (Fig. 1, *C*; with this burn-up K_{eff} = 1 when the lower ends of the control rods are set at the height of the core center). According to estimates, this download can be implemented after the reactor output will be about 85,000 megawatt-hours on low-enriched fuel.

In general, the spectra and the flux densities on the horizontal beams are similar to those that were when the reactor operated on highly-enriched fuel. Changes in the flux densities and its components are the following:

HEC-1. Thermal flux will be restored quite, epi-thermal and fast fluxes will increase threefold.

HEC-2. All components (thermal, epi-thermal and fast) will be restored.
HEC-3. Epi-thermal flux will increase by 69 %, fast flux will fall by 14 %.
HEC-4. All components of the flux will increase by about a third.
HEC-5. Thermal flux will be doubled, epi-thermal increase by four, fast – by five times.
HEC-6. Thermal flux will be doubled, epi-thermal increase by six times, fast – by eight times.
HEC-7. All components will increase about a third.
HEC-8. All components will remain almost unchanged.
HEC-9. All components will decrease approximately by 20 %.
HEC-TC. The total flux will be reduced by a quarter (thermal – by 27 %, epi-thermal – 11 %, fast – 34 %).

4. Conclusions

It was shown by model calculations that conversion of the research reactor WWR-M from highly-enriched fuel (initial enrichment in ^{235}U 36 %) on the low-enriched (19.7 %) substantially modifies both neutron spectra and fluxes at the outlets of horizontal experimental channels. These changes are caused not so much with the transition to a different fuel as with the need to start a company with "fresh", i.e. unburned, fuel rods and with consequent need to fill the core with fuel assemblies only by 28 % to compensate the excess reactivity. Partially these changes are also associated with the removal of two large water cavities out of the core.

During the subsequent operation of the reactor, as fuel will be burned out, beryllium displacers in the core will be replaced by fuel assemblies. After full filling the core parameters of neutron beams will be close to those which were before conversion to a new fuel. The remaining differences are mainly due to the absence of water cavities in the core.

REFERENCES

1. *Briesmeister J.F.* (Ed.), MCNP - A General Monte Carlo N-particle Transport Code. Version 4C. - Los Alamos National Laboratory, NM (USA). Report No. LA-13709 -M, March 2000. - 788 p.
2. *Ворона П.М., Разбудей В.Ф.* Розрахункові дослідження та аналіз характеристик дослідницького реактора ВВР-М як джерела нейтронів для вирішення наукових та прикладних задач // Ядерна фізика та енергетика. - 2010. - Т.11, №1. - С. 57 - 65.

DIFFERENCE TEMPERATURE DEPENDENCE OF THE THERMAL SOURCE MOX FUEL AND FUEL DIOXIDE AND RELATED FEATURES ACCIDENT THIRD BLOCK OF THE NPP "FUKUSHIMA-1"

V. D. Rusov, V. A. Tarasov, S. A. Cherneshenko,
A. A. Kakaev, E. V. Grehan, S. I. Kosenko, O. I. Pantak

Odesa National Polytechnic University, Odesa, Ukraine

Before the accident, nuclear power plant "Fukushima-1" prospect of expanding nuclear fuel base also linked with the use of MOX (mixed oxide uranium-plutonium fuel). Accident plant "Fukushima-1", which led to the melting of the reactor core, revealed a lack of knowledge of fuel temperature properties of nuclides in a wide temperature range (more than 1000 K) than the operating temperature of reactors. The results of calculations of the temperature dependence of the average of the thermal neutron spectrum cross sections of nuclear fission and radiation capture of uranium-238, uranium-235 and plutonium 239. Observed and explained for the temperature range investigated the fundamental difference of temperature dependence of the average of the thermal neutron spectrum nuclear reaction cross sections of uranium-235 and plutonium 239. We also obtain the temperature dependence of the calculated dependence of densities of heat sources for MOX fuel and uranium oxide fuel for thermal reactors. Temperature range for the test for the first time showed a fundamental difference of temperature dependence of the density of heat sources for MOX fuel and uranium oxide fuel.

1. Introduction

The most important objectives of a strategy for further development of nuclear energy is the safe operation of nuclear power plants, expansion of base fuel and reprocessing of spent nuclear fuel.

Safety requirements for new generation reactors to respond fully developed wave uranium-plutonium reactor, characterized by internal security [1 - 3]. This new type of reactor eliminates a nuclear fuel cycle procedure for enrichment of nuclear fuel and use it is natural (and even technical) uranium, and, therefore, spent nuclear fuel.

Basic kinetics reactor (neutron kinetics and nuclides) are related forward and backward linkages with the kinetics of heat and radiation defects fuel [4, 5]. Kinetics of defect fuel through dimensional changes caused by plastic deformation, swelling or disruption of fuel under load and irradiation, and by changing its density affects the reactivity of the reactor. Studying the stability of the reactors require application of nonlinear dynamics. At the same time, the kinetics of the wave reactor has a number of fundamental importances for the theory of non-linear characteristics of dissipative structures, one of which is the disequilibrium of uranium-plutonium fissile environment in high-density neutron field and high temperatures. Formation of dissipative thermal structures, dissipative structures defects uranium-plutonium fissile environment, the implementation of temperature regimes with peaking Kurdyumov [6] can significantly affect the kinetics of the reactor, in particular, on the implementation of the very slow waves in a wave of nuclear burning reactor and its stability.

Before the accident, nuclear power plant "Fukushima-1" prospect of expanding nuclear fuel base also linked with the use of MOX (mixed oxide uranium-plutonium fuel).

Accident plant "Fukushima-1", which led to the melting of the reactor core, revealed a lack of knowledge of fuel temperature properties of nuclides in a wide temperature range (more than 1000 K) than the operating temperature of reactors.

The hypothesis of georeaktore wave type, located on the border of the liquid and the solid core of the Earth, it requires studies of the kinetics at temperatures of 5000K, 7000K. [7]

Therefore, in this study we investigated the properties of thermal reactor fuel nuclides in a wide range of temperatures (more than 1000 K), temperature dependence of the heat source for the MOX fuel (a mixture of uranium dioxide and plutonium 239) and uranium oxide fuel (a mixture of uranium dioxide urana238 and 235) in order to identification of possible differences of these relationships that identify and may explain a number of characteristic features of the temperature of the accident at the third block plant "Fukushima-1", where one-third of the reactor fuel load was MOX fuel.

2. Dependence of the average over the thermal neutron spectrum, sections of temperature reactor fuel

Since the accident at the AEC, "Fukushima-1" occurred in reactors BWR (boiling water reactor, the neutron spectrum that - heat), the paper presents the results of calculations and the temperature dependence of the thermal spectrum-averaged neutron cross sections of nuclear fission and radiation capture for uranium 238, uranium-235 and plutonium 239.

Obtained calculated temperature dependence of the average of the thermal neutron spectrum cross sections of nuclear fission and radiation capture of plutonium-239 and uranium-235 are shown in Fig. 1 and 2, respectively. The Fig. 2 also presents the calculated temperature dependence of the thermal spectrum averaged neutron radiative capture cross sections for uranium-238.

Table 1. **Westcott factor for fission and radiation capture of plutonium-239 [11]**

T	g_c	g_f	T	g_c	g_f
300	1,154	1,058	1300	5,314	3,091
400	1,374	1,150	1500	5,782	3,328
500	1,713	1,305	1600	5,947	3,412
600	2,159	1,518	1800	6,164	3,521
700	2,672	1,768	1900	6,226	3,552
900	3,724	2,290	2100	6,269	3,572
1100	4,630	2,746			

Table 2. **Westcott factor for fission and radiation capture of uranium-235 [11]**

T	g_c	g_f
300	0,978	0,976
400	0,964	0,954
500	0,960	0,938
700	0,970	0,920
800	0,978	0,914
900	0,987	0,910
1000	0,993	0,907
1100	0,998	0,903
1200	1,000	0,900
1300	1,001	0,893
1400	0,999	0,891
1500	0,996	0,887
1700	0,986	0,887
2100	0,958	0,885

Table 3. **Westcott factor for the radiative capture of uranium-238 [11]**

T	g_c
300	1,002
400	1,004
600	1,008
700	1,011
1300	1,024
1700	1,034
2100	1,044

Table 4. **Nuclear reaction cross section for thermal neutron energy [10]**

Nuclide	ν^T*	σ_f^T, b	σ_c^T, b	$\alpha^T = \sigma_c/\sigma_f$	I_c, b	I_f, b
U-235	2.42	580	107	0.184	142	277
U-238		0	2.7	0	277	0
Pu-239	2.88	750	315	---	188	312

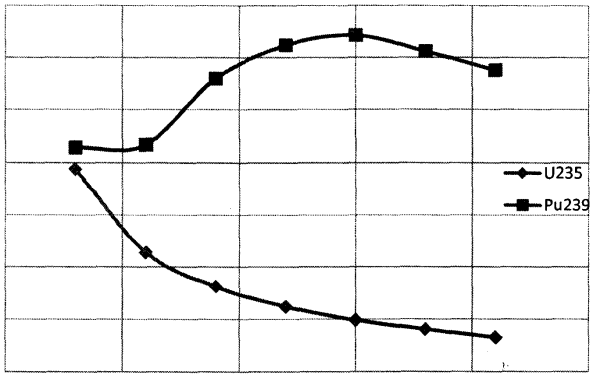

Fig. 1. The dependence of the cross sections of the fission of uranium-235 and plutonium-239, the average of the thermal neutron spectrum, the temperature, the fissile fuel environment (cross sections are normalized to σ_f^T - thermal micro-cross).

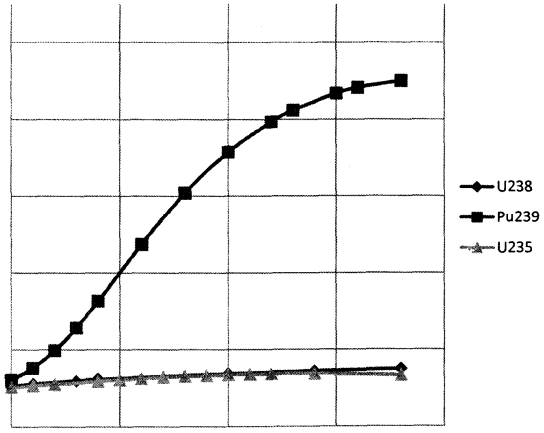

Fig. 2. The dependence of the radiative capture cross section of uranium-235, uranium-238 and plutonium-239, averaged thermal neutron spectrum, temperature, dividing the fuel temperature (cross sections are normalized to σ_f^T -thermal micro-cross).

Shown in Fig. 2 depends show a significant increase in radiative capture cross section of plutonium-239 with increasing temperature and a slight increase in radiative capture cross section for uranium-235, uranium-238.

3. According to averaging over the total neutron spectrum cross-sections on temperature reactor fuel

As noted above in Section 2 for computation averaged thermalized part of the spectrum of sections with the aid of (3), which includes tabulated values Westcott factor, perhaps to heat with a water-moderated reactors and moderators, consisting of nuclei of low atomic number, and therefore have a high ability to slow, but for heavier nuclei as the main moderator, such as carbon and oxygen, are already having problems with the calculations of (3) due to the lack of tabulated values for factor Westcott neutron gas at temperatures above 2100K.

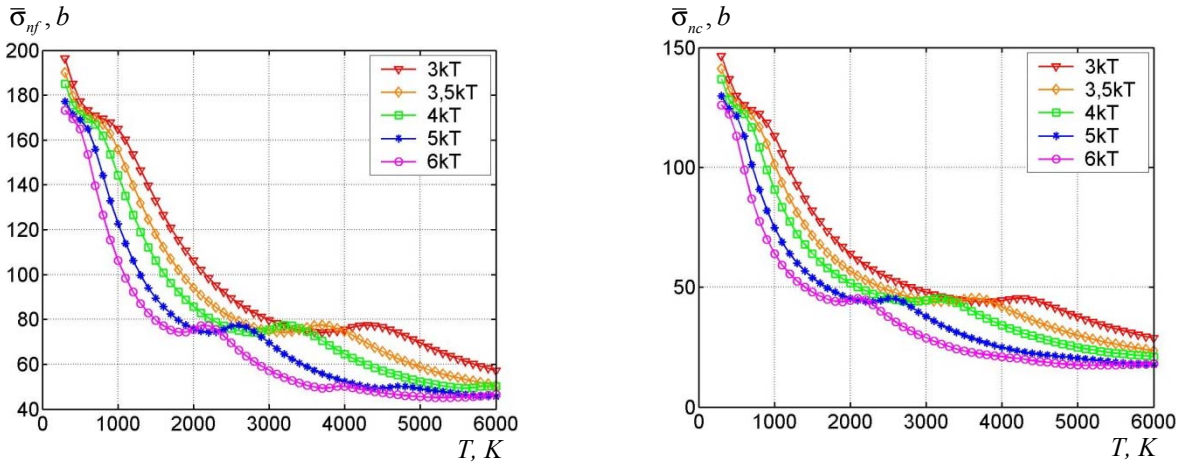

a *b*

Fig. 3. The cross section of division (*a*) and radiative capture cross section (*b*) ^{235}U, averaged a combined range of Maxwell and Fermi temperature dividing the environment and for different values of the boundary energy spectra of Fermi and Maxwell.

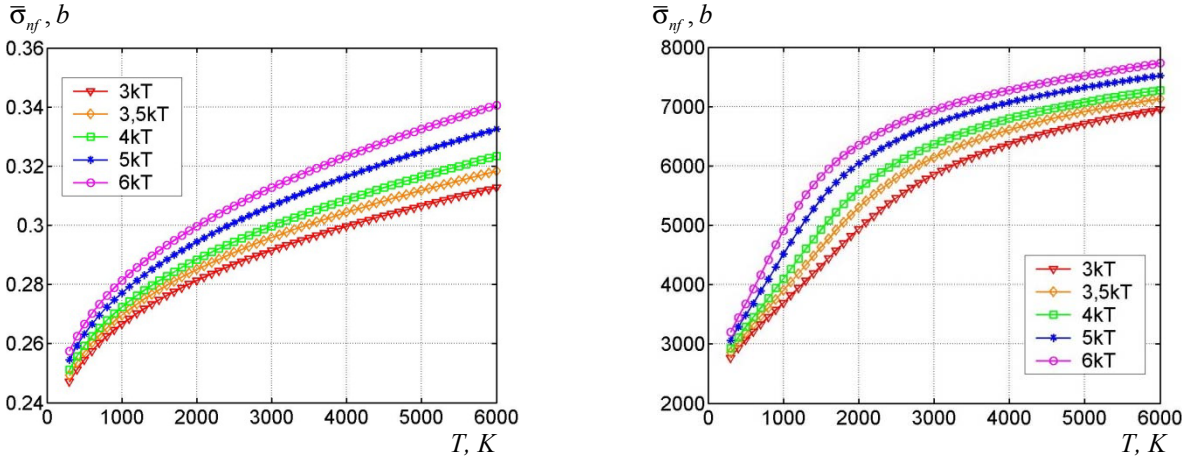

a *b*

Fig. 4. The cross section of division (*a*) and radiative capture cross section (*b*) $^{238}_{92}U$, averaged over the spectrum of the combined Maxwell and Fermi temperature dividing the environment and for different values of the boundary energy spectra of Fermi and Maxwell.

Shown in Fig. 4, *b* $^{238}_{92}U$ data to confirm the dependence of the radiative capture cross-section of the temperature, because it has the resonance region is as low as that $^{239}_{94}Pu$ of the (average fission cross section $^{238}_{92}U$ is due to the high threshold of division 1 MeV, as shown in Fig. 4, *a* is practically insensitive to hardening of the neutron spectrum caused by the increased temperature of the fuel).

4. Dependence of the density of the heat source MOX fuel and uranium Dioxide fuel temperature reactor fuel

Obtained calculated density dependence of the heat source of MOX fuel and uranium Dioxide temperature reactor fuel are shown in Figs. 5 and 6, respectively.

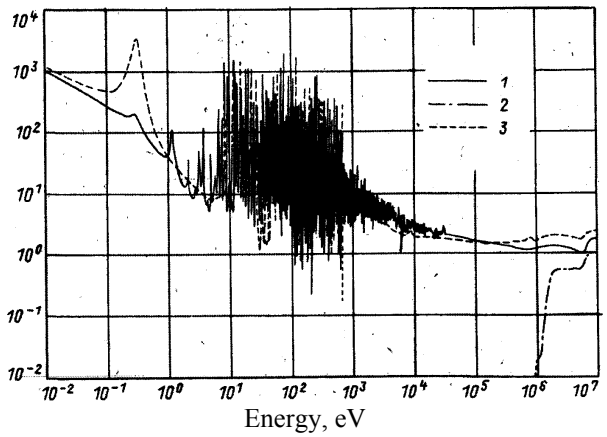

Fig. 5. Fission cross section of uranium-235 (*1*); uranium-238 (*2*); plutonium-239 (*3*) as a function of neutron energy [16].

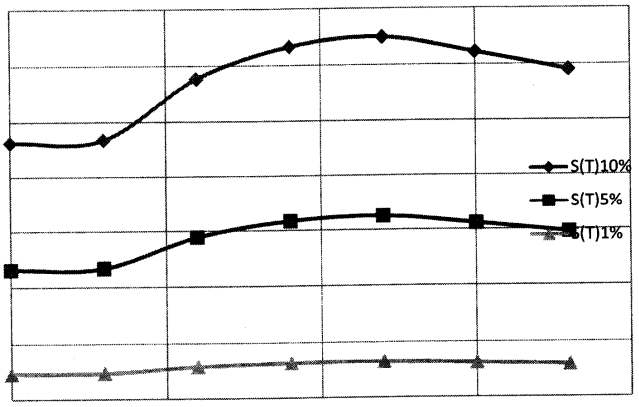

Fig. 6. Depending on the density of the heat source on the temperature of the medium from the fissioning fuel mixture of uranium dioxide-238 and plutonium-239 for three compositions (enrichment of plutonium-239 1 %, 5 %, 10 %).

5. Conclusions

The results of calculations of the temperature dependence of the average of the thermal neutron spectrum cross sections of nuclear fission and radiation capture of uranium-238, uranium-235 and plutonium-239. Observed and explained for the temperature range investigated the fundamental difference of temperature dependence of the average of the thermal neutron spectrum nuclear reaction cross sections of uranium-235 and plutonium 239. We also obtain the temperature dependence of the calculated dependence of densities of heat sources for MOX fuel and uranium oxide fuel for thermal reactors.

Observed and explained for the temperature range investigated the fundamental difference of temperature dependence of the density of heat sources for MOX fuel and uranium oxide fuel. The temperature dependence of the heat source for the fissile fuel environment, have identified and justify the characteristics of the accident at the 3-rd block AES 'Fukushima-1."

REFERENCES

1. *Феоктистов Л.П.* Нейтронно-делительная волна // ДАН. - 1989. - Т. 309, № 4. - С. 864 - 867.
2. *Феоктистов Л.П.* Безопасность - ключевой момент возрождения ядерной энергетики // Успехи физических наук. - 1993. - Т. 163, № 8. - С. 89 - 102.
3. *Rusov V.D., Linnik E.P., Tarasov V.A. et al.* Traveling wave reactor and condition of existence of nuclear burning soliton-like wave in neutron-multiplicating media // Energies. - 2011. No. 4, P. 1337 - 1361; doi: 10.3390/en4091337.
4. *Тарасов В.А., Бориков Т.Л., Крыжановская Т.В. и др.* Теория диссипативных структур кинетической системы для дефектов нелинейной физической системы «металл+нагрузка+облучение». Части 1, 2 // Вопросы атомной науки техники. Серия «Физикарадиационных повреждений и радиационное материаловедение. - 2007. - № 2(90). - С. 63 - 75.
5. *Тарасов В.А., Бориков Т.Л., Крыжановская Т.В. и др.* Теория диссипативных структур кинетической системы для дефектов нелинейной физической системы «металл+нагрузка+облучение». Части 3, 4 // Вопросы атомной науки техники. Серия «Физикарадиационных повреждений и радиационное материаловедение. - 2007. - № 6(91). - С. 18 - 35.
6. *Русов В.Д., Тарасов В.А., Чернеженко С.А.* Режимы с обострением в уран-плутониевой делящейся среде технических ядерных реакторов и геореактора // Вопросы атомной науки техники. Серия «Физикарадиационных повреждений и радиационное материаловедение. - 2011. - № 2(97). - С. 112 - 121.
7. *Rusov V.D., Pavlovich V.N., Vashenko V.N. et al.* Geoantineutrino spectrum and slow nuclear burning on the boundary of the liquid and solid phases of the Earth's core // Journal of Geophysical Research. - 2007. - Vol. 112. - P. 1 - 16; B09203, doi: 10.1029/2005JB004212.
8. *Вейнберг А., Вигнер Е.* Физическая теория ядерных реакторов. - М.: Изд-во Иностр. лит-ры, 1961.
9. *Бартоломей Г.Г., Бать Г.А., Байбаков В.Д., Алхутов М.С.* Основы теории и методы расчета ядерных энергетических реакторов. - М.: Энергоатомиздат, 1989.
10. *Фейнберг С.М., Шихов С.Б., Троянский В.Б.* Теория ядерных реакторов. Т. 1. - М.: Атомиздат, 1978.
11. *Абагян П.Л., Базазянц Н.О., Николаев М.Н., Цибуля А.М.* Групповые константы для расчета реакторов и защиты. - М.: Энергоиздат, 1981.
12. *Украинцев В.Ф.* Эффекты реактивности в энергетических реакторах. - Обнинск: ИАТЭ, 2000.

13. *Федоров Н.Д.* Краткий справочник инженера-физика. Ядерная физика и атомная физика // М.: Государственное издательство литературы в области атомной науки и техники, 1961. - 507 с.
14. *Владимиров В.И.* Практические задачи по эксплуатации ядерных реакторов. - М.: Энергоатомиздат, 1986, 304 с.
15. *Широков С.В.* Физика ядерных реакторов // К.: Наук. думка, 1992. - 288 с.
16. *Кеслер Г.* Ядерная энергетика. - М.: Энергоатомиздат, 1986.
17. *Heinz Neeb.* The radiochemistry of nuclear power plants with light water reactors. - Berlin, New York: WalterdeGruyter, 1997.
18. *Самойлов О.Б., Усынин Г.Б., Бахметьев А.М.* Безопасность ядерных энергетических установок. - М.: Энергоатомиздат, 1989.
19. *Safety* and security of commercial spent nuclear fuel storage: public report. - Washington, D.C.: National Academies Press, 2006.
20. *Кабакчи С.А., Булгакова Г.П.* Радиационная химия в ядерном топливном цикле. - РХТУ им. Д.И. Менделеева, 1997.

RECENT DEVELOPMENTS IN NUCLEAR DATA COMPILATION, EVALUATION AND VALIDATION AT THE IAEA NUCLEAR DATA SECTION

V. Semkova[1], N. Otuka[1], S. P. Simakov[1], V. Zerkin[1], O. O. Gritzay[2]

[1] Nuclear Data Section, International Atomic Energy Agency, Vienna, Austria
[2] Neutron Physics Department, Institute for Nuclear Research, National Academy of Sciences of Ukraine, Kyiv, Ukraine

The IAEA Nuclear Data Sections coordinates the activities of the International Network of Nuclear Reaction Data Centres (NRDC) for collection and compilation of experimental nuclear reaction data in the EXFOR database. The paper will present recent NDS initiatives related to the EXFOR developments such as: compilation of neutron source spectra used for spectrum average cross sections measurements; compilation of experimental covariance matrix; compilation of delayed neutron data, renormalization of EXFOR data to new standards, etc. The NDS data evaluation and validation projects will be discussed as well. The International Reactor Dosimetry and Fusion File (IRDFF) v.1.0 was released in May 2012. The energy range was extended from 20 to 60 MeV. The NDS plans to validate the 74 dosimetry reaction cross sections and related decay data in different neutron fields.

1. Introduction

The International Network of Nuclear Reaction Data Centres (NRDC, http://www-nds.iaea.org/nrdc/) constitutes a worldwide cooperation of 14 data centres from 10 countries and 2 international organisations under the auspices of the International Atomic Energy Agency. The NRDC Network coordinates the world-wide collection, compilation and dissemination of nuclear reaction data and related bibliographic information in the EXFOR and CINDA databases [1]. The EXFOR database presently contains information and numerical data from more than 19600 experiments consisting of more than 146000 datasets. The database includes integral, differential and partial cross sections as well as angular distributions, secondary particle spectra, polarization data, resonance parameters, nu-bar, fission product yields, reaction rates etc. for neutron-, charged-particle-induced and photonuclear reactions in the energy range up to 1 GeV. In its more than 60 years of history EXFOR has accumulated a large amount of valuable information and the database is continuously evolving in order to be up-to date and meet the needs of its diverse community of users.

2. Recent developments

Neutron sources with spectral energy distributions play an important role in a wide range of science and applications, such as: nuclear physics, astrophysics, fission and fusion reactor technologies, material research, medical applications etc. In many cases nuclear reaction data, included in the EXFOR database, have been obtained by experiments with neutron sources that have relatively broad energy (or non-monoenergetic) distribution, for example: fission reactors (thermal/fast/filtered fields), accelerators (thick targets, quasi monoenergetic fields) etc. Description and numerical data for the standard and reference neutron fields as well as different codes for calculation of the accelerator based neutron production are available from NDS web. However, the effective spectrum in the volume of the interaction sample could be different from the source spectrum due to the specific experimental conditions. Information on neutron source spectra and on the effective spectra at the sample position are an integral part of cross section measurements. The IAEA Nuclear Data Section has undertaken an initiative to compile spectral distributions and other relevant information for the data measured with non-menoenergetic neutron sources, which will allow correct interpretation of measured results, complete specification of physical process, and comparison with other measurements, evaluations and nuclear model calculations. Several types of neutron fields applied in spectrum average cross section measurements, compiled in EXFOR, were discussed during the CM "Neutron Sources Spectra for EXFOR"[2], namely: the fast neutrons spectrum supplied by the Yayoi reactor [3], the cold neutron source spectra at the Budapest PGAA-NIPS facilities [4], neutron spectra after the interference neutron filters at Kyiv research reactor [5], the quasi-stellar neutron spectrum produced by the ^{7}Li(p, n)^{7}Be reaction at a proton energy Ep = 1912 keV after integration over all emission angles [6], the neutron spectra produced by the ^{9}Be(d, xn) reaction at Ed = 30, 53 MeV [7], and Fast neutron sources with white and quasi-monoenergetic spectra of the Nuclear Physics Institute Řež [8]. The EXFOR format provides rules for coding of the incident source. New coding riles have been proposed for the compilation of neutron spectra and correlations between spectrum average cross section data and effective spectra at the sample position for the particular experiment.

Special attention has been paid recently to the development of the coding and tools for processing of the uncertainty components reported by authors in order to provide proper description of uncertainty and covariance information in EXFOR. According to the latest NRDC documents [9,10] the sources of uncertainties in a free text and data headings are given under the keyword ERR-ANALYS and corresponding numerical values are reported in COMMON or DATA section. In order to differentiate uncertainty components different headings are assign to statistical uncertainty (ERR-S), systematic uncertainties (ERR-SYS) or partial systematic uncertainties (ERR-1, ERR-2, etc.). The coding also includes minimum, maximum values and correlation properties (F-fully correlated, U-uncorrelated, P-partially correlated, C-correlated)) for the specific component. New rules for coding of covariance matrices have been approved during the 2012 NRDC meeting [11]. The matrices $Z_{i,j}(X_i,Y_i)$ will be presented as symmetric squared matrix with correlation

coefficients given as a lower triangle. The code for every array X, Y, Z will present the following parameters: type, length, data type and units. A web tool for construction of covariance matrix from EXFOR uncertainties has been recently developed by V. Zerkin and is available from the IAEA-NDS web (examples can be found at http://www-nds.iaea.org/exfor/exfor.htm) The tool allow to confirm or change uncertainty codes in an EXFOR Entry, modify the correlation type of the partial uncertainties. Different outputs are provided for the calculated covariance data: tables in ENDF-6 and EXFOR formats; interactive 2D/3D plots, and data formatted for input to a FORTRAN program. An example with uncertainty information/data retrieved from ERR-ANALYS, COMMON and DATA section from an EXFOR Entry and two of the output options for the constructed covariance matrix are shown in Table 1.

Table 1. **A web tool for construction of covariance matrix from EXFOR uncertainties**

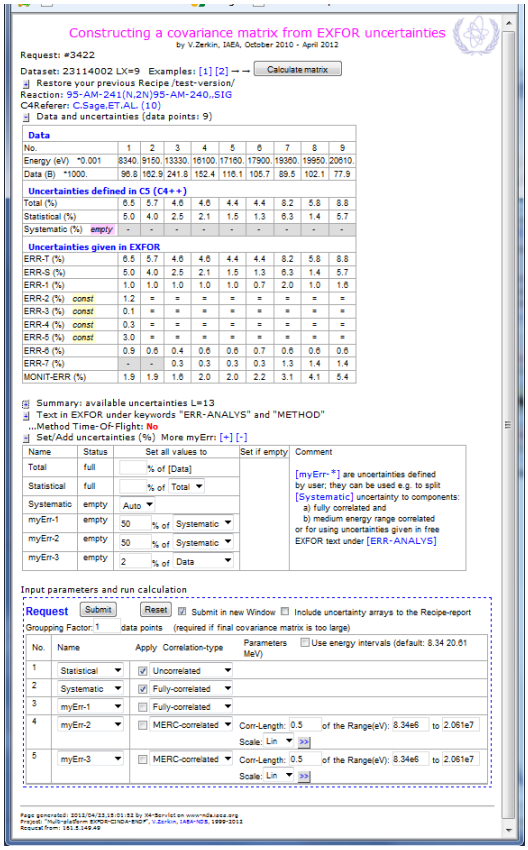

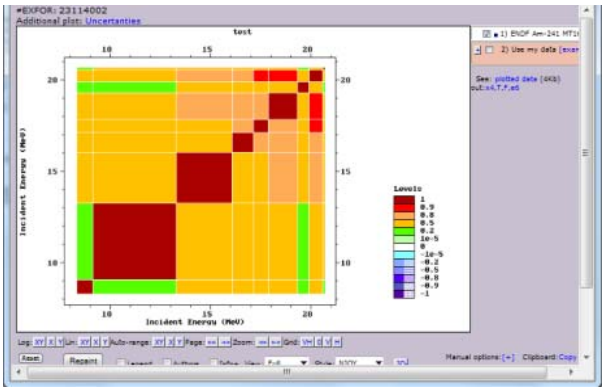

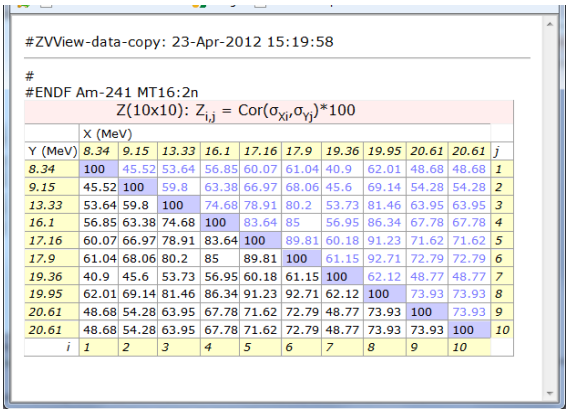

A tool has been developed by V. Zerkin for applying renormalization of data sets compiled in EXFOR database. Based on the information provided by the authors for the monitors or standards used in the experiment the data are renormalized to the latest evaluations. The procedure results in better agreement in the data from different experiments and improvement in the characteristics of the fitting. A collection of neutron cross section standards as well as documents and reports are provided at http://www-nds.iaea.org/standards for users.

New rules have been approved for gamma elastic and inelastic scattering at the NRDC meeting 2012. Novel non-destructive method for detecting clandestine materials has been developed recently based on Nuclear Resonance Fluorescence (NRF). The inelastic gamma scattering (γ, γ′) with excitation of strong dipole resonances in the nucleus and consecutive prompt g-ray decay can be applied for the identification of the isotopes (stable, radioactive or actinide). The reaction will be coded as elastic or inelastic scattering when the authors specify the observed transition as population the ground or an excited state. Otherwise the reaction is treated as partial scattering. The reaction code include the modifier ARE (resonance area) in sub-field SF6, because the resolution (keV) of the High-Purity Germanium detectors used for measurement of the scattered photons is much higher that the width of the resonances (meV) of the levels excited in NRF.

3. Further developments

A new cross section library for reactor dosimetry and fusion application "International Reactor Dosimetry and Fusion File (IRDFF 1.0)" [12] has been recently released at the IAEA/NDS web: http://www-nds.iaea.org/IRDFF. The library contains cross sections and covariance matrices for 74 reactions for the energy range from 10^{-11}MeV up to 60 MeV in ENDF-6 format. Development of the new library has been based on IRDF-2002 by upgrading with 37 new evaluations of cross sections and their uncertainties. The data above 20 MeV are retrieved from TENDL-2010 library and normalized to the IRDF-2002 data at highest neutron energy. Intercomparisons were made with integral

measurements in reference neutron fields (thermal Maxwellian (300K), 1/E and ^{252}Cf(sf)) [14]. The preliminary validation will be further developed. Benchmark measurements in energy smoothed and quasi-monoenergetic neutron fields generated by protons and deuterons on thick or thin targets (e.g., 8-40 MeV deuteron beam stopped in a thick Be target or 113 and 256 MeV protons incident on Al and U targets) will be extremely valuable for the validation of the cross sections at higher energies. New experiments below 20 MeV for some of the reactions are needed as well. Examples of some well characterized neutron fields considered for validation of the IRDFF (1.0) library are presented in Table 2.

Table 2. **Neutron fields considered for validation of the IRDFF (1.0) library**

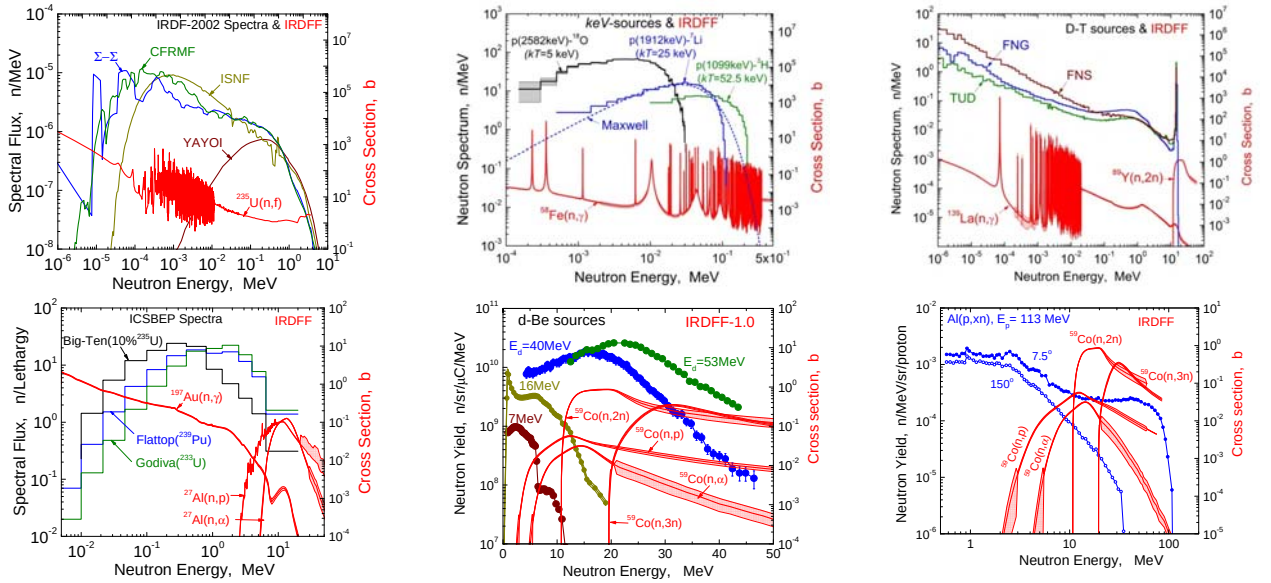

The compilation of beta-delayed neutron data in EXFOR database has also been discussed during the NRDC meeting 2012. The priority of compilation has been rather low for these data in the past, because they are on the boundary between reaction data and decay data. Studies devoted to the production and identification of delayed-neutron precursors have been carried out recently and the results have not been included in any database. The new generation of radioactive beam facilities will allow nuclear structure studies of neutron-rich nuclides for which (multiple) β-delayed neutron emission is allowed. However contributions from the fewer neutrons reach isotopes is indispensible in order to receive proper results. Existence of a number of delayed-neutron precursors has been predicted from mass measurements and evaluations and theoretical studies, however many of them have not been experimentally investigated yet [12]. Such data are of interest for nuclear and reactor studies as well. So, availability of experimental database is important for different fields of experimental and theoretical studies. EXFOR already contains data relevant to the beta-delayed neutron emission and the compilation of such data will continue to the database more complete.

REFERENCES

1. *Otuka N., Dupont E., Schwerer O. et al.* The role of the nuclear reaction data centres in experimental nuclear data knowledge sharing // Korean Phys. Soc. – 2011. – Vol. 59. – P. 1292 - 1296.
2. *Simakov S.* (Ed). Summary Report of the Consultants' Meeting on Neutron Sources Spectra for EXFOR // INDC(NDS)-0590, International Atomic Energy Agency, 2011.
3. *Harada H. et al.* Measurements of Neutron Capture Cross Section of 237Np for Fast Neutrons // Nucl. Sci. Tech. – 2009. – Vol. 46. – P. 460 - 468.
4. *Belgya T.* Target preparation for in-beam thermal neutron capture experiments // JRC Sci & Tech Report EUR 23883 EN (2010) 21-26.
5. *Gritzay O.* Neutron spectra after the interference neutron filters at Kyiv research reactor // INDC(NDS)-0590. - 2011. – 15 - 19.
6. *Ratynski W., Käppeler F.* Neutron capture cross section of 197Au: A standard for stellar nucleosynthesis // Phys. Rev. – 1988. – Vol. C37. – P. 595 - 504.
7. *Schweimer G.W.* Fast neutron production with 54 MeV deuterons // Nucl. Phys. – 1967. – Vol. A100. – P. 537 - 544.
8. *Simakov S.P. et al.* Analysis of the dosimetry cross sections measurements up to 35 MeV with a 7Li(p, xn) quasi-monoenergetic neutron source // J. of Kor. Phys. Soc. – 2011. – Vol. 59. – P. 1856 - 1859.

9. *Otsuka N.* (Ed.). LEXFOR (EXFOR Compiler's Manual) // IAEA-NDS-208Rev.2011/01.
10. *Otsuka N.* Summary Report of the Technical Meeting on International Network of Nuclear Reaction Data Centres // INDC(NDC)-0618.
11. *Zerkin V.* Development of a Web Tool for construction a covariance matrix from EXFOR uncertainties // http://www-nds.iaea.org/nrdc/nrdc_2012/working/wp2012-42rev.pdf
12. *Zsolnay E.M., Capote Noy R., Nolthenius H.J., Trkov A.* Summary description of the new international reactor dosimetry and fusion file (IRDFF release 1.0) // INDC(NDS)-0616.
13. *Capote R., Zolotarev K.I., Pronyaev V.G., Trkov A.* Validation of the ENDF-B/VII 23 % U(nth, f) prompt fission neutron spectrum using updated dosimetry cross sections, PHYSOR 2012.

SPECIFIC NEUTRON DATA LIBRARY FOR NUCLEAR DATA SUPPORT OF RADIOISOTOPE ACCUMULATION CALCULATIONS AT THE RESEARCH REACTOR

P. M. Vorona, O. O. Gritzay, O. I. Kalchenko, N. A. Klimova

Institute for Nuclear Research, National Academy of Sciences of Ukraine, Kyiv, Ukraine

At the research reactor WWR-M during the long period, the study of neutron cross sections for nuclei, important as for nuclear physics investigations, so as for applied purposes have been fulfilled [1]

Applied purposes include, among others, the production of radioactive isotopes for practical use. This paper covers the results of radioisotope program development, based on the neutron fluxes in the reactor core [2], and also the formation of the specific neutron data library for nuclear data support of radioisotope accumulation calculations at reactor

Potential program of radioisotope production was developed, at first, under the analysis of national needs in Ukraine in radioisotope production for different spheres of use (science, medicine, industry, etc.) The following special-purpose isotopes are included into the developed program : ^{32}P, ^{51}Cr, ^{55}Fe, ^{59}Fe, ^{60}Co, ^{75}Se, ^{85}Sr, ^{89}Sr, ^{90}Sr, ^{90}Y, ^{99}Mo / ^{99m}Tc, ^{103}Ru, ^{110m}Ag, ^{109}Cd, ^{117m}Sn, ^{131}Te / ^{131}I, ^{134}Cs, ^{141}Ce, ^{143}Pr, ^{147}Nd, ^{151}Sm, ^{153}Sm, ^{152}Eu, ^{154}Eu, ^{155}Eu, ^{153}Gd, ^{160}Tb, ^{169}Yb, ^{177}Zu, ^{182}Ta, ^{183}Ta, ^{181}W, ^{185}W, ^{187}W, ^{188}W / ^{188}Re, ^{186}Re, ^{188}Re, ^{192}Ir, ^{198}Au, ^{197}Hg.

The most important values for evaluation of special-purpose isotope activity attainment, except reactor neutron flux, are the neutron capture cross sections of selected nuclei.

Specific neutron data library includes the data for 30 elements, isotopes of which are presented into the radioisotope program development. This library includes also the data for all accompanying isotopes that may be presented in the start material and for other isotopes that would be accumulated during irradiation. There are the files in different formats, and also the digital data in Table form.

Files in ENDF format are collected as the result of analysis of the last versions of ENDF libraries of common use : ENDF/B-VII, JEFF-3.1, JENDL-3.3, BROND-2.2, CENDL-2. For most calculations two libraries of five were chosen: JENDL-3.3 (Japan) and JEFF3.1 (OECD).

For some isotopes the data from ENDF/B-VII and JENDL-4 new versions that appeared during the work under our library, and for several ones from BROND-2 library were used. Total number of selected files is equal to 154, they are written at separate CD for further operation with them.

ACE-formatted files are necessary for calculations of radioisotopes accumulated in reactor using the computer code package MCNP [3]. Even the last versions of this code don't contain all files for our isotopes, or they are too outdated. So we prepared ourselves the files in ACE format for $^{94,95,96,97,99}Mo$, $^{181,182}Ta$, $^{182,183,184,186}W$, $^{185,187}Re$ and $^{70,72,73,74,76}Ge$.

Numerical data, presented in Tables, include the values of thermal capture cross sections, resonance integrals and Westcott factors. The calculations of accumulated isotopes have to include the activation for neutrons of all energies in reactor spectrum. For this moment, the Table includes the following data: σ_γ^0 - thermal neutron capture cross section (at energy 0.0253 eV)

I_γ – Resonance Integral, g(T) – Westcott factor. Neutron data are taken from recent compilation [4] and also from several publications of experimental data. Table includes also evaluated values σ_γ^0 and I_γ from new ENDLs. There are also the isotope composition of elements and half-lives of radioactive isotopes. One of the used methods is Westcott method of spectral characteristics, where thermal $g(T)$ and resonance $s(T)$ cross section indexes exist and also r – above-thermal parameter of neutron field [5]. The average (effective) neutron cross sections may be calculated using the following equation: $\Sigma_{eff} = \sigma_\gamma^0 (g + r \cdot s)$. Westcott indexes g and s are connected with the cross section energy dependence (degree of cross section deviation from *1/v* - dependence at thermal and epithermal energies). Values g and s for different isotopes are calculated and tabulated by Westcott [5] and others. Values r for neutron field are defined from cadmium ratio, which may be measured in experiment using the activation detection technique (thin foils of Au, Cu, Co, etc.) in different irradiated regions of the used reactor.

This work was supported by STCU contract № Uz-25.

REFERENCES

1. *Vorona P.M., Gritzay O.O., Kalchenko O.I, Koloty V.V.* // 40 years of neutron investigations at Research Reactor in Kyiv. - Kyiv, 2000. - P. 20 - 33 (in Ukrainian).
2. *Vorona P.M, Razbudey V.F.* // Nuclear Physics and Atomic Energy. - 2010. - No. 1(11) - P. 574.
3. *Vorona P.M, Razbudey V.F.* // Nuclear Physics and Atomic Energy. - 2011. - No. 3(12). - P. 235.
4. *Mughabhab S.F.* Atlas of Neutron Resonanses / Fifth Edition. - NNDC, USA, 2006.
5. *Westcott C.H.* // AECL-352, CRRP-362, 1956, AECL - 1101, 1960.

List of neutron data for selected nuclei for calculations of radioisotope accumulation at irradiation in nuclear reactor

Target radio-isotope, half-life	Isotope composition of natural element target			Neutron data							Comment
				σ_γ^0			Westcott g-factor	I_γ, barn			
	Chemic element Starting isotope	Isotope	%	Atlas [1]	JENDL-3.3	JEFF-3.1		Atlas [1]	JENDL-3.3	JEFF-3.1	
1	**2**	**3**	**4**	**5**	**6**	**7**	**8**	**9**	**10**	**11**	**12**
	24-Cr-nat.			3.17(.08)+0		3.031864+0		2.1(.2)+0		1.521949+0	BROND-2
Cr-51											
27.7025 days	Cr-50	Cr-50	4.345	1.54(.02)+1*	1.603539+1	1.592893+1	1.0002	1.17(.02)+1	7.500710+0	7.482844+0	
		Cr-52	83.789	8.6(.2)-1*	7.752092-1	7.601409-1	1.0003	4.8-1**	4.687905-1	4.648568-1	
		Cr-53	9.501	1.86(.06)+1*	1.759208+1	1.806709+1	1.0003	1.23+1**	8.361593+0	8.429464+0	
		Cr-54	2.365	4.1(.4)-1*	3.426588-1	3.600814-1	1.0003	2.5(.4)-1**	1.783729-1	2.018690-1	
	26-Fe-nat			2.56(.03)+0*		2.616912+0				1.375334+0	BROND-2
Fe-55											
2.73 year	Fe-54	Fe-54	5.845	2.25(.18)+0*	2.252035+0	2.252035+0	1.0002	1.27(.10)+0**	1.212551+0	1.205718+0	
		Fe-56	91.754	2.59(.14)+0*	2.590818+0	2.585874+0	1.0002	1.36(.15)+0**	1.348415+0	1.343078+0	
		Fe-57	2.119	2.48(.30)+0*	2.463337+0	2.486274+0	1.0002	1.51(.15)+0**	1.423986+0	1.906982+0	
		Fe-58	0.282	1.32(.03)+0	1.300378+0	1.273861+0	1.0012	1.50(.07)+0	1.357975+0	1.402978+0	
	27-Co-nat										
Co-60											
1925.1 days		**Co-58**	**70.8 days**	1.9(.2)+3*	1.651417+2	1.651417+2		7.(1.)+3	6.253548+0	1.277542+5	ENDF/B-7
		Co-58m	**9.04 hour**	1.4(.1)+5		1.008948+5				1.277542+5	
	Co-59	Co-59	100	3.718(.006)+1	3.720244+1	3.717595+1	1.0004	7.4(.2)+1	7.584753+1	7.579747+1	
Y-90	39-Y-nat										
64.0 hour											
	Y-89	Y-89	100.00	1.28(.02)+0	1.277667+0	1.285675+0	1.0002	9.6(.6)-1	8.682513-1	9.213997-1	
		Y-90	**2.667 days**	<6.5	3.3+0	3.501345+0			2.62+0	4.757299+0	ENDF/B-7
		Y-91	**58.51days**	1.4(.3)	1.400535+0	1.400538+0			2.843213+0	2.85+0	ENDF/B-7
	42-Mo-nat			2.52(.04)+0*			1.0003				
Mo-99				n	8.003069+0	1.700656+0		n	4.157293+1	2.737629+1	
2.747 days		Mo-92	14.84	8.(2.) -2*	2.075784-2	2.075784-2	0.93947	8.3-1**	9.672444-1	9.672444-1	
		Mo-94	9.25	3.4(.6)-1*	1.311341-2	1.311341-2	1.0003	1.12+0**	1.400176+0	1.400176+0	

Continuation of the Table

1	2	3	4	5	6	7	8	9	10	11	12
		Mo-95	15.92	1.34(.03)+1*	1.399664+1	1.399664+1	1.0000	1.18(.07)+2**	1.185415+2	1.185415+2	
		Mo-96	16.68	5.(2.)-1*	5.955521-1	5.955521-1	1.0004	1.7(.3)+1**	1.753200+1	1.753200+1	
		Mo-97	9.55	2.2(.2)+0*	2.100426+0	2.100426+0		1.44(.3)+1**	1.712769+1	1.712769+1	
	Mo-98	Mo-98	24.13	1.30(.06)-1	1.300264-1	n		6.7(.3)+0	6.552611+0	n	
		Mo-100	9.63	1.99(.03)-1*	1.990813-1	1.990813-1	1.0003	3.76(.15)+0	3.903175+0	3.903175+0	
	44-Ru-nat			2.56(.13)+0*				4.1(.4)+1**			
Ru-103				1.2+0				5+0			
39.26 days		Ru-96	5.54	2.9(.2)-1	2.901120-1	2.486834-1		6.36(.23)+0	7.280462+0	1.288447+1	
		Ru-98	1.87	< 8*	8.003057+0	7.958971+0	1.202		1.149680+1	1.193077+1	
		Ru-99	12.76	7.24(1.)+0	7.311536+0	7.103223+0	1.0024	1.62(.20)+2**	1.709214+2	1.627385+2	
		Ru-100	12.60	5.8(.4)+0	5.023347+0	5.802199+0	1.0003	1.12(.11)+1	1.118537+1	8.176178+0	
		Ru-101	17.06	5.2(.3)+0	3.360353+0	3.414846+0	1.0017	1.02(.10)+2	1.001857+2	1.111421+2	
	Ru-102	Ru-102	31.55	1.27(.04)+0	1.229603+0	1.300427+0	1.0001	4.9(.3)+0	4.310576+0	3.212351+0	
		Ru-103	**39.26days**	1.2+0	8.003085+0	6.683604+1		5.+0**	9.206764+1	5.943731+2	
		Ru-104	18.62	4.91(.10)-1	3.227030-1	2.972752-1	1.0003	6.3(.2)+0	6.559340+0	5.809100+0	
		Ru-105	**4.44 hour**	3.9(.6)-1	3.866663-1	2.000772-1			6.875900+0	7.351737+0	ENDF/B-7
		Ru-106	**371.6 days**	1.46(.45)-1	1.460563-1	1.460562-1		2.(.6)+0	2.002168+0	2.093093+0	
	47-Ag-nat			6.33(.04)+1				7.56(.20)+2			
Ag-110m				8.2(1.1)+1	8.199653+1			3.1(.6)+1**	9.389544+1		
249.76 days		Ag-107	51.839	3.76(.12)+1	3.863039+1	3.761640+1	0.9981	1.07(.05)+2	1.038749+2	1.075566+2	
	Ag-109	Ag-109	48.161	9.1(.1)+1	9.057057+1	9.074488+1	1.0057	1.470(.048)+3**	1.471703+3	1.474145+3	
		Ag-111	**7.45 days**	3.(2.)+0*		3.001160+0		1.05(.20)+2		1.039618+2	
Cd-109	48-Cd-nat			2.52(.05)+3*	2.463547+3			7.0(1.0)+1	7.222666+1		ENDF/B-6
461.4 days											
		Cd-106	1.25	~ 1 *	9.698532-1	1.118409+0	0.9999	4.1+0**	1.039880+1	1.457196+1	
	Cd-108	Cd-108	0.189	7.2(1.3)-1*	1.086859+0	1.101238+0	1.0002	1.07+1**	2.692357+1	1.719826+1	
		Cd-110	12.49	1.1(.1)+1*	1.105721+1	1.101396+1	1.0000	3.9(.04)+1	3.911035+1	4.161367+1	
		Cd-111	12.80	6.9(.8)+0	2.394122+1	2.402999+1	0.9939	4.17(.03)+1**	4.933971+1	5.031422+1	
		Cd-112	24.13	2.2(.5)+0*	2.192908+0	2.195479+0	1.0000	1.25(.1)+1**	1.323869+1	1.348727+1	
		Cd-113	12.22	2.061(.04)+4	2.075712+4	2.072508+4	1.3604	3.90+2**	3.944336+2	3.921651+2	
		Cd-114	28.73	3.30(.18)-1*	3.405450-1	3.360875-1	1.0002	1.26(.1)+1	1.686653+1	1.315020+1	

Continuation of the Table

1	2	3	4	5	6	7	8	9	10	11	12
		Cd-115m	**44.56 days**		5.001888+0	3.101200+1			9.401956+0	1.963046+2	ENDF/B-7
		Cd-116	7.49	7.5(1.)-2*	7.486517-2	7.499613-2	1.0000	1.5(.2)+0**	1.695849+0	1.677259+0	
	50-Sn-nat			6.03(.09)-1*	6.250878-1			4.1(.3)+0	6.559030+0		BROND-2
Sn-117m											
13.60 days											
Sn-119m											
293.1 days		Sn-112	0.97	8.5(.4)-1*	1.009272+0	1.009272+0	1.006	2.9(.2)+1	3.048488+1	3.048488+1	
		Sn-113	**115 days**	8.8(1.2)+0*	8.869483+0			2.17(.05)+2**	2.277854+2		ENDF/B-7
		Sn-114	0.66	1.25(.03)-1*	1.253062-1	1.253062-1	1.0003	6.3(1.5)+0**	6.665647+0	6.665647+0	
		Sn-115	0.34	5.8(.8)+1*	2.985567+1	2.985567+1	1.0003	2.79(.6)+1**	1.381292+1	1.381292+1	
	Sn-116	Sn-116	14.54	1.3(.4)-1*	1.277365-1	1.277365-1	1.0004	1.19(.1)+1**	1.238326+1	1.238326+1	
		Sn-117	7.68	1.07(.05)+0*	2.173804+0	2.173804+0	1.0004	1.57(.25)+1**	1.814831+1	1.868210+1	
	Sn-118	Sn-118	24.22	2.20(.50)-1*	2.179247-1	2.179247-1	1.0004	3.4(.4)+0**	5.340734+0	5.340734+0	
		Sn-119	8.59	2.19(.06)+0	2.176567+0	2.176567+0	1.0003	2.9(.5)+0**	5.324087+0		
		Sn-120	32.58	1.4(.3)-1*	1.392480-1	1.392480-1	1.0005	1.14+0**	1.219914+0	1.219914+0	
		Sn-122	4.63	1.46(.08)-1*	1.837313-1	1.837313-1	1.0005	8.1(.4)-1	9.317416-1	9.317416-1	
		Sn-123	**129.2 days**		3.001156+0	3.301281-2			6.275317+1	2.684344+0	
		Sn-124	**5.79 days**	1.3(.05)-1*	1.354994-1	1.354994-1	1.0008	8.3(2.5)-2	7.848264+0	7.894614+0	
		Sn-125	**9.64 days**		1.502632-1	5.502136-1			8.821928+0	1.484937+1	ENDF/B-7
		Sn-126	**2.3+5 year**		9.003497-2	3.001166-1			1.498065-1	1.851979-1	
	52-Te-nat			4.6(.1)+0*				5.6(.3)+1			
I-125											
59.4 days											
I-131				8.(5.)+1							
8.02 days		Te-120	0.09	2.34(.30)+0*	2.340907+0	2.287440+0	1.209		2.245556+1	1.999127+1	
		Te-122	5,55	3.9(.4)+0*	3.376159+0	2.801327+0	1.0006	8.8(1.)+1**	8.015346+1	7.408387+1	
		Te-123	0.89	4.18(.3)+2*	4.183881+2	4.100494+2	1.0126	5.630(.3)+3**	5.648338+3	5.543112+3	
		Te-124	4.74	6.3(.7)+0*	6.786161+0	6.802527+0	1.0003	5.3(.7)+0**	5.610979+0	8.391856+0	

Continuation of the Table

1	2	3	4	5	6	7	8	9	10	11	12
		Te-125	7.07	1.29(.16)+0*	1.520816+0	1.550667+0	1.0003	2.07(.03)+1**	2.192922+1	2.318180+1	
		Te-126	18.84	4.4(0.6)-1*	1.035124+0	1.035399+0	1.0003	8.0(.6)+0	8.146325+0	1.037277+1	
		Te-128	31.74	2.0(1.8)-1*	2.140828-1	2.150152-1	1.0003	1.66(.05)+0**	1.306429+0	1.750671+0	
		Te-130	34.08	1.95(.10)-1*	2.700613-1	2.901143-1	1.0003	4.0(.5)-1	2.842004-1	3.605678-1	ENDF/B-7
		Te-132	**3.204 days**			2.000779-3				5.625667-3	
	55-Cs-nat										
Cs-134											
754.5 days daysdays		Cs-133	100	3.03(.11)+1	2.901203+1	2.900671+1	1.0030	4.37(.26)+2	3.962325+2	4.209775+2	
		Cs-134	**2.065 year**	1.4(.12)+2*	1.397247+2	1.397222+2			1.053061+2	7.894945+1	
		Cs-135	**2.3+6 year**	8.3(.3)+0*	8.703739+0	9.008678+0		3.79(.27)+1	6.245796+1	6.118695+1	
		Cs-136	**13.16 days**		1.300508+1	1.300563+0			5.737369+1	3.855702+1	
		Cs-137	**30.07 year**	2.7(.3)-1*	2.500975-1	1.414731-1			3.564353-1	6.291361-1	
	58-Ce -nat			6.3(.4)-1*				3.7(1.7)+0			
Ce -141				2.9(.3)+1				1.51+2			
32.501 days	Ce-140	Ce-136	0.185	7.45(1.)+0*	7.458325+0			7.7(1.2)+1**	7.719345+1		ENDF/B-7
		Ce-138	0.251	1.035(.240)+0*	1.037237+0			6.7(3.4)+0	9.498869+0		ENDF/B-7
		Ce-140	88.45	5.8(.2)-1*	5.703766-1	5.746478-1	1.0003	5.4(.5)-1	3.421576-1	3.365303-1	
		Ce-141	**32.51daysssss**	2.9(.3)+1*	2.912601+1	3.27374+1		1.51+2**	5.026603+2	1.650931+2	
		Ce-142	11.114	9.7(.2)-1*	1.004022+0	9.004774-1	1.0003	1.15(.05)+0	9.311024-1	1.014308+0	
		Ce-143	**33.0 hour**	6.(.7)+0*	6.0	6.00234+0			4.32+1	4.155159+1	ENDF/B-7
		Ce-144	**284.9 days**	1.(.1)+0*	1.000391+0	1.12860+0		2.6(.3)+0	2.540586+0	2.858657+0	
	59-Pr-nat										
Pr-143				9.(1.)+1				1.30+2			
13.57 days			100	1.15(.03)+1	1.150471+1	1.148409+1	0.9993	1.74(.02)+1	1.839069+1	1.794511+1	
		Pr-142	**19.12 hour.**	2.(.3)+1*	2.001353+1	2.000782+1			8.227226+1	1.449526+2	ENDF/B-7
		Pr-143	**13.57 days**	9.(1.)+1	9.003520+1	8.903480+1		1.9(.25)+2	1.863466+2	1.895064+2	
	60-Nd-nat			5.01(.14)+1*				3.9(.5)+1			
Nd-147											
10.98 days		Nd-142	27.2	1.87(.07)+1*	1.870561+1	1.863910+1	1.0003	3.4(1.1)+1	8.660686+0	6.166418+0	

Continuation of the Table

1	2	3	4	5	6	7	8	9	10	11	12
Pm-147		Nd-143	12.2	3.25(.1)+2	3.250764+2	3.359528+2	0.9964	1.29(.30)+2**	1.288289+2	1.328293+2	
2.623 year		Nd-144	23.8	3.6(.3)+0*	3.603895+0	3.583410+0	1.0003	4.2(.5)+0**	4.297893+0	4.195993+0	
		Nd-145	8.3	5.(.1)+1	4.386135+1	4.186169+1	1.0000	2.30(.35)+2	2.040332+2	2.314835+2	
	Nd-146	Nd-146	17.2	1.49(.06)+0	1.399872+0	1.400486+0	1.0002	2.57(.14)+0	2.907114+0	2.816236+0	
		Nd-147	**11.0 days**	4.4(1.5)+2*	4.311128+2	4.399971+2		4.30+2**	6.302774+2	6.058716+2	
	58-Ce -nat	Nd-148	5.7	2.58(.07)+0	2.493442+0	2.500845+0	1.0004	1.55(.15)+1	1.472430+1	1.989540+1	
		Nd-150	5.6	1.04(.04)+0	1.202261+0	1.186972+0	1.0003	1.52(.08)+1	1.589462+1	1.580155+1	
	Ce-140			5.670(.1)+3			1.699*	1.4(.2)+3			
		Sm-151	**90 year**	1.517(.03)+4	1.512777+4	1.518453+4	0.9274*	3.765(.16)+3**	3.408564+3	3.465765+3	
		Sm-144	3.07	1.64(.10)+0*	1.640809+0	6.961054-1		2.38(.17)+0	1.902978+0	1.959884+1	
		Sm-147	14.99	5.7(.3)+1	5.801939+1	5.719413+1	0.9965	7.77(.30)+2	7.801158+2	7.947236+2	
Pr-143		Sm-148	11.24	2.4(.6)+0*	2.413757+0	2.701058+0		2.7(1.4)+1	4.515679+1	2.766163+1	
13.57 days		Sm-149	13.82	4.014(.06)+4	4.054446+4	4.174405+4	1,7102	3.390+3**	3.493515+3	3.487212+3	
		Sm-150	7.38	1.00(.04)+2	1.085943+2	1.033525+2	0.9985	3.58(.50)+2	3.248146+2	3.395022+2	
	59-Pr-nat	**Sm-153**	**46.28 hour**	4.20(1.80)+2*	4.201656+2	3.301328+2		n	7.222490+2	2.863932+3	
		Sm-152	26.74	2.06(.06)+2	2.062804+2	2.060227+2		2.970(.100)+3	2.764030+3	2.978249+3	
Nd-147	Pr-141	Sm-154	22.75	8.3(.5)+0*	8.395188+0	8.402232+0		3.6(.4)+1	3.631340+1	3.353951+1	
10.98 days		Nd-142	27.2	1.87(.07)+1*	1.870561+1	1.863910+1	1.0003	3.4(1.1)+1	4.515679+1	2.766163+1	
Pm-147		Nd-143	12.2	3.25(.1)+2	3.250764+2	3.359528+2	0.9964	1.29(.30)+2**	3.493515+3	3.487212+3	
2.623 year	60-Nd-nat	Nd-144	23.8	3.6(.3)+0*	3.603895+0	3.583410+0	1.0003	4.2(.5)+0**	3.248146+2	3.395022+2	
		Nd-145	8.3	5.(.1)+1	4.386135+1	4.186169+1	1.0000	2.30(.35)+2	3.408564+3	3.465765+3	
	Nd-146	Nd-146	17.2	1.49(.06)+0	1.399872+0	1.400486+0	1.0002	2.57(.14)+0	2.764030+3	2.978249+3	
		Nd-147	**11.0 days**	4.4(1.5)+2*	4.311128+2	4.399971+2		4.30+2**	7.222490+2	2.863932+3	
		Nd-148	5.7	2.58(.07)+0	2.493442+0	2.500845+0	1.0004	1.55(.15)+1	3.631340+1	3.353951+1	
		Nd-150	5.6	1.04(.04)+0	1.202261+0	1.186972+0	1.699*	1.52(.08)+1	1.589462+1	1.580155+1	
	62-Sm-nat			5.670(.1)+3			0.9274*	1.4(.2)+3			
Sm-151		**Sm-151**	**90 year**	1.517(.03)+4	1.512777+4	1.518453+4		3.765(.16)+3**	3.408564+3	3.465765+3	
90 year		Sm-144	3.07	1.64(.10)+0*	1.640809+0	6.961054-1	1.699*	2.38(.17)+0	1.902978+0	1.959884+1	
		Sm-147	14.99	5.7(.3)+1	5.801939+1	5.719413+1	0.9965	7.77(.30)+2	7.801158+2	7.947236+2	
		Sm-148	11.24	2.4(.6)+0*	2.413757+0	2.701058+0		2.7(1.4)+1	4.515679+1	2.766163+1	
		Sm-149	13.82	4.014(.06)+4	4.054446+4	4.174405+4	1,7102	3.390+3**	3.493515+3	3.487212+3	
	Sm-150	Sm-150	7.38	1.00(.04)+2	1.085943+2	1.033525+2	0.9985	3.58(.50)+2	3.248146+2	3.395022+2	
Sm-153		**Sm-153**	**46.28 hour**	4.20(1.80)+2*	4.201656+2	3.301328+2		n	7.222490+2	2.863932+3	ENDF/B-7
1.93 days	Sm-152	Sm-152	26.74	2.06(.06)+2	2.062804+2	2.060227+2		2.970(.100)+3	2.764030+3	2.978249+3	
		Sm-154	22.75	8.3(.5)+0*	8.395188+0	8.402232+0		3.6(.4)+1	3.631340+1	3.353951+1	
	63-Eu-nat			4.565(.1)+3			0.9018*	2.32(.15)+3			ENDF/B-7

Continuation of the Table

1	2	3	4	5	6	7	8	9	10	11	12
Eu-152		**Eu-152g**	**13.50 year**	1.28(.06)+4	1.275166+4	1.275166+4	0.967*	1.58+3**	2.178876+3	2.178876+3	
13.52 year	Eu-151	Eu-151	47.81	9.2(.1)+3	9.168513+3	9.165976+3	0.8940	3.3(.3)+3	3.108974+3	3.355076+3	
		Eu-153	52.19	3.12(.07)+2	3.126925+2	3.311164+2	0.986	1.42(.10)+3	1.410199+3	1.410199+3	
Eu-154		**Eu-154**	**8.593 year**	1.34(.13)+3	1.846988+3	1.845157+3	0.8979*	8.02+2**	1.176513+3	1.359160+3	
8.593 year	Eu-153										
Eu-155		**Eu-155**	**4.761 year**	3.95(.125)+3*	3.760448+3	3.758180+3	1.022(jendl)	2.32(.03)+4**	1.551579+4	1.528022+4	
4.761 year	Eu-153										
		Eu-156	**15.19 days**		1.00+2	4.822161+2	1.00(jendl)		1.449+3	1.492209+3	
		Eu-157	**15.18 hour**		1.108+2	1.900569+2			9.478+2	1.302294+3	ENDF/B-7
	64-Gd-nat			4.889(.104)+4			0.8467*	3.9(.1)+2			
Gd-153		**Gd-153**	**240.4 days**	2.231(.3)+4*	2.231049+4				2.975421+2		ENDF/B-7
240.4 days	Gd-152	Gd-152	0.20	7.35(.20)+2*	1.056159+3	1.056159+3		2.02(.16)+3	9.892703+2	9.892703+2	
		Gd-154	2.18	8.5(1.2)+1	8.501538+1	8.503369+1	0.9967	2.45(.30)+2	2.149146+2	2.476914+2	
		Gd-155	14.80	6.09(.05)+4	6.074062+4	6.074063+4	0.8390	1.537(.1)+3**	1.534103+3	1.545582+3	
		Gd-156	20.47	1.8(.7)+0*	2.188166+0	1.536148+0	1.0007	1.04(.15)+2	1.204530+2	1.008299+2	
		Gd-157	15.65	2.54(.00815)+5	2.536806+5	2.532920+5	0.84715	7.54(.20)+2**	7.616639+2	7.629854+2	
		Gd-158	24.84	2.2(.2)+0	2.497074+0	2.501244+0	1.0009	7.3(.7)+1	6.393311+1	6.307262+1	
		Gd-160	21.86	1.4(.3)+0*	7.963470-1	7.703350-1	0.9954*	7.4(1.0)+0**	1.201817+1	8.552585+0	
	65-Tb-nat										
Tb-160				3.34(.64)+2	n	5.251664+2		2.994+3**	n	1.134617+3	
72.3 days	Tb-159	Tb-159	100.00	2.34(.04)+1	2.649747+1	2.321236+1		4.18(.20)+2	4.705913+2	4.139417+2	
	70-Yb-nat			3.48(.06)+1				1.54(.09)+2			
Yb-169				3.6(.3)+3*				5.2(.5)+3**			
32.026 days	Yb-168	Yb-168	0.13	2.30(.17)+3	**2.30796+3**			2.13(.10)+3**	**2.13543+4**		JENDL-4
		Yb-170	3.04	9.9(1.8)+0	**9.91527+0**			3.10(.30)+2	**3.12058+2**		JENDL-4
		Yb-171	14.28	5.83(.38)+1	**5.83131+1**			3.18(.30)+2	**3.26639+2**		JENDL-4
		Yb-172	21.83	1.3(.8)+0	**1.31272+0**			2.5(.3)+1	**2.71557+1**		JENDL-4
		Yb-173	16.13	1.55(.15)+1*	**1.55000+1**			3.8(.3)+2	**3.84592+2**		JENDL-4
		Yb-174	31.83	6.32(.15)+1	**6.32090+1**			2.7(.3)+1	**2.54842+1**		JENDL-4
		Yb-176	12.76	2.85(.5)+0	2.82339+0			6.9(.6)+0	6.97643+0		JENDL-4
	71-Lu-nat			7.49(.2)+1				6.22(.50)+2			
Lu-177											
6.734 days		Lu-175	97.416	2.33(.11)+1	n	2.587533+1	0.972*	6.20(.50)+2	n	6.466754+2	
	Lu-176	Lu-176	2.584	2.02(.07)+3	n	1.962023+3	1.7579	1.087(.040)+3	n	9.188284+2	
	73-Ta-nat										

Continuation of the Table

1	2	3	4	5	6	7	8	9	10	11	12
Ta-182				8.2(.6)+3	n	8.289160+3		9.43(.50)+2**	n	1.043314+3	
114.4 days		Ta-180	0,0123	5.63(.60)+2				1.346(.1)+3**			
	Ta-181	Ta-181	99,9877	2.05(.05)+1	0	2.067907+1	1.0041	6.55(.2)+2	6.599718+2	6.599718+2	
	74-W -nat			1.84(.03)+1			1.0018	3.52(.25)+2			
W -181				5.50+0 ***							
121.2 days	W -180	W -180	0.135	3.73(.24)+1 ***				2.14(.3)+2**			
		W -182	26.40	1.99(.03)+1	2.071551+1	2.071551+1	1.0031*	6.0(.6)+2**	6.283083+2	6.283083+2	
		W -183	14.40	1.04(.02)+1	1.011681+1	1.011681+1	0.9989*	3.55(.30)+2**	3.347526+2	3.347526+2	
W -185		**W-185**	**75.1 days**	2.1(.3)+0*				1.16+2**			
75.1 days	W -184	W -184	30.60	1.7(.1)+0	1.698141+0	1.698141+0	0.9989*	1.47(.15)+1	1.622415+1	1.622415+1	
W -188											
69.4 days	W -186	W -186	28.40	3.81(0.05)+1	3.946035+1	3.789768+1	1.0014*	4.80(.15)+2	5.286293+2	3.468191+2	
	75-Re-nat			8.97(.14)+1				8.31(.20)+2			
Re-186											
3.718days		Re-185	37.40	1.12(.02)+2	n	1.121760+2	1,0053	1.727(.050)+3	n	1.729951+3	
Re-188		**Re-188**	**17.005 hour**	<2*							
17.005 hour		Re-187	62.60	7.64(.01)+1	n	7.670604+1	0,9942	3.00(.20)+2	n	2.942693+2	
	77-Ir-nat			4.253(.024)+2	n	4.171530+2		2.15(.10)+3	n	2.192318+3	
Ir-192		**Ir-192g**	**73.83 days**	1.588(.200)+3				3.410+3**			
73.83 days	Ir-191	Ir-191	37.27	9.54(.10)+2	9.544651+2	n	0,9964	3.55(.10)+3	3.324121+3	n	ENDF/B-7
		Ir-193	62.73	1.11(.05)+2	1.111736+2	n	1.0180	1.35(.10)+3	1.376125+3	n	ENDF/B-7
	38-Sr-nat			1.28(6)+0				1.1(.2)+1			
Sr-85		Sr-84	0.56	8.22(1.2)+1*	8.221617-1	8.126506-1		9.31(.47)+0	1.155064+1	1.052556+1	
64.84 days		Sr-86	9.86	1.04(.07)+0*	1.040305+0	2.841199+0	1.0003	4.8(.2)+0	4.813803+0	5.177171+0	
		Sr-87	7.00	1.7(.3)+1*	1.600854+1	1.601118+1	1.0064	1.17(.30)+2**	1.210010+2	1.184301+2	
Sr-89	Sr-88	Sr-88	82.58	5.8(.4)-3*	5.802270-3	5.802264-3	1.0003	6.5-2**	6.322859-2	1.242817-2	
50.53 days		**Sr-89**	**50.53 days**	4.2(.4)-1*	4.201613-1	4.201614-1			4.135189-1	5.270341-1	
		Sr-90	**28.79 year**	1.04(.14)-2*	1.500576-2	9.003456-1		1.04(.16)+2	8.987153-2	5.109931-1	
	79-Au-nat										
Au-198				2.510(.037)+4			0.98*				
2.69517 days	Au-197	Au-197	100,0000	9.86(,09)+1	9.870099+1	9.874477+1	1.0051*	1.550(.028)+3	1.570565+3	1.562755+3	ENDF/B-7
	80-Hg-nat			3.723(.40)+2		3.834666+2		7.3(.5)+1		1.191528+2	

Continuation of the Table

1	2	3	4	5	6	7	8	9	10	11	12
Hg-197											
64.14 hour	Hg-196	Hg-196	0.15	3.08(.18)+3 *	3.078770+3	3.078770+3		4.71(.15)+2**	4.201417+2	4.201417+2	ENDF/B-7
		Hg-198	9.97	2.0(.3)+0*	1.985936+0	1.985936+0		7.2(.2)+1**	7.446641+1	7.446641+1	ENDF/B-7
		Hg-199	16.94	2.15(.048)+3	2.150167+3	2.150167+3		4.34(.20)+2**	4.386910+2	4.386910+2	ENDF/B-7
		Hg-200	23.10	1.4+0	1.443144+0	1.443144+0		1.5+0**	2.576334+0	2.576334+0	ENDF/B-7
		Hg-201	13.18	4.9(.6)+0	7.784657+0	4.903971+0		3.0(.3)+1**	3.447050+1	3.343023+1	ENDF/B-7
		Hg-202	29.86	4.89(.05)+0	4.955143+0	4.955143+0		2.9+0**	3.209761+0	3.209761+0	ENDF/B-7
		Hg-204	6,87	4.3(1.0)-1*	4.316372-1	4.316372-1		8.5(2.0)-1	2.725222+0	2.725222+0	ENDF/B-7

Westcott g-factors marked with * were taken from Atlas [1] - Atlas of Neutron Resonances, Fifth Edition, NNDC, USA, 2006.
Other g-factors were taken from [2] - Reprint INDC (NDS)-440 by S. F. Mughabhab
"Thermal Neutron Capture Cross Sections, Resonance Integrals and G-factors", IAEA, Vienna, 2003

Notations to the Table

σ_γ^0 – capture cross section for neutron energy at 2200m/sec (0,0253e V)

*) 1 - σ_γ – capture cross section measured in a Maxwellian flux;

2 - σ_γ^r – capture cross section measured with reactor neutrons;

3 - σ_γ^c – capture cross section calculated from resonance parameters;

4 - σ_t – total cross section;

5 - $\sigma_\gamma[T_{1/2}, I^\pm]$ – part of capture cross section leading to isomeric state or to ground state of radioactive nuclei.

I_γ – radiative capture resonance integral (total, measured)

**) 1 - I_γ^c – radiative capture resonance integral calculated from resonance parameters;

2 - $I_c\,[T_{1/2}, I^\pm]$ – radiative capture resonance integral for isomeric state (or ground state of radioactive nuclei).

***) – experimental data obtained in our laboratory and absent in Atlas 2006.

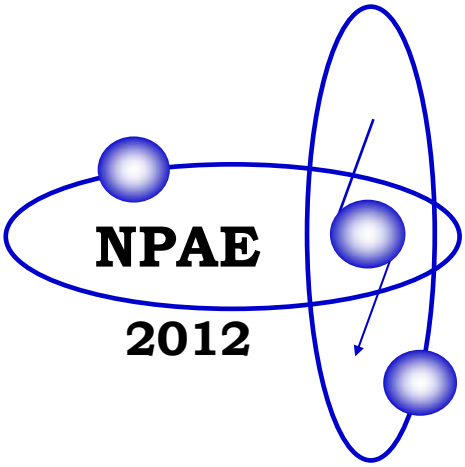

Section 6

Problems of Atomic Energy

STUDY OF ACCELERATED UNIT UNLOADING MODE INITIATED BY TURBINE FEED PUMP TRIP WITH TVSA FUEL ASSEMBLIES OPERATION IN WWER-1000

V. I. Borysenko[1,2], I. N. Kadenko[2], D. V. Samoilenko[3]

[1] *Institute for Safety Problems of Nuclear Power Plants, National Academy of Sciences of Ukraine, Kyiv, Ukraine*
[2] *International Nuclear Safety Center of the Taras Shevchenko National University of Kyiv, Kyiv, Ukraine*
[3] *Scientific and Technical Centre, National Nuclear Energy Generating Company "Energoatom", Kyiv, Ukraine*

This paper provides the study results of accelerated unit unloading mode (AUU) initiated at WWER-1000 unit operated at 100 % power and its expediency in the event of single Turbo Feed Pump (TFP) failure. Modeling was performed using an advanced calculation code RELAP/SCDAPSIM/Mod3.4 and relevant model for KhNPP Unit No. 2. As the study shows, SCRAM cannot be prevented in case of failure of 3 main circulation pumps (MCPs) due to steam generators (SG) level drop. Based on the results obtained, it is reasonably justified to allow SCRAM signal instead of AUU activation in case of single TFP failure at power level more than 90 % of N_{nom}. This will provide more sparing temperature modes for fuel assemblies and equipment, as well as prevent additional thermal cycling loads and violation of safe operation limits as SG water levels.

1. Introduction

To attain high technical and economic indices of electricity generation from NPPs aimed, inter alia, at providing competitiveness generating utilities all over the world seek to reduce the fuel component, which can reach 30 % of the total electricity generating cost. This makes the tasks of optimizing the fuel component obvious [1]. One of the main ways to solve the problem of optimizing the fuel component is to increase the level of nuclear fuel burnup. At the same time, fuel manufacturers tend both to increase an initial enrichment of nuclear fuel and an amount of fuel in the core. However, alteration of water-uranium ratio may also change the coefficient of reactivity, i.e. higher fuel burnup enlarges a reactivity coefficient range. These changes can be significant and lead to deviations from the anticipated behavior of a number of transients in the reactor facility (RF), including neutron power change rate due to feedback action. This paper provides the modeling results and analysis of AUU behavior induced by TFP failure in the WWER-1000 unit at N_{nom} = 100 %.

The variation range of core reactivity coefficient during the fuel campaign with water-uranium ratio specific for alternative fuel assemblies, such as TVSA, used at Ukrainian NPPs with WWER-1000 units is much greater compared to previous generation fuel. Such trend will continue in future when using next generation FAs, in particular fuel rods with increased fuel column height or pellets without central opening. An increase of reactivity coefficients in absolute value has significant impact on AUU anticipated behavior.

In recent years, several NPPs with WWER-1000 units operating in AUU mode have recorded significantly higher neutron power excursion than ever observed since the start of WWER-1000 operation. Despite the fact that such modes proceed in the subcritical state the AUU operation is accompanied by reaching safe operation limits for neutron power growth rate leading to drop of SG levels below SCRAM setpoints.

2. Problem description

Since 2007 a number of NPPs with WWER-1000 units have recorded activation of AUU mode reaching SCRAM setpoints by period of reactor that has not been previously observed. On the one side, this could be due to introduction of the state-of-the-art neutron flux monitoring system (NFMS), which, unlike previous generations, allows to keep records of more rapid and dynamic processes with specific times of an order of seconds.

On the other side, the parameters of neutron power changes:

- level of neutron power drop upon AUU activation;
- rate of neutron power raise due to the feedback action;
- level of neutron power excursion,

differ significantly from the neutron power behavior (Fig. 1) recorded under PHARE SRR 1/95 [2] that addressed AUU mode in the WWER-1000 as an international test problem investigated in various scientific centers using different software programs (Table 1).

Table 1. **List of institutes and verified programs under PHARE SRR 1/95**

Institute	Code
FZR, Germany	DYN3D/ATHLET
VTT, Finland	HEXTRAN/SMABRE
KI, Russia	BIPR8KN/ATHLET
STCNRC, Ukraine	DYN3D/ATHLET
INRNE, Bulgaria	DYN3D/ATHLET

The reasons for such differences include, inter alia, as follows:

- decrease of mean drop time for control rod (CR) of control and protection system (CPS) from ~ 3 s in the late 90's to ~ 1.5 s now;
- increase in absolute value of reactivity coefficients by coolant and fuel temperature.

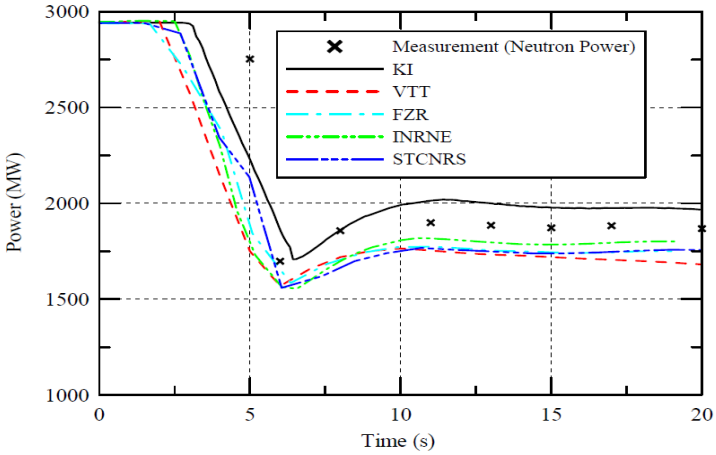

Fig. 1. Comparison of the measured power variation with calculation results obtained using different programs for AUU mode. The results of dynamic tests performed during Balakovo Unit 4 startup were used as the experimental data.

The [2] specifies that there are no reasons to consider AUU mode dangerous in terms of nuclear safety and fuel thermal reliability.

The validity of this statement for AUU mode recorded, for example, at Khmelnitsky Unit No. 2 in 2007 with some parameters having significant difference (Table 2) from the study results [2], should be the subject of further investigation.

Table 2. **Some parameters of reactor in AUU mode**

Parameter	Design of SRR 1/95	KhNPP-2, 22.09.2007
Drop time of AUU control group, s	3.5	1.37
Minimum neutron power, %	52	48
Maximum neutron power during feedback action, %	60	70 as per design 61 – SCRAM actuated
Maximum rate of neutron power raise	62 – 100 MW/s	162 MW/s

After the AUU mode is actuated the operation of WWER-1000 series power unit of V-320 type is accompanied by dropping of CPS control group named an AUU group and triggering of reactor power unloading and limiting device that should render unit to 50 % power level by interacting with CPS control group. An alteration of neutron power in AUU mode depends on efficiency of AUU group and its drop time having significant impact on feedback action intensity. The decrease of the drop time for AUU control group from 3.5s to 1.37s will increase the power ascension rate from 62-100 MW/s [2] to 162 MW/s [3 - 6]. It should also be noted that neutron power ascension rate significantly depends on feedback parameters in terms of reactivity coefficients and their time constants. For example, the reactivity coefficient by coolant temperature changes in absolute values in ~ 2 times during the fuel campaign from the start till the end of boron control.

Therefore, AUU behavior at KhNPP Unit No. 2 c significantly different from that simulated under the Project SRR 1/95. The most significant concern relates to the so called neutron power excursion that can exceed 20 % without account of further power raise due to colder coolant coming as a result of closing primary circulation.

The power excursion mode up to 20 % is provided for in the fuel documentation [7, 8]. The number of such excursions during the design lifetime is 15 for usual fuel assemblies (FA) and 20 for TVSA.

Therefore, significant divergences between the anticipated behavior of AUU mode and the actual behavior observed recently at a number of WWER-1000 units [3 - 6, 9] generate specific interest to simulating this mode.

3. Computer code and the model used in the investigations

In this paper, for modeling AUU mode in case of single TFP failure the thermal-hydraulic code RELAPSCDAPSIM/Mod3.4 with point reactor kinetics model was used [10]. Such approach is applicable due to absence at AUU asymmetric perturbation of the neutron field in the reactor core.

In order to study the behavior of processes with reducing neutron reactor power (working in a subcritical state), the model of WWER-1000 for the RELAP5/Mod3.2 code was applied. The calculations at the same time were performed with using the RELAPSCDAPSIM/Mod3.4 code, which is a fusion of later RELAP5/Mod3.x versions and SCDAP models. The RELAP5 models allow to calculate the general thermal hydraulics, the interaction of control systems, reactor kinetics and transport of non-condensed gases. The SCDAP models simulate the core behavior during a severe accident.

RELAPSCDAPSIM/Mod3.4 code allows to perform a realistic analysis of the design, beyond the design and severe accidents with severe core damage before the destruction of the reactor vessel, at the same time modeled in detail the

processes in the reactor facility. The neutron kinetics is presented in the point approximation, it does not take into account changes in the spatial profile of energy release during local reactivity changes.

For the calculations the three loops WWER-1000 model of the KhNPP Unit No. 2 (loop 3 is double and corresponds to the 2-nd and 3-rd real loops) was used. It was previously developed and validated in framework of the safety analysis work [11]. The model includes the basic equipment of the normal operation systems and safety systems of the first and second circuits. Also in the model takes into account changes in thermal-hydraulic characteristics of the first reactor circuit caused by the operation TVSA in the core, moreover clarified the characteristics of the gas gap fuel element.

Particular attention in model was paid to the correct description of the reactor kinetics input data, since they have the greatest influence to the results of the modes simulation associated with the reactivity change. At the same time the neutron-physical characteristics for the beginning- and end-of-core-lifetime of seventh fuel loading on KhNPP Unit No. 2 [12] was used.

The reactivity at transient is defining as the sum of the reactivity inserted by the displacement of the CR CPS, and released reactivity due to feedback action. During operation of the seventh fuel loading on KhNPP-2 in case of AUU activation drop into the core of the 4th group of CR takes place.

To determine the reactivity, released due to feedback actions, the code takes into account the following reactivity coefficients: reactivity coefficient by average temperature of the fuel, $\frac{\partial \rho}{\partial T_U}$; reactivity coefficient by average coolant temperature without changing the density, $\frac{\partial \rho}{\partial T_{H2O}}$; reactivity coefficient by coolant density, $\frac{\partial \rho}{\partial T_\gamma}$.

To account for the radial distribution of energy release, the reactor core is conventionally divided into two unequal volumes, at one of which the heat exchange of coolant with a "hot" fuel assemblies takes place and at other heat exchange with the "average" fuel assemblies. In addition, at the hot and average FA select "hot" and "average" fuel elements, this is also taken into account when modeling the heat exchange. In this case the coefficient of nonuniformity of energy release by fuel assemblies of the core k_q and coefficient of nonuniformity of energy release by fuel elements of the core k_r is used.

To account for the distribution of energy release by height, the reactor core in the model, namely the volume in which heat exchange of coolant with hot and average FA takes place, divided into 10 equal control volumes. For each such volume calculated weights coefficients, according to which the defined contribution to the total reactivity some reactivity released in a separate volume, when is changing the thermal-hydraulic parameters of the coolant in it.

4. Calculation results

Using the model, which takes into account features discussed in the previous section, a study AUU mode initiated by single FWP failure was performed. For this mode the calculation results of the neutron reactor power are shown in Fig. 2, which shows how, after a rapid decrease in neutron power to ~ 50 % Nnom due to fall of AUU group (time of fall ~ 1.3 s), under the feedback action is a growth of neutron power to a level more than 67 % Nnom that differ significantly from the simulation results obtained in the framework of the project [2].

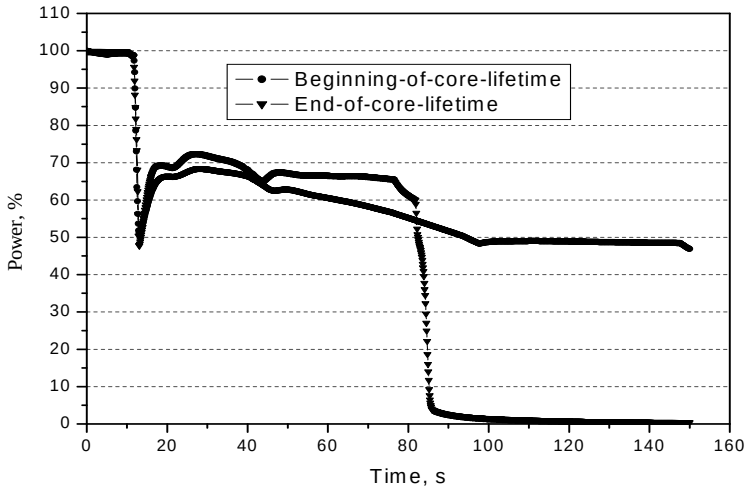

Fig. 2. Changes of reactor neutron power in case of single TFP failure for the beginning- and end-of-core-lifetime.

Simultaneously with AUU activation after TFP failure begins to drop rapidly the water level in the steam generators (Figs. 3 and 4) due to the decrease of SG feeding. When the level becomes below 500 mm from the nominal 2.25 m, as shown in Fig. 4, according to the operating limitations [13] in the emergency mode shuts down the corresponding MCP. In case of failure of 3 MCPs the scram activation takes place (by a condition «Failure of the 3 MCPs from the 4 which

is working at power > 5 %»). Such AUU mode behavior for the end-of-core-lifetime (see Fig. 2), due to large integrated power released at transient as a result of the feedback action by reactivity, despite the work of unloading power system (UPS), and the rate of water evaporation exceeds the rate of SG feeding.

At single TFP failure from two working and AUU activation, also signal to close the turbine control valves in order to reduce the turbine unit power to 55 % Nnom. In same time turbine electro-hydraulic control system (EHCS), operates in the PC-1 mode of maintaining the pressure in the main steam collector (MSC) - [14]. Steam relief device such as BRU-A and BRU-K are closed.

The coolant temperature changes at the inlet and outlet of the reactor is shown in Figs. 5 and 6.

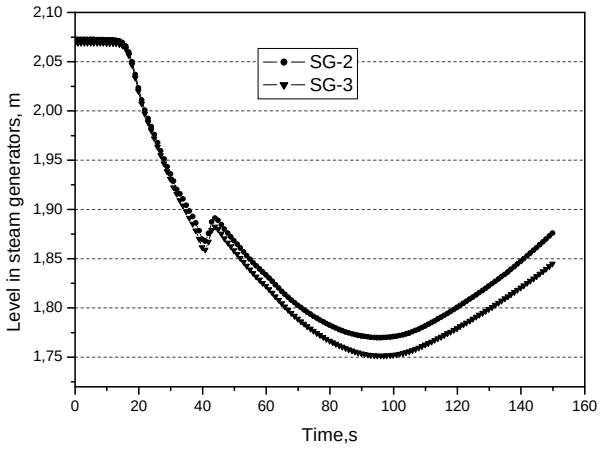

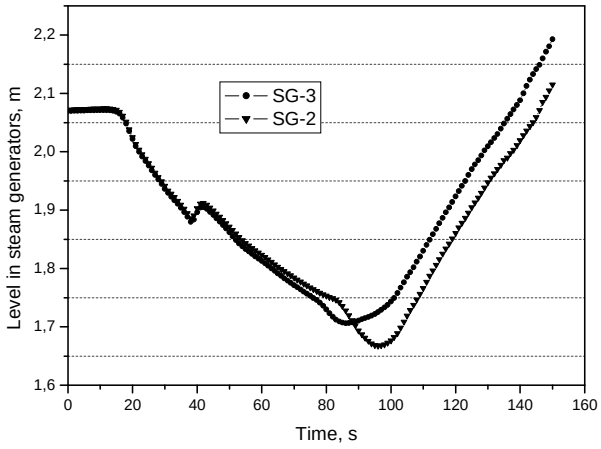

Figs. 3 and 4. Levels in SG-2 and SG-3 in case of single TFP failure for the beginning- and end-of-core-lifetime.

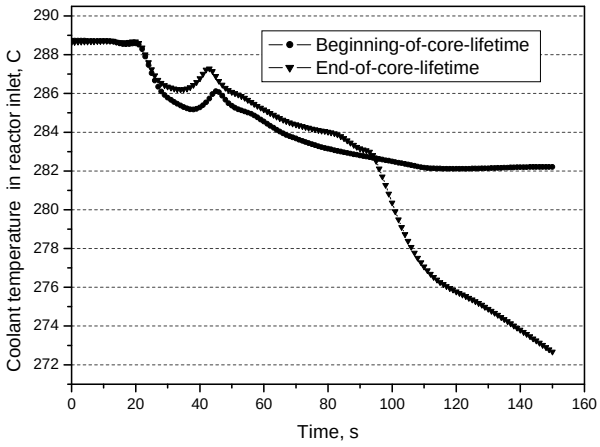

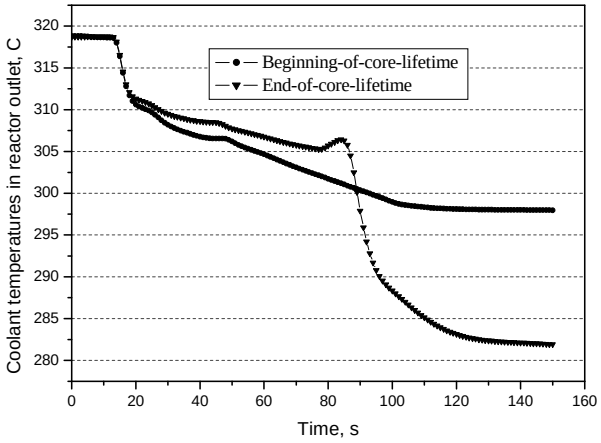

Figs. 5 and 6. The coolant temperature at the inlet and outlet of the reactor for the beginning- and end-of-core-lifetime.

The coolant temperature growth at the outlet of the reactor after 75s for the end-of-core-lifetime due to a sharp decrease of water flow through the reactor. This associated with third MCP failure due to a reduction in the water level of the corresponding generator and achievement of setpoint 1.75 m. Such temperature growth continues until the scram activation, caused by third MCP failure. In Fig. 2, this corresponds to region of a power reduction after 75 seconds to the time of scram activation.

5. Conclusions

According to WWER-1000 design in case of single TFP failure at power more than 75 % of nominal, in order to transfer power unit quickly to a lower power level the AUU mode is made. In AUU mode the AUU group of control rods drops into the core, at the same time the UPS begin work and power is corrected to level of 50 % of Nnom. Simultaneously with the reactor unloading the turbine unloading takes place, that is, steam power and electric power (as a consequence) of the power unit is reduced. At the same time provides stabilization of the pressure in the main steam collector according to a specific mode [14]. According to the design when AUU triggered the power unit must move to a new steady state at half nominal power.

However the results of analysis which was carried out in this work for the seventh fuel loading of KhNPP Unit No. 2, shows that during AUU activation due to TFP failure the neutron reactor power increases to 73 % Nnom after rapid drop. In this case, the efficiency of the UPS is not enough for rapidly reduce the heat power to ~ 50 %, and TFP works cannot to maintain boiler water level at SG. Further, during evaporation the water level in the steam generators is reduced to emergency setpoints which corresponding MCP failure. After the three MCP failures the SCRAM activation

takes place. According to the received results of calculations, such transient takes place at end-of-core-lifetime.

Therefore, since SCRAM cannot be prevented after AUU activation, in this case, the AUU mode is not expedient because it leads to additional thermal cycling loads of fuel and equipment, and also violated the safe operation limits as the SG levels.

REFERENCES

1. *Arkhangelskaya A.I.* Economic policy in reforming conditions of the electric energy market and power and the investment program of OJSC "Concern Rosenergoatom" // Reports collection of seventh IRTC "Safety efficiency and safety of nuclear power. - Moscow, 2010 - P. 22 - 25.
2. EUROPEAN COMMISSION. PHARE PROGRAMME / SAFETY RELATED RESEARCH PROJECT SRR 1/95. Validation of coupled neutron kinetic / thermal hydraulic codes against transients measured in VVER reactors. Final Technical Report Compiled by S. Mittag. Reference: FZR/SRR195/FIN2.1.
3. Technical Report “Modernization of design AUU mode of the reactor facility WWER-1000. SAR development to modernize the AUU mode”. - LLC “FIZAR”, 2008.
4. *Bykov M.A, Alekhin G.V. Petkevich I.G*. Indications analysis of the neutron flux systems at accelerated unit unloading mode for reactor facility with WWER-1000 // Sixth Int. scientific and technical conf. "Safety providing of NPP with WWER." - 6-29.05.2009 (OKB "GIDROPRESS", Podolsk, Russia).
5. *Technical* reference. NPC analysis and reliability of fuel of Khmelnitsky Unit No. 2 at transient after accelerated unit unloading activation. - M.: Kurchatov Institute, 2008.
6. *Borysenko V.I., Kadenko I.M., Samoilenko D.V*. WWER-1000 accelerated unit unloading activation transient features // Nucl. Phys. At. Energy. - 2009. - Vol. 10, No. 2. - P. 157 - 164.
7. *Complex* components of the WWER-1000 core. Catalog description. U 0401.21.00.000 DKO.
8. *Complex* components of the WWER-1000 core. Catalog description. U 0401.04.00.000 DKO.
9. *About* safety and stability of operation NPPs with VVER-1000 at dynamic conditions with AUU activation (Report) / OJSC "VNIIAES", 2008.
10. SCDAP/RELAP5/MOD3.2 Code Manual, Volume I: SCDAP/RELAP5 Interface Theory, NUREG/CR-6150, INEL-96/0422, October 1997.
11. *43-923.203.031.RM06.* Khmelnytska NPP. Power unit 2. Safety analysis report. Chapter 15. Design accidents analysis. Calculation model description for RELAP code.
12. *43-923.203.254.OB04.03.* Khmelnytska NPP. Power unit 2. Safety analysis report. Chapter 4. Reactor. Part 3. Neutron-physical calculations.
13. *43-923.203.007.DB02.* Khmelnytska NPP. Power unit 2. Final safety analysis report. Chapter 15. Design accidents analysis. NSGF Database. Part 2. Basic components of RF.
14. *43-923.203.007.DB06.* Khmelnytska NPP. Power unit 2. Final safety analysis report. Chapter 15. Design accidents analysis. NSGF Database. Part 6. Control systems, automation, protection and interlock.

THE PROBLEMS OF THE USAGE OF POWERFUL ELECTRONS ACCELERATORS FOR THE IRRADIATION OF NUCLEAR POWER STATIONS' EQUIPMENT AND MATERIALS

T. V. Kovalinska[1], N. V. Khalova[1], I. A. Ostapenko[1], V. I. Sakhno[1], V. V. Shlapatska[2], A. G. Zelinskyy[1]

[1] Institute for Nuclear Research, National Academy of Sciences of Ukraine, Kyiv, Ukraine
[2] Government enterprise "RADMA", Institute of Physical Chemistry, National Academy of Sciences of Ukraine, Kyiv, Ukraine

The possibilities of making the qualification of the materials and equipment of nuclear power stations on modern electrons accelerators of high power are researched. The problems of using this powerful sources of radiation for modern methods of nondestructive control of functional characteristics of the equipment and materials are discussed. The purpose of researches is the determination of the possibility of such works from the point of view of radiation safety of the personnel and the environment. First of all, this problem is connected with the increase of the intensity of secondary irradiation in such processes. The character of secondary irradiation is researched, as well as the dynamics of its energetic spectrum in rooms of powerful industrial accelerator (with beam power of more than 20 kW and average energy of electrons of 1.6 MeV) in regimes of irradiation of the equipment with contents of heavy elements. The original way of solving this problem is suggested. Experimentally proved, that during the usage of the set of compensatory measures, it is also possible to make tests of NPPs' materials and equipment on industrial accelerators of high power.

1. Introduction

Equipment qualification (EQ) is the confirmation and maintenance of performance and technical characteristics of the equipment to ensure its functionality in "hard" environmental conditions and seismic actions.

EQ is recommended by the IAEA [1] and should be one of the most important directions of the activity to ensure the necessary level of safety of NPPs' power units.

The purpose of the qualification is to establish (define) a period of time during which the equipment will definitely perform its functions taking into account aging effects.

The recommendations concerning the EQ process are outlined in IAEA standards [2]. The upgraded general structural scheme of the equipment qualification estimation process (Fig. 1) was suggested. In this scheme the EQ process includes three basic stages:

- the preparation of basic data;
- qualification estimation;
- the development of qualification enhancing methods.

2. The Preparation of Basic data

In general, the qualification is fulfilled for all of the equipment. However, this leads to the substantial expenses of material and labor resources. For example, the IAEA recommends firstly to fulfill the qualification for the equipment of systems, which are important for safety. [2].

In accordance with these recommendations, based on the general list of the equipment of NPP's power unit, the detailed list of the equipment, which should be qualified, is developed. This list is the basic document of the qualification, and must contain all the necessary and sufficient information for the definition of the qualification status of each equipment unit.

In the process of the detailed list development, the input data is collected and documented, that can be divided into two groups [3, 4]:

1) qualification characteristics – project parameters of the equipment (name, label, type, class of safety, group, seismic category, etc.)

2) qualification requirements to the equipment on the basis of calculated characteristics of environmental influences in conditions of the original event of an accident (OEA) from the analysis of project accidents (original events, where the functioning of this equipment is needed; necessary time of functioning; the parameters of "hard" environmental conditions; the parameters of seismic influences).

With the purpose the advancement of EQ works, certain measures concerning qualification optimization process – grouping and categorization – are recommended in international documents.

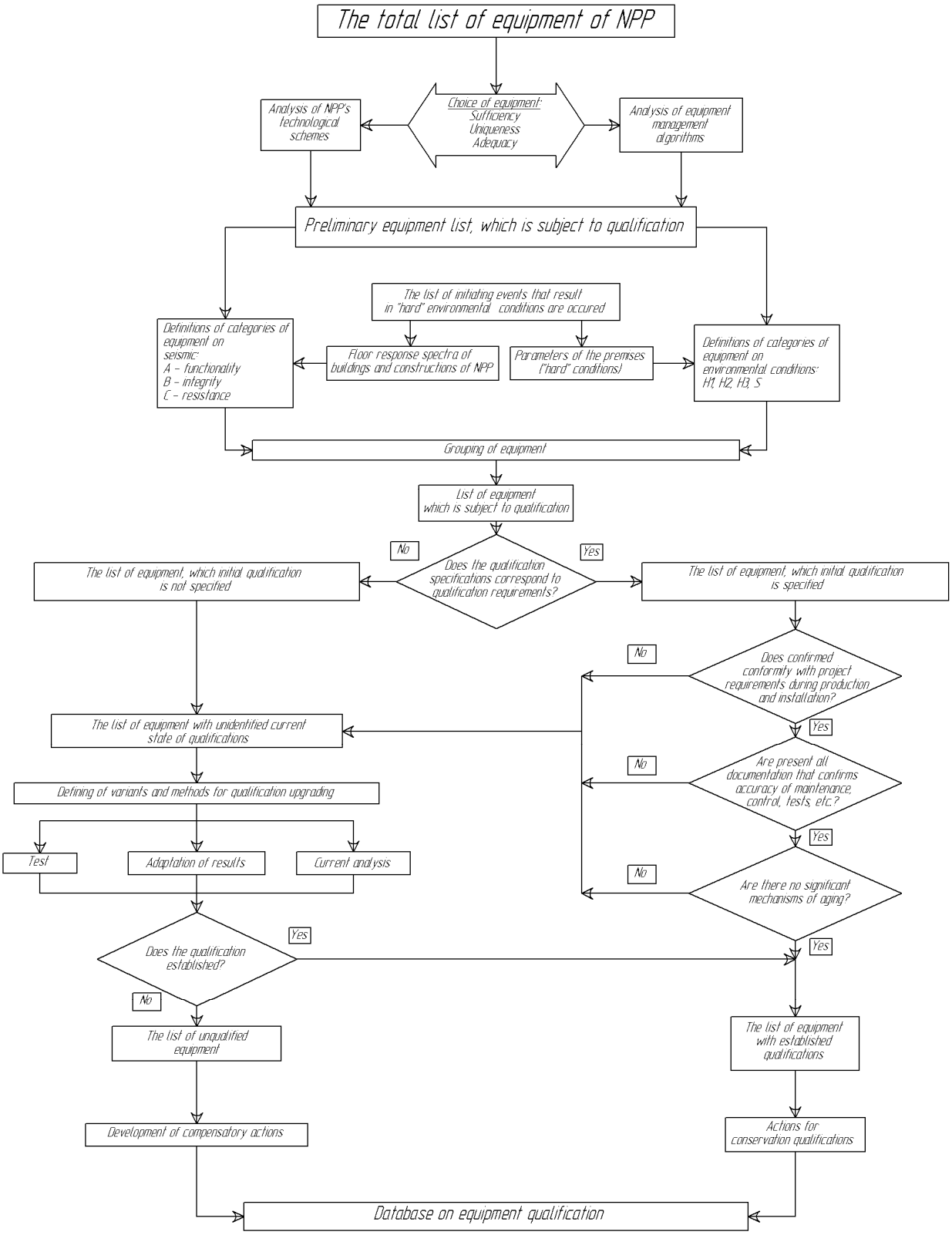

Fig. 1. General structural scheme of the equipment qualification fulfillment.

3. Establishing the Status of EQ

At the end of the stage of basic data preparation, we have the list of the equipment which contains the following data [4]:

- project (passport) parameters for each group of equipment (qualification characteristics);
- operating conditions, including environmental conditions, in which functioning of the equipment is required (qualification requirements).

In general, the point of qualification estimation is in comparing qualification requirements and qualification characteristics.

If all passport characteristics meet or exceed qualification requirements, the equipment qualification is determined (QD); otherwise it is not determined (QND).

Matching qualification characteristics and qualification requirements allows to determine in what extent requirements to the equipment of systems, important for safety, were considered during its projection and production (basic qualification status).

However, even if initially (according to passport data) the equipment is qualified, the deviation from technical requirements may occur during its installation. We should also take into account that the requirements concerning equipment operation may not be followed in the operation process. Besides, any equipment falls under aging in the operation process. These factors may lead to the changes of qualification characteristics of the equipment and, consequently, the state of the qualification.

The impact of these changes is taken into account in the estimation of the current state of the EQ.

Thus, the current state of the equipment qualification is determined, if:

1. during visual inspections the compliance with project requirements in the production and installation is confirmed;

2. all the necessary documentation which confirms the correctness of technical maintenance and repair, verification, testings, etc. is present on the nuclear power plant;

3. there are no significant aging mechanisms.

The equipment, which current state of qualification is impossible to estimate (for the reason of deviations during inspections, the lack of necessary operational documentation or inability of the estimation of the influence degree of significant aging mechanisms) is added to the list of the equipment with unspecified qualification. Methods of qualification enhancing are appointed for this equipment.

4. Measures on Qualification Enhancing

To enhance the EQ, different methods, depending on the group and category of the equipment and environmental conditions, may be used. They may include:

1. Qualification testings method – obtaining real equipment qualification characteristics during accelerated thermal, radiation and operational aging.

2. Method of analysis – determining qualification characteristics, by using appropriate analytical models.

3. The experience of operation – determining the qualification, by using the experience of the operation of comparable equipment of other nuclear power plants.

4. Adapting the results – analytically reasonable dissemination of the qualification results of similar equipment installed on other nuclear power plants, taking into account the experience of operation.

The equipment, qualification characteristics of which satisfy qualification requirements after measures on the qualification enhancement, are added to the list of the equipment with determined qualification. For such equipment measures on qualification preservation are developed and added to the database.

For the equipment, which qualification is not determined after the qualification enhancement, compensatory measures are developed and implemented. According to [1] and [2], such activities may include:

- the development and implementation of compensatory measures (for example, installation of protective shields, additional reinforcements, etc.);
- additional calculations and tests;
- modification (replacement of separate components, parts);
- replacement of the equipment with the new, modernized one.

The results of the implementation of compensatory measures are also added to the database on the equipment qualification.

5. Modernization of Methods and Technical Qualification Means. Development of Exploratory Radiation Stands of the Electrical Equipment Qualification

Long-term researches, fulfilled in the sector of radiation technologies NSD INR NAS of Ukraine, showed that the only possibility to realize complex qualification processes is the usage of electrophysical technique. It was demonstrated that on its basis it is possible to create specialized exploratory stands which combine all the necessary parameters of measurements of the components of qualification processes and allow to obtain the most correct information about resource capacities of the equipment. General structural scheme of such specialized radiation stand with advanced possibilities was developed taking into account the results of previous methodological researches.

The researches of modern technical possibilities of nuclear branch in Ukraine showed that the most available way of creating a technical complex which is necessary for functional radiation testings (stand) is the usage of two electrophysic sources of electrons, combined with the common program and hardware provision of the research of parameters of the experimental equipment. In the Fig. 2 the structure of such stand, which is developed, taking into account the conclusions of previous theoretical researches is presented.

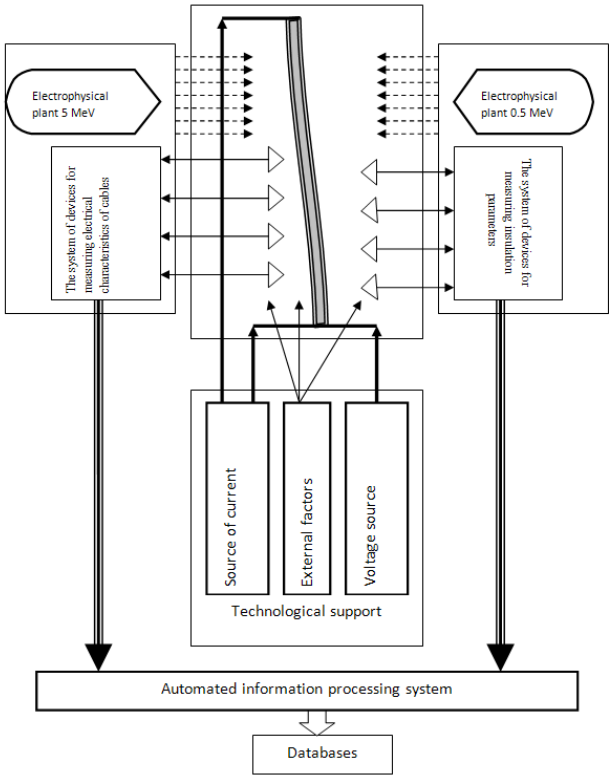

Fig. 2. Scheme of the stand for functional radiation testings.

The stand of such structure allows to fulfill complex and target researches of functional suitability of the electrical equipment, polymeric constructions and materials of nuclear installations as a whole or its components. This ability, in terms of the equipment qualification, may seem to be excessive, because during the qualification you should only find out, whether the equipment is suitable or not. But taking into account the necessity of the fulfillment of the complex program on enhancing the operational reliability of nuclear energetic and the extension of after-project operation terms, such complications of the stand structure are quite reasonable, because they allow to obtain much new valuable information.

In early stages the stand will be used for complex tests of various cable products and electrical equipment. It consists of the basic set of control and measurement devices, data processing systems, experimental modules for combining the possibilities of continuing material science researches (various insulation materials and coverings) and new technologies of functional testings. The stand is provided with the system of formation of all operational (up to the extreme ones) and external unfavorable factors including radiation.

The project of the stand takes into account new qualification methods. Unlike the typical method of consecutive testings with various operating factors (according to STD) [4 - 9]), new methods are developed for stands. They provide complex testing of electro-technical products under the influence of simultaneously the whole set of operational and external factors. With this purpose, various sources of current supply, chains of maximum voltage supply to the elements of the equipment, various technological devices for the formation of toxic chemical and temperature factors in the chamber, high- and low-energy source of ionizing radiation are provided in the equipment of the stand. By means of these technical facilities, it is provided not only to get answers concerning functional suitability of the equipment for the operation on the nuclear installation, but also to research the dependences of functions of the equipment on the influence of any operational or unfavorable factors. With this purpose, the power of information system should be high enough taking into account the necessity of the formation of a special base of new data about the processes which take place in the equipment, from the results of testings and researches.

The basis of this stand is the existing radiation technique in INR NAS of Ukraine – the experimental scientific and technologies installation with 4 MeV electron accelerator, which has been already adapted for the qualification tasks by means of appropriate technical modernization. The existing structure of this installation meets all the requirements of industrial radiation installations of wide usage.

An important part of the developed structure of the stand is the supplement of 4 MeV electron source with the additional electrophysical source of electrons of "Compton" energy (0.4 MeV) which are also of electro-physical type. This provides appropriate intensities of such source (current of the beam) and the possibility of very smooth regulation of electrons' energy. Previous estimates of energetic characteristics of the researched radiation-induced chemical processes in cables' insulation revealed the necessity to provide a stationary electron beam with the power of at least 20 kW, what is quite available for electrons' accelerators of direct action (Aurora, Electron etc.). They are rather cheap and have good industrial indexes (efficiency), what will improve production possibilities of new exploratory stands.

Conclusions

The provision of nuclear power plants' safety should be the priority in the construction, building and operation of power units. The process of the estimation of the equipment qualification level, recommended by the IAEA, is one of the most reliable methods of the verification of the equipment performance capacity.

In the process of the collection and analysis of technical documentation, while determining the initial state of the qualification, it is estimated, in what extent qualification requirements were considered during the projection of the equipment.

While estimating the current level of the qualification, all errors, made during the installation of the equipment, are identified and eliminated. Besides, the analysis of the the correctness of the operation of the equipment is fulfilled, what allows to identify and consider further possible non-project modes of work. In addition, the degree of degradation of the equipment because of aging under the influence of various operating factors is identified and taken into account.

During the estimation of the state of the qualification the recommendations concerning the preservation of the qualification for the equipment with determined qualification and compensatory measures for non-qualified equipment are developed.

As a result of the estimation of the current qualification level for NPPs' equipment the qualifying period is determined – the guarantee of nuclear power plants' safety during this period of time. The qualifying period also allows to repair and replace the equipment (or its parts) according to real indexes of the depreciation, what significantly improves economic indexes of the power unit.

REFERENCES

1. *Convention* on Nuclear Safety. INFCIRC/449. – Vienna: International Atomic Energy Agency, 1994.
2. *Equipment* Qualification in Operational Nuclear Power Plants: Upgrading, Preserving and Reviewing. Safety Reports Series No. 3.
3. *STP 0.03.050-2009*. The standard of the enterprise. Qualification of equipment and technical devices of NPP. General requirements.
4. *PM-D.0.03.476-09*. The program of works on the NPP equipment qualification NNEGC “Energoatom”.
5. *STP 0.03.083-2009*. Qualification of equipment on the environmental conditions. General requirements.
6. *IEEE* Standard 627-1980. Design Qualification of Safety Systems Equipment Used in Nuclear Generating Stations.

TIME TO REACH A GIVEN LEVEL OF NUMBER OF NEUTRONS IS STOCHASTIC ANALOG OF REACTOR PERIOD

V. V. Ryazanov

Institute for Nuclear Research, National Academy of Sciences of Ukraine, Kyiv, Ukraine

In theory and in practice the operation of nuclear reactors to control the safety of the reactor is widely used deterministic value - the period of the reactor. It is proposed along with the period of the reactor using a stochastic analogue of this magnitude - a random amount of time to achieve a given level of a random process for the number of neutrons in the reactor. The paper discusses various features of the behavior of the mean and variance of time to achieve a specified level. This kind of features can be associated with impaired behavior of the reactor system. Introduced the value of time required to reach the level can be used to monitor and improve the safety of nuclear power plants.

1. Introduction

In [1] the random variable characterizing the evolution of neutron time intervals, the time to reach the level of the number of neutrons in the reactor. Time to reach the level of neutron number is a random time to obtain the random process of the total number of neutrons in the reactor of a given level. In [1] is show that this value can be regarded as a stochastic analogue of the reactor period. In this paper we investigate the value fundamentally different from the reactor period - the time to reach the level of the number of neutrons in the reactor. It is defined from other assumptions in comparison with the period and has a physical meaning, corresponding to its name. The relations obtained for the statistical quantities - time to reach the level of the number of neutrons in the reactor, and distribution of this quantity are important, reflecting the behavior of real-life physical quantities finite time to achieve a given level of the number of neutrons in the reactor. The characteristics and behavior of this quantity will be useful in various problems of physics, the theory and methods of calculation of nuclear power reactors.

In [1] the distribution of time to achieve the level of the number of neutrons in the reactor, from which you can record not only the average level of achievement, but also all moments of this value, and such probabilistic characteristics as the probability that the time to reach the level of the number of neutrons in certain prescribed limits are calculate. The advantage of this approach is that at the points of a dangerous change in reactivity, which can lead to emergency situations, the moments (e.g. mean and variance) of the random variable time to achieve the level of the number of neutrons in the reactor have singularities. They may, for example, take the complex or negative values. Estimate of the average time required to reach the level of the number of neutrons in the reactor and of the variance of this quantity may serve as one of the practical applications of the proposed description of the various options by changes in reactivity over time. These changes are assumed to be given. Features of the behavior of the moments of time required to reach level will indicate the instability of the neutron system. Thus, taking into account the different effects that contribute to the reactivity, it is possible to choose a safe change. Mathematical expressions for the mean time to achieve the level of neutron number is simpler and clearer relations connecting the period of reactor with reactivity. These expressions are easily calculated. The algorithm is as follows: given change in reactivity over time. According to the obtained relations and graphs are determined the moments in which the change in reactivity can lead to the values of the average time required to reach the level of neutron number corresponding to the low periods of the reactor.

2. Features of the behavior of the moments of time required to reach level

For the average time to achieve, calculated in accordance with the expressions of [1], the numerical calculation gives the following feature at a value of reactivity is equal to β, reactivity jump on the prompt neutrons (Fig. 1). We also give an example of behaviors of dispersion of time to achieve the level for the case of a jump to the prompt neutrons, Fig. 2.

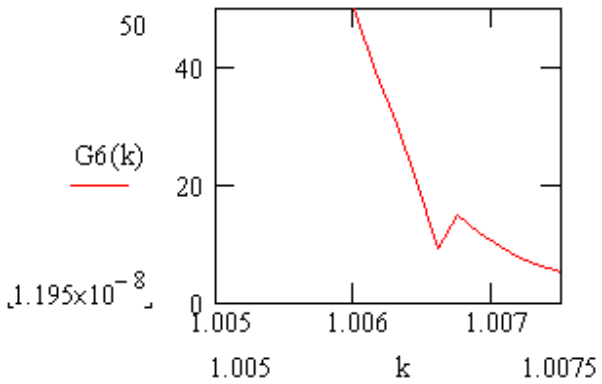

Fig. 1. Average time to achieve of level by ρ = β.

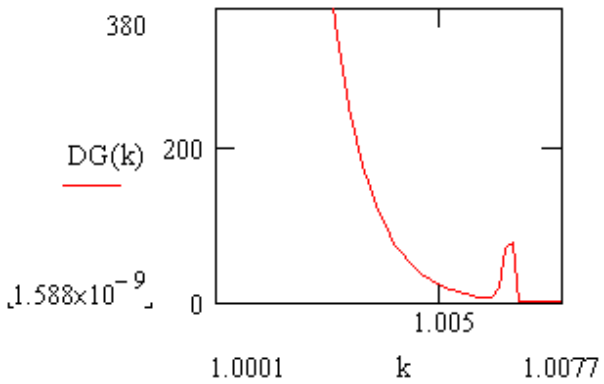

Fig. 2. Dispersion of time to achieve the level by ρ = β.

By simulating the behavior of these moments in the various processes in the reactor, it is possible to track their characteristics, thereby controlling the safety of the reactor. In [1] are obtained expressions for the moments that take into account the dynamics of changes in reactivity over time. But on the same temporary value the averaging is carried out. Therefore, in this paper, we propose to distinguish two times: we must distinguish between the integration over the possible time required to reach the level of Γ, the averaging time and the current time t. These are different times. In [1] is assumed as the same time, $\rho(t = \Gamma)$. This, apparently, can serve as a first approximation. In the general case, we must distinguish $\rho(t,\Gamma)$. The dependence of the time required to reach the level of the current point in time can be allowed, for example, by introducing dependence of the effective neutron multiplication factor k from the current point in time t, and from the moment of the lifetime of Γ:

$$k(t,\Gamma), \quad \Gamma=\begin{cases} t, & t\le\Gamma_f \\ 0, & t>\Gamma_f \end{cases}, \tag{1}$$

where Γ_f is a random moment of the end of the lifetime. In terms of the form (2) (after substituting in them (1)) can be integrated over Γ, and the dependence on the current time counted by $k(t)$. By the time Γ averaging is carried, and the current time t takes into account the real dynamics of the system, occurring in the system changes due to external influences and internal factors. Another approach is possible, when taken into account the dependence of reactivity from the current time $\rho(t)$. As in [1], carried out the averaging on t. In the above relations substituted time-dependent reactivity $\rho(t)$. It is assumed that spent an averaging over time to achieve the level at one point in the current time can also be performed at any other time of the current time, and write the relation [1]

$$l_{ef}Z(t)=(1-\beta)(\exp[R\omega_0(t)]-1)/\omega_0+\beta b(\exp[R\omega_1(t)]-1)/\omega_1 \tag{2}$$

$$P(\Gamma,t)=[(1-\beta)\exp[\Gamma\omega_0(t)]+\beta b\exp[\Gamma\omega_1(t)]]/l_{ef}Z(t)$$

$$\langle\Gamma(t)\rangle=\{(1-\beta)[\exp[R\omega_0(t)](R\omega_0(t)-1)+1]/\omega_0^2+\beta b[\exp[R\omega_1(t)](R\omega_1(t)-1)+1]/\omega_1^2\}/l_{ef}Z(t)$$

(or a more general expression of the type $l_{ef}Z_{\gamma_L}=\int_0^R e^{ty(t)/R}dt,\ldots$ $y(t)$ is function from $k(t)$ [2]), where the notation of [1]: $l_{ef}=1/v\Sigma_a\approx 10^{-8}$- 10^{-3} s is mean effective neutron lifetime; v, Σ_a are the average velocity and the cross section of neutron absorption, respectively; for thermal neutrons $l_{ef}=1/v\Sigma_a\approx 10^{-3}$ s, $Z(t)$ is partition function, $\rho=(k-1)/k$ is the reactivity of the reactor; $\lambda=0,077\ s^{-1}$ is the effective decay constant of delayed neutron precursors, $\beta=0,0065$ is the fraction of delayed neutrons, $\omega_{1,2}$ are return value for a period of effective groups of delayed neutrons, $b=\lambda l_{ef}$, $\Gamma_{\max}=R$ is maximum possible time to reach of level.

Thus, there are three main possibilities describing of the temporary change of reactivity.

1. As in [1]. Current time coincides with the space of possible averaging time of averaging, $\rho(\Gamma = t)$.
2. For each current time t is carried out averaging over Γ, then take into account the dependence of $\rho(t)$, as in (1). Considering the dependence of $\rho(\Gamma, t)$.
3. Just as in (2), but not allocated time Γ, and assume that for each time averaging is carried out, and after averaging takes into account the dependence of $\rho(t)$, as in (2). When $\Gamma = t$, averaging over Γ is carried out taking into account that $\rho(\Gamma = t)$. That is, first averaging over Γ in $\rho(\Gamma, t)$, and then take into account the dependence of $\rho(., t)$.

This calculation gives a more "smooth" dependences on the increase in reactivity, the average time to reach the level falls are not as dramatically as without depending on the current time in considered in the following example- in the case of two peaks of reactivity when connecting of loop of main coolant pump (*MCP*).

Estimates of moments of time to achieve the level of the number of neutrons can be made when the reactivity is changes due to in the composition of the core, fuel burn, poisoning of the reactor, xenon oscillations and other phenomena that accompany the reactor.

Consider the following example. In [2] investigated the connection of a loop which has not previously worked when reactor plant on two *MCP*s. In the regime of "connection *MCP* previously broken loop" increase consumption and decrease the temperature of the coolant at the reactor inlet of the plug-in loop causes a pronounced asymmetric behavior of the characteristics of the active zone. As a result, the connection previously broken hinges on the first ten seconds of the transition process is an increase in coolant flow through the reactor. The increase in consumption leads to a decrease in heating the coolant to the core and, consequently, to reduce the average temperature of the coolant in the reactor. Due to the negative temperature coefficient of reactivity in the reactor is introduced positive reactivity (Fig. 3, the first peak of reactivity was 0.13 %). The introduction of positive reactivity leads to an increase in neutron and thermal power of reactor (Fig. 3).

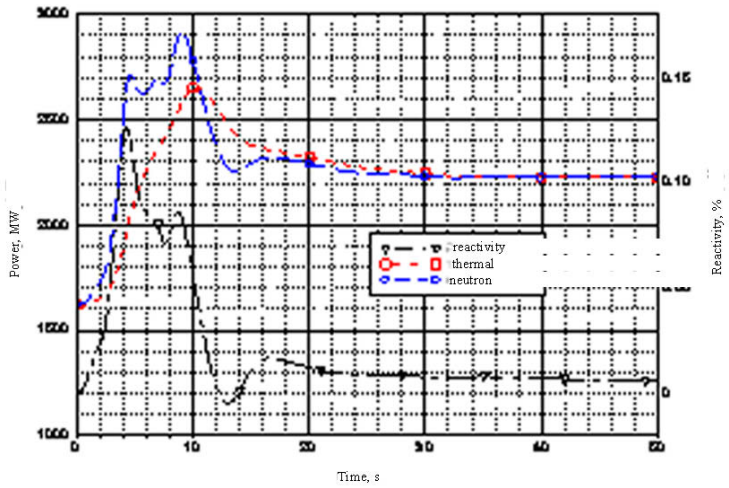

Fig. 3. Changing the reactivity and the neutron and thermal power in the transition process.

At the seventh seconds cold coolant of the connected loop begins to flow into the core, causing an additional increase in reactivity (Fig. 3, the second peak) and a further increase of the neutron power of reactor (Fig. 3), the maximum value of which reaches 2924 MW on 9.1 s. The second peak of reactivity is lower of the first and is 0.09 %. The maximum value of the thermal reactor power in the transition process is 2653 MW. In the future due the feedback, the reactivity tends to zero, and neutron and thermal power are stabilized at the level of 2255 MW by the end of the transition process.

A pronounced imbalance of energy release causes an increase of integrated neutron power of the maximum loaded fuel rod with 55 kW to 126 kW (129 % power ramp-down), and the heat power from 55 kW to 110 kW (power ramp-down 100 %). In this case, the maximum fuel temperature in the transition process reaches 1998˚C for the fuel rod, and the minimum value of the safety factor is 1.15, ie observed the eligibility criteria for this type of accident.

Consider the changes in magnitude of the first and second peaks of positive reactivity and the effect of these changes on the average time to achieve the level. *m* denote the value of the first peak of reactivity. Numerical calculation of the dependence of the average time to achieve the level from *m* is shown in Fig. 4.

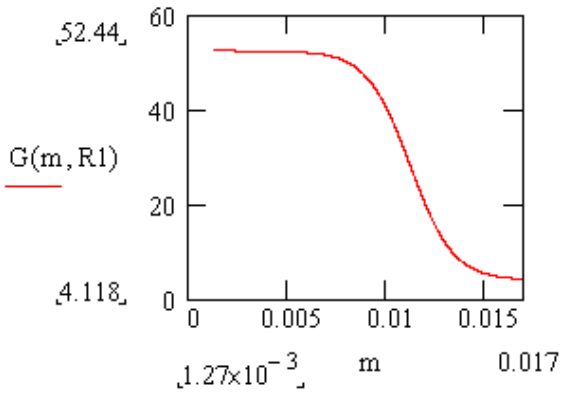

Fig. 4. The dependence of the average time to achieve the level from *m*.

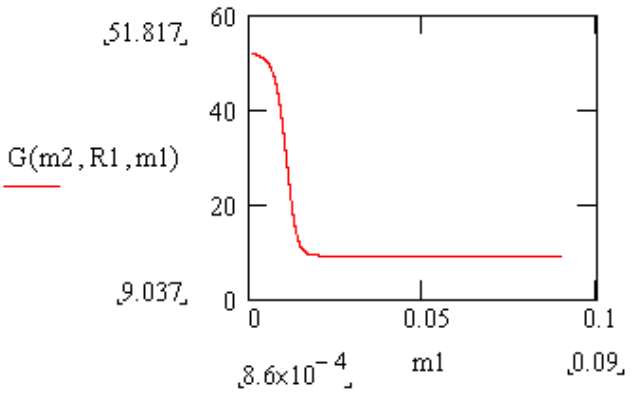

Fig. 5. The dependence on the magnitude of the reactivity of the second peak, designated m_1.

It is seen that with increasing *m* values of the average time required to reach a level corresponding to the period of the reactor, are reduced to dangerously low values (less than 10 seconds). Similarly, the dependence on the magnitude of the reactivity of the second peak, designated m_1. This dependence with $m = m_2 = 0{,}127 \cdot 10^{-2}$ shown in Fig. 5.

In Fig. 6 shows the dependence from m_1 for $m = 0{,}0069$.

In Fig. 7 shows the dependence of the average time required to reach the level for the example considered in [1] from [4] for different values of the initial perturbation of reactivity $\rho_{pert} = p$. It is seen that for certain values $\rho_{pert} = p$ there is no value of the average time to achieve the level of Tm (R, p).

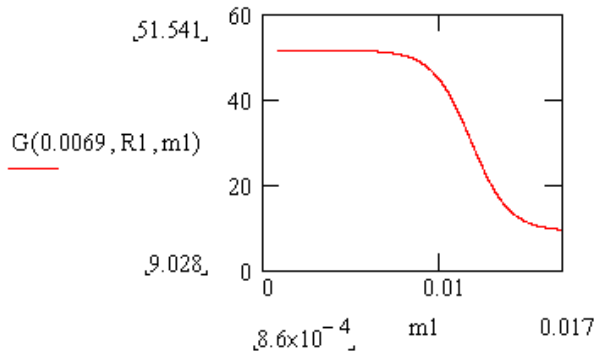

Fig. 6. The dependence of the average time from m_1 for m = 0,0069.

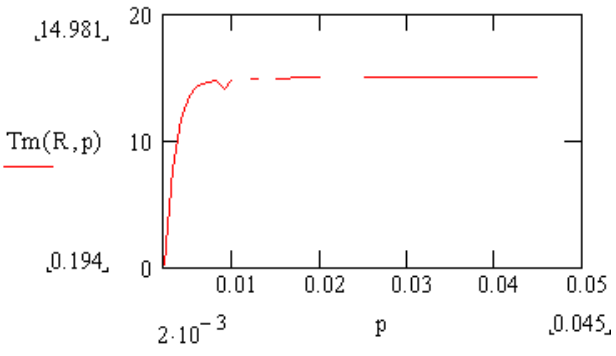

Fig. 7. The dependence of the average time required to reach the level for different values of the initial perturbation of reactivity $\rho_{pert} = p$.

3. Conclusions

There are many examples of various features of the behavior of the average time to achieve the level. The goal is to systematize such examples, to identify patterns in them. It should also investigate in detail the ways to incorporate these temporal behavior of the time required to reach the level, analyzing their advantages and disadvantages.

REFERENCES

1. *Ryazanov V.V.* Distribution of time to achieve the level of neutron number and the period of the reactor // Atomic energy. - 2011. - Vol. 110, No. 6. - P. 307 - 317.
2. *Ryazanov V.V.* Stochastic analog of reactor period - time to reach a given level of number of neutrons // Problems of nuclear power plants safety and of Chornobyl. - 2012. - Vol. 19. - P. 8 - 18.
3. *Ovdienko N.* Safety assessment of VVER-1000 transients and reactivity accidents operation using the model of the spatial kinetics: Thesis for the degree of candidate of technical sciences. - Kyiv, 2010.
4. *Sarkisov A.A., Puchkov V.N.* Physical principles of operation of nuclear steam supply systems. - Moscow: Energoatomizdat, 1989. - 504 p.

AUTOMATED INSTALLATION FOR THE REMOTE CAPSULATION OF AMPULE RADIATION SOURCES FOR THE INDUSTRIAL DEFECTOSCOPY ON BASIS OF RADIOISOTOPE IRIDIUM-192

P. M. Vorona[1], V. M. Shevel[1], V. P. Levchenko[2], S. V. Dubovetskiy[3], O. E. Frolov[3]

[1] Institute for Nuclear Research, National Academy of Sciences of Ukraine, Kyiv, Ukraine
[2] LTD "RADIOFARM", Kyiv, Ukraine
[3] Research and Production Company "NAVKO-TEH", Kyiv, Ukraine

The installation for the remote welding of the thin-walled capsules with the gamma-emitting radioactive substance was created at the WWR-M research reactor for the goal of manufacturing of the radionuclide ionizing radiation sources using the ^{192}Ir isotope. The installation allows carrying out the TIG welding (Tungsten Inert Gas) by the automatic mode without an incorporation of the additive materials of annular seams to the low-carbon, alloyed and structural steels for the seam diameters in the range from 4 to 20 mm.

1. Introduction

The program aimed on the organization of the domestically produced radionuclide materials for the science and various applied uses (medicine, techniques and other areas) is in progress now in the Institute for nuclear research NAS of Ukraine. The structure of technological cycle for the production of radioactive materials [1] consists of following components: the generation of radionuclides by means of irradiation in the reactor; the remote treatment of high-active material in the hot-cells and the manufacturing of the desired product; the certification of this product; the organization of the product supply to the end-users. Recently, the development of each component aimed on the scientific and technical provision of the technological process was completed under support of the STCU and CNCP international funds [2 - 12]. This paper presents the development of the technical provision for the manufacturing of the closed high-active ionizing radiation sources with the reactor radioisotopes.

2. Closed ionizing radiation sources with ^{192}Ir

Closed ionizing radiation sources (further – IRS) with the radioisotopes are widely used in the modern practice, in particular, in the industrial defectoscopy for the gamma-raying of the metal constructions and welded seams as well as in the medicine for the medical treatment of cancer (for example, by the brachytherapy method). The radioisotopes of various chemical elements are used in such IRS as the gamma-emitters. One of the most used IRS is the radioisotope source on the base of reactor radioisotope ^{192}Ir with the half-life of 74.02 hours. The typical value of the IRS activity, which are used in the industrial defectoscopy, lies in the range form 3 to 9 TBq. This value is corresponding to the gamma-ray exposure dose rate in the range from 20 to 110 R/h at the distance of 1 m.

The generation of the ^{192}Ir radioisotope is carried out at the irradiation of the Iridium targets by the reactor neutrons in the nuclear reactions ^{191}Ir(n, γ) ^{192}Ir(n, γ) ^{193}Ir(n, γ). The dynamics of nuclear reactions is depending on the neutron reaction cross-sections, the neutron flux and the neutron spectrum. The calculations of the neutron flux and their relevant spectral characteristics in the irradiated areas were performed for the obtaining of neutron data, which are necessary for the irradiation optimization and the estimation of ^{192}Ir accumulation [7]. The experimental measurements of the neutron cross-sections with the Iridium isotopes (^{191}Ir, ^{192}Ir, ^{193}Ir) were performed too [13, 14]. On the base of both calculation and experimental investigations of the ^{192}Ir accumulation it was shown that the ^{192}Ir specific activity about of 5.8 GBq/g (per 1 g of the natural Iridium) can be generated from the Iridium target in the reactor Beryllium reflector at the twenty irradiation days. This provides the possibilities for the manufacturing of the powerful sources, which are corresponding to the requirements of the industrial defectoscopy for the IRS activities. Thus, for example, the experimental ^{192}Ir sample prepared for the neutron cross-section measurements has the activity of 4.2 TBq [13, 14].

The challenging problem at the manufacturing of such IRS for the industrial application is the provision of reliable insulation of the source's radioactive material from the contact with the environment as well as the prevention of its dispersion and the guarantee of the IRS safe operation during the whole operation period. One of the most reliable methods for the provision of these requirements is the capsulation of the radioactive substance into the metal capsule by means of welding. For this goal the technology of remote treatment of the high-active samples in the hot-cells and the automated installation for the remote welding of the capsules were developed.

3. Automated installation for the remote welding of the closed IRS capsule

The technical characteristics of developed installation allow the welding of the standard IRS capsules, which are using by the "GAMMARID" industrial defectoscopes. The IRS working part consists of the irradiated disk-shaped Iridium foils made from the natural iridium. The thin-walled capsules for such IRS made from the stainless steel; the capsule diameter is equal to 5-6 mm, the height – 6-7 mm.

The TIG (Tungsten Inert Gas) technology is used in the installation, i.e. the arc electrical welding by means of the infusible tungsten electrode in the atmosphere of the protective gas argon. The installation's basic units are following: 1) the welding tool; 2) the mechanism for the welding tool moving (up-down); 3) the adjuster of the welding tool

position; 4) the welding rotator; 5) the device for the assembling-welding; 6) the takeout; 7) the assembling frame; 8) the pneumatic automation; 9) the control unit; 10) the high-voltage power supply; 11) the operator's console. The units assigned for the welding are assembled on the separate frame (the executing mechanisms unit). The common view of this unit together with the technical characteristics is shown in Fig. 1.

Technical characteristics

Circular seam diameter, mm	4 - 20
Welding position	lower
Drive for the welding tool moving	pneumatic
Fixing	mechanical clip
Welding current regulation range, A	8 - 160
Welding rate regulation range, mm/s	0 - 10
Protective gas	Argon
Welding tool cooling	air
Compressed air pressure, MPa	≥ 0,4

Fig. 1. The executing mechanisms unit and the technical characteristics of the installation for the remote welding of the thin-walled capsules.

The installation is located in the reactor's hot-cells, which are the constituent of the radioisotope generation technological cycle at the reactor [1]. The installation's principal part, namely, the executing mechanisms unit, is installed in the protective box of the hot-cell No. 4. The auxiliary mechanisms destined for the installation operation are located in the operator room of this hot-cell for the maintenance simplification. The technology destined on the mounting of the IRS working part into the stainless steel thin-walled capsules with the consequent welding of their covers are already developed and tested in the hot-cells. All working operations are carried out distantly by means of the manipulators and additional remote tools aimed for the works with the high-active substances.

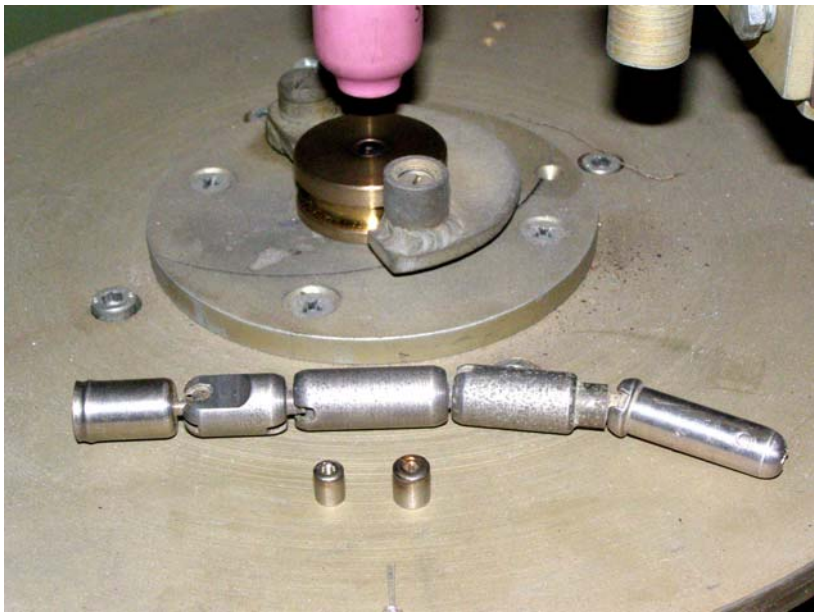

Fig. 2. The welded IRS capsules (two pieces ahead) and the technological chain of the industrial defectoscope "GAMMARID".

The starting-up and adjustment of the welding remote control was performed, which allows to obtain the high-quality seams at the different diameters. The welded capsules (two pieces ahead) are shown in Fig. 2; the technological chain of the industrial defectoscope "GAMMARID" is shown on this figure too; the prepared IRS is placed remotely to the front end (left) of this technological chain; all details are shown on the rotating face-plate of the welding installation.

The commissioned installation is ensuring surely a following:

1) The program control of all installation's mechanisms and tools as well as their reliability diagnostics by means of the computer;
2) The control of the equipment readiness, the welding tool position and the pressure in the system;
3) The execution of the welding operations, i.e. the lowering of welding tool to the starting point of jointing; the arc firing at the immovable ampoule; the rotation of capsule with the welding speed; the jointing closing; the lifting of welding tool and the return of face-plate into starting position.
4) The exact setup of the welding parameters and the overlapping length;
5) The smooth regulation of the face-plate rotating rate.

The commissioned welding installation will be used for the capsulation of the IRS thin-walled capsules using the ^{192}Ir isotope, which is used not only in the industrial defetoscopy, but in the medical treatment of cancer by the brachytherapy method. It is necessary to mention that the performed testing has confirmed the broad possibilities of the installation for the automatic TIG welding without an incorporation of the additive materials of annular seams to the low-carbon, alloyed and structural steels.

This work was supported by SSTU, project No P437.

REFERENCES

1. *Vorona P.M.* The use of the WWR-M reactor for the manufacturing of radionuclide products // 40th anniversary of the neutron investigations on the WWR-M reactor: Proc. of the scientific conf. INR NASU. - Kyiv, 2000. - P. 48 - 55.
2. *Vorona P.M., Isakas I.E., Shustov V.O.* Optimization of the neutron and physical parameters of the research reactor for the experimental investigations of the radioactive nuclei neutron cross-sections // Nuclear and radiation technologies. - 2006. - Vol. 6, No. 3 - 4. - P. 67 - 72.
3. *Vorona P.M., Razbudey V.F.* WWR-M research reactor as the neutron source for the radioisotopes generation and scientific investigations // 6th Int. Conf. "Nuclear and radiation physics" (Almaty, Kazakhstan, 4 - 7 June 2007): Book of abstracts. - Almaty, 2007. - P. 607 - 609.
4. *Berlizov A.N., Vorona P.M., Malyuk I.A. et al.* Non-destructive method of the certification of the ^{90}Sr - ^{90}Y sources by means of high-resolution gamma-spectrometry // 6th Int. Conf. "Nuclear and radiation physics" (Almaty, Kazakhstan, 4 - 7 June 2007): Book of abstracts. - Almaty, 2007. - P. 617 - 618.
5. *Vorona P.M., Razbudey V.F.* Calculation-analytical investigations of neutron-physical characteristics of WWR-R nuclear reactor of INR NAS of Ukraine // Proc. of the 2nd Int. Conf. "Current Problems in Nuclear Physics and Atomic Energy" (Kyiv, 9 - 15 June, 2008): Book of Abstracts. - Kyiv, 2008. - P. 70 - 71.
6. *Berlizov A.N., Vorona P.M., Malyuk I.A. et al.* Gamma-spectrometry of the radioisotope products at the WWR-M reactor // Annual report / Institute for Nuclear research NASU. - Kyiv, 2009.
7. *Vorona P.M., Razbudey V.F.* Calculation investigations and analysis of the characteristics of the WWR-M research reactor as the neutron source for the scientific and applied tasks // Nucl. Phys. At. Energy. - 2010. - Vol. 11, No. 1. - P. 57 - 62.
8. *Vorona P.M., Razbudey V.F.* Calculational investigator for optimization of radionuclides production technology in the research reactor WWR-M // Proc. of the 3-rd Int. Conf. "Current Problems in Nuclear Physics and Atomic Energy" (Kyiv, 7 - 12 June, 2010). - Kyiv, 2011. - Part II. - P. 576 - 580.
9. *Vorona P.M., Shevel V.M.* Stationary processing line for series manufacture of the ^{99m}Tc-pertechnetate radiopharmaceutical production on the WWR-M reactor // Proc. of the 3-rd Int. Conf. "Current Problems in Nuclear Physics and Atomic Energy" (Kyiv, 7 - 12 June, 2010). - Kyiv, 2011. - Part II. - P. 581 - 583.
10. *Vorona P.M., Razbudey V.F.* Influence of the neutron energy on the generation of the radionuclides at the target irradiation in the reactor // Nucl. Phys. At. Energy. - 2011. - Vol. 12, No. 3. - P. 235 - 241.
11. *Vorona P.M., Gritzay O.O., Kalchenko O.I., Klimova N.A.* Specific neutron data library for radioisotope accumulation calculations at the research reactor // Proc. of the 4-rd Int. Conf. "Current Problems in Nuclear Physics and Atomic Energy" (Kyiv, 3 - 7 Sept., 2012): Book of Abstracts. - Kyiv, 2012. - P. 114.
12. *Tryshyn V.V., Ageev V.A., Shevel V.M., Bezdrobna L.K.* Development of technologies and organization of radiopharmaceuticals production at the Institute of Nuclear Research of the National Academy of Sciences of Ukraine // Ukrainian Journal of Radiology. - 2011. - Vol. XIX, No. 3. - P. 329 - 331.
13. *Vertebnyi V.P., Vorona P.N., Kaltchenko A.I. et al.* Neutron cross-sections for the iridium isotopes // Neutron Physics: Proc. of the 5th All-Union Conference (Kiev, 15 - 19 Sept. 1980). - Moscow, 1980. - Part 2. - P. 114 - 118.
14. *Vertebnyi V.P., Vorona P.N., Kaltchenko A.I., Krivenko V.G.* Neutron Resonances of ODD-ODD Radioactive Isotopes // Nuclear Cross Sections Technology: Proc. of the Int. Conf. (Knoxville, TN, October 22 - 26, 1979). - Washington, 1980. - P. 881 - 885.

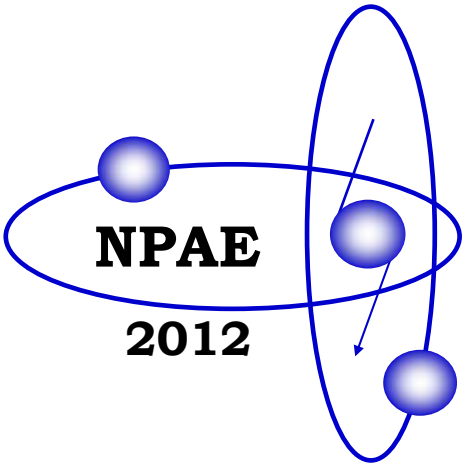

Section 7

Applied Nuclear Physics, Experimental Facilities and Detection Techniques

LOW-BACKGROUND CHAMBER FOR THE GERMANIUM GAMMA SPECTROMETER

A. V. Andreev[1], Yu. M. Burmistrov[1], E. S. Konobeevski[1], M. V. Mordovskoy[1], S. V. Zuyev[1], V. I. Firsov[2]

[1] Institute for Nuclear Research, Russian Academy of Sciences, Moscow, Russia
[2] State Atomic Energy Corporation "Rosatom", JSC "GIREDMET", Moscow, Russia

The goal of the project is a development of low-background setup based on a high-purity Germanium detector and a complex of external and internal shielding to reduce the background of external gamma radiation, space radiation and radiation from shielding materials. Various variants of external and internal shielding were studied. The achieved backgrounds level on this moment the ~ 3.8 cps and should be lowered in the near future by using materials with lower contents of natural radioactive elements (steel, copper). First results have been obtained also using "active shielding", consisting of plastic scintillator and DPP technic.

Low-background measurements using germanium detectors are held in underground or surface laboratories. The background level in underground laboratories, are generally much lower than in the ground. By placing gamma spectrometers underground we reduce the natural background caused by cosmic particles. Choice of the mines containing very little uranium and thorium (serpentine rock) reduce background too.

However, measuring the activity of the samples (particularly those containing short-lived isotopes), irradiated in accelerators and neutron generators, should be carried out near the irradiating apparatus (i.e. in surface laboratories).

One of the main characteristics of the setup is the integrated background (counts per second, cps) in the given range of energy gamma-ray. This value is most often used to compare different setups.

We was used this parameter to evaluate the performance of configurations, choosing the optimal variant of the external protection and construction of low-background chamber.

However, but if your set is not designed to search for rare processes, this parameter may not be the most important. For measuring the content of certain substances is often requires knowledge of the intensity of certain gamma lines.

For further comparison we will use data from other laboratories which were reduced to the efficiency of our detector (Tab. 2). And we'll discuss only the "ground" setups with the cost is not too overwhelming ours.

In 2011, the low-background setup was installed based on a germanium gamma-ray spectrometer to measure the background and content of the nano-impurity in materials. For measurement of gamma-ray spectra was used the detector made of high purity germanium crystal of 130 cm^3 and 30 % relative efficiency.

For the processing of the measured gamma-ray spectra were used programs «Angamma» and «SpectraLineGP» (GammaPrecision) - for the precision machining of gamma-ray spectra, identification and activity calculation (LLC "LSRM", it supports all analyzers manufactured by JSC SPC "Aspect").

In the present work we tested two versions of low-background chambers of various configurations and sizes to use as materials for the external protection of two types of lead different by producing country - the "Russian" (Pb-1, the ring - the outer diameter of 420 mm, inner - 220 mm, height 100 mm) and the "Bulgarian" (Pb-2, curly bricks) and with the internal protection of electrolytic copper thickness of 20 mm (Fig. 1, *a* and *b*).

Comparative measurements of U and Th contents in protective materials showed (Table 1) that the contents of the U and Th in the "Bulgarian" lead lower than in "Russian". Therefore, the Bulgarian lead was used as the basis for creating low-background chamber for further research, and the Russian lead was used for the other chamber, designed for already existing methods of neutron activation analysis.

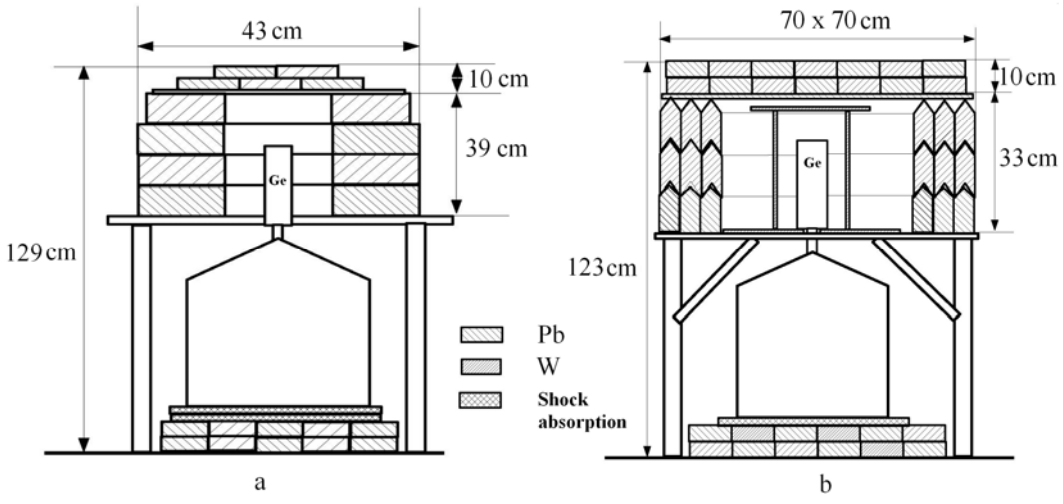

Fig. 1. Low-background chamber: *a* – Pb - ring; *b* Pb - curly bricks.

Table 1. **Contents of the U and Th in protective materials**

Defined element, % by weight	Analyzed material		
	Pb-1*	Pb-2**	Cu***
U	$3{,}5{\cdot}0^{-5}$	$<3{\cdot}10^{-5}$	$<5{\cdot}10^{-5}$
Th	$1{,}0{\cdot}10^{-4}$	$4{\cdot}10^{-5}$	$7{\cdot}10^{-5}$

* "Russian", ** "Bulgarian", *** Oxygen-free electrolytic copper.

The spectrometer is placed on a concrete platform with the detector's Dewar underneath. It was found that one must use a massive external protection under the Dewar detector to reduce the contribution of the gamma-line of isotope K-40.

During the long-term measurements of the background sometimes is observed instability of the intensities of some gamma-ray lines decay products Ra-226. This is possible due to the changes in the concentration of radon near detector, and indoors. Sealing and venting with nitrogen working chamber is the next step of work.

When testing various options of protection of the camera made from the lead ring the integral background values of 8 cps were obtained. The choice of the external protection made from the Bulgarian lead and the internal protection made from tungsten (20 mm thickness) reduces this amount to 5 cps that is a good indicator for ground installations without the active protection

Further reduction of the integral background was achieved via the subsequent optimization of protection by reducing the internal volume of the chamber to 15*20*30 cm3 and via the use for self-protection (together with tungsten) the sheet of electrolytic copper with thickness of 20 mm. This reduced the total background to 3.8 cps.

Fig. 2 shows the spectrum of the background, measured from the highest purity germanium detector in a low-background chamber made from the Bulgarian lead for 24 hours. Table 2 shows area of the most intense gamma-ray lines of the spectrum.

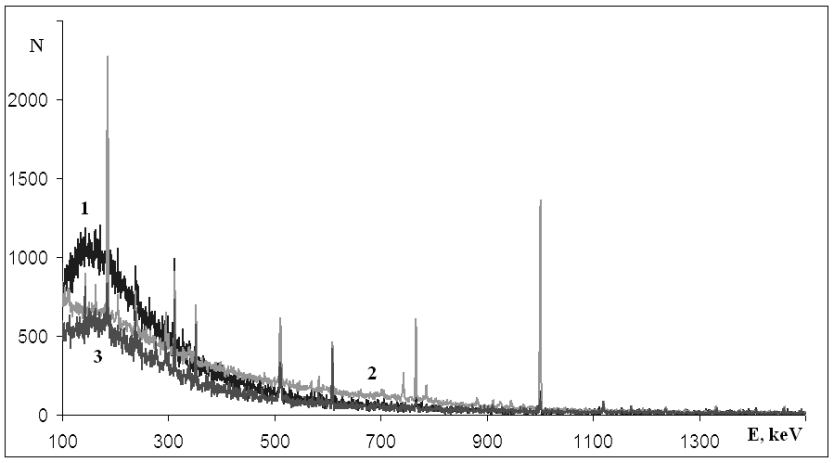

Fig. 2. Gamma spectrum of the natural background depending of different sets of materials:
1 - Pb; 2 - Pb + W; *3* - Pb + Cu + Sn + Cu.

Table 2. **Intensity of some gamma-ray lines of the natural background detector**

Element	Isotope	The energy of the gamma line, keV	The intensity of the main lines of gamma background, imp / c				
			Rossendorf* [1]	LRK-1 MEPhI [2]	ORTEC LAB [3]	NIST** [3]	INR RAS (this work)
U	U–235	185.7	$7.3 \cdot 10^{-3}$	$2.8 \cdot 10^{-3}$	$0.4 \cdot 10^{-3}$	–	$3.6 \cdot 10^{-3}$
Th	Pb–212	238.7	$25 \cdot 10^{-3}$	$3.1 \cdot 10^{-3}$	$1.0 \cdot 10^{-3}$	$0.4 \cdot 10^{-3}$	$1.5 \cdot 10^{-3}$
U	Pb–214	295.2	$10 \cdot 10^{-3}$	$0.4 \cdot 10^{-3}$	$0.7 \cdot 10^{-3}$	$0.3 \cdot 10^{-3}$	-
U	Pb–214	351.9	$16 \cdot 10^{-3}$	$1.0 \cdot 10^{-3}$	$1.1 \cdot 10^{-3}$	$0.8 \cdot 10^{-3}$	$4.0 \cdot 10^{-3}$
Th	Tl–208	583.2	$9.0 \cdot 10^{-3}$	$1.2 \cdot 10^{-3}$	$0.8 \cdot 10^{-3}$	$0.2 \cdot 10^{-3}$	$0.8 \cdot 10^{-3}$
U	Bi–214	609.3	$17 \cdot 10^{-3}$	$1.2 \cdot 10^{-3}$	$1.2 \cdot 10^{-3}$	$0.8 \cdot 10^{-3}$	$4.1 \cdot 10^{-3}$
Th	Ac–228	911.2	$9.6 \cdot 10^{-3}$	$0.7 \cdot 10^{-3}$	–	–	–
K	K–40	1460.6	$1.1 \cdot 10^{-3}$	$0.8 \cdot 10^{-3}$	$7.0 \cdot 10^{-3}$	$0.2 \cdot 10^{-3}$	$0.18 \cdot 10^{-3}$
Co	Co-60	1173	$1.7 \cdot 10^{-3}$	$0.1 \cdot 10^{-3}$	$0.2 \cdot 10^{-3}$	$0.5 \cdot 10^{-3}$	$0.3 \cdot 10^{-3}$

* Zentralinstitute fur Kernforschung, Rossendorf.
**Center for Analytical Chemistry, National Institute of Standards and Technology, Gaithersburg, USA.

The next step will be purging the chamber with nitrogen, optimizing the geometry of the protection under the detector and the use of "active shielding".

Active shielding is supposed to use scintillation detector located outside the lead shielding, and working in a mode of anticoincidence with a germanium detector.

The first debug measurements with organic scintillator dimensions 50 × 50 × 5 cm located above the main camera protection Ge detector were conducted. Measurements were taken by means of the digital pulse processing module DPP (Mod. DT5720C, 2 Channel, 12bit, 250MS/s Waveform Digitizer developed by CAEN - Costruzioni Apparecchiature Elettroniche Nucleari SpA [4]), the waveforms of the Ge detector signals and the signals from the two ends of the scintillator were recorded. The amplitude range allows recording the entire spectrum of the signals of detectors, the time range corresponded to the 50 microseconds scan and allows one to see the entire time picture of the passing of coincident events. Then, from the three-dimensional diagram (time, relative to the signal Ge detector, the amplitude of the Ge detector, the individual amplitudes or the sum amplitude of the signals of PMT) were selected loci of coincident events.

Preliminary results show a decrease in the background is about 1.5 times in the range 1 - 3 MeV and a little less in the 100 - 500 keV. These are only first preliminary data.

In the near future it is proposed to surround the chamber with additional 4 similar scintillation detectors. Perhaps the data collection system will be similar for all them.

The experimental results correspond to world level of researches in considered area. This is confirmed by comparing the reached characteristics with published data from other setups (see Table 2).

This work was supported by RFBR grant number 11-03-01262.

REFERENCES

1. *Kiseleva T.T. et al.* The use of a low-background underground laboratory in activation analysis of pure substances and radiometry low activity naturally radioactive // Journal of Analytical Chemistry (Russia). - 1994. - Vol. 49. - No. 1. - P. 12 - 17.
2. *Laboratory* of Environmental Radioactivity «LRK-1 MEPhI» of Moscow Engineering Physics Institute. Environment samples radioactivity investigation multi-detector low-background gamma-spectrometry // http://www.radiation.ru/eng/project/laborat.htm.
3. *ORTEC*. Low-Background Germanium Gamma-Ray Detectors // http://www.ortec-online.com/download/Low-Background.pdf.
4. *CAEN*. Application Note AN2506. Digital Gamma Neutron discrimination with Liquid Scintillators // http://www.caen.it.

ELECTRON LINEAR ACCELERATOR LUE-8-5 WITH W-Be PHOTONEUTRON TARGET AS A NEUTRON SOURCE

A. V. Andreev[1], Yu. M. Burmistrov[1], A. M. Gromov[1], E. S. Konobeevski[1], M. V. Mordovskoy[1], G. V. Solodukhov[1], S. V. Zuyev[1], V. I. Firsov[2], Yu. M. Zipenyuk[2]

[1] Institute for Nuclear Research, Russian Academy of Sciences, Moscow, Russia
[2] Federal State Research and Design Institute of Rare Metal Industry "Giredmet" JSC, Moscow, Russia

We describe a neutron source based on electron linear accelerator LUE-8-5 of the Institute for Nuclear Research and neutron-producing target consisting of tungsten bremsstrahlung converter and beryllium photoneutron target. The estimates performed show that for average electron current of 30 μA, using a W-converter with thickness of 3 - 5 mm and Be photoneutron target (~ 20 cm), the neutron yield will be ~ 3 - 5 · 10^{10} n/s. The use of polyethylene moderator around the Be-target will lead to the thermal neutron flux near the target ~ 10^8 - 10^9 n/(cm^2 · s). Such a flux will ensure the metrological characteristics of neutron-activation determination of the content of most rare and precious metals.

1. Introduction

Neutron activation analysis (NAA) is widely used in the analysis of high-purity substances and geological samples [1, 2]. Especially attractive because of the high sensitivity, productivity and relative cheapness are the instrumental methods. Attention recently drawn to the development of analytical methods is appreciably due to a reduction in the number of research reactors, increased demands to radiation safety, and problems with licensing when working on them. At the same time there are more accessible and, undoubtedly, more radiation-safe sources of activating (in particular, neutron) radiations. These are accelerators of the charged particles (microtrones, linear accelerators, neutron generators) [3 - 6].

Lower, in comparison with the reactor, neutron fluxes (especially of thermal energies) restrict the use of these facilities for the analysis of pure substances and materials. However, for the analysis of geological samples (ores, products of their processing and enrichment, breed, waste products of the ore enrichment enterprises, etc.), these methods can be applied successfully and compete with other activation methods, not yielding and often exceeding their limits of content determination. The advantages of this approach include high performance, the ability to simultaneously determine the content of several elements during a single irradiation and representativeness of the results of the analysis. It is important also that, irradiating the samples by neutron fluxes of 10^8 - 10^9 n/(cm^2 · s) during up to several hours, most of the samples can be returned in 3 - 4 weeks to the customer in unmodified form for the further research. Especially, it is important for the unique or expensive samples.

2. W-Be source of fast neutrons

Table 1. **Mean characteristics of the LUE-8-5 electron LINAC**

Energy of accelerated electrons	8 MeV
Repetition r ate	Up to 600 Hz
Power in beam	Up to 5 kW
Pulse duration	3 μs
Average current at 50 Hz	30 μA

It is of interest to consider the possible use as a neutron source for NAA of industrial low-energy electron accelerators. Linear electron accelerators with energies of 8 - 10 MeV are widely used in practice in many fields of science, engineering and technology. Their attractive properties compared with reactor neutron sources and neutron generators are relatively low cost, compactness, reliability, industrial availability and safety.

Such accelerators with average characteristics given in Table 1 may provide the thermal neutron flux of about 10^8 n/(cm^2 · s) with a sufficiently low gamma background and satisfactory size of the irradiation field. Let us consider as an example the linear electron accelerator LUE-8-5 of the Institute for Nuclear Research of Russian Academy of Sciences. Its main characteristics are presented in Table 1 as follows:

The neutron flux at electron accelerators can be obtained or by direct photofission reaction or by photoproduction of neutrons in a material with low atomic number. In view of that the effective energy of the bremsstrahlung gamma from tungsten converter is about 2 - 3 MeV, the choice of the target material is limited by ^{9}Be ((γ, n) threshold = 1.67 MeV) or deuterium (the threshold of 2.26 MeV (Fig. 1).

Despite the fact that the (γ, n) cross section for deuterium is twice higher than for beryllium, the use of beryllium is preferable by the criteria of accessibility, good thermal conductivity and relative cheapness. Thus, for W-convertor and Be-target using 8 MeV electrons with average current of 30 μA, fast neutron yield of (3 - 5) · 10^{10} neutrons/s can be obtained (Fig. 2).

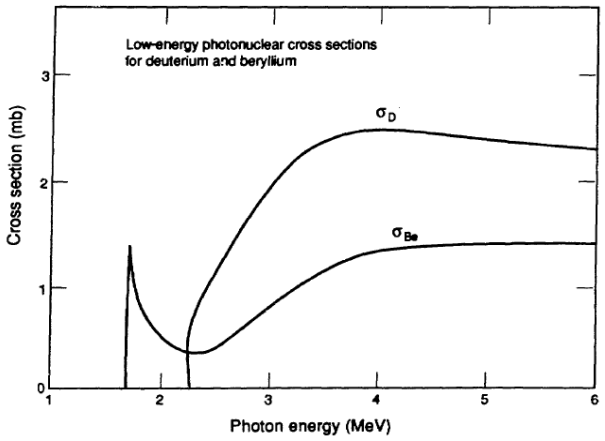

Fig. 1. Low-energy photonuclear cross sections for D and Be.

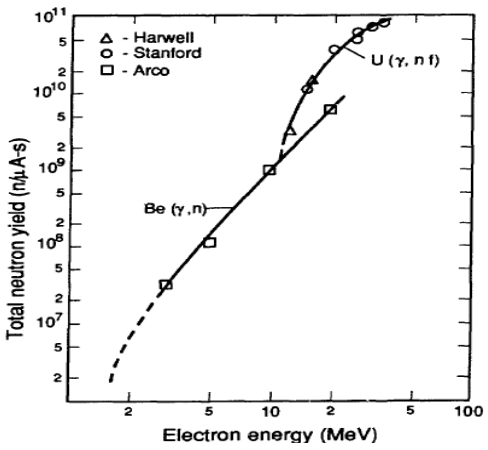

Fig. 2. Total neutron yield for Be and U targets

3. Moderator-source of thermal neutrons

The use of moderators will greatly extend the application of fast neutrons for analytical purposes. This applies particularly to the development of non-destructive methods for determining the elements that are poorly analyzed by fast-neutron activation These elements include some precious metals, a number of refractory metals and rare earth elements. In addition, the source of slow neutrons gives the opportunity to develop methods for determining the macro-content of elements (from 5 to 100 % by weight). The use of a pneumatic transport system allows to develop techniques using short-lived isotopes with half-life $T_{1/2}$ <10 min, which are very rarely used in the reactor variant of analysis.

There are several types of devices to slow the neutron flux for use in accelerators. Optimal construction should maximize the thermal neutron flux at a minimum amount of background gamma radiation and the maximum reduction of the fast neutron flux in the moderator. One needs also to take into account such requirements as simplicity, low cost and compactness of installation.

The use of neutron converters in developing thermal neutron sources can improve the source characteristics compared to pure-polyethylene moderator for the following reasons. The average energy of secondary neutrons generated in the converter as a result of nuclear reactions (inelastic scattering, (n, 2n), fission) is ~ 1 MeV. This leads, on one hand, to a reduction of the fast-neutron flux, and on the other hand to an increase of the density of thermal and resonance neutrons near the converter due to a reduced thermalization length for neutrons with lower energy. The increase of neutron flux can be achieved also as a result of neutron multiplication in the (n, 2n) reaction.

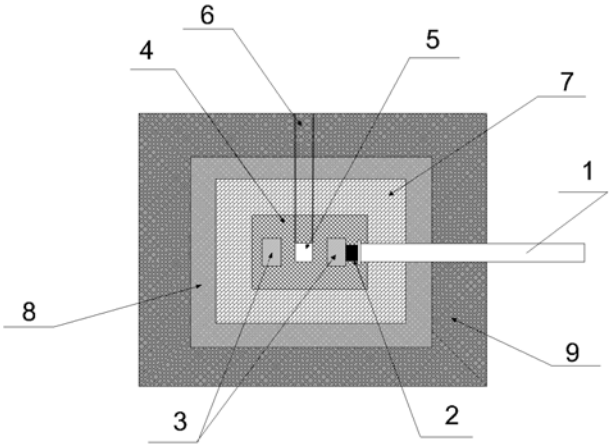

Fig. 3. Photoneutron source of thermal neutrons: *1* - electron source; *2* - tungsten converter of brems-strahlung gamma rays; *3* - beryllium photoneutron target; *4* - polyethylene moderator; *5* - cavity for irradiated samples; *6* - inlet for placing irradiated samples; *7* - converter-reflector; *8* - heavy metal shielding; 9 - borated polyethylene neutron shielding.

Electrons from the accelerator LUE-8-5 (*1*) with a maximum energy of 8 MeV hit the tungsten converter (*2*) with thickness of 0.5 radiation length and form the flux of bremsstrahlung gamma rays with maximum energy of 8 MeV. These gamma rays incident on the beryllium target (material with low photoneutron threshold) form the fast neutrons with average energy of ~2 MeV. Fast neutrons in the polyethylene moderator (*4*) undergo collisions with hydrogen nuclei, resulting in diminishing of energy to 0.07 eV, which is close to the energy of thermal neutrons. Thermal neutrons permeate the cavity (*5*), in which the studied samples are irradiated. The size of the cavity depends on the required number of irradiated samples and range from 1 × 1 × 1 cm^3 to 10 × 10 × 10 cm^3), while the position of its center inside the moderator should coincide with a maximum of thermal neutron flux in the moderator. The imposition of samples for irradiation is performed through the hole (*6*). During the irradiation this hole is closed with a stopper made from the same materials as the walls of the block-moderator. Neutrons emitted outward the moderator, are collided with the material of converter (*7*) and some of them have reflected back into the moderator. Additionally, the converter-reflector multiplicates the not yet slowed-down fast neutrons by the reaction (n, 2n). The most effective materials for use as converter are Be, W, Pb and U.

Neutrons, which are not reflected in the moderator, flow outward and are partially absorbed in a layer of heavy metal shield (*8*). Protection layer of borated polyethylene (*9*) slow-down the fast neutrons, which escaped out of the

moderator and passed through the converter and heavy metal shield, and absorbs the slow and thermal neutrons. Gamma radiation produced by the interaction of neutrons with the moderator and converter materials is attenuated in the converter and in the additional layers of heavy metal shield.

The efficiency of neutron moderation is determined by the thermalization factor K, defined as:

$$K = \frac{Total\ Fast\ Neutron\ Yield}{Peak\ Thermal\ Flux}.$$

This factor depends upon both the design and materials of the moderator and the average energy of the fast-neutron flux. On the basis of published data for a ^{252}Cf source with average neutron energy of 2.3 MeV [7] we can estimate K as ~30 - 50. For the LUE-8-5 Neutron Source this yields the maximum thermal neutron flux of ~ $2 \cdot 10^8$ - 10^9 n/cm$^2 \cdot$ s at fast-neutron yield of $1 - 5 \cdot 10^{10}$ n/s.

4. Conclusions

Such a value of the thermal neutron flux is comparable to those obtained at the installations for NAA on the basis of 30 MeV microtron [3] and T-400 and NG-150 neutron generators [6], for which the thermal-neutron moderators have been designed, manufactured and tested. A distinctive feature of these moderators, made of polyethylene, was a large enough cavity for sample irradiation. At the microtron this cavity was equal to 3500 cm^3, at NG-400 - 1000 cm^3. This allowed the simultaneous irradiation of several dozen samples with mass of 20 - 50 g at the microtron and up to 20 pcs with mass of 10-20 g at the NG-400. Thermal neutron flux was ~ ~$1 \cdot 10^9$ n/(cm$^2 \cdot$s) and $3 \cdot 10^9$ n/(cm$^2 \cdot$s) at the microtron and NG-400 neutron generator, respectively. The exposure time was between 10 minutes and several hours.

Table 2. **Lower limits of content determination of some elements in ores**

Elements	η, % mass
Cr, Zn, Mo, Ce, Hg, Ta, Te	$(1 - 3) \cdot 10^{-2}$
Sc, Co, Cu, As, Ga, Hf, U, Th	$(1 - 3) \cdot 10^{-3}$
REE (La, Eu, Dy, Sm, Yb, Lu), Sb, Re, W, Ir	$(2 - 4) \cdot 10^{-4}$

On the basis of numerous analyzes of hundreds of types of geological samples (10 - 50 g each) – ores and products of their processing and enrichment, the lower limits of content determination (η, % mass) of Au, U, Th, rare-earth elements, rare and refractory metals were estimated (Table 2) [6, 7].

In conclusion it should be mentioned that the experimental values of the lower limit of content determination clearly demonstrates the capabilities of the NAA, which can be implemented on a modernized electron linac LUE-8, completed by the moderator with relevant characteristics and low-background germanium gamma spectrometer.

This work was supported by RFBR grant number 11-03-01262.

REFERENCES

1. *Firsov V.I., Schulepnikov M.N.* The present state neutron activation method of analysis of semiconductor silicon // Journal of Analytical Chemistry. - 1988. - Vol. 43, No. 5. - P. 773 - 784.
2. *Kiseleva T.T., Rabinovich B.S., Firsov V.I., Schulepnikov M.N.* Neutron activation analysis of pure substances with use of high-flux nuclear reactor // Journal of Analytical Chemistry. - 1987. - Vol. 42, No. 2. - P. 256 - 262.
3. *Kapitsa S.P., Samosyuk V.N., Firsov V.I. et al.* Analytical capabilities of electron accelerators // Journal of Analytical Chemistry. - 1984. - Vol. 39, No. 12. - P. 2101 - 2119.
4. *Andreev A.V., Makarov S.A., Skorkin V.M.* Moderator of fast neutrons of neutron generator for activation analysis // Proc. of the XII Int. Conf. on Electrostatic Accelerators. - Obninsk, Russia, 2000. - P. 94 - 98.
5. *Andreev A.V., Firsov V.I., Tsipenyuk Yu.M.* Neutron activation analysis of geological samples using microtron and neutron generator // Zavodskaya laboratoriya. - 2012. - Vol. 78, No. 5. - P. 19 - 23.
6. *Andreev A.V., Burmistrov Yu.M., Firsov V.I.* Estimation of possibilities of thermalized neutrons on the basis of neutron generator for activation analysis // Zavodskaya laboratoriya. - 2010. - Vol. 65. - P. 1283 - 1289.
7. *Stokes J. et al*. // IRT 46110-019, IRT Corp. (1981).

MODEL-INDEPENDENT EVALUATION OF RECOILS CHANNELING IMPACT ON VISIBLE ENERGY SPECTRA IN DARK MATTER PARTICLES CRYSTALLINE DETECTORS

S. V. Dyuldya, M. I. Bratchenko

National Scientific Centre "Kharkiv Institute of Physics and Technology", Kharkiv, Ukraine

Proposed is a direct method of Dark Matter crystalline scintillation detectors calibration by means of an atomistic molecular dynamics modeling of their responses to ~10 keV recoil atoms. Simulations show that the recoils channeling exists in NaI lattice with probabilities of ~5 - 15 %. It does not affect the mean values of quenching factors but gives rise to high visible energy spectral tails absent in disordered detectors. As a result, the lattice ordering manifests the ~100 % effect on NaI(Tl) visible energy spectra at 2÷6 keV window.

Channeling [1, 2] is widely discussed in the Dark Matter (DM) community concerning its impact on interpretation of low-background DM direct detection with scintillation counters. The standard weakly interacting massive particles (WIMP) scenario of DM particles (DMp) assumes the detector light response to be only due to primary knock-on atoms (PKA) recoiled at DMp-nucleon elastic scattering. The PKA energies E_R range in $\sim 10^{(0\div 2)}$ keV at WIMP masses $M \sim 10^{0\div 2}$ GeV/c^2. A part $\Delta E_{el} = q_{el} \cdot E_R$ of E_R is transferred to electrons of a detector via ionization energy losses of the PKA induced atomic collision cascade. But the detected (*visible*) energy $E_{det} = q \cdot \Delta E_{el}$ is only a fraction $Q(E_R) = q_{el}(E_R) \times \times q(E_R)$ of E_R due to detector and PKA type specific quenching $q < 1$ of electronic excitations [3, 4]. Since one can identify E_R of a monoenergetic PKA source using the instrument probability distribution function (p.d.f.) $p_{det}(E_{det}|E_R) = \delta(E_{det} - Q \cdot E_R)$, proper quenching factors $Q(E_R) < 1$ are of key importance for reliable calibration of DMp scintillation detectors.

Channeling has been first introduced into this agenda by Drobyshevski's [5] hypothesis that certain fraction $P_{ch} < 1$ of the recoils are channeled in a crystalline detector, and have abnormally high quenching factors $Q_{ch} = 1$. Thus actually $p_{det}(E_{det}|E_R) = P_{ch} \cdot \delta(E_{det} - E_R) + (1 - P_{ch}) \cdot \delta(E_{det} - Q \cdot E_R)$. The P_{ch} estimation model of DAMA collaboration [6] has predicted an enhancement of NaI(Tl) crystal counting efficiency in the near-threshold 2÷6 keV window of their 8σ significant observation of DM attributed annual modulation signal. They evaluated $P_{ch}(E_R)$ by means of the Monte Carlo (MC) procedure of ray-tracing of a point isotropic source of recoils, and qualified the channeled ones as those directed within the Lindhard critical angles $\psi_c(E_R)$ [1] of open axial and planar channels of NaI(Tl) single crystal. It resulted in a very significant ($P_{ch} \sim 25$ % for 4 keV I) channeling.

But the foundations of Refs. 5 and 6 look very questionable. An ansatz $Q_{ch} = 1$ [5] is definitely violated at keV energies since the elastic (nuclear) energy loss ΔE_n of well channeled heavy ions is non-negligible. The ΔE_{el} dominance at channeling was suggested in early 1960's to predict [7, 8] its impact on a number $\nu(E_R)$ of atomic displacements in neutrons induced collision cascades in metals. But all attempts to observe the $\nu(E_R)$ reduction have lost out. The collaboration model [6] also omitted the blocking effect [1] of PKA strong scattering by the nearest neighbors of the lattice site of emergence. It has been critically revised in a semi-analytical model of Bozorgnia - Gelmini - Gondolo (BGG) group [9, 10] that suggested that the PKA capture into a channel requires its initial transversal thermal displacement beyond the critical distance $r_c(E_R) \sim 0.1 \div 1$ Å of stable channeling. Such a model has been first introduced by Kumakhov [8] in 1972, and similarly to his estimates for metals, the BGG model calculations for various detector materials result in exponentially small $P_{ch} < 1$ %.

One can see that the situation remains far from clear since the results of application of different models differ by orders of magnitude. The essentially quantitative problem of DM detector calibration conflicts with the mostly qualitative nature of the low energy channeling analytical criteria. Besides, channeling is highly unstable due to intrinsic dechanneling on thermal vibrations and electrons, and is known to interfere with other competitive directional effect of crystal lattice ordering.

In the present work, we perform the channeling/blocking models independent atomistic simulation of the impact of NaI lattice ordering on detector readings. We compare responses in a crystalline and entirely disordered (amorphized) representations of the same detector material at preservation of all other simulation parameters. Our approach is free of *a priory* introduction of channeling that emerges by oneself in lattices. However, the *a posteriori* statistical analysis of collision cascade dynamics allows us to clarify its role and to suggest proper values of P_{ch} and Q_{ch}.

We use the in-house developed molecular dynamics (MD) code *MICKSER* [11]. It implements the restricted version of MD valid for simulation of atomic collisions in crystals and amorphous materials down to ~1 eV with special attention paid to accurate modeling of ion implantation, channeling, and other directional effects. Algorithmic details can be found in Ref. 11. Current version of the code is capable to model the full collision cascade by trajectory tracking of all atoms recoiled with energies exceeding the lattice binding energy $E_b < 10$ eV. The "universal" Ziegler - Biersack - Littmark (ZBL) interatomic potential was used in combination with the inhomogeneous electron densities calculated within the Isolated Atomic Density Superposition (IADS) method. Ionization stopping was calculated according the well-established Firsov and Brandt - Kitagawa models. The statistics of MC sampling of collision cascades was $\sim 10^4$ for each PKA energy E_R. The energies ΔE_n and ΔE_{el} deposited in a cascade into the nuclear and electronic subsystems of

NaI were tallied, while the cascade total energy $E_R = \Delta E_n + \Delta E_{el}$ was monitored to conserve within 0.1 % of E_R.

To calculate visible energies $E_{det} = q \cdot \Delta E_{el}$, applied is the novel modification of the classical Birks formula $q = (1 + kB \cdot |dE/dx|)^{-1}$ [3] with an empirically adjustable Birks constant kB. Instead, we use $q(E_R) = [1 + kB \cdot \Delta E_{el}(E_R)/R(E_R)|]^{-1}$ where ΔE_{el} is the total inelastic energy deposition in the PKA induced collision cascade and R is the PKA total range. It is based on the fact that the size of the coherent light response formation domain ($\sim 10^{1\div 3}$ nm) considerably exceeds the size of ~keV energy cascades ($\sim R$). The quantities $\Delta E_{el}(E_R)$ and $R(E_R)$ are readily computable by our *MICKSER* code as well as by the *SRIM* code, www.srim.org. It allows direct modeling of $Q(E_R)$, see Fig. 1 for this method validation. But further to *SRIM*, our code can also tally $q(E_R)$ as a random variate on a per-event (per-cascade) basis to make it possible the MC tallying of the visible energy E_{det} spectra.

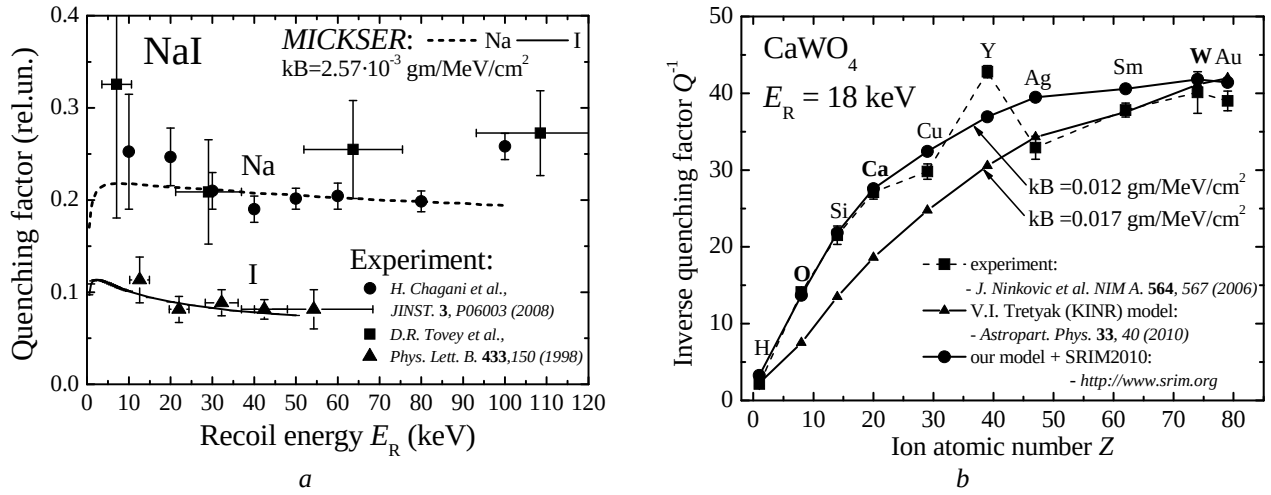

Fig. 1. The *MICKSER* and *SRIM2010* calculated quenching factors Q for various ions in disordered NaI (*a*) and $CaWO_4$ (*b*) compared to the experimental data and the results of Tretyak model calculations [4].

We start from the clear evidence of directional effects (incl. channeling) at recoil dynamics in NaI crystal lattice of NaCl type, lattice unit (l.u.) 6.473 Å. In Fig. 2, all ion flux angular maps are highly anisotropic, and correlated with NaI crystallography. Blocking dominates at 1÷2 l.u. from the PKA start point while at large distances r it gives place to relatively stable channeling. The momentum isotropization (that forms the uniformly grey maps in disordered NaI) is never reached here: due to energy losses only well channeled ions can be delivered to distances exceeding their range in the amorphized NaI. A similar dynamics appears for all other $E_R \subset (1\div 100)$ keV. It means that the lattice driven anisotropy is characteristic for collision cascades under consideration.

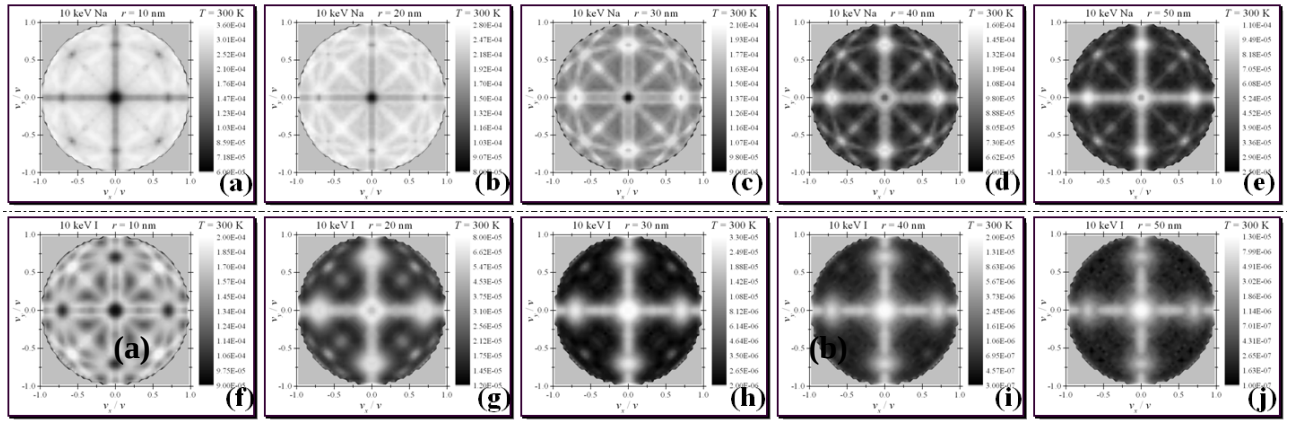

Fig. 2. Radial projections of total angular distributions of 10 keV Na (a→e) and I (f→j) PKA plotted at increasing distances $r = 10,20,\rightarrow,50$ nm from the NaI lattice site of their isotropic emergence at 300 K. Dark spots at small r correspond to blocking while light spots and strips indicate axial and planar channeling.

The *MICKSER* code capability of channeling identification (see details in Ref. 11) have enabled its quantitative rating by means of routine calculation of transversal energies $E_\perp$ in several dozens of channels and their comparison with theory supplied critical values. Fig. 3 presents the probabilities $P_{ch}(r)$ to find a recoil channeled at a distance r from the lattice site of its emergence.

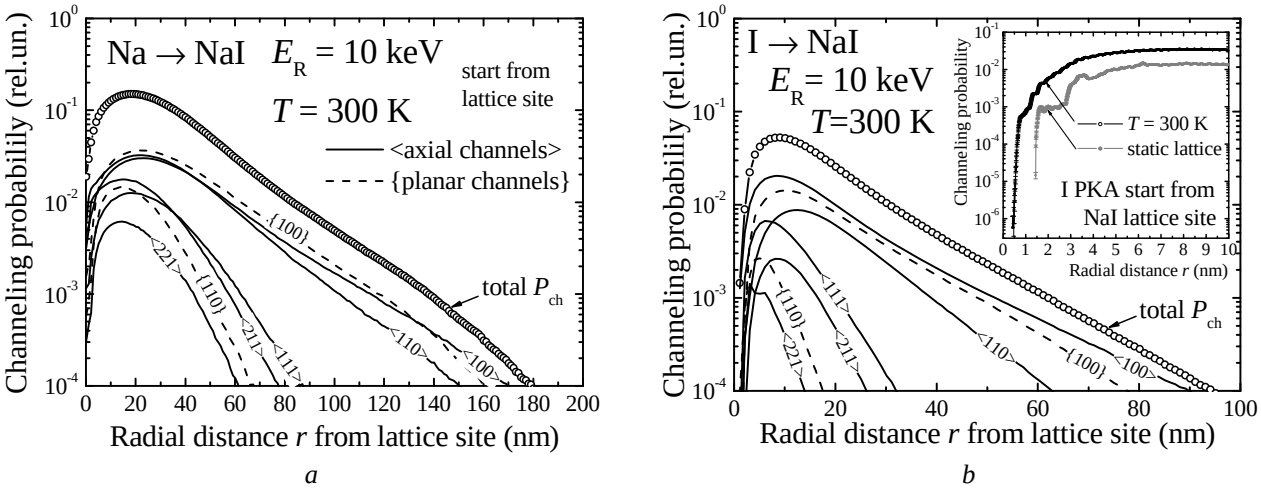

a *b*

Fig. 3. Radial dechanneling functions $P_{ch}(r)$ of 10 keV Na (*a*) and I (*b*) isotropically emerged recoils together with partial $P_{ch}(r)$ of the most significant axial <*hkl*> and planar {*hkl*} channels.

Evidently, and opposite to model assumptions of [5, 6, 9], $P_{ch} \neq$ const but is a "dechanneling function" of r. Due to blocking, P_{ch} is marginal (<0.1 %) at $r \leq (1\div2)\cdot$l.u. from a site. It agrees well with the analytical results of BGG group [9] and those of Kumakhov [8]. But a rapid volume capture [2, 11] into the channeling mode of recoil motion takes place at greater distances. It populates P_{ch} maxima to ≈15 % (Na) and ≈5 % (I) at $r \sim (10\div20)\cdot$l.u. Then $P_{ch}(r)$ decays exponentially. The inset of Fig. 3, *b* indicates that the capture is not exclusively owned [8, 9] to thermal displacements of the PKA start point. It occurs also in a regular static lattice at multiple small-angle scattering of recoils. We summarize the Fig. 3 data with the conclusion that the attempts [8, 9] to describe the recoil channeling probability P_{ch} by whatever local measure of its emergence initial conditions are insufficient. Channeling is populated non-locally in the bulk up to several percents high probability.

But does it affect the quenching factors of NaI(Tl) detectors? Fig. 4 argues that the answer is (most likely) negative. The lattice effect is significant (~10÷25 %) for PKA emergence from interstitial locations but is much smaller (~1÷5 %) for actual emergence from lattice sites. This is a challengingly small difference to be resolved experimentally, see Fig. 4, *a*. Fig. 4, *b* shows that Q_I in a crystalline NaI is ≈5 % smaller then in the disordered one. This effect cannot be due to channeling.

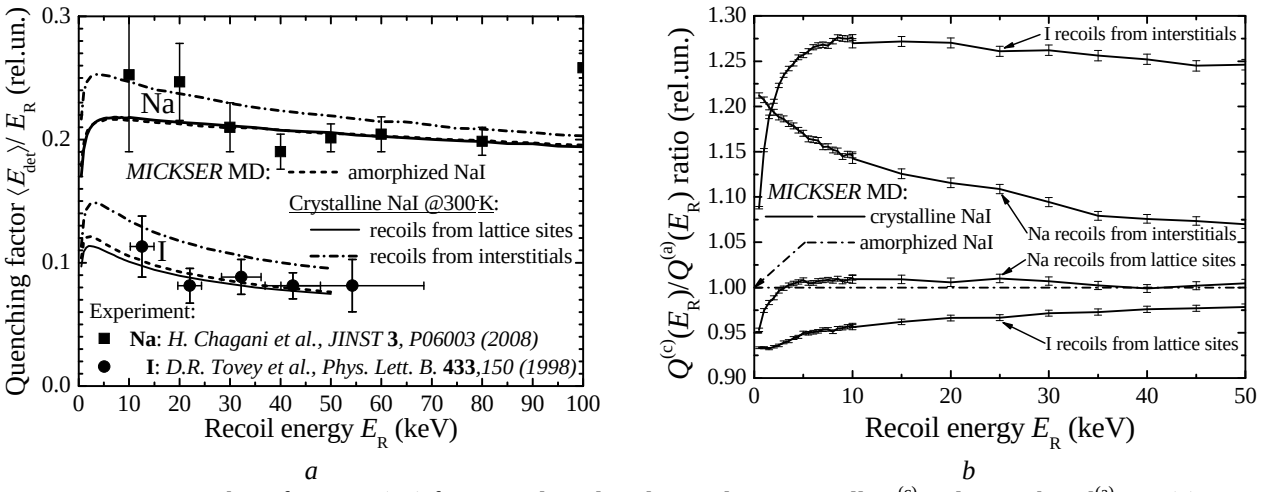

a *b*

Fig. 4. Quenching factors $Q(E_R)$ for Na and I induced cascades in crystalline$^{(c)}$ and amorphized$^{(a)}$ NaI (*a*) and comparative measure $Q^{(c)}/Q^{(a)}$ of lattice impact for different conditions of PKA emergence (*b*).

The weakness of $Q = \langle E_{det}\rangle / E_R$ lattice ordering sensitivity agrees with Lindhard's reversibility rule [1, 2] that predicts the *in toto* compensation of channeling and blocking impacts on all mean (integral) yields of isotropic recoils' atomic collisions (as noted above, the same is valid for $\nu(E_R)$).

However, this rule does not impose constraints on differential statistical distributions (p.d.f.) of measurable quantities. Fig. 5 shows that they are different in lattices and in disordered media. Unlike the Gaussian shaped spectra in amorphized NaI, both ΔE_{el} and E_{det} in a crystal manifest (i) exponential high-energy tails more pronounced for interstitial emergence and (ii) certain increase of probability of low-energy loss and E_{det}. The former feature is well attachable to channeling since it is statistically similar to the "channeling tails" of ion ranges, a known issue of ion implantation [11]. The less obvious root of the latter one is quasichanneling [12] at focusing of recoils onto atomic

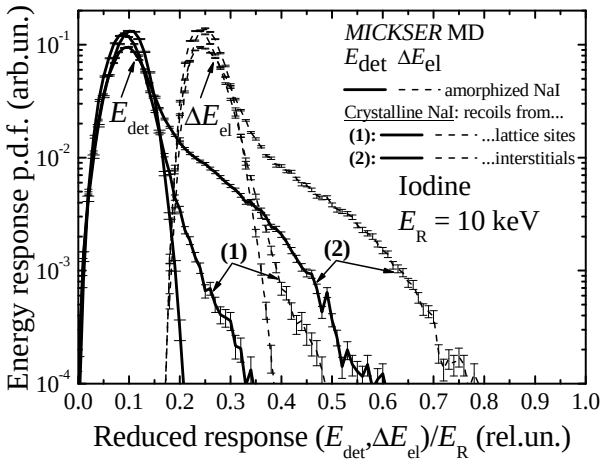

Fig. 5. Differential spectra of ionization energy losses and quenched visible energies for 10 keV cascade at different conditions of Iodine PKA emergence.

rows/planes. Quasichanneled ions experience a large nuclear energy loss that is localized at $r \leq (3\div5)\cdot$l.u. and thus renormalizes (softens) the energy available to the subsequent part of cascade. It is also responsible for the reduced Q of heavy Iodine in Fig. 4.

For Na PKA, the Fig. 5 spectra shift to the right and broaden. The same spectral shape is observed at all relevant PKA energies E_R. So, these lattice effects are common for crystal detectors. They can be qualified quantitatively by means of the Fig. 6, *a* 3-fractional fit representing the E_{det} p.d.f. $f(E_{det}) = \sum_{j=1}^{3} P_j f_j(E_{det})$ as a P_j-weighted sum of partial p.d.f. f_j of random chaotic (*rand*), channeled (*ch*) and quasichanneled (*qch*) fractions of cascade dynamics, and making the only assumption that the $f_{rand}(E_{det})$ shape is the same one that is modeled in an amorphized version of NaI.

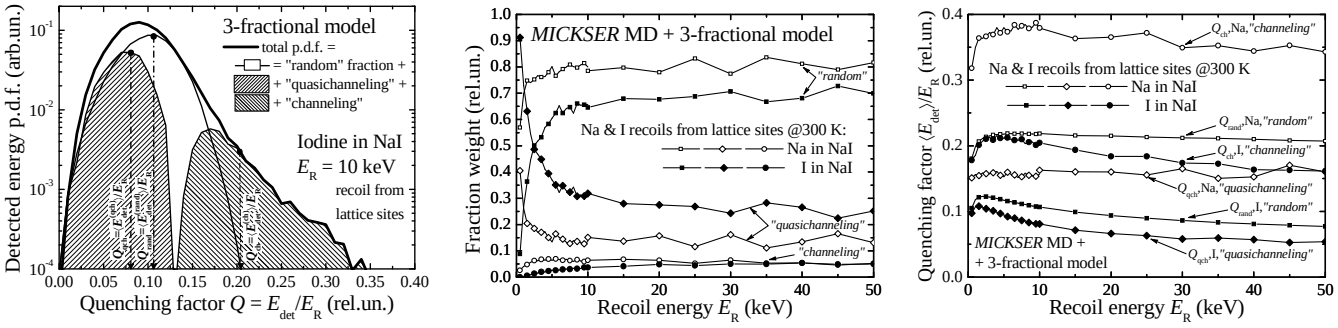

a *b* *c*

Fig. 6. 3-fractional model partitioned p.d.f. of Q (*a*); populations P_j (*b*); partial Q_j (*c*) of fractions.

One can see in Fig. 6, *b* that $P_{ch} \sim (3\div7)$ % for both Na and I PKA in a broad range of E_R. By order of magnitude, it agrees with the Fig. 3 data obtained using just another trajectory point dependent channeling criterion. The total population $P_{ch}+P_{qch}$ of lattice driven directional effects is ~20÷30 %. It is greater for Iodine due to more pronounced quasicahnneling of a heavier recoil. The first moments $\langle E_{det}\rangle_j = \int dE_{det}\, E_{det}\, f_j(E_{det})$ define the fractional quenching factors $Q_j = \langle E_{det}\rangle_j / E_R$ plotted in Fig. 6, *c*. The basic model assumption $Q_{ch} = 1$ of Refs. 5, 6, 9 definitely fails: though $Q_{ch} \sim 2\cdot Q_{rand}$, all $Q_{ch} < 40$ %. The representative Q_{ch} are ≈0.35 (Na) and ≈0.2 (I). It is also notable that $Q_{qch} < Q_{rand}$.

We note that the simulated E_{det} spectra and the obtained "effective" (P_{ch},Q_{ch}) values differ substantially from those used in current treatments of the channeling impact. So, it is of great interest to examine how they affect the visible energy spectrum in the DAMA detector. It can be studied using the standard approach of the Lewin-Smith compendium [13] but applying the MD simulated p.d.f. $f(E_{det}|E_R)$ instead of conventional δ-shaped $p_{det}(E_{det}|E_R)$. We have carried out a pilot evaluation using the PKA energy spectra dR/dE_R for spin-independent WIMP-nucleon elastic scattering with total $\sigma_0 = 10^{-6}$ pb and Helm form factor. The Ref. [13] galactic halo model was used: the Earth velocity annual span $v_E = 244\pm15$ km/s, the DMp escape velocity $v_{esc} = 600$ km/s, the near-earth DM mass density $\rho_{DM} = 0.74\,\mathrm{GeV}\cdot c^{-2}\cdot cm^{-3}$. For NaI, the composite $dR(E_R)/dE_R$ is upper bounded by the kinematical maximal energy transfer $E_R^{(max)}$ of Na (≈80 keV at WIMP mass 20 GeV/c^2), and decays *abt* exponentially with an inflection at $E_R^{(max)} \approx 40$ keV of I. The properly interpolatable database of pre-modeled $f(E_{det}|E_R)$ for $E_R \subset 10^{(0\div2)}$ keV was used in calculations. The results are shown in Fig. 7.

In Fig. 7, *a*, DAMA model [6] shows the ubiquitous impact of channeling. According to BGG model [9], it appears only above the quenched limit $E_{det}^{(max)} = Q_{Na}\cdot E_R^{(max)} = 24$ keV. The MD based data of Fig. 7, *b* - *d* manifest just an intermediate case: the relative magnitude of lattice driven effects is ~100 % at 2÷6 keV visible energies (*cf.* ~1000 % of DAMA and ~1 % of BGG models; note that our results tend to DAMA ones for unrealistic interstitial emergence). The lattice effect in these bins is due to Iodine recoils. In Fig. 7, *c*, its amplitude grows *abt* linearly with WIMP mass while shifting to higher E_{det} and thus leaving the window of the collaboration observed DMp signature.

The reason of the obtained lattice ordering provided increase of detector response consists in the existence of channeling tails of Fig. 5. Owing to them, the recoils of lower E_R can contribute to the specific bin of visible energy E_{det}. Recently, such tails have been also observed, and correlated to anomalously high recoil ranges, by the South Korean group [14] at their simulations of CsI(Tl) detector. The *MARLOWE* code simulated [14] tail in CsI crystal for E_R = 18.4 keV is populated to ≈4.5 % fairly consistently with our MD evaluation of Fig. 6, *b* for NaI crystalline detector.

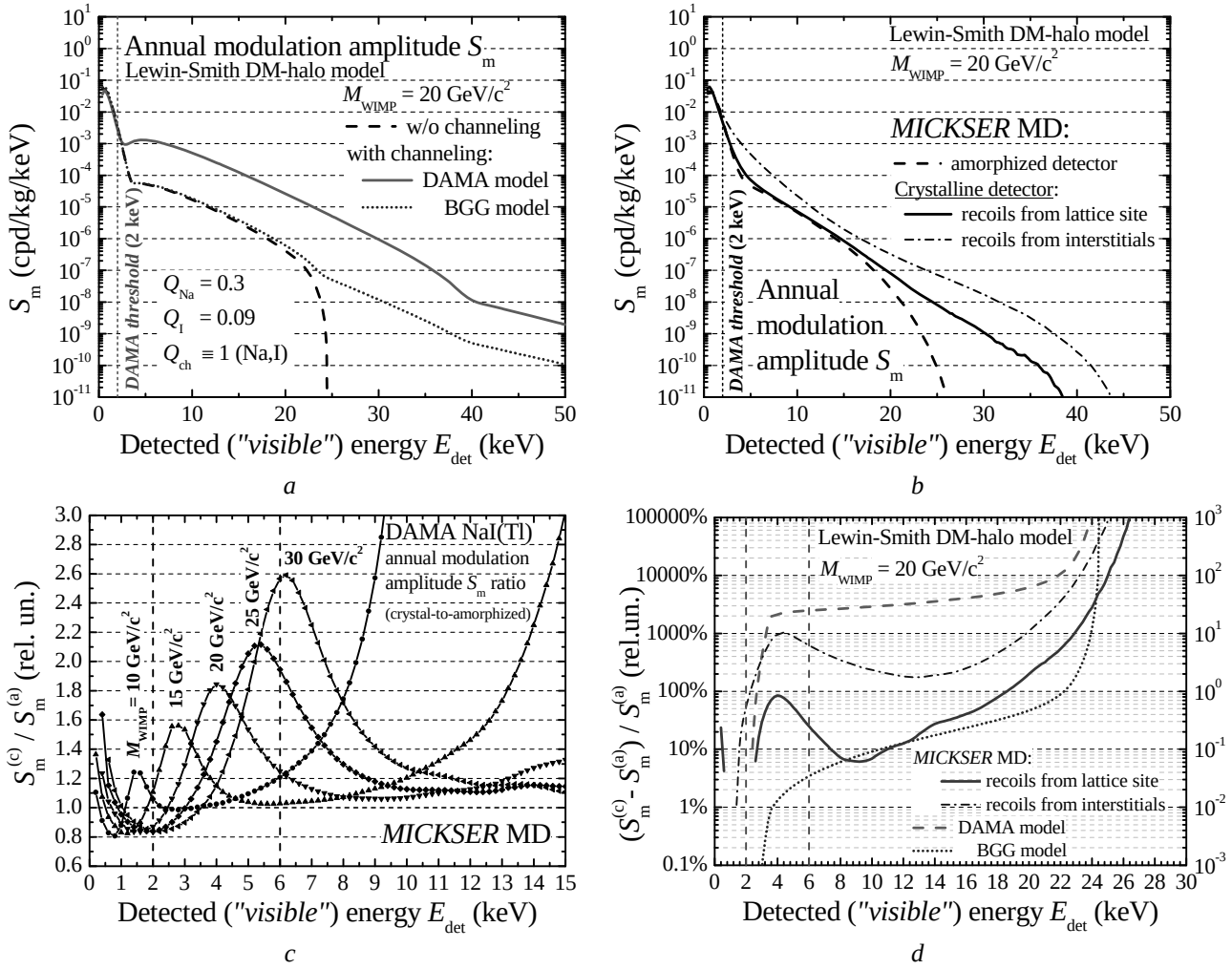

Fig. 7. Absolute (*a* and *b*) and relative (*c* and *d*) representations of modulated visible energy spectra in NaI detector calculated within the scope of existing models [6, 9] (*a* and *d*) and MD simulation of the present work (*b* - *d*).

Numerous ion implantation and radiation damage studies argue that similar tailed distributions are very characteristic for keV energies ions transport and collision cascades in crystals. In our case, their impact on visible energy spectra is notable enough to be included into calibrations and analysis of DM experiments, also for other DMp models and other (CsI, $CaWO_4$, Si, Ge, *etc.*) detectors. It can be done by means of the developed simulation method and computer code, *MICKSER*.

REFERENCES

1. *Lindhard J.* Influence of crystal lattice on motion of energetic charged particles // Mat. Fys. Medd. Dan. Vid. Selsk. - 1965. - Vol. 34, No. 14. - P. 1 - 64.
2. *Kumakhov M.A., Schirmer G.* Atomic collisions in crystals. - NY: Gordon & Breach, 1989. - 260 p.
3. *Birks J.B.* The theory and practice of scintillation counting. - NY: Pergamon Press, 1967. - 662 p.
4. *Tretyak V.I.* Semi-empirical calculation of quenching factors for ions in scintillators // Astropart. Phys. - 2010. - Vol. 33. - P. 40 - 53.
5. *Drobyshevski E.M.* Channeling effect and improvement of the efficiency of charged particle registration with crystal scintillators // Mod. Phys. Lett. - 2008. - Vol. A23. - P. 3077 - 3085.
6. *Bernabei R., Belli P., Montecchia F., Nozzoli F., Cappella F. et al.* Possible implications of the channeling effect in NaI(Tl) crystals // Euro. Phys. J. - 2008. Vol. C53. - P. 205 - 213.
7. *Oen O.S., Robinson M.T.* The effect of channeling on displacement cascade theory // Appl. Phys. Lett. - 1963. - Vol. 2. - P. 83 - 85.
8. *Kumakhov M.A.* The effect of channeling on the radiation cascade in solid // Radiation physics of crystals and *p-n* junctions. - Minsk: Nauka i tehnika, 1972. - P. 18 - 27 (in Russian).
9. *Bozorgnia N., Gelmini G.B., Gondolo P.* Channeling in direct Dark Matter detection (I-III) // JCAP. - 2010. - No. 11. - 019,028,029. [arXiv:astro-ph.CO/1006.3110,1008.3676,1009.3325].
10. *Bozorgnia N., Gelmini G.B., Gondolo P.* Channeling in solid Xe, Ar and Ne direct Dark Matter detectors // NIM. - 2011. - Vol. A654. - P. 162 - 169. [arXiv:astro-ph.CO/1011.6006].

11. *Bratchenko M.I., Bakai A.S., Dyuldya S.V.* The effect of dynamically unstable channeling on off-axis ion implantation // Journal of Physical Studies. - 2009. - Vol. 13. - P. 1601 (14 p.).
12. *Chadderton L.T.* Comments on the scattering of charged particles by single crystals. IV. Quasichanneling, flux peaking and atom location // Rad. Eff. - 1975. - Vol. 27. - P. 13 - 21.
13. *Lewin J.D., Smith P.F.* Review of mathematics, numerical factors, and corrections for dark matter experiments based on elastic nuclear recoil // Astropart. Phys. - 1996. - Vol. 6. - P. 87 - 112.
14. *Lee J.H., Bhang H. et al.* Simulation and measurement of quenching and channeling effects in CsI(Tl) for dark matter search // IEEE Trans. Nucl. Sci. - 2012. - Vol. PP, No. 99 - 1 p.

NON-CLASSICAL RADIATION TRANSPORT IN RANDOM MEDIA WITH FLUCTUATING DENSITIES

S. V. Dyuldya, M. I. Bratchenko

National Scientific Centre "Kharkiv Institute of Physics and Technology", Kharkiv, Ukraine

The ensemble averaged propagation kernels of the non-classical radiation transport are studied by means of the proposed application of the stochastic differential equation random medium generators. It is shown that the non-classical transport is favored in long-correlated weakly fluctuating media. The developed kernel models have been implemented in GEANT4 and validated against the "double Monte Carlo" modeling of absorptions curves of disperse neutron absorbers and γ-albedos from a scatterer/absorber random mix.

We deal with the problem of description and Monte Carlo (MC) modeling of neutrons and photons transport in media having practically unresolved heterogeneities of a small (as against the system scale Λ) spatial correlation scale l_c, and specifically consider the challenging case $\lambda \sim l_c \ll \Lambda$ where $\lambda = \Sigma^{-1} = \mathbf{M}(s)$ is a representative mean (m.f.p.) of a free-path (f.p.) length s. It arises in various applications of radiation transport (RT) theory [1] ranging from nuclear engineering to optics of cloudy atmosphere. The theory treats it as a doubly stochastic RT in random fields $\{n_i\}$ of i-indexed elemental (or nuclide) number densities, and attempts to find moments $\langle Y^{k\geq 1}\rangle$ of a medium response Y to irradiation (hereinafter $\langle\circ\rangle$ denotes an ensemble average over the realizations of the random field having the specified probability measure). At j-enumerated discrete interaction processes with deterministic microscopic cross-sections $\{\sigma_{ij}\}$, it leads to random total macroscopic cross-section $\Sigma = \sum_{i,j} n_i \sigma_{ij}$, and thus to random coefficients of the Boltzmann type RT equation that is hard to be solved without simplifications. Most of them consider the RT problem homogenization to preserve the classical form of the Boltzmann equation (BE) propagation kernel (PK) $I(s) = e^{-\Sigma \cdot s}$ (the spatially homogenized $\Sigma = \text{const}$ describes the regular Beer-Lambert extinction law). Generally, the "naive" homogenization to the smallest scale (as in an Atomic Mix Model, AMM, with $\Sigma = \Sigma_{\text{mix}}$) is invalid: since $I(s)$ is concave, $\langle I\rangle(s) > e^{-\Sigma_{\text{mix}} \cdot s}$ due to Jensen inequality [2]. The "effective" homogenization theory [3] and models succeed in renormalization of Σ with self-shielding factors $f_{\text{ss}} = \Sigma_{\text{eff}}/\Sigma_{\text{mix}} < 1$. But they cannot describe the case $s \sim l_c$ under consideration.

For some kinds of participating media (e.g., random binary mixtures), the statistically accurate "benchmark" solution of the problem is found by the double-MC RT simulation [4, 5] in a large number of random medium samples followed by the explicit ensemble averaging of responses. Unfortunately, double-MC has huge computational costs and complexity, and also is poorly applicable to other relevant cases (e.g. turbulent media, or heterophase density fluctuations). It favors more efficient MC schemes conceptually similar to those of Woodcock or Chord Length Sampling (CLS) [6] algorithms currently used in certain MC packages. We try to contribute to these developments by the MC implementation of properly generalized effective propagation kernels.

Recently Davis et al. have pointed out that the f.p. dependence Σ(s) is non-negligible in spatially correlated media. Thus instead of $e^{-s/\lambda}$, the PK general form $I(s) = \exp\left[-\tau(s) \equiv -\int_0^s \Sigma(s')\,\mathrm{d}s'\right]$ (common to optics of variable media) shall be used [7]. They have noticed that it makes sense also for Lebesgue measurable random functions Σ(s) when treating the optical length $\tau(s)$ as a stochastic integral [8]. Moreover, they have applied the 1-point invariant f.p. dependent ensemble averaged PK (EAPK) $\Im(s) = \langle I\rangle$ to the (at least qualitative) description of radiation extinction in random media, and have obtained the sub-/super-exponential deviations from the Beer-Lambert law as well as the wider-then-exponential f.p. distributions peculiar to the anomalous "non-classical" transport phenomena extensively studying in modern statistical physics [9]. Assuming $\Sigma = \Sigma(s)$, Larsen [10] has derived a Generalized Boltzmann Equation (GBE) of non-classical RT. It includes s as an explicit "memory variable" to account for the spatial correlation of scattering events. The existence of GBE solution has been recently proved by Frank and Goudon [11]. The iterative procedure of their proof shows that the GBE solution is representable as a per-collision Neumann type series. It means that GBE can be solved using the terminating MC algorithm that has to make use of EAPK.

In the present work, we study the non-classical EAPK $\Im(s)$ systematically basing on the stochastic processes (s.p.) generating models of f.p. statistics in spatially correlated random media, and calculate exactly the EAPK for some stochastic differential equation (SDE) medium generators.

Let's remind that the PK $I = e^{-\tau}$ measures an uncollided flux of particles traveled the path length s since the previous interaction at $s = 0$. The collision probability at ds is $\mathrm{d}\tau = \Sigma(s)\cdot\mathrm{d}s$, thus $I(s)\cdot$is a nonincreasing solution of the differential equation $\mathrm{d}I(s) = -\Sigma(s)\cdot I(s)\cdot\mathrm{d}s$, $I(0) = 1$. At random Σ, it is the multiplicative SDE of the Anderson-Kubo oscillator [12]. Its statistical properties are determined by those of imaginary frequency $i\Sigma$ that, in turn, follow from those of the random medium.

Let's describe the number density $\{n_i\}$ fluctuations along the travel ray $\mathbf{r} = \mathbf{r}_0 + \mathbf{\Omega}\cdot s$, with the SDE system $\{\mathrm{d}n_i = \hat{\mathrm{S}}_i[\mathrm{d}s; \{n_i\}, \delta W]\}$ where δW is a noise and linear operators $\{\hat{\mathrm{S}}_i\}$ offer the specific medium model. The system $\{\mathrm{d}n_i\}$ reduces to a single SDE for dΣ at fixed stoichiometry $\{c_i\}$ fluctuations of mass density. This is the case we only

consider here for the sake of simplicity having in mind possible generalizations. We also limit ourselves to the statistically homogeneous isotropic media: $\Sigma(s|\mathbf{r}_0,\mathbf{\Omega}) = \Sigma(s)$, and require the nonnegatively valued s.p. $\Sigma(s) \ge 0$ to be ergodic and strongly stationary: all moments $\langle \Sigma^{k\ge 0} \rangle < +\infty$ are s independent at $s >> l_c$ where $l_c = \delta\Sigma^{-2} \int_0^\infty C_2(s)\,\mathrm{d}s$ is the correlation length, $C_2(s)$ is the autocovariance of $\Sigma(s)$ and $\delta\Sigma^2 = C_2(0)$ is its variance, the squared volatility $\delta\Sigma$. At finite constant $\langle \Sigma^k \rangle$, one can calibrate the s.p. $\Sigma(s)$ parameters from the known first moments and l_c of the random medium. The triplet $\{\langle\Sigma\rangle, \delta\Sigma^2, l_c\}$ we adopt as a minimal set of the medium model phenomenological parameters. They can be either measured or evaluated using the statistical analysis of its certain benchmark model. Without loss of generality, we use $\langle\Sigma\rangle = \Sigma_{mix}$ (AMM), then the random medium turns into a homogeneous atomic mix in the absence of noise.

The made model assumptions are in fact very restrictive. The simple Gaussian noise based models [8] include negative Σ and/or have infinite $\delta\Sigma$, and thus are excluded from consideration. One has only treat colored [12] positive mean-reverting s.p. with finite variances. For example, within the diffusion type s.p. model the PK is described by the SDE sequence:

$$\mathrm{d}I(s) = -\Sigma(s) \cdot I(s) \cdot \mathrm{d}s\,, \tag{1a}$$

$$\mathrm{d}\Sigma(s) = a(\Sigma) \cdot \mathrm{d}s + b(\Sigma) \cdot \delta W\,, \tag{1b}$$

where (1b) is the Itô's SDE with drift $a(\Sigma)$, diffusion $b(\Sigma)$, and Wiener noise δW. To obtain solutions $\Sigma(s) \ge 0$, one needs $a(\Sigma) \ge 0$, $b(\Sigma) \to 0$ at $\Sigma \to +0$. The existence of 1-point density (p.d.f.) $f_1(\Sigma)$ such that $\partial_\Sigma \left[a(\Sigma) \cdot f_1(\Sigma) \right] - \tfrac{1}{2} \cdot \partial_\Sigma^2 \left[b^2(\Sigma) \cdot f_1(\Sigma) \right] = 0$, $\partial_x^n(\cdot) = \partial^n(\cdot)/\partial x^n$, is also required for ergodic stationary solutions. Then we identify the averaging over all s-ended paths of the s.p. Σ with the ensemble average over the joint probability density $f(I,\Sigma|s)$, and calculate the EAPK $\Im(s)$ as follows:

$$\Im(s) = \langle I \rangle\big|_s = \left\langle \exp\left[-\int_0^s \Sigma(s')\,\mathrm{d}s' \right] \right\rangle = \int_0^\infty \mathrm{d}\Sigma \int_0^1 \mathrm{d}I' \cdot I' \cdot f(I', \Sigma|s)\,, \tag{2}$$

$$\partial_s f(I,\Sigma|s) - \partial_I \left[\Sigma \cdot I \cdot f(I,\Sigma|s) \right] + \partial_\Sigma \left[a(\Sigma)\, f(I,\Sigma|s) \right] - \tfrac{1}{2} \cdot \partial_\Sigma^2 \left[b^2(\Sigma)\, f(I,\Sigma|s) \right] = 0\,. \tag{3}$$

Eq. 3 is the standard Fokker - Plank equation (FPE) for $f(I,\Sigma|s)$. The 1-point invariant $\Im(s)$ is its solution with the initial condition (i.c.) $f(I,\Sigma|0) = f_1(\Sigma)$. The i.c. $f(I,\Sigma|0) = \delta(\Sigma - \Sigma_0)$ determines the conditional EAPK $\Im(s|\Sigma_0)$ at the non-random Σ_0. In MC, it is of particular need to maintain one-step medium correlations for the transport continuation from the interaction point where the medium state Σ is predetermined by sampling from the p.d.f. $f(\Sigma|s) = \int_0^1 \mathrm{d}I \cdot I\, f(I,\Sigma|s)$ for particles interacting at s. It obeys the FPE $\partial_s f(\Sigma|s) + \Sigma \cdot f(\Sigma|s) + \partial_\Sigma \left[a(\Sigma) \cdot f(\Sigma|s) \right] - \tfrac{1}{2} \partial_\Sigma^2 \left[b^2(\Sigma) \cdot f(\Sigma|s) \right] = 0$ obtained from Eq. 3 by integration, and in view of the boundary condition $f(1,\Sigma|s) = 0$. Evidently, $\Im(s) = \int_0^\infty \Im(s|\Sigma')\,\mathrm{d}\Sigma'$.

Other analytical and numerical methods of the EAPK calculation can be used for other s.p. based models of $\Sigma(s)$. If known is the characteristic functional $G_\Sigma\left(\left[k(t)\right]\right) = \left\langle \exp \int_{-\infty}^\infty ik(t)\Sigma(t)\,\mathrm{d}t \right\rangle$ [13] then $\Im(s) = G_\Sigma([k(t) = -i \cdot \Theta(s) \cdot \Theta(s-t)])$ where $\Theta(x)$ is the Heaviside step function. The EAPK is also obtainable as an infinite sum of the zero mean s.p. $Z(s) = \Sigma(s) - \langle\Sigma\rangle$ cumulant expansion: $\Im(s) = \exp\left(-\langle\Sigma\rangle \cdot s + \sum_{m=1}^\infty \frac{1}{m!} \int_0^s \mathrm{d}x_1 \int_0^s \mathrm{d}x_2 \ldots \int_0^s \mathrm{d}x_m \left\langle\left\langle Z(x_1) Z(x_2) \ldots Z(x_m) \right\rangle\right\rangle \right)$. The finite-terms summation gives a qualitatively feasible approximation. But it can violate the $\Im(s)$ monotonic decrease at large $\delta\Sigma$ and $s >> l_c$. Such an artifact is common [8] to Gaussian ($m \le 2$) s.p. based models when $\Im(s) \cong \exp\left(-\langle\Sigma\rangle \cdot s + \int_0^s (s-x) \cdot C_2(x)\,\mathrm{d}x \right)$ [5] is only covariance dependent. We notice that it is also relevant to nonnegatively valued s.p. like, e.g., the exponential Ornshein - Uhlenbeck (expOU) s.p. [13]. So, one must use the infinite statistical sum for colored s.p., that is a known analytical issue.

But one can always apply the EAPK MC sampling. The nondecreasing stochastic integral $\tau(x)$ is accumulated from the $\Sigma(x)$ realization obtained either from an analytical solution of SDE (1b) (the expOU is an example) or by discrete numerical schemes [14] of SDE integration. The f.p. s is sampled when $\tau(s = x) = -\ln\xi$ where ξ is uniformly distributed on (0,1]. It is statistically equivalent to the solution of equation $\Im(s) = \xi$ that applies the cumulative s distribution (c.d.f.) $1 - \Im(s)$.

Let's proceed to the exact analytical solutions we have found for EAPK $\Im(s)$ of different stochastic medium models to clarify certain general regularities of the non-classical RT behavior. We show that they are essentially dependent on two non-dimensional parameters that measure the relative volatility $\delta_\Sigma = \delta\Sigma/\Sigma_{mix}$ and the correlation scale variability $\delta_c = \delta\Sigma \cdot l_c$ of the generating s.p.

1. The **Bessel - Feller** mean-reverting diffusion s.p. (1b) has $a(\Sigma) = -\beta \cdot (\Sigma - \alpha)$, $b(\Sigma) = \sigma \cdot \Sigma^{1/2}$ and is calibrated as

follows: $\beta = l_c^{-1}$, $\alpha = \Sigma_{mix}$, $\sigma^2 = 2\delta\Sigma^2/\Sigma_{mix}l_c$. The 1-point density is a Γ-distribution p.d.f. $f_1(\Sigma) = \delta_\Sigma^{-2}\cdot\Gamma^{-1}\left(\delta_\Sigma^{-2}\right)\cdot\Sigma_{mix}^{-1}\times\left(\delta_\Sigma^{-2}\,\Sigma/\Sigma_{mix}\right)^{\delta_\Sigma^{-2}-1}\exp\left(-\delta_\Sigma^{-2}\,\Sigma/\Sigma_{mix}\right)$. The FPE (3) derived solution for $f(\Sigma|s) = \exp[-g(s)]\cdot f_1[q(s)\cdot\Sigma]$, $g(0) = 0$, $q(0) = 1$, leads to an analytical expression for EAPK: $\Im(s) = \exp\left(-\frac{2}{\delta+1}\Sigma_{mix}s\right)\cdot\left\{\frac{(\delta+1)^2}{4\delta}\cdot\left[1-\left(\frac{\delta-1}{\delta+1}\right)^2\exp\left(-\delta\frac{s}{l_c}\right)\right]\right\}^{-\delta_\Sigma^{-2}}$, where $\delta = \sqrt{1+4\delta_\Sigma\delta_c} > 1$.

In Fig. 1, *a*, **(i)** $\Im(s) >> \exp(-\Sigma_{mix}\cdot s)$ at all f.p. $s > \lambda_{mix} = \Sigma_{mix}^{-1}$; **(ii)** $\Im(s)$ manifests the non-exponential non-classical behavior at $s \sim s_c = \delta^{-1}l_c$ (here $\Sigma_{mix}\cdot s_c \approx 3$); **(iii)** $\Im(s) \cong \Im_0\cdot e^{-\Sigma_{eff}\cdot s}$ at $s >> s_c$, thus homogenizing to $\Sigma_{eff} = f_{ss}\cdot\Sigma_{mix}$ with the self-shielding factor $f_{ss} = 2/(1+\delta) < 1$. But unlike in the classical ($\Im_0 = 1$) homogenization theory, $\Im_0 = \left[4\delta/(1+\delta)^2\right]^{\delta_\Sigma^2} < 1$.

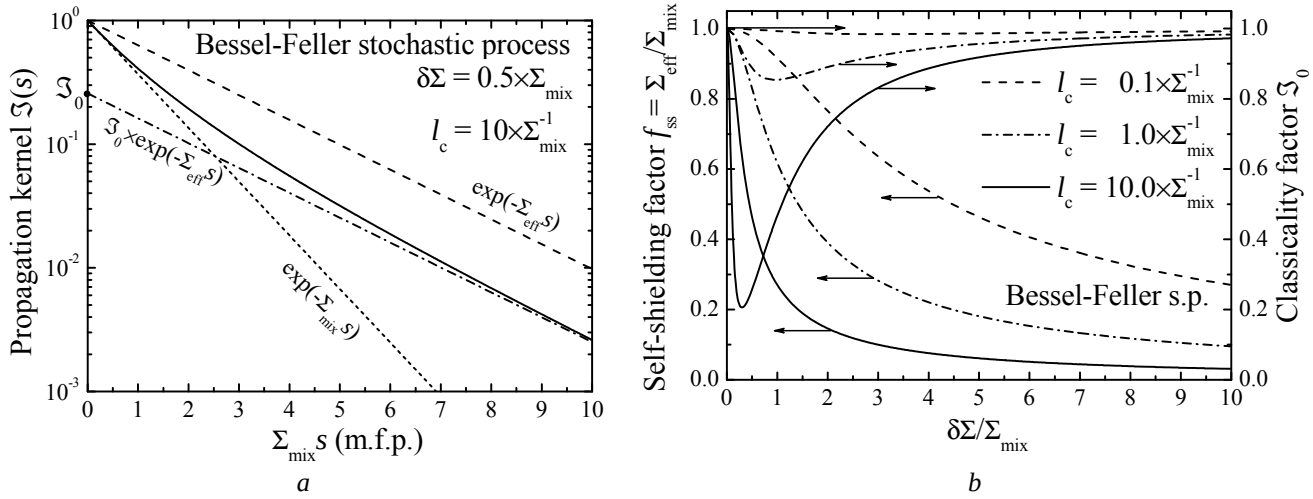

Fig. 1. The calculated Bessel-Feller s.p. EAPK $\Im(s)$ (*a*) and the indices of its far asymptotic behavior (*b*).

The introduced factor $\Im_0 \subset (0,1]$ is determined by the EAPK transient behavior at $s < l_c$. We rate it as the non-trivial "classicality factor" of the generalized RT. Fig 1(b) shows that the non-classical ($\Im_0 < 1$) behavior is favored in long-correlated ($\delta_c >> 1$) weakly fluctuating ($\delta_\Sigma \le 1$) media.

2. The **Campbell noise** is the well studied point [15] s.p. $\Sigma(s) = \sum_{k=-\infty}^{+\infty}\psi(s+x_k)$ where $\psi(x) \ge 0$ is a smooth deterministic shape function of the Poisson distributed (with frequency ν) pulses localized at x_k. Assuming $\psi(-x) = \psi(x)$, we calibrate it according to Campbell theorem: $\nu = \left(2l_c\delta_\Sigma^2\right)^{-1}$, $\nu\cdot\int_{-\infty}^{\infty}\psi(x)\,dx = \Sigma_{mix}$, $\nu\cdot\int_{-\infty}^{\infty}\psi^2(x)\,dx = \delta\Sigma^2$. The characteristic functional of this s.p. is [13] $G_\Sigma\left(\left[k(x)\right]\right) = \exp\left\{\nu\cdot\int_{-\infty}^{+\infty}\left[\exp\left(i\int_0^{+\infty}k(y)\psi(y-x)\,dy\right)-1\right]dx\right\}$, and immediately leads to the EAPK $\Im(s) = \exp\left\{-\nu\cdot\int_{-\infty}^{+\infty}\left[1-\exp\left(-\int_0^s\psi(y-x)\,dy\right)\right]dx\right\}$. At $s >> l_c$, again, it is homogenized with the universal ψ-independent $f_{ss} = \frac{1-\exp(-2\delta_\Sigma\delta_c)}{2\delta_\Sigma\delta_c} \approx \begin{cases}1-\delta_\Sigma\delta_c, & \delta_\Sigma\delta_c << 1\\ (2\delta_\Sigma\delta_c)^{-1}, & \delta_\Sigma\delta_c >> 1\end{cases}$ while the factors $\Im_0 < 1$ vary with pulse shape. For stepwise shaped pulses $\psi(x) = (\delta\Sigma^2/\Sigma_{mix})\cdot\Theta(x - l_c)\cdot\Theta(l_c - x)$, $\Im_0$ is found analytically: $\Im_0 = \exp\left\{-\delta_\Sigma^{-2}\cdot\left[\left(1-\delta_\Sigma^{-1}\delta_c^{-1}\right)+\left(1+\delta_\Sigma^{-1}\delta_c^{-1}\right)\exp\left(-2\delta_\Sigma\delta_c\right)\right]\right\}$. The subsequent analysis shows that $\Im_0 \to \Im_0(\delta_c) \approx$ $\approx \exp\left(-\frac{2}{3}\delta_c^2\right)$ at $\delta_\Sigma\delta_c << 1$ while $\Im_0 \to \Im_0(\delta_\Sigma) \approx \exp\left(-\delta_\Sigma^{-2}\right)$ at $\delta_\Sigma\delta_c >> 1$. Again, one can see that the non-classical RT requires long correlations $\delta_c >> 1$ at moderate variability $\delta_\Sigma \sim 1$.

3. The **Markov binary mixture** of two ($\Sigma_{1,2}$) materials is described with the renewal s.p. [1] statistics of intersections of particle rays with their boundaries. It is characterized by the mean chord lengths $L_{1,2}$. They are concordant with the materials volume shares $\nu_{1,2} = L_{1,2}/L$, $L = L_1 + L_2$. Then the s.p. is stationary, and is calibrated to $\Sigma_{mix} = (\Sigma_1L_1 + \Sigma_2L_2)/L$, $\delta\Sigma = |\Sigma_1 - \Sigma_2|\sqrt{L_1L_2}/L$, $l_c = L_1L_2/L$. But one more parameter $\nu_1 = 1 - \nu_2$ remains free. The EAPK of this s.p. can be

calculated exactly by solving the L–P equations [1, 4], using the dichotomic s.p. characteristic functional [13], or by diagram technique of the statistical sum calculation [5]. All these ways result in the same expression: $\Im(s) = \exp(-\Sigma_{12}s)\cdot\left\{\left[l_c^{-1} - (\nu_1 - \nu_2)(\Sigma_1 - \Sigma_2)\right]\frac{\sinh \delta\Sigma_{12}s}{2\delta\Sigma_{12}} + \cosh \delta\Sigma_{12}s\right\}$ where $\delta\Sigma_{12} = \sqrt{\left(\frac{\alpha_1 - \alpha_2}{2}\right)^2 + \frac{1}{L_1 L_2}}$, $\Sigma_{12} = (\alpha_1 + \alpha_2)/2$, $\alpha_{1,2} = \Sigma_{1,2} + L_{1,2}^{-1}$. As well, the mix is effectively homogenized to $\Sigma_{eff} = \Sigma_{12} - \delta\Sigma_{12}$, and the correspondent self-shielding factor f_{ss} was obtained and MC benchmarked in Ref. 5. Now we can supplement it with the calculation of classicality factor $\Im_0 = \frac{1}{2} - \left[(\nu_1 - \nu_2)\cdot(\Sigma_1 - \Sigma_2) - l_c^{-1}\right]/4\delta\Sigma_{12}$. Though the non-classical RT signature $\Im_0 < 1$ is obvious, the analysis of this, in fact, 4-parametric formula is rather complicated. But the advantage of this s.p. consist in the possibility to confront the theory with the statistically accurate benchmark MC calculations of the RT in the same system.

The developed approach is implemented in our GEANT4 [16] based MC code *RaT* 3.1 [5]. It has requested the all-out upgrade of the GEANT4 object model that is primordially dealing only with classical exponential PK The stochastic materials (SM) concept has been introduced to model the unresolved heterogeneity of random media. They are attributed with the non-classical EAPK (calculated using the methods described above) as well as with some other p.d.f.'s required for correlated sampling of final states to provide the statistically consistent iterative algorithm of particles' transport. One should emphasize that the non-classical RT in SM is modeled within the single-stage MC (1-MC) thereby avoiding the double-MC benchmark method extended dimensionality and thus upgrading efficiency by orders of magnitude. Certain validation results are discussed below.

In Fig. 2, the problem of thermal neutrons transport in a random packings of spherical inclusions in a matrix is illustrated (we applied the double-MC to this problem earlier, see details in [5]). One can see that the benchmark results are well reproduced by the Markov binary mixture non-classical RT model for both primary (see Fig. 2, *a*) and secondary (see Fig. 2, *b*) effects of neutron-material interactions, *incl.* the near-surface buildup maximum of Helium production in $^{10}B(n, \alpha)^7Li$ reactions.

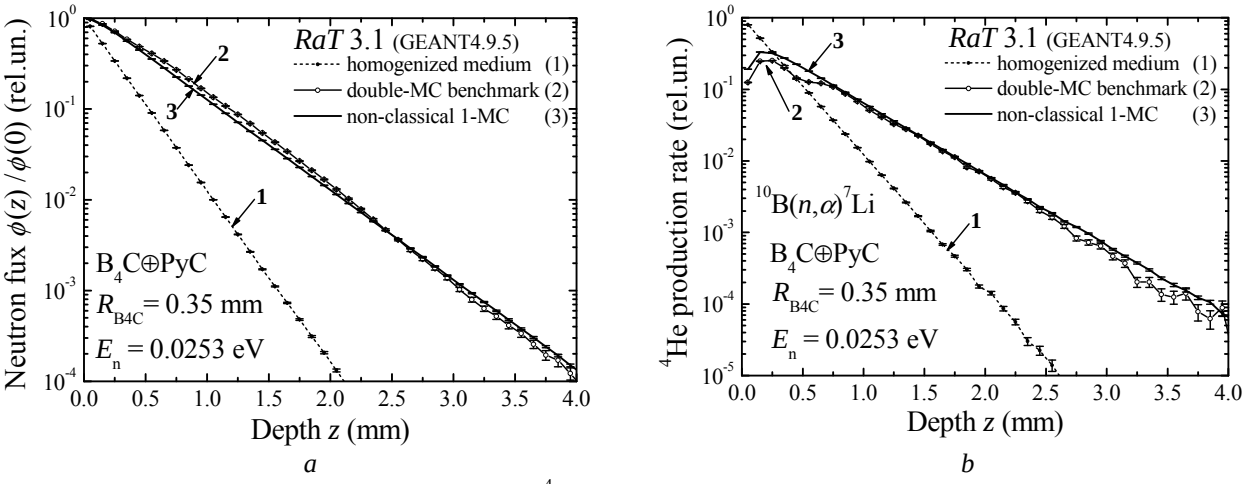

Fig. 2. Neutron flux attenuation curves (*a*) and ^{4}He production rates (*b*) in a B_4C binary mix with PyC simulated using the method of the present work and compared to the results of benchmark double-MC modeling.

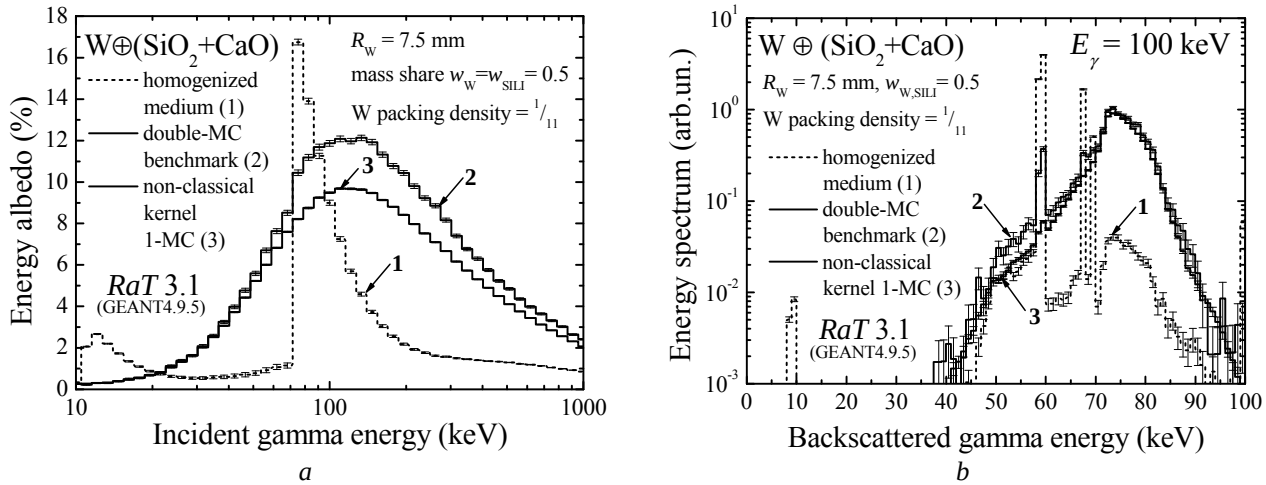

Fig. 3. Energy albedo (*a*) and reflected gamma spectrum (*b*) for random mix of W spheres in a silicone mass.

The more complex validation case is shown in Fig. 3. We considered the backscattering of broad γ-beams of various energies E_γ normally incident on the 60 cm thick slab of absorber (W) spheres randomly mixed with the scatterer, a silicone mass SiO_2+CaO. This effect is entirely due to the scattered and secondary components of the gamma flux, and thus is very sensitive to the RT transport model. Within the "naively" homogenized AMM, backscattering is marginal everywhere except of the fluorescent yields E_γ of the Tungsten *K*- ($K_\beta \in 67 \div 69$ keV, $K_\alpha \approx 59$ keV) and *L*-series (7.4÷9.7 keV). The benchmark model by default includes all scattering-absorption correlations and gives much greater albedos. Their reproduction by the non-classical RT model is accurate to 20% that is satisfactory for practical purposes. Note that the 1-MC simulation is about ten times quicker.

One can conclude that the developing stochastic approach of incorporation of the non-classical RT concept into theoretical and MC transport calculations is fruitful. In particular, it is prospective to apply this method and models to the reactivity calculations of GenIV HTGR/VHTR/PBMR TRISO fuels and to the modeling of coolant gamma heating in super-critical water-cooled reactors (SCWR) having heterophase coolant density fluctuations in the vicinity of a pseudocritical point.

This work was supported in part by the STCU partner project #P4841.

REFERENCES

1. *Sanchez R.* Linear kinetic theory in stochastic media // J. Math. Phys. - 1989. - Vol. 30. - P. 2489 - 2511.
2. Jensen J.L.W.V. Sur les fonctions convexes et les inegalities entre les valeurs moyennes // Acta Math. - 1906. - Vol. 30. - P. 175 - 193.
3. *Bernard E., Golse F., Salvarani F.* Homogenization of transport problems and semigroups // Math. Meth. Appl. Sci. - 2010. - Vol. 33. - P. 1228 - 1234.
4. *Adams M.L., Larsen E.W., Pomraning G.C.* Benchmark results for particle transport in a binary Markov statistical medium // J. Quantit. Spectr. Rad. Transf. - 1989. - Vol. 42. - P. 253-266.
5. *Dyuldya S.V., Bratchenko M.I.* Monte Carlo simulation of radiation transport in stochastically heterogeneous absorbers // Proc. of the 3rd Int. Conf. "Current Problems in Nuclear Physics and Atomic Energy" (Kyiv, 7 - 12 June, 2010). - Kyiv, 20011. - Part II. - P. 463 - 467.
6. *Zimmerman G.B., Adams M.L.* Algorithms for Monte Carlo particle transport in binary statistical mixtures // Trans. Am. Nucl. Soc. - 1991. - Vol. 64. - P. 287 - 292.
7. *Davis A.B., Marshak A.* Photon propagation in heterogeneous optical media with spatial correlations: Enhanced mean-free-paths and wider-than-exponential free-path distributions // J. Quantit. Spectr. Rad. Transf. - 2004. - Vol. 84. - P. 3 - 34.
8. *Davis A.B., Mineev-Weinstein M.* Radiation transport through random media represented as measurable functions: Positive versus negative spatial correlations // Proc. of Int. Conf. on Math., Comp. Meth. & Reactor Phys. (Saratoga Springs, NY, 2009). - Vol. 2. - P. 1137 - 1149.
9. Anomalous Transport: Foundations and Applications. - Weinheim: Wiley-VCH, 2008. - 584 p.
10. *Larsen E.W.* A generalized Boltzmann equation for "non-classical" particle transport // Proc. M&C+SNA-2007. - Available on CD-ROM from Am. Nucl. Soc., LaGrange Park, IL. - 13 p.
11. *Frank M., Goudon T.* On a generalized Boltzmann equation for non-classical particle transport // Kinet. Relat. Models. - 2010. - Vol. 3. - P. 395-407.
12. *Hanggi P., Jung P.* Colored noise in dynamical systems // Adv. Chem. Phys. - 1995. - Vol. 89. - P. 239-326.
13. *Caceres M, Budini A.* The generalized Ornstein-Uhlenbeck process // J. Phys. A: Math. Gen. - 1997. - Vol. 30. - P. 8427 - 8444.
14. *Higham D.J.* An algorithmic introduction to numerical simulation of Stochastic Differential Equations // SIAM Review. - 2001. - Vol. 43. - P. 525 - 546.
15. *Lowen S., Teich M.* Fractal-based point processes. - Wiley-Interscience: John Wiley & Sons, Inc., 2005. - 613 p.
16. *Agostinelli S., Allison J., Amako K., et al.* Geant4 - a simulation toolkit // Nucl. Instr. Meth. Sec. A. - 2003. - Vol. A22. - P. 250 -303.

LOW-ENERGY ELECTRON SPECTRA ARISING FROM THE BOMBARDMENT OF A TITANIUM TARGET BY β-PARTICLES OF TRITIUM AND α-PARTICLES OF ^{238}PU

A. I. Feoktistov, V. T. Kupryashkin, L. P. Sidorenko, N. F. Kolomiets, A. V. Kovalenko, V. A. Lashko

Institute for Nuclear Research, National Academy of Sciences of Ukraine, Kyiv, Ukraine

Low-energy spectrum of electrons arising from the bombardment of the titanium target by β-particles from tritium decay was investigated by (β,e)-coincidence method. To compare effects of different charge particles similar measurements were performed with α-particles from ^{238}Pu decay, in the same experimental conditions and with the same target. It is shown that ionization of atoms bombarding by charge particles can be represented as the effect of shake-off in both cases.

1. Introduction

Low-energy spectrum of electrons arising from the bombardment of a titanium target by β-particles of tritium can be represented as a result of the effect of shake-off, the quantum-mechanical transition from the initial unperturbed state of the system (atom) *i* to a final state *f* under the influence of a sudden perturbation caused by the interaction of atomic electron charge with the charge of flyingβ-particle. We assume the condition of "suddenness" of the shake-off process is condition that time of change of chargeτ is significantly less than the period of transition of atom from initial *i* to final state *f*, $\tau_\beta = \frac{r}{v_\beta} \ll 2\pi\omega_{fi}^{-1}$, where ω_{fi} is transition frequency.

The effect of shake-off can be observed in the case when a sudden disturbance occurs spontaneously in the system in a state of rest, for example in β-decay of nuclei, and in the case of moving charge particle in the moment of its closest approach with target atoms*r*, when shake-off probability becomes dependent on velocity v_β [1, 2].

We have found several types of electron emission depending on their origin from the angular distribution investigation of electrons emitted from the target surface under α-particle bombardment [3]. This is near-zero energy electrons e_0 which takes off from the surface of target to continuum due to its interaction with suddenly arisen motionless charge of ionized atoms near the surface. The kinetic energy of e_0-electrons is no larger than several electron volts and its binding energy at the surface is less 1 eV as will be discussed later.

Other types of electron emission which we call the fast electrons e_f are connected with perturbation of atoms at the moment of charge particle flight. If these atoms are located inside the target shake-off leads to the transition of electron to unfilled level of atom and formation of vacancy at the place where it was before. Fast electrons e_f^A associated with these processes can migrate toward the surface and move into the vacuum. Their angular distribution is isotropic [3]. Finally, when charge of flying particle at the exit of target causes an electron shake-off from atoms located on the surface the emission of fast electrons e_f^i into vacuum electron spectrum of e_f^i-electrons do not distort and can be compared with theoretical one.

We compare measured low energy electron spectra with theoretical one for α-particle transmission through targets of Al, Cu and Au [4 - 6] and they indicate the validity of our representation of atom ionization by flying α-particle as shake-off process.

In this work we want to continue these investigations in this work and use β-particles from tritium decay as charge particle with low energy and titanium target. To compare the influence of α- and β-particles on shaking process we decide to carry some measurements with α-particles in the same experimental conditions and with the same target.

2. Physical quantities relationship in the shake-off effect

The main formula describing the probability of emitting surface e_f^i-electron into vacuum due to perturbation by flying charge particle has such form:

$$dW(E) = \frac{c}{V_p}\left(\frac{Z_p e^2}{r}\right)^2 \left|\int \psi_f^* \psi_i^{(0)} dq\right|^2 \frac{b\sqrt{E}}{(E+E_n)^2} dE. \quad (1)$$

The first two multipliers define the probability of obtaining perturbation by electron; it increases with time of perturbation, but under conservation of shake-off condition $\tau_\beta \ll 2\pi\omega_{fi}^{-1}$, of course. Minimal probability of perturbation is at the motion of particle with speed of light c. Though the dimension of transferring perturbation is the square of energy it is divided by square of energy $(E + E_n)^2$ in formula (1). The probability of system transition from the state *i* to the state *f* with vacancy at the place of emitted electron is defined by the square of matrix element consisting of wave functions which are coordinate parts of stationary states $\psi(q,t) = \psi(q) exp\left(-iE\frac{t}{\hbar}\right)$. Finally, the last multiplier is energy differential distribution of electrons in continuum after shake-off. Here $b = \frac{\sqrt{2}m^{3/2}V_e}{\pi^2\hbar^3}$, m is electron mass and $V_e = x^3$ are volume and mean distance between electrons able to shake-off into the vacuum. Thus, first two multipliers describe first stage of shake-off process; they determine the probability of the perturbation transfer dependent on

velocity and charge of particles, while other multipliers relate to second stage of shake-off process: they describe transition probability from initial to final state and electron distribution on energy in continuous spectrum. Second stage does not depend on kind and motion of particles, though it does not occur without first stage.

The first-order perturbation theory for time-dependent transitions [2 - 7] was used in obtaining of formula (1), which is added by the expression to describe the electron shake-off to continuum and by multiplier c/v_p, which takes into account the motion of the charge at the moment of disturbance transfer [8]. Disturbance entirely and completely transfers to shaking electron and system remains with a vacancy in the shell of shaken electron. The for e_f^i-electrons on the surface

$$\left(\frac{Z_p e^2}{r}\right) = E + E_n. \tag{2}$$

Though the transmission probability of system from initial state *i* to final one *f* does not depend on the energy and such condition must be $r < r_{max}$, where $r_{max} = \frac{Z_p e^2}{E_n}$ for e_f^i-electrons. From the uncertainty relation it follows that in the moment of perturbation transfer from charge particle to an atomic electron the uncertainty of transferred energy $\Delta E = \frac{\hbar}{\tau}$ is several times larger than the magnitude of this perturbation, so the main condition of "suddenness" can be rewritten in the form $\frac{\Delta E}{E} = \frac{\omega^{-1}}{\tau} \gg 1$. Transferred to electrons energy becomes uncertain at the moment of perturbation. Therefore, the value of the perturbation can only be determined after the measurement of emitted electron energy and calculation according to formula (2). The distance of approaching of particle to electron *r* can be established at this moment only.

The yield of e_f^i-electrons with energy from 0 to E from the surface of the target passed by charge particle is

$$Y(E) = \pi \frac{c}{v_p} \left(\frac{Z_p e^2}{x}\right)^2 \left| \int \psi_f^* \psi_i^{(0)} dq \right|^2 b \int_0^E \frac{\sqrt{E} dE}{(E+E_n)^2} = B \int_0^E \frac{\sqrt{E} dE}{(E+E_n)^2} = BF(E), \tag{3}$$

where

$$F(E) = \int_0^E \frac{\sqrt{E} dE}{(E+E_n)^2} = \frac{1}{\sqrt{E_n}} arctg \sqrt{\frac{E}{E_n}} - \frac{\sqrt{E}}{E+E_n}, \; F(0) = 0. \tag{4}$$

3. Experimental procedure

The study of low-energy electron ionization spectrum, which arises after β-particles of tritium pass through titanium target was carried out by method of timing (βe)-coincidences by means of applying braking voltage U (retarding potential) in the channel of electron detection. The counting rate dependence of timing coincidences on the retarding voltage was measured.

The measurements were performed in two geometries represented in Fig. 1. In "transmission" experiment tritium source S together with a collimator K were placed close to the target T, as shown in the Figure. The target was a self-supporting Ti film with 0.4 μm thickness, arranged at the angle of 45° relative β-particle beam, so the total thickness for β-particles was 0.57 μm. β-particles after passing of the target and 6 cm distance hit on the detector MCP_1, which is an assembly of two microchannel plates in a chevron configuration, and were recorded by them. Emitted from the target e_0-, e_f^A-, e_f^i-electrons were detected by second detector MCP_2. MCP_2 detector was fixed in a vacuum chamber immovably while all other elements of construction (MCP_1, S, K, T) were fixed on the axis of rotation O which made it possible to measure the angular distribution of electrons hitting on MCP_2 in coincidence with β-particles. The target, a collimator and a source had the same potential U, which is varied during the measurements. The pressure in vacuum chamber was maintained near $5 \cdot 10^{-6}$ Torr.

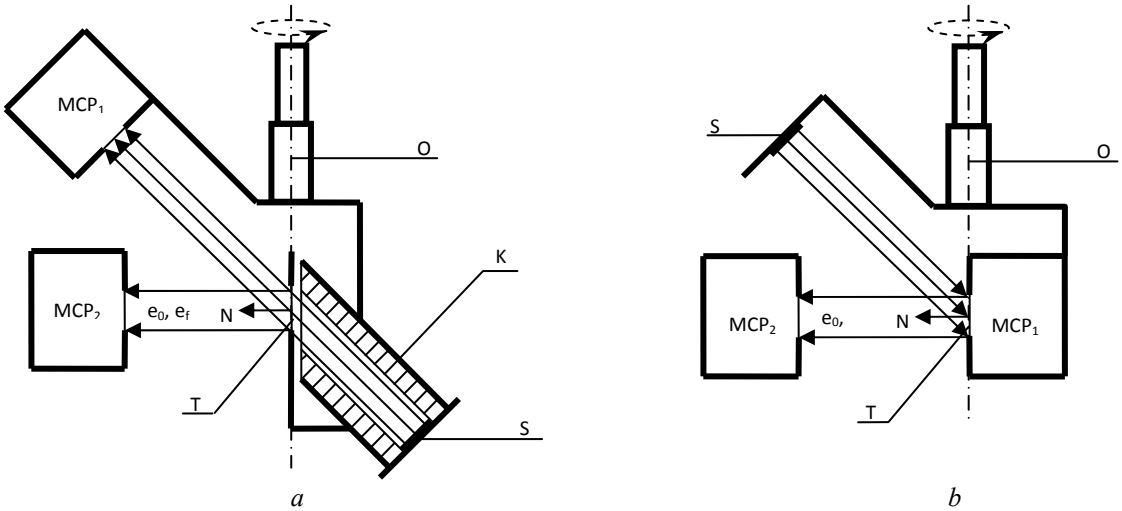

Fig. 1. The schemes of experiments: *a* - "transmission" geometry; *b* - "reflection geometry", S – source, T – target, MCP_1 and MCP_2 – detectors, K – collimator, O – axis of rotation.

In the "reflection" experiment β-particle detector MCP_1 was located directly behind the target (see Fig. 1, *b*) while the source S (without collimator) was moved into the place of MCP_1. In this geometry detector MCP_2 registered e_0- and e_f-electrons, arising at the entrance of β-particles into the target, which was applied by potential U in measuring time. In both geometries the same target surface was investigated.

The radioactive source was a tritium spot of 22 mm diameter on a 35 mm diameter of titanium substrate. The average energy of its continuous β-spectrum is 5.69 ± 0.02 keV at the end-point energy 18 keV, the activity of the source was $5 \cdot 10^7$ Bq. In "transmission" geometry due to absorption of β-particles in the target detector recorded only electrons with initial energy above 8.4 keV, which corresponds to the mean range of electrons in the target thickness. Average speed of β-particles at the exit of the target was $v_\beta = 3.8 \cdot 10^9$ cm·s^{-1}, and the average energy was E = 3.7 keV. In "reflection" geometry mean energy of β-particles at the entrance to the target, which are able to pass through the target and be registered by MCP_1 is 11 keV, which corresponds to mean velocity $v_\beta = 6.3 \cdot 10^9$ cm·s^{-1}.

In the measurements with α-particle source of tritium was replaced by ^{238}Pu source from the OSAI set (an exemplary spectrometric α-source with energy $E_\alpha = 5.5$ MeV). Since for α-particles target was thin enough, we can assume that the input and output energies of α-particles are practically the same and speed $v_\alpha = 1.6 \cdot 10^9$ cm·s^{-1} was adopted in both cases the same.

We have studied the properties of e_0-electrons in works [9 - 12], so now we mention about them only shortly. Distribution N(E = eU) of coincidence number of (e_0 + e_f)-electrons with tritium β-particles in "transmission" geometry for U in range from +24 eV to -10 eV is shown in Fig. 2 (curve *1*) as visual example. We will consider the distribution of e_0-electrons on energy which is the difference of the coincidence numbers N(0) and N(E): $N_\Delta(E)=N(0)-N(E)=AF(E)$, where F(E) is the theoretical distribution of shaking e_0-elctrons, defined by formula (4). The experimental distribution $N_\Delta(E)$ is in a good agreement with theoretical one (Fig. 3, curve *3*).

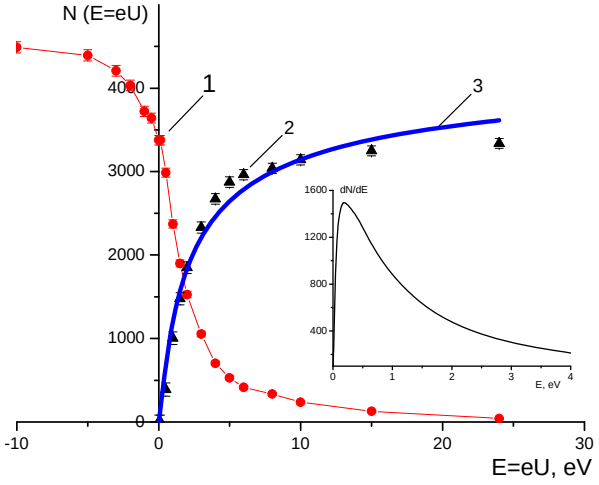

Fig. 2. Spectra of e_0-electrons from tritium β-particles in "transmission" measurements: *1* – retarding curve (integral spectrum of e_0-electrons in the range from E_{max} to E = eU); *2* – integral distribution of e_0-electrons in the range from 0 to E; *3* – energy distribution of e_0-electrons calculated from (4) as shake-off for E_n=0.6 eV. Insert – differential distribution of e_0-electrons at the same binding energy calculated by formula (3).

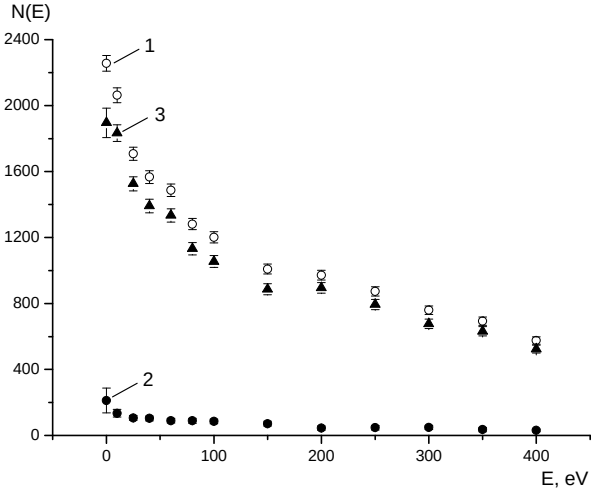

Fig. 3. Dependence of the number of coincidences of β-particles with fast electrons e_f on energy: *1* – "transmission" experiment; *2* – "reflection" experiment; *3* – dependence for e_f^i-electrons shaking to continuum.

All spectra are aligned with registration of $3.6 \cdot 10^6$β-particles and $1.8 \cdot 10^5$ α-particles per one hour (but for clarity "reflection" spectra with β-particles are increased five-fold in Fig. 2). We measured coincidence time spectra in the range of retarding potential from 0 to 400 V, it was measured 13 points with 1 h exposure in all.

4. Presentation of measurement results

Let us turn to a discussion of the properties of fast e_f-electrons. Fig. 3 shows the distribution 1, representing the numbers of (β,e_f)-coincidences in "transmission" geometry as a function of energy $N_{\beta 1}$(eU), this numbers is a sum of e_f^A- and e_f^i-electrons. Distribution 2 is a numbers of (β,e_f^A)-coincidences $N_{\beta 2}$(eU), measured in "reflection" geometry, and distribution 3 represents the numbers of (β,e_f^i)-coincidences, which is the difference $N_{\beta 3}(eU) = N_{\beta 1}(eU)-1.7N_{\beta 2}(eU)$. The coefficient 1.7 reflected different probabilities of electron shake-off at the exit of target, where $v_\beta = 3.8 \cdot 10^9$ cm·s^{-1}, and at the entrance of target, where $v_\beta = 6.3 \cdot 10^9$ cm·s^{-1}.

The same dependences as in Fig. 4 are showed in Fig. 5, but for α-particles passage through the target. In this case $N_{\alpha 3}(eU) = N_{\alpha 1}(eU) - N_{\alpha 2}(eU)$, because titanium target is thin for α-particles and numbers of e_f^A-electrons at the entrance of target and at its exit are the same.

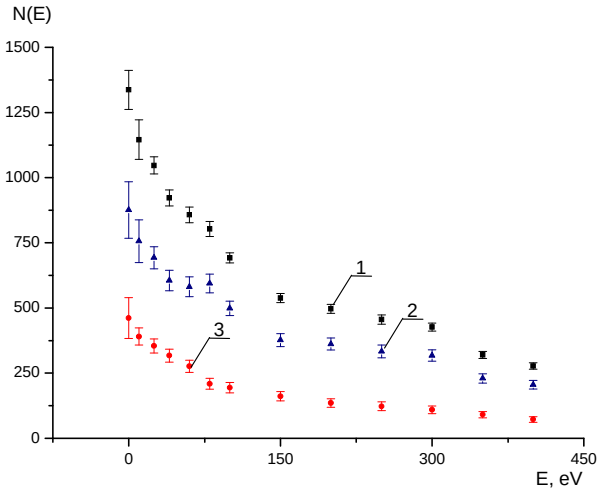

Fig. 4. Dependence of the coincidence number of α-particles with fast electrons e_f on energy of e_f: *1*, *2*, *3* – the same as in Fig. 3.

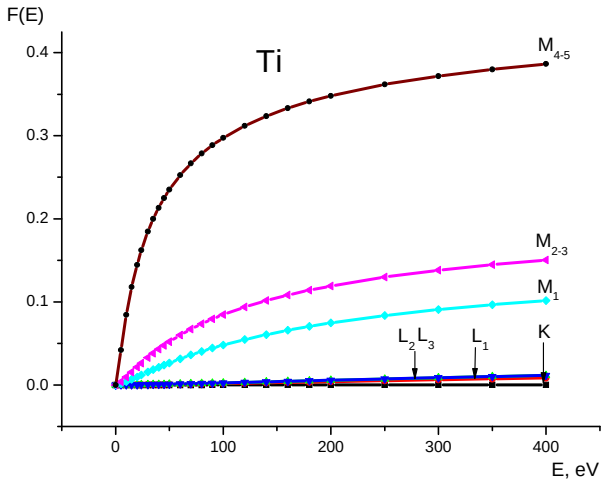

Fig. 5. The function of integral e_f^i-electron distribution F(E) (see formula (4)) for shaking from different subshells of Ti atom.

Based on formula (1) we can compare distributions $N_{\beta 3}(eU)$ and $N_{\alpha 3}(eU)$, which shows the similarity of shake-off curves for α- and β-particles.

The integral spectrum of ionization electrons in the energy range from 0 to E can be obtained by means of transformation which corresponds to the change of integration limits $\int_0^E = \int_0^{E_{max}} - \int_E^{E_{max}}$, i.e. $N_{\beta 4}(E) = N_{\beta 3}(0) - N_{\beta 3}(E)$, and can be compared with theoretical distribution $N_{\beta 4}(E) = \sum_l A_{\beta l} F_l(E)$, where index l denotes different shells of atom involved in shake-off process, multiplier $A_{\beta l}$ independent on e_f^i energy distribution is defined as $A_{\beta l} = = \eta\pi\frac{c}{V_\beta}\left(\frac{Z_\beta e^2}{x_l}\right)^2 \left|\int \psi_f^* \psi_i^{(0)} dq\right|_l^2 bn_\beta$, where η depends on experimental conditions and is the production of detection efficiency of electrons ε on part of its collection δ_{eff} by MCP_2 detector and n_l is number of electrons in l-subshell. All sign β should be substitute by α, when process with α-particle is considered.

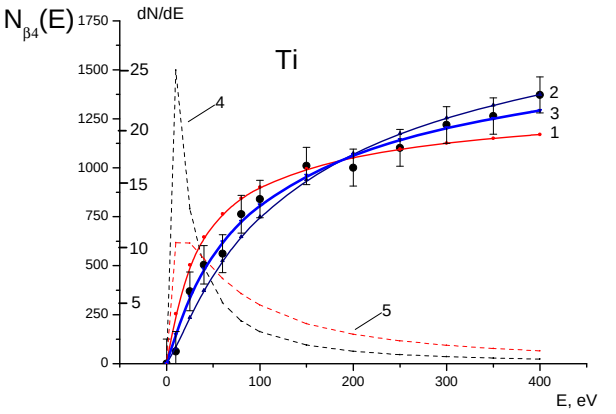

Fig. 6. The comparison of experimental and calculated e_f^i-electron distributions for shaking by β-particles of tritium: *1* – shaking on $M_{4,5}$-subshells of Ti; *2* – $M_{1,2,3}$-subshells; *3* – their mixture. Differential distribution of e_f^i-electrons on energy for $M_{4,5}$ – (*4*) and $M_{1,2,3}$ – (*5*) subshells are showed by dotted lines.

Calculations of e_f^i-electron integral energy distribution for different subshells of titanium atom obtained from the formula (4) are presented in Fig. 6. As it will be seeing from the further only shaking from M-subshells electron distribution is comparable with experimental distribution, K- and L-shells influence on shake-off in this range of e_f^i-electron energy is small.

The comparison of experimental and calculated energy distributions for e_f^i-electrons from shake-off by tritium β-particles by means of RMS fitting is presented in Fig. 6. Experimental values are drawing as points with statistical bars. Curve *1* corresponds to the calculations of e_f^i-shake-off from $M_{4,5}$-subshells of titanium atom, and curve *3* is the same for $M_{1,2,3}$-subshells. Thick curve *2* corresponds to the calculation for the mixture

$$N_{\beta 4}(E) = N_\beta(E) = xA_{M_{4,5}}F_{M_{4,5}}(E) +$$

$$+(1-x)A_{M_{1,2,3}}F_{M_{1,2,3}}(E),$$

where x = 0.4 and (1 - x) = 0.6.

A similar analysis was made for the shake-off electrons from Ti target under bombardment by ^{238}Pu α-particles. In accordance with results for tritium β-particles distribution of ionization electrons e_f^i can be mainly represented as a shake-off of electrons from M-shell for α-particles, too, moreover, this occurs in 40 % of events at $M_{4,5}$-subshells and other 60% at $M_{1,2,3}$-subshellsof titanium atom. The dashed lines show in Fig.6 calculated differential spectra of electrons e_f^i according to formula (3) for these components of curve $N_{\beta 4}$.

5. Conclusions

The investigations of energy distribution of e_f^i-electrons emitted from titanium target under bombardment by tritium β-particles indicated a good agreement of experimental distribution with theoretical one by formula (1). This allows us to draw conclusion about correct description of atom ionization by flying particle as quantum-mechanical transition of the system under the influence of sudden perturbation from initial state to final one with the emission of electron into continuum and the formation of vacancy in the atom on the site of emitted electron, i.e. as the shake-off effect. Previously such a statement was made after investigations of ionization of different targets by flying α-particles [4 - 6].

A comparison of the properties of shake-off process induced by β- and α-particles penetrating Ti target was made. For this purpose a measurements with α-particles were carried out in the same experimental conditions and with the same target as for β-particles. It was found the similarity of energy distributions of e_f^i-electrons and the total probability of shake-off proportional to $\frac{(Z_p e^2)^2}{v_p}$.

Shake-off process can be represented as taking place in two stages [13]. Sudden perturbation of the system take place in the first stage and we experimentally see difference in perturbation transfer for α- and β-particles, it is determined by multipliers before matrix element $\pi\frac{c}{v_p}\left(\frac{Z_p e^2}{r_a}\right)^2$ in the formula (1). In the second stage the transition of system from the initial state i to the final state f occurs. Second stage which is determined by the remaining terms of (1) is the same for different particles independently of the first stage, although it cannot occur without it presence. This also was confirmed by comparing of the measurement results in our work.

REFERENCES

1. *Dykhne M., Yudin G.L.* // Usp. Fiz. Nauk. - 1978. - Vol. 125. - P. 377.
2. *Landau L.D., Lifshitz E.M.* Course of Theoretical Physics. Vol. 3. Quantum Mechanics: Non-Relativistic Theory. - Moscow, Nauka, 1974; Oxford: Butterworth-Heinemann, 1981. - P. 179.
3. *Kupryashkin V.T., Sidorenko L.P., Feoktistov A.I., Shapovalova I.P.* // Izv. Akad. Nauk. Ser. Fiz. - 2004. - Vol. 68. - P. 1208.
4. *Sidorenko L.P., Kupryashkin V.T., Feoktistov O.I., Rovens'kikh E.P.* // Ukr. J. Phys. - 2010. - Vol. 55. - P. 757.
5. *Kupryashkin V.T., Sidorenko L.P., Feoktistov O.I., Rovenskikh E.P.* // JETP. - 2011. - Vol. 139. - P. 679.
6. *Kupryashkin V.T., Sidorenko L.P., Feoktistov O.I., Rovenskykh E.P.* // Ukr. J. Phys. - 2012. - Vol. 57. - P. 5.
7. *Davydov A.S.* Quantum Mechanics. - Moscow: Nauka, 1963. - P. 326.
8. *Feoktistov A.I.* // Ukr. J. Phys. - 2010. - Vol. 55. - P. 165.
9. *Feoktistov A.I.* // Ukr. J. Phys. - 2008. - Vol. 53. - P. 1043.
10. *Kupryashkin V.T., Sidorenko L.P., Feoktistov A.I., Shapovalova I.P.* // Izv. Akad.Nauk. Ser. Fiz. - 2003. - Vol. 67. - P. 1446.
11. *Feoktistov A.I., Valchuk A.A., Kupryashkin V.T. et al.* // Izv. Akad.Nauk. Ser. Fiz. - 2008. - Vol. 72. - P. 281.
12. *Feoktistov A.I., Valchuk A.A., Kupryashkin V.T. et al.* // Izv. Akad. Nauk. Ser. Fiz. - 2008. - Vol. 72. - P. 285.
13. *Dykhne M., Yudin G.L.* // Usp. Fiz. Nauk. - 1977. - Vol. 121. - P. 157.

DATA REDUCTION FOR HIGH GAMMA-RAY COMPTON SPECTROSCOPY

Samir Ahmed Hamouda

Department of Physics, University of Benghazi, Benghazi, Libya

General aspects of the Compton Scattering theory are introduced. Data analysis procedure for the γ-ray experiment is outlined. The Background, detector response function, geometrical broadening function and source broadening function corrections are discussed.

1. Introduction

Compton scattering is a technique for determining the momentum distribution of electrons in condensed matter. When monochromatic photons are Compton scattered (inelastically scattered) in a fixed direction, the observed energy spectrum of the scattered photons is Doppler-broadened due to the motion of the target electrons. This broadened line shape, referred to as the Compton profile, $\mathbf{J(p_z)}$**,** can be analyzed to yield detailed information about the electron momentum distribution, **n(p**), in the scatterer**.** Within the impulse approximation [1], the Compton profile, $J(p_z)$, is defined as the projection of the ground state electron momentum density distribution, n(p), along the scattering vector (chosen as the p_z axis) and is given by:

$$J(p_z) = \int\int n(p_x, p_y, p_z)\, dp_x dp_y. \quad (1)$$

Therefore, in Compton scattering experiment all the available information about the electrons initial state is contained in the distribution of the inelastically scattered radiation, i.e. the Compton profile. A detailed review of this topic can be found in [2 - 3].

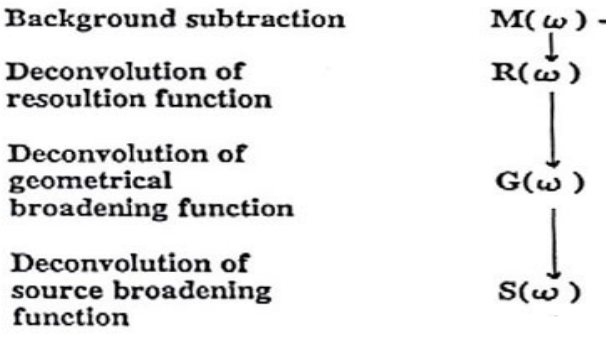

Fig. 1. The order of data correction.

Over the range of energies below 1 MeV, the Compton cross-section is proportional to the atomic number Z whereas the photoelectric cross-section is approximately proportional to Z^4/ω_1^3 where $\boldsymbol{\omega_1}$ is the incident photon energy. This implies that the ratio of Compton to photoelectric cross section is approximately proportional to ω_1^3/Z^3. For 662 keV gamma ray radiation, the Compton cross section is greater than the photoelectric cross section up to about Z = 90 [4 - 7]. For example, if Compton profile measurement is to be carried out using x-ray energy of 15 keV compared to gamma ray energy of 662 keV, the gamma ray experiment will gain a factor of about 10^5 in time for the same sample and the same source strength. As a result, the higher energy of the gamma ray makes Compton profile measurements to be performed on a wide range of high Z-materials and their alloys which are completely impractical at the present x-ray energies.

However, before the data can be interpreted, a series of energy dependent corrections have to be applied [8]. In this paper an outline of the data corrections is presented and the background, detector response function, geometrical broadening and source broadening functioncorrections are discussed. The order of data corrections is illustrated schematically in Fig. 1.

2. Background Subtraction

The background is defined as the signal obtained with the source opened and no sample in position. The main sources of the background are: (1) the natural radioactivity such as cosmic rays. (2) stray radiation from the source. (3) scattering from the sample chamber, sample holder, air in the scattering chamber, and detector collimator. Therefore, it is necessary to measure the background spectrum and then subtract this from the Compton scattering data before the remaining data processing procedures can be used.

Since in gamma-ray experiments the background can be measured independently compared with x-ray experiments an appropriate energy calibration of the spectra is required. It is important to emphasize the point that the experimental condition (i.e. geometry, collimation, shielding arrangement) in which the Compton data is obtained should not differ from the experimental condition in which the background is measured. In the background measurement only the sample is removed, and everything else must remain the same. This will allow for the background measurement to be consistent and minimize the systematic error.

When using high energy gamma- ray source for Compton profile measurements with a long half-life such as the 137-Cs source which has a half-life (30 years), the background contribution is considered to be time-independent. Since the background spectrum is subtracted from the Compton data on point-by-point basis, the background measurement should have good statistics so that time scaling is properly performed.

3. The Energy Resolution of the Instrument

In gamma ray Compton scattering experiments, the energy analysing system consists of a SSD and associated electronics. The instrumental resolution function of a Compton spectrometer consists of two parts: (i) the energy resolution of the detector, $\mathbf{\Delta E_{det}}$, which is the convolution of the detector response function with the source broadening function (i.e. due to inelastic scattering within the source material); and (ii) the geometrical resolution, $\mathbf{\Delta E_{geom}}$, due to finite collimation. The total instrumental resolution function, $\mathbf{\Delta E_{inst}}$ is the convolution of these two functions defined as FWHM (keV) and is given by

$$\Delta E_{inst} = [(\Delta E_{det})^2 + (\Delta E_{geom})^2]^{1/2}. \quad (2)$$

4. The Energy Resolution of the Detector

The detectorresolution function is defined as a measure of the amount of broadening of a monoenergetic radiation line in the Compton peak range. The energy resolution of the SSD is given by

$$\Delta E_{det} = (\alpha + F\varepsilon\omega_1)^{1/2}, \quad (3)$$

where ω_1 is the incident energy, α represents the noise term and is constant, **F** is the Fano factor, and $\boldsymbol{\varepsilon}$ is the average energy to produce a pair of positive hole and electron.

The main features of the Compton line are a Gaussian peak and an extended tail on the low energy side of the line [9]. The low energy tail originates from partial absorption processes such as imperfect charge collection within the germanium crystal. The existence of the low energy tail in the detector response function influences the shape of the true symmetric Compton profile in such a way that the measured Compton peak is the convolution of the detector response function and the true symmetric Compton profile. When the resolution function is convoluted with the true symmetric Compton profile it produces a progressive asymmetric broadening on the low energy side of the profile, leaving the high energy side of the profile largely unaffected. Therefore, the extraction of the true symmetric Compton profile from the measured data requires the removal of the low energy tail (i.e. deconvolution) from the measured data.

5. Geometrical Broadening Function Correction

The geometrical broadening results from the beam divergence due to finite collimation. The uncertainty of the scattering angle, due to beam divergence, results in an energy dispersion which broadens the experimental profile. Therefore, in order to minimize the asymmetry as well as improving the accuracy of the experimental profile, the effects produced by the geometrical broadening must be removed from the measured profile.

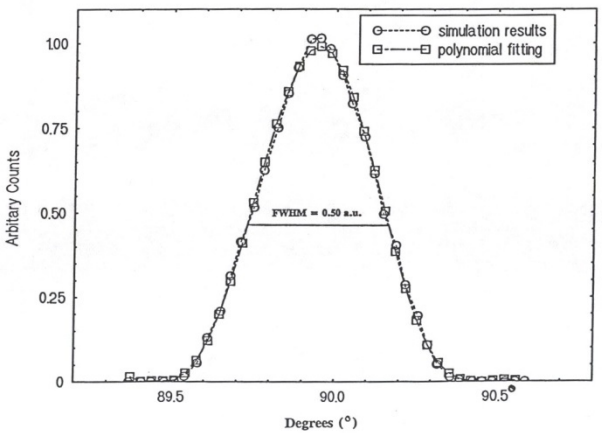

Fig. 2. The calculated geometrical resolution function for the 137-Cs spectrometer.

Since the geometrical broadening cannot be measured in an independent experiment, it is calculated by Monte Carlo simulation of the ray path. In this calculation only one slit collimator for both source and detector was considered. Fig. 2 shows the shape of the geometrical resolution function obtained from the simulation for 100,000 photons. The simulated angular intensity distribution curve is approximated by a polynomial of an 8^{th} order in order to remove the random statistical fluctuations from the calculated intensity distribution. As can be seen from Fig. 2, the geometrical resolution function is a Gaussian with FWHM = 0.5 a.u. The objective of data correction discussed in this section is to deconvolute the geometrical resolution function from the experimental profile.

In the data analysis, the geometrical resolution function is convoluted with the detector resolution function (see Fig. 1) and then deconvoluted from the experimental data by means of the fast Fourier transform method.

6. Source Broadening Function Correction

The source broadening arises from the fact that the incident mono-energetic photon radiation can be degraded by inelastic scattering within the source and emerge with a wide range of lower energies, thus contributing to Compton profile asymmetry. Therefore, in order to minimize the Compton profile asymmetry, the spectral distribution of the inelastic scattering within the source has to calculated and removed from the experimental profile. In the present studies, the source broadening function of the 137-Cs disc source (of 6 mm diameter and 4 mm thick) was calculated by Mote Carlo simulation developed by Rollason et al. [10]. To remove the effects produced by the inelastic scattering

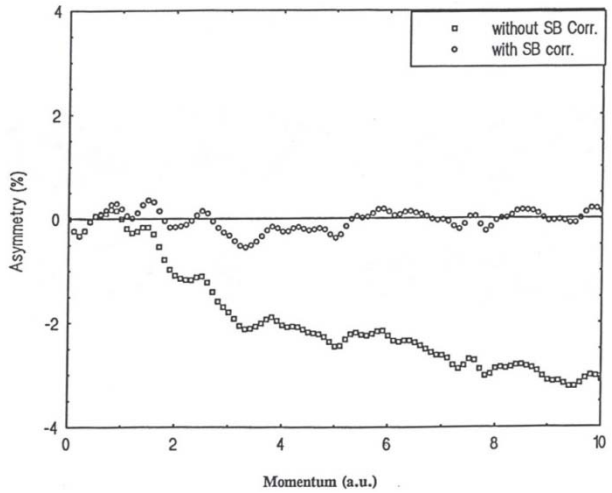

Fig. 3. The effect of the source broadening correction on the final Compton profile symmetry $[(+p_z)-(-p_z)]$ in %.

within the source, an additional deconvolution correction is required. When this correction is applied, the deconvoluted profile is then convoluted with a Gaussian of FWHM equal to the experimental resolution. Fig. 3 shows the effect of this correction on the Compton profile asymmetry.The overall effect of all the deconvolution corrections discussed in the present data analysis procedure is to remove the low energy asymmetry and smooththe experimental data. Accordingly, the theoretical profile must also be convoluted with a Gaussian of FWHM equal to the experimental resolution before comparing it with experimental profile.

Conclusions

In the previous sections the sensitivity of the Compton line shape to data corrections has been discussed in detail. Therefore, in order to minimize the asymmetry as well as improving the accuracy of the experimental profile, the effects produced by the background, the detector response function,the geometrical broadening and source broadeningmust be removed from the measured profile.if undetected error is introduced in these corrections it will make the interpretation of the final results very difficult.

ACKNOWLEDGEMENT

I would like to express my gratitude to the Compton group at the University of Warwick for providing the data reduction software package used in this work, and to Dr. M. J. Cooper for his fruitful discussions about this work.

REFERENCES

1. *Eisenberger P., Platzmann P.M.* Compton Scattering of x-ray from Bound Electrons // Phys. Rev. - 1970. - Vol. A2. - P. 415.
2. *Williams B.* (Ed.) Compton Scattering. - New York: McGraw-Hill, 1977.
3. *Hamouda S.A.* Compton Scattering Theory // Scientific Magazine Issued by Renewable Energies and Water Desalination Research Center (Tajuora, Tripoli). - 2006. - Vol. 6, No. 8. - P. 36.
4. *DuBard J.L.* Compton profile measurements of aluminum and iron with 662 keV γ-radiation // Phil. Mag. - 1078. - Vol. B37. - P. 273 - 283.
5. *Hamouda S.A.* Compton and Bremsstrahlung Cross Sections Ratio. AL - NAWAH // Scientific Magazine Issued by Nuclear Research Center (Tripoli, Libya). - 2009. - Vol. 8, No. 12. - P. 5.
6. *Hamouda S.A.* A 137-Cs Spectrometer for Compton Scattering studies // Industrial Research Journal. - 2007. - No. 22.
7. *Hamouda S.A.* Compton profile measurement of iron with 662 keV γ-radiation // Proc. of the 4th Arab Congress on Material Sciences (ACMS-IV, Tripoli, Libya). - 2005. - Vol. 2. - P. 506.
8. *Timms D.N.* Ph.D. Thesis (unpublished). - England: University of Warwick, 1989.
9. *Hamouda S.A.* The influence of the Detector Response Function of Gamma-Ray Spectrometer on the asymmetry of Compton Profiles. AL - NAWAH // Scientific Magazine Issued by Nuclear Research Center (Tripoli, Libya). - 2008. - Vol 7, No. 11. - P. 66.
10. *Rollason A.J., Felsteiner J., Bauer G.E.W., Schneider J.R.* // Nucl. Instr and Meth. - 1987. - Vol. A256. - P. 532.

QUALITY ASSURANCE AND RADIATION SAFETY IN POSITRON EMISSION TOMOGRAPHY

Ya. V. Kmetyuk[1], H. V. Rabosh[1], O. A. Bezshyyko[2], L. O. Golinka-Bezshyyko[2], I. M. Kadenko[2], O. A. Kazinova[2], A. O. Nagai[2]

[1] All-Ukrainian Center for Radiosurgery of the Clinical Hospital "Feofania", Kyiv, Ukraine
[2] Taras Shevchenko National University of Kyiv, Ukraine

Scientific studies, clinical experience and economic analysis have shown that the positron emission tomography (PET) is clinically and cost effective cancer diagnostics method. Combined PET and computed tomography (PET/CT) has proven clinical utility, particularly in the diagnosis, staging or restaging malignant disease and metastases, surgical planning, radiation therapy planning and evaluation of treatment response. The use of PET/CT has grown substantially in the past few years, with an increasing number of hospitals and installations of PET/CT imaging centers each year. In the same time combination of 2 procedures, each of which impart a radiation dose and, as a result, increases the deleterious influence for health, creates additional radiation safety issues. In these conditions the role of quality assurance (QA) and quality control (QC) programs is getting more and more important. We considered main QA and radiation safety requirements for whole PET technology chain from radio-pharmacy facilities to PET/CT scanning and patient release criteria. All these issues were considered and assessed having the example of PET facilities and technology chain of All-Ukrainian Center for Radiosurgery of the Clinical Hospital "Feofania".

1. Introduction

Positron emission tomography has become one of the most important diagnostic tools in the cancer detection and treatment in last ten-fifteen years. Main advantage and uniqueness of this method is possibility to find and identify any malignant neoplasms of small sizes (for new metastatic formations less than one centimeter), which are in the stage of active growth phase, studying a tumor`s activity, clear identification of the stage of specific disease, prognostication of the effectiveness of treatment targeted to finally define the quality of medical process in a post-therapeutic period. In the recent years the active progress and development of new PET-procedures take place and the characteristics of equipment and analyzing software are being improved with increasing rate. The combination of positron emission tomograph with computerized X-ray tomographic system into one tandem has provided essential advantages and improvement of scanner `characteristics for positron emission tomography. At the present stage of progress practically all such systems are produced with X-ray computer tomograph (CT) with modified name PET/CT scanner (or PET/CT tomograph). For the past few years with appearance of effective semiconductor electronic photomultipliers (SiPM), which have a small sensitivity to magnetic field, the tendency of integration PET scanner and magnetic resonance tomograph appears, new time-of-flight methods allow to improve background conditions for obtaining high quality diagnostic scans.

2. Basic physical and biological principles of PET tomography

In the early thirties of the last century it was noticed that the significant part of malignant neoplasms is characterized with higher level of glucose uptake. It is due to quick growth and reproduction of cancer cells, and such a rapid metabolism requires large quantity of biological construction and energy resources, among which glucose occupies the most important place. In the seventies years it was suggested to use labeled glucose analogues for the metabolism study in a human organism. Initially radioactive carbon was used as an irradiation source, but application of radioactive isotope ^{18}F in the fluorodeoxyglucose (FDG) has become especially widespread. FDG is a glucose analogue at several stages of its metabolism, but unlike glucose FDG metabolism is broke off too soon and its product with the radioactive marker of fluorine being accumulated in live tissues. If one defines the concentration of fluorine-18 in tissue then ^{18}F accumulation in the tumor can be localized with quite good accuracy and high value of probability (corresponding to high metabolism level). Some important organs of human body (like brain, heart) also have high metabolism level. That complicates partly the determination of malignant tumors in such areas, but it allows studying cerebral and cardiac activity directly in a dynamics which is very important for corresponding fields of medicine. A nucleus of fluorine-18 emits positrons of sufficiently low energy while decaying. This process makes it possible to identify the point where a nucleus disintegrated with quite good accuracy and low background. Let's consider the physics of this process. As a result of β^+-decay a positron is emitted with energy not higher than 0.63 MeV. It is captured in a human body and annihilates with one of environment electrons after achievement of kinetic energy close to zero. As a result of annihilation two photons with the same energy equal 511keV escape in opposite directions (angle 180^0). Matrix of scintillation detectors forms a circle around patient, in these detectors the energy of photons and time of their appearance are detected. According to a signal coincidence from two matrix detectors the straight line is defined (at two "points"-detectors). There is a radiation source on that line, and place of the cross points of such lines is to be used to determine the point of positron emission.

For the synthesis of FDG which is to be injected into a patient, it is necessary to produce radioactive fluorine-18 every day with activity about of 1 - 4 Ci, because the half-life of ^{18}F is 110 min, i.e. this isotope decays fast enough.

Quite short half life on the one hand leads to the relative isotope safety (within few days nuclei of fluorine-18 will mostly decay), on the other hand it limits the distances to use fluorine-18 produced in one PET center and implies the requirement to produce FDG close to clinics equipped with PET scanners (within one-two hours of a transport movement). Therefore different medical cyclotrons and automated FDG synthesis systems are dedicated for the production of fluorine-18 in one large clinical institution. One of the most justified methods of ^{18}F production is 15 MeV protons irradiation of nuclei ^{18}O (as a rule in water, containing stable isotope ^{18}O with enrichment exceeding 90 %). In nuclear reaction $p+^{18}O \rightarrow n+^{18}F$ the needed fluorine isotope is produced but meanwhile a considerable neutron flux is generated as a side harmful process. Once irradiated, the water (containing ^{18}O converted into ^{18}F) needs to be squeezed out into automated FDG synthesis system where all the processes of material cleaning and pharmaceutical synthesis take place without human help in the automatic mode. Then prepared pharmaceuticals do pass the quality control to be lately packed for utilizing in the same medical institute where FDG was produced or for transportation to other medical institute which has PET scanners. FDG is injected into a patient by using a syringe for effective extension in blood-vascular system and after 20-40 minutes (for the achievement of the corresponding metabolism stages) diagnostic scanning is ready to be carried out at PET (PET/CT) tomograph. All technological chain to get diagnostic PET images of high quality is difficult enough and has substantial differences from the processes of X-ray imaging not only in basic physical principles but also in the area of radiation safety and development of quality assurance management systems.

3. Radiation safety in PET application

Numerous features of PET technology chain do require special rigorous measures to provide high level of radiation safety for patients, personnel and other people in the hospital and nearby. This includes very thorough consideration of corresponding building design, system for radiation monitoring, internal and external audits, prevention of accidental radioactive releases into atmosphere, etc. One can note first of all the following issues:

1. Annihilation gamma-quanta (with energy 511 keV) are major contributors to radioactive irradiation from positron emitting isotopes. This energy is high enough relative to x-ray generated by roentgen diagnostic equipment and even gamma ray energy of the most widespread isotopes in nuclear medicine (such as ^{99m}Tc). For 511 keV gamma ray energy attenuation a contribution of photoabsorption does not prevail and a part of Compton scattering is quite significant. Therefore strong dependence (ordinary for radiation safety specialists in the field of nuclear medicine and x-ray diagnostics) of quanta absorption from atomic number of material is absent practically. From this conclusion such result arises – low effectiveness of lead and barite plaster (standard materials for X-ray diagnostics field). For example the tenth value layer (TVL) for radiation of ^{99m}Tc is nearly 0.9 mm of lead, for X-ray tube with anode voltage 100 kV TVL in lead less than 0.25 mm (with 2mm aluminium filtration), but for annihilation gamma-quanta of ^{18}F this value is nearly 1.6 cm. One can derive the following conclusions from this:

a. the most effective shielding against annihilation gamma-quanta is concrete walls and main optimal effective method is to increase a distance between radiation source and point of dose applying, taking into account the ratio shield/shield cost;

b. radiation safety system for personnel is complicated, first of all for nurses who applies syringe injection of FDG to patient blood. Thus, lead or tungsten syringe covers make it possible to solve this problem partially only (herewith the injection procedure is essentially complicated due to large mass of cover), minimization of injection time is main approach in these conditions to minimize radiation dose on nurse fingers and hands;

c. radiation doses for patients in PET are not very high – the dose rate from ^{18}F is about one order of magnitude higher than for ^{99m}Tc, but due to short half-life the total cumulative patient dose nearly equals to value of Technetium.

One can find more detail information about radiation safety and shielding of PET diagnostics in ref. [1, 2].

2. If one use reaction $p+^{18}O \rightarrow n+^{18}F$ to obtain ^{18}F, intensive neutron flux is generated as side harmful product. For example for production of ^{18}F few Ci, a neutron fluence may reach about 10^{15} neutrons in 4π solid angle. Intensive flux of thermal and resonance neutrons may be formed due to slow down at the cyclotron construction elements and shielding vault. Neutron capture reactions lead to formation of several radioactive isotopes. All such interactions (neutron capture and reactions with primary neutrons) cause essential radioactive background of induced radiation in the cyclotron vault. To lowering this background the vendors prefer to manufacture the target unit materials with low neutron cross section values or with short living radioactive isotopes in output channel of neutron induced reactions. One must avoid using in the vault (especially around target unit) the elements with high values of cross sections for cyclotrons without built-in shielding. Besides constructive materials of accelerator and vault itself, the activation of air causes accumulation of radioactive isotope ^{41}Ar with half-life nearly two hours [3] in the cyclotron vault. To minimize the influence of such radioactive sources a using of built-in complex neutron cyclotron shielding is considered as the most effective approach. For this case only small air inner volume in shield is irradiated in area around target (dozens liters). Then the air with induced activity has to be diluted in a large volume of clean air to obtain the permitted concentrations of ^{41}Ar and further release into the atmosphere. Another approach is used for cyclotrons without built-in shielding. In this case volume of air in cyclotron vault can exceed dozens of cubic meters and its dilution to get permitted concentrations of radiation in air can be problematic or even impossible. The alternative solution of such problem could be the ventilation of cyclotron systems without releasing the air into the atmosphere. Then upon completion of ^{18}F production the air with induced activity is to be pumped into large balloons and after cooling time (as

a rule – one day and night for argone-41 decay) the air may be released into the atmosphere with continuous radiation monitoring.

3. During technology chain of positron emitting isotopes, especially in the processes with gases or volatile components (frequently in ^{11}C production chain) the risk of leakage of highly radioactive discharges to ventilation system might be essential. The consequences of accident like this can lead to radioactive pollution of PET chain rooms and even outer atmosphere [4]. Therefore continuous radiation monitoring in ventilation system is mandatory. It is not simple task because direct measurements by detector systems without concentration of radioactive isotopes is very problematic for pollution concentrations nearly permitted values [5].

4. Quality assurance procedures in the PET technology chain

Taking into account a very complex PET technology chain one have to build Quality Assurance (QA) system in the all segments of chain in their interconnections. This QA system should cover all the activities from the development of PET diagnostics departments and further to operate routine procedures with equipment and software. Some leading organizations of national and international level developed sets of documents, which are devoted to these problems. Among them: the IAEA documents [6, 7], accreditation procedures of American College of Radiology (ACR accreditation, [8]), standards of 2001 and 2007 years of the Association of Electrical Equipment and Medical Imaging Manufacturers (NEMA standards for positron emission tomography, [9]).

5. PET diagnostics in All-Ukrainian Center for Radiosurgery of the Clinical Hospital “Feofania”

More than one year department of PET/CT diagnostics is in operation at All-Ukrainian Center for Radiosurgery of the Clinical Hospital “Feofania” in Kyiv. Complete technological chain (from a fluorine-18 production with medical cyclotron and FDG synthesis to the scanning procedures on the PET/CT tomograph) is developed, recognized and fully certified. . The cyclotron has its own built-in protection that substantially improves and simplifies the conditions to provide high level of radiation safety. Ukrainian normative documents and best international practices [5 - 8] were taken into account for the development of QA procedures. Biograph 64 TruePoint PET/CT by Siemens is used for a tomographic scanning. Within the framework of quality control system the NEMA IEC Body phantom according to the standard of NEMA NU2-2007, ACR phantom «Flangeless Deluxe ECT Phantom» according to the ACR accreditation program of nuclear medicine, dose calibrator Atomlab™ 500 Calibrator (Biodex) and other modern equipment are in full scope operation for patients treatment and experience gaining.

REFERENCES

1. *Mark T. Madsen et al.* AAPM Task Group 108: PET and PET/CT Shielding Requirements // Med. Phys. - 2006. - Vol. 33(1). - P. 4 - 15.
2. *Radiation* protection in newer medical imaging techniques: PET/CT // SRS No.58. - Vienna: IAEA, 2008. - 41 p.
3. *Bezshyyko O., Golinka-Bezshyyko L., Kadenko I.* Argon activation in air at medical cyclotron RDS ECLIPSE during production of ^{18}F // VANT. - 2009. - No. 5. - P. 37 - 39.
4. *Calandrino R., del Vecchio A., Todde S., Fazio F.* Measurement and Control of the Air Contamination Generated in a Medical Cyclotron Facility for PET Radiopharmaceuticals // Rad. Safe. J. - 2007. - Vol. 92. - Suppl. 2. - P. 70 - 77.
5. *Nechay D., Bezshyyko O., Golinka-Bezshyyko L. et al.* Optimization of radiation impact on environment using positron emission tomography // Sci. Bull. Uzhgorod Univ. - 2009. - No. 24. - P. 131 - 135.
6. *Planning* a Clinical PET Centre // IHHS No. 11. - Vienna: IAEA, 2010. - 143 p.
7. *Quality* Assurance for PET and PET/CT Systems. IHHS No.1. - Vienna: IAEA, 2009. - 145 p.
8. http://www.acr.org/Quality-Safety/Accreditation/Nuclear-Med-PET.
9. http://www.nema.org/Standards/ComplimentaryDocuments/Contens-and-Scope-NU-2-2007.pdf

MAGNETO-RESISTANCE OF $SI_{0,97}GE_{0,03}$ WHISKERS IRRADIATED BY REACTOR FAST NEUTRONS

N. T. Pavlovska[1], P. G. Litovchenko[1], A. Ya. Karpenko[1], Yu. O. Uhryn[2], Yu. V. Pavlovskyj[2], I. P. Ostrovskii[3], Yu. M. Khoverko[3]

[1] Institute for Nuclear Research, National Academy of Sciences of Ukraine, Kyiv, Ukraine
[2] Drohobych Ivan Franko State Pedagogical University, Drohobych, Ukraine
[3] Lviv National Polytechnic University, Lviv, Ukraine

The influence of reactor fast-neutrons irradiation by the fluence of $8,6 \cdot 10^{17}$ n/cm^2 and strong magnetic field (up to 14 T) on resistance of $Si_{1-x}Ge_x$ (x = 0,03) whiskers in the temperature range of 4,2 - 300 K is studied. The activation energy of the of impurity levels is calculated. The interpretation of changes in the magneto-resistance is proposed.

Introduction

Whiskers crystals are characterized by high structural perfection, chemical stability, and also by strength, which for the crystals of small transverse sizes reaches theoretically possible limit [1].

Whiskers crystals find a number of scientific and practical applications. For example, from semiconductor whiskers crystals it is possible to obtain highly sensitive strain gauges [2]. On their base the sensors of physical quantities [3 - 5] are created. For a period of recent decades the work is conducted on creation on the basis of the whiskers crystals of composite materials with special properties [6]. It is established also a number of size effects in Si whiskers crystals. With the decrease of the diameter of sub-micron whiskers crystals the decrease of lattice parameter [7] and the displacement of the edge of optical absorption to the side of high energies occur [8]. The observed special features of Si whiskers crystals relate either with the absence of defects in crystal lattice, or the special arrangement of defects in the crystals or with the influence of surface. From other side, the high perfection of the structure of initial whiskers crystals makes it possible to simulate the defects, which are formed in the process of irradiation. Thus, in the works [9] and [10] the influence of irradiation by electrons and γ quanta (up to 10^{18} cm $^{-2}$) on the *p*-$Si_{1-x}Ge_x$ whiskers crystals, respectively, were investigated. It was shown; the second radiation defects of the interstitial atoms of boron are basic defects in the crystals. Today, the influence of neutron irradiation on the electrophysical properties of $Si_{1-x}Ge_x$ whiskers crystals is not practically studied. The purpose of this work is a study of the magneto-resistance of $Si_{1-x}Ge_x$ whiskers crystals, irradiated by the neutrons.

Procedure

SiGe whiskers growing were carried out by the method of chemical transport reactions in the closed bromide system with the use of gold as the initiators of growth. Growth material (silicon, germanium), alloying admixtures (boron) and halogen (bromine), which is used as the transportation agent, are load in the growth ampule. Ampule is pumped out up to a pressure of 10 - 5 Torr and then placed into the tube furnace with the gradient of temperature. The temperature of the source zone is 900 ^{o}C, temperature of crystallization zone is 550 - 750 ^{o}C. The content of germanium in the solid solution of $Si_{1-x}Ge_x$ was determined by the method of microprobe analysis on the installation CAMEBAX and accounts: X = 0,03 mole percents. For the study of neutron irradiation influence whiskers crystals with diameter 40 ± 2 μm and with length of 2 - 3 mm were selected. They are p-type crystals with the specific resistance ρ = 0,018 Ohm · cm.

Crystals were irradiated by fast neutrons with the fluence of $8,6 \cdot 10^{17}$ n/cm^2 at reactor BBP 10M of the institute for nuclear research National Academy of Sciences of Ukraine. After irradiation the measurements of magneto-resistance in the magnetic fields up to 14 T in the temperature interval from 4,2 to 300 K in the international laboratory of strong magnetic fields and low temperatures (Vrotslav, Poland) were carried out.

Results and their consideration

After irradiation of samples their resistances at room temperature have increased to about 5 orders of magnitude. It has not given the ability to perform low temperature measurements of magneto-resistance. Then the annealing of irradiated samples was carried out ranging from 50 to 350^{o}C in increments of 25 ^{o}C. Samples were annealed at each temperature for 20 min, then they were cooled to room temperature and their resistance was measured. It was determined that at temperatures above 280 ^{o}C resistance of irradiated crystals decreases sharply coming close to the original value before irradiation (Fig. 1). Only after this you can carry out the temperature measurements of field dependencies of resistance (Fig. 2). As you can see from the picture, magneto-resistance slightly changes in weak magnetic fields and increases with magnetic field increasing. Also a change of magneto-resistance curvature has been observed.

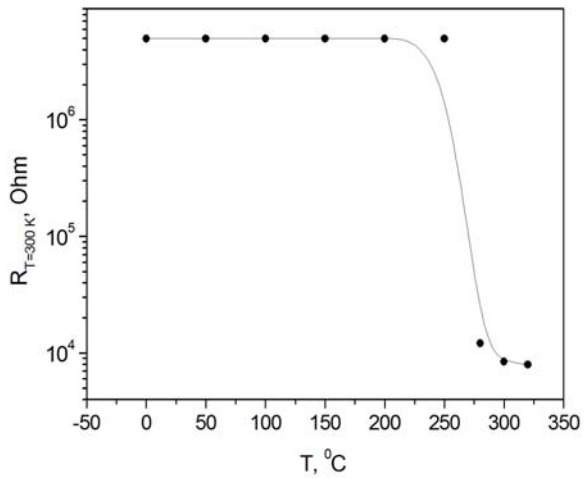

Fig. 1. The dependence of the resistance of irradiated $Si_{1-x}Ge_x$ (x = 0,03) whiskers with specific resistance ρ = 0,018 Ohm · cm on annealing temperature.

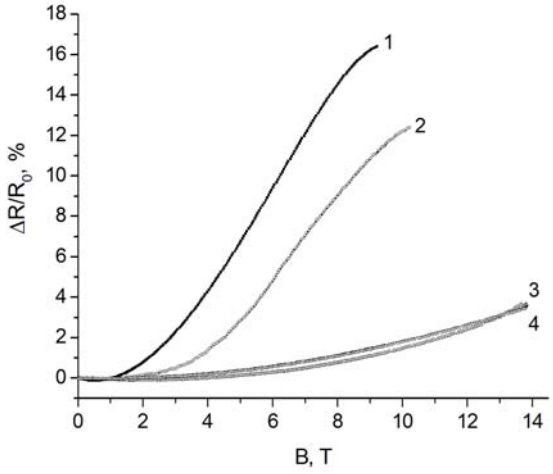

Fig. 2. The field dependencies of the resistance relative change of neutron irradiated $Si_{1-x}Ge_x$ (x = 0,03) whiskers with specific resistance ρ = 0,018 Ohm · cm at different temperatures: *1* - 4,22 K; *2* - 6 K; *3* - 25 K; *4* - 45 K.

The change of magneto - resistance curvature from concave to convex at temperature 4,22 K indicates that in this magneto - resistance contribute light carriers of charge (electrons or light holes) that have high mobility and very low concentration, that is, they are free minority carriers of charge [11]. Let us calculate parameters of these minority carriers of charge [11].

$$\mu = \frac{\sqrt{3}}{B_n}\left(\frac{4\rho(B_n)}{3\rho_0} - 1\right), \tag{1}$$

$$n = \frac{4\sqrt{3}B_n}{e\rho} \cdot \frac{\frac{\rho(B_n)}{\rho_0} - 1}{\left(4\frac{\rho(B_n)}{\rho_0} - 3\right)^2}, \tag{2}$$

where μ and n are mobility and concentration of minority carriers of charge, respectively; B_n is magnetic field point of the magnetoresistance curve fold; $\rho(B_n)$ is the resistivity at the point of magnetoresistance curve fold, ρ_0 is resistivity in the absence of a field.

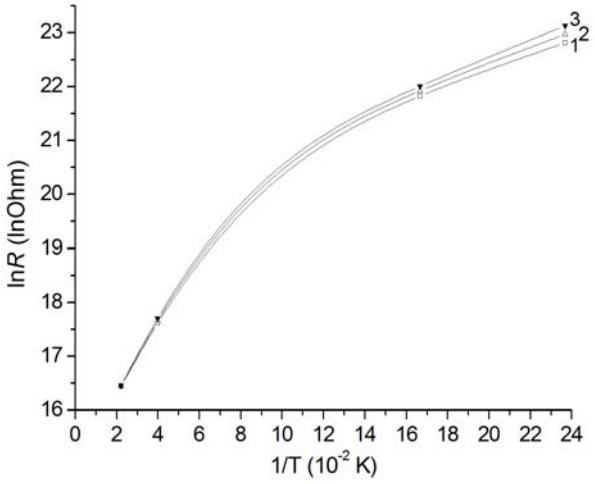

Fig. 3. The dependence of resistance on temperature for $Si_{1-x}Ge_x$ (x = 0,03) whiskers with specific resistance ρ = 0,018 Ohm cm at different values of magnetic field induction: *1* - 0 T; *2* - 6 T; *3* - 10 T.

These formulas for T = 4,22 K give us: μ = 1400 $cm^2/(V \cdot s)$, $n = 2{,}9 \cdot 10^9 cm^{-3}$; that is for this temperature very small quantity of light charge carriers with high mobility is making a contribution to the conductivity. Let's calculate relation of minority charge carriers conductivity to conductivity of majority charge carriers under the formula [1].

$$\frac{\sigma_н}{\sigma_0} = 4 \cdot \left(\frac{\rho(B_n)}{\rho_0} - 1\right),$$

which gives: $\sigma_н/\sigma_0$ = 0,32, that is the minority charge carriers are making a significant contribution to the conductivity at this temperature. The energy of activation of the impurities that cause these charge carriers, calculated from resistance temperature dependence, is: ε = 2,1 meV (Fig. 3).

In order to ascertain the effect of the magnetic field on the parameters of free charge carriers the dependences of lnR (1/T) at different values of the magnetic field (see Fig. 3) were constructed and the activation energy of impurity for these field values were calculated. From this Figure it is visible, that at low temperatures the slope of the line = lnR (1/T) increases considerably, reflecting the growth of the activation energy with the growth of the magnetic field. Under the field of 10T this activation energy is 2,5 meV, that is, it significantly exceeds the activation energy in the absence of the field (2,1 meV). This suggests that for low temperatures resistance increases with the magnetic field due not only to decrease of the mobility of free charge carriers, which is unavoidable in these fields, but also as a result of magnetic field reducing their concentration. At higher temperatures (about 40 K), as can be seen from Fig. 3, for all values of the magnetic field the curves almost merge with each other, which testifies to the independence of the activation energy 11,5 meV from the field, which in turn speaks about the independence of the concentration of free charge carriers on the magnetic field and thus magneto resistance is determined by the decrease in the mobility of the charge carriers (for these temperatures - holes).

Conclusions

The analysis of magnetoresistance curves for neutron irradiated $Si_{1-x}Ge_x$ (x = 0,03) whiskers crystals gave the following results: at low temperatures (about 4,2 K) significant contribution to the conductivity (about 32 %) are from the light charge carriers (electrons and light holes), of which there are very few ($n = 10^9$ cm^{-3}) and that have a high mobility ($\mu = 1400$ $cm^2/(V \cdot s)$). Level, which supplies the charge carriers has an energy $\varepsilon = 2,1$ meV, which in magnetic field of about 10 T increases to ε = 2,5 meV that encourages us to draw a conclusion on what caused the magnitoresistance, except magnetic field decrease in mobility, is also magnetic field decrease in the concentration of free charge carriers. At higher temperatures (about 40 K), conductivity are realized by holes with activation energy $\varepsilon = 11,5$ meV, and which practically does not depend on magnetic field.

REFERENCES

1. *Гиваргизов Е.И*. Рост нитевидных и пластинчатых кристаллов из пара. - М.: Наука, 1977. - 304 с.
2. *Baitsar R., Voronin V., Krasnogenov E., Bogdanova N*. Mechanical sensors based on Si-Ge whiskers // Sensors and Actuators. - 1992. - Vol. A30. - P. 175 - 181.
3. *Voronin V., Maryamova I., Zaganyach Y., Karetnikova E., Kutrakov A*. Silicon whiskers for mechanical sensors // Sensors and Actuators. - 1992. - Vol. A30. - P. 27 - 33.
4. *Maryamova I.J, Karetnikova E.N., Gortynskaya I.D, Yatzuk Ju.S.* Mechanical sensors for cryogenic temperatures // Int. Conf. Actual Problems of Electronics Instrument Enginiring (APEIE-92). - Novosidirsk, 1992. - Vol. 4. - P. 96 - 99.
5. *Maryamova I., Druzhinin A., Lavitska E. et al.* Low temperature semiconductor mechanical sensors // Sensors and Actuators. - 2000. - Vol. A85. - P.153 - 157.
6. *Baitsar R.I., Kurylo I.V., Varshava S.S., Ostrovskii I.P.* Mechanical properties of silicon-germanium alloy whiskers // Functional materials. - 2001. - Vol. 8, No. 2. - P. 398 - 400.
7. *Климовская А.И., Островский И.П., Байцар Р.И.* Рентгенометрическое исследование субмикронных нитевидных кристаллов кремния *n*-типа // Изв. РАН, Сер. физ. - 1993. - Т. 57, № 11. - С. 210 - 213.
8. *Gule E.G., Rudko G.Yu., Klimovskaya A.I. et al.* Visible light emission from free-standing filament crystals of silicon // Physica Status Solidi. - 1997. - Vol. 161. - P. 565 - 571.
9. *Дружинин А.А., Марьямова И.И., Кутраков А.П. и др.* Исследование влияния электронного облучения на кремниевые тензорезисторы // Технология и конструирование в электронной аппаратуре. - 2010. - № 1(85). - С. 26 - 29.
10. *Дружинин А.О., Островский И.П., Ховерко Ю.Н. и др.* Влияние облучения γ-квантами на свойства нитевидных кристаллов Si-Ge // Физика и химия твердого тела. - 2010. - Т. 11, № 1. - С.89 - 92.
11. *Ougrin Y.* About the Absence of the Halleffect anomaly in superconductors / The 1977 Int. Workshop on superconductivity co-sponsored by ISTEC and MRS (Big Island, Hawaii, USA, June 15 - 18, 1977). - P. 403 - 405.

CHARGE-SENSITIVE AND SHAPING AMPLIFIER MICROASSEMBLIES FOR DOSIMETRY AND SPECTROMETRY ON CZT-DETECTORS

V. L. Perevertaylo, I. L. Zaitsevsky, L. I. Tarasenko, A. V. Perevertaylo, E. A. Shkirenko

SE Institute of Microdevices STC "Institute for Single Crystals", National Academy of Sciences of Ukraine, Kyiv, Ukraine

Developments of new spectrometric channel electronics on the basis of microassemblies, which allowed to reduce the noise and increase of signal-to-noise ratio, lowering power consumption and dimensions. The complete line of front-end electronics for CZT detectors implemented as micro-assemblies is described, the design concept, operation details and application features of charge sensitive amplifier (CSA) and shaping amplifier (SA) microassemblies are discussed, and the results obtained when registering low energy X-ray spectra are shown. It has a high energy resolution ΔE at the level of the leading companies. For direct detection with silicon p-i-n-diode new electronic channel can resolve ^{241}Am peaks up to 8 keV with a resolution of about 2 keV at room temperature. New electronics is universal and can be used with different semiconductor detectors – Si, CdZnTe, Scintillator-photodiode, as shown in the spectra. Low power consumption and reduced dimensions allows the using in portable equipment. Manufacturability of micro assembly opens up the possibility for mass production and low cost opens up the possibility to supply them with detectors as "Start kit" for the construction of radiometric and spectrometric devices.

1. Introduction

Prospects of use of CdZnTe (CZT) detectors result from their efficiency of registering Gamma- and X-ray radiation, high energy resolution at home temperatures, increased signal-to-noise ratio due to low dark currents and wide forbidden gap of materials.

To implement the advantages of CZT detectors for use in portable spectrometric, radiometric and dose-metering instruments and to facilitate the use of such detectors in other fields, we developed the integrated line of detection equipment. The customer in this case obtains ready to use complete detection system with CZT detector together with front-end electronics, including the low noise charge sensitive amplifier (CSA) and the active filter shaping amplifier (SA) with wide range gain control. The CSA gives an output voltage pulse with the amplitude proportional to the amount of the charge generated in the detector. The SA provides optimal filtering for signal-to-noise ratio improvement and amplifies the signal for the digital registration system. Such signal processing technique is effective for recovering signals delivered by the variety of light, radiation and particle detectors [1]. Some examples of these detectors are photodiodes, X-ray detectors and detectors for nuclear and particle physics.

The complete line of detection equipment for CZT detectors includes microassemblies of CSA and SA based on the Active Filters (AFS electronic modules), having following advantages: low dimensions and power consumption, high reliability, versatility in applications with CZT detectors used for measuring dose rate in the instruments for emergency dose control and NPP monitoring, as well as in many other applications. The microassembly design approach has previously been successfully applied to the development of spectrometric instruments for silicon detectors [1]. The prospects of CZT detectors with CSA and AFS microassemblies are in applied research (X-ray spectroscopy in medicine, biology) and in basic research (high energy physics, nuclear physics, astrophysics).

2. Goals and Tasks of Development

During the development of microassemblies for CZT detectors main attention was paid to obtaining high energy resolution and good technological features of microassemblies, guaranteeing reproducible parameters in batch manufacturing as well as stability, reliability and versatility in applications.

The energy resolution of detection system depends on the noise level of front-end amplifier. The CSA with JFET input stage is inherently the most low noise amplifying configuration. But there commonly exist some sources of excess noise. One of the evident noise sources is a high-Ohmic resistor, usually used for DC stabilization of input JFET. Great efforts have been made to reduce the CSA noise level by excluding this high-Ohmic resistor, and stabilizing the CSA by means of optical pulse feedback [2], by implementing of drain pulse reset [3], drain DC feedback loop [4], or by use of active current divider feedback network [5]. The absence of a resistor in parallel with a capacitor in a feedback loop would effectively reduce the CSA noise level. However the configurations without a high-Ohmic resistor listed above require a complicated and power consuming circuitry, need fine individual trimming of each device, lack stability and are hardly applicable in the microassembly design for batch production.

In [6] the effect of JFET gate potential self-stabilizing is described and the low noise CSA with a constant current source connected to the JFET drain is proposed. The JFET gate potential is self-stabilized due to the internal feedback based upon its output I-V characteristics. This effect is also utilized in low noise CSA, DC stabilized without a feedback resistor described in [7].

3. CSA Microassembly Design Approach

During the development of CSA microassembly for CZT detectors we integrated in our design the approaches of [6] and [7], and modified the amplifier circuit to obtain improved gain, speed and stability parameters, resulting in CSA microassembly with Floating Gate Mode of input JFET (Fig. 1). The design concept was aimed at the CSA microassembly circuit which is easily reproducible, needs no post-production trimming, as well as reliable and versatile in applications.

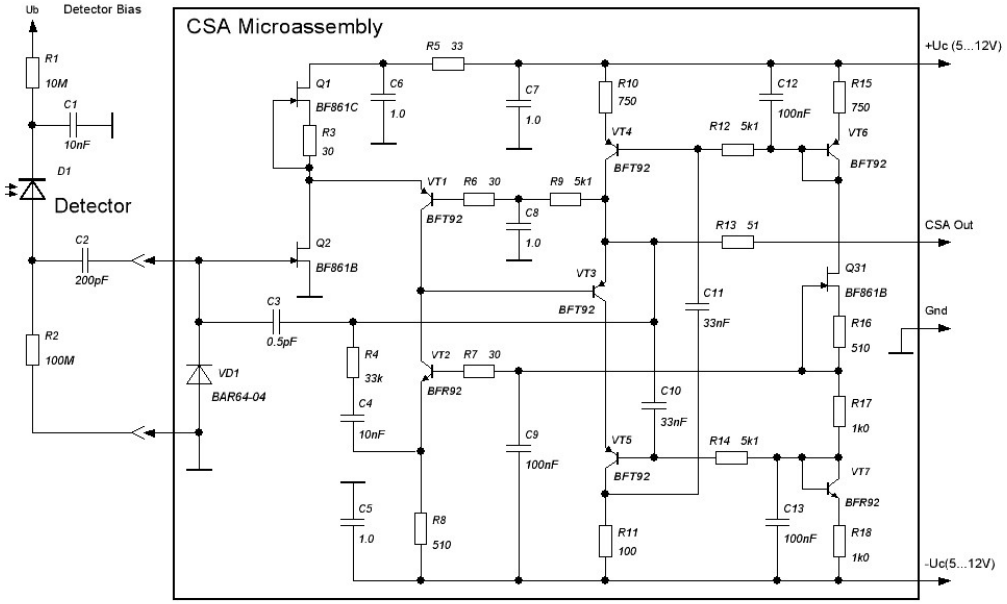

Fig. 1. CSA microassembly application circuit diagram.

The high-Ohmic resistor, usually used for DC stabilization of CSA input JFET, is excluded and the JFET is used in Floating Gate Mode with zero gate leakage current towards the external circuits. The constant current source connected to the JFET drain provides DC stabilization and improves input stage gain, and the DC feedback through the common-base transistor keeps CSA output DC level within linear margins. High speed of operation is provided by double-boosted output emitter follower stage, and another gain boosting circuit is used to provide independence of CSA gain from the detector capacitance. The temperature compensated bias circuit ensures stable operation over wide temperature and supply voltage ranges. The gate of input JFET transistor is protected with use of p-i-n-diode with an extremely low capacitance, which introduces practically no extra noise and dramatically speeds up the power-on transition process, in case the detector is used with DC decoupling capacitance (as shown in Fig. 1).

CSA microassembly features low noise level with low and medium capacity detectors, connected with or without DC decoupling capacitor. Output rise time under the detector capacitance of 5 pF does not exceed 20 ns. CSA microassembly can be used with CZT, Si and Scintillator + Si-Photodiode Detector Assemblies under the bias voltage up to 250V, which is important for CZT detectors. Energy resolution for CZT detectors is about 2.5 keV. Supply voltages range from ±5V to ±12V. Use of miniature SMD active and passive components minimizes the board dimensions, allowing installation of CSA microassembly in 14 pin DIP metal-glass package for the hybrid ICs.

4. SA Microassembly and Equipment Application Facilities

The energy resolution of detection system depends not only on the noise level of the front-end amplifier, but also on proper spectrometric pulse shaping. The SA microassembly is developed using the classic Bessel active filters (Fig. 2). SA forms highly symmetric pseudo-Gaussian pulse and can be implemented for FWHM range (0.3÷16) μs with variable gain Ku = (10 ÷ 140) set by the external resistor. SA input noise is ~ 5 μV. Two OPA in SSOP packages and miniature SMD passive components are used in SA microassembly. As well as CSA microassembly, it is installed in 14-pin DIP metal-glass package for the hybrid ICs.

To facilitate the customer's application of CSA and AFS microassemblies for CZT detectors the prototyping board was developed, intended for installation of microassemblies in 14 pin DIP metal-glass packages for the hybrid ICs (Fig. 3). The detector input connectors with or without DC decoupling capacitors are installed, the detector bias voltage is supplied through the RC-filtering circuits. Power supply ±Vc lines with decoupling elements, ground and signal lines are properly connected to the sockets contacts. Pole/zero cancellation fine control, DIP switches with resistor set for SA step gain control as well as 8-pin socket for optional buffer/inverter OP amp with configuration jumpers are installed. Additionally to the sockets for CSA and AFS microassemblies, one spare 14-pin DIP socket is installed, intended for future use of DC restorer microassembly. The prototyping board is mounted in aluminum case with Dsub connector for output signal, detector bias voltage and power supply voltages.

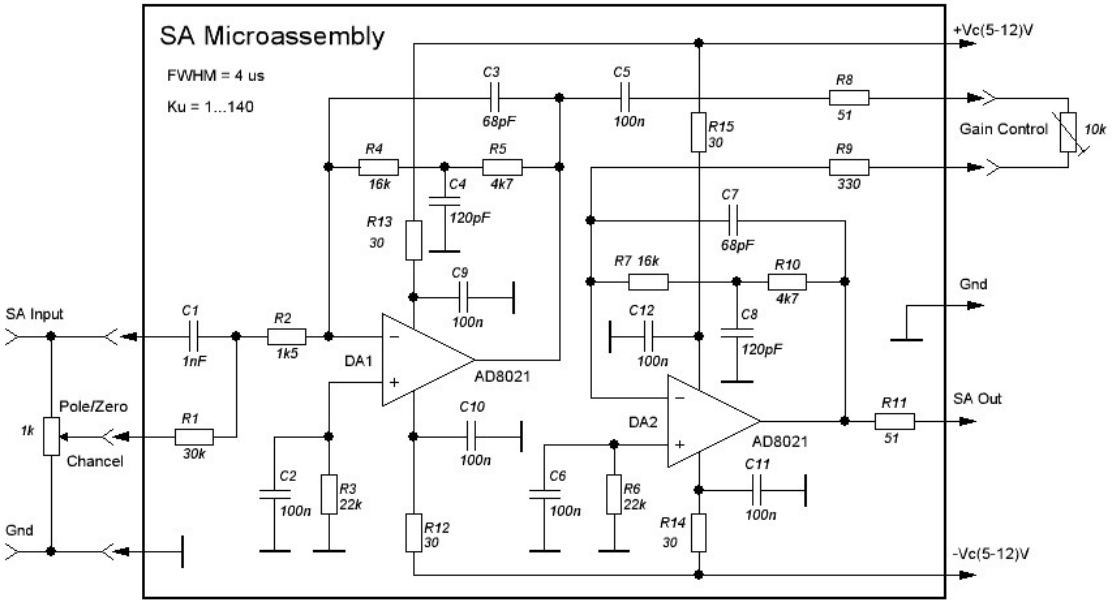

Fig. 2. SA microassembly application circuit diagram.

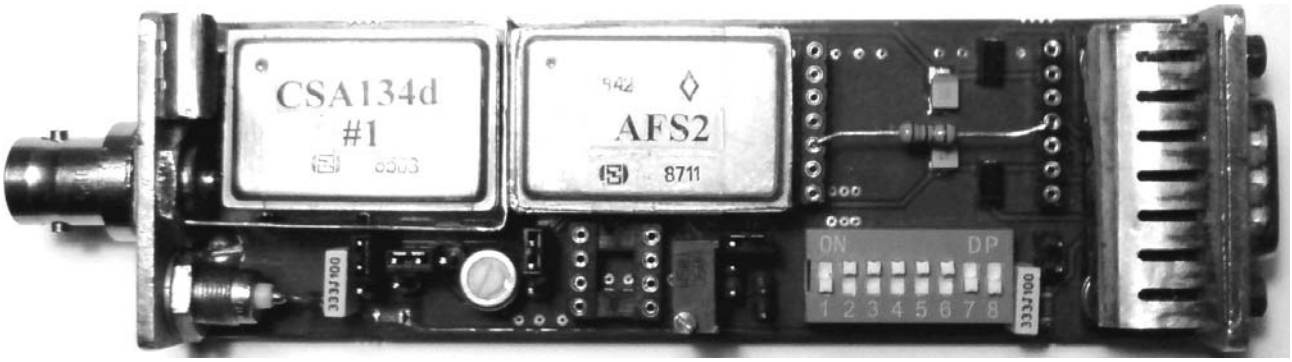

Fig. 3. CSA and SA microassemblies prototyping board [8].

5. Spectrometric Results

The results obtained with use of the microassemblies for CZT detectors in registering medium and low energy X-ray spectra are shown in Figs. 4 and 5.

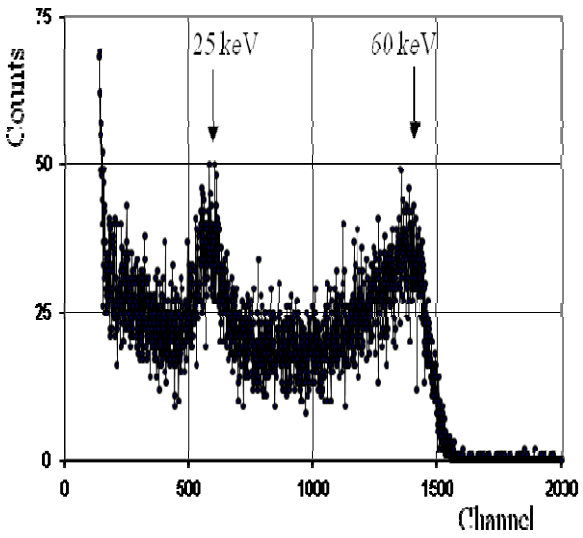

Fig. 4. Spectrum of ^{241}Am with CdZnTe-detector $4 \times 4 \times 1$ mm^3 (Fe-filter 0,2 mm and Sn-filter 0,2 мм): $\tau_{FWHM} = 3$ μs, $U_b = 100$ V, t = 300 s, T = 27 ºC.

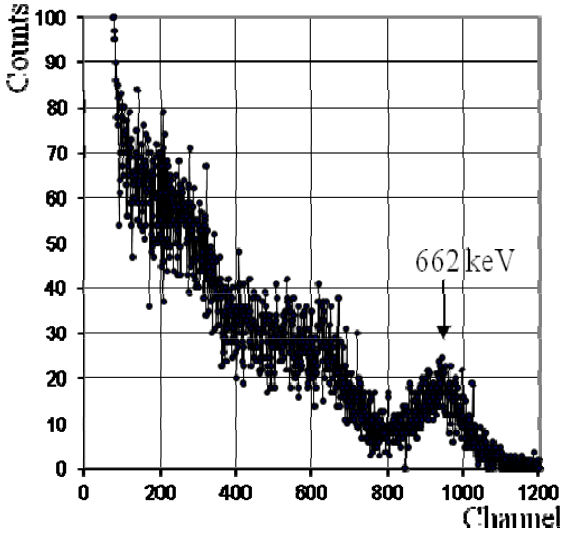

Fig. 5. Spectrum of ^{137}Cs with CdZnTe-detector $5 \times 5 \times 3$ mm^3 (teflon-filter 10 mm), $\tau_{FWHM} = 3$ μs, $U_b = 100$ V), (t = 5000 s).

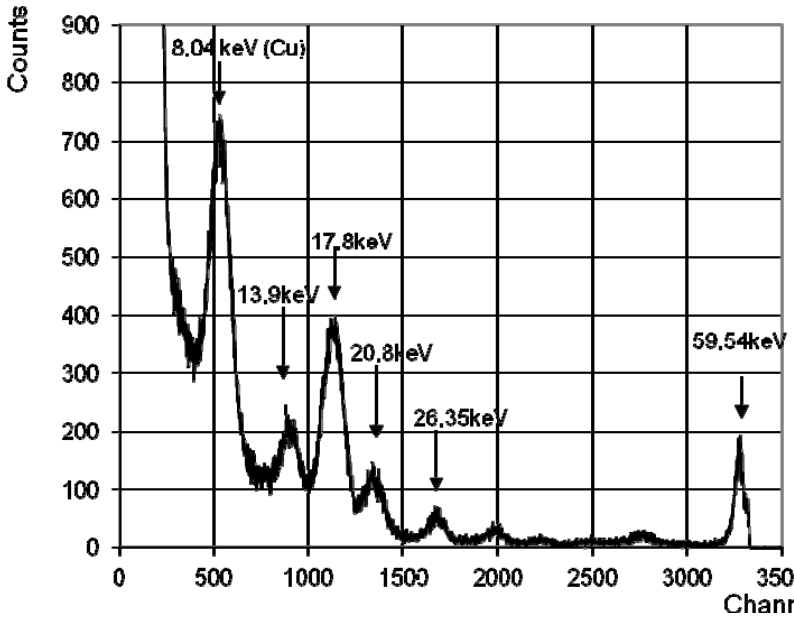

Fig. 6. Spectrum of ^{241}Am with Si-pin-detector 0,9 × 3,5 × 0,35 mm^3, [8];
(Cu-filter 0,03 mm): τ_{FWHM} = 3 μs, U_b = 50 V, t = 5000 s, T = 18 ºC, ΔE ~ 2 keV.

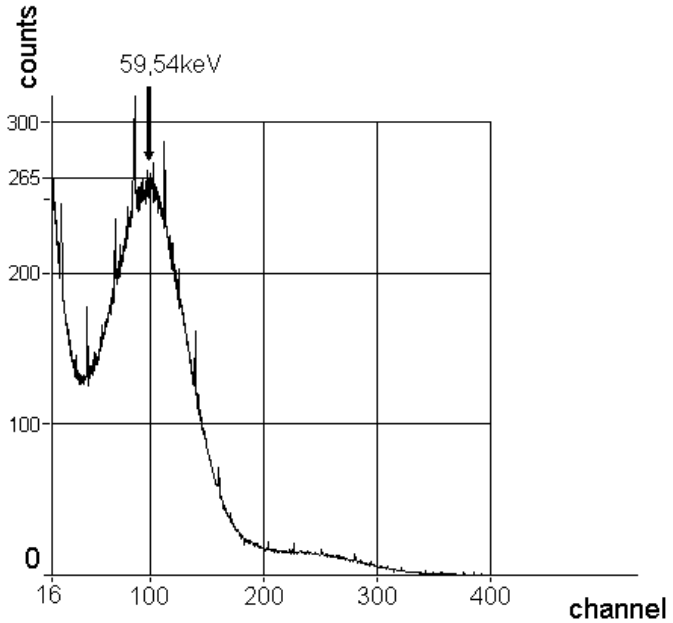

Fig. 7. ^{241}Am Spectrum. Detector CsJ(Tl)-10 × 10 × 10 mm^3- P-I-N-Photodiode 5 × 5mm^2, [8]; U_b = 20 V, t = 300 s.

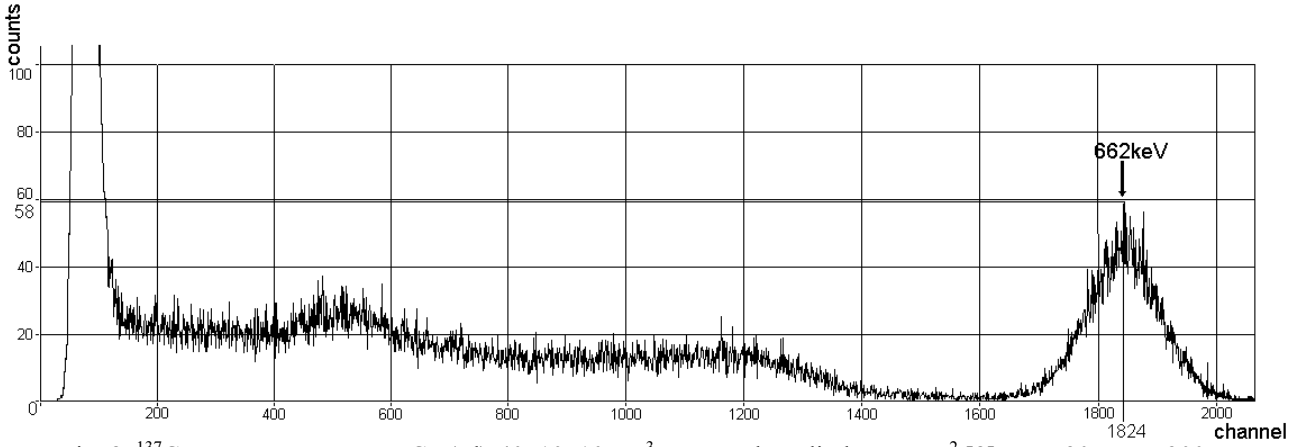

Fig. 8. ^{137}Cs spectrum. Detector-CsJ(Tl)-40x10x10mm^3- P-I-N-Photodiode 5x5mm^2 [8]; U_b = 20 V, t = 200 s.

6. Conclusions

CSA with JFET in Floating Gate Mode and Bessel active filter SA, implemented as microassemblies for use with CZT detectors, provide good resolution in registering low energy X-ray spectra, feature high versatility in application with various types of detectors. For direct detection with silicon p-i-n-diode new electronic channel can resolve ^{241}Am peaks up to 8 keV with a resolution of about 2 keV at room temperature. The CSA an SA microassemblies satisfy the requirements for use in the instruments for emergency dose control and NPP monitoring, as well as in many other applications. Supplied as a complete set with detector and a prototyping board, they form a Start Kit, easy to use for the customer.

REFERENCES

1. *Arkhipkin A.N., BrovchenkoV.G., Kirichenko A.M. et al.* Spectrometric amplifier: a hybrid microassembly // Instruments and Experimental Techniques. - 2003. - No. 3. - P. 84 - 87.
2. *Goulding F.S. et al*. Charge sensitive preamplifier using optoelectronic feedback // US Patent. 3,611,173. - 1971.
3. *Ohkawa S. et al.* Charge integration preamplifier for use in radiation detection circuitry // US Patent. 5,322,995. - 1994.
4. *Sinitsyn V.N., Ginzburg Yu.N.* Charge sensitive preamplifier with drain feedback for X-ray spectrometer // Instruments and Experimental Techniques. - 1986. - No. 5. - P. 99 - 102.
5. *Артемов С.В, Зайцевський І.Л., Кожушко Б.В., Шевченко С.В*. Зарядово-чутливий попередній підсилювач з низьким рівнем шуму // Пат. України № 84314. - 2008.
6. *Kumahara T. et al.* Self-feedback type low-noise charge sensitive amplifier // US Patent. 4,053,847. - 1977.
7. *Bertuccio G. et al*. Low noise charge sensitive preamplifier DC stabilized without a physical resistor // US Patent. 5,347,231. - 1994.
8. http://www.detector.org.ua - website of Scientific-Production Company "BIT" (Ukraine).

INFLUENCE OF PRODUCTION TECHNOLOGY AND DESIGN ON CHARACTERISTICS NEUTRON-SENSITIVE P-I-N DIODES

V. L. Perevertaylo, V. I. Kovrygin

SE Institute of Microdevices STC "Institute for Single Crystals"
National Academy of Sciences of Ukraine, Kyiv, Ukraine

This paper presents the results of tests on neutron-sensitive p-i-n diode with local p-n junction, which allows to measure not only the integral dose by nonionizing energy loss (NIEL), but also the real-time dose and dose rate because of ionizing energy losses (IEL). The influence of design and process parameters and the lifetime of minority carriers on the radiation characteristics of the device considered. Sensitivity at low doses (from one to ten rad) is limited due to a decrease in the lifetime because of influence of lateral sides of cut. The sensitivity and accuracy of dose can be increased by moving of p-n junction away from the cut surface. The dependence of the voltage drop across the diode on the neutron dose irradiation up to 5 krad received, and the sensitivity was 2 - 3 mV/rad. We have demonstrated that replacement of the bulk p-i-n diode with total p-n junction by new diodes with local p-n junction allow for increase sensitivity, accuracy of dose and application in NIEL and IEL measurements simultaneously. Explanation for the extinction of a direct current through the diode with increasing doses of neutron irradiation proposed.

1. Introduction

The use of p-i-n diodes for determining of neutron dose by measuring parameters related to damage of the crystal structure of a semiconductor material under irradiation, is attractive due to the small size of the detector, a simple measuring circuit, a low (or zero) supply voltage, high mechanical strength. Despite the disadvantages of this method (fading, the temperature dependence, the dispersion), it is widely used in neutron dosimetry [1 - 7].

The measurement of the dose based on the effect of damages of the semiconductor detector material crystal structure in the interaction with neutrons, which in the case of p-i-n diode leads to increased forward voltage across the diode U_F with increasing doses of neutron irradiation. Formation of various point defects and defect clusters in silicon irradiated with neutrons leads to a change of two key characteristics of the material. First, a change in the concentration of deep levels in the band gap of silicon, which leads to a change in the lifetime τ of minority carriers in the base [8]. Second, a change in the effective concentration of shallow donors and acceptors, which leads to a change in resistivity ρ in the base [1]. Changing either of these parameters (ρ and τ) under irradiation contributing to the change in the current-voltage characteristics (I-V). Both parameter can influence on the accuracy of the dose, the sensitivity and the minimum threshold of the measured dose. And given the high sensitivity τ to the effects of technological factors, it is necessary to investigate its behavior in the manufacturing process of the diode, influence on the I-V characteristics of the diode and contribution to the error in determining the dose that was done in this study. In addition, it is important to know the influence of p-i-n diode geometry on the τ, to predict described above electrical and radiation parameters of the detector. Therefore, when designing the diodes we specified various geometries of the sensitive area of diodes to create different conditions for the generation-recombination processes in the edge regions. The studies were conducted during testing and experimental operation of several batches neutron-sensitive p-i-n diodes.

2. The bulk neutron-sensitive p-i-n diode with long base and total implanted layer.

The traditional structure of neutron-sensing p-i-n diode wth long base is presented in [1] and shown in Fig. 1. Initial material - silicon of zone melting (FZ) n-type with a resistivity $\rho_o \geq 10^3$ Ohm·cm, the samples with a thickness (length) of the base 1,2; 2,2; and 3,2 mm and a cross section of the base 1x1 mm were investigated. The lifetime of the initial silicon τ_o~300 μs. Formation of p-n junction (p +-region) conducted by ion implantation of boron totally over the whole surface of the wafer, the depth of the p-n junction was 0,8 μm. The wafers were divided into individual chips with a cross section 1x1 mm by cutting directly on the p-n junction. To reduce surface recombination and other negative consequences of cutting side surfaces of the crystal diodes were etched and protected with a special varnish. Minority carrier lifetime in the base, defined by [8] and the experimental data, was 10 μs. Diodes were irradiated in the central channel of the reactor BR-1 by neutrons with an average energy 1,25 MeV in quasistatic and pulsed mode.

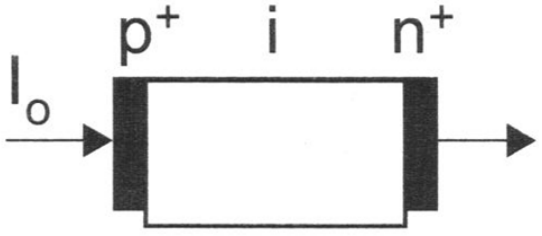

Fig. 1. Design of the bulk neutron-sensitive p-i-n diode with long base according to [1].

The sensitivity of the diodes according to the data [1] was 200mV/Gy for a diode with a thickness of base 1,2 mm and increased with increasing thickness of the base.

One drawback of the design and technology is disruption of the p-n junction by cutting, which leads to an increase in dark current leakage through the p-n junction, the appearance of regions with increased generation-recombination activity in the p-n junction, the growth of the saturation current of the p-n junction I_S, which reduces the sensitivity of the diodes to violations introduced by neutrons, i.e., to raising the threshold for the detection of small doses. In addition, because of the large leakage current these diodes cannot be used for the measurement of ionization currents in reverse bias p-n junction for the detection of gamma-, X-rays or other ionizing radiation or particles.

3. Design and technology of the new bulk p-i-n diode with local p-n junction

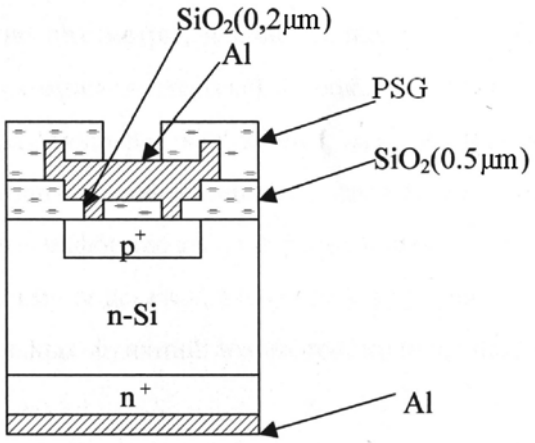

Fig. 2. Design of the new bulk neutron-sensitive p-i-n diode with thick base and local p-n junction.

Given the above, we have proposed the design of a neutron-sensitive p-i-n diode with the formation of a local p-n junction, using planar technology of integrated circuits (IC), shown in Fig. 2. To provide high sensitivity used high-resistance n-type silicon (FZ) with ρ_o~2 × 10^3 Ohm · cm, with an initial value of τ_o ~ 300 μs. Thickness of the base of the diode was 1200 μm. Cross-section of the crystal 1000 × 1000 μm. The boundaries of the p+-region moved away from the side surfaces (cutting planes) at 200 (300) μm, the size of the p+ region was 600 × 600 (400 × 400) μm, respectively (Table). Also, we have been made inspection lot diodes with n-type silicon of high quality with ρ_o = 1 kOhm · cm and an initial τ = 1700 μs and wafers thickness of 375 μm (see Table).

Technological features making p-i-n diodes, presented in Fig. 2 are described in [9 - 10], process provides high reproducibility of manufacturing the devices for leakage current, lifetime, breakdown voltage and other parameters due to processes through the use of soft-temperature conditions, cleaning, gettering impurities and suppress the defect formation. Fig. 3, *a* shows the crystal p-i-n diodes with different sizes of p+-region (600 × 600 and 400 × 400 μm), and Fig. 3, *b* - assembled neutron-sensitive devices.

Change in the lifetime of minority carriers in silicon at different stages of manufacturing p-i-n diode and neutron irradiation

The geometry of the p-i-n diode	Minority carrier lifetime τ, μs				
The size of p +-region and wider. diode, μm	In the initial silicon, (ρ_o~2 KOhm × × cm)	After production (before cutting)	After cutting, the average over the diode	Without the contribution of cutting edges ***	After neutron irradiation **
400 × 400 × 1200	300	~275	23	190	10**
600 × 600 × 1200	300	~ 275	23	190	10
600 × 600 × 375	1700****	~1200	30	300	-
5000 × 5000 × 375	1700****	~1200	220	400	15
1000 × 1000 × 1200*	300****	~ 275	10	-	-

***** p-i-n diode with the formation of p+-region of the p-n junction by implantation of boron totally over the whole surface and separated into chips by cutting (size 1000 × 1000 μm) [1].

****** Neutron irradiation dose 3500 rad (E = 1,25 MeV).

******* Measurements at dipping of the cut diode in liquid polar dielectric with ε = 81.

******** silicon with a resistivity ρ_o~1,0 KOhm · cm.

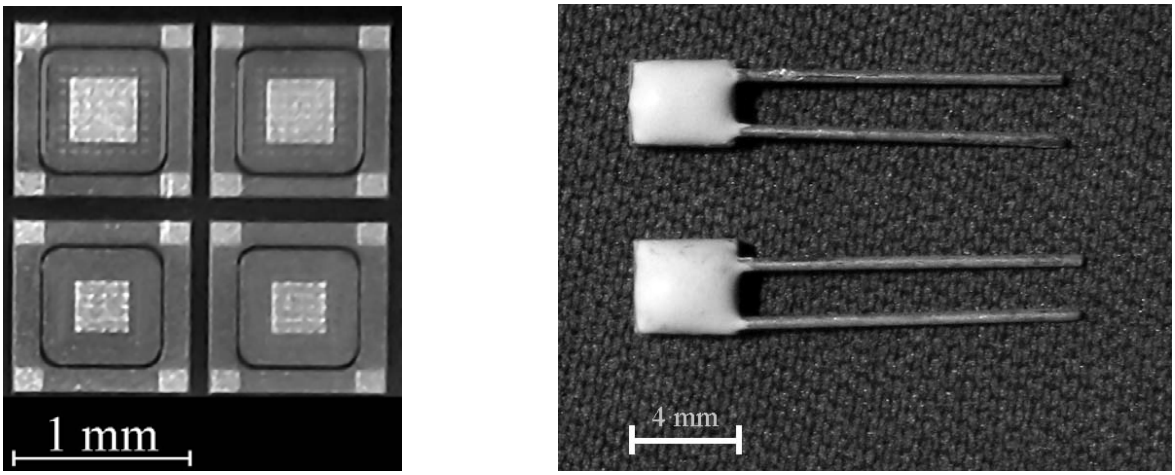

a *b*

Fig. 3. Crystals of new p-i-n diode with thick base and local p-n junction (*a*) and assembled neutron-sensitive devices (*b*).

4. The lifetime of minority carriers in silicon at different stages of p-i-n diode manufacturing and neutron irradiation

Analysis of the results of the effect of geometry, technology and irradiation on the lifetime of minority carriers in silicon τ given in the Table, led to a number of conclusions about the relationship τ with these factors. From the Table it is clear that in comparison to the technology of total doping and cutting of the p-n junction, the technology of local p-n junction formation gives τ increase about 2 - 3 times (23 - 30 μs compared to 10 μs) by moving aside the boundaries of the p+-region from the edges of the crystal, even without any treatment side surfaces of the cut. In addition, measurements τ before cutting and after cutting the crystals show a very strong influence of this operation, leading to a decrease in τ on the order of magnitude (e.g., from 275 μs to 23 - 30 μs). On the other hand, dipping of the cut crystals in a liquid with a high dielectric constant increases τ and almost restores it to the original value (190 μs). These facts suggest the existence on the cut edges of crystal the regions with increased generation-recombination activity due to the presence of deep levels with high concentrations, making a major contribution to the reduction in the measured lifetime by generation-recombination processes (Fig. 5).

5. Effect of the lifetime on current of directly-biased p-i-n diode and shape of the I-V characteristic

The effect of lifetime on the currents of direct-biased p-n junction and shape of the I-V can be seen from Fig. 4, which shows the direct branch of the I-V studied p-i-n diodes with a different value of the lifetime: lower curves for the samples on the wafers before cutting (τ ~ 275 - 300 μs) and upper curves for the same samples after cutting (τ ~ 20 - 30 μs). It is seen that with decreasing τ I-V has shifted towards increasing of the "heel" and the decrease in the slope of the I-V.

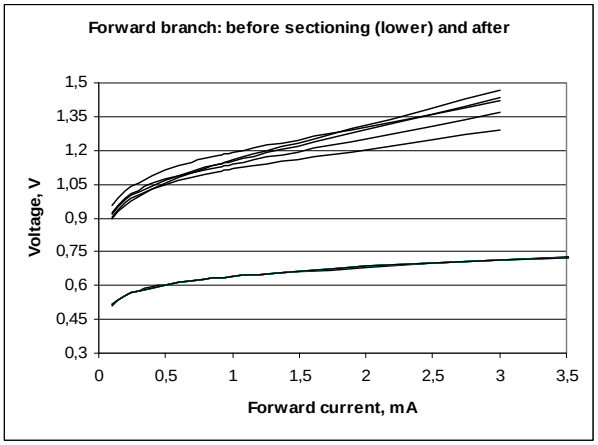

Fig. 4. Direct branches of I-V characteristics for p-i-n diodes with different value of the life time: before cutting (lower curves) and after cutting (upper curves).

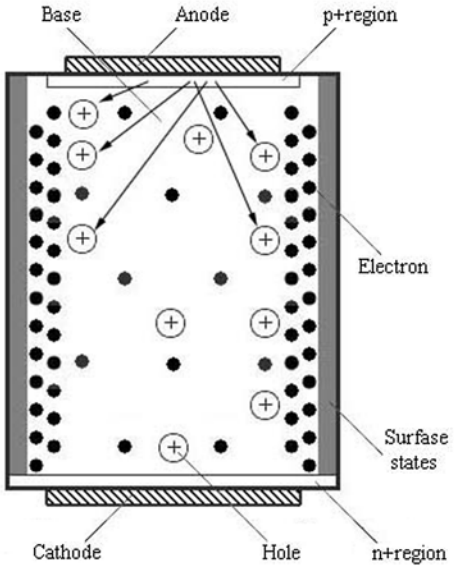

Fig. 5. The depletion of the base due to the effects of surface state at the cut sides leading to a decrease in conductivity base and preferential recombination of injected holes at the side faces. Arrows indicate the preferred direction of motion of the carriers.

Forward voltage U_F on pin-diode is the sum of voltages on p-n junction and on base (V_i) and is described by [11]:

$$U_F = U_{p-nS} + V_i = \varphi_T \ln \frac{I_F}{2qp_n \frac{DS}{\sqrt{D_p \tau_p}}} + \frac{3\pi kT}{8q} \exp\left(\frac{W}{2\sqrt{D_a \tau_a}}\right), \quad (1)$$

where D_a – ambipolar diffusion coefficient; τ_a – ambipolar lifetime; $L_p = \sqrt{D_p \tau_p}$ for holes; p_n – hole concentration in the n-base; φ_T – temperature potential; I_F – current through the diode; W – width of the base of a diode; S – area of p+-region; expression $I_S = 2qp_n \frac{DS}{\sqrt{D_p \tau_p}}$ characterizes the saturation current, $L_a = \sqrt{D_a \tau_a}$ – ambipolar diffusion length.

Expression (1) shows that the voltage across the diode depends essentially as on the length of the base of diode, and on the lifetime τ. Similar relations for ΔU_F are given in [12]. When you use the right branch of a parabolic relationship, described in [12], for estimation ΔU_F under irradiation using the value of ratio W_b/L_a close to 2,75, get the value ΔU_F, harmonizing with the received experimental sensitivity at neutron dose measurements. According to given in [11, 12] dependences for our construction 600 × 600 × 1200 mm, τ at the point of conversion should be ≈ 190 μs, and at W_b/L_a = 2,75 - 100 μs, in this case original U_F will be about 0,6 V. A further increase in sensitivity of the diode is

possible by increasing τ while maintaining (W_b/L_a = 2,75). The easiest way to increase τ is moving of p-n junction away from the cut surface of the crystal at the distance 3*L* considering τ, measured on a wafer. It is necessary to implement in the following modifications of the device. Really, the Table shows that for the diodes with the size of 55 × 0,375 mm, in which p-n junction is away from the cut surface at a distance 500 μm, has value of τ ~ 220 μs in comparison with 30 μs for the diode with the distance from the p-n junction to the cut surface 200 μm.

Described above the deep levels in the cut crystal surfaces also have the ability to capture the majority carriers, obtaining a negative charge, and thus depleting the base (see Fig. 5). This was evidenced by the increase in own base resistance, which turned out when it was measured, more than 30 % higher than the calculated value specified of the geometry of the crystal.

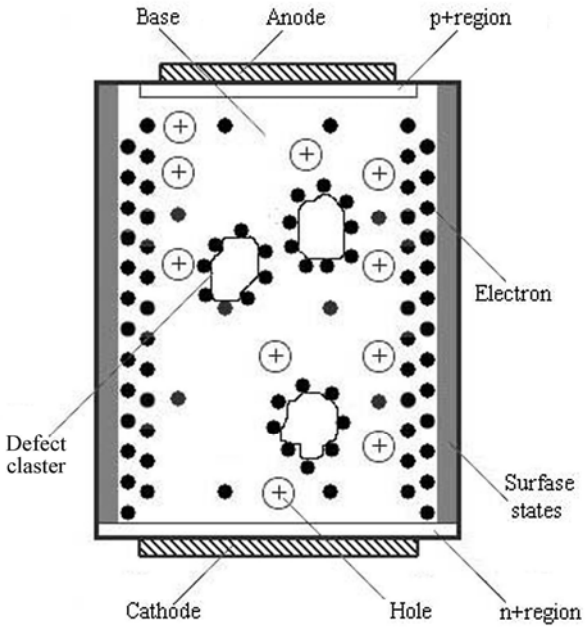

Fig. 6. Recombination of injected holes on defects and damage caused by radiation and on surface state at the cut faces.

The interaction with the flow of particles contributes to the semiconductor as point defects, and the whole cluster of disordering with the size of the space-charge region to 200 nm [13 - 14], (Fig. 6). These areas collect the majority carriers, immobilizing them, causing the growth of the resistivity and the increase in the recombination of minority carriers in the base, which reduces τ. Appearance of similar defects is expected also at the sides after cutting, as confirmed by the similarity of growth patterns U_F after cutting and after irradiation. With increasing doses of neutron irradiation effect is observed when the p-i-n diode is non-conductive, so that only an intrinsic current measurements are possible. According to the authors this is due to the fact that the concentration of clusters of defects increases with irradiation until they overlap over the section of base, so that the base is fully depleted region and does not pass current in direct inclusion as in the diode cannot begin the process of setting current. This effect was observed in diodes that have received large doses of neutron irradiation. For in this article pin-diodes, this effect occurs beginning doses of 3000 - 5000 rad. With further increase in the voltage across the diode can beginning field breakdown, leading to the appearance of the current in the diode just as is the case with latch-up.

6. Effect of the lifetime on characteristics of reverse-biased p-i-n diode and the measurement of ionizing energy losses

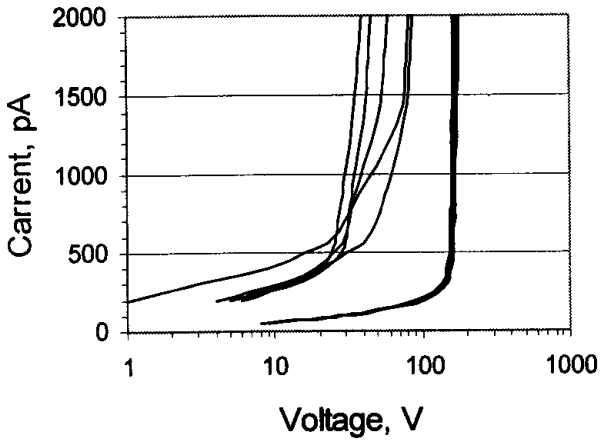

Fig. 7. Current-voltage characteristic reverse-biased p-i-n diode (size of the p+-region 600 × 600 mm^2).

Developed in this paper, the neutron-sensitive p-i-n diodes are also planned for the measurement of ionization currents in mode of reverse-biased p-n junction at the gamma-irradiation, X-rays or other ionizing radiation or particles.

In Fig. 7 shows the current-voltage characteristic reverse-biased p-i-n diode with the size of the p+-region of 600 × 600 mm^2, which shows that the decrease in τ after cutting has led to an increase in leakage current of p-i-n diode and their spread, reduce the breakdown voltage and the appearance of a soft (field) breakdown in prebreakdown area. If the initial leakage current is a few pA, after cutting it increased by an order.

Due to such low dark leakage current at a sufficiently low capacitance of diode (0,5 - 1 pF/mm^2) becomes possible registration of gamma-ray, X-rays with low energies in the spectrometric mode. In [15] presented minidozimeter used in low dose rate brachytherapy with isotope ^{125}I, in which was applied reverse-biased p-i-n diode (fully depleted) with cross-section base less than 1 mm^2, similar to that described above, which resolved ^{125}I isotope peaks in the energy range 22 - 35 keV when measuring the spectral characteristics. In [10] the results

of spectrometry by pin-diode, with close to the above parameters (leakage current of ~ 10 pA/mm^2, capacity ~ 0,5 - 1 pF/mm^2), but has a relatively large capacity (~ 50 pF) which at the direct detection diodes of X-ray radiation of the isotope ^{241}Am resolved peak 59.5 keV. Thus, the use of local p-n junction allows dosimetry and spectrometry in real-time reverse-biased p-n junction, provided sufficiently small leakage currents. This allows to measure not only the integral dose by NIEL, but also the real-time dose and dose rate of IEL simultaneously by one diode.

7. Dose characteristics of p-i-n diodes under the neutron irradiation

Made p-i-n diodes were exposed by two sources of fast neutrons - reactor BR-1 with an average energy 1.25 MeV neutron doses up to 600 rad and reactor GIR - 2 with an average energy of 0.9 MeV neutron doses up to 5000 rad.

Prior to the exposure the diodes of the same type were divided into three groups. Group 1 consisted of a number of diodes, selected by the close values of τ and initial base R_{B0}. Group 2 consisted of a number of devices that simply satisfied the 20 % variation of electrical parameters. Both groups were exposed to low doses in the first reactor. The group division was to determine the influence of τ and R_{B0} scatter to repeatability of $U_F(D)$. The third group also consisted of diodes with a 20 % variation of electrical parameters and was exposed in the second reactor. Dosimetry support ensured track dosimeter DINA.

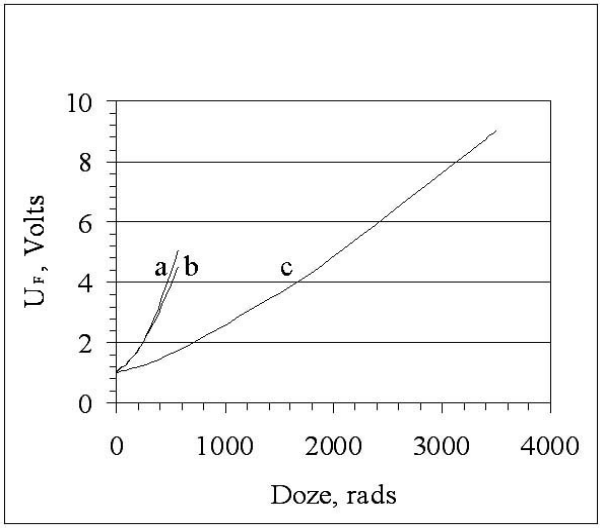

Fig. 8. The dependence of the forward voltage drop on the p-i-n diode on the dose of neutrons: *a* – the first group; *b* – second group ($E_{av\ n}$ = 1,25 MeV); *c* – the third group ($E_{av\ n}$ = 0,9 MeV).

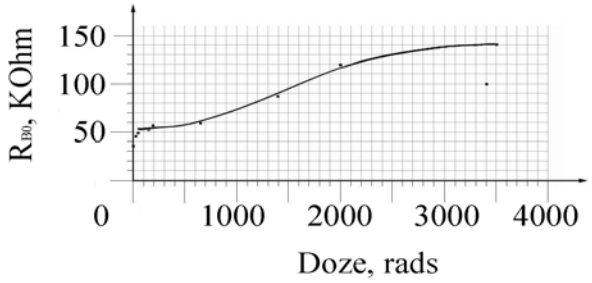

Fig. 9. The resistance of the p-i-n diode base on the dose of neutrons.

The top difference of measured U_F in the first group was within 2 %, and U_F of the first group and the worse of the second – 13%.

Dependences of U_F on the dose of neutrons are different for different reactors. The slope of the curve (and hence sensitivity) determined by the spectrum of the neutron energy in the flow and flow power that are unique to each reactor. For example, in [7] was observed differences in the sensitivity of p-i-n diode under neutron irradiation in various reactors. But for a good repeatability of the dependence $U_F(D)$, that allows you to use a correction factor KERMA [16] for the dose correction, you can use the final random calibration of the devices used to make with the features of the energy spectrum of the neutron source for the measurements.

Also of interest is a dependence of R_{B0} on the dose. As can be seen from Fig. 9 base resistance first increased with increasing dose because of defects, leading to a decrease in the concentration of majority carriers in the base, and then the value of R_{B0} is stabilized as approaching intrinsic values [14, 17].

The measurement of the base resistance was carried out by the pulse method, by feeding the diode by an amplitude of 30 V, 1mA, registering drop voltage on the diode in conduction mode.

8. Conclusions

Restrictions of the bulk p-i-n diode with total p-n junction in the measurement of small neutron doses were analyzed. Presented the results of tests on neutron-sensitive pin-diode with local p-n junction, which allows to measure not only the integral dose by nonionizing energy loss (NIEL), but also the real-time dose and dose rate because of ionizing energy losses (IEL). The influence of design and process parameters and the lifetime of minority carriers on the radiation characteristics of the device considered. Sensitivity at low doses (from one to ten rad) is limited due to a decrease in the lifetime because of the influence of lateral sides of cut. The sensitivity and accuracy of dose can be increased by moving of p-n junction away from the cut surface. The dependence of the voltage drop across the diode on the neutron dose irradiation up to 5 krad received, and the sensitivity was 2 - 3 mV/rad. Replacement of the bulk p-i-n diode with total p-n junction by new diodes with local p-n junction allow for increase sensitivity, accuracy of dose and application in NIEL and IEL measurements simultaneously. Explanation for the extinction of a direct current through the diode with increasing doses of neutron irradiation proposed.

REFERENCES

1. *Литовченко П.Г., Розенфельд А.Б., Хиврич В.И. и др*. Использование структур на основе кремния как датчиков в аварийной дозиметрии смешанных гамма- нейтронных полей // Весці АН БССР. Серыя фіз.-мат. навук. - 1991. - № 3. - С. 93 - 98.
2. *Lee N., Kim S., Youk G., Kim Y.* Development of a semiconductor neutron dosimeter with a PIN Diode // IEEE Nuclear Science Symposium Conference Record (19 - 25 Oct. 2003). - Vol. 5. - P. 3473 - 3477.
3. *Rosenfeld A.B. et al*. Neutron dosimetry with planar silicon p-i-n diodes // IEEE Trans. Nucl. Sci. - 2003. - Vol. NS-50. - No. 6. - P. 2367 - 2372.
4. *Carolan M.G., Rosenfeld A.B.* A method for measuring tissue-equivalent dose using a pin diode and activation foil in epithermal neutron beams with $E_N < 100$ keV // Radiation Protection Dosimetry. - 2006. - Vol. 120(1 - 4). - P. 337 - 340.
5. *Ravotti F. Glaser M., Rosenfeld A.B. et al*. Radiation Monitoring in Mixed Environments at CERN: From the IRRAD6 Facility to the LHC Experiments // IEEE Trans. Nucl. Sci. - 2007. - Vol. NS-54. - P. 1170 - 1177.
6. *Panwar L., Chaudhary, H S. Vaijapurkar, S G. et al*. Silicon PIN diode neutron dosimetry // Indian Journal of Pure & Applied Physics. - 2010. - Vol. 48. - P. 813 - 816.
7. *Lee N., Oh S., Lee H. et al*. Differences in Calibration Factors of a neutron diode dosimeter at Different. Facilities // Progress in Nuclear Science and Technology. - 2011. - Vol. 1. - P. 190 - 193.
8. *Swartz J.M., Thurston M.O.* Analysis of the Effect of Fast Neutron Bombardment on the Current-Voltage Characteristic of a Conductivity Modulated p-i-n Diode // Journal of Applied Physics. - 1966. - Vol. 37(2). - P. 745 - 755.
9. *Перевертайло В.Л.* Разработка и характеристики кремниевых координатно-чувствительных детекторов для физики высоких энергий и ядерной физики // Ядерна фізика та енергетика. - 2008. - № 1 (23). - С. 88 - 95.
10. *Перевертайло В.Л.* Характеристики і технологія виготовлення кремнієвих планарних p-i-n фотодіодів для сцинтиелектронних детекторів // Электроника и связь. Тематический выпуск «Проблемы электроники», Часть 1. - 2007. - С. 15 - 23.
11. *Sze S.M.* Physics of Semiconductor Devices. New York: A. Wiley-interscience Publication, 1981. - P. 130 - 131.
12. *Афанасьев В.Н., Уваров Е.Ф.* Динамика изменений прямого падения напряжения на p-i-n диодах в процессе импульсного нейтронного облучения // Физика и техника полупроводников. - 1996. - Т. 30, вып. 4. - С. 682 - 685.
13. *Bertolotti M.* // Radiation Effects in Semiconductors / Ed. by F. L.Vook. - New York: Plenum Press, 1968. - P. 311.
14. *Коршунов Ф.П., Богатырев Ю.В., Вавилов В.А.* Воздействие радиации на интегральные микросхемы. - Минск: Наука и Техника, 1986. - 254 с.
15. *Cutajar D.L. et al.* Intraoperative Solid-State Based Urethral Dosimetry in Low Dose Rate Brachytherapy // IEEE Trans. Nucl. Sci. - 2006. - Vol. NS-53. - No. 3. - P. 1408 - 1412.
16. *ASTM* Committee E-10. "Standard Practice for Characterising Neutron Energy Fluence Spectra in Terms of an Equivalent Monoenergetic Neutron Flueiice for Radiation Hardness Testing of Electronics". - 1993. - ASTM E 722-93. - American Society for Testing and Materials.
17. *Ларк-Горовиц К.* Бомбардировка полупроводника нуклонами // Полупроводниковые материалы / Под ред. В.М. Тучкевича. - М: Изд-во Иностр. лит-ры, 1954. - С. 62 - 94.

THE EFFECTIVENESS OF REGISTRATION OF FISSILE MATERIALS BY VARIOUS METHODS

V. D. Petrenko, A. V. Khugaev, A. D. Avezov, G. R. Alimov, U. N. Ismailov

Institute of Nuclear Physics, Uzbekistan Academy Sciences, Tashkent, Uzbekistan

Fission process of nuclear materials is accompanied by the yield of fission fragments and corresponding emission of γ-quanta and fission neutrons. In this work comparative analysis of effectiveness of registration of radioactive elements by two various methods: double γ-quanta coincidence and neutron detection methods. In the frame of developed approach the analysis of comparative effectiveness of registration methods for some fissile materials was done.

1. Introduction

Presently there are various methods of detection of fissile materials [1 - 4]. Our experience of using radiation portal monitors at Uzbekistan borders shows rather well their effectiveness [5]. But the modern trends of society development demand increasing of registration effectiveness of radioactive materials. First of all it is related to strengthening non-proliferation regime and prevention of illicit trafficking of nuclear and other radioactive materials. Besides, modern nuclear technologies are oriented on use of low-enrichment nuclear materials thus increasing the demands on nuclear security and radiation safety control. The methods of control should be more effective and fast. Earlier we studied the possibility of detection of fissile nuclear materials by double γ-γ coincidence method [4]. In present work we continue to study registration effectiveness with inclusion into consideration multi-particle correlations of registered γ-quanta and prompt fission neutrons.

2. Basic approach

Let's consider any radioactive element with atomic number A. Its mass is m, molar mass is μ_A half-life is $T_{1/2}$. Then the radioactivity of this material – number of nuclear decays per time unit is defined as: $A_{Rad} = \frac{\ln 2}{T_{1/2}} \frac{m}{\mu_A} N_A$, where N_A - Avogadro's number. As registered particle we'll consider prompt neutrons and multiple γ-quanta being accompanying fission products. Let's designate their number in each fission act as ν_n and ν_γ. Supposing the isotropic character of fission products distribution we consider effectiveness of registration of one neutron n and one γ - quantum in each fission act. Let probability of registration by detector of one neutron and one γ-quantum be q_n and q_γ correspondingly. Then using binomial distribution we get:

$$P_\gamma = C^1_{\nu_\gamma} \cdot q_\gamma (1-q_\gamma)^{\nu_\gamma - 1}. \quad (1)$$

Note that in case of γ-quanta registration radiation background is the factor to be excluded. Neutron background is much lower and in this case problem of background exclusion is nor so crucial. For solving the background problem the method of double γ - γ coincidence demanding two detectors is used. Then we have:

$$P_{\gamma\gamma} = \nu_\gamma(\nu_\gamma - 1) q_\gamma^2 (1-q_\gamma)^{2\nu_\gamma - 3} \equiv \frac{\nu_\gamma - 1}{\nu_\gamma (1-q_\gamma)} \cdot P_\gamma^2 . \quad (2)$$

We supposed here that two registering detectors are equivalent. For detection of one neutron, as it follows from (1) we have:

$$P_n = C^1_{\nu_n} \cdot q_n (1-q_n)^{\nu_n - 1}. \quad (3)$$

So, detection effectiveness of on neutrons and double γ - γ coincidence is given from comparison of relations (2) and (3). Here it's necessary to note that analysis of detection problem should include peculiarities knowledge of which is necessary for elaboration of effective registration methods. As an example we'll consider actinides, namely $^{235}_{92}U$, $^{238}_{92}U$, $^{239}_{94}Pu$ and $^{252}_{98}Cf$. The main thing representing fundamental difficulty is the following: during the fission of studied nuclei through various fission channels the main channel is α-decay. By this, as it is easy to show using half-lives, their specific activities are several orders higher than those of spontaneous fission (excluding $^{252}_{98}Cf$ nucleus). This fact nevertheless does not make task of detection of heavy radioactive elements easier because even in the presence of minimal lead shield (with thickness ~ 2 mm), the total absorption of fission products in lead is provided. It is due to the fact that characteristic radiation originating during α-particle movement is close by its energy parameters to lead

absorption band. Therefore it's impossible to register fission products by external detectors with shields. In case of products of spontaneous fission channel, though fission products pass through lead shield (thickness ~ 30mm), but their specific activity is low on background level. So, in case of registration of fissile elements on their spontaneous fission products, the problem of separation of fission products registered by detectors from background appears. Note that in this case spontaneous fission is characterized by emission of accompanying prompt neutrons and γ-quanta. One of effective methods to solve this problem is the method of double γ-γ coincidence. The problem of separation from background in case of neutrons became urgent at low activities of registered radioactive elements. Let the effectiveness of detection of one neutron and one γ-quantum be written as:

$$q_n = \frac{S_D}{4\pi R^2}(1-\exp[-\bar{\sigma}_n n_D L]), \quad q_\gamma = \frac{S_D}{4\pi R^2}(1-\exp[-\bar{\sigma}_\gamma n_D L]), \tag{4}$$

where L - thickness of detector; n_D - concentration of atoms of working substance of detector; $\bar{\sigma}_n$ and $\bar{\sigma}_\gamma$ - averaged over energy cross sections of interaction with atoms of working substance of detector; S_D - working square of detector and R-characteristic distance from radioactive source to detector. Supposing that detector thickness $L >> \lambda$ mean free path in detector, one may assume neglecting edge effects that:

$$q_n = q_\gamma = q = \frac{S_D}{4\pi R^2}. \tag{5}$$

Then registration effectiveness of double γ-γ coincidence detection or neutron detection one can define as:

$$\eta = \frac{P_{\gamma\gamma}}{P_n} = \frac{\nu_\gamma(\nu_\gamma - 1)}{\nu_n} q(1-q)^{2(\nu_\gamma - 1)-\nu_n}. \tag{6}$$

Let us consider the further generalization of method of double γ-γ coincidence to increase the reliability of detection of fissile material. If one considers triple correlations of type γ-γ-γ or γ-γ-n coincidence, it is easy to obtain the following useful relations:

$$P_{\gamma\gamma\gamma} = \nu_\gamma \cdot (\nu_\gamma - 1)\cdot(\nu_\gamma - 2) q_\gamma^3 (1-q_\gamma)^{3\nu_\gamma - 6}, \tag{7}$$

$$P_{\gamma\gamma n} = \nu_\gamma \cdot \nu_n \cdot (\nu_\gamma - 1) q_n q_\gamma^2 (1-q_\gamma)^{2\nu_\gamma - 3}(1-q_n)^{\nu_n - 1}. \tag{8}$$

These relations may be generalized on case of arbitrary number of detectors, for example let them be N, then for coincidence scheme $\underbrace{\gamma-\gamma-\gamma....-\gamma-\gamma}_{N}$ we'll get the following relation:

$$P_{N\gamma} = C_{\nu_\gamma}^N q_\gamma^N (1-q_\gamma)^{N\cdot\nu_\gamma - N(N-1)/2}, \tag{9}$$

where $N \le \nu_\gamma$.

3. Numerical calculations

Let's consider registration effectiveness of nuclear materials by various methods on some examples. We'll calculate specific activities of: ^{235}U, ^{238}U, ^{239}Pu и ^{252}Cf. Registration effectiveness of fissile material depends on intensity of emitted radiation of fission product and the amount of radioactive substance. We'll make calculations of specific activity per 1 g of radioactive substance. If we consider the half-lives of fissile material in case of SF are known then specific activity of source may be calculated as follows:

$$A_R = \frac{N_A \ln 2}{A \cdot T_{1/2}} = \frac{const}{A \cdot T_{1/2}}, \tag{10}$$

where A- atomic number; N_A - Avogadro's number; $T_{1/2}$ - half-life in decay channel. Calculation results are shown in Table 1.

Table 1. **Specific activities of fissile materials at SF**

Nucleus	$T_{1/2}(SF)$, years	A_R, Bq
^{235}U	$(1\pm0.3)\cdot10^{19}$	$4.3\cdot10^{-6}$
^{238}U	$(8.2\pm0.1)\cdot10^{15}$	$6.7\cdot10^{-3}$
^{239}Pu	$(1\pm0.3)\cdot10^{19}$	$5.54\cdot10^{-3}$
^{252}Cf	86 ± 1	$6.04\cdot10^{11}$

The obtained absolute activity of source needs measuring during detection taking into account its shielding (as a rule lead shield). Accounting shield the main fission products emitted outside are prompt neutrons and γ-quanta. For them

we'll take number of neutrons and γ-quanta per one SF act at an average as 2 - 3 and 8 - 12, correspondingly. If we consider probability of detection of prompt neutrons and γ-quanta, then we take for estimation the following parameters:

$$S_D = 100 \ \ cm^2 ; \ r = 100 \ cm. ; \ \varepsilon_{eff\,(n)} = 0.2 ; \ \varepsilon_{eff\,(\gamma)} = 0.4 \tag{11}$$

Table 2. **Probabilities of neutron registration in one SF act**

Nucleus	ν_n	P_n, $\frac{n}{\text{sec}}$
^{235}U	2.407	$3.83 \cdot 10^{-4}$
^{238}U	2.05	$3.26 \cdot 10^{-4}$
^{239}Pu	2.874·	$4.57 \cdot 10^{-4}$
^{252}Cf	3.724	$5.92 \cdot 10^{-4}$

In this case, taking into account obtained relations we may write: $q_\gamma \approx 3.176 \cdot 10^{-4}$ and $q_n \approx 1.592 \cdot 10^{-4}$. Results of probabilities of one neutron registration for spontaneous fission are shown in Table 2.

Here for ν_γ we took $\nu_\gamma = 8$. Having it in mind one can see that in accordance with relations (1) and (2) we get that registration probability $P_\gamma \approx 2.54 \cdot 10^{-3}$ and $P_{\gamma\gamma} \approx 1.5 \cdot 10^{-4}$. The values ν_n were taken from [6 - 8].

4. Conclusions

Table 3. **The registration effectiveness of neutrons and of events of γ-γ coincidence**

Nucleus	ε
^{235}U	1.3
^{238}U	1.8
^{239}Pu	0.76
^{252}Cf	0.41

The number of registered by detector particles is determined as product of registration probability of one particle multiplied by the number of particle emitted by fissile material. Let's suppose that $N\gamma = A_{Rad} \cdot \nu_\gamma$ and $Nn = A_{Rad} \cdot \nu_n$ correspondingly. Then the registration effectiveness of neutrons and of γ-γ coincidence events may be estimated by the following relation: $\varepsilon = \frac{\nu_\gamma}{\nu_n} \frac{P_{\gamma\gamma}}{P_n}$. Calculation results are presented in Table 3.

Here we took lower limit of value $\nu_\gamma = 8$. In case if higher value is taken, registration effectiveness of double γ-γ coincidence increases approximately1.5 times. So in this work the approach was developed and possibility of determining the registration effectiveness of prompt γ-quanta by double γ-γ coincidence method in comparison with neutron registration method was studied. This statement needs more detailed study using calculations made in spirit of work [9]. But from Table 3 it is possible already to make conclusion for elaboration of detection technique based on results obtained.

REFERENCES

1. *Gurevich I.I., Tarasov L.V.* Fizika nejtronov nizkikh ehnergij. - Moscow: Nauka, 1965. - 607 p.
2. *Kramer-Ageev E.A., Lavrenchik V.N., Samosadnyj V.T., Protasov V.P.* Ehksperimental'nye metody nejtronnykh issledovanij. - Moscow, 1990. - 272 p.
3. *Reilly D., Ensslin N., Smith H., Kreiner S.* Passive Nondestructive Assay of Nuclear Materials. LA-UR-90-732, Los Alamos National Laboratory, Los Alamos, New Mexico, 1991.
4. *Karimov Yu.N., Shipilov N.N., Fazilov M.I. et al.* // J. of Applied Radiation and Isotopes. - 2005. - Vol. 63. - P. 655 - 658.
5. *Petrenko V.D., Yuldashev B.S., Ismailov U.N. et al.* // AIP Proceedings. - 2009. - Vol. 1194. - P. 49 - 55.
6. *Gorbachev V.M., Zamyatin Yu.S., Lobov A.A.* Vzaimodejstvie izluchenij s yadrami tyazhelykh ehlementov i delenie yader. - Moscow: Atomizdat, 1976. - 461 p.
7. *Holden N. E., Hoffman D. C.* // Pure and Applied Chemistry. - 2000. - Vol. 72, No. 8. - P. - 1525.
8. *NuDAT 2.5*, http://www.nndc.bnl.gov/nudat2/, (National Nuclear Data Center, Brookhaven National Laboratory, Uoton, NY, 2009).
9. *Khokonov A.A., Savojskij Yu.V., Kamarzaev A.V.* // Yadernaya Fizika. - 2010. - Vol. 73, No. 9. - P. 1528 - 1532.

MESON PHOTOPRODUCTION AND BARYON RESONANCES

M. V. Romaniuk[1,2]
(on behalf of the BGO-OD, CB@MAMI and A2 collaborations)

[1] *Dipartimento di Fisica, Università di Messina, Messina, Italy*
[2] *Institute for Nuclear Research, National Academy of Science of Ukraine, Kyiv, Ukraine*

The study of the nucleon structure is one of primary interests in the strong interaction physics and has been the subject of experimental and theoretical studies for several decades. One of the primary manifestations of the complex internal structure of the nucleon is the existence of its excited states, i.e. baryon resonances. The availability of high intensity and high duty cycle electron and photon facilities open new possibilities for the study of baryon resonances using electromagnetic probes. These provide information on the resonances and nucleon wavefunctions through the measurement of the helicity amplitudes. Photoproduction of pions on light nuclei is important to obtain information on nuclear structure, in particularity for understanding of the nucleon spin structure. Preliminary results on charged pion photoproduction on ^{3}He target will be present.

1. BGO-OD collaboration

In present time in the question of hadron structure still exist problems in understanding of some specific states in range of quark models. To investigate baryon resonances we use the photoproduction of mesons. Electro-magnetic probe is a good tool for study of nucleon resonances since it is possible to get access to resonance states coupled to photons and also polarization observables are accessibles, wich gives us separation of overlapping resonances. In order to obtain full information about baryonic resonances it is need to study different channels: non-strange pseudoscalar mesons with charge combinations, strange and vector mesons.

The new experimental setup of the recently established BGO-OD collaboration consists of the combination of an open-dipole forward spectrometer and the BGO ball which cover the central angular region. This configuration is ideally suited to investigate the photoproduction of multi-particle final states with mixed charges. In addition it will allow nucleon polarization measurements in single-meson photoproduction. Due to the excellent forward acceptance it opens the possibility to investigate vector-meson production in order to understand the reaction mechanism and the role of resonances. The BGO-OD collaboration presently includes individuals and groups from Germany (Bonn), Italy (Rome, Frascati, Pavia, Messina), Russia (Gatchina, Moscow), UK (Edinburgh, Glasgow) and Ukraine (Kharkov), and is open for further extension.

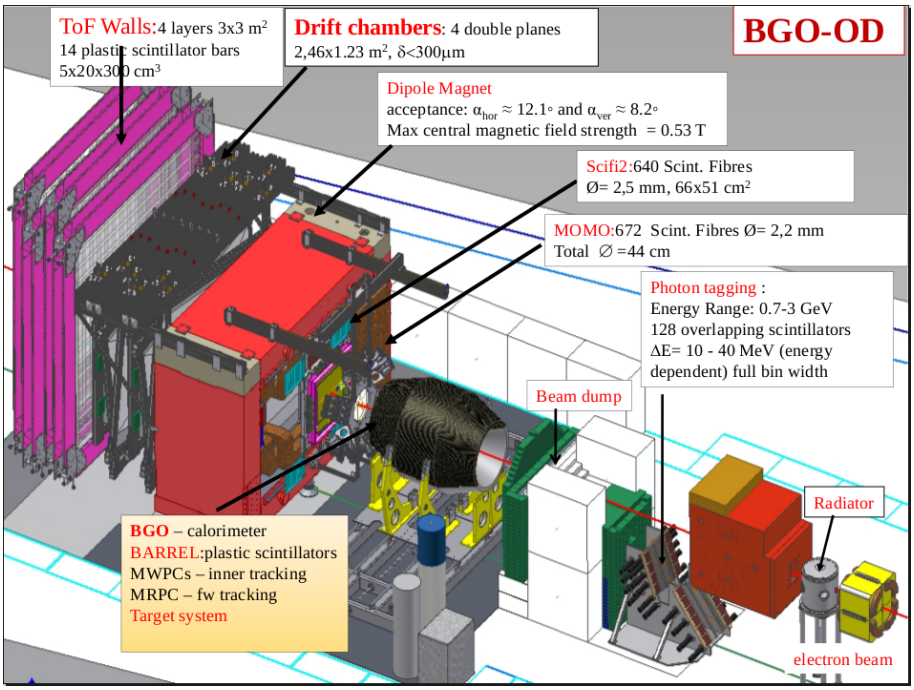

Fig. 1. Overview of the experimental set up of the BGO-OD experiment.

The experimental set-up (Fig. 1) consists of a large 90 ton dipole magnet, tracing detectors, two scintillating fiber detectors, MOMO and SciFi2 (to allow for momentum reconstruction of charged particles bent through the magnetic field), an aerogel Cherenkov detector (discriminates pions against protons and particularly improves the $K^{\pm}$-identification substantially), a time-of-flight (TOF) detector (provides flight-time measurements for charged particles

and neutrons), the BGO Ball which is optimized for photon detection, good performances with protons (energy and angle reconstruction) and good neutron detection efficiency. BGO hermetically encloses the target (polar angular range 25 - 155 degrees). Main features of BGO-OD beam: Beam energy γ: E_γ = 0.7 - 2.8 GeV; linear polarization degree up to 2.0 - 2.2 GeV; High intensity (10^7 γ/s) for low cross section reactions [1]. The Quantumcooler Hydrogen/Deuterium is a two stage closed-cycle refrigerator. The working fluid in all stages is an high purity helium gas. The nominal operating temperatures of each stage is 70 and 20K respectively. Both stages are based on the Gifford-McMahon (G-M) cycle. The target cell is a 3 cm diameter aluminum cylinder, closed by thin mylar windows at the two sides. Two different lengths of the cell 6 and 11 cm are available. The target cell could be filled with liquid Hydrogen (H2) or Deuterium (D2). The hydrogen/deuterium gas is cooling down by the helium through heat exchangers and liquefied inside the cell. In order to ensure the movement of the target system and and extraction of the nose out of the BGO the rails system was build (Fig. 2).

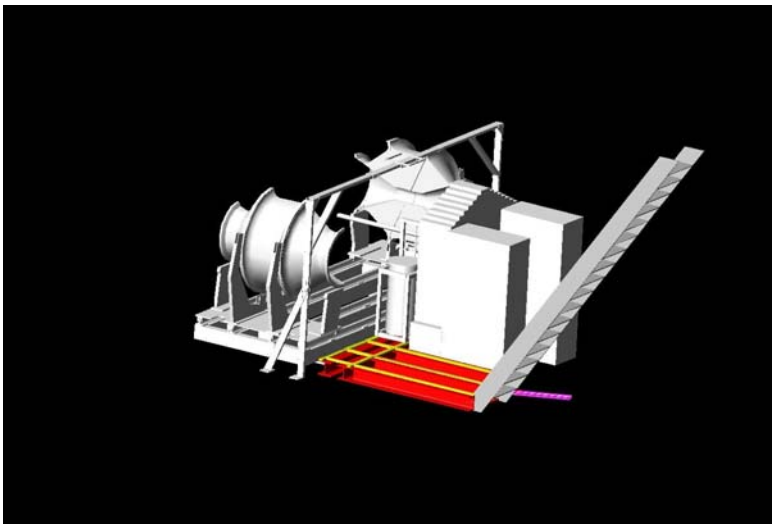

Fig. 2. Schematic view of the target system, BGO ball and rails system.

Initial cool-down of the H_2 from room temperature take about 8 hours, it is possible to empty cell in ~ 20 minutes using electric heater, refill target in ~ 2 hour (Fig. 3).

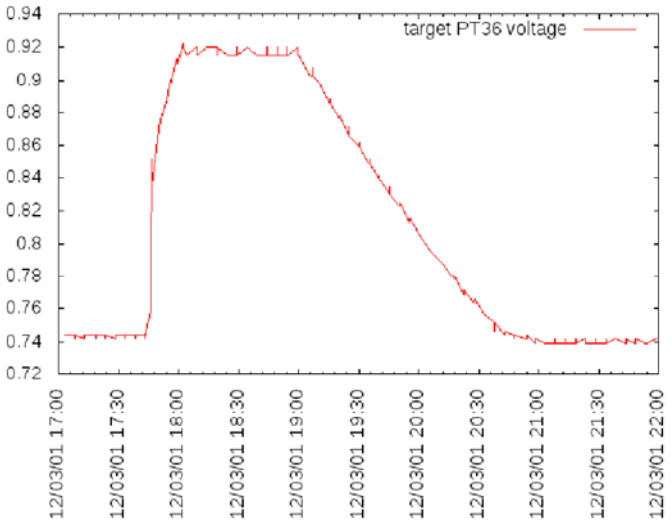

Fig. 3. Pressure (PT36) on H2 tank, emptying and refill, beam-time, March 1st, 2012.
Pressure +0.74 bar - cell is full; pressure +0.92 bar - target cell is empty [2].

During commissioning beam time at the March 2012 BGO detector setup, testing, calibrations and first analysis of data from the BGO ball were performed. No charged particle identification was available (no data from the plastic scintillator barrel or MWPC) and no data from the photon tagger or any information from the forward spectrometer was used in the analysis.

Fig. 4, *a* is the invariant mass of two photon clusters plotted against the total energy of the two clusters, there is a

concentration of events with the invariant mass close to the expected π^0 mass of 134 MeV and a smaller shoulder above 500 MeV consistent with the η mass [3].

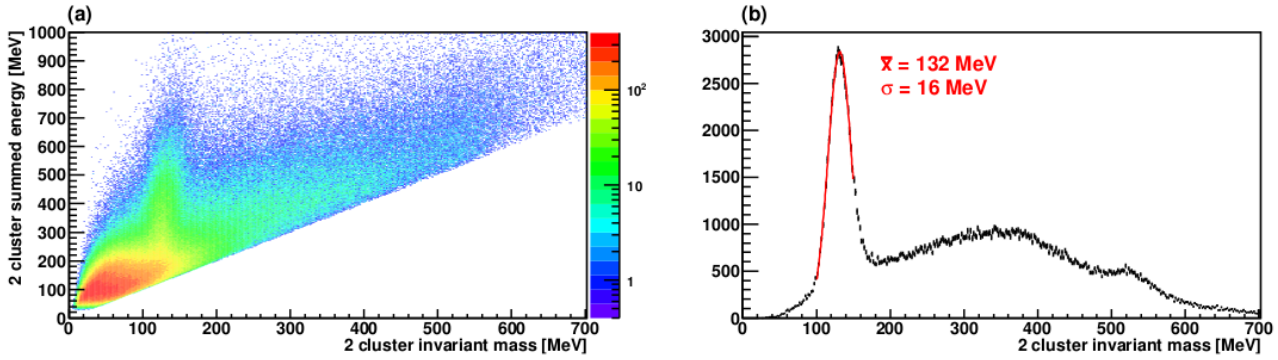

Fig. 4. Two photon invariant mass *a* - Two photon energy versus the invariant mass. *b* - Invariant mass when the two photon energy is greater than 400 MeV. A Gaussian distribution is fitted to the peak at the expected π^0 mass, mean ($\bar{x}$) and width (σ) inset [3].

2. GDH sum rule

The sum rules, which connect information from all energies to fundamental parameters of the present interaction models, could be a good tool for study of the internal structure of the nucleon, in particular of its spin structure. The Gerasimov-Drell-Hearn (GDH) sum rule is consequences of general principles: forward Compton scattering, the optical theorem and the low energy one [4, 5]. It relates the anomalous magnetic moment (AMM) κ of a particle of spin S and mass M to the integral over the weighted helicity asymmetry of the total absorption cross section for circularly polarized photons on a longitudinally polarized target:

$$I_{GDH} = \int_{\upsilon_{th}}^{\infty} \frac{\sigma_p - \sigma_a}{\upsilon} d\upsilon = 4\pi^2 \kappa^2 \frac{e^2}{M^2} S \,, \tag{1}$$

where ν is the photon energy and σ_p (σ_a) denotes the total absorption cross section for parallel (antiparallel) orientation of photon and particle spins. The lower limit of the integral, ν_{th}, corresponds to pion production and photodisintegration threshold for a nucleonic and nuclear target, respectively.

Contributions of different partial reaction channels to the GDH sum rule

	I_{GDH} proton	I_{GDH} neutron
$\gamma N \to N\pi$	172 [164]	147 [131]
$\gamma N \to N\pi\pi$	94	82
$\gamma N \to N\rho$	−8	−6
$\gamma N \to K\Lambda(\Sigma)$	−4	2
$\gamma N \to N\rho(\omega)$	0	2
Regge contribution ($E_\gamma > 2\,\mathrm{GeV}$)	−14	20
TOTAL	∼ 239 [231]	∼ 247 [231]
GDH sum rule	204	233

In the Table the current theoretical estimate of the GDH sum rule values is given for the proton and the neutron. Predictions for Nπ are from the SAID [6] and (within brackets) MAID [7] multipole analysis; estimates for Nππ are from [8]; estimates for Nη are from [7]; kaon channel contributions are from [9]; predictions for vector meson production are from [10]; Regge contributions are from [11]. This estimate disagrees with the expected GDH sum rule value for the proton while it roughly reproduces the neutron GDH value. However, the (proton-neutron) difference has a different sign with respect to the GDH expectation. These discrepancies emphasized the need of a precise test of the GDH sum rule for both the neutron and proton and for precise double polarization data for all γN→Nπ(π) channels, which give the dominant contribution to the GDH integral to obtain a complete understanding of the γN interaction. For the neutron case, an additional complication arises due to the lack of free neutron targets. The use of neutrons bound in ^{2}H and/or ^{3}He is necessary. The comparison between the two different "free neutron" values that are extracted both from the deuteron and ^{3}He targets using different nuclear models will give a fundamental cross-check of the reliability of the extraction procedures. While in the deuteron the proton and the neutron are essentially in s states of relative motion with aligned spins, ^{3}He is a system of two protons with spins paired off and an "active" unpaired neutron, again in relative s states. As a result we then find that

$$\mu_d \approx \mu_p + \mu_n \,, \quad \mu_{^3He} \approx \mu_n \,, \tag{2}$$

so that the ^{3}He spin structure function is much closer to the free neutron than the deuteron. Therefore, it is expected that the measured GDH integrand function for ^{3}He above the pion photoproduction threshold will already be a good first approximation of the I^n_{GDH} value.

3. A2 collaboration

The experiment was done at the tagged photon facility of the MAMI accelerator in Mainz. Circularly polarized photons were obtained by bremsstrahlung of longitudinally polarized electrons with an average polarization of 75 %, the bremsstrahlung photons were tagged using the Glasgow-Mainz magnetic spectrometer (energy resolution ~ 2 MeV). The relative tagging efficiency was monitored by a CCD photon camera and absolute measurements were made using a lead-glass detector. The reaction products were detected by the central detector system, see Figure, consisting of the Crystal Ball (CB) NaI spectrometer, complemented by the Multi-Wire Proportional Chambers (MWPCs), used to identify and track the charged particles, and the cylindrical Particle Identification Detector (PID), used to distinguish the charged from the neutral particles detected by the CB. The combined information provided by these three detectors provides accurate energy, angle and particle identification in the azimuthal (φ) and polar (θ) angular regions from 0º to 360º and from 21º to 159º, respectively.

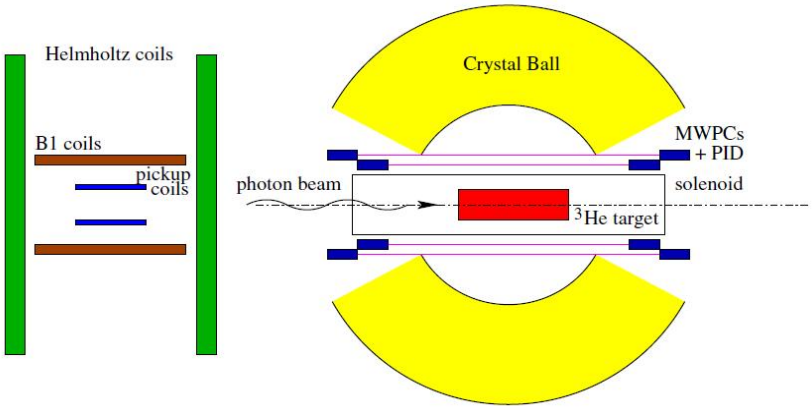

Fig. 5. Side view of the ^{3}He experimental setup.

The ^{3}He gas target density is relatively low (N_T~$2.5 \times 10^{21} cm^{-2}$) compared to that of a solid or liquid target (about 100 times less). Despite this, the ^{3}He gas target has a greater fraction of polarised neutron with respect to the deuterated butanol target [12].

4. Results and conclusions

Using dE/dx vs E technique, PID and MWPCs information pion/proton separation has been done. Preliminary results obtained for unpolarised total (differential) cross section as a function of the incoming photon energy up to 500 MeV for $\gamma\ ^3He \to \pi^{\pm}X$ channels are shown in Figs. 6 and 7, where data (blue spots) are compared to the predictions from the model of A. Fix (red line) [13]. Fix model take into account Fermi motion of the interacting nucleons inside the nuclei and the nuclear effects, which damp and broaden the peak due to the excitation of then Δ(1232) resonance.

In the Figs. 8 and 9 the total (differential) helicity dependent cross section difference, $\Delta\sigma_{\pi} = \Delta\sigma_{\pi,a} - \Delta\sigma_{\pi,p}$, for the $\gamma\ ^3He \to \pi^{\pm}X$ channels is shown in comparison to the model predictions from A. Fix.

For the first time unpolarised and polarized cross sections of the channel $\gamma\ ^3He \to \pi^{\pm}X$ in the Δ-resonance region has been measured. Present calculations are not able to describe in a good way helicity dependence of πX channels, futher theoretical and experimental research are needed.

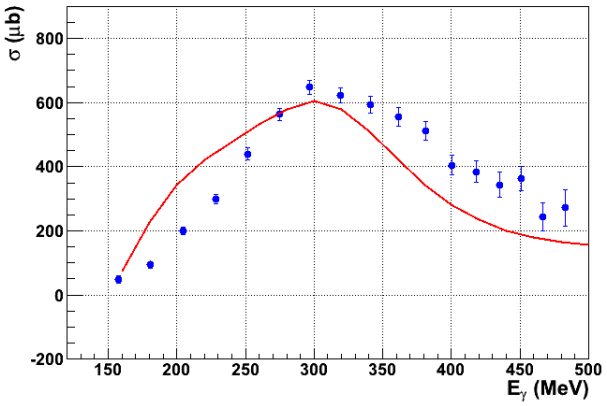

Fig. 6 Preliminary results of the unpolarised total cross section for $\gamma\ ^3He \to \pi^{\pm}X$ channels compared to the Fix model (red line).

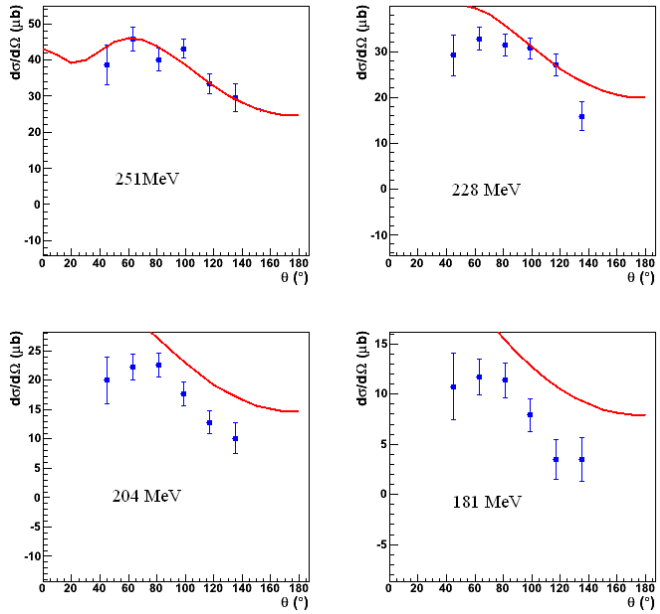

Fig. 7. Preliminary results of the unpolarised differential cross section for $\gamma\ ^3He \rightarrow \pi^{\pm}X$ channels compared to the Fix model (red line).

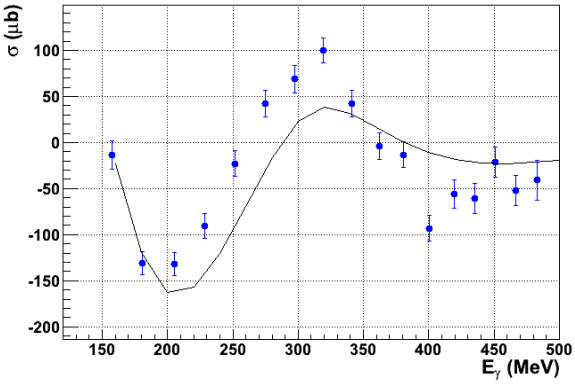

Fig. 8. The helicity dependent total cross section for the $\gamma\ ^3He \rightarrow \pi^{\pm}X$ channel are compared to the prediction from A. Fix model in the Δ-resonance region.

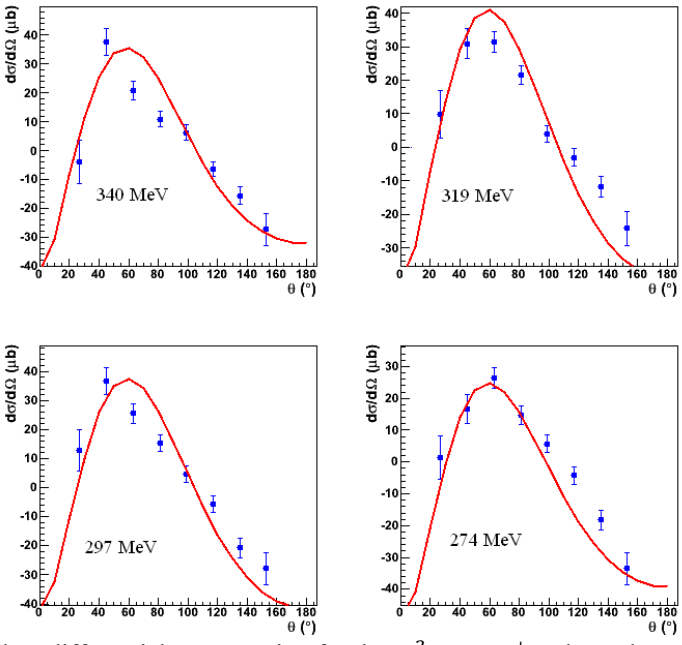

Fig. 9. The helicity dependent differential cross section for the $\gamma\ ^3He \rightarrow \pi^{\pm}X$ channel are compared to the prediction from A. Fix model in the Δ-resonance region

REFERENCES

1. *Letter* to intent to the PAC, ELSA (2009).
2. *Romaniuk M*. Target system // Internal Note - BGO-OD Collaboration - May 2012 - P. 1 - 30.
3. *Jude T.* First analysis of BGO data from the March 2012 commissioning beam time BGO-OD Collaboration - April 2012. - P. 1 - 11.
4. *Gerasimov S.*B. // Sov. J. Nucl. Phys. - 1966. - Vol. 2. - P. 430.
5. *Drell S.D., Hearn A.C.* // Phys. Rev. Lett. - 1966. - Vol. 16. - P. 908.
6. *Arndt R. A. et al* // Phys. Rev. - 2002. - Vol. C66. - P. 055213.
7. *Drechsel D. et al* // Phys. Rev. - 2001. - Vol. D63. - P. 114010.
8. *Fix. A., Arenhoevel H.* // Eur. Phys. J. - 2005. - Vol. A25. - P. 115.
9. *Sumowigado S., Mart T.* // Phys. Rev. - 1999. - Vol. C60. - P. 0282201.
10. *Zhao Q., Al-Khalili J.S., Bennhold C.* // Phys. Rev. - 2002. - Vol. C65. - P. 032201.
11. *Bianchi N., Thomas E.* // Phys. Lett. - 1997. - Vol. B404. - P. 223.
12. *Pedroni P.* Double polarization experiments at MAMI // Eur. Phys. J. Topics. - 2011. - Vol. 198. - P. 181 - 198.
13. *Fix A.* Private communication.

POSSIBILITIES TO INVESTIGATE ASTROPHYSICAL PHOTONUCLEAR REACTIONS IN UKRAINE

Ye. Skakun[1], I. Semisalov[1], V. Kasilov[1], V. Popov[1], S. Kochetov[1], N. Avramenko[1], V. Maslyuk[2], V. Mazur[2], O. Parlag[2], D. Simochko[2], I. Gajnish[2]

[1]NSC KIPT, Institute of High Energy and Nuclear Physics, Kharkiv, Ukraine
[2] Institute of Electron Physics, National Academy of Sciences of Ukraine, Uzhgorod, Ukraine

Reactions of proton capture (***rp***-process) and sequences of photodisintegrations of the (γ,n), (γ,α) and (γ,p) types (***γ***-process) play the key role in stellar nucleosynthesis of the so-called ***p***-nuclei – a group of stable proton rich nuclides which could be created by none of *slow* (***s***) and *rapid* (***r***) radiative neutron capture reactions. There is need of knowledge of thousands of reaction rates to simulate natural abundances of the p-nuclei. Using bremsstrahlung beams from thin tantalum converters of the electron linear accelerator of NSC KIPT (Kharkiv) and the microtron of IEP (Uzhgorod) and conventional activation technique applying high resolution gamma-spectrometry we measured the integral cross sections of the (γ,n)-reactions on the nuclei of the ^{96}Ru, ^{98}Ru, ^{104}Ru, ^{102}Pd, and ^{110}Pd isotopes the first two of which and palladium-102 are p-nuclei, and determined the reaction rates by a procedure of superposition of several bremsstrahlung spectra with different endpoints in the range from the thresholds to 14 MeV. The experimental reaction cross sections were compared to available data in overlapping energy range and the derived reaction rates to the predictions of the Hauser - Feshbach statistical model of nuclear reactions. In most cases theory underestimates the observed reaction rates in not great extent.

1. Introduction

Occurring in nature chemical elements and their isotopes were synthesized in stars via different type low-energy nuclear reactions from pre-existing nucleons. The lightest nuclei were created through the process called the Big Bang nucleosynthesis while nuclei having masses up to iron (Z = 26) were produced through the successive fast nuclear fusion mechanisms in the cores of stars. The majority of trans-iron nuclei were synthesized by *rapid* (***r***) and *slow* (***s***) (compared to the intervening beta-minus decays) neutron capture processes, i.e. (n, γ)-reactions [1]. However there are 35 nuclei between ^{74}Se (Z = 34) and ^{196}Hg (Z = 80) which cannot be formed through these scenarios since they are screened from the r-process by another stable isotope in the same isobar chain and bypassed by the s-process. They were called by ***p***-nuclei since they are located at the proton-rich side of the valley of stability and the scenario of their synthesis by ***p***-*process* complemented by β^+, electron capture and (n, γ)-reactions.

Several isotopes of p-type are placed in the A = 90÷110 mass number region. The chains of the ruthenium and palladium isotopes and the ways of their star synthesis are shown in Fig. 1. The most of the natural ruthenium (having masses 99 and more) and palladium (masses 104 and more) isotopes were synthesized in the s (the thick broken arrow line in Fig. 1) and r (the individual thin solid arrows) processes. However both of these scenarios are bypassing the ^{96}Ru, ^{98}Ru and ^{102}Pd p-nuclei. The ^{96}Ru (^{98}Ru) nuclide cannot be formed because of the ^{95}Ru (^{97}Ru) isotope radioactivity and the ^{96}Mo (^{98}Mo) isotope stability. The ^{102}Pd nuclide is blocked by the radioactive ^{101}Pd and stable ^{102}Ru isotopes. A possible chance of these nuclei creation is p-process representing a combination of proton induced reactions (***rp***-*process*) and (γ, n), (γ, p) or (γ, α) photonuclear reactions (***γ***-*process*) on pre-existing s- and r-nuclei and the ***νp*** as an alternative process [2]. So if r-process widens the valley of stability and s-process elongates it then p-process moves backward from heavier nuclei to lighter ones.

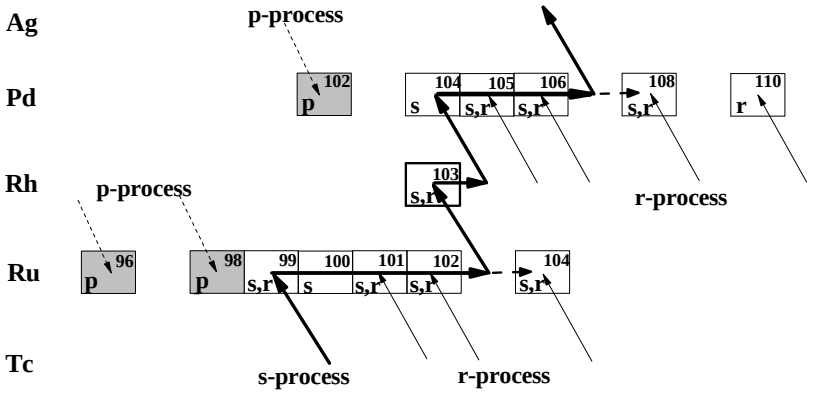

Fig. 1. The main nucleosynthesis mechanisms of the ruthenium and palladium isotopes production.

The widely believed candidate site for the p-process are the deep O-Ne-rich layers of massive stars of SNe-II type exploding as core-collapse supernovae at the stellar plasma temperatures of $T_9 = 1.8 \div 3.3$ (T_9 is the temperature in 10^9 Kelvin units). The primary stimulus to the cosmos nucleosynthesis theory development is to understand the shape of the abundance curve when plotted on a graph as a function of atomic mass and the strongly differing (by factors up to ten millions) abundances of the chemical elements and their several isotopes. The p-nuclei represent only a small fraction

(usually 0.01÷1 %) of the isotopic content of corresponding elements in the solar system. This fact is hopeful to believe in formation of the p-nuclei from pre-existing s and r seed nuclei. The (p,γ)-reactions require a high-temperatures of stellar plasma to overcome the proton Coulomb barrier. So photonuclear reactions can play larger role in the heavier p-nuclei synthesis. Available astrophysical nucleosynthesis simulation codes have probably their own uncertainties but they must be provided with such high precision nuclear data as reaction rates converted from cross sections, nuclear masses, decay data, structure features of many nuclei etc. p-Process involves thousands of photonuclear reactions on around 2000 nuclei-"targets" many of which are radioactive even in the ground state and often populated in excited states according to the Boltzman statistics of star gas at high temperatures. Impossibility to measure cross sections of nuclear reactions on unstable and excited nuclei increases the importance of theoretical calculations of nuclear reaction cross sections in the frame of the statistical Hauser - Feshbach model [3]. Therefore experimental values of nuclear reaction cross sections are both nuclear data for star nucleosynthesis simulation and to test predictive power of the statistical theory of nuclear reactions.

Large efforts were applied in recent years to measure charged particle (see, e.g. [4] and references therein) and gamma induced ([5, 6] and references therein) reaction cross sections in astrophysically interesting energy range. However, current databases (cf. KADoNIS database [7]) show the scarce of available data in question. We present the results of our measurements of cross sections of (γ, n)-reactions on ruthenium (^{96}Ru, ^{98}Ru, ^{104}Ru) and palladium (^{102}Pd, ^{110}Pd) isotopes: in the bremsstrahlung photon energy range from the respective threshold to 14 MeV, the proton rich ^{96}Ru, ^{98}Ru, and ^{102}Pd isotopes of which are p-nuclei. The cross sections are transformed to the reaction rates by the superposition method proposed by Darmstadt group [8, 9] and compared to the prediction of the NON-SMOKER code [10] utilizing the statistical theory of nuclear reactions.

2. Generalities of photonuclear reactions

We concentrate on the dominant (γ, n)-reaction. The reaction rate $\lambda_{(\gamma,n)}(T)$ for (γ, n)-process depending on temperature T of a thermal photon bath of a star is expressed by the equation:

$$\lambda_{(\gamma,n)}(T) = \int_0^\infty cn_\gamma^{Planck}(E,T)\sigma_{(\gamma,n)}(E)dE\ , \tag{1}$$

where c is the speed of light, $n_\gamma^{Planck}(E,T)$ represents the blackbody Planck distribution, *i. e.* the number of photons of a star environment per unit energy and volume interval

$$n_\gamma^{Planck}(E,T) = \frac{1}{\pi^2}\frac{1}{(c\hbar)^3}\frac{E^2}{\exp\left(E/kT\right)-1}$$

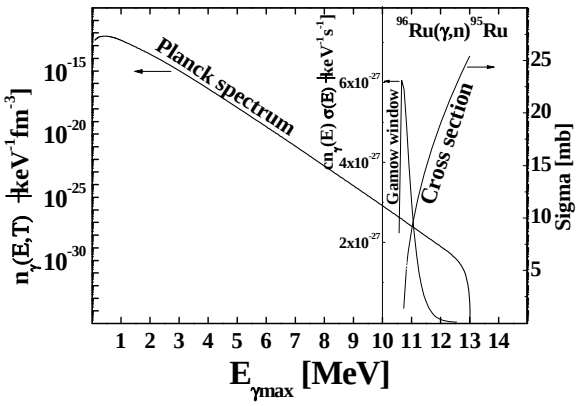

Fig. 2. Astrophysically relevant energy region ("Gamow window" peak in the right panel) determined as the product of the Planck spectrum and the ^{96}Ru(γ, n)^{95}Ru reaction cross section for the stellar temperature $T_9 = 3$.

and $\sigma_{(\gamma,n)}(T)$ corresponds to the cross section of the (γ, n)-reaction. The photon flux cn_γ^{Planck} (of Eq. 1) decreases exponentially with increasing energy (the dropping curve in Fig. 2 marked as "Planck spectrum") while the (γ, n)-reaction cross section steeply increases from the threshold to the giant dipole resonance curve maximum (the growing curve "Cross section" at the right panel in Fig. 2). The product of these quantities (i. e. the integrand of Eq.1) is a narrow peak located at about kT/2 above the reaction threshold which was called by the Gamow window by analogy with the similar picture for the charged particle reactions.

Bremsstrahlung spectra of our electron accelerators are approximately described by the Schiff distribution [11] for a thin converters. Darmstadt group found [8, 9] that the Planck and bremsstrahlung distributions have rather similar shapes in the limits of the narrow high energy region and showed that a superposition of several (6 or more) bremsstrahlung spectra with differing end point energies can reproduce the Planck spectrum over enough high-energy range:

$$cn_\gamma(E,T) \approx \sum_i a_i(T)N_\gamma^{brems}(E_{o,i},E),$$

where N_γ^{brems} represents the bremsstrahlung spectrum with the end point energy E_0 and $a_i(T)$ the strength coefficients adjusting for each temperature T. The experimentally determined bremsstrahlung spectrum photonuclear reaction yield Y is proportional to the integrated product of the $N_\gamma^{brems}(E_{o,i}, E)$ and the reaction cross section $\sigma(E)$:

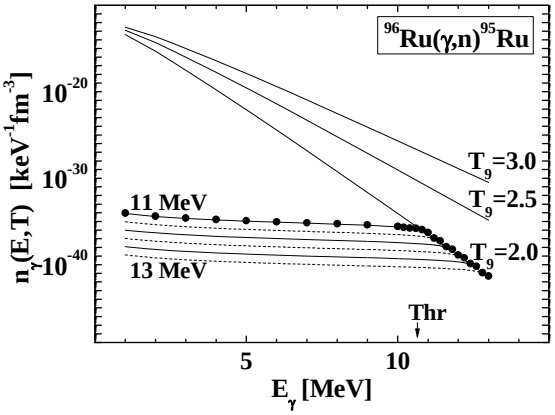

Fig. 3. Thermal Planck spectra at temperatures $T_9 = 2$, $T_9 = 2.5$ and $T_9 = 3$ and simulation of photon spectrum at $T_9 = 2$ by summation of the six bremsstrahlung spectra with the end-point energies between 11 and 13 MeV for ^{96}Ru(γ, n)^{95}Ru reaction.

$$Y \sim \int_{S_n}^{E_0} \sigma(E) N_\gamma^{brems}(E, E_0) dE.$$

Combining the two last equations one can obtain the next expression for the reaction rate instead of Eq. (1):

$$\lambda_{(\gamma,n)}(T) \sim \sum_i a_i(T) \int_{Thr}^{E_0} \sigma(E) N_\gamma^{brems}(E, E_0) dE \propto \sum_i a_i(T) Y_i.$$

Fig. 3 shows the Planck spectra for three temperature values of a star photon bath ($T_9 = 2.0$, 2.5, and 3.0) and simulation of one of them ($T_9 = 2$) from the six Schiff bremsstrahlung spectra in the energy range 13÷11 MeV intended for the ^{96}Ru(γ, n)^{95}Ru reaction analysis. The six lower curves (the alternating solid and dash ones) present the bremsstrahlung spectra for the 13.0, 12.6, 12.2, 11.8 11.4, and 11.0 MeV end-point energies. The sum of these six spectra is given by the dark points. As follows the Planck spectrum in the range from the ^{96}Ru(γ, n)^{95}Ru reaction threshold (Thr = 10.693 MeV) to 13 MeV is reproduced rather well. The large difference between the Planck spectrum and the summary bremsstrahlung one at lower energies does not matter. So to determine the reaction rate the task comes to measurements of the photonuclear reaction yields at 6 or more values of the bremsstrahlung end-point energy.

3. Experimental

Our measurements of the (γ,n)-reaction cross sections on the nuclei of the ^{96}Ru, ^{98}Ru, ^{104}Ru, ^{102}Pd, and ^{110}Pd isotopes were performed by conventional photoactivation technique using high-resolution spectrometry at the two accelerators: the Kharkiv electron linear accelerator and the Uzhgorod microtron capable to accelerate electrons up to the 30 MeV maximum energy. The monoenergetic electron beams of incident energies from the reaction thresholds up to 14 MeV which are best suited for astrophysical interest were stopped in the thin (200 μm) tantalum radiator foils to generate the bremsstrahlug radiation of the Schiff distribution. The Kharkiv irradiation setup contained a collimator made of lead to cut the bremsstrahlung beam hitting to the targets under study. At the Uzhgorod microtron the targets were put at the certain small distance behind the radiator foil with no collimator to get larger photon intensity.

As targets we used the pressed tablets with the 10 mm diameter and masses around 400 mg of metallic powder of ruthenium of natural isotopic composition. Besides we disposed the self-supporting metallic foils of the ^{104}Ru enriched (99.6 %) isotope with the 20 mm diameter and the surface thicknesses around 5 mg/cm^2. In the case of palladium samples the natural and enriched foils of the ^{102}Pd (54 %) and ^{110}Pd (99 %) isotopes were used.

In time of irradiations the ruthenium and palladium targets were sandwiched with the gold foils of the known surface thicknesses (around 15 mg/cm^2) and suitable diameter which were activated in order to determine the absolute photon intensity by measuring the yields of the standard ^{197}Au(γ, n)^{196}Au reaction. The threshold of this reaction is rather low (8.071 MeV), the cross sections are well known in the astrophysically interesting energy region [12, 13], the decay properties of the ^{196}Au nucleus-product are very suitable and known with the high accuracy.

After irradiations during several hours (depending on the half-life of the expected product), the targets were mounted in front of the shielded gamma-detector located in the low-background room to count γ-rays following the decay of the nucleus-product.. The Ge(Li)-detector was used at the Kharkiv measurements and the Ge(Li) and HPGe detectors at the Ughgorod ones. The integral cross sections were derived from the peak intensities of the decay γ-transitions using the conventional activation equation applying a standard reaction.

4. Experimental results and theory predictions

Our measurements pursue the aim to determine the reaction rates of photonuclear (γ,n)-processes on some p-nuclei and their neighbours and to compare them with the theoretical predictions. Most of theoretical calculations of the cross section network of nucleosynthesis interest are relied on the Hauser - Feshbach statistical model [3] the main ingredients of which are optical model potential, nuclear level density and radiation strength functions. The properties of the ground and excited states are also important to be able to calculate the cross sections for excited and exotic nuclei for which the data cannot be derived experimentally. One of the computer codes implementing the statistical model is the NON-SMOKER code of Rauscher [10] with the predictions of which we compare our experimental data.

The results of our measurements are presented in Fig. 4. The left column of panels gives the (γ, n)-reaction yields relative to the standard ^{197}Au(γ, n)^{196}Au reaction yields. The values obtained at the Kharkiv linear accelerator are depicted by the dark circle points while the Uzhgorod data are the dark square points. The data of both accelerators are in a good agreement. The results of Tickner et al [14] of the several end-point bremsstrahlung energies (light points) agree with our ones rather well.

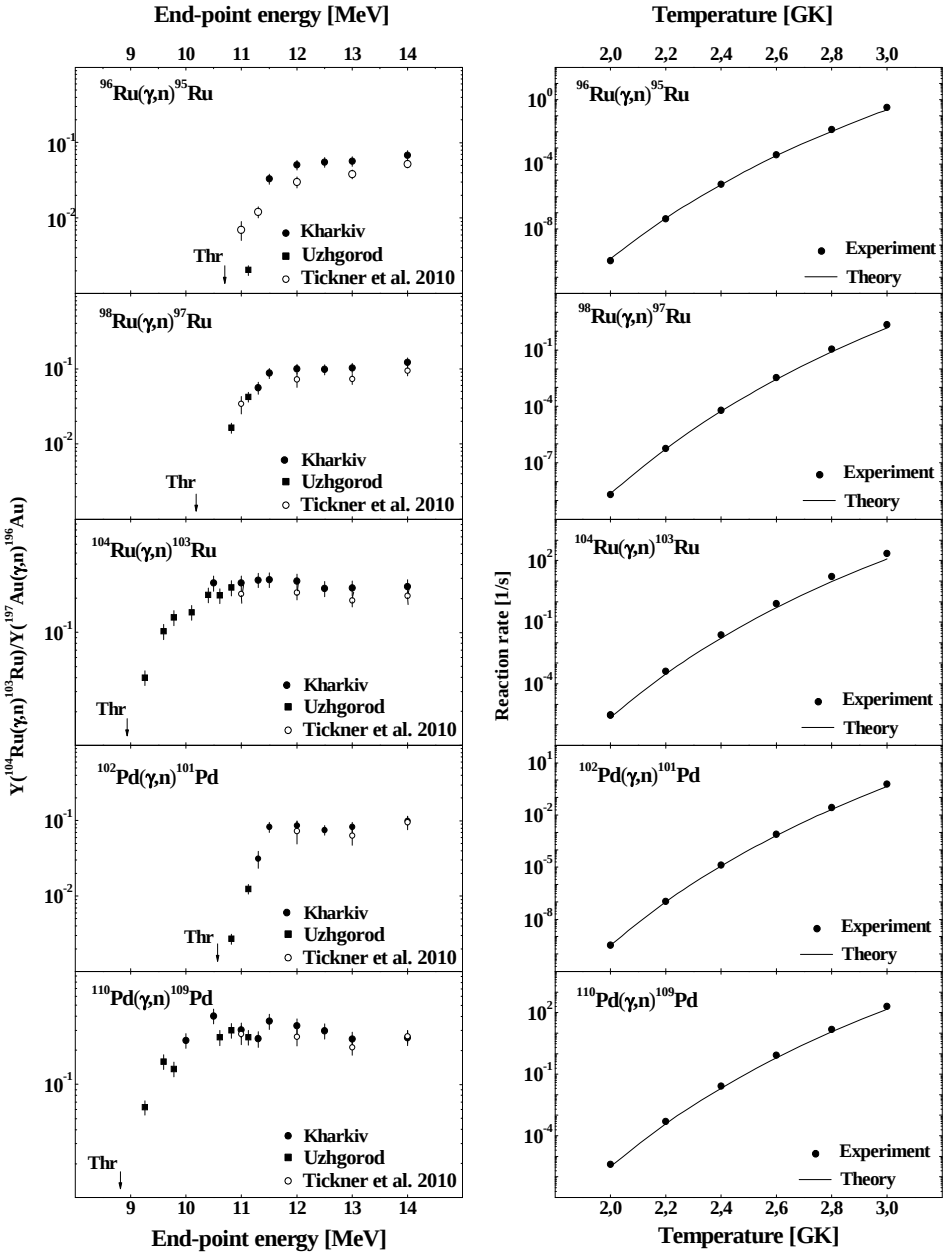

Fig. 4. Yields of (γ, n)-reactions on the ruthenium and palladium isotope nuclei relative to the standard ^{197}Au(γ, n)^{196}Au reaction (*left column*) and reaction rates (*right column*). Points are experimental values, curves are theory predictions.

The right panel column presents the experimental (dark points) and the NON-SMOKER code theoretical reaction rates (curves) of the photonuclear reactions studied. The most of the experimental to theory ratios of the reaction rates lie in the range between 1 and 2 and agree with previously observed systematics for the nuclei in the mass number A = 190÷200 [9, 15].

5. Conclusions and outlook

Several scenarios including γ-process are responsible for a stellar nucleosynthesis of the p-nuclei, a sizeable part of which is located in the nuclear mass region A≈100. In view of a scarce of the corresponding experimental information further activation/decay measurements of the photonuclear reaction cross sections are desirable and can be performed in the near and above threshold region using the bremsstrahlung beams of the Ukraine accelerators. The derived reaction rates can be used as input data for the astrophysical nucleosynthesis simulation and to test the predicting power of the statistical theory of nuclear reactions.

REFERENCES

1. *Burbidge E. M., Burbidge G. R., Fowler W. A., Hoyle F.* Synthesis of the elements in stars // Rev. Mod. Phys. - 1957. - Vol. 29. - P. 547 - 650.
2. *Arnould M., Goriely S.* The p-process of stellar nucleosynthesis: astrophysics and nuclear physics status // Phys. Rep. - 2003. - Vol. 384. - P. 1 - 84.
3. *Hauser W., Feshbach H.* The inelastic scattering of neutrons // Phys. Rev. - 1952. - Vol. 87. - P. 366 - 373.
4. *Skakun Ye.* Launch of proton reaction cross section investigation for astrophysical needs at KIPT // Proc. of the 2-nd Int. Conf. “Current Problems in Nuclear Physics and Atomic Energy” (Kyiv, Ukraine, June 9 - 15, 2008). - Kyiv, 2009. - P. 482 - 488.
5. *Utsunomiya H., Mohr P., Zilges A., Rayet M.* Direct determination of photodisintegration cross sections and the p-process // Nucl. Phys. - 2006. - Vol. A777. - P. 459 - 478.
6. *Nair C. et al.* Photodisintegration studies on p-nuclei: the case of Mo and sm isotopes // J. Phys. (London) - 2008. - Vol. G35. - P. 014036.
7. http://nuclear-astrophysics.fzk.de/kadonis/.
8. *Mohr P. et al.* Experimental simulation of a stellar photon bath by bremsstrahlung: the astrophysical γ-process // Phys. Lett. - 2000. - Vol. B488. - P. 127 - 130.
9. *Vogt K. et al.* Measurement of the (γ, n) reaction rates of the nuclides ^{190}Pt, ^{192}Pt, and ^{198}Pt in the astrophysical γ process // Phys. Rev. - 2001. - Vol. C63. - P. 055802.
10. *Rauscher T., Thielemann F.-K.* Predicted cross-sections for photon-induced particle emission // At. Data Nucl. Data Tables - 2004. - Vol. 88. - P. 1 - 81.
11. *Schiff L.I.* Energy-Angle Distribution of Thin Target Bremsstrahlung // Phys. Rev. - 1951. - Vol. 83. - P. 252 - 253.
12. *Vogt K. et al.* Measurement of the (γ,n) cross section of the nucleus ^{197}Au close above the reaction threshold // Nucl. Phys. - 2002. - Vol. A707. - P. 241 - 252.
13. *Nair C. et al.* Photoactivation experiment on 197Au and its implications for the dipole strength in heavy nuclei. // Phys. Rev. - 2008. - Vol. C78. - P. 055802.
14. *Tickner J. et al.* Measurement of activation yields for platinum group elements using Bremsstrahlung radiation with end-point energies in the range 11 - 14 MeV. // Nucl. Instr. Meth. in Phys. Res. - 2010. - Vol. B268. - P. 99 - 105.
15. *Sonnabend K. et al.* Systematic study of (γ, n) reaction ratesfor $Z \geq 78$ isotopes. // Phys. Rev. - 2004. - Vol. C70. - P. 035802.

STUDY OF NEUTRON CAPTURE BY MEDICAL NUCLIDES AT IRRADIATION FACILITIES OF INR RAS

V. M. Skorkin, S. V. Akulinichev, A. V. Andreev

Institute for Nuclear Research, Russian Academy of Sciences, Moscow, Russia

A thermal neutron absorption by materials containing ^{157}Gd and ^{168}Yb nuclides was studied for use in neutron capture therapy and high-dose brachytherapy. We have used a DT neutron generator NG-400 for irradiation a cell suspension containing liquid-crystal particles consist of deoxyribonucleic acid molecules and gadolinium ions. For a beam current of about 1 mA a fast neutron yield was $1 \cdot 10^{11}$ n/s. The fast neutrons produced the thermal neutrons in a tungsten converter and a polyethylene moderator. The thermal neutron fluence of about $5 \cdot 10^{11}$ n·см$^{-2}$ resulted in full cells killing. A ytterbium oxide with the enriched 1 mg ^{168}Yb was irradiated thermal neutrons at RADEX facility of the proton linac at the energy of 209 MeV and current of 30 μA to create interstitial gamma sources. A photon spectrum of ^{169}Yb was measured with used HPGe detector IGC-45. The contributions from other radionuclides were small. The anisotropy of the source radiation was about 20 %.

1. Introduction

The materials containing ^{157}Gd and ^{168}Yb nuclides are promising for use in neutron capture therapy (NCT) and high-dose brachytherapy. These nuclides have high thermal neutron capture cross section and create nuclides with second radiation at the neutron capture [1, 2].

$^{157}\text{Gd} + n_{\text{th}} \rightarrow \gamma + {}^{158}\text{Gd} \rightarrow$ internal conversion electrons + Auger electrons + X-rays.

$^{168}\text{Yb} + n_{\text{th}} \rightarrow \gamma + {}^{169}\text{Yb}$ (e -capture) $\rightarrow {}^{169}\text{Tm} + \gamma$- rays (average energy 93 keV).

The thermal neutron absorption cross section of ^{157}Gd and ^{168}Yb are 242 000 barns and 11 000 barns respectively.

The liquid-crystal particles containing deoxyribonucleic acid (DNA) molecules and gadolinium ions as a biomaterial can be used for NCT [3]. The particle of DNA-Gd has a size about of 0.5 μm and contains 10^7 nuclides of ^{157}Gd. The conversion electrons (the energy ≥ 30 keV) and X-rays (the energy about of 50 keV) can induce DNA double strand breaks in tumor cell nucleus (Fig. 1). The secondary radiation can cause cancer cells killing in case of ^{157}Gd concentration of 1 mg/g [4]. DNA-Gd particle density should be of 10^3 per cell.

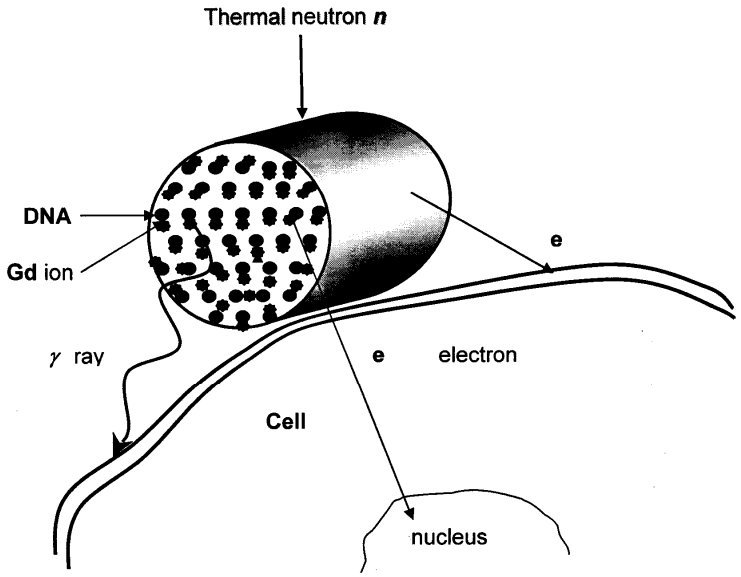

Fig. 1. A thermal neutron capture by DNA-Gd particle creates gamma rays and electrons, which kill neighbor tumor cell.

^{169}Yb interstitial source for the high-dose brachytherapy with half-life of 32 days and energy of photons from 50 to 308 keV can be created at thermal neutrons irradiating ^{168}Yb nuclide [5]. The titanium capsule a diameter of about 1 mm and a length of about 6 mm contains 3 mg of ytterbium oxide with the 20 % enriched ^{168}Yb isotope (Fig. 2).

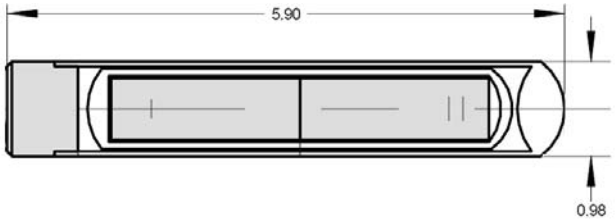

Fig. 2. Configuration of the Ytterbium High Dose Rate Source.

2. Neutron irradiation of DNA-Gd particles

In our experiments with DNA-Gd particles we have used neutron irradiation facilities based on a DT neutron generator NG-400 (Fig. 3). In this generator primary neutrons with the energy about 14 MeV and the total intensity of about $1 \cdot 10^{11}$ n/s are generated in the tritium target, irradiated by the initial deuteron beam with the average current of about 1 mA. Fast neutrons produced the thermal neutrons in a moderator system consisted of a tungsten converter and polyethylene.

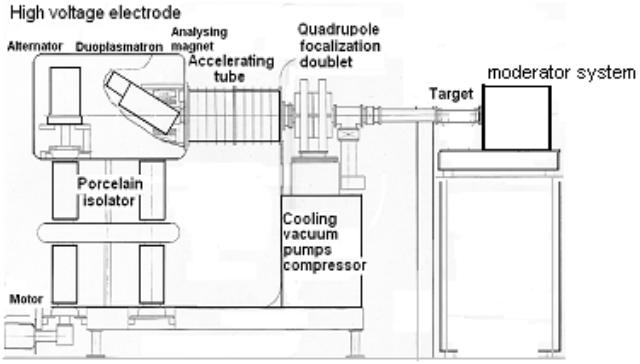

Fig. 3. The neutron generation NG-400.

The biological samples were fixed at the depth of 5 cm in the polyethylene phantom of the size $20 \times 20 \times 20$ cm^3 (Fig. 4).

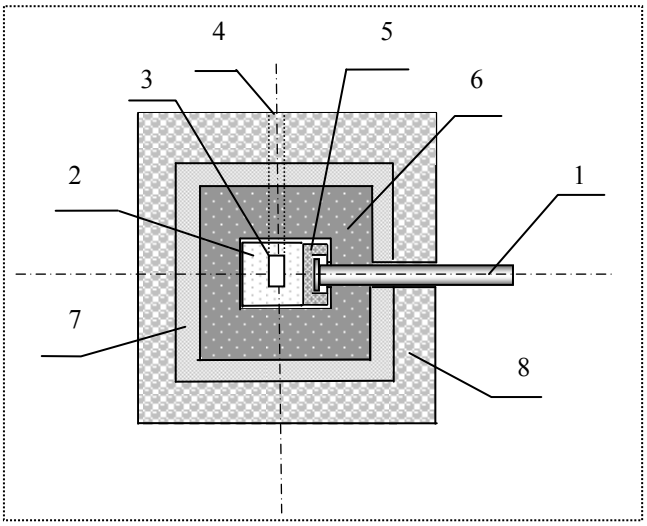

Fig. 4. The moderator system of the neutron generation NG-400. *1* - a target of neutron generator; *2* - polyethylene moderator of a fast neutrons; *3* - a irradiated sample; *4* - inlet to accommodate the samples; *5* - tungsten converter; *6* - a lead reflector; *7* – a protection layer of against gamma radiation; *8* - protection layer of borated polyethylene.

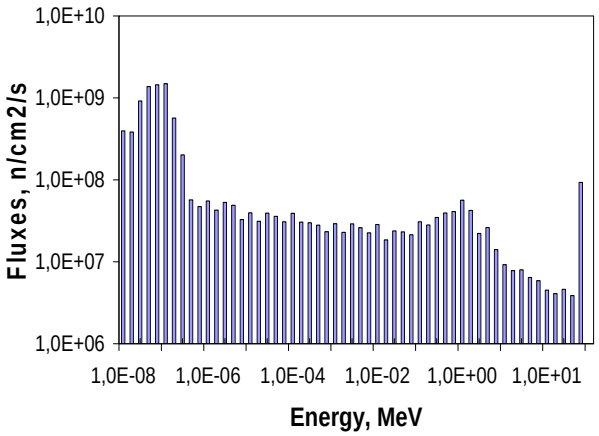

Fig. 5. The neutron spectrum in NG-400 moderator system.

A Monte-Carlo transport program NCNP4B was used to calculate neutron and gamma fluxes in the biological samples (Fig. 5). A certain amount of fast neutrons was still reaching the biological samples The calculated thermal and fast neutron fluxes in the biological samples are $1.4 \cdot 10^8$ см$^{-2} \cdot$ s^{-1} and $3.5 \cdot 10^7$ см$^{-2} \cdot$s^{-1} correspondingly. Biological samples containing 100 mg of a cell suspension and 2 mg of DNA-Gd particles was irradiated into the moderator system at NG-400 In order to extract the net biological effect of the thermal neutron capture in DNA-Gd particles, we have identically irradiated two sets of biological samples: one with DNA-Gd particles containing gadolinium and another one without it. The radiobiological effect produced by fast neutrons must be identical in both cases since fast neutrons have no specific interaction with gadolinium. The difference in the tumor cell killing efficacy for two sets of samples might be due to the thermal neutron capture by DNA-Gd particles only.

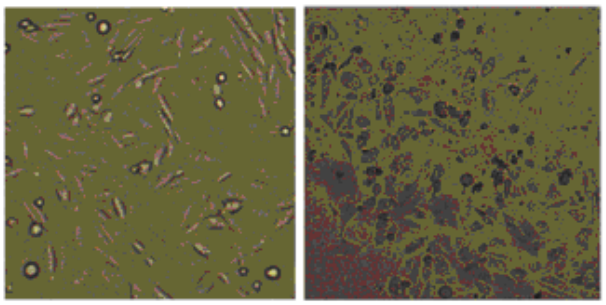

Fig. 6. The images of cells layers taken after neutron irradiation. *1* - the image with thermal neutron irradiation without gadolinium carrier; *2* – the image after 1 hour of the thermal neutron irradiation with gadolinium carrier.

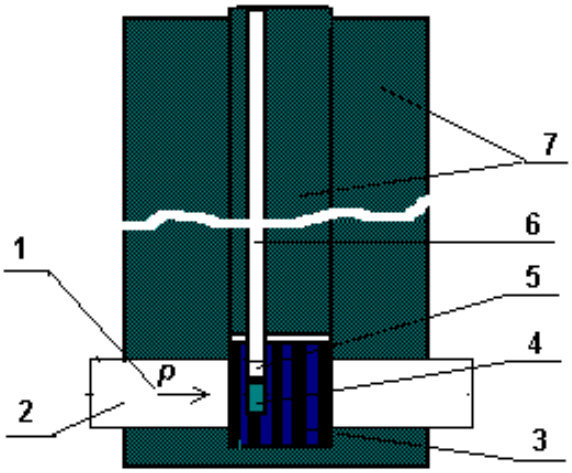

Fig. 7. RADEX irradiation facility *1* - proton beam; *2* - vacuum channel; *3* - tungsten target; *4* - irradiated channel; *5* - moderater with ytterbium capsule; *6* - vertical channel; *7* - iron shield.

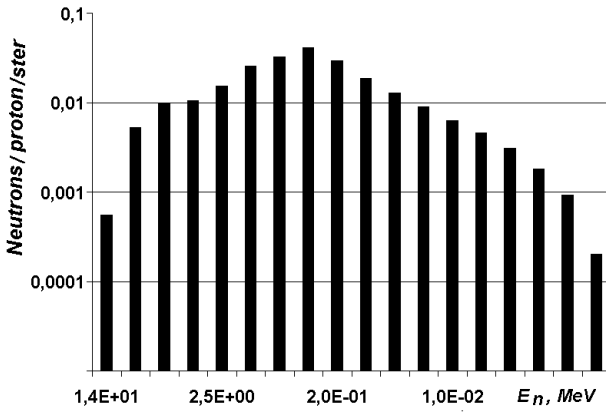

Fig. 8. The spectrum of the evaporation neutrons from W target of RADEX.

The thermal and fast neutron fluxes for each biological sample were measured by means of a neutron activation analysis. The irradiation time was about 1 hour and the thermal neutron fluence was of the order of $5 \cdot 10^{11}$ n·cm^{-2}. In the experiment under consideration the fast neutron flux was estimated as $(1 - 3) \cdot 10^7$ n · cm^{-2} · s^{-1}. The experiment thermal neutron flux in the same experiment was $1.5 \cdot 10^8$ n · cm^{-2}·s^{-1}. The irradiation of the cell material in presence of radiation from DNA-Gd particles results in full cells killing and absence of live cells (Fig. 6).

3. Study of ^{169}Yb interstitial source

Ytterbium sources are produced by irradiation of the starting material with the isotope ^{168}Yb thermal neutrons in a nuclear reactor. This method is costly. Moreover, the presence fast neutron component (over 10 %) of a fission spectrum leads to activation of the titanium shell in the reaction ^{46}Ti (n, p) ^{46}Sc. The resulting radioactive ^{46}Sc isotope has long half-life (83.3 days) and a high energy photon (889 keV and 1120 keV). This increases the radiation burden on staff and patients. In our investigation the titanium capsule with ^{168}Yb nuclide was activated at RADEX facilities at a proton energy of 209 MeV and a current of 30 μA. The irradiation facility RADEX at the beam-stop is placed on the direct card track of the proton beam (Fig. 7). The RADEX irradiation facility has vacuum proton channel (Ø 20 cm), tungsten target (Ø 30 cm) and vertical channel (Ø 7 cm) and irradiated channel (Ø 6 cm) (Fig. 7).

The tungsten target is placed 4 m beneath the surface of the beam-stopper. The secondary spallation neutrons are produced when hydrogen ions interact with the target nuclei of tungsten.

The spallation reactions result in the yielding of $3 \cdot 10^{14}$ n/s fast neutrons from the target (Fig. 8).

The irradiated channel is placed into the tungsten target. The neutron flux level available in the irradiation channel is up to 10^{12} n · cm^{-2}s^{-1}. A polyethylene moderator contained ytterbium capsule is placed into the irradiation channel of RADEX facility. The thermal neutron flux in the moderator is about of 10^{10} n · cm^{-2}s^{-1}.

After irradiation ytterbium capsule during 5 days up to 0.3 mCi was measured ^{169}Yb source photon spectrum using the gamma-spectrometers based on the 200 cm^3 coaxial HPGe detector IGC-45 (ORTEC). This detector had a energy resolution of 2.2 keV and a relative efficiency of 45.5 % at 1.33MeV. On the spectrum are clearly visible emission lines of the main radionuclide ^{169}Yb (Fig. 9).

The contributions from other radionuclides are small (Table).

From the analysis of instrumental gamma-ray spectrum of the test sample that the spectrum contains peaks at energy of 283 keV and 396.32 keV from radionuclide ^{175}Yb. The ratio of the peak areas of ^{169}Yb (307.8 keV) and ^{175}Yb (283 keV + 396.32 keV) is about of 26.

The spatial distribution of the absorbed dose of ^{169}Yb source radiation was measured in a water equivalent phantom using MD-55 film (Fig. 10).

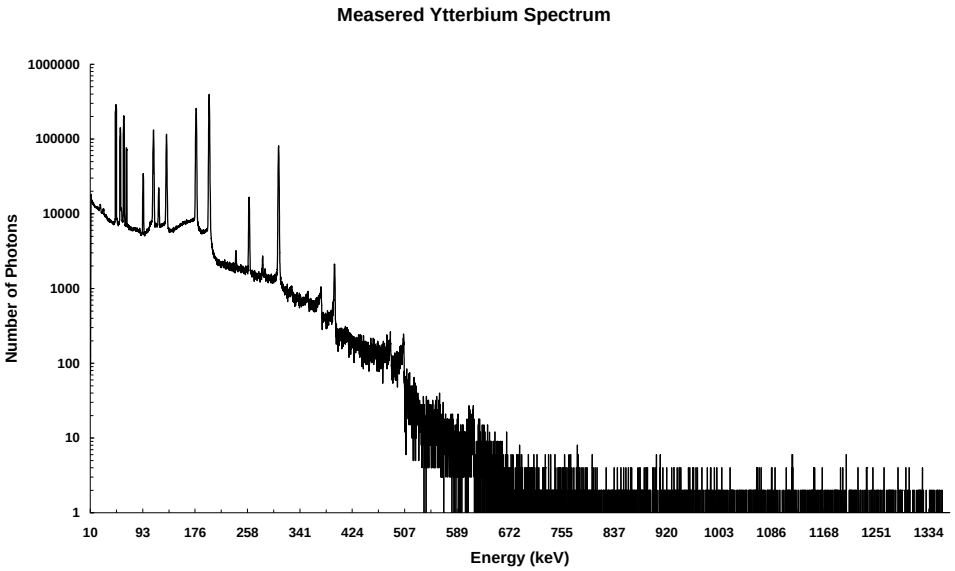

Fig. 9. Measured ^{169}Yb source photon spectrum using a HPGe detector IGC-45 (ORTEC).

The most significant photon energies, emission probabilities of ^{169}Yb source

^{169}Yb (John J. Munro. Implant Sciences Corp.**)**		**^{169}Yb (**RADEX**)** (^{175}Yb)	
E_γ, keV	n_i (γ/decay)	E_γ, keV	Intensity, s^{-1} (%)
50.74	93.4	50.6	1066500
57.50	38.3	57,5	1084056
63.11	43.7	63.1	1119660
93.61	2.7	93.6	154770
109.78	17.4	109.8	863880
118.19	1.9	118.2	86116
130.52	11.1	130.5	633616
177.21	21.4	177.2	1476136
197.95	34.9	197.9	2624414
261.07	1.8	261.1	128079
		283 (^{175}Yb)	8316 (3.7 %)
307.73	10.8	307.7	737316
		396 (^{175}Yb)	20384 (6.0 %)

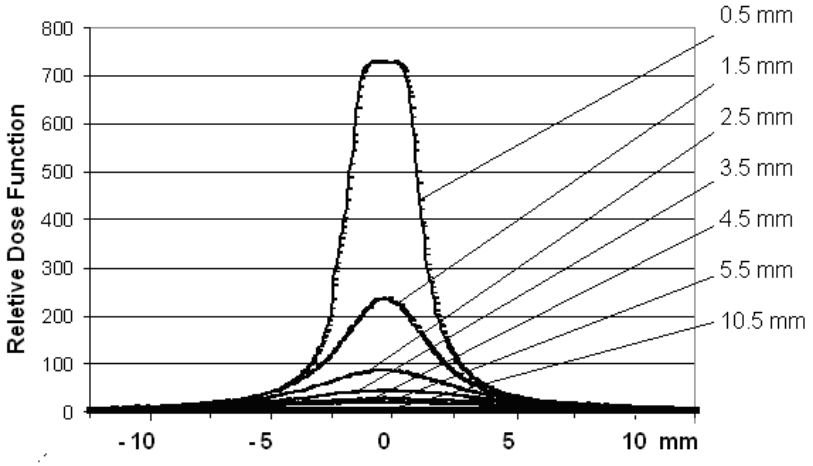

Fig. 10. A distribution of the absorbed dose of ^{169}Yb source radiation.

The measured anisotropy of the source radiation is about 20 %.

REFERENCES

1. *Greenwood R. C., Reich C. W., Baader H. A. et al*. Collective and two-quasiparticle states in ^{158}Gd observed though study of radiative neutron capture in ^{157}Gd // Nucl. Phys. - 1978. - Vol. A304. - P. 327 - 428.
2. *Piermattei A., Azario L., Montemaggi P.* Implantation guidelines for ^{169}Yb seed interstitial treatments // Phys. Med. Biol. - 1995.- Vol. 40. - P. 1331 - 1338.
3. *Yevdokimov Yu. M., Salyanov V. I., Kondrashina O. V. et al*. Particles of liquid-crystalline dispersions formed by (nucleic acid-rare earth element) complexes as a potential platform for neutron capture therapy // Int. J. Biol. Macromol. - 2005. - Vol. 370. - P. 165 - 173.
4. *Goorley T., Zamenhof R., Nikjoo H.* Calculated DNA Damage from Gadolinium Auger Eletrons and Relation to Dose Distributions in a Head Phantom // Int. J. Radiat. Biol. - 2004. - Vol. 80. - P. 933 - 940**.**
5. *David C. M., Mark A. T., John J. M. et al*. Monte Carlo characterization of an ytterbium-169 high dose rate brachytherapy source with analysis of statistical uncertainty // Med. Phys. - 2007. - Vol. 34. - P. 3614 - 3619.

APPROACH TO GAMMA SPECTRUM ANALYSIS WHEN ENERGY CALIBRATION IS UNKNOWN

A. M. Sokolov

Institute for Nuclear Research, National Academy of Sciences of Ukraine, Kyiv, Ukraine

In this paper an approach to gamma spectrum analysis for the purpose of determining the activity concentrations of nuclides in natural samples is presented. In proposed method procedure of energy calibration for spectrometer is not needed. Approach may by especially convenient for portable and mobile spectrometer at measuring in the field.

1. Introduction

If a gamma spectrometer is used to determine the quantity of gamma emitters present in the source the measured spectrum usually described as a sum of spectra of the gamma-emitting nuclides contained in the source [1]:

$$Sp_j = \sum_{i=0}^{N} c_i \cdot sp_j^{(i)}\,, \tag{1}$$

where Sp_j - the spectrum, represented by the number of counts $Sp(j)$ in the j-th channel of a spectrometerж c_i – the coefficients to be determined; $sp_j^{(i)}$ – particular components (e.g. the spectra of specific nuclides); j – channel number; i – particular component number.

However usually at measuring components and spectrum a background is present. Therefore instead of components we have spectra of type $sp_j^{(i)} + Fon1_j$ and instead of spectrum measuring gives $Sp_j + Fon2_j$. To take that *Fon1* and *Fon2* into account, they are measured separately (*Fon1* in the same conditions with components, and *Fon2* in one conditions with the first spectrum in the series of measuring). In addition, if the series of spectra are measured, then the conditions of these measuring can vary. That is reflected in a change of energy calibration for the channels of spectrometer. Thus a spectrum is shifted and stretched (or compressed) with respect to the spectra of radiation of components, measured at other energy calibration. For scintillation detectors such effect is related to sensibility of their characteristics on a temperature variation [2].

For correctness of equation (1) it is necessary to bring results of measuring of spectrum and separate components to one system of channels with identical calibration on energy. For this purpose usually energy calibration is provided for a spectrum and for separate components. Such procedure can require additional measuring with the use of gauge standard sources.

2. Spectrum analysis without energy calibration

The worked out method and program does not require information of calibrations on energy, and suppose only, that calibrations for components and for background *Fon1* are identical, calibration for *Fon2* and for first in the series of spectra is the same, and for subsequent spectra can be different. It is assumed also, that relationship between energy and channel number for spectrum and for components, which we denote as $E = Fs(k)$ and $E = Fc(k)$, satisfy the condition: $Fc(k) = Fs(a \cdot k + b)$. A special case of this situation - the linear calibration on the energy $E = as \cdot k2 + bs$ for the spectrum and $E = ac \cdot k1 + bc$ for the components. In this case, for parameters $a = ac$ /as and $b = (bc - bs)$ /*as* the condition $Fc\ (k1) = Fs\ (a \cdot k1 + b)$ is satisfied. The program that implements the method works with the relative calibration $k2 = a \cdot k1 + b$, which establishes a relation between the channels corresponding to the same energy.

The program does not use the explicit form of functions $Fs(k)$ and $Fc(k)$ and finds itself the coefficients a and b. A task in a form (1) will be transformed in a task for minimum

$$\min_{a,b}\left(\min_{c_i}\left\|\sum_{i=0}^{N} c_i \cdot sp_j^{(i)} - Sp^*_{a\cdot j+b}\right\|^2\right), \tag{2}$$

which is solved in two stages (linear for c_i and nonlinear for a and b). At that a spectrum Sp^* in (2) is obtained from the spectrum Sp by special procedure "of pouring", similar to that described in [3].

The spectrum is transformed from one system of channels onto a system of channels that correspond to the relative calibration with the parameters a and b. Fig. 1 shows the spectrum in the original form (solid line) and the spectrum, converted in accordance with the change of variable with parameters a and b, that were founded at solution of the problem (2) (dotted line).

Later the activities of particular nuclides in the sample can be obtained on the basis of the found coefficients c_i, on known activity of gauge sources and taking into account time of measuring of separate components and spectrum.

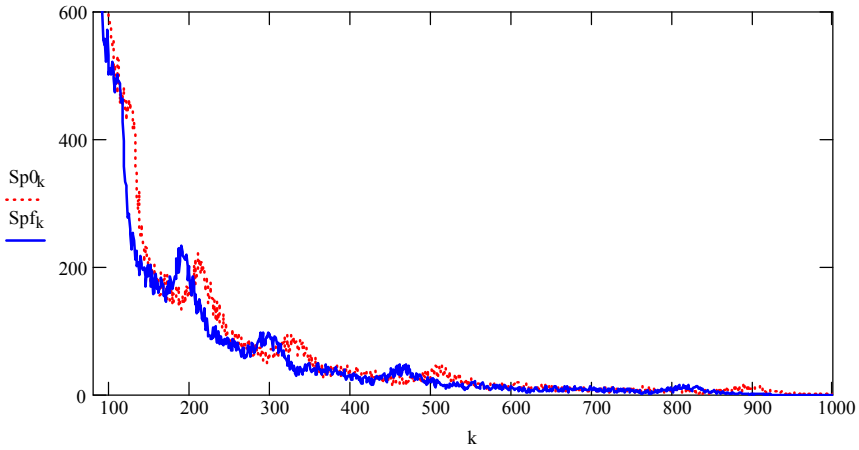

Fig. 1. The original spectrum (solid line) and the spectrum, converted in accordance with the change of variable with parameters *a* and *b*, that were founded at solution of the problem (2) (dotted line).

For the transformed spectrum the task (1) is solved by traditional least squares method [4]. Typical result is shown in Fig. 2.

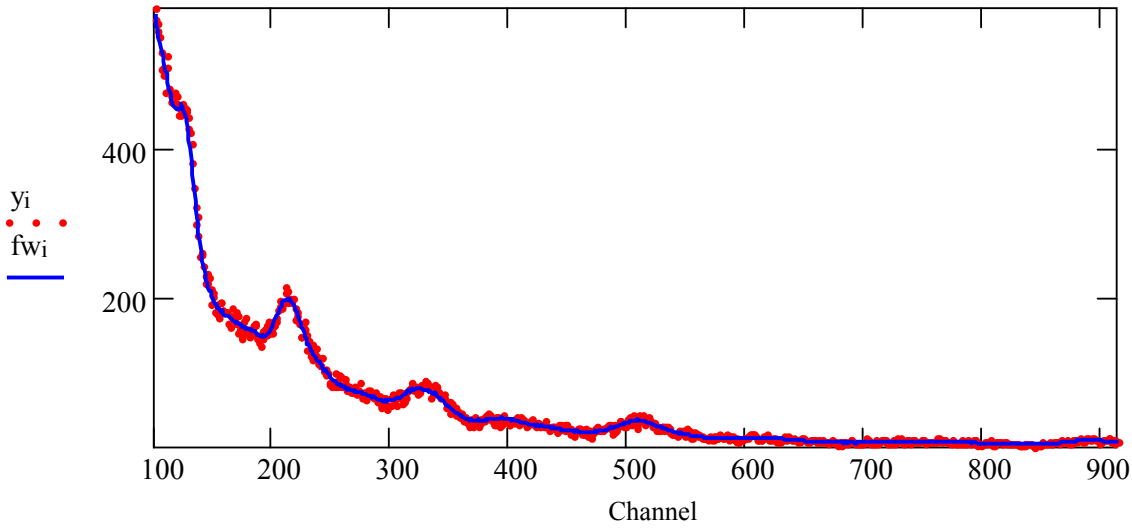

Fig. 2. The converted spectrum (dotted line) and it's approximation by linear model (solid line).

3. Organization of work when series of spectra are processing

Processing of the first spectrum in the series and subsequent spectra is different in the background *Fon2* subtraction. Direct subtraction can be made, if the spectrum and the background measured at the same energy calibration, or if they are transformed into a system of channels that corresponds to the same gauge. For the first spectrum in series and for background *Fon2* the measurements are executed with the same energy calibration and so the subtraction can be performed. For the next spectrum in series the calibration of energy can vary. So for the first spectrum we, at first, make a subtraction $(Sp_j + Fon2_j) - Fon2_j$, and then for the "refined" spectrum we solve the problem (2). In particular, will the values of parameters *a* and *b*, knowing that we will translate *Fon2* in channels corresponding calibration energy component. We denote the result as *Fon2**. When processing next spectra of a series background subtraction from the spectrum can be carried out in the framework of task (2) that will slightly change to:

$$\min_{a,b}\left(\min_{c_i}\left\|\sum_{i=0}^{N} c_i \cdot sp_j^{(i)} - ((Sp + Fon2)^*_{a\cdot j+b} - Fon2^*_j)\right\|^2\right)$$

Eventually, estimation of interested activity of individual components in the sample is obtained by the found coefficients ci, according to the activity of standard sources and by the time of measuring of the individual components and the spectrum (viz, Ai = ci · ai · Ti / Ts).

4. Conclusions

Proposed method for the spectrum analysis does not require calibration on energy of the spectrometer. Necessary harmonization of the measured spectra and the standard sources is achieved by transforming the spectrum on the scale of channels on which the spectra of the individual components have been measured. For this purpose the relative calibration $k2 = a \cdot k1 + b$, determined by the parameters a and b, is used. To find them, we have to solve the problem (2) and (3). That increases the amount of computation in comparison with the traditional approach, but for modern computers it is not a problem. Processing time per spectrum in typical conditions (2048 channels, 4-6 components in the spectrum) is usually less than 1 second. Method is stably applicable for parameter a in range of (0.5 ÷ 2.). Program also contains a stage of statistical analysis of the results, according to well known rules [5]. During statistical analysis the estimation of accuracy of obtained activities is performed. This takes into account the statistical error in data (in the spectrum), the error of the method and the uncertainty in the values of the activity of the gauge sources. The program checks also are the set of components enough for description of spectrum and whether all components significantly deviate from zero.

The method would be especially useful for portable spectrometers [6], for which the calibration on energy 'in situ' is burdensome.

ACKNOWLEDGEMENTS

The author is grateful to E. E. Petrosian and V. D. Balakin for the discussions of the problem.

REFERENCES

1. *Hendriks P.H.G.M., Limburg J., De Meijer R.J.* Full-spectrum analysis of natural g-ray spectra. Journal of Environmental Radioactivity. - 2001. - Vol. 53. - P. 365 - 380.
2. *Кочергин А.В., Мороз Н.Г., Плахотник Ю.В.* Автоматическая стабилизация энергетической шкалы спектрометрического тракта гамма сканера кругового обзора с кодирующей маской //Вісн. Донецького Нац. ун-ну. Сер. А: Природничі науки. - 2011. - № 1. - С. 67 - 71.
3. *Третяк В.И.* TS2 - диалоговая система обработки одномерных спектров. - К., 1990. - 23 с. - (Препр. / АН УССР. Инт- ядерных исслед.; КИЯИ-90-35).
4. *Соколов А.М.* POMNK - программа приближения экспериментальных данных линейной комбинацией функций. - К., 1985. - 40 с. - (Препр. / АН УССР. Ин-т ядерных исслед.; КИЯИ-85-32).
5. *Худсон Д.* Статистика для физиков. - М.; Мир, 1970. - 296 с.
6. *Бесшейко О.А., Вишневский И.Н., Денисенко Р.В. и др.* Портативный сцинтилляционный гамма-спектрометр для измерения радиоактивности объемных сред в полевых условиях // Ядерна фізика та енергетика. - 2011. - Т. 12, № 4. - С. 400 - 406.

NEUTRON DETECTOR ARRAY FOR REACTIONS AROUND COULOMB BARRIER

P. Sugathan[1], J. Antony[1], K. S. Golda[1], A. Jhingan[1], Rajesh Kumar[1], V. V. Satyanarayana[1], R. P. Singh[1], S. K. Suman[1], T. Varughese[1], S. Venkataramanan[1], R. K. Bhowmik[2]

[1] Inter University Accelerator Centre, Aruna Asaf Ali Rd, New Delhi, India
[2] Guru Ghasidas University, Koni, Bilaspur, Chhattisgarh, India

A large neutron detector array being built for the study of fusion-fission dynamics is described. The array consists of 100 liquid scintillators mounted on a nearly semi spherical geometry. Each scintillator coupled to Hamamatsu R4144 photo multiplier tube is readout using custom designed electronic circuits. Homemade integrated electronics module performs the n-γ separation by zero-cross timing and time of flight method. Compact remote controlled high voltage power supply built from DC-DC converters are used to operate the detector. The neutrons are detected in coincidence with fission fragments using multi wire proportional chambers. The performance tests of n-γ discrimination using ^{252}Cf neutron source showed excellent discrimination at the energy threshold of 110 keV recoil electron energy.

1. Introduction

The study of heavy ion induced fusion-fission dynamics is a topic of considerable research interest, both experimentally and theoretically. The recent experimental observations suggest that many reaction mechanisms are possible in heavy ion induced fission near and above the Coulomb barrier energies. It has been shown that, the now well established reaction process such as fusion-fission and quasi-fission exhibit their own characteristics reaction times that can be probed by measuring pre-scission neutron and charged particle multiplicities [1 - 3]. The pre-scission neutron multiplicity has a strong correlation with the evolution of the composite system in the nuclear deformation space [4]. Over the years, the measurement of pre-scission and post-scission neutron multiplicity in coincidence with fission fragment has been used as a powerful tool to study the dynamics of the fissioning system and a large number of such experiments have been performed [5 - 9].

At Inter University Accelerator Centre (IUAC, formerly known as Nuclear Science Centre), New Delhi, heavy ion beams from the Pelletron tandem and LINAC accelerators are used for nuclear reaction studies around the Coulomb barrier energies. Using DC and pulsed beams, we have performed a number of experiments probing the fusion-fission dynamics in our scattering chamber and neutron array facility [10 - 13]. The scattering chamber facility consists of a 1.5 m diameter vacuum chamber and a time of flight (TOF) spectrometer for fission fragment angular distribution and mass measurements. The neutron detector array consists of 24 liquid scintillators (at a flight distance of 2 m from target) and a pair of multi-wire proportional counters (MWPC) for fission-fragment detection. These facilities are being used for experiments measuring the fission fragment mass distribution, angular distribution and extraction of pre and post scission neutron multiplicities. To distinguish the time scale of different dynamical process in fission, it is also necessary to experimentally extract the correlation between the pre- and post scission multiplicities and their evolutions with the parent nucleus excitation energy. For these types of experiments, a bigger neutron detector array is required to make any measurement of multiplicity distributions in coincidence with fission fragments. Already, one such detector array DEtecteur MOdulaire de Neutron (DEMON) in France and Belgium [14], has been used for similar studies. To enhance further studies in this field, we had proposed to build a new detector array of 100 detectors and got the approval and financial support from the Department of Science and technology, Govt. of India. The new detector array will use the TOF technique for the determination of neutron energy and the pulse shape discrimination (PSD) technique to discriminate the neutrons from gamma rays. This detector array would be a national facility being built as a collaboration of IUAC and other participating universities within the country.

2. Large Neutron detector array at IUAC

The upcoming new facility will have 100 individual neutron detectors installed in a fixed radius semi sphere configuration. The detectors are made of 5” × 5” organic liquid scintillator cell BC501A coupled to 5” photo multiplier tube (PMT). They will be mounted on a metallic geodesic dome structure at a radial distance of 1.75 m from the target. A one meter diameter spherical vacuum chamber will be installed to house the targets and the fission fragment detectors. The center of the target chamber is located at 1.4 m above the ground level and all the neutron detectors are mounted on eight rings on the geo-dome structure, the lowest ring being 15^{o} below the target plane. The total solid angle coverage of the neutron detector array in this geometry is ~3.3 % of 4π. The first phase of the project will have 50 neutron detectors operational and the remaining 50 detectors will be installed on later stage. The BC501A liquid scintillators have the best pulse shape discrimination properties giving good n-γ discrimination. Though the detectors in our existing setup used Philips XP4512B PMTs, their unavailability led us to choose Hamamatsu R4144 PMT for all new detectors. According to the manufacturer this tube has good timing characteristics and from the comparative study made by Moszynski et.al [15], it was found to be the second best recommended tube for liquid scintillators. To process signals from detectors, we have planned to use standard analog NIM electronics and data readout using CAMAC/VME data acquisition system. For this purpose, custom made electronics have been built and tested using detector signals. Later stage, we may upgrade the electronics using digital processing techniques.

3. Instrumentation for Neutron detector array

From each detector cell, the light output, pulse shape discrimination and time of flight are recorded using standard NIM electronics. The anode signal from PMT is used for timing as well as pulse shape discrimination whereas the dynode signal is used for energy (light output) information. A custom made PSD module [16] has been used for the signal readout. This module contains the integrated electronics for n-γ discrimination, time of flight and energy. It is a single width NIM module having two independent channels that can accept signals from two detectors. For each detector, the anode and dynode (through a charge sensitive pre amplifier) signals are fed to the inputs of the PSD module which process them and provide energy, constant fraction timing and a time to amplitude signal corresponding to zero-crossing time distribution for n -γ separation at its outputs. Other logic signals and monitoring signals are also provided on its front panel. Total 50 channels of PSD modules have been fabricated and tested for its performance.

In our experimental setup, the PMTs are normally operated below -2000 volt. To apply the high voltages, we plan to use home made voltage divider bases, which contains the high voltage resistive divider circuit compatible to R4144 tube. The base also contains an integrated charge sensitive pre-amplifier for dynode signals. To take care of the large number of high voltage channels required for the full array, custom made compact high voltage power supply has been made at IUAC. The high voltage (0 - 2000 V) is generated using commercial DC-DC high voltage converter chip (PICO make) mounted on a control board that can be controlled over a private Local Area Network. The digital section of this board consists of a microprocessor and an Ethernet controller where as the analogue section contains one 12-bit digital to analog converter. Each board has its own unique MAC and IP address so that each can be specifically selected at a time for read & write operations. A 24 channel power supply system, each channel having the compact DC-DC converter has been assembled in a 2U box (19" rack mount) and tested successfully by biasing the detectors. A network of 120 such boards has been planned for the final phase of detector array. A graphical user interface developed in Qt framework is used to control the high voltages over the network.

The fission fragments are detected in low-pressure position sensitive multi wire proportional counters mounted inside the spherical vacuum chamber. Two MWPCs are mounted at folding angles so that the complimentary fission fragments are detected in coincidence. The MWPC has three electrodes, having a central cathode foil electrode sandwiched between two wire/strip frames. The cathode frame is made of double-sided aluminized Mylar foil (thickness of 2 micron). The horizontal position (X) sensing wire frame is made of 10 micron thick gold plated tungsten wires stretched (pitch of 0.63 mm) on a printed circuit board (PCB). The vertical position (Y) sensing electrode is made of 2.5 mm strip on a PCB. The position information is derived using delay lines chips. The electrodes are enclosed in vacuum tight rectangular aluminum chamber having thin Mylar foil entrance window (of active area 126 mm × 75 mm). The detector was operated with iso-butane gas. The detectors mounted at a distance of 25 cm from the target spans an angular coverage of $\pm 14^{o}$ in the horizontal(X) plane and $\pm 8^{o}$ in the vertical(Y) plane respectively. Fast rise time about 3 ns and a position resolution about ~1 mm has been observed in beam experiments on-line. To increase the efficiency further, an array of four MWPC will be used in future to cover a large solid angle for fission detection.

4. Performance tests

All the 50 detectors for the first phase have been tested for its performance characteristics using standard gamma ray as well as neutron sources. The n-γ discrimination test was carried out with home made PSD electronics and compared with commercial electronics. Though the detectors and PMTs are all identical, the operating voltage varied slightly among detectors. Nominal operating voltage on each detector was determined by keeping the anode signal amplitude for ^{137}Cs gamma rays around 450 mV for best timing & zero-cross separation. The light output (the dynode signal) from the detector was calibrated using the Compton edges of gamma rays from ^{22}Na, ^{137}Cs and ^{60}Co. All the signals were digitized and collected event by event using conventional analog to digital converters and time to digital converters on a CAMAC based data acquisition system. A typical energy (light output) spectrum for gamma ray from ^{137}Cs source is shown in Fig. 1.

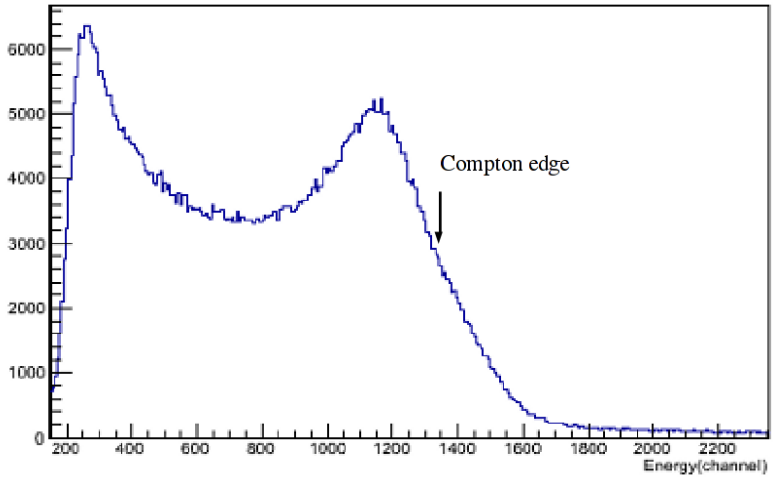

Fig. 1. Light output corresponding to 662 keV gamma rays from ^{137}Cs source.

The performance of the n-γ separation was tested thoroughly using home made as well as commercial PSD electronics. Fig. 2 shows the two dimensional histogram showing zero cross time distribution plotted against the energy output for one detector using neutrons and gamma radiations from 252 Cf source. Distinct separation between neutron and gamma events from the source is clearly visible illustrating the performance of the pulse shape discrimination of the setup. A one dimensional histogram showing the n-γ discrimination corresponding to the energy threshold of 110 keV recoil electron energy is shown in Fig. 3. The PSD performance at a given energy threshold is quantified by using a figure of merit (FOM), defined as the ratio of peak separation to the sum of full width at half maximum (FWHM) of the peaks. The typical FOM for the detector and electronics combinations is found to be 1.62 at 110keV recoil electron energy.

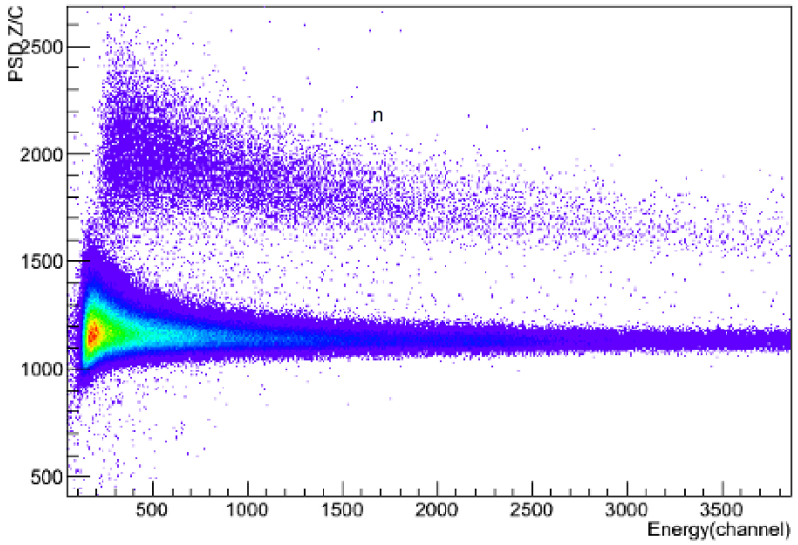

Fig. 2. Zero cross time distribution versus energy for neutrons and gamma rays from ^{252}Cf source.

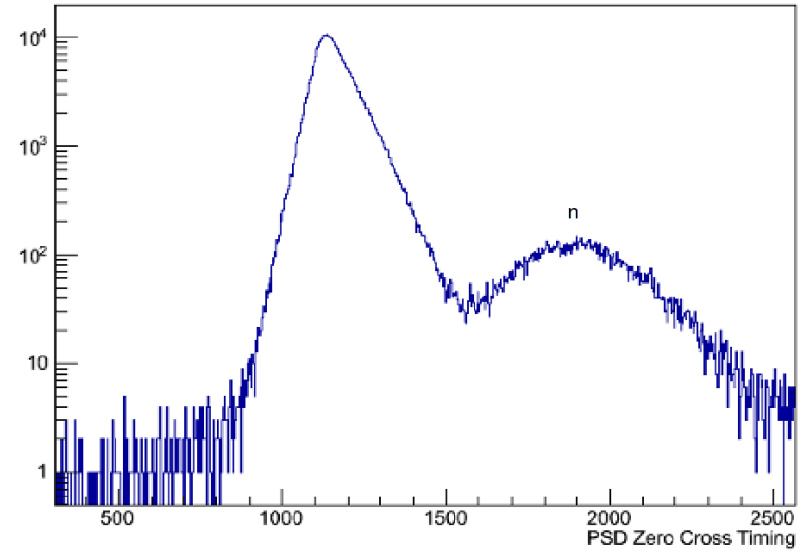

Fig. 3. Neutron-γ discrimination at the energy threshold of 110 keV recoil electron energy.

5. Summary

The new facility for studying fusion fission reaction dynamics using 100 neutron detectors and multi wire proportional counters for fission fragment detection is being setup at IUAC. All the 50 detectors for the first phase have been tested for its performance using standard radioactive sources. The n-γ discrimination tests using custom made pulse shape discrimination module showed good separation of neutron events with a figure of merit of 1.62 at the detection threshold of 110 keV recoil electron energy. Multi channel high voltage power supply system with remote control over the Ethernet has been fabricated using compact DC-DC converters.

ACKNOWLEDGMENTS

We acknowledge the Department of Science and Technology, Govt. of India for supporting this project under the grant no IR/S2/PF-02/2007. We are grateful to Prof Mihir Chatterjee, SINP for providing us neutron detectors for the initial setup. The support and help received from other investigators and collaborators are acknowledged. We thank Dr. Roy for his constant encouragement and continuous support.

REFERENCES

1. *Hilscher D., Rossner H.* Dynamics of nuclear fission // Ann. Phys. Ft. - 1992. - Vol. 17. - P. 471.
2. *Hinde D.J. et al.* Neutron emission as a probe of fusion-fission and quasi-fission dynamics // Phys. Rev. - 1992. - Vol. C45. - P. 1229 - 1259.
3. *Toke J. et al.* Quasi fission- The mass drift mode in the heavy ion reactions // Nucl. Phys. - 1985. - Vol. A440. - P.327 -365
4. *Aritomo Y., Ohta M., Materna T. et al.* Analysis of fusion-fission dynamics in super heavy mass region by pre-scission neutron multiplicities // Nucl. Phys. - 2004. - Vol. A738. - P. 221 - 225.
5. *Rossner H. et al*. Analysis of pre- and post-scission neutrons emitted in the reaction ^{169}Tm(^{36}Ar,f) at E_{lab} = 205 MeV // Phys. Rev. - 1989. - Vol. C40. - P. 2629 - 2640.
6. *Saxena A. et al*. Entrance channel effects in the fusion-fission time scales from studies of pre-scission neutron multiplicities // Phys. Rev. - 1994. - Vol. C49. - P. 932 - 940.
7. *Hilscher D. et al*. Observation of cold scission of highly excited fissioning nuclei // Phys. Rev. Lett. - 1989. - Vol. 62. - P. 1099 - 1102.
8. *Cabrera J. et al.* Fusion-fission and fusion-evaporation processes in ^{20}Ne + ^{159}Tb and ^{20}Ne + ^{169}Tm interactions between E/A = 8 and 16 MeV // Phys. Rev. - 2003. - Vol. C68. - P. 034613.
9. *Lestone J. P*. Determination of the time evolution of fission from particle emission // Phys. Rev. Lett. - 1993. - Vol. 70. - P. 2245 - 2248.
10. *Golda K. S. et al.* National Array of Neutron Detectors (NAND) - a versatile setup for studies on reaction dynamics // Proc. of the DAE symposium on Nuclear Physics / Ed. by S. Kailas et al. - 2006. - Vol. 51. - P. 626.
11. *Hardev Singh et al*. Measurement of neutron multiplicity from fission of ^{228}U and nuclear dissipation // Phys. Rev. - 2009. - Vol. C80. - P. 064615
12. *Varinderjit Singh et al*. Search for an effect of shell closure on nuclear dissipation via a neutron-multiplicity measurement // Phys. Rev. - 2012. - Vol. C86. - P. 014609
13. *Banerjee K. et al*. Evidence of quasi fission in the ^{16}O+^{238}U reaction at sub-barrier energies// Phys. Rev. - 2011. - Vol. C83. - P. 024605.
14. *Tilquin I. et al*. Detection efficiency of the neutron modular detector DEMON and related characteristics // Nucl. Instr. Meth. - 1995. - Vol. A365. - P. 446 - 252.
15. *Moszyński M. et al.* Comparative study of new 130 mm diameter fast photo multipliers for neutron detectors // Nucl. Instr. Meth. - 1991. - Vol. A307. - P. 97 - 109
16. *Venkataramanan S. et.al.* A compact pulse shape discriminator module for large neutron detector arrays // Nucl. Instr. Meth. - 2008. - Vol. A596. - P. 248 - 252.

CHARACTERISTICS OF WIDE BAND-GAP GAMMA-RADIATION DETECTORS BASED ON MERCURY COMPOUNDS

A. A. Zakharchenko[1], A. I. Skrypnyk[1], M. A. Khazhmuradov[1], E. M. Prokhorenko[2], V. F. Klepikov[2], V. V. Lytvynenko[2]

[1] National Scientific Centre "Kharkiv Institute of Physics and Technology", Kharkiv, Ukraine
[2] Institute of Electrophysics and Radiation Technologies, National Academy of Sciences of Ukraine, Kharkiv, Ukraine

We used Monte-Carlo method to compare characteristics of HgI_2- and HgS-detectors which work in the mode of pulse amplitude analysis. The GEANT4 Simulation Toolkit version 4.9.4p03 and EGSnrc version 4.r2.3.2 were used for gamma-quantum trajectory modeling and response function calculation in the gamma-quantum energy range between 25 keV and 3 MeV. We supposed that simulated HgI_2- and HgS-detectors were equipped with planar contacts and their geometric sizes were of ∅2 mm × 1 mm. Gamma-quantum registration efficiency $\varepsilon(E_\gamma)$ and detector sensitivity $\delta(E_\gamma)$ dependence on energy for energy range from 0.025 to 3 MeV are obtained basing on calculated detector response functions. Statistical characteristics of theoretical response functions and pulse amplitude distributions are studied taking into account noise and incomplete charge collection distortions of theoretical response functions. Results of simulation show that in the high energy region the efficiency of energy conversion of gamma-quanta in charge signal for HgS detectors can exceed the same characteristic for HgI_2-detectors up to 10…12 %.

1. Introduction

Mercuric iodide (HgI_2) is a promising material for gamma-radiation registration at room temperatures. Theoretical detection capability of HgI_2 exceeds the characteristics of most materials produced for gamma-radiation spectroscopy [1]. Present technologies of HgI_2 growth allow to obtain specific resistance ρ of semiconductor compound in the range between 10^{13} Ohm · cm and 10^{14} Ohm · cm [2]. Using the single carrier collection techniques (for wide band-gap semiconductor detectors it is only electron collection) [3] the resolution of HgI_2-detectors can exceeds the resolution of the same CdZnTe-detectors.

However, detectors based on HgI_2 did not become commercially available because crystals from this semiconductor compound have essential defects. In particular, the higher sublimation rate of iodine leads to sample surface enrichment with iodine (stoichiometric impurity), and the transition from tetragonal α-HgI_2 phase to the orthorhombic β-HgI_2 phase destroys order of the material structure [4]. As a result grown material is an excessively soft. Besides it easy delaminates along iodine planes.

Although other wide band-gap semiconductor compounds which include iodine (for example, PbI_2) do not undergo phase changes but they are also not suitable for mechanical treatment (ingot cutting, polishing of the detector surface) because of high fragility of the grown crystals [1].

The disturbance of the crystalline structure leads to formation of the electrically active defects in HgI_2 which essentially deteriorate charge collection in the planar detectors [4, 5]. Therefore in the majority of published investigations the thickness of the HgI_2-detector does not exceed 1 mm. Such detectors can be used for registration of X-rays and low energy gamma-quanta (E_γ is below 100 keV). Since ratio of the lateral side value (or diameter for cylindrical detectors) to the thickness of HgI_2-detector is usually not less than 10 to 1 that value of anisotropy of detector sensitivity is specified as tens or even hundreds percents (at 90° angle). Field of application of anisotropic detectors is mainly confined to stationary devices where detector orientation toward axis of gamma-radiation beam is not changed.

Above mentioned disadvantages of iodine-containing semiconductor compounds became the reason of search of other materials which have the same detection characteristics as HgI_2. But at the same time new materials must be more suitable for mechanical treatment and they must provide the reproduction of good detection characteristics of detector. Mercuric sulphide (HgS) is one of the new promising materials for gamma-radiation detection [6]. It is the most widely distributed stable mercuric mineral (cinnabar). As shown in Ref. [6] even impure natural HgS-crystals have sufficiently good characteristics of charge carrier transport for creation of gamma-radiation detectors which could work in the energy range up to 100 keV.

In this work Monte-Carlo method is used for comparison between detection characteristics of planar HgS gamma-radiation detectors working in the mode of registration of single gamma-quanta [7, p. 110] and characteristics of the same HgI_2-detectors. Statistical characteristics of theoretical response functions and pulse amplitude distributions have been investigated taking into account the distortions of theoretical response functions due to noises and incomplete charge collection. Basing on the calculated detector response functions the dependencies of gamma-quantum registration efficiency $\varepsilon(E_\gamma)$ and detector sensitivity $\delta(E_\gamma)$ on energy E_γ were obtained for energy range from 0.025 to 3 MeV.

2. Simulation of response function of room-temperature semiconductor detectors

The calculation model of response functions of room-temperature semiconductor detector (SCD) was originally developed and tested for CdTe- and CdZnTe-detectors with planar contacts [8, 9]. Subsequently, this model has been applied for analysis of characteristics of other wide band-gap semiconductor materials [10]. The universal

EGSnrc and Geant4 codes for the Monte-Carlo simulation of the passage of photons, electrons and positrons through matter [11, 12] was used for computation. Besides of interaction of gamma-quanta and charged particles with detector matter the model [8] allow to take into account the influence of noises and losses of nonequilibrium charge on the output signal amplitude.

Fig. 1 and Fig. 2 show calculated response function of HgI_2-detector with planar contacts on gamma-quanta with energy E_γ = 662 keV (^{137}Cs source) and its transformation in the measuring channel. The plot ordinate is defined as the ratio of pulse counts N_i in i-th channel of the simulated analog-digital converter (ADC) to total pulse counts $N_{tot} = \sum_i N_i$. Detector parameters correspond to data Ref. [13]: sizes of 1 × 1 × 1 cm^3, charge transport characteristics (mobility-lifetime product) – $(\mu\tau)_e = 5 \cdot 10^{-3}$ cm^2/V, $(\mu\tau)_h = 3 \cdot 10^{-5}$ cm^2/V, SCD bias U = 2.5 kV. Fig. 1 demonstrates processes of gamma-quantum energy absorption and nonequilibrium charge production in the detector. The investigated detector has sufficiently high probability of the complete absorption (photoeffect) of gamma-quanta with energy E_γ = 662 keV. Simulation shows that about fifty percents of the interacted quanta are fully absorbed. The efficiency of gamma-quanta registration for energy E_γ = 662 keV is about 42 % and so absolute theoretical intrinsic probability of scattering in the photopeak is about 21 %. It means that less than 25 % of input gamma-quantum flow is fully absorbed in HgI_2 at the length 1 cm. It coincides with simulation results using MCNP code [1]. Escape peaks corresponded to characteristic gamma-quanta of the mercury and iodine which have left the detector volume are clearly visible on the Compton valley background (0.45 < E < 0.65 MeV). The ratio of photopeak amplitude E_γ to the average pulse amplitude in the Compton continuum region (0 < E < 0.45 MeV) exceeds two orders of magnitude. Small peak spreading comes from fast electron energy losses due to the generation of lattice vibrations (losses up to 5 %).

Fig. 2 shows changes of response function of HgI_2-detector (Fig. 1) after the output of the measuring channel. A main part of pulse amplitudes is shifted to the Compton continuum region. The escape peaks are almost completely spreaded. The ratio of the photopeak amplitude E_γ to the average amplitude in the Compton continuum region (i.e. where 0 < E < 0.45 MeV) is less than 1.3. In whole the response function (Fig. 2) has satisfactory agreement with calculation in Ref. [13].

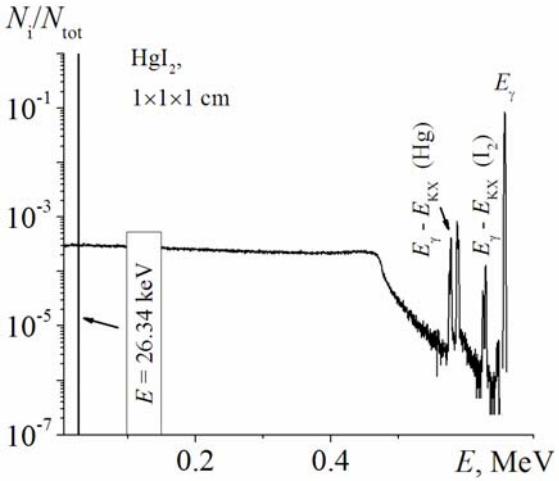

Fig. 1. The response function of HgI_2-detector on gamma-quanta with energy 662 keV without taking into consideration the charge collection and noises.

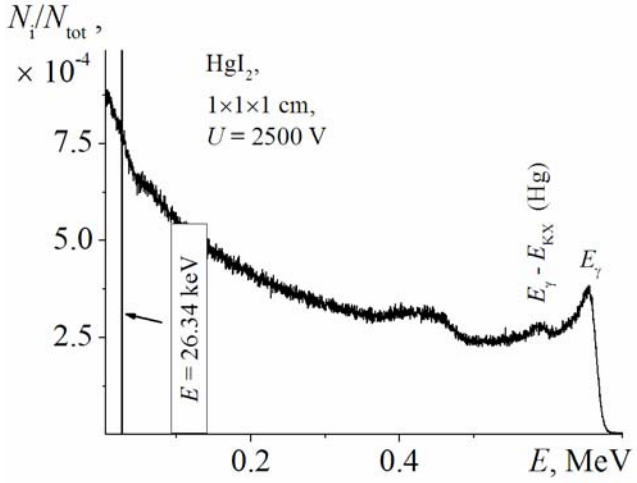

Fig. 2. The response of HgI_2-detector after the output of the measuring channel corresponded to Ref. [13].

Results of simulation (Fig. 2) are satisfactorily conformed to calculations that presented in the Ref. [13] but the shape of the showed in that Ref. experimental ^{137}Cs spectrum differs from the shape of calculated spectrum. The most important distinctions are the photopeak lack and higher value of experimental ratio N_i/N_{tot} at the initial energy range in comparison with simulation. The variation of the model parameters showed that we can achieve such spectral distribution if the intensity of internal electric field inside the detector is much less than expected value that is U/d = 2500 V/cm for planar detectors. It can be a consequence of the distortion of the internal electric fields near numerous growth defects of semiconductors as in Ref. [14, 15]. This case can be reproduced within the used model at lower bias U (Fig. 3). From

Fig. 3 it follows that the photopeak is absent as it occurs for the real spectrum of ^{137}Cs source that was presented in Ref. [13]. The pulse number in the initial channels exceeds the average value of pulse number in the Compton continuum up to one order of magnitude.

Fig. 4 shows change $CCE(x)$ corresponding to reduction of the internal electric field intensity inside the detector. At the same time the detector thickness-averaged collection efficiency CCE is decreased from 57.6 % to 42.9 %. It leads to

complete degradation of the 662 keV photopeak (Fig. 3). Thus, the developed model of room-temperature semiconductor gamma-radiation detector allows to obtain the response function of HgI_2-detector which has satisfactory agreement with known experimental and simulation data. It permits to use the described model for comparison between detection characteristics of HgI_2- and HgS-detectors.

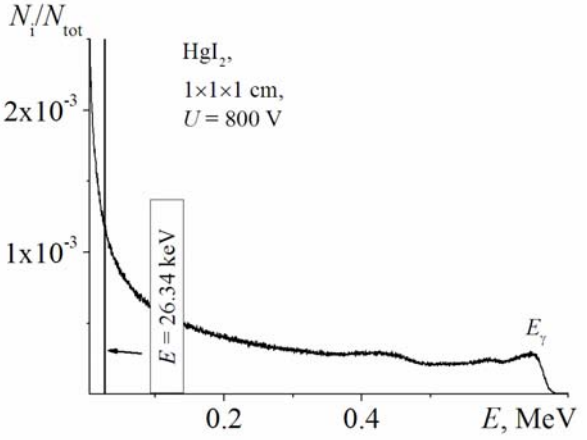

Fig. 3. The change of HgI_2-detector response at the bias reduction.

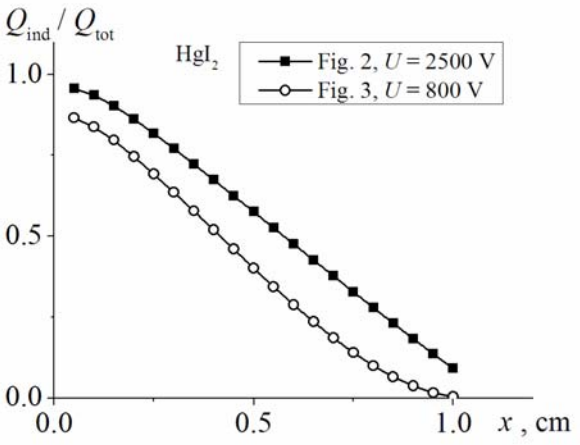

Fig. 4. The change of the charge collection efficiency CCE(x) in the HgI_2-detector.

3. Characteristics of HgI_2- and HgS-detectors

The calculations of response functions were carried out for the planar HgI_2- and HgS-detectors with ohmic contacts. Their geometric sizes were of ∅2 mm × 1 mm. The detector operation spectrometric mode was simulated. In the both cases bias voltage was 100 V. The equivalent noise charge was 400 units of electron charge (e^-). Mobility-lifetime products were chosen $(\mu\tau)_e = 1 \times 10^{-4}$ cm^2/V for electrons and $(\mu\tau)_h = 4 \times 10^{-5}$ cm^2/V for holes in both detectors. At the first stage of HgS-detector simulation with electron and holes mobilities $\mu_e = 15$ cm^2/(V · s) and $\mu_h = 2$ cm^2/(V · s) respectively (detector no. 1) was studied. HgI_2-detector mobilities were $\mu_e = 67$ cm^2/(V · s) and $\mu_h = 8$ cm^2/(V · s). At the second stage of HgS-detector simulation with the same electron and hole mobilities as for HgI_2-detector (detector no. 2) was investigated.

As the calculation shows (Fig. 5) the sensitivity δ of HgS-detector no. 1 is essentially lower than the sensitivity of HgI_2-detector. The detector thickness-averaged charge collection efficiency *CCE* for HgS-detector no. 1 was changed in the range from about 42 % for energy of gamma-quanta 26.34 keV to about 4 % for 3 MeV. At the same time for HgI_2-detector *CCE* change was observed in the range between about 65 % and about 36 %. We suppose that the main reason of comparatively low sensitivity of HgS-detectors is a ballistic deficiency due to low mobility of charge carriers [16].

In order to check the last assumption the theoretical response of HgS-detector no. 2 with the same mobility of charge carriers as for HgI_2-detector was computed. As follows from data of Fig. 5 the sensitivity δ of HgI_2-detector is practically equal to sensitivity δ of HgS-detector no. 2 in the range of gamma-quantum energy up to about 80 keV. Jump increase of sensitivity of HgS-detector no. 2 is observed in the energy region above 80 keV. This jump corresponds to transition over *K*-edge of absorption of mercury (83.1 keV). Interestingly, that this jump is almost invisible for HgI_2 (Fig. 6). The jump change of sensitivity have to be taken into account at calculation of parameters of correction of energy dependence of sensitivity of HgS-detectors in dosimetry application.

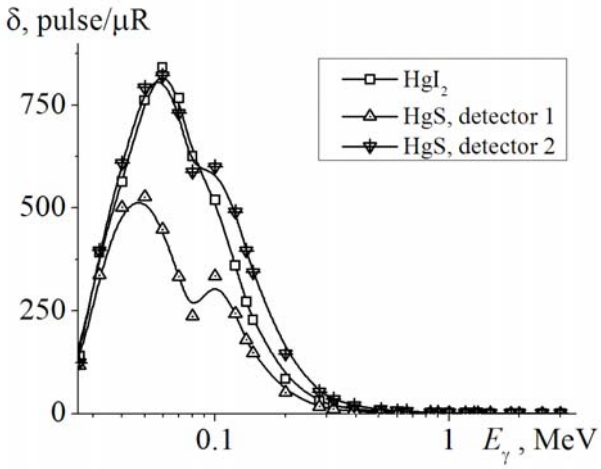

Fig. 5. The dependence of sensitivity δ vs gamma-quantum energy for HgI_2-and HgS-detectors.

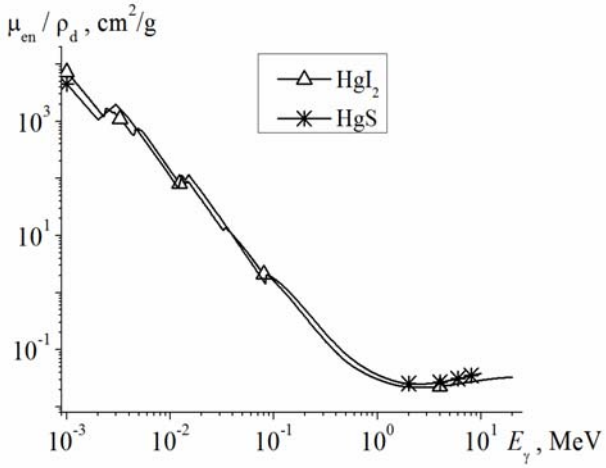

Fig. 6. The energy dependence of mass energy coefficient in the HgI_2- and HgS-detectors.

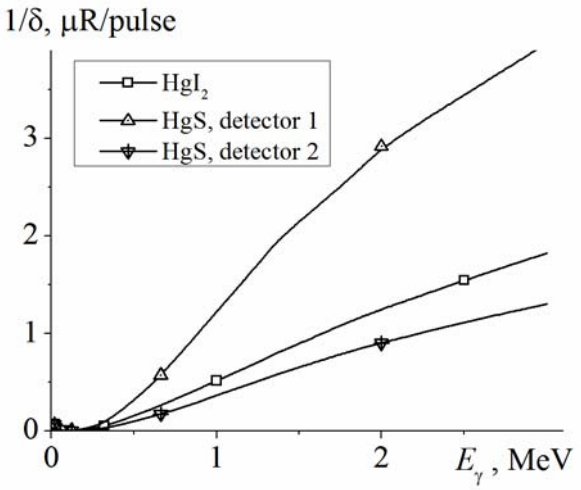

Fig. 7. The dependence of 1/δ value vs gamma-quantum energy for HgI_2- and HgS-detectors.

The comparison between dependencies of investigated detector sensitivity on energy in the range above 300 keV can be most easily made for inverse function $1/\delta = f(E_\gamma)$ (Fig. 7). The calculation data show (plot – HgS, detector no. 1) that HgS-detectors which can be made from currently available material cannot compete with detectors based on mercuric iodide. In the high energy region the sensitivity of HgS gamma-radiation detectors is lower in 2 or more times in comparison with the same HgI_2-detectors.

In order to use advantages of HgS semiconductor compound (chemical stability, mechanical strength) it is necessary to improve the growth technologies of mercuric sulfide. The principle problem consists in increasing values of charge carrier transport in HgS up to level of averaged values which are typical for currently available mercuric iodide. In this case, as the simulation shows (Fig. 7, plot – HgS, detector no. 2), the sensitivity of HgS-detector can exceed the sensitivity of the same HgI_2-detector in the high energy gamma-quantum range at 10 - 12 %. The thickness of serial HgS-detectors can be increased up to 3 mm. In this case the theoretical value of their sensitivity in the high energy gamma-quantum range can exceed the sensitivity of serial HgI_2-detectors up to 15 %. For further improvement of characteristics of HgS-detectors the grown single crystals of mercuric sulfide have to allow to use higher bias.

4. Conclusions

Mercuric sulfide (HgS) is a new promising material for production of room-temperature gamma-radiation detectors. The our calculation showed that for using advantages of HgS (chemical stability, mechanical strength) it is necessary to improve the growth technology of mercuric sulfide in order to increase mobility of charge carriers. Achieving mobility values of electrons and holes which are typical for currently available mercuric iodide the sensitivity of HgS-detectors in the high energy gamma-quantum range (above 1 MeV) can exceed the sensitivity of the same HgI_2-detectors up to 15 %. For further increasing sensitivity it is necessary to obtain the mercuric sulfide crystals with higher values of electrons and holes mobility.

REFERENCES

1. *Lintereur A., Qiu W., Nino J. et al.* Iodine based compound semiconductors for room temperature gamma-ray spectroscopy // Proc. of SPIE. - 2008. - Vol. 6945. - P. 694503-1 - 3.
2. *Vaccaro F., van den Berg L., Szubart L. et al.* The long-term spectral stability of HgI_2 gamma-ray detectors // Proc. SPIE. - 2001. - Vol. 4507. - P. 108 - 118.
3. *Owens A., Kozorezov A.* Single carrier sensing techniques in compound semiconductor detectors // Nucl. Instr. & Meth. A. - 2006. - Vol. 563. - P. 31 - 36.
4. *Van Scyoc J., James R., Schlesinger T. and Gilbert T.* Defects and Impurities in Mercuric Iodide Processing // MRS Proceedings. - 1995. - Vol. 378. - P. 795 - 802.
5. *Schieber M., Zuck A., Lukach M.* Non-destructive evaluation of purified HgI_2 starting materials // Journal of Optoelectronics and Advanced Materials. - 2001. - Vol. 3. - P. 757 - 761.
6. *Squillante M., Higgins W., Kim H. et al.* HgS: A Rugged, Stable Semiconductor Radiation Detector Material // Proc. of SPIE - 2009. - Vol. 7449, 74491U. - P. 74491U-1 - 6.
7. *Knoll G.* Radiation Detection and Measurement / 3rd ed. - New York: Wiley, 2000. - 802 p.
8. *Zakharchenko A., Verevkin A., Kutnij V., Rybka A., Khazhmuradov M.* Modelirovanie funkcii otklika CdZnTe detektorov dlia dozimetrii gamma-izlucheniia // Visnik harkivs'kogo natsional'nogo universitetu. Seriia fizichna "Yadra, chastinki, polia". - 2008. - Vol. 832. - P. 71 - 76 (in Russian).
9. *Zakharchenko A.* Verifikaciia modelej poluprovodnikovyh detektorov gamma-izlucheniia // Visnyk harkivs'kogo natsional'nogo unsversitetu. Seriia fizichna "Yadra, chastinki, polia". - 2011. - Vol. 955. - P. 51-59. (in Russian).
10. *Skrypnyk A., Zakharchenko A., Khazhmuradov M.* Comparison of GEANT4 with EGSnrc for simulation of gamma-radiation detectors based on semi-insulating materials // Problems of atomic science and technology, Series: Nuclear Physics Investigations (56). - 2011, no 5. - P. 93 - 100.
11. *Kawrakow I., Mainegra-Hing E., Rogers D.* EGSnrcMP, the new multiplatform version of EGSnrc // Med. Phys. - 2004. - Vol. 31. - P. 1731.

12. *Agostinelli S. Allison J., Amako K. et al.* Geant4 - a simulation toolkit // Nucl. Instr. & Meth. A. - 2003. - Vol. 506. - P. 250 - 303.
13. *Baciak J.E., He Z.* Spectroscopy on Thick HgI_2 Detectors: A Comparison Between Planar and Pixelated Electrodes // IEEE Trans. Nucl. Sci. - 2003. - Vol. 50, No. 4. - P. 1220 - 1224.
14. *Yang G., Bolotnikov A., Camarda G. et al.* Electric field distribution of cadmium zinc telluride (CZT) detectors // Proc. of SPIE. - 2009. - Vol. 7449. - P. 74490C-1 - 7.
15. *Klimenko I., Komar' V., Migal' V., Nalivajko D.* Vliianie uprugih polej rostovyh defektov na fotodielektricheskij otklik kristallov $Cd_{1-x}Zn_xTe$ // Fizika i tehnika poluprovodnikov. - 2001. - Vol. 35. - P. 139 - 142 (in Russian).

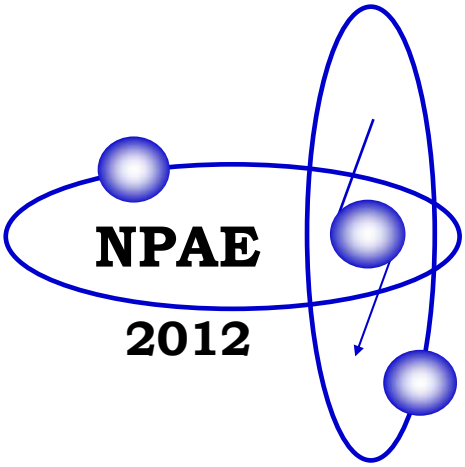

Section 8

High Energy Physics

NUCLEON NONEQUILIBRIUM DISTRIBUTION FUNCTIONS IN RELATIVISTIC HEAVY-ION COLLISIONS

D. Anchishkin[1], V. Naboka[2], S. Yezhov[2], J. Cleymans[3]

[1] *M. M. Bogolyubov Institute for Theoretical Physics, National Academy of Sciences of Ukraine, Kyiv, Ukraine*
[2] *Taras Shevchenko National University, Kyiv, Ukraine*
[3] *University of Cape Town, Rondebosch, South Africa*

We investigate the evolution of the nucleon system created in relativistic nucleus-nucleus collision, but we parameterize this development by the number of collisions of every particle during evolution rather than by the time variable. It is assumed that the group of nucleons which leave the system after the same number of collisions can be joined in a particular statistical ensemble. The nucleon nonequilibrium distribution function which depends on a certain number of collisions of a nucleon before freeze-out is derived. The collision smearing of the nucleon momenta about their initial values during nucleus-nucleus collisions is investigated.

1. Introduction

The main goal of the investigations of the collisions of relativistic nuclei is extraction of a physical information about nuclear matter and its constituents. It is a matter of fact that we can get know more about quarks and gluons (constituents) just under extreme conditions, i.e. at high densities and temperatures. In the present paper we propose a transparent analytical model of the nucleon spectrum which occur in relativistic heavy-ion collisions. Our model is aimed at the extraction of the physical information from the nucleon spectra for such collision energies when the number of created nucleon-antinucleon pairs is much less than the number of net nucleons. This means that the model can be applied to AGS and SPS energies.

Let us look on the cross-section of the multiparticle production during collision of relativistic nuclei, where $P = P_A + P_B$ is the initial total 4-momentum of two colliding nuclei "A" and "B". For the description of the nucleon subsystem one can parameterize the final state of the nucleon ensemble by 4-vector $K_N = (E_N, \mathbf{K}_N)$. In the center of mass of the N-nucleon subsystem, where $\mathbf{K}_N = 0$, the total cross-section reads

$$\left[\prod_{n=1}^{N}\omega_n \frac{d^N\sigma_{nucleon}}{d^3p_1 d^3p_2 \ldots d^3p_N}\right]_{E_N} = W(\mathbf{p}_1,\mathbf{p}_2,\ldots,\mathbf{p}_N)\,\delta[E_N - \sum_{n=1}^{N}\omega_n], \tag{1}$$

where $\omega_n = \omega(\mathbf{p}_n) = \sqrt{m^2 + \mathbf{p}_n^2}$. Due to the presence of the δ-function, which "fixes" the energy of the nucleon system, the last expression (1) looks like a probability in the microcanonical ensemble. Then, it is reasonable to make the Laplace transform with respect to the energy E_N of the nucleon ensemble

$$\left[\prod_{n=1}^{N}\omega_n \frac{d^N\sigma_{nucleon}}{d^3p_1 d^3p_2 \ldots d^3p_N}\right]_{\beta} = W(\mathbf{p}_1,\mathbf{p}_2,\ldots,\mathbf{p}_N)\prod_{n=1}^{N} e^{-\beta\omega_n}\,. \tag{2}$$

It turns out that now one can describe the final state of the nucleon subsystem through one of the two parameters: the total energy E_N or the parameter β. The statistical model [1 - 3] neglects all dynamics, which is accumulated in the transition probability W, in favor of the features of the phase space. Formally this is expressed like approximation: $W(\mathbf{p}_1,\mathbf{p}_2,\ldots,\mathbf{p}_N) \approx \text{const}$. This description gives a certain information about the spectrum of the registrated particles. Meanwhile, any dynamical information about rescattering processes during collision is lost. At the same time, it is well understood that a microscopic description can be done just on some level of approximation. For instance, if possible to factorize the transition probability W we come to factorization of the multi-nucleon cross-section

$$\left[\prod_{n=1}^{N}\omega_n \frac{d^N\sigma_{nucleon}}{d^3p_1 d^3p_2 \ldots d^3p_N}\right]_{\beta} = \prod_{n=1}^{N}\left[e^{-\beta\omega_n} W(\mathbf{p}_n)\right]. \tag{3}$$

The approximation of the sequential rescatterings of a particle during collision of nuclei which is proposed in the present paper is exactly in this framework: we follow the chain of reactions (rescatterings) of every nucleon, which goes through the number of hadron transformations, and as a result we obtain a single-particle spectrum of the nucleon $W_M(\mathbf{p})$, which depends on the number M of collisions (reactions) of the nucleon.

We argue that the number of nucleon collisions (reactions) at AGS and SPS energies is finite and the maximal number of collisions M_{max} is not more than $M_{max} = 43$. Besides this all nucleons, which are freezed out during

particular nucleus-nucleus collision, can be partition into groups; in every group the nucleons went through the same number M of collisions. We determined that the most populated groups are for number of collisions M which are in the range: $M = 16–18$. Starting from initial time moment of the nucleus-nucleus collision we follow the sequential collisions of every nucleon through the opposite nucleus (Fig. 2), nevertheless the original nucleon can be transformed during particular collision into another particle, for instance into delta isobar Δ^+, (Fig. 1). Then, we follow a new particle which carries the same charges (the baryon number, electrical charge etc.) as the original nucleon. During the last collision (it can be a decay) all these "intermediate" particles transform back into nucleons, hence we can investigate just nucleons in the final state. With growing the number of collisions the actual number of "active" nucleons goes down because of radiation of nucleons. From this point every group of nucleons in the final noninteracting state is the subject of the statistical model. For the multiscattering stage of evolution we treat UrQMD [4, 5] as a source of “experimental data” which we use to adjust the parameters of our model.

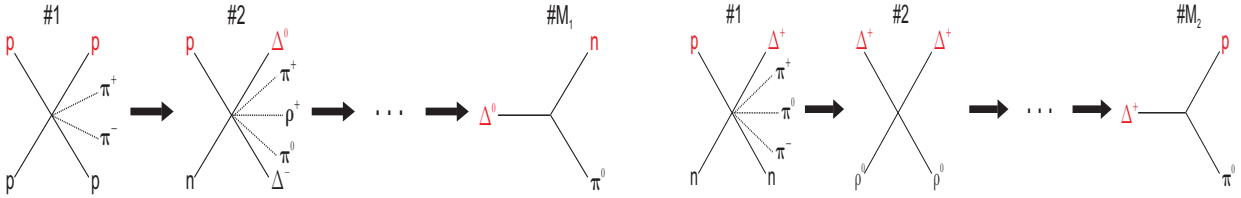

Fig. 1. Sequential reactions of the initial nucleon, $1 \le M_{1,2} \le 43$.

We propose the mutually complementary combination of these two approaches: the approximate description of the dynamical stage of evolution of nucleons during the nucleus-nucleus collision which is completed by the statistical description of the nucleon freezed out stage. We named this approach as "The multiscattering-statistical model".

2. The multiscattering-statistical model

Consider successive variations of the momentum of a nucleon from nucleus A (see Fig. 2) which moves along the collision axis from left to right through nucleus B. Every m-th collision induces the momentum transfer, $\mathbf{q}_m$, for this nucleon. So that, after M collisions, the nucleon acquires the momentum $\mathbf{k}$:

$$\mathbf{k}_0 \rightarrow \mathbf{k}_0 + \mathbf{q}_1 \rightarrow \mathbf{k}_0 + \mathbf{q}_1 + \mathbf{q}_2 \rightarrow \cdots \rightarrow \mathbf{k}_0 + \mathbf{Q} = \mathbf{k}. \qquad (4)$$

where $\mathbf{Q} = \sum_{m=1}^{M} \mathbf{q}_m$ is the total momentum transfer finally obtained by our nucleon after M collisions (Fig. 3). If M-th collision is the last one, then the nucleon is free after it or the nucleon has been freezed out from the system. As a matter of fact it will be a group of such nucleons which experienced the same number of collisions M before freeze-out. The relation of these nucleon groups (nucleon sub-ensembles) to the spectrum is discussed in the next section.

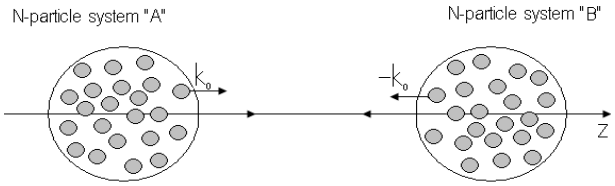

Fig. 2. Two colliding identical nuclei. Two-stream system is created during collision of every nucleon from nucleus "A" with nucleons from nucleus "B" and vice versa.

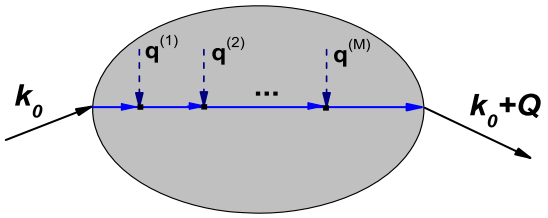

Fig. 3. Transformation of the initial nucleon momentum, $\mathbf{k}_0$, as a result of M collisions; $\mathbf{Q} = \sum_{m=1}^{M} \mathbf{q}_m$ is the total momentum transfer after M collisions, $\mathbf{q}_m$ is the momentum transfer in the m-th collision.

We assume that all momentum transfer obtained by the nucleon from nucleus "A" during its traveling through the system "B" are the random quantities [6, 7].

2.1 Two-stream dynamics

The description of a two-stream system which is created in relativistic nucleus-nucleus collisions is based on the following assumptions:

1) Starting from the initial state (first touch of the colliding nuclei), at the arbitrary moment of time there are two system of nucleons: one system consists of nucleons with positive z-component of the nucleon momentum, i.e. $p_z \ge 0$

(we name this system as "A") and the second system consists of nucleons with negative z-component of the nucleon momentum, i.e. $p_z \le 0$ (we name this system as "B", see Fig. 2). Even after freeze-out there is a good enough separation of these systems along p_z-axis.

2) The number of collisions of every nucleon (hadron) is finite because the lifetime of the fireball is limited. To determine the maximal number of collisions, M_{max}, in a particular experiment we use the results of UrQMD simulations [4,5].

3) Because the colliding nuclei are restricted spatially, the different nucleons experience a different number of collisions: it is intuitively clear that the collision histories of the inner nucleons and surface nucleons will be different. That is why, we partition all amount of freezed out nucleons (nucleon ensemble) into different nucleon sub-ensembles in accordance with a number of collisions M the nucleons went through before being freezed out. Then, the nucleons from every sub-ensemble give their own contribution to the total nucleon spectrum.

If we denote the number of particles in a particular nucleon sub-group (sub-ensemble), where the nucleons experienced M collisions by N_M, then in the c.m.s. of colliding nuclei the total nucleon spectrum looks like [6, 7]

$$\frac{dN}{d^3p} = \sum_{M=1}^{M_{max}} N_M \mathbb{F}_M(\mathbf{p}), \quad with \quad \sum_{M=1}^{M_{max}} N_M = N_{total}, \tag{5}$$

where N_{total} is the total number of net nucleons. The number of nucleons N_M in every sub-ensemble calculated for different energies with the help of the microscopic transport model UrQMD [4,5] is depicted in Fig. 4. Every sub-ensemble of nucleons (these nucleons are already emitted) can be imaging as an ideal gas which moves with some collective velocity.

Normalized to unity two-stream distribution function $\mathbb{F}_M(\mathbf{p})$, which in accordance with the first assumption should take into account the spectrum produced from both particle streams "A" and "B", in the Gaussian approximation looks like (for details see Refs. [6, 7])

$$\mathbb{F}_M(\mathbf{p}) = \frac{1}{2}\left[f_M^{(a)}(\mathbf{p}) + f_M^{(b)}(\mathbf{p}) \right], \tag{6}$$

where

$$f_M^{(a)}(\mathbf{k}) = \frac{1}{z_M(\beta_M)} \exp\left\{ -\beta_M \omega(\mathbf{k}) - \frac{\mathbf{k}_\perp^2}{2\left(\sigma_\perp^2\right)_M} \right\} \exp\left\{ -\frac{(k_z - k_{0z} - \langle Q_z \rangle_M)^2}{2\left(\sigma_z^2\right)_M} \right\}, \tag{7}$$

and

$$f_M^{(b)}(\mathbf{k}) = \frac{1}{z_M(\beta_M)} \exp\left\{ -\beta_M \omega(\mathbf{k}) - \frac{\mathbf{k}_\perp^2}{2\left(\sigma_\perp^2\right)_M} \right\} \exp\left\{ -\frac{(k_z + k_{0z} + \langle Q_z \rangle_M)^2}{2\left(\sigma_z^2\right)_M} \right\} \tag{8}$$

with $\mathbf{k}_0 = (0,0,k_{0z})$ and we assume $\langle \sigma_x^2 \rangle_M = \langle \sigma_y^2 \rangle_M \equiv \langle \sigma_\perp^2 \rangle_M$. Here the single-particle partition function reads $z_M(\beta_M) = \int d^3k / (2\pi)^3 f_M^{(a)}(\mathbf{k})$.

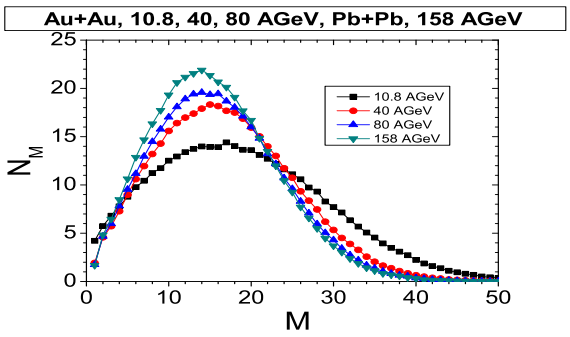

Fig. 4. The populations N_M of the nucleon sub-ensembles which depend on the number of collisions M. The result is obtained from the UrQMD simulations for the most central collisions.

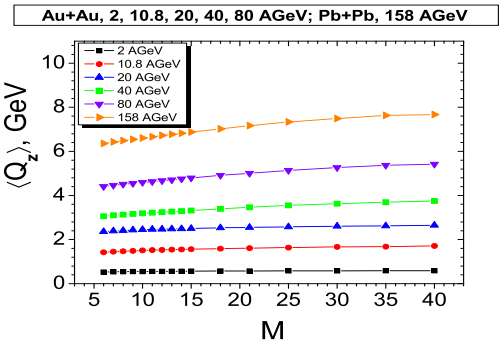

Fig. 5. The z-component of the mean momentum ransfer versus number of collisions.

3. Extraction of physical parameters from the data

First we obtain from UrQMD [4, 5] the longitudinal distribution of nucleons for every M-th sub-ensemble. The distributions for the stream "A" (positive p_z) and the stream "B" (negative p_z) were obtained separately. This pool of

distributions we quoted as "urqmd data". We fit the "urqmd data" on the longitudinal distribution of nucleons of the M -th sub-ensemble of the stream "A" exploiting the theoretical distribution function (7) integrated over transverse momentum. The variations of the theoretical distribution function were provided by four parameters: $\langle Q_z \rangle_M$, β_M, $\left(\sigma_\perp^2\right)_M$ and $\left(\sigma_z^2\right)_M$. The results of the fit of the "urqmd data" (nucleon longitudinal distributions) for the energies 10.8,20,80 and 158 AGeV are depicted in Fig. 6.

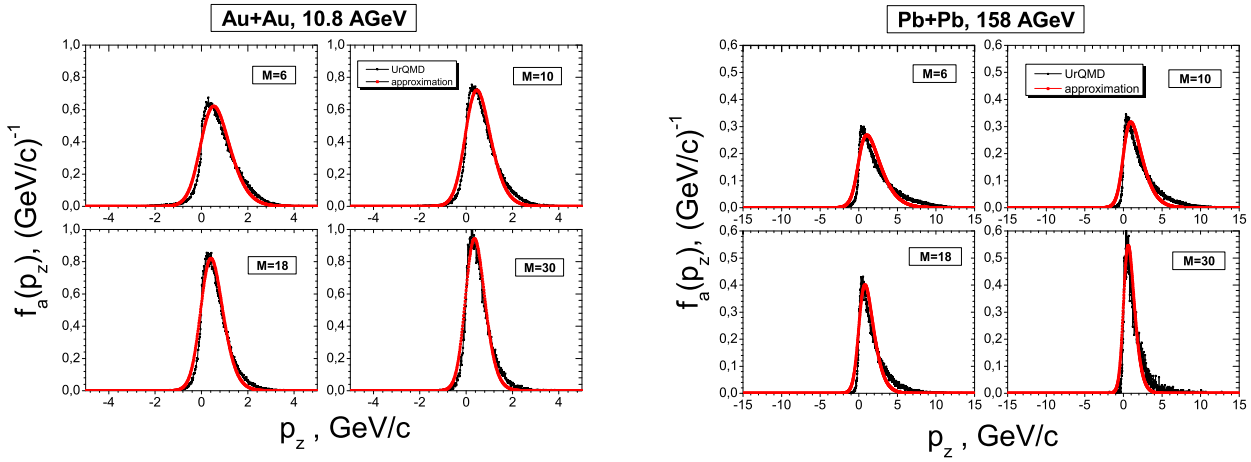

Fig. 6. The spectrum of the M -th nucleon sub-ensemble ($M = 6,10,18,30$) with respect to p_z -component of the nucleon momentum calculated using the UrQMD transport model for Au+Au collision (black curve). The red curve is the fit of the UrQMD data in the framework of the proposed multiscattering-statistical model.

The dependence of the parameters with respect to the number of reactions, M , of the nucleon before freeze-out is shown in the following Figures: The slope parameter $T_M = 1/\beta_M$ in Fig. 8 (red curves) and the temperature T_0 (blue curves); The mean value of the shift of the distribution function, $\langle Q_z \rangle_M$, in Fig. 5; The longitudinal variance $\left(\sigma_z^2\right)_M$ in Fig. 7.

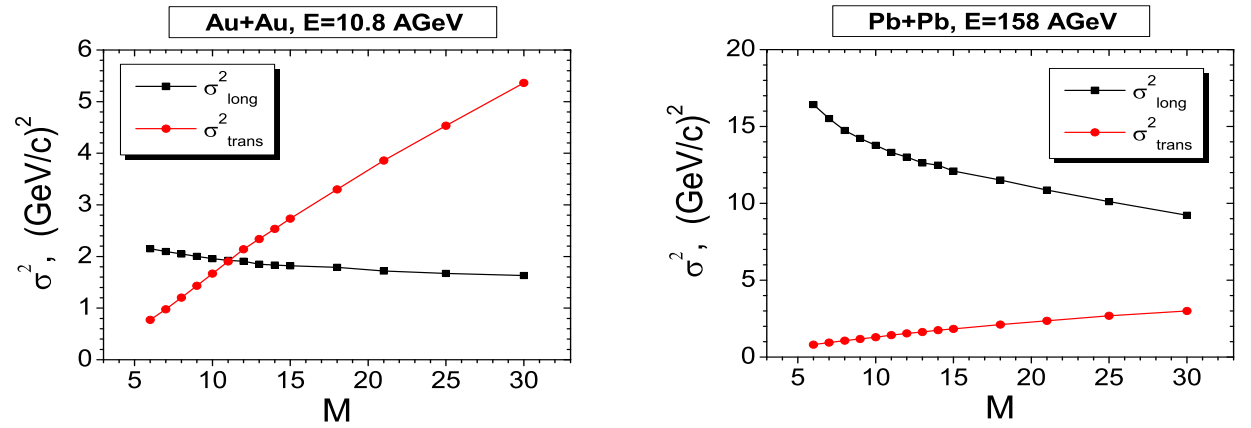

Fig. 7. Longitudinal and trasverse variances, $\left(\sigma_z^2\right)_M$ and $\left(\sigma_\perp^2\right)_M$,
versus the number of collisions M for collision energies 10.8 and 158 AGeV.

Temperature of the hot ideal gas is determined in the local rest frame of the gas. This temperature is connected with the total kinetic energy of N particles (nucleons) in the local rest frame in the following way:

$$\frac{E_{r.f.}}{N} = 3T_0 + m_N \frac{K_1(m_N/T_0)}{K_2(m_N/T_0)}. \qquad (9)$$

In our model $E_{r.f.}$ is the total kinetic energy of the sub-ensemble of nucleons in the rest frame of this group of particles, m_N is the nucleon mass ($E_{r.f.} = \gamma[E - V P_z], \gamma = 1/\sqrt{1-V^2}$).

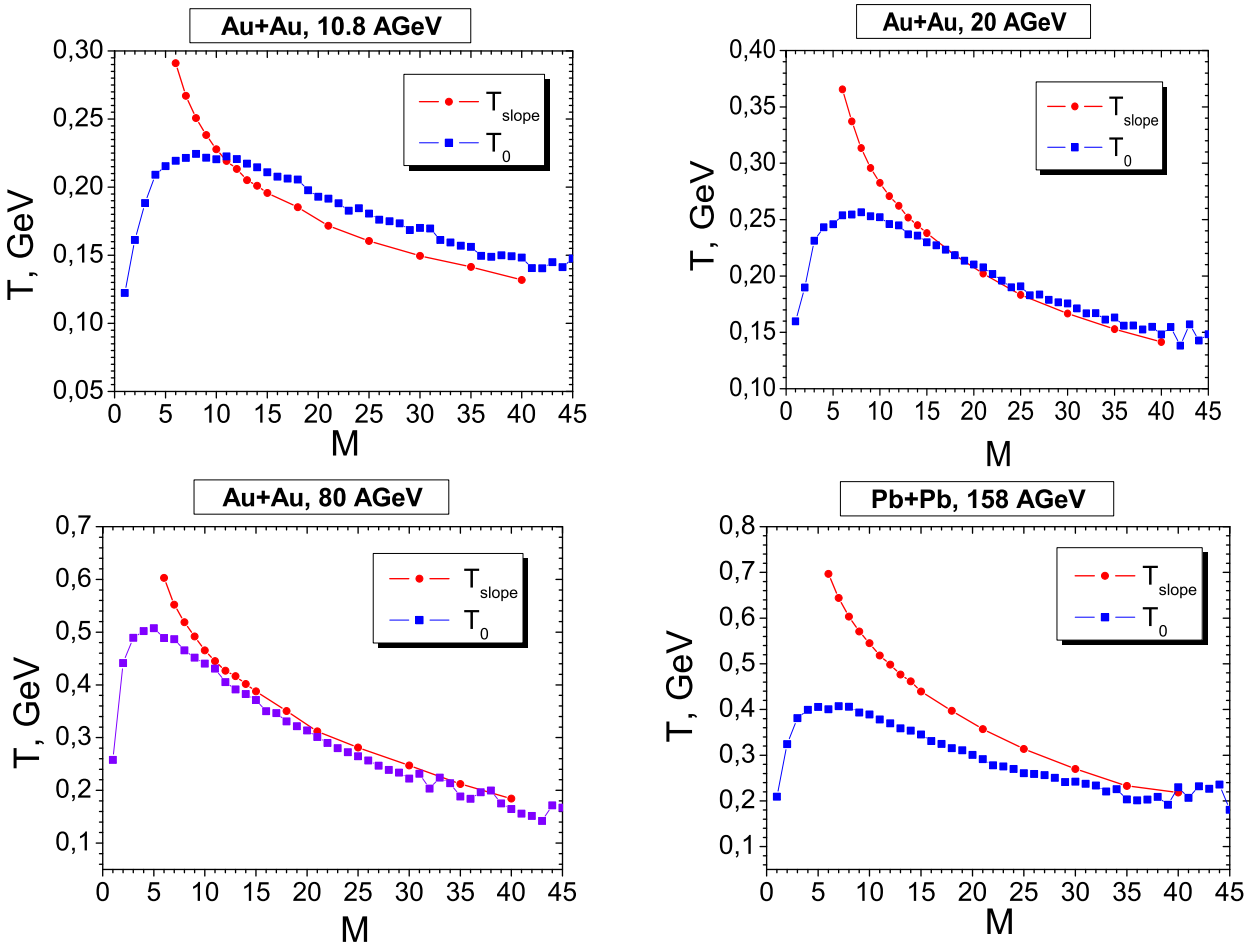

Fig. 8. Dependence of the slope parameter T_M (red curve) and temperature T_0 (blue curve) on the collision number M for different energies of the nucleus-nucleus collision: 10.8, 20, 80, 158 AGeV.

To obtain the transverse distribution we integrate the "A"-stream distribution function (7) over the longitudinal component of the nucleon momentum. The results of the description of the "urqmd data" on nucleon transverse distribution for the energy 20 AGeV is depicted in Fig. 9 (*left panel*). For this description we use the same values of parameters $\langle Q_z \rangle_M$, β_M, $(\sigma_z^2)_M$ and $(\sigma_\perp^2)_M$, which were obtained during the fit to the "urqmd data" on nucleon longitudinal distributions.

The experimental data for transverse nucleon distributions in central Au+Au reactions at $p_{lab} = 11.6$ A GeV/c [8] were described with making use of the formula (5), the result is depicted in Fig. 9 (*right panel*). We see a good agreement of the description with experiment.

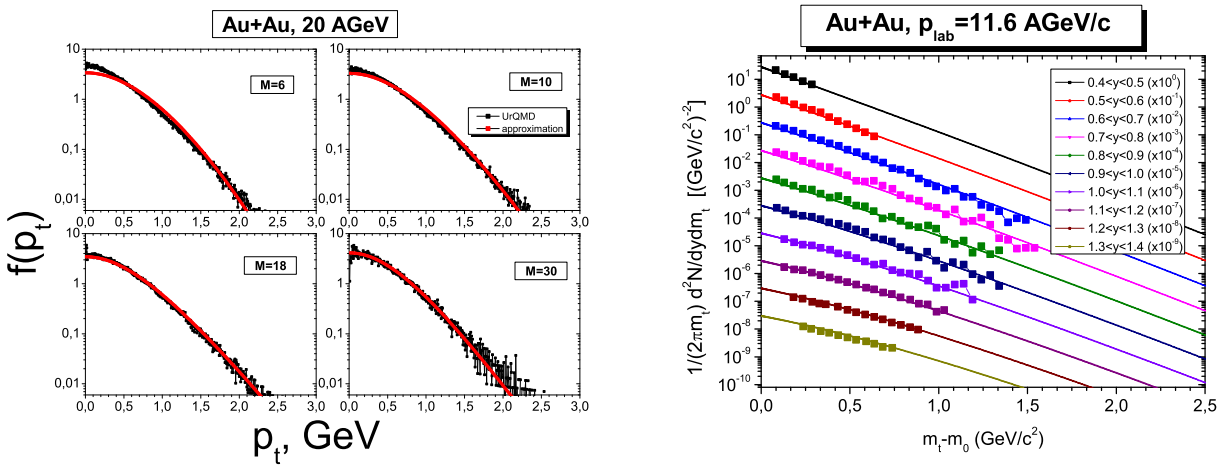

Fig. 9. Fit of the UrQMD data (*left panel*) and description of the experimental data [8] on nucleon transverse distribution in central Au+Au reactions at $p_{lab} = 11.6$ A GeV/c (*right panel*).

4. Discussion and conclusions

• Description of a many-particle system, which is in the thermal equilibrium state, can be regarded as understood by means of the temperature and chemical potential if the latter is needed. Then, to obtain the value of the temperature one has to fit particle spectrum data with the help of single-particle distribution function. The fitting procedure is nothing more as an extraction of the physical quantity, "temperature", from the data.

• If we transfer to the description of the nonequilibrium many-particle system, the natural question arises: what a set of parameters is necessary to have a relevant physical picture of the many-particle system which state evolves in time? Of course, under the words "physical picture" one means a physical interpretation of the parameters of the model. The set of parameters of a model, a behavior of evolution of parameters become a specific language on which we investigate, describe and "understand" the nonequilibrium many-particle system and the processes inside it.

"The Multiscattering-Statistical Model" reveals four parameters, which describe the nonequilibrium distribution function:

1. The slope parameter $T(M) = 1/\beta_M$.

2. The mean value of z -component of the total momentum transfer $\langle Q_z \rangle_M = \sum_{m=1}^{M} \langle q_z \rangle_m$.

3. The variances of the Gaussian distribution, $\left(\sigma_\perp^2\right)_M$ and $\left(\sigma_z^2\right)_M$.

We can conclude that evolution of the physical parameters of "The Multiscattering-Statistical Model" elaborated in the present paper gives a transparent insight into dynamics of the net nucleons during relativistic nucleus-nucleus collisions. The appearance of the Gaussian distribution as a factor in the nonequilibrium distribution function of nucleons, see for instance (7) or (8), is common for description of any multiscattering process with big but finite number of rescatterings of the particle when every particular scattering can be regarded as independent of others. This condition is satisfied especially for nucleons during high energy heavy-ion collisions when the particle wave length $\lambda = \hbar / p$ is much smaller then the mean distance between nucleons in colliding nuclei.

ACKNOWLEDGEMENTS

D. Anchishkin was partially supported by the program "Microscopical and phenomeno-logical models of fundamental physical processes at micro and macro scales" (Section of physics and astronomy of the NAS of Ukraine).

REFERENCES

1. *Lurçat F., Mazur P.* Statistical Mechanical Evaluation of Phase-Space Integrals // Nuovo Cimento. - 1964. - Vol. 31. - No. 1. - P. 140 - 163.
2. *Byckling E., Kajantie K.* Particle Kinematics. - , London - NY - Sydney - Toronto: John Willey and Sons, 1973.
3. *Rémi Hakim.* Introduction to Relativistic Statistical Mechanics. - World scientific, 2011.
4. *Bass S.A., Belkacem M., Bleicher M. et al.* Microscopic Models for Ultrarelativistic Heavy Ion Collisions // Prog. Part. Nucl. Phys. - 1998. - Vol. 41. - P. 225.
5. *Bleicher M., Zabrodin E., Spieles C. et al.* Relativistic Hadron-Hadron Collisions in the Ultra-Relativistic Quantum Molecular Dynamics Model // J. Phys. G: Nucl. Part. Phys. - 1999. - Vol. 25. - P. 1859.
6. *Anchishkin D., Muskeyev A., Yezhov S.* Full and Partial Thermalization of Nucleons in Relativistic Nucleus-Nucleus Collisions // Nucl. Phys. - 2009. - Vol. A820. - P. 307C; arXiv:0902.0999 [nucl-th].
7. *Anchishkin D., Muskeyev A., Yezhov S.* Collision Thermalization of Nucleons in Relativistic Heavy-Ion Collisions // Int. J. Mod. Phys. - 2009. - Vol. A24. - P. 4437 - 4456; arXiv:0902.4171 [nucl-th].
8. *Ahle L., Akiba Y., Ashktorab K. et al.* (*E-802 Collaboration*). Particle production at high baryon density in central Au + Au reactions at 11.6A GeV/c // Phys. Rev. - 1998. - Vol. C57**.** - No. 2. - P. R466.

PHOTOPRODUCTION OF JETS AND DETERMINATION OF α_s AT LEPTON-PROTON COLLIDER HERA

V. E. Aushev, I. M. Kadenko, D. I. Lontkovskyi, I. V. Makarenko

Taras Shevchenko National University, Kyiv, Ukraine

Recent measurements of inclusive-jet cross sections in the reaction $ep \rightarrow e + jet + X$ for small photon virtualities are presented. Single- and double-differential cross sections measured using $k_T$jet algorithmare discussed. In addition, extraction of values of $\alpha_s(M_Z)$ and energy-scale dependence of strong coupling constant is descibed.

1. Introduction

The study of jet production in ep collisions at HERA has been well established as a testingground of perturbative QCD (pQCD). Jet cross sections provided precise determinationsof the strong coupling constant, α_s, and its scale dependence. Jet observables in NC DIS [1] and photoproduction [2] were used as input [3] in a QCD analysis to extract the parton distribution functions (PDFs) of the proton; these data helped to constrain the gluon density at medium- to high-x values, where x is the fraction of the proton momentum carried by the gluon.These studies also demonstratedthat the $k_T$cluster algorithm in the longitudinally invariant inclusive mode resultsin the smallest uncertainties in the reconstruction of jets in ep collisions. The $k_T$algorithm is well suited for ep collisions and yields infrared- and collinear-safe crosssections at any order of pQCD. The results tested the performanceof these jet algorithms with data in a well understood hadron-induced reaction and it wasshown that pQCD calculations with up to four partons in the final state provide a gooddescription of the differences between jet algorithms.Measurements of inclusive-jet cross sections in photoproduction are presented in thispaper.

Two types of QCD processes contribute to jet production in photoproduction;at leading order they can be separated into [4, 5] the direct process, in which thephoton interacts directly with a parton in the proton, and the resolved process, in whichthe photon acts as a source of partons, one of which interacts with a parton in theproton.

Single-differential inclusive-jet cross sections as functions of the jet transverseenergy, E_{Tjet}, and pseudorapidity, η_{jet}, are presented based on the $k_T$jet algorithm [6]. In addition, measurements of cross sections are also presented as functions of E_{Tjet}in differentregions of η_{jet}, which have the potential to constrain further the gluon density at high$x$. Next-to-leading-order (NLO) QCD calculations using recent parameterisations of theproton and photon PDFs are compared to the measurements. A determination of $\alpha s(M_Z)$as well as of its energy-scale dependence are also presented. The analyses presented hereare based on a data sample with a more than three-fold increase in statistics with respectto the previous study [7].

2. Experimental set-up

A detailed description of the ZEUS detector can be found elsewhere [8, 9]. A brief outline of the componentscrusualfor this analysis is given below. The high-resolution uranium-scintillator calorimeter (CAL) [10] consisted of three parts: the forward (FCAL), the barrel (BCAL) and the rear (RCAL) calorimeters. Each part was subdivided transversely into towers and longitudinally into one electromagnetic section (EMC) and either one (in RCAL) or two (in BCAL and FCAL) hadronic sections (HAC). The smallest subdivision of the calorimeter was called a cell. The CAL energy resolutions, as measured under test-beam conditions, were $\sigma(E)/E = 0.18/\sqrt{E}$ for electrons and $\sigma(E)/E = 0.35/\sqrt{E}$ for hadrons, with E in GeV. The luminosity was measured using the Bethe-Heitler reaction $ep \rightarrow \gamma ep$by a luminosity detector which consisted of a lead-scintillator calorimeter [11] and an independent magnetic spectrometer [12]. The fractional uncertainty on the measured luminosity was 1.8 %.

3. Data selection

The data were collected during the running period 2005–2007, when HERA operated with protons of energy Ep = 920 GeV and electrons or positronsof energy Ee = 27.5 GeV, at an epcentre-of-mass energy of $\sqrt{\sqrt{s}}$ = 318 GeV, and correspond to an integrated luminosity of 299.9 ± -5.4 pb^{-1}. A three-level trigger system was used to select events online [9, 13].

Events from collisions between quasi-real photons and protons were selected offline using following criteria:

- a reconstructed event vertex along the Z axis within 35 cm of the nominal interaction point was required;
- cuts based on tracking information were applied to remove the contamination from beam-gas interactions, cosmic-ray showers and beam-halo muons;
- charged current DIS events were rejected by requiring the total missing transverse momentum, $p_{T,miss}$, to be small compared to the total transverse energy, $E_{T,tot}$, i.e. $p_{T,miss}/\sqrt{E_{T,tot}} < 2\ \sqrt{GeV}$;
- any NC DIS event with an identified scattered-electron candidate in the CAL was rejected (in the following, the term electron will refer to both the electron and positron, unless otherwise stated);
- the events were restricted to γpcentre-of-mass energies in the region 142 <Wp<293 GeV,where Wp = $\sqrt{sy}$; y is

the inelasticity and was estimated as $y_{JB} = (E - p_Z)/2E_e$, where E is the total energy measured in the CAL and p_Z is the longitudinal component of the total momentum.

After these selection criteria were applied, the contamination from beam-gas interactions, cosmic-ray showers and beam-halo muons was found to be negligible. The remaining background from NC DIS events was estimated by Monte Carlo (MC) techniques to be around 1 % and was neglected. The contamination from charged current DIS events was found to be even smaller. The selected sample consisted of events from ep interactions with $Q^2 < 1$ GeV^2, where Q^2 is the virtuality of the exchanged photon, and a median $Q^2 \approx 10^{-4}$ GeV^2, estimated using MC techniques.

3.1. Jet search

In photoproduction, jets are usually defined using the transverse-energy flow in the pseudorapidity-azimuth (η - φ) plane of the laboratory frame. The procedure to reconstruct jets with the $k_T$algorithm from an initial list of objects (e.g. final-state partons, final-state hadrons or energy deposits in the calorimeter) is described below in some detail. In the following discussion, $E_{T,i}$ denotes the transverse energy, $\eta_i$the pseudorapidity and $\varphi_i$the azimuthal angle of object i. For each pair of objects, the quantity $d_{ij} = \min((E_{T,i})^2, (E_{T,J})^2)\ [(\eta_i - \eta_J)2 + (\varphi_i - \varphi_j)2]/R_2$ is calculated, where Ris the jet radius. For each individual object, the distance to the beam, $d_i = (E_{T,i})^2$, is also calculated. If, of all the values $\{d_{ij}, d_i\}$, $d_{kl}$is the smallest, then objects kand lare combined into a single new object. If, however, $d_k$is the smallest, then object kis considered a jet and removed from the sample. The procedure is repeated until all objects are assigned to jets. For the measurements presented in this paper, the jet radius Rwas set to unity and the jet variables were defined according to the Snowmass convention. The k_T jet algorithmwas used to reconstruct jets in the hadronic final state from the energy deposits in the CAL cells. The jets reconstructed from the CAL cell energies are called calorimetric jets and the variables associated with them are denoted by $E_{T,jet,cal}$, $\eta_{jet,cal}$and $\varphi_{jet,cal}$.Sample of events was selected for further analysis, which contain at least one jet satisfying $E_{T,jet,cal} > 13$ GeV and $-1 < \eta_{jetcal} < 2.5$.

4. Monte Carlo simulations

Samples of events were generated to determine the response of the detector to jets ofhadrons and the correction factors necessary to obtain the hadron-level jet cross sections.In addition, these samples were used to estimate hadronisation corrections to the NLOcalculations.The MC programs Pythia6.146 and Herwig 6.504 were used to generateresolved and direct photoproduction events. Samples of Pythia including multiparton interactions (Pythia-MI) with a minimum transverse momentum for the secondary scatter, $p_{Tsec,min}$, of 1, 1.5 or2 GeV were used to simulate contributions from non-perturbative effects not related tohadronisation (NP), such as the underlying event. All the samples of generated eventswere passed through the Geant 3.21-based ZEUS detector- and trigger-simulationprograms. They were reconstructed and analysed by the same program chain as thedata. The jet search was performed on the MC events using the energy measured in the CALcells as described in Section 3. In addition, the jet algorithm was also appliedto the final-state particles (hadron level) and partons (parton level).

5. Results

Single- and double-differential inclusive-jet cross sections were measured in the kinematic region given by $Q^2 < 1$ GeV^{2}and $142 < Wp < 293$ GeV. These cross sections include every jet of hadrons with $E_{T,jet} > 13$ GeV and $-1 < \eta_{jet} < 2.5$ in each event. The *x* region covered by the measurements was determined to be $3\ 10^{-3} < x < 0.95$.

5.1. Single-differential cross sections

The measurements of the single-differential cross sections based on the k_T jet algorithmas functions of $E_{T,jet}$ and η_{jet} are presented in Fig. 1. The measured $d\sigma/dE_{T,jet}$ falls by over four orders of magnitude in the measured range. The measured $d\sigma/d\eta_{jet}$ displays a maximum around $\eta_{jet} \approx 1$.

The NLO QCD predictions are compared to the measurements in these Figures. The calculation reproduces the measured $d\sigma/dE_{T,jet}$ well. The measured $d\sigma/d\eta_{jet}$ is well described for $\eta_{jet.} < 2$; however, an excess of data with respect to the theory is observed for larger η_{jet} values. Such discrepancies have already been observed in previous studies of jet photoproduction [14, 15].The influence of non-perturbative effects not related to hadronisation in the predictions was investigated by using the NLO$\otimes$NP QCD calculations. The comparison of these calculations to the data is shown in Fig. 2.

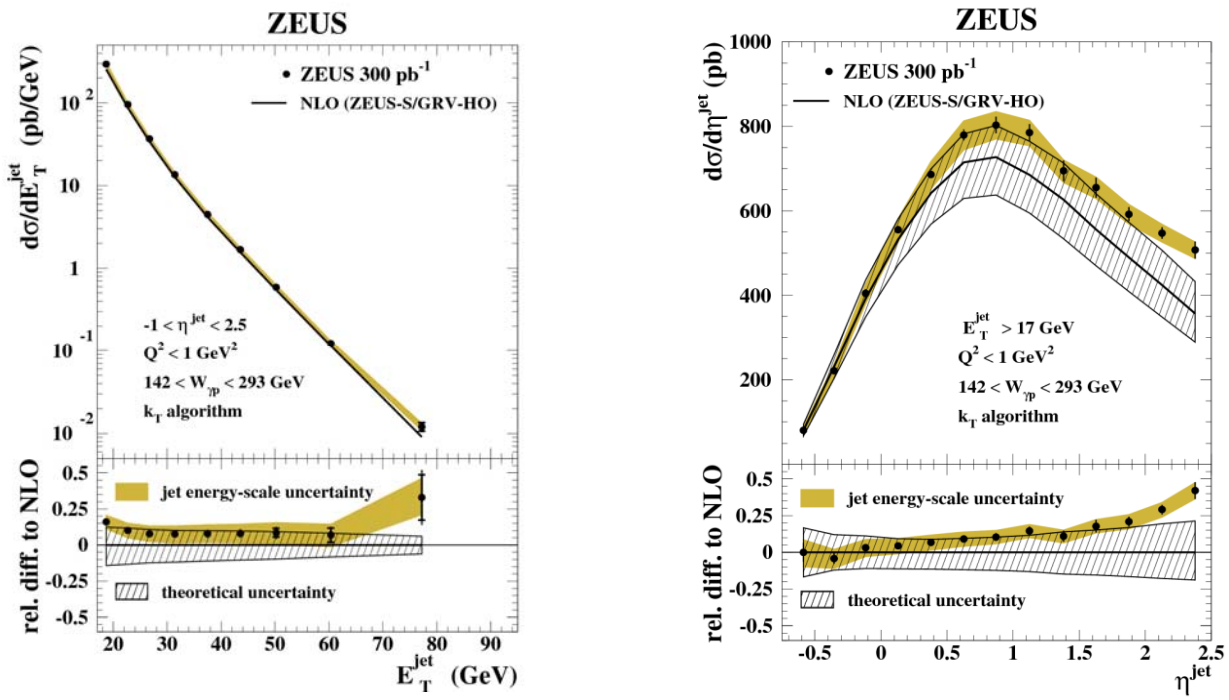

Fig. 1. *a* – The measured differential cross-section $d\sigma/dE_{T,jet}$ based on the $k_T$jet algorithm for inclusive-jet photoproduction with $-1 < \eta_{jet} < 2.5$ (dots) in the kinematic region given by $Q^2 < 1$ GeV^2 and $142 < Wp < 293$ GeV. The NLO QCD calculation (solid line), corrected to include hadronisation effects and using the ZEUS-S (GRV-HO) parameterisations of the proton (photon) PDFs, is also shown; bottom panel: therelative difference between the measured $d\sigma/dE_{T,jet}$ and the NLO QCD calculation(dots). *b* – The measured differential cross-section $d\sigma/d\eta_{jet}$ based on the $k_T$jet algorithm for inclusive-jet photoproduction. Other details as in the caption to Fig. 1, *a*.

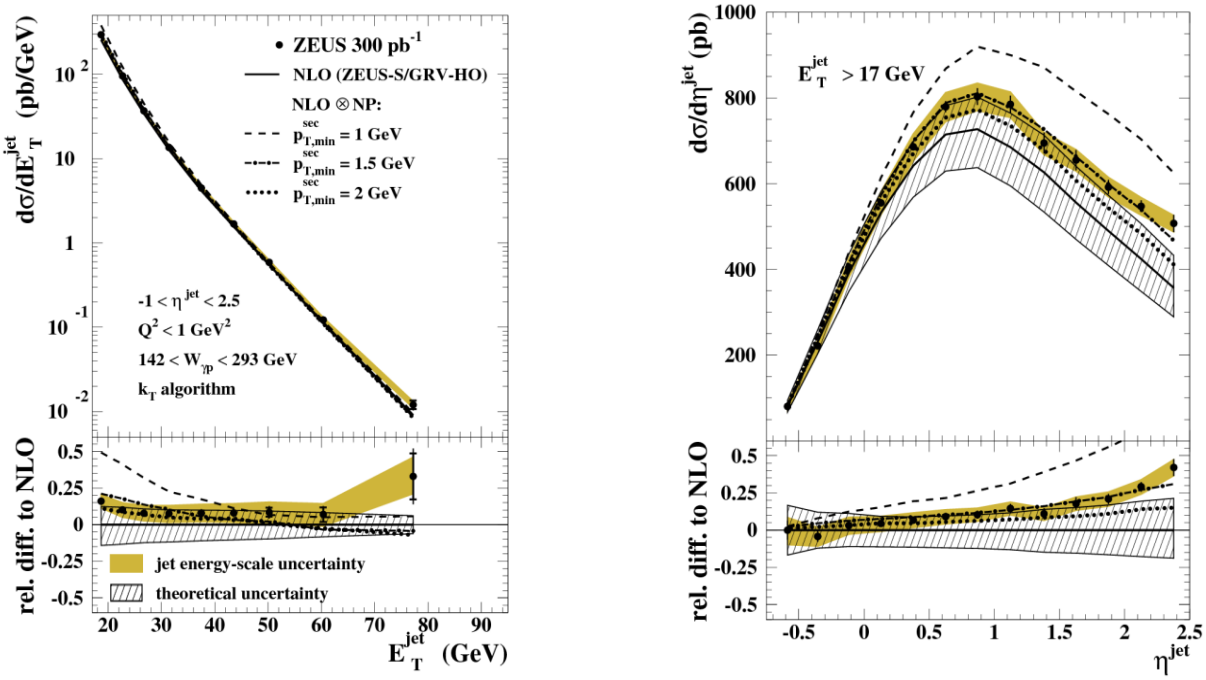

Fig. 2. The measured differential cross-sections (*a*) $d\sigma/dE_{T,jet}$ and (*b*) $d\sigma/d\eta_{jet}$ based on the $k_T$jet algorithm for inclusive-jet photoproduction with $E_{Tjet} > 17$ GeV and $-1 < \eta_{jet} < 2.5$ (dots) in the kinematic region given by $Q^2 < 1$ GeV^2 and $142 < Wp < 293$ GeV. For comparison, the NLO QCD calculations including an estimation of non-perturbative effects (see text) are also shown. Other details as in the caption to Fig. 1, *a*.

It is observed that the NLO⊗NP QCD calculations predict a larger jet rate at low $E_{Tjet}$and high η_{jet}, in the region where the NLO QCD prediction fails to describe the data. The NLO⊗NP QCD prediction with $p_{T,sec,min} = 1.5$ GeV is closest to the data. These observations indicate the possible presence of effects such as the underlying event in the data,

which are not included in the NLO QCD calculation. These non-perturbative contributions are expected to be unrelated to the hard scattering and approximately constant with the scale of the interaction, so that the ratio of this non-perturbative contribution to the jet transverse energy becomes smaller as E_{Tjet} increases, as seen in Fig. 2, *a*. This is supported by the good description of the data by the NLO QCD calculation for E_{Tjet}> 21 GeV (see Fig. 2, *a*) and by the inclusive-jet cross section as a function of $\eta_{jet}$for E_{Tjet}> 21 GeV (Fig. 3, *a*): the NLO QCD calculation gives a good description of the data in the whole measured range; in particular, discrepancies between data and theory are no longer observed at high values of η_{jet}. In addition, the differences between the NLO⊗NP predictions with different $p_{Tsec,min}$ values become smaller, as seen in Fig. 3, *b*.

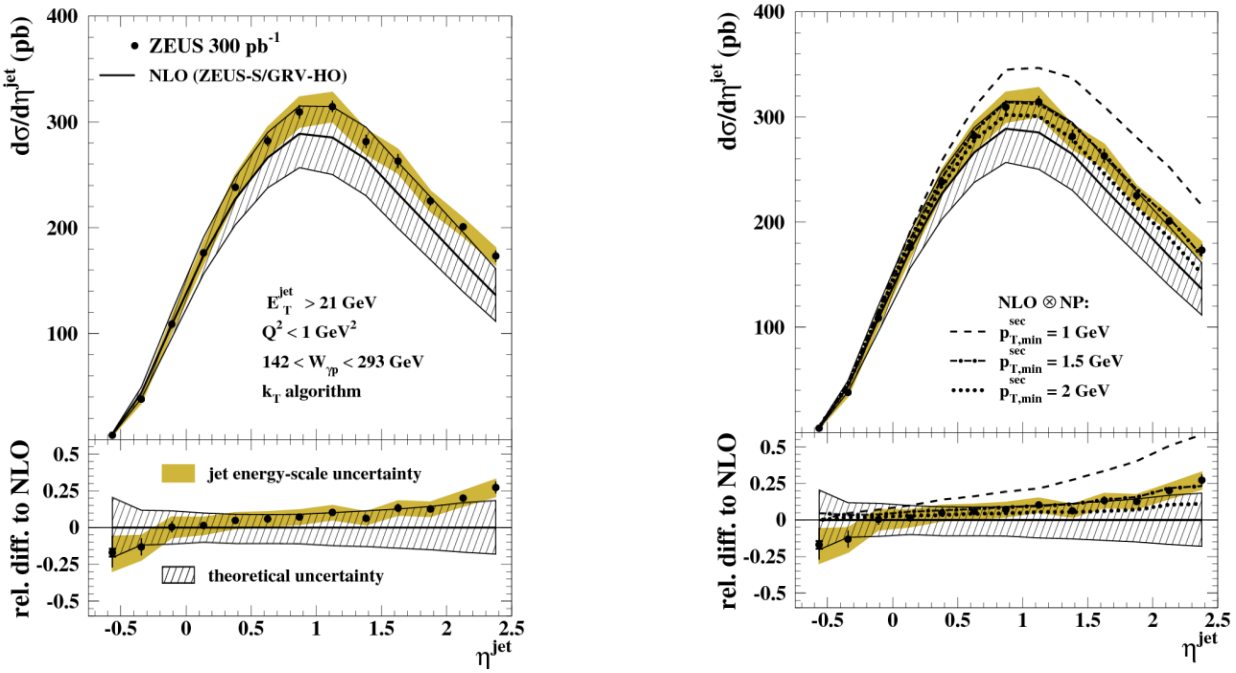

Fig. 3. The measured differential cross-section $d\sigma/d\eta_{jet}$ based on the $k_T$jet algorithm for inclusive-jet photoproduction with E_{Tjet}> 21 GeV (dots). In (*b*), the NLO QCD calculations including an estimation of non-perturbative effects (see text) are also shown. Other details as in the caption to Fig. 1, *a*.

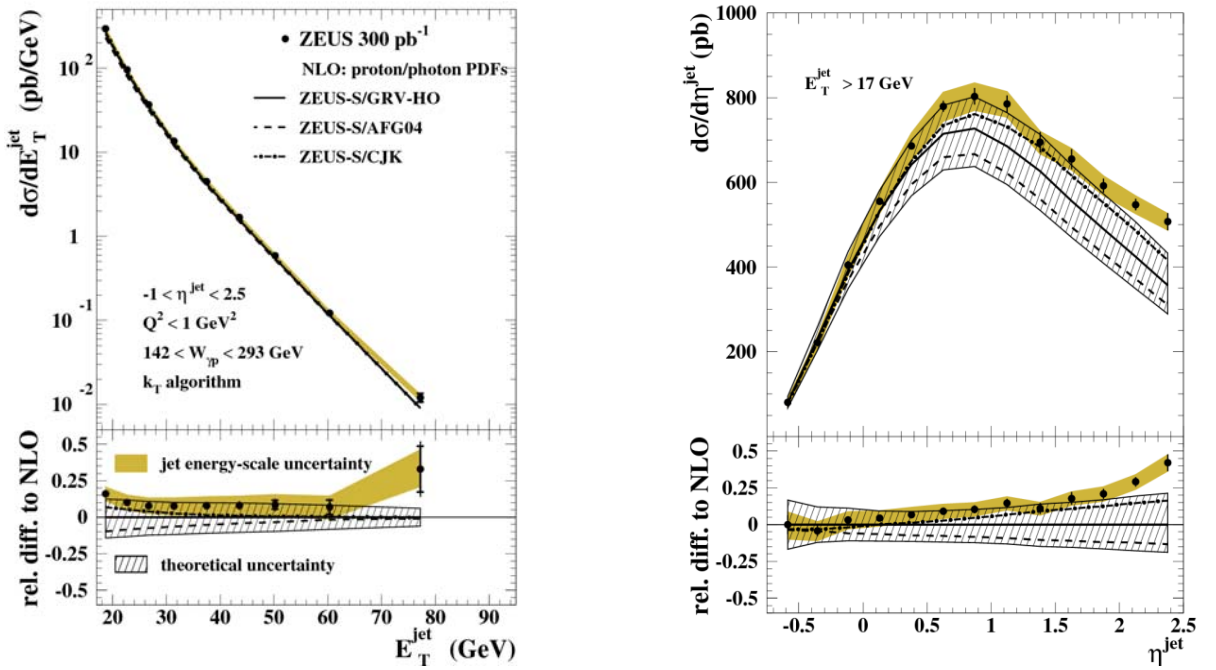

Fig. 4. The measured differential cross-sections (*a*) $d\sigma/dE_{T,jet}$ and (*b*) $d\sigma/d\eta_{jet}$based on the kT $k_T$jet algorithm for inclusive-jet photoproduction with E_{Tjet}>17 GeV and $-1 < \eta_{jet} < 2.5$(dots). For comparison, the NLO QCD calculations using different parameterisations of the photon PDFs are also shown. Other details as in the caption to Fig. 1, *a*

The influence of the poorly constrained photon PDFs on the predictions was investigated by comparing calculations based on different PDF sets to the data. Fig. 4 shows the measurements together with the NLO QCD predictions using alternatively the AFG04 and CJK sets of photon PDFs, together with the predictions based on the GRV-HO set. Some differences are observed between the three predictions, especially at low E_{Tjet} and high η_{jet}. In particular, the predictions based on AFG04 (CJK) are lower (higher) than those based on GRV-HO.

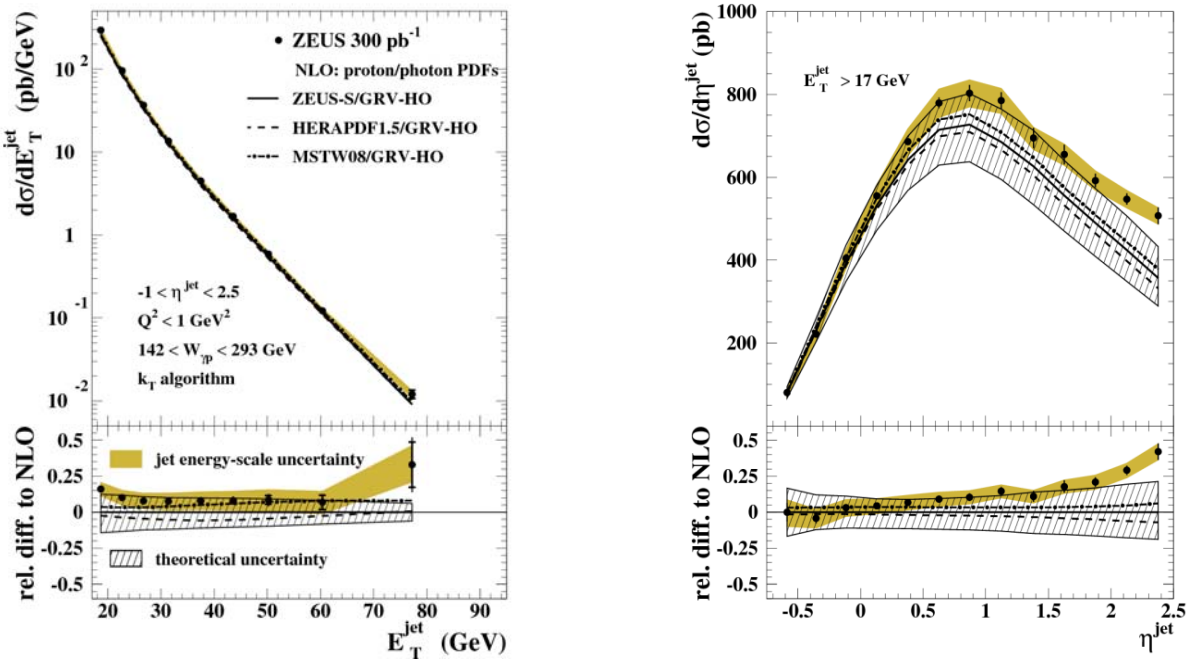

Fig. 5. The measured differential cross-sections (*a*) $d\sigma/dE_{T,jet}$ and (*b*) $d\sigma/d\eta_{jet}$based on the $k_T$jet algorithm for inclusive-jet photoproduction with E_{Tjet}>17 GeV and $-1 < \eta_{jet} < 2.5$ (dots). For comparison, the NLO QCD calculations using different parameterisations of the proton PDFs are also shown. Other details as in the caption to Fig. 1, *a.*

The influence of the proton PDFs on the predictions was investigated by comparing calculations based on different PDF sets to the data. Fig. 5 shows the measurements together with the NLO QCD predictions using alternatively the MSTW08 and HERAPDF1.5 sets of proton PDFs, together with the predictions based on the ZEUS-S set. The prediction based on HERAPDF1.5 is lower than that based on the ZEUS-S set in most of the phase space, whereas the MSTW08 prediction is higher at high E_{Tjet}. This region of phase space is not well constrained since the main contribution comes from the high-*x* gluon density in the proton. In summary, the measurements of inclusive-jet cross sections in photoproduction have the potential to constrain the proton and the photon PDFs. To study in more detail the sensitivity of the inclusive-jet cross sections to the proton and photon PDFs and findthe regions of phase space in which the data can add information to constrain further these PDFs, double-differential cross sections were measured and are presented in the next section.

5.2. Double-differential cross sections

The measurements of the inclusive-jet cross sections based on the $k_T$jet algorithm as functions of E_{Tjet}in different regions of η_{jet} are presented in Fig. 6, *a*. The measured cross sections exhibit a steep fall-off within the E_{Tjet} range considered. The E_{Tjet} dependence of the cross section becomes less steep as η_{jet} increases. The NLO QCD predictions are compared to the measurements in Fig. 6, *a*. They give a good description of the data, except at low E_{Tjet} and high η_{jet}. Fig. 6, *b* shows the relative difference of the measured differential cross sections to the NLO QCD calculations.

The data are well described by the predictions for $-1 < \eta_{jet} < 2.5$ in the whole E_{Tjet} range measured. For the region $2 < \eta_{jet} < 2.5$, where it is observed that non-perturbative effects not related to hadronisation might contribute significantly, the data are well described only for E_{Tjet}> 21 GeV. In the regions, in which the gluon-induced contribution is substantial and the possible presence of non-perturbative effects is expected to be minimised, the data have the potential to constrain the gluon density in the proton. Therefore, these high-precision measurements also have the potential to constrain the photon PDFs in these regions of phase space.

5.3. Determination of $\alpha_s(M_Z)$

The measured single-differential cross-sections $d\sigma/dE_{T,jet}$ based on the three jet algorithms were used to determine values of $\alpha_s(M_Z)$using the method presented in [1]. Only the measurements for E_{Tjet}> 21 GeV were used in the procedure to minimise the effects of a possible non-perturbative contribution in addition to that of hadronisation and the uncertainty coming from higher orders. The fit was restricted to E_{Tjet}< 71 GeV because of the relatively large

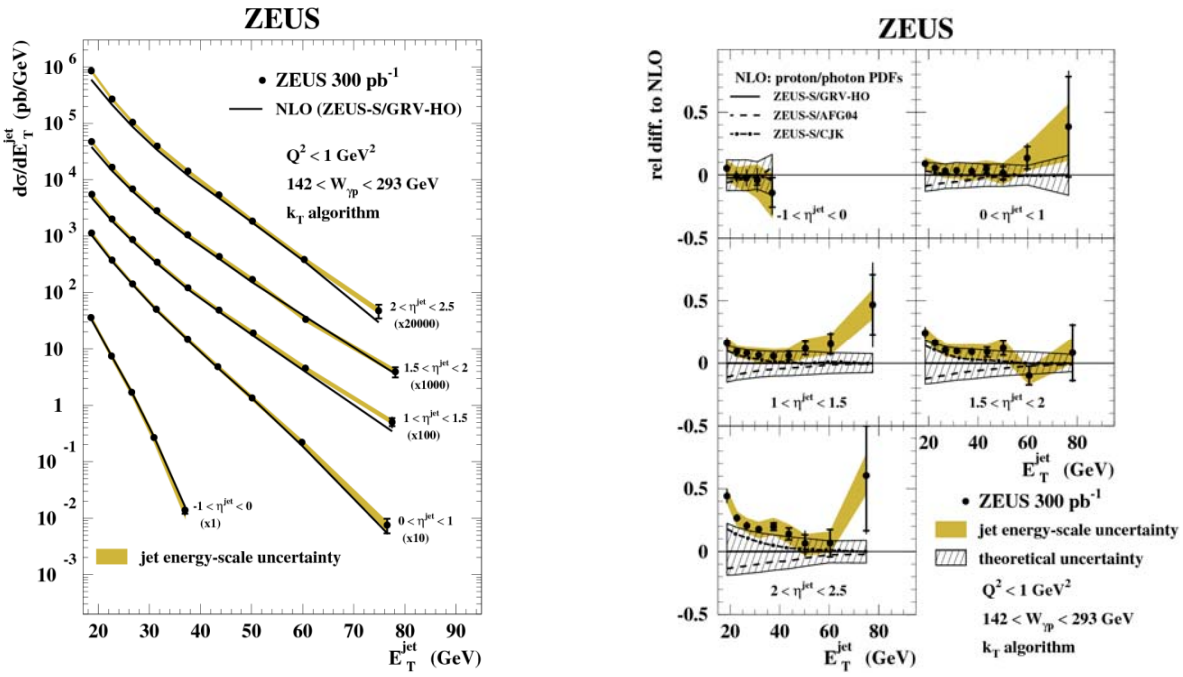

Fig. 6. *a* – The measured differential cross-sections $d\sigma/dE_{T,jet}$ based on the $k_T$jet algorithm for inclusive-jet photoproduction with $E_{Tjet}>17$ GeV in different regions of η_{jet} (dots). *b* – The relative differences between the measured differential cross-sections $d\sigma/dE_{T,jet}$ presented in Fig. 6, *a* and the NLO QCD calculations (dots). The relative differences between the predictions based on different photon PDFs and that based on the ZEUS-S/GRV-HO sets are also shown.

uncertainty coming from the proton PDFs for higher E_{Tjet} values. The experimental uncertainties on the extracted values of $\alpha_s(M_Z)$ were evaluated by repeating the analysis for each systematic check. The overall normalisation uncertainty from the luminosity determination was also included. The largest contribution comes from the uncertainty in the absolute jet energy scale. The largest contribution arises from the terms beyond NLO, which was estimated by using the method of Jones et al. [16]. The uncertainty due to the photon PDFs is of the same order as that arising from higher orders. The uncertainty due to the proton PDFs and that arising from the hadronisation effects were also estimated.The value of $\alpha_s(M_Z)$ obtained from the measured $d\sigma/dE_{T,jet}$ is

$$\alpha_s(M_Z) = 0.1206^{+0.0023}_{-0.0022}(exp.)^{+0.0042}_{-0.0035}(th.)$$

This determinationis consistent with previous determinations in NC DIS at HERA, with the results obtained in proton-antiproton collisions and have a precision comparable to those obtained in individual determinations from e^+e^- experiments. These values are also consistent with the world average, as well as with the HERA 2004 average and the HERA 2007 combined value.

5.4. Energy-scale dependence of α_s

The energy-scale dependence of α_s was determined from a NLO QCD fit to the measured $d\sigma/dE_{T,jet}$ cross section. Values of α_s were extracted at each mean value of measured E_{Tjet} without assuming the running of α_s. The method employed was the same as above, but parameterising the α_s dependence of $d\sigma/dE_{T,jet}$ in terms of $\alpha_s(<E_{Tjet}>)$ instead of $\alpha_s(M_Z)$, where $<E_{Tjet}>$i is the average E_{Tjet} of the data in each bin. The extracted values of α_s as a function of E_{Tjet} are shown in Fig. 7.

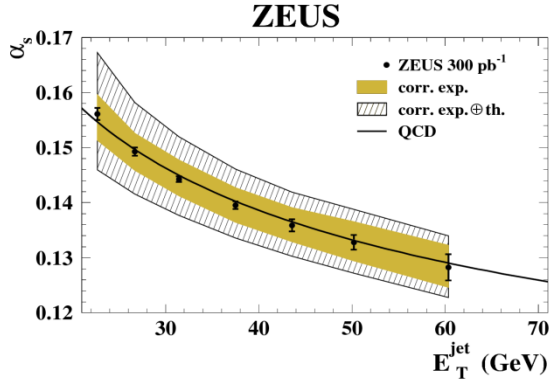

Fig. 7. The $\alpha_s$values determined in each $<E_{Tjet}>$ value from the analysis of themeasured $d\sigma/dE_{T,jet}$ cross section based on the kT jet algorithm (dots). The error bars represent the uncorrelated experimental uncertainties; the shaded area represents the correlated experimental uncertainties and the hatched area represents the correlated experimental and theoretical uncertainties added in quadrature. The solid line indicates the renormalisation-group prediction at two loops obtained from the corresponding $\alpha_s(M_Z)$ value determined in this analysis.

The data demonstrate the running of α_s over a large range in E_{Tjet} from a single experiment. The predicted running of the strong coupling calculated at two loops is in good agreement with the data.

6. Summary and conclusions

Measurements of differential cross sections for inclusive-jet photoproduction at a centre-ofmassenergy of 318 GeV using an integrated luminosity of 300 pb^{-1} collected by the ZEUSdetector have been presented. The cross sections refer to jets of hadrons of $E_{Tjet}>17$ GeV and $-1 <\eta_{jet}<2.5$ identified in the laboratory frame with the k_T jetalgorithm with jet radius R = 1. The cross sections are given in the kinematic region of $Q^2< 1$ GeV^2 and $142 <Wp<293$ GeV.

Measurements of single-differential cross sections were presented as functions of E_{Tjet} and η_{jet}t. The NLO QCD calculations provide a good description of the measured cross sections, except at high η_{jet}t. Non-perturbative effects not related to hadronisation and the influenceof the photon PDFs were found to be most significant in this region.Extracted value of α_s is in good agreement with the world and HERA averages. The extracted valuesof α_s as a function of E_{Tjet} are in good agreement with the predicted running of the strongcoupling over a large range in E_{jetT}.

REFERENCES

1. *Chekanov S. et al.* [ZEUS Collaboration] // Phys. Lett. - 2002. - Vol. B547. - P. 164.
2. *Chekanov S. et al.* [ZEUS Collaboration] // Eur. Phys. J. -2002. - Vol. C23. - P. 615.
3. *Chekanov S. et al.* [ZEUS Collaboration] // Eur. Phys. J. - 2005. - Vol. C42. - P. 1.
4. *Smith C.H. Llewellyn* // Phys. Lett. - 1978. - Vol. B79. - P. 83; *Kang I., Smith C.H. Llewellyn* // Nucl. Phys. - 1980. - Vol. B166. - P. 413; *Owens J.F.* // Phys. Rev. - 1980. - Vol. D21. - P. 54; *Fontannaz M., Mantrach A., Schiff D.* // Z. Phys. - 1980. - Vol. C6. - P. 241.
5. *Stirling W.J., Kunszt Z.* // Proc. HERA Workshop / R.D. Peccei (ed.). - Hamburg, Germany: DESY, 1987. - Vol. 2. - P. 331; *Drees M., Halzen F.* // Phys. Rev. Lett. - 1988. - Vol. 61. - P. 275; *Drees M., Godbole R.M.* // Phys. Rev. Lett. - 1988. - Vol. 61. - 682; *Drees M., Godbole R.M.* // Phys. Rev. - 1989. - Vol. D39. - P. 169; *Baer H., Ohnemus J., Owens J.F.* // Z. Phys. - 1989. - Vol. C42. - P. 657; *Baer H., Ohnemus J., Owens J.F.* // Phys. Rev. - 1989. - Vol. D40. - P. 2844.
6. *Abramowicz H. et al.* [ZEUS Collaboration] // Nucl. Phys. - 2012. - Vol. B864. - P. 1 - 37.
7. *Chekanov S. et al.* [ZEUS Collaboration] // Phys. Lett. - 2003. - Vol. B560. - P. 7.
8. *Derrick M. et al.* [ZEUS Collaboration] // Phys. Lett. - 1992. - Vol. B293. - P. 465.
9. *ZEUS Collaboration* / U. Holm (ed.). The ZEUS Detector. Status Report (unpublished), DESY(1993), available on http://www-zeus.desy.de/bluebook/bluebook.html
10. *Derrick M. et al.* // Nucl. Instr. Meth. - 1991. - Vol. A309. - P. 77.
11. *Andruszk´ow J. et al.* - DESY, 1992. - (Preprint DESY-92-066).
12. *Helbich M. et al.* // Nucl. Instr. Meth. - 2006. - Vol. A565. - P. 572.
13. *Smith W.H., Tokushuku K., Wiggers L.W.* // Proc. Computing in High-Energy Physics (CHEP) / Ed. by C. Verkerk, W. Wojcik (Annecy, France, Sept. 1992). - Geneva, Switzerland: CERN. - 1992. - P. 222. Also in preprint DESY 92-150B.
14. *Chekanov S. et al.* [ZEUS Collaboration] // Phys. Rev. - 2007. - Vol. D76. - P. 072011.
15. *Chekanov S. et al.* [ZEUS Collaboration] // Nucl. Phys. - 2008. - Vol. B792. - P. 1.
16. *Jones R.W.L. et al.* // JHEP. - 2003. - Vol. 0312. - P. 007.

EXCLUSIVE VECTOR MESON PRODUCTION

V. Aushev[1], D. Szuba[2], A. Levy[3], S. Kananov[3], V. Bondar[1], R. Shevchenko[4]

[1] Taras Shevchenko National University, Kyiv, Ukraine
[2] Hamburg University, Institute of Experimental Physics, Hamburg, Germany
[3] Raymond and Beverly Sacker Faculty of Exact Sciences, School of Physics, Tel Aviv University, Tel Aviv, Israel
[4] National Technical University of Ukraine "Kyiv Polytechnic Institute", Kyiv, Ukraine

The production of ground state vector mesons, V = ρ, ω, φ, J/ψ,Y, has been extensively studied at ep collider. Latest results were obtained from the study of two pion exclusive electroproduction in the mass range $0.4 < M_{\pi\pi} < 2.5$ GeV using 82 pb^{-1} of integrated luminosity collected during 1998 - 2000 on ep collider with center-of-mass energy 318 GeV. The analysis was carried out in the kinematic range of $2 < Q^2 < 80$ GeV^2, $32 < W < 180$ GeV and $|t| < 0.6$ GeV^2. The two-pion invariant mass distribution is interpreted in terms of the pion electromagnetic form factor, $|F(M_{\pi\pi})|$, assuming that the studied mass range includes the contributions of the ρ, ρ' and ρ'' vector meson states. The masses and widths of resonances are obtained and subsequently the Q^2 dependence of the cross-section ratios $\sigma(\rho' \to \pi\pi)/\sigma(\rho)$ and $\sigma(\rho'' \to \pi\pi)/\sigma(\rho)$ was extracted. The pion form factor obtained in the present analysis is compared to that obtained in $e^+e^- \to \pi^+\pi^-$.

1. Introduction

Exclusive electroproduction of vector mesons, $\gamma^* p \to Vp$, at large centre-of-mass energy, W, and large γ^* virtuality, Q^2, is usually viewed as a three-step process: the virtual photon γ^* fluctuates into a qq pair which then interacts with the proton through a two gluon ladder and hadronizes into a vector meson, V. The production of ground state vector mesons, V = ρ, ω, φ, J/ψ,Y , which are 1S triplet qq states, has been extensively studied at ep collider, paritcularly in several recent publications [1–4]. It was found that the process becomes hard with the increase of the photon virtuality Q^2 and can be described in perturbative Quantum Chromodynamics (pQCD).

Few main results in vector-mesons study were obtained: cross-sections have been measured as a function of W, Q^2 and t, also effective pomeron trajectory has been obtained. Also, helicity structure have been measured through the angular distributions of the decay particles. The extracted spin-density matrix elements strongly support the hypothesis of s-channel helicity conservation [1 - 4].

The ψ(2S) state is the only radially excited 2S triplet qq state studied so far has [4]. In this study only the photoproduction reaction was investigated and the low cross-section ration of ψ(2S) to the ground-state J/ψ supported the existance of a suppression effect, expected if a node in the ψ(2S) wave-function is present.

Other excited vector-meson states, in particular those consisting of light quarks, can be used to study the effect caused by changing the scanning size. The $\pi^+\pi^-$ mass distribution shows a complex structure in the mass range of 1 - 2 GeV [5]. Evidence for two excited vector-meson states has been established; the ρ' (1450) is assumed to be predominantly a radially excited 2S state and the ρ''(1700) is an orbitally excited 2D state, with some mixture of the S and D waves. In addition, there is also the $\rho_3(1690)$ spin 3 meson which has a ππ decay mode. These resonances can be studied through their two-pion decay mode, related to the pion electromagnetic form factor, Fπ(Mππ) [6].

The study of exclusive electroproduction of two pions, $\gamma^* p \to \pi^+\pi_-$, is presented in two-pion mass range $0.4 < M_{\pi\pi} < 2.5$ GeV, in the kinematic range $2 < Q^2 < 80$ GeV^2, $32 < W < 180$ GeV and $|t| < 0.6$ GeV^2.

The analyzed data were collected at the ep collider in the years 1998 - 2000, when 920 GeV protons collided with 27.5 GeV electrons or positrons with center-of-mass energy 318 GeV. The sample used for this study corresponds to 81.7 pb^{-1}.Details of data selection and reconstruction can be found in [7].

2. The ππ mass fit

The $\pi^+\pi^-$ mass distribution, after acceptance correction, is shown in Fig. 1. A clear peak is seen in the ρ mass range. A small shoulder is apparent around 1.3 GeV and a secondary peak at about 1.8 GeV.

The two pion invariant mass distribution was fitted as a sum of two terms,

$$\frac{dN(M_{\pi\pi})}{dM_{\pi\pi}} = A\left(1-\frac{4M_\pi^2}{M_{\pi\pi}^2}\right)\left[\left(F_\pi(M_{\pi\pi})\right)^2 + B\left(\frac{M_0}{M_{\pi\pi}}\right)^n\right], \quad (1)$$

where A is an overall normalization constant and M_π is the pion mass. The second term is a parameterization of the non-resonant background with constant parameters B, n and $M_0 = 1$ GeV. The other parameters (the masses and widths of the resonances and their relative contributions β and γ) enter through the pion form factor F_π. The fit, which includes 11 parameters, gives a good description of the data (χ^2/ndf = 28.8/24 = 1.2). The result of the fit is shown in Fig. 1 together with the contribution of each of the two terms of Eq. (1). The ρ and the ρ'' signals are clearly visible. The negative interference between all the resonances results in the ρ' signal to appear as a shoulder. For better illustration of these phenomena, the data is shown in Fig. 2 in linear scale and limited to $M_{\pi\pi} > 1.2$ GeV, with separate contribution of the background, three resonant amplitudes as well as their total interference term. The fit parameters are listed in Table 1.

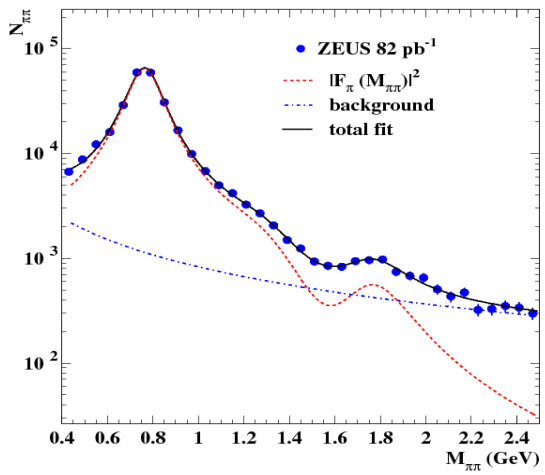

Fig. 1. The two-pion invariant-mass distribution, $M_{\pi\pi}$: $N_{\pi\pi}$ – the acceptance-corrected number of events in each bin of 60 MeV; dots – the data; solid line – the result of a fit using the Kuhn - Santamaria parameterization; dashed line – the result of the pion form factor normalized to the data; the dash-dotted line – the background contribution.

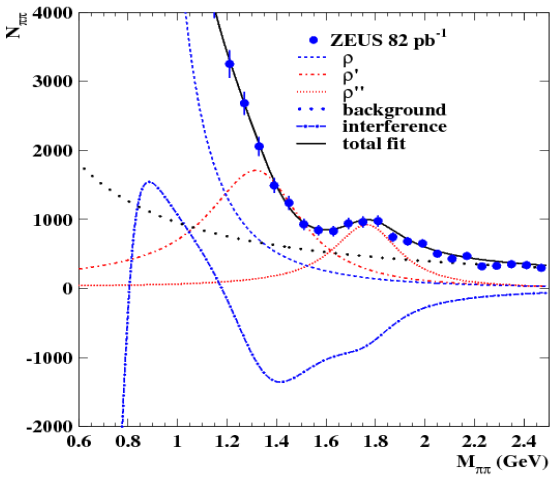

Fig. 2. The two-pion invariant-mass distribution, $M_{\pi\pi}$: $N_{\pi\pi}$ – the acceptance-corrected number of events in each bin of 60 MeV; dots – the data; solid line – Kuhn - Santamaria parameterization fit. The contributions of the three resonances ρ, ρ' and ρ'' are shown as dashed, dash-dotted and dotted lines, respectively. The sum of their interferences is shown by the long-dash-dotted line; sparse dotted line – the background.

Table 1. **Fit parameters obtained using $F_\pi(M_{\pi\pi})$ parameterization. The first uncertainty is statistical, the second one – systematic. Also the masses and widths from PDG are shown**

Parameter	ZEUS	PDG
M_ρ (MeV)	$771 \pm 2^{+2}_{-1}$	775.49±0.34
Γ_ρ (MeV)	$155 \pm 5 \pm 2$	149.1±0.8
β	$-0.27 \pm 0.02 \pm 0.02$	
$M_{\rho'}$ (MeV)	$1350 \pm 20^{+20}_{-30}$	1465±25
$\Gamma_{\rho'}$ (MeV)	$460 \pm 30^{+40}_{-45}$	400±60
γ	$0.10 \pm 0.02^{+0.02}_{-0.01}$	
$M_{\rho''}$ (MeV)	$1780 \pm 20^{+15}_{-20}$	1720±20
$\Gamma_{\rho''}$ (MeV)	$310 \pm 30^{+25}_{-35}$	250±100
B	$0.41 \pm 0.03 \pm 0.07$	
n	$1.30 \pm 0.06^{+0.18}_{-0.13}$	

The negative value of β and positive value of γ implies that the relative signs of the amplitudes of the three resonances ρ, ρ' and ρ'' is +,−,+, respectively. A similar pattern was observed in $e^+e^- \to \pi^+\pi^-$ and τ-decay experiments [8 - 11], which also showed a dip in the mass range around 1.6 GeV, resulting from destructive interference. There is a single experiment where a constructive interference was obtained around 1.6 GeV, namely $\gamma p \to p\pi^+\pi^-$, a result which is not understood.

3. Q^2 dependence of the pion form factor

The Q^2 dependence of the relative amplitudes was determined by performing the fit to $M_{\pi\pi}$ in three Q^2 regions, 2 - 5, 5 - 10 and 10 - 80 GeV^2. The masses and widths of the three resonances were fixed to the values found in the overall fit and listed in Table 1. The results are shown in Fig. 3. A reasonable description of the data is achieved in all three Q^2 regions.

The corresponding values of β and γ are given in Table 2. The absolute value of β increases with Q^2 while the value of γ is consistent with no Q^2 dependence, within large uncertainties.

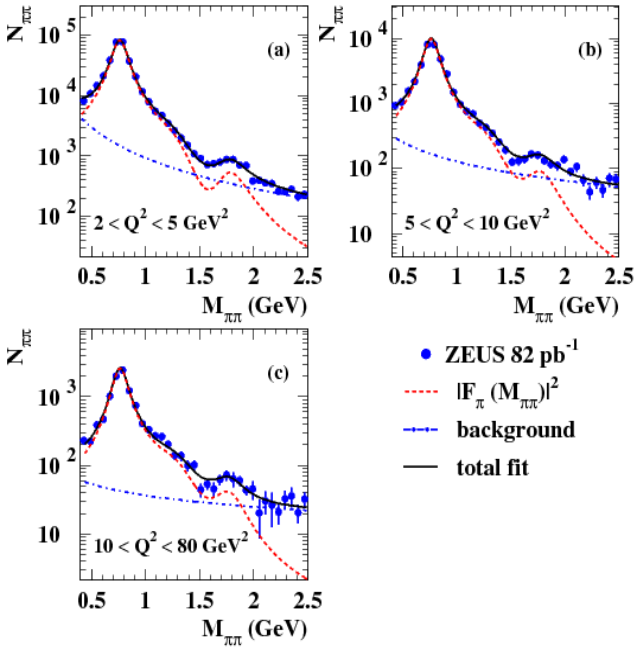

Fig. 3.The two-pion invariant-mass distribution, $M_{\pi\pi}$: $N_{\pi\pi}$ – the acceptance-corrected number of events in each bin of 60 MeV,; dots – the data; solid line – Kuhn-Santamaria parameterization fit; dashed line – the pion form factor normalized to the data; dash-dotted line denotes the background contribution.

Table 2. **The Q^2 dependence of the β and γ parameters. Masses and widths are fixed to the values given in Table 1. The first uncertainty is statistical, the second one – systematic**

$Q^2(\mathrm{GeV}^2)$	2–5	5–10	10–80
β	$-0.249 \pm 0.008^{+0.005}_{-0.003}$	$-0.282 \pm 0.008^{+0.005}_{-0.008}$	$-0.35 \pm 0.02 \pm 0.01$
γ	$0.100 \pm 0.009 \pm 0.003$	$0.098 \pm 0.012^{+0.005}_{-0.003}$	$0.118 \pm 0.022^{+0.008}_{-0.006}$

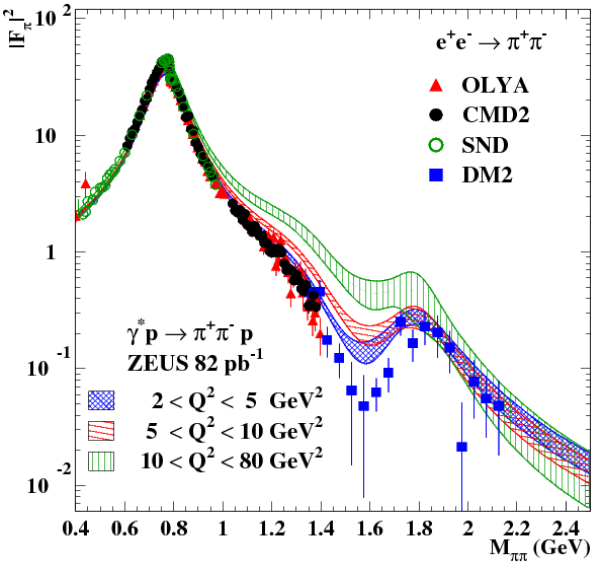

Fig. 4. The square of the pion form factor $|F_\pi|^2$ as a function of the $\pi^+\pi^-$ invariant mass, $M_{\pi\pi}$, as obtained from the reaction $e^+e^- \to \pi^+\pi^-$ [5, 10], shaded bands: crossed lines – the pion form factor squared obtained in the present analysis within Q^2: 2 - 5 GeV^2; horizontal lines – 5 - 10 GeV^2 and vertical lines – 10 - 80 GeV^2.

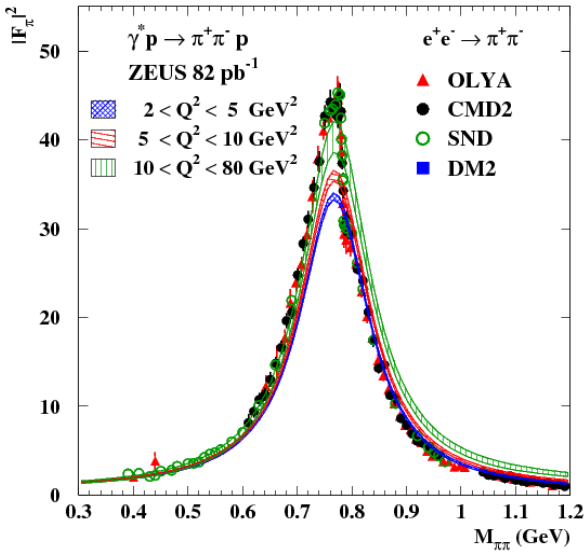

Fig. 5. The square of the pion form factor $|F_\pi|^2$, in the ρ mass region, as a function of the $\pi^+\pi^-$ invariant mass, $M_{\pi\pi}$, as obtained from the reaction $e^+e^- \to \pi^+\pi^-$, shaded bands: crossed lines – the pion form factor squared obtained in the present analysis within Q^2: 2 - 5 GeV^2; horizontal lines – 5 - 10 GeV^2 and vertical lines – 10 - 80 GeV^2.

The $|F_\pi(M_{\pi\pi})|^2$ obtained from the reaction $e^+e^- \to \pi^+\pi^-$ is shown in Fig. 4. It is also shown the curves representing the pion form factor as obtained in the present analysis for the three Q^2 ranges: 2–5, 5–10, 10–80 GeV^2. In general, the features of the $|F_\pi(M_{\pi\pi})|^2$ distribution observed here are also observed in e^+e^-, i.e., the prominent ρ peak, a shoulder around the ρ' and a dip followed by an enhancement in the ρ'' region. Above the ρ region, where the interference between the ρ' and the ρ'' start to dominate, we observe a Q^2 evolution which bring the lowest Q^2 range results from the present analysis close to those of e^+e^-. However, in the ρ peak reagion, shown in Fig. 5, the pion form factor $|F_\pi(M_{\pi\pi})|^2$ is highest at the highest Q^2 value, like in the ρ'-ρ'' interference region, while the e^+e^- data are higher than the highest Q^2 range. They are equal within errors for $M_{\pi\pi} > 1.8$ GeV.

4. Cross-section ratios as a function of Q^2

The ππ branching ratios of ρ' and ρ'' are poorly known. Therefore we study here the ratio R_V defined as

$$R_V = \frac{\sigma(V) \cdot Br(V \to \pi\pi)}{\sigma(\rho)}, \tag{2}$$

where σ is the cross section for vector meson production and $Br(V \to \pi\pi)$ is the branching ratio of the vector meson V (ρ', ρ'') into ππ. The ratio R_V may be directly determined from the results of the $M_{\pi\pi}$ mass fit,

$$R_{\rho'} = \beta^2 \frac{I_{\rho'}}{I_\rho} \quad R_{\rho''} = \gamma^2 \frac{I_{\rho''}}{I_\rho}, \tag{3}$$

$$I_V = \int dM_{\pi\pi} BW_V M_{\pi\pi}^2, \tag{4}$$

and the integration is carried out over the range $2M_\pi < M_{\pi\pi} < M_V + 5\Gamma_V$.

Fig. 6 shows and Table 3 lists the ratio R_V for V = ρ', ρ'' , as a function of Q^2.

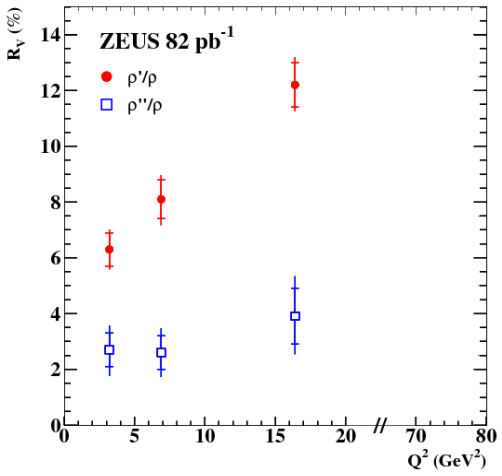

Fig. 6. The ratio R_V as a function of Q^2 for V = ρ' (full circles) and ρ'' (open squares). The inner error bars indicate the statistical uncertainty, the outer error bars represent the statistical and systematic uncertainty added in quadrature.

Table 3. **The dependence of the Q^2 value on the ratio R_V for V = ρ' and ρ''. The first uncertainty is statistical, the second one – systematic**

$Q^2(\mathrm{GeV}^2)$	2–5	5–10	10–80
$R_{\rho'}$	$0.063 \pm 0.006 \pm 0.004$	$0.081 \pm 0.007^{+0.006}_{-0.005}$	$0.122 \pm 0.008^{+0.005}_{-0.006}$
$R_{\rho''}$	$0.027 \pm 0.006^{+0.004}_{-0.003}$	$0.026 \pm 0.006 \pm 0.003$	$0.039 \pm 0.010^{+0.003}_{-0.005}$

One can clearly state that the value of $R_{\rho'}$ increases with Q^2. This rise has been predicted by several models. The suppression of the 2S state (ρ') is connected to a node effect which results in cancellations of contributions from different impact parameter regions at lower Q^2 value, while at higher value of Q^2 the effect of cancellation vanishes.

5. Summary

Exclusive two pion electroproduction has been studied in the mass range $0.4 < M_{\pi\pi} < 2.5$ GeV, $2 < Q^2 < 80$ GeV^2, $32 < W < 180$ GeV and $|t| \leq 0.6$ GeV^2.

The mass distribution is well described by the pion electromagnetic form factor which includes three resonances, ρ, ρ'(1450) and ρ''(1700).

A Q^2 dependence of $|F_\pi(M_{\pi\pi})|^2$ is observed, visible in particular in the interference region between ρ' and ρ''. The electromagnetic pion form factor obtained from the present analysis is lower (higher) than the one obtained from $e^+e^- \to \pi^+\pi^-$ for $M_{\pi\pi} < 1$ GeV ($1 < M_{\pi\pi} < 1.8$ GeV). They are equal within errors for $M_{\pi\pi} > 1.8$ GeV.

The Q^2 dependence of cross section ratios $R_{\rho'} = \sigma(\rho' \to \pi\pi)/\sigma(\rho)$ and $R_{\rho''} = \sigma(\rho'' \to \pi\pi)/\sigma(\rho)$, has been studied. The ratio $R_{\rho'}$ rises strongly with Q^2, as expected in QCD-inspired models in which the wave-function of the vector meson is calculated within the constituent quark model, which allows the presence of the nodes in the wave-function.

REFERENCES

1. *Aaron F.D. et al.* [H1 Collaboration]. Diffractive Electroproduction of rho and phi Mesons at HERA // JHEP. - 2010. - Vol. 05. - P. 032.
2. *Breitweg J. et al.* [ZEUS Collaboration]. Measurement of exclusive ω electroproduction at HERA // Phys. Lett. - 2000. - Vol. B487. - P. 273.
3. *Aktas A. et al.* [H1 Collaboration]. Elastic J/ψ production at HERA // Eur. Phys. J. - 2006. - Vol. C46. - P. 585.
4. *Adloff C. et al.* [H1 Collaboration]. Diffractive photoproduction of ψ(2S) mesons at HERA // Phys. Lett. - 2002. - Vol. B541. - P. 251.
5. *Barkov L.M. et al.* Electromagnetic pion form factor in the timelike region. // Nucl. Phys. - 1985. - Vol. B256. - P. 365.
6. *Polyakov M.V.* Hard exclusive electroproduction of two pions and their resonances // Nucl. Phys. - 1999. - Vol. B555. - P. 231.
7. *Abramowicz H. et al.* [ZEUS Collaboration]. Exclusive electroproduction of two pions at HERA // Eur. Phys. J. - 2012. - Vol. C72 - P. 1869.
8. *Bisello D. et al.* [CDM2 Collaboration]. The pion electromagnetic form factor in the time-like energy range $1.35 < \sqrt{s} < 2.4$ GeV // Phys. Lett. - 1989. - Vol. B220. - P. 312.
9. *Akhmetshin R.R. et al.* [CDM2 Collaboration]. Measurement of $e^+e^- \to \pi^+\pi^-$ cross section with CMD-2 around ρ meson // Phys. Lett. - 2002. - Vol. B527. - P. 161.
10. *Aul'chenko V.M. et al.* [CDM2 Collaboration]. Measurement of the pion form factor in the range 1.04 - 1.38 GeV with the CMD-2 detector. // JETP. - 2005. - Vol. Lett. 82. - P. 743.
11. *Aubert B. et al.* [BABAR Collaboration]. Precise measurement of the $e^+e^- \to \pi^+\pi^-$ (γ) cross section with the initial state radiation method at BABAR // Phys. Rev. - 2009. - Vol. Lett. 103. - P. 231801.

INFLUENCE OF TUBULAR INITIAL CONDITIONS ON PION SPECTRA IN A + A COLLISIONS

M. S. Borysova[1], Iu. A. Karpenko[2], Yu. M. Sinyukov[2]

[1] *Institute for Nuclear Research, National Academy of Sciences of Ukraine, Kyiv, Ukraine*
[2] *M. M. Bogolyubov Institute for Theoretical Physics, National Academy of Sciences of Ukraine, Kyiv, Ukraine*

The long-range structure of two-particle angular correlation functions is modified significantly by the presence of sharp inhomogeneities in a hot and dense matter formed in relativistic heavy ion collisions. It has been argued that the ridge phenomenon observed in two-particle angular correlations in relativistic A + A collisions is rooted probably in the initial conditions (IC) of the thermal evolution of the system. The aim of this study is to analyze the IC of the system leading to the ridge structures. As motivated by the glasma-flux-tube scenario, the IC were modeled by the sets of different number of high energy-density tube-like fluctuations with longitudinally homogeneous structure within some space-rapidity region in a boost-invariant 2D geometry. The influence of a fluctuating bumping structure of the IC on bulk observables and the collective evolution of matter created in A+A collisions in the frameworks of the Hydro-Kinetic Model (HKM) is investigated. The description of spectra with the 2+1 HKM, which allows describing all the stages of the system evolution as well as a formation of the particle momentum at the decoupling stage is done with inclusion of tubular IC. Its impact on the transverse pion spectra, integrated spectra and the flows is analyzed.

Introduction

The structure and properties of the matter under extremely hot and/or dense conditions are of fundamental interest and provide unique environments for studying the strongest force of Nature. The hot deconfined matter, the so-called quark-gluon plasma (QGP), was part of the history for cosmic evolution after the Big Bang and has now been created via relativistic heavy ion collisions (the "Little Bang") and explored in laboratory experiments at the Relativistic Heavy Ion Collider (RHIC) and the Large Hadron Collider (LHC). Correlations and fluctuations are an invaluable tool for probing the dynamics of heavy-ion collisions. Data from the experiments at RHIC revealed interesting features in the two-particle correlation landscape [1 - 4]. Specifically, an excess of correlated particles are observed in a narrow "ridge" near $\Delta\varphi = 0$ and the away side peak at $\Delta\varphi = \pi$, that was firstly measured in the relativistic heavy-ion collisions by the STAR collaboration [1]. The discovery of the ridge has provoked a lot of theoretical analyses. Early models of the "soft" or untriggered ridge formation proposed at times strikingly different explanations. The novel observation of Alver and Roland that the correlations arising from geometrical fluctuations result in odd flow harmonics such as triangular flow, v_3, suggests that v_3 , together with flow harmonics of all higher orders, explains this excess [5]. It has recently been shown in measurements [6 - 9] and demonstrated in various modelings [10 - 12] that there are fairly strong fluctuations in the initial matter profile from event to event. Such fluctuations contain various higher order harmonics in azimuthal angle $\sim \cos(n\varphi)$. In the collective expansion of the bulk matter, these fluctuations lead to observed harmonic flows up to about n = 6 and explain the soft di-hadron azimuthal correlations (the "soft-ridge"). This suggests that what were formerly thought to be indications of jet-medium interactions may well result simply from the presence of higher-order flow harmonics, arising through a combination of nucleon position fluctuations and viscous effects.

If the "soft ridge" structure is caused by the peculiarities of the bulk matter, then the explanations based on the hydrodynamics models of A + A collisions are to the point. During more than 50 years the hydrodynamic models were based on the smooth initial energy density profiles (see, e.g. [13, 14] for the ridge problem). However, it has been shown that fluctuations in the positions of nucleons within the colliding nuclei may lead to significant deviations from the smooth profiles event-by-event [15]. They result in lumpy IC which has no particular symmetry, and this lumpiness should be taken into account in fluid dynamical calculations [16 - 19]. More precisely, one should calculate the azimuthal distribution for each initial condition, then average over IC.

It was proposed in [20] to study the possible typical (or "representative") configuration of initial fluctuations which are already maximally symmetric in the azimuthal plane, instead of averaging the result over many fluctuations. It was found that for the different initial energy-density configurations, the effect of the initial bumping-like fluctuations is not washed out during the system expansion and preserve in the final energy density of hadronic matter [21, 22]. To test the influence of this effect on the observed particle spectra and appearance of the ridge structure, this paper examines the angular dependence of the particle (pion) spectra for such IC. For this purpose we use the Hydro-Kinetic Model (HKM) [23] which incorporates description of all the stages of the system evolution as well as a formation of the particle momentum at the decoupling stage, with longitudinally homogeneous and a transversally bumping IC. To highlight the role of pure fluctuations, we limit our study in the present paper only by the most central collisions, and to be specific we do calculations for RHIC $\sqrt{s}$ = 200 GeV collisions. Unlike to non-central collisions with strong anisotropy already in the average geometry and dominated by the 2nd harmonics, in the perfectly central collisions (b = 0) the average background geometry is isotropic and the anisotropy from various harmonic fluctuations will be best manifested.

Methods, results and discussion

In this section the results obtained by numerical calculations on the basis of the 2 + 1 HKM that includes the transversally bumping tube-like IC with the aim to study how the initial fluctuations in the energy density distribution affect the spectra are presented and discussed. For the sake of simplicity, the emission of the only one kind of particles (negative pions, π^-) from the expanding fireball is considered. The analysis is based on the Boltzmann equations of the hydrodynamic approach to relativistic nucleus-nucleus (A + A) collisions. It is consistent with the conservation laws and accounts for the opacity effects. We use Bjorken-type IC of quasi-inertial flow at proper time: boost-invariance of the system in the longitudinal *z*-direction and zero initial longitudinal flow without transverse collective expansion in *xy*-plane. The hydrodynamic evolution starts at the time τ_0 = 0.2 fm/c. Two types of initial configurations were examined. The first one corresponds to the smooth Gaussian profile with a radius *R* and energy density *E* as was considered in [23]. The second type of initial scenarios is based on bumping tube-like initial fluctuations at τ_0. These tubes are rather thin transversally and relatively long in the direction of beam axis, with the transverse (gaussian) radii a_i in the energy density *E*. The general initial energy-density distribution *E* at τ_0 is given by

$$E = E_b \exp\left[-\frac{x^2+y^2}{R^2}\right] + \sum_{i=0}^{N_t} E_i \exp\left[-\frac{(x-x_i)^2+(y-y_i)^2}{a_i^2}\right], \quad (1)$$

where $R_i = x_i^2 + y_i^2$ are the positions of the fluctuation locations and N_t is the number of tubes mentioned above. E_b is the maximum value of the average energy-density distribution while E_i are the values of energy density maxima of the tube-like fluctuations.

The calculations with following parameters of the tube-like IC were performed:

The configuration without fluctuation: distribution of initial energy density corresponds to the Gauss distribution with R = 5,4 fm and maximum energy density at r = 0 is E_b = 90 GeV/fm^3;

The configuration with one tube shifted from the center: E_b = 90 Gev/fm^3; R = 5,4 fm; E_0 = 270 GeV/fm^3; R_0 = 3 fm and 5.6 fm; a_0 = 1 fm (Fig. 1, *a*).

The configuration with four tubes (fluctuations): E_b = 85 GeV/fm^3; R = 5,4 fm; E_i = 250 GeV/fm^3; R_i = 5,6 fm; a_i = 1 fm [24] (Fig. 1, *b*).

The configuration with ten tubes (fluctuations): E_b = 25 GeV/fm^3; R = 5,4 fm; R_0 = 0 fm; $R_{1,2,3}$ = 2,8 fm; $R_{i,j>3}$ = = 4,7 fm; a_i = 1 fm; $E_i = 4E_b \exp\left(-R_i^2 / R^2\right)$ (Fig. 1, *c*).

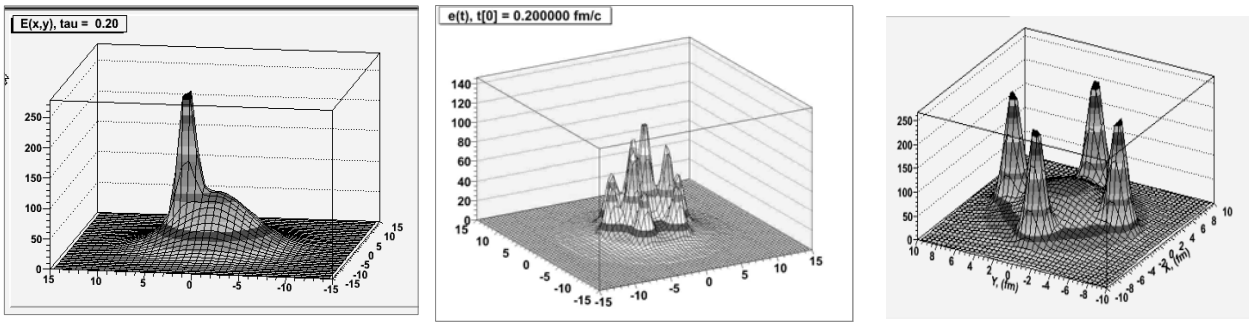

a *b* *c*

Fig. 1. 3D plots of energy density profiles with tube-like IC for τ = 0.2 fm/c:
a - 1 displaced tube; *b* - 4 tubes; *c* - 10 tubes.

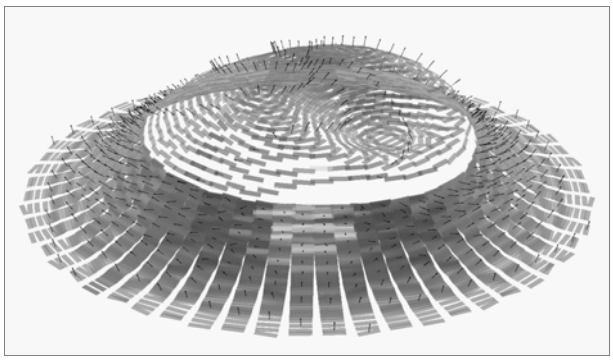

Fig. 2. The chemical freeze-out hypersurface τ (x, y) at the T = 165 MeV for one displaced tube at 3 fm with the field of velocities.

The chemical freeze-out hyper-surface at the T = 165 MeV that corresponds to the end of chemically and thermally equilibrated evolution and start of the hydro-kinetic stage of A+A collision process is presented in the Fig. 2 for the case 1 a). One can see that the fluctuation in initial distribution leads to the appearance of concavity in corresponding to the fluctuation location on freeze-out hyper-surface.

As it was shown in [25] there is a significant impact of particle emission from the boundary surface of the hot and dense system formed in the high energy heavy ion collisions on the observed spectra. To calculate spectra the yield of particles from volume and surface parts of the chemical freeze-out hyper-surface were taken into account.

For all the considered sets of tubes the traces of the initial fluctuations (the bumping final energy distributions) remain after the system evolution and lead to a non-trivial structures in observed spectra. The corresponding pronounced peaks could be seen in the calculated pion spectra (also see [24]). In Fig. 3 the comparison between different cases of the initial energy-density distribution for integrated spectra is presented. The upper lines (black) at the Figures correspond to the integration for $p_T > 0.9$ GeV and grey one to - $p_T > 2.5$ GeV.

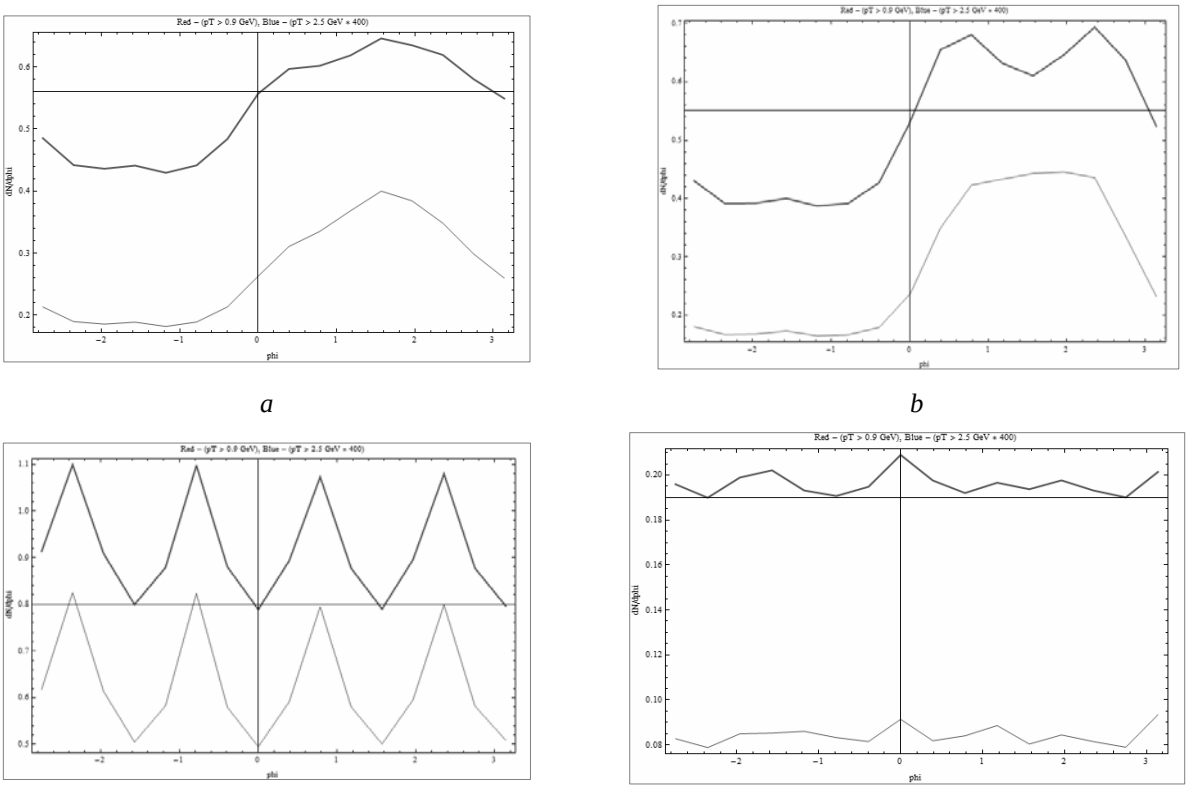

a *b*

c *d*

Fig. 3. The black line corresponds to the integration for $p_T > 0.9$ GeV and grey one to - $p_T > 2.5$ GeV for: *a* - 1 displaced tube at 3 fm; *b* - 1 displaced tube at 5.6; *c* - 4 tubes; *d* - 10 tubes.

As expected, the azimuthal dependencies of pion spectra have shown the remnants of bumping structures in IC especially pronounced for the case of 4 tube-like fluctuations for the medium transversal momenta. As shown in Fig. 3 the results demonstrate that if one particle with relatively large p_T is triggered, most probably, its azimuthal direction will correspond to one of the peaks in the distributions dN/dφ. Then, as follows from dN/dφ distribution, the probability to find the second particle with the same or smaller transverse momentum will be maximal in a narrow range Δφ near this peak. Inclusive correlations between the triggered particle and particle corresponding to other peaks will be relatively weak since these peaks will change from the event to the event of their angular location as for the "triggered peak". It happens because the fluctuations in the bumping structure will washed out the two particle correlations in the inclusive spectra. This is the mechanism of the formation of the so called "soft ridges".

Conclusions

In contrast to the traditional hydrodynamic description of the relativistic nuclear collisions with smooth IC, the transversally bumping tube-like fluctuations in the initial energy-density distributions are considered with the aim to study the influence of its presence on the pion spectra and ridge formation. These very dense color-field flux tubes are formed at a very initial stage of the nucleus-nucleus collision leftovers. It was found that the presence of transversally bumping tube-like fluctuations in IC strongly affects the hydrodynamic evolution and leads to emergence of conspicuous structures in azimuthal distributions of the pion spectra pronounced especially for the medium transverse momenta. As the result, the hydrodynamic mechanism of the "soft ridges" formation becomes sufficiently plausible. To constrain the IC for hydrodynamic expansion in A + A collisions and to study of two-particle correlations a further systematic analysis within the HKM is needed.

ACKNOWLEDGMENTS

The research was carried out within the scope of the European Ultra Relativistic Energies Agreement (EUREA) of the European Research Group GDRE: Heavy ions at ultrarelativistic energies and is supported by National Academy of Sciences of Ukraine (Agreement F3/2012) and by the State fund for fundamental researches of Ukraine (Agreement F33/42-2012).

REFERENCES

1. *Horner M.G.* [STAR Collaboration]. Low- and intermediate-p_T di-hadron distributions in Au + Au collisions at sqrt(s_NN) = 200 GeV from STAR // J. Phys. G: Nucl. Part. Phys. – 2007. – Vol. 34. - P. S995 - 998.
2. *Putschke J.* [for the STAR collaboration]. Near-side Δη Correlations of High p_T Hadrons from STAR // Nucl. Phys. A. – 2007. – Vol. 783. – P. 507 - 510.
3. *McCumber M.P*. [for the PHENIX Collaboration]. The 'shoulder' and the 'ridge' in PHENIX // J. Phys. G: Nucl. Part. Phys. – 2008. – Vol. 35. - P. 104081.
4. *Alver B., Back B.B., Baker M.D. et al.* [PHOBOS Collaboration]. High Transverse Momentum Triggered Correlations over a Large Pseudorapidity Acceptance in Au + Au Collisions at sqrt(s_NN) = 200 GeV // Phys. Rev. Lett. – 2010. – Vol. 104. – P. 062301-4.
5. *Alver B., Roland G.* Collision geometry fluctuations and triangular flow in heavy-ion collisions // Phys. Rev. – 2010. – Vol. C81. - P. 054905-8, arXiv:1003.0194 [nucl-th].
6. *Lacey R.* [for the PHENIX Collaboration]. PHENIX Measurements of Higher-order Flow Harmonics in Au + Au collisions at Root_s = 200 GeV // J. Phys. G. – 2011. – Vol. 38. - P. 124048 [arXiv:1108.0457 [nucl-ex]].
7. *Grosse-Oetringhaus J.F.* Hadron Correlations in Pb-Pb collisions at sqrt(s_NN) = 2.76 TeV with ALICE // J. Phys. G. – 2011. – Vol. 38. - P. 124028 [arXiv:1107.0556 [nucl-ex]].
8. *Jia J.* Measurement of elliptic and higher order flow from ATLAS experiment at the LHC // J. Phys. G. – 2011. – Vol. 38. - P. 124012 arXiv:1107.1468 [nucl-ex].
9. *Li W.* [CMS Collaboration]. Correlations and fluctuations measured by the CMS experiment in pp and PbPb // J. Phys. G. – 2011. – Vol. 38. - P. 124027 [arXiv:1107.2452 [nucl-ex]].
10. *Alver B. H., Gombeaud C., Luzum M., Ollitrault J.-Y.* Triangular flow in hydrodynamics and transport theory // Phys. Rev. – 2010. – Vol. C 82. - P. 034913-10.
11. *Luzum M.* Flow fluctuations and long-range correlations: elliptic flow and beyond // J. Phys. – 2011. – Vol. G38. – P. 124026-10. [arXiv:1107.0592 [nucl-th]].
12. *Qin G.-Y., Petersen H., Bass S.A., Muller B.* Translation of collision geometry fluctuations into momentum anisotropies in relativistic heavy-ion collisions // Phys. Rev. – 2010. – Vol. C82. - P. 064903-15. [arXiv:1009.1847 [nucl-th]].
13. *Moschelli G., Gavin S.* Soft Contribution to the Hard Ridge in Relativistic Nuclear Collisions // arXiv:0910.3590v2 .
14. *Hirano T., Tsuda K.* Collective flow and two-pion correlations from a relativistic hydrodynamic model with early chemical freeze-out // Phys. Rev. – 2002. – Vol. C66. – P. 054905-14.
15. *Manly S. et al.* [PHOBOS Collaboration]. System size, energy and pseudorapidity dependence of directed and elliptic flow at RHIC // Nucl. Phys. - 2006. - Vol. A774. - P. 523 – 526. [arXiv:nucl-ex/0510031].
16. *Aguiar C.E., Hama Y., Kodama T., Osada T.* Event-by-event fluctuations in hydrodynamical description of heavy-ion collisions // Nucl. Phys. – 2002. – Vol. A698. – P. 639 - 642.
17. *Petersen H., Steinheimer J., Burau G. et. al.* Fully integrated transport approach to heavy ion reactions with an intermediate hydrodynamic stage // Phys. Rev. – 2010. – Vol. C82. – P. 044904-1 - 044904-26.
18. *Werner K., Karpenko Iu., Pierog T. et. al.* Event-by-event simulation of the three-dimensional hydrodynamic evolution from flux tube initial conditions in ultrarelativistic heavy ion collisions // Phys. Rev. – 2008. – Vol. C78. – P. 044901-18; arXiv:1004.0805.
19. *Andrade R.P.G., Grassi F., Hama Y., Qian W.-L.* Hydrodynamics: Fluctuating Initial Conditions and Two-particle Correlations // Nucl. Phys. – 2011. – Vol. A854. - P. 81 – 88.
20. *M Borysova M.S., Sinyukov Yu.M., Karpenko Iu.A.* Fluctuations in Initial Energy Density Distributions In A + A Collisions // Nucl. Phys. At. Energy. – 2010. - Vol. 11, No. 3. - P. 269 – 274.
21. *Borysova M.S., Sinyukov Yu.M., Karpenko Iu.A.* Evolution of energy density fluctuations in A + A collisions // Physics of Particles and Nuclei Letters. – 2011. - Vol. 8, No. 9. - P. 915 – 917. arXiv:1102.2084v1 [nucl-th].
22. *Akkelin S.V., Hama Y., Karpenko Iu., Sinyukov Yu.M.* Hydro-kinetic approach to relativistic heavy ion collisions // Phys. Rev. – 2008. – Vol. C78. – P 034906-15.
23. *Sinyukov Yu.M., Karpenko Iu.A., Nazarenko A.V.* Spacetime scales and initial conditions in relativistic A + A collisions // J. Phys. G: Nucl. Part. Phys. – 2008. – Vol. 35. – P. 104071 – 104075.
24. *Borysova M.S.* Bumping structure of initial energy density distributions and peculiarities of pion spectra in A + A collisions // Nucl. Phys. At. Energy. – 2012. – Vol. 13, No. 1. - P. 39 - 45.
25. *Borysova M.S., Sinyukov Yu.M., Akkelin S.V.et al.* Hydrodynamic source with continuous emission in Au + Au at $\sqrt{s}$ = 200 GeV // Phys. Rev. - 2006. – Vol. C73. - P. 024903-8. ArXiv: nucl-th/0507057.

COMPARISON OF DIGITAL METHODS FOR STORAGE, SORTING AND DISPLAYING OF THE SPECTROMETRIC INFORMATION

I. P. Dryapachenko, E. M. Mozhzhukhin, V. V. Ostashko, Yu. M. Pavlenko, O. I. Rundel, A. F. Sharov

Institute for Nuclear Research, National Academy of Sciences of Ukraine, Kyiv, Ukraine

During ten years at the Kyiv tandem EGP-10K beam of accelerated hydrogen ions was used extensively in the inclusive and exclusive experiments with scattering and nuclear reactions on different nuclei. Charged particles (protons, deuterons, ^{4}He), γ-quanta and neutrons were registered in the outgoing channels of the studied nuclear processes. This required to use of different methods of radiation spectrometry. The most used (ΔE × E)-method for spectrometry of charged particles and the time-of-flight method for registration and the separation of neutrons and γ-rays. The current need of the algorithm universalization for measurement and data processing was led to the development, installation and use of computerized multiparameter setup that was used successfully in this time in the beam experiments. This paper discusses the results of the facility modernization in accordance with the development of digital technology, above all, communication devices for measuring apparatus and control computer, and related changes and improves of the operating systems and software for data processing.

1. Introduction

The authors have long experience of preparing and using various methods for the spectrometry analysis of the nuclear interaction products in inclusive and exclusive experiments with of the low energy accelerator beams [1 - 4]. Many years ago the possibility of such methods to register and accumulate the experimental data was limited on very small volumes of "memory" devices and accompanying devices - from counters and analyzers to disk drives of the small electronic computers. This required developing of the complex and bulky electronic equipment for pre-selection and sorting signals from using detectors. But this in turn was one of the driving levers of the digital technology revolutions, which helped improve the quality of the nuclear-physics experiments due to miniaturization, multichannelity, manyparametries of measuring collect data systems. These processes are closely associated with computerization support nuclear-physical experiments based on its hardware unification and soft universalization for the accumulation and sorting of data and processing and analyzing the results. In this paper, we are talking about using of the any interface instrumentations with control computer and comparison of the some base characteristics and their impact on the quality of the experiment and results.

2. Experimental procedure

2.1. Measuring methods

The aim of this work was to compare the performance capabilities, characteristics and their impact on the results for several variants used systems of accumulation. A telescope of two silicon semiconductor detectors of charged particles was used as a radiation detector. It consisted of ΔE-detector with 18 microns thick and E-detector thickness of 200 microns. Traditional block diagram for processing signals of the detector consists of two "lines" of electronic blocks, each of which includes a preamplifier, main amplifier and a differential discriminator for adjusting of the up and down levels of signal registration from each detector. There are organized the "slow" (within microseconds) pulses coincidences as letting signal (strobe) for linear "gate", which provide two-parameter identification of the registered charged particle variety with simultaneous determination of its energy. These three signals - two analog, as a amplitude range for energy spectrum of registered particles and one logical (in this case – from the slow coincidence circuit) which can be as detector number (in this case - the telescope) or the coincidence range (double, triple...) – are entering and digitizing in CAMAC-crate, and then are sent to the administrator computer to collect statistical information (with the possible pre-visualization in the on-line control of initial measurement conditions). There is using after measurement stopping the off-line sorting of an all final volume of accumulated information and its subsequent processing and analysis by using of the chosen algorithm. Those options for communication of the recording electronics and a control computer were compared in this paper.

CAMAC-crate controller FK4410-1 (Vilnius) was used most widely in experiments on the accelerator beams at the Institute for Nuclear Research in last time. This is combined with a control computer by through connection fee, which was designed and manufactured in our institute. It should be recalled that originally the all referred equipment was used in measuring-computing complex based on small computer machines: M6000, CM-2, -4, -1420 - Soviet counterpart of the famous PDP-brand. And then the algorithm and appropriate ASSEMBLER-software have been developed for support of the universal multichannel measuring techniques, which used for accumulation of the multiparameter spectrometric information on the variety and energy products, which are registered the study of nuclear interactions. Objectively, this was a necessary transitional stage for widespread use of new generation of digital technology - personal computers.

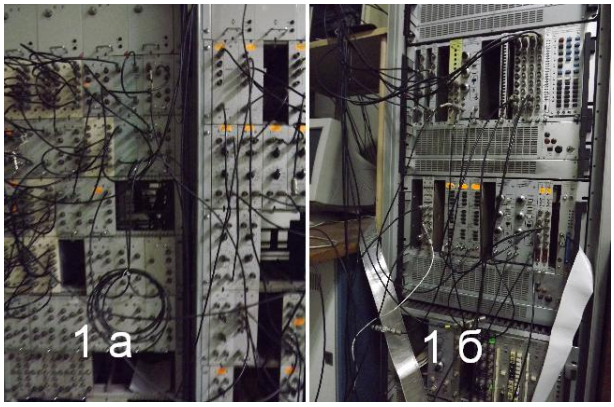

Fig. 1. Electronic of the EGP-10K measuring complex.

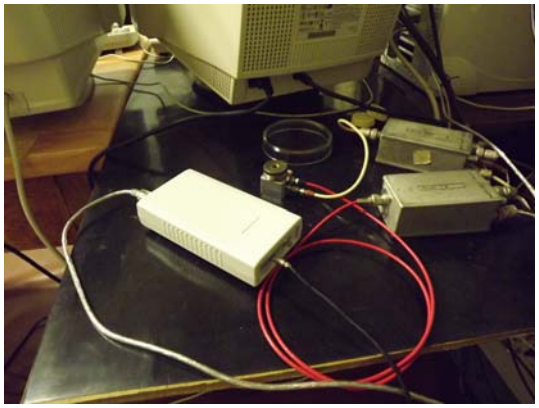

Fig. 2. Single USB-ADC.

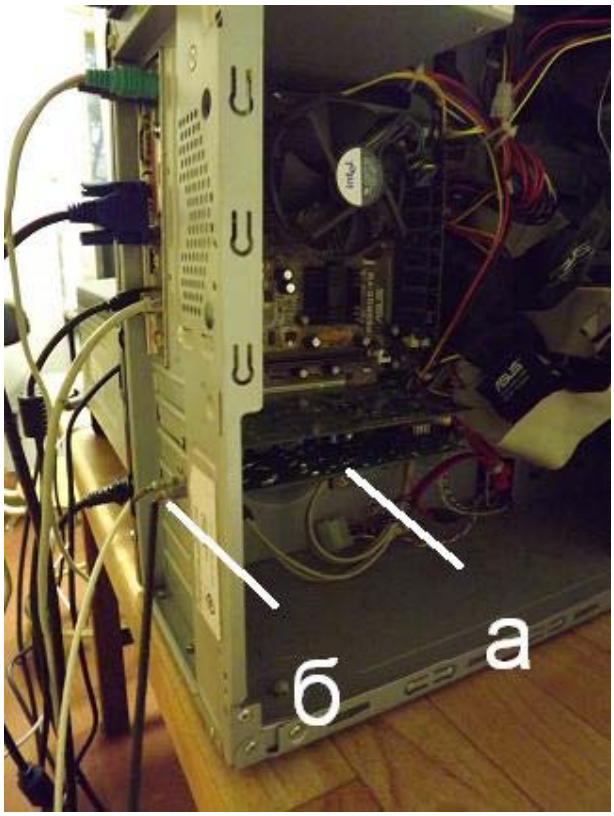

Fig. 3. Two-parameter ADC controller.

Gained previous experience has sufficiently quickly used with new technology. Existing software, primarily interfaces for control of the experiment and processing of collected data, were processed under DOS-shell [5]. There was using namely this technique to provide support experiments on the accelerator beam for over ten years. This Figure illustrates the hardware components of the measuring complex: in Fig. 1, *a* – low level equipment for receiving and processing pulses from working detectors and in Fig. 1, *b* – blocks in the standard CAMAC for digitizing and connection with managing personal computer.

Explosive development of digital technology and computers, "unlimited" speed and memory resources, the objective necessity of universalization and even informational and methodological globalization require continuous "tracking" and modernization of using methods. In our case, it was could to realize the transition to computer-support the above mentioned measuring methods under modern Windows-shell based on new digital devices. For logic statement must begin with a new CAMAC-crate controller CC02 [6]. This device, which was developed at the Kharkov National University, provides the accumulation of digitized analog information in the 4096 channels range. Control interface is designed and operates under the Windows-shell by using common software package National Instruments LabVIEW. The exit file after processing under Compaq Fortran converted to text format, suitable for processing in standard packages (Excel, Origin, etc.). The results with CC02 controller were shown in previous work [7]. The following steps have been taken already on modernizing the system of accumulation. Through information available in the global network it was found ready spectrometric analog-digital converter on 4096 channels with USB bus powered (4L-SATSP-USB), which connected through USB-port into a personal computer. With added software (driver ADC and convenient "friendly" interface), this small device weight of 300 g (Fig. 2) completely replaces the above installation (see Fig. 1) in using for the accumulation of one-dimensional spectra. Finally, a decisive step to «Windows»-modernization of multiparameter accumulation technique now was made. We launched in collaboration with Dubna colleagues two-parameter ADC controller (pci2_m1k), which through PCI card slot is compatible with PC under the chosen version of Windows. This PCI card (“a” in Fig. 3) has three LEMO-inputs (“b” Fig. 3) for two spectral signals and one for control signals (strobe). So just this device could used to above without cumbersome intermediate equipment.

Within the preparing frame-up to measurements on the beam accelerator were carried out measuring of the ^{226}Ra-decay α-particles spectra with (ΔE × E)-telescope of two silicon detectors in one- and two-dimensional mode using new devices, when running together with the accumulation on the traditional measuring installation (let us use for it the name “DOS-acquisition”).

2.2. Results and discussion

In Fig. 4 shows a screen-shot measurement interface, which running in the method DOS-acquisition. It is given the number parameters (ADC) from 1 to 5, the code (number) detector or a combination of the registrated coincidences, options of visualization for collected data, and last, number of parameter (specific range) in one-dimensional variant (Fig. 5) or two for two-dimensional imaging mode (Fig. 6). File results after sorting and processing in the off-line mode the accumulated statistics special DOS-program reformats a text file, suitable for common applications handling numeric arrays - Excel, Origin, etc.

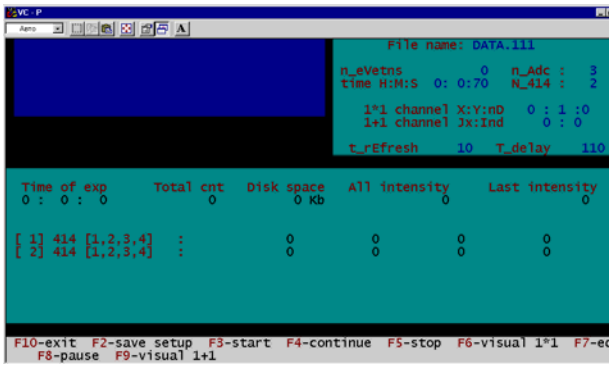

Fig. 4. Measurement interface
in the method DOS-acquisition.

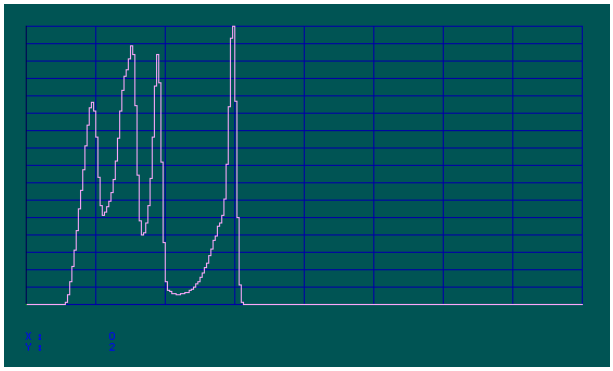

Fig. 5. Data visualization in one-dimensional variant.

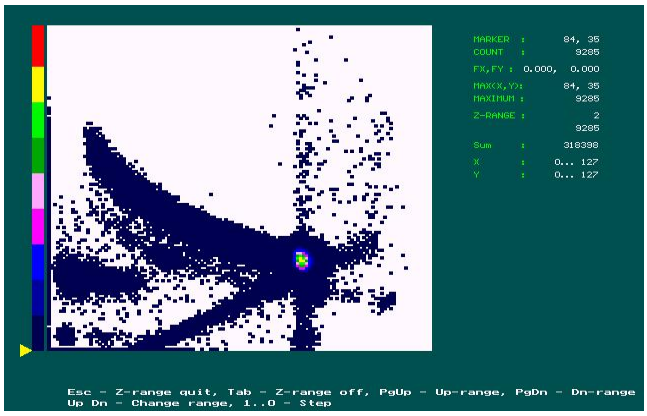

Fig. 6. Data visualization in two-dimensional variant.

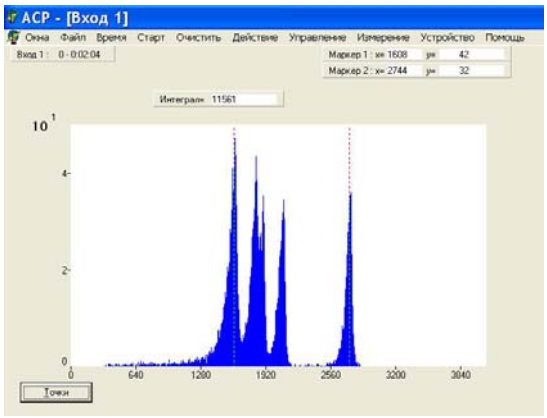

Fig. 7. Windows-interface
for one-dimensional USB-ADC.

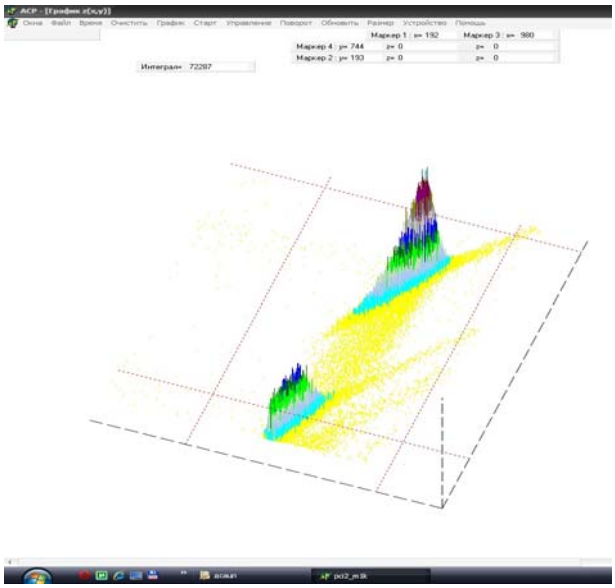

Fig. 8. Windows-interface
for two-dimensional USB-ADC.

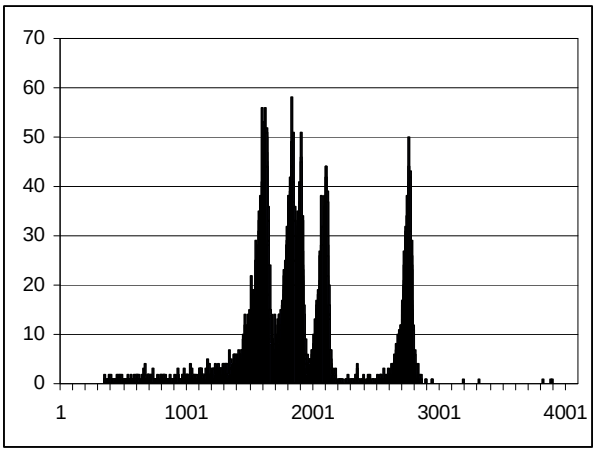

Fig. 9. Text format result in Excel.

In Fig. 7 submitted the screen-shot Windows-interface management and measurement using one-dimensional USB-ADC. In the conventional view, there are the available Windows shell options, which determine the start (stop) and the time length of exposure, selection of threshold check in the spectrum and so on Also available conventional options of opening a new file and its saving in text format for reading (download) accumulated and saved the file. Finally, in Fig. 8 represented the result of accumulation of two-parameter range of α-particle decay of ^{226}Ra using two-dimensional ADC. On one axis (input) was given spectrum of the "fine" detector, and on the second axis (second input) - from thick detector (range up to full stopping of charged particles). Digitized file of the accumulated statistical information consists of "words" with three numbers - the channel number on the axis "X", the channel number on the axis of «Y» and the number of counts on the axis of «Z». With the help of FORTRAN-program in the standard package Visual Compaq this source file is converted to a text table, available in any Windows-applications. Below are the results of off-line processing (sorting and reformatting) using accumulated statistical information for the above three methods of obtaining data.

DOS-acquisition: Numerical result is only available in one-dimensional version. Therefore, processing must end for the two-dimensional information (see Fig. 6) by selection of area of the two-dimensional plane and its projection (summation statistics) on the selected axis to get the final one-dimensional spectrum, which is presented in Fig. 5.

One-dimensional USB-ADC: In Fig. 7 provides accumulated using this device range. The signals were presented on different devices from a single analog breeder and were blocked for simultaneous start (and stop) one and the same strobe. Then those are saved in text format result by importing data, which are introducing in Excel (Fig. 9). The principal is the coincidence of the amounts of statistical information in the accumulated spectra in different acquisition systems.

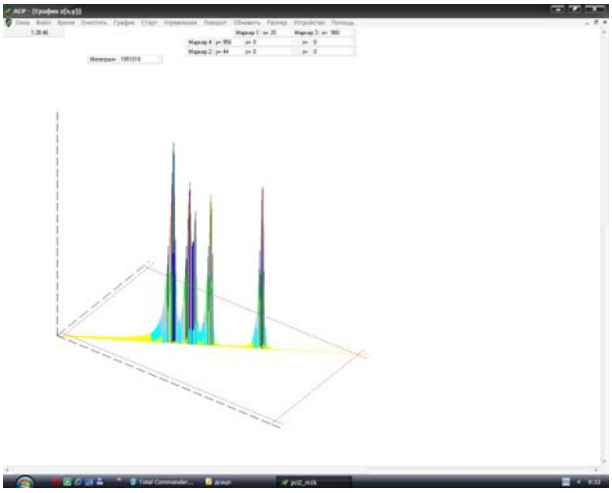

Fig. 10. Spectrum of ^{226}Ra α-particles.

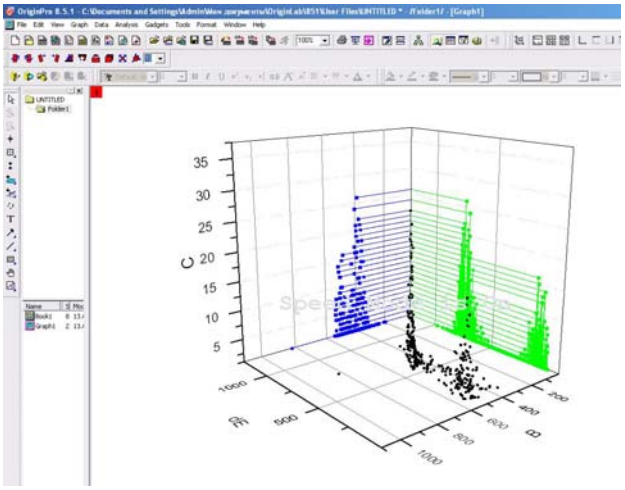

Fig. 11. Two-dimensional spectrum.

Two-dimensional PCI-ADC: For illustrative purposes, if in the two-dimensional mode on two inputs is one the same signal, we get on a plane two-dimensional statistical data accumulated diagonal, which in the projection on any axis will give one dimensional spectrum, registered elected (on both axis) detector. In Fig. 10 shows the accumulated two-dimensional spectrum. Data obtained for single "thick" detector for ^{226}Ra α- particle (with four "passport" energy: 7687, 6002, 5490 and for the two telescope detectors 4599 keV). In Fig. 11 represented by two-dimensional spectrum for the two telescope detectors (see Fig. 8) after offline processing and exporting the exit text file into standard Origin code. It remains to recall the difference in the "hardware" between these two options by Figs. 1 and 3.

3. Conclusions

The results demonstrate the adequacy of selected procedures accumulation and sort of experimental data in low beam accelerator energies. Created opportunities experiment control on the present level to universalize used methods to obtain and process data based on current and unified devices and software.

ACKNOWLEDGMENTS

The authors would like to thank P. A. Iordanskij (Dubna, Russia) for the given digital blocks and related software.

Work performed with financial support in the target program, NAS of Ukraine.

REFERENCES

1. *Дряпаченко І.П., Можжухін Е.М.* Розсіяння та реакції пучків протонів та дейтронів з енергією 1.6 - 7.3 МеВ київського тандему ЕГП-10К // Ядерні та радіаційні технології. - 2004. - Т. 4, №2. - С. 76.
2. *Zadro M., Di Pietro A., Figuera P. et al.* Stopping power of helium gas for ions from 2 to 31 MeV // Nuclear

Instruments and Methods in Physics Research. - 2007. - Vol. B259. - P. 836.
3. *Dryapachenko I., Mozhzhukhin E., Salo V., Voronov O.* Accelerator Beam Method for Fast Neutron Scintillation Tests // LUMDETR 2009 (Krakow, Poland, 12 - 17 July, 2009): Book of Abstracts. - P. 307.
4. *Павленко Ю.Н., Теренецкий К.О., Вербицкий В.П. и др.* Подбаръерное взаимодействие дейтронов с ядрами ^{58,62}Ni // 61 Междунар. конф. по проблемам ядерной спектроскопии и структуре атомного ядра «Ядро-2011» (Саров, Россия, 10 - 14 окт. 2011 г.) - С. 79.
5. *Павленко Ю.М., Кива В.О., Коломієць І.М. та ін.* Методика багато параметричних кореляційних вимірювань для досліджень ядерних реакцій // Зб. наук. праць Ін-ту ядерних досл. - 2005. - № 2(15). - С. 151.
6. *Ляшенко В.Н., Турчин А.А., Перминов А.И., Рева С.Н.* Контролер крейда СС02: Руководство пользователя / Лаборатория интеллектуальных электронных систем, кафедра электроники и управляющих систем Национального университета им. В.Н. Кармазина. - Харьков, 2006. - 70 с.
7. *Дряпаченко І.П., Ковтун В.С., Можжухін Е.М. та ін.* Оновлення методик вимірювань на пучку тандем-генератора ЕГП-10К з використанням цифрової техніки // Ядерна фізика та енергетика. - 2012. - Т. 13, № 2. - С. 203.

RARE b-DECAYS AT LHCb EXPERIMENT

V. M. Iakovenko (on behalf of LHCb collaboration)

Institute for Nuclear Research, National Academy of Science of Ukraine, Kyiv, Ukraine

Studies of rare effects in B-physics provide a possibility to precision tests of the Standard Model and discover the evidences of New Physics. Precise measurements of rare B decays are performed with the LHCb experiment at Large Hadron Collider. We report recent measurements of leptonic $B^0_{(s)}\to\mu^+\mu^-$, semileptonic $B^0\to K^{*0}\mu^+\mu^-$ and radiative penguin rare decays $B^0\to K^*\gamma$ and $B^0_s\to\varphi\gamma$ using 1 fb^{-1} of data taken at $\sqrt{s}$ = 7 TeV with the LHCb detector.

Introduction

Flavor changing neutral current (FCNC) processes are highly suppressed in the standard model (SM) and thus constitute a stringent test of the current description of particle physics. Measurements of FCNCs provide sensitivity to the contributions of heavy virtual particles in the loop diagram. Loop diagrams are well described theoretically and easily accesible experimentally through many observables which we can measured, e.g. branching fractions, CP and isospin asymmetries and photon polarization. Thus, studies of the rare *B*-decays can yield powerful constraints on many New Physics scenarios, including models with supersymmetry.

Large Hadron Collider beauty

The LHCb detector [1] is a single-arm forward spectrometer at the LHC covering the pseudo-rapidity range2 <η< 5, designed for the study of particles containing *b* or *c* quarks. The detector includes a high precision tracking system consisting of a silicon-strip vertex detector surrounding the *pp* interaction region, a large-area silicon-strip detector located upstream of a dipole magnet with a bending power of about 4 Tm, and three stations of silicon-strip detectors and straw drift tubes placed downstream. The combined tracking system has a momentum resolution Δp/p that varies from 0.4 % at 5 GeV/c to 0.6 % at100 GeV/c, and an impact parameter (IP) resolution of 20 μm for tracks with high transverse momentum (pT). Charged hadrons are identified using two ring-imaging Cherenkov detectors (RICH). Photon, electron and hadron candidates are identified by a calorimeter system consisting of scintillating-pad and preshower detectors, an electromagnetic calorimeter and a hadronic calorimeter. Muons are identified by a system composed of alternating layers of iron and multiwire proportional chambers. The trigger consists of a hardware stage, based on information from the calorimeter and muon systems, followed by a software stage which applies a full event reconstruction.

Search of leptonic $B^0_s\to\mu^+\mu^-$ and $B^0\to\mu^+\mu^-$ decays

Rare decays $B^0_s\to\mu^+\mu^-$ and $B^0\to\mu^+\mu^-$ are highly suppressed in the SM, as they can occur only via helicity suppressed loop diagrams. Precise predictions of their branching fractionsare provided in [2]:

$$\mathrm{B}(B^0_s\to\mu^+\mu^-) = (3.23 \pm 0.27)\cdot 10^{-9},$$

$$\mathrm{B}(B^0\to\mu^+\mu^-) = (1.07 \pm 0.10)\cdot 10^{-10}$$

make these modes powerful probes in the search for deviations from the SM, especially in models with a non-standard Higgs sector, which can give rise to higher branching fractions.

The entire 2011 dataset for the search of both channels was used [3]. Dimuon candidates were classified in the bins of a two dimensional space made of a multivariate discriminant variable and the dimuonin variant mass. The probability of a signal event to fall in each bin is obtained from the data sample itself using $B^0_{(s)}\to h^+ h^-$decays. The expected number of combinatorial background events is extracted from a fit to the invariant mass side bands. The invariant mass of dimuon candidates in the highest multivariateb in is shown in Fig. 1.

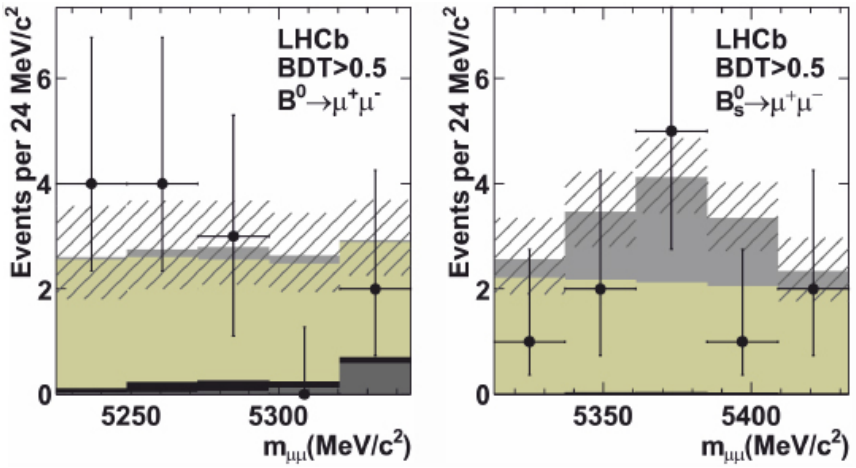

Fig. 1. The invariant mass of dimuon candidates with the highest multi-variate discriminant classification from 1 fb^{-1} of LHCb data taken at $\sqrt{s}$ = 7 TeV. The limits for each are $B(B^0_s\to\mu^+\mu^-)< 4.5\cdot 10^{-9}$ @ 95 % C.L. and $B(B^0\to\mu^+\mu^-) < 1.0\cdot 10^{-9}$ @ 95 % C.L.

Upper limits on the branching fractions are determined to be:

$$B(B^0_s \to \mu^+\mu^-) < 4.5 \cdot 10^{-9} \text{ @ 95 \% C.L.}$$

$$B(B^0 \to \mu^+\mu^-) < 1.0 \cdot 10^{-10} \text{ @ 95 \% C.L.}$$

These results are compatible with SM theoretical predictions.[1]

Measurements of semileptonic $B^0 \to K^{*0}\mu^+\mu^-$ decay

The helicity structure of $B^0 \to K^{*0}\mu^+\mu^-$ decay can be determined by measuring the angular distribution of the B daughters. It comprises the helicity angle of the kaon, θ_K, between the kaon in the K^{*0} meson rest frame and the K^{*0} in the B^0 meson rest frame; the helicity angle of the μ^+ (μ^-), θ_l, between the muon in the dimuon rest frame and dimuon in the B^0 ($\bar{B}^0$) meson rest frame; and the angle, φ, between the decay planes of the dimuonand the K^{*0} systems in the B^0 meson rest frame. The four-body decay is completely described by three angles ($\cos\theta_l$, $\cos\theta_K$, φ) and the dimuon invariant mass squared (q^2). This gives access to angular observables which are relatively free from hadronic uncertainties: A_{FB}, the forward backward asymmetry of the $\mu^+\mu^-$ pair in B rest frame, F_L, the fraction of longitudinal polarisation of the K^{*0} and S_3, proportional to the asymmetry of the K^{*0}transverse polarisation and fourth term(S_9). The angular analysis of $B^0 \to K^{*0}\mu^+\mu^-$ at LHCb has measured these four observables [5, 6]. The values of these observables are shown in Fig. 2.

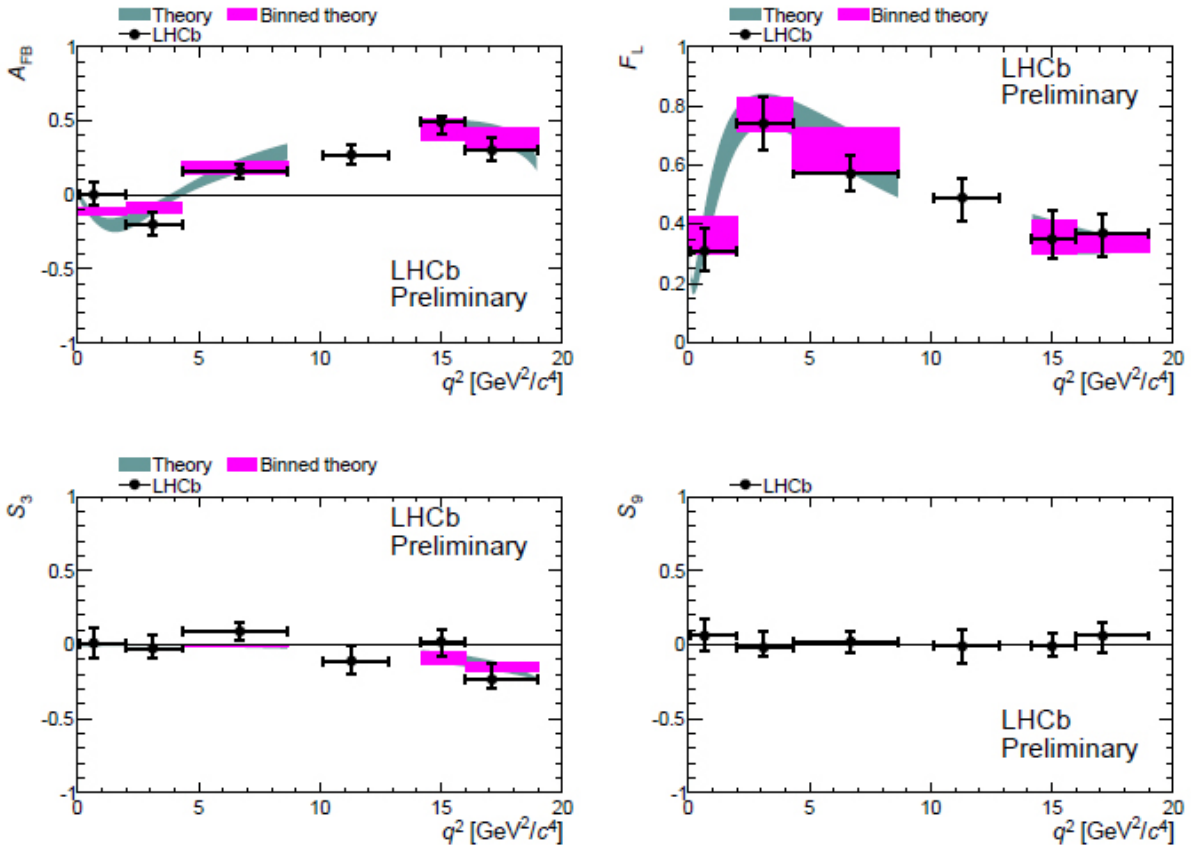

Fig. 2.The values of angular observables $A_{FB,}$ F_L, S_3 and S_9 for $B^0 \to K^{*0}\mu^+\mu^-$ as a function of q^2, based on the analysis of 1 fb^{-1} of data collected at $\sqrt{s}$ = 7 TeV in LHCb. The observables are measured in six bins of q^2 and determined from a simultaneous fit to the angular distribution [5]. The SM predictions are taken from [7].

The LHCb results are the most precise, where all results agree with the SM. These measurements put strong constraints (> 10 TeV) on non-MFV new physics affecting the Wilson coeffcients C_7, C_9 and C_{10}[8]. LHCb collaboration has made the first measurement of the zero crossing point for A_{FB} at $4.9^{+1.1}_{-1.3}$ Gev^2/c^4 [5], that is in agreement with SM predictions which range from 4.0 - 4.3 GeV^2/c^4.

[1] With the combination of 1 fb^{-1} 2011 data and 1.1 fb^{-1} of the first part of 2012 data the first evidence for $B^0_s \to \mu^+\mu^-$ were produced [4].

Measurement of isospin asymmetry in $B^0 \to K^{*0}\mu^+\mu^-$

The isospin asymmetry of $B \to K^{(*)}\mu^+\mu^-$ decays is defined as

$$A_I = \frac{B(B^0 \to K^{(*)0}\mu^+\mu^-) - \frac{\tau_0}{\tau_+} B(B^+ \to K^{(*)+}\mu^+\mu^-)}{B(B^0 \to K^{(*)0}\mu^+\mu^-) + \frac{\tau_0}{\tau_+} B(B^+ \to K^{(*)+}\mu^+\mu^-)},$$

where $B(B \to f)$ is the branching fraction of the $B \to f$ decay and τ_0/τ_+ is the ratio of the lifetimes of the B^0 and B^+ mesons. The value of A_I is expected to be close to zero in the SM [9] and a measurement of A_I is a test of the spectator model of quark interactions. The value of A_I for $B \to K\mu^+\mu^-$ within SM is also predicted to be around zero. In 2009, the BaBar collaboration reported a significantly negative deviation from zero for both $B \to K^{(*)}\mu^+\mu^-$ and $B \to K\mu^+\mu^-$ decays in the q^2 region below the J/ψ resonance, which provides the main motivation for the measurement [10].

The LHCb measurement of the $B \to K^{(*)}\mu^+\mu^-$ isospin asymmetry was performed for both B decays to pseudoscalar and vector mesons [11]. This requires the measurement of the differential branching fraction for the four decays: $B^+ \to K^+\mu^+\mu^-$, $B^0 \to K^0_S\mu^+\mu^-$, $B^0 \to (K^{*0} \to K^+\pi^-)\mu^+\mu^-$ and $B^+ \to (K^{*+} \to K^0_S\pi^+)\mu^+\mu^-$ decays. The decays involving a K^0_S are more difficult than the K^+ decays due to the long lifetime of the K^0_S and lower visible branching fractions. The differential branching fractions of $B^0 \to K^0\mu^+\mu^-$ and $B^+ \to K^{*+}\mu^+\mu^-$ measured by LHCb [11] are shown in Fig. 3. The value of isospin asymmetry, A_I, for $B^0 \to K^0\mu^+\mu^-$ and $B^+ \to K^{*+}\mu^+\mu^-$ are shown in Fig. 4. For $B^0 \to K^*\mu^+\mu^-$ LHCb results are consistent with SM predictions. Due to the deficit of $B^0 \to K^0_S\mu^+\mu^-$ seen in Fig. 3, LHCb measures a negative isospin asymmetry, deviating from the SM expectation of zero asymmetry by 4.4σ [11].

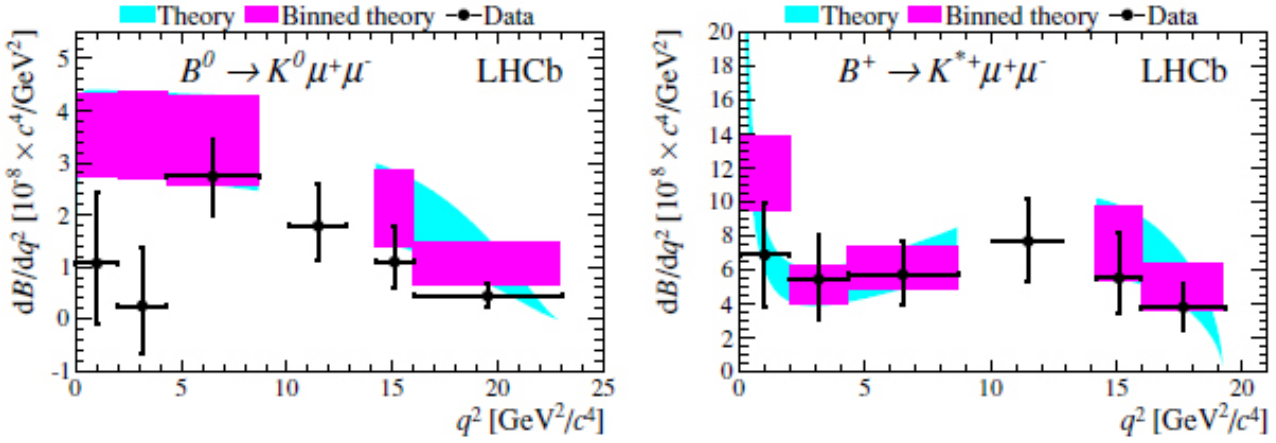

Fig. 3. Differential branching fractions of (*l*eft) $B^0 \to K^0\mu^+\mu^-$ and (*right*) $B^+ \to K^{*+}\mu^+\mu^-$ measured using 1.0 fb^{-1} of data collected at $\sqrt{s}$ = 7 TeV at LHCb in 2011. The theoretical SM predictions are taken from [7, 12].

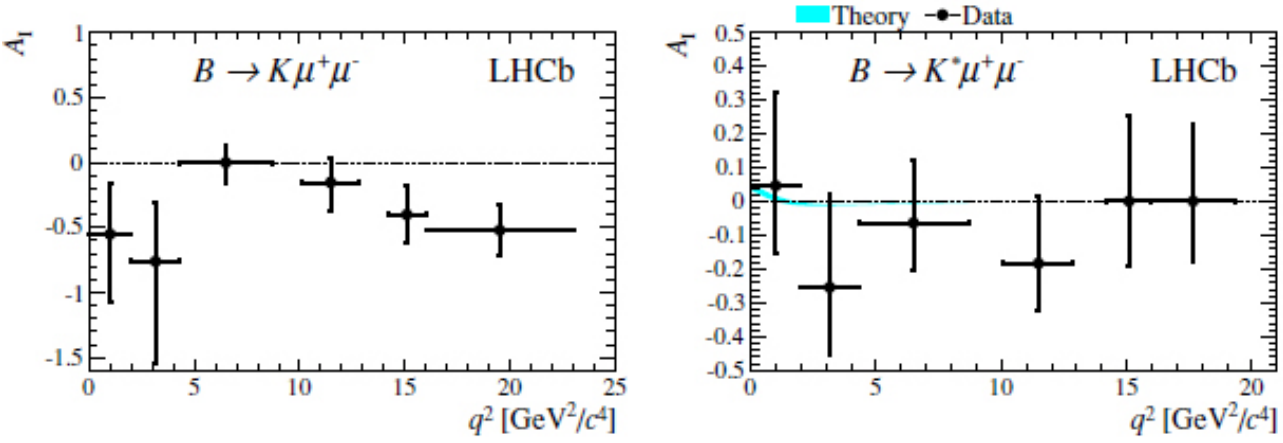

Fig. 4. Isospin asymmetry of (*left*) $B \to K\mu^+\mu^-$ and (*right*) $B \to K^*\mu^+\mu^-$.
For $B \to K^*\mu^+\mu^-$ the theoretical SM prediction, which is very close to zero, is shown for q^2 below 8.68 GeV/c^2.

Radiative penguin $B^0 \to K^*\gamma$ and $B^0_s \to \varphi\gamma$ decays

In the SM, the decays $B^0 \to K^*\gamma$ and $B^0_s \to \varphi\gamma$ proceed at leading order through the electromagnetic penguin transitions, $b \to s\gamma$. At one-loop level the setransitions are dominated by a virtual intermediate top quark coupling to a W boson.

Radiative decays of the B^0 meson were first observed by the CLEO collaboration in 1993 in the decay mode $B^0 \to K^* \gamma$ [13]. The latest theoretical predictions from NNLO calculations using soft-collinear effective theory give us the values of branching fraction for decays $B^0 \to K^* \gamma$ and $B^0_s \to \varphi\gamma$ [14]:

$$B(B^0 \to K^* \gamma) = (4.3 \pm 1.4) \cdot 10^{-5},$$

$$B(B^0_s \to \varphi\gamma) = (4.3 \pm 1.4) \cdot 10^{-5},$$

which suffer from large uncertainties from hadronic form factors. A better-predicted quantity is the ratio of branching fractions, as it benefits from partial cancellations of theoretical uncertainties.

The data used to measure the ratio of $B(B^0 \to K^* \gamma)/B(B^0_s \to \varphi\gamma)$ corresponds to 1.0 fb^{-1} of pp collisions collected in 2011 at the LHC with a centre-of-mass energy of $\sqrt{s}$ = 7 TeV. The invariant mass distribution of the $K\pi\gamma$ candidates and the K^+K^- candidates are shown in Fig. 5.

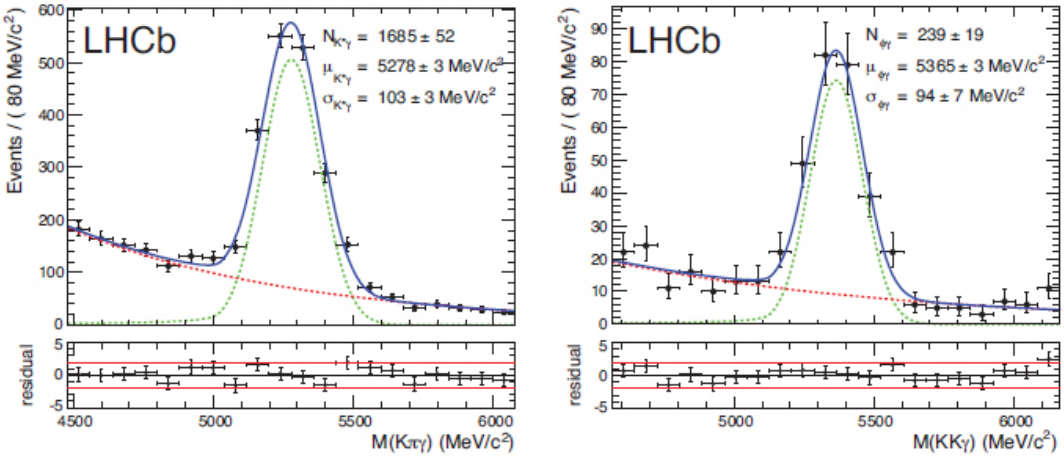

Fig. 5. The invariant mass distribution of selected (*left*) $B^0 \to K^* \gamma$ and (*right*) $B^0_s \to \varphi\gamma$ candidates selected from 1.0 fb^{-1} of data collected at $\sqrt{s}$ = 7 TeV during 2011 [15].

The ratio of branching fractions is measured as:

$$\frac{B(B^0 \to K^* \gamma)}{B(B^0_s \to \varphi\gamma)} = \frac{y_{B^0 \to K^{*0}\gamma}}{y_{B^0_s \to \varphi\gamma}} \frac{B(\varphi \to K^+K^-)}{B(K^{*0} \to K^+\pi^-)} \frac{f_s}{f_d} \frac{\varepsilon_{B^0_s \to \varphi\gamma}}{\varepsilon_{B^0 \to K^{*0}\gamma}}, \quad (1)$$

where N are the observed yields of signal candidates, $B(\varphi \to K^+K^-)/B(K^{*0} \to K^+\pi^-) = 0.735 \pm 0.008$ [16] is the ratio of branching fractions of the vector mesons, $f_s/f_d = 0.267^{+0.021}_{-0.020}$ [17] is the ratio of the B^0 and B^0_s hadronization fractions in pp collisions at $\sqrt{s}$ = 7 TeV, and $\varepsilon_{B^0_s \to \varphi\gamma}/\varepsilon_{B^0 \to K^{*0}\gamma}$ is the ratio of total reconstruction and selection efficiencies of the two decays.

The value of the ratio of branching fractions is measured and the value of $B(B^0_s \to \varphi\gamma)$ is calculated using the world average for $B(B^0 \to K^* \gamma)$ [16]:

$$\frac{B\left(B^0 \to K^* \gamma\right)}{B\left(B^0_s \to \varphi\gamma\right)} = 1.12^{+0.23}_{-0.20},$$

$$B(B^0_s \to \varphi\gamma) = (3.9 \pm 0.5) \cdot 10^{-5},$$

where the quoted error is a combination of the statistical and systematic uncertainties.The measurement of the ratio of branching fractions ensures the cancellation of most of the systematic errors. This is the most precise measurement of $B(B^0_s \to \varphi\gamma)$ to date.

Conclusions

Using an integrated luminosity of 1.0 fb^{-1} of pp collision data collected by the LHCb experiment at a centre-of-mass energy of $\sqrt{s}$ = 7 TeV we have presented recent results on search of very rare decays $B^0_{(s)} \to \mu^+\mu^-$, isospin analysis with semileptonic $B^0 \to K^{*0}\mu^+\mu^-$ decay and measurements of ratio of the branching fractions of $B^0 \to K^* \gamma$ and $B^0_s \to \varphi\gamma$ decays. LHCb provides us information to constrain many models of New Physics.

REFERENCE

1. *Alves A.A. Jr. et al.* [LHCb Collaboration]. The LHCb detector at the LHC // JINST. - 2008. -3 S08005. - 217 p.
2. *Buras J., Girrbach J., Guadagnoli D., Isidori G.* On the standard model prediction for B ($B^0_{s,d} \to \mu^+ \mu^-$) // Eur. Phys. J. - 2012. - Vol. C72. - 14 p.; arXiv:1208.0934.
3. *Aaij R. et al.* [LHCb Collaboration]. Strong constraints on the rare decays $B^0_s \to \mu^+ \mu^-$ and $B^0 \to \mu^+ \mu^-$ // Phys. Rev. Lett. - 2012. - Vol. 108. - P. 231801. - 8 p.; arXiv:1203.4493.
4. *Aaij R. et al.* [LHCb Collaboration].First evidence for the decay $B^0_s \to \mu^+ \mu^-$; arXiv:1211.2674.
5. *LHCb Collaboration.* Differential branching fraction and angular analysis of the $B^0 \to K^{*0} \mu^+ \mu^-$decay // Proc. of 47th Rencontres de Moriond on QCD and High Energy Interactions (La Thuile, Italy, 2012). - 20 p.; LHCb-CONF-2012-008.
6. *Aaij R. et al.* [LHCb Collaboration]. Differential branching fraction and angular analysis of the $B^0 \to K^{*0} \mu^+ \mu^-$decay // Phys. Rev. Lett. - 2012. - Vol. 108. - P. 181806. - 11 p.; arXiv:1112.3515.
7. *Bobeth C., Hiller G., Van Dyk D.* More benefits of semileptonic rare B decays at low recoil: CP Violation // JHEP. - 2011. - Vol. 07. - 18 p.; arXiv:1105.0376.
8. *Altmannshofer W., Straub D.M.* Cornering new physics in b→s transitions; arXiv:1206.0273.
9. *Feldmann T., Matias J.* Forward-backward and isospin asymmetry for $B \to K^{(*)} l^+ l^-$ decay in the Standard Model and in supersymmetry // JHEP. - 2003. - Vol. 01. - 21 p.; arXiv:hep-ph/0212158.
10. *Aubert B. et al.* [BaBar Collaboration]. Direct CP, lepton flavor and isospin asymmetries in the decays $B \to K^{(*)} l^+ l^-$ // Phys. Rev. Lett. - 2008. - Vol. 102. - P. 091803. - 7 p.; arXiv:0807.4119.
11. *Aaij R. et al.* [LHCb Collaboration]. Measurement of the isospin asymmetry in $B \to K^{(*)} \mu^+ \mu^-$ decays // JHEP. - 2012. -Vol. 07. - 21 p.; arXiv:1205.3422.
12. *Bobeth C., Hiller G., Van Dyk D., Wacker C.* The decay $B \to K l^+ l^-$ at low hadronic recoil and model-independent $\Delta B = 1$ constraints // JHEP. - 2012. -Vol. 01. - 23 p.; arXiv:1111.2558.
13. *Ammar R. et al.* [CLEO Collaboration]. Evidence for penguin-diagram decays: First observation of $B^0 \to K^*(892)\gamma$ // Phys. Rev. Lett. - 1993. - Vol. 71. - 5 p.
14. *Ali A., Pecjak B.D., Greub C.* Towards $B \to V\gamma$ decays at NNLO in SCET // Eur. Phys. J. - 2008. - Vol. C55. - P. 577; arXiv:0709.4422.
15. *Aaij R. et al.* [LHCb Collaboration]. Measurement of the ratio of branching fractions $B(B^0 \to K^* \gamma)/B(B^0_s \to \varphi\gamma)$ and direct CP asymmetry in $B^0 \to K^* \gamma$ // Nucl. Phys. - 2013. - Vol. B867. - P. 1; arXiv:1209.0313.
16. *Beringer J. et al.* [Particle Data Group]. Review of particle physics // Phys. Rev. - 2012. - D86,010001.

EQUATION OF STATE OF STRANGE QUARK MATTER IN A STRONG MAGNETIC FIELD

A. A. Isayev[1,2], J. Yang[3]

[1] *National Science Center "Kharkov Institute of Physics and Technology", Kharkiv, Ukraine*
[2] *V. N. Karazin Kharkiv National University, Kharkiv, Ukraine*
[3] *Department of Physics and the Institute for the Early Universe Ewha Womans University, Seoul, Korea*

Thermodynamic properties of strange quark matter (SQM) in strong magnetic fields H up to 10^{20} G are considered at zero temperature within the MIT bag model. The effects of the pressure anisotropy, exhibiting in the difference between the pressures along and perpendicular to the field direction, become essential at $H > H_{\rm th}$, with the estimate $10^{17} < H_{\rm th} \lesssim 10^{18}$ G. The longitudinal pressure vanishes in the critical field H_c, which can be somewhat less or larger than 10^{18} G, depending on the total baryon number density and bag pressure. As a result, the longitudinal instability occurs in strongly magnetized SQM. The appearance of such instability sets the upper bound on the magnetic field strength which can be reached in the interior of a neutron star with the quark core. The longitudinal and transverse pressures as well as the anisotropic equation of state of SQM are determined under the conditions relevant for the cores of magnetars.

1. Introduction

Strange quark matter (SQM), composed of deconfined u, d and s quarks, can be the true ground state of matter, as was suggested in Refs. [1, 3]. This conjecture, if will be confirmed, would have important astrophysical implications. In particular, strange quark stars can exist in the form of stable SQM self-bound by strong interactions [4]. Also, if SQM is metastable at zero pressure, it can appear in the high-density core of a neutron star as a result of the deconfinement phase transition. In this case, the stability of SQM is provided by the gravitational pressure from the outer hadronic layers. Then a relevant astrophysical object is a hybrid star having a quark core and the crust of hadronic matter.

Another important aspect related to the physics of compact stars is that they are endowed with the magnetic field. For magnetars, the field strength at the surface can reach the values of about 10^{14} - 10^{15} G. In the interior of a magnetar the magnetic field strength can reach even larger values of about 10^{20} G [5]. In such ultrastrong magnetic fields, the effects of the $O(3)$ rotational symmetry breaking by the magnetic field become important [5]-[8]. In particular, the longitudinal (along the magnetic field) pressure is less than the transverse pressure resulting in the appearance of the longitudinal instability of the star's matter if the magnetic field exceeds some critical value. The effects of the pressure anisotropy should be accounted for in the consistent study of structural and polarization properties of a strongly magnetized stellar object. In this research, we consider the effects of the pressure anisotropy in SQM under the presence of a strong magnetic field within the framework of the MIT bag model.

2. General formalism

In the simplest version of the MIT bag model, quarks are considered as free fermions moving inside a finite region of space called a "bag". The effects of the confinement are accomplished by endowing the finite region with a constant energy per unit volume, the bag constant B. The energy spectrum of free relativistic fermions (u, d, s quarks and electrons) in an external magnetic field has the form

$$\varepsilon_\nu^i = \sqrt{k_z^2 + m_i^2 + 2\nu |q_i| H}, \quad \nu = n + \frac{1}{2} - \frac{s}{2}\mathrm{sgn}(q_i), \quad i = u, d, s, e, \tag{1}$$

where $\nu = 0, 1, 2...$ enumerates the Landau levels, n is the principal quantum number, $s = +1/2$ corresponds to a fermion with spin up, and $s = -1/2$ to a fermion with spin down. The lowest Landau level with $\nu = 0$ is single degenerate and other levels with $\nu > 0$ are double degenerate.

Further we will consider magnetized SQM at zero temperature. In the zero temperature case, the thermodynamic potential for an ideal gas of relativistic fermions of i th species in the external magnetic field reads [9]

$$\Omega_i = -\frac{|q_i| g_i H}{4\pi^2} \sum_{\nu=0}^{\nu_{\max}^i} (2 - \delta_{\nu,0}) \left\{ \mu_i k_{F,\nu}^i - \bar{m}_{i,\nu}^2 \ln \left| \frac{k_{F,\nu}^i + \mu_i}{\bar{m}_{i,\nu}} \right| \right\}, \tag{2}$$

where the factor $(2 - \delta_{\nu,0})$ takes into account the spin degeneracy of Landau levels, g_i is the remaining degeneracy factor [$g_f = 3$ for quarks (number of colors), and $g_e = 1$ for electrons], μ_i is the chemical potential, and

$$\bar{m}_{i,\nu} = \sqrt{m_i^2 + 2\nu\,|q_i|\,H}\,, \quad k_{F,\nu}^i = \sqrt{\mu_i^2 - \bar{m}_{i,\nu}^2}\,.$$

In Eq. (2), summation runs up to $\nu_{\max}^i = I\left[\frac{\mu_i^2 - m_i^2}{2\,|q_i|\,H}\right]$, $I[...]$ being an integer part of the value in the brackets. The number density $\varrho_i = -(\frac{\partial\Omega_i}{\partial\mu_i})_T$ of fermions of i th species is given by

$$\rho_i = \frac{|q_i|\,g_i H}{2\pi^2}\sum_{\nu=0}^{\nu_{\max}^i}(2-\delta_{\nu,0})k_{F,\nu}^i\,. \tag{3}$$

In order to find the chemical potentials of all fermion species, we will use the following constraints:

$$\frac{1}{3}(\rho_u + \rho_d + \rho_s) = \rho_B\,, \tag{4}$$

$$2\rho_u - \rho_d - \rho_s - 3\rho_{e^-} = 0\,, \tag{5}$$

$$\mu_d = \mu_u + \mu_{e^-}\,, \tag{6}$$

$$\mu_d = \mu_s \tag{7}$$

being the conditions of the total baryon number conservation, Eq. (4) (ϱ_B is the total baryon number density), charge neutrality, Eq. (5), and chemical equilibrium, Eqs. (6), (7), with respect to the weak processes occurring in the quark core of a neutron star [4].

At zero temperature, the energy density $E_i = \Omega_i + \mu_i\varrho_i$ for fermions of i th species reads

$$E_i = \frac{|q_i|\,g_i H}{4\pi^2}\sum_{\nu=0}^{\nu_{\max}^i}(2-\delta_{\nu,0})\left\{\mu_i k_{F,\nu}^i + \bar{m}_{i,\nu}^2\ln\left|\frac{k_{F,\nu}^i + \mu_i}{\bar{m}_{i,\nu}}\right|\right\}. \tag{8}$$

In the MIT bag model, the total energy density E, longitudinal p_l and transverse p_t pressures in quark matter are given by [5]

$$E = \sum_i E_i + \frac{H^2}{8\pi} + B, \tag{9}$$

$$p_l = -\sum_i \Omega_i - \frac{H^2}{8\pi} - B, \quad p_t = -\sum_i \Omega_i - HM + \frac{H^2}{8\pi} - B, \tag{10}$$

where B is the bag constant, and $M = \sum_i M_i = -\sum_i(\frac{\partial\Omega_i}{\partial H})_{\mu_i}$ is the total magnetization. It is seen that the magnetic field strength enters differently to the longitudinal and transverse pressures that reflects the breaking of the $O(3)$ rotational symmetry in a magnetic field. In a strong enough magnetic field, the quadratic on the magnetic field strength term (the Maxwell term) will be dominating, leading to increasing the transverse pressure and to decreasing the longitudinal pressure. Hence, there exists a critical magnetic field H_c, at which the longitudinal pressure vanishes, resulting in the longitudinal instability of SQM. In the astrophysical context, this means that in the magnetic fields $H \geqslant H_c$ a neutron star with the quark core will be subject to the gravitational collapse along the magnetic field.

3. Numerical results and conclusions

As was mentioned in Introduction, SQM can be in absolutely stable state (strange quark stars), or in metastable state, which can be stabilized by high enough external pressure (hybrid stars). Note that the analysis of the absolute stability window in the parameter space for magnetized superconducting color-flavor-locked strange matter in Ref. [10] shows that the maximum allowed bag pressure decreases with the magnetic field strength (cf. Eq. (32) of that work). The same holds true for magnetized nonsuperconducting SQM because the arguments of Ref. [10] can be reiterated in the given case with the only change that in Eq. (32) of Ref. [10] one should use the potential $\Omega = \sum_i \Omega_i$ with Ω_i given

by Eq. (2) of the present study. In numerical calculations, we adopt two values of the bag constant, $B = 100$ MeV/fm^3 and $B = 120$ MeV/fm^3, which are slightly larger than the upper bound $B \simeq 90$ MeV/fm^3 from the absolute stability window at zero magnetic field strength [3]. The core densities corresponding to these bag pressures are chosen equal to $\varrho_B = 3\varrho_0$ and $\varrho_B = 4\varrho_0$, respectively, which are, in principle, sufficient to produce deconfinement ($\varrho_0 = 0.16$ fm^{-3} being the nuclear saturation density). Therefore, in the astrophysical context, we assume a scenario in which SQM can be formed in the core of a strongly magnetized neutron star. For the quark masses, we use the values $m_u = m_d = 5$ MeV, and $m_s = 150$ MeV [9].

In order to calculate the energy density E of the system, transverse p_t and longitudinal p_l pressures, we, first, find the chemical potentials of all fermion species from the self-consistent Eqs. (4) - (7) and then determine the quantities E, p_t, p_l from Eqs. (9), (10). Fig. 1 shows the longitudinal p_l and transverse p_t pressures at zero temperature as functions of the magnetic field strength. It is seen that, first, the transverse and longitudinal pressures stay practically constant and indistinguishable from each other. This behavior of the pressures p_t and p_l corresponds to the isotropic regime. Beyond some threshold magnetic field H_{th}, the transverse pressure p_t increases with H while the longitudinal pressure p_l decreases with it, clearly reflecting the anisotropic nature of the total pressure in SQM in such strong magnetic fields (anisotropic regime). In the critical magnetic field H_c, the longitudinal pressure p_l vanishes. This happens at $H_c \approx 7.4 \cdot 10^{17}$ G for $\varrho_B = 3\varrho_0, B = 100\text{MeV/fm}^3$, and at $H_c \approx 1.4 \cdot 10^{18}$ G for $\varrho_B = 4\varrho_0, B = 120\text{MeV/fm}^3$. Above the critical magnetic field, the longitudinal pressure is negative leading to the longitudinal instability of SQM. Therefore, the thermodynamic properties of SQM should be considered in the magnetic fields $H < H_c$.

Let us now make the estimate of the threshold magnetic field H_{th} at which the anisotropic regime enters. Fig. 2 shows the normalized difference between the transverse and longitudinal pressures $\delta = (p_t - p_l)/p_0$ as a function of the magnetic field strength for the cases under consideration (p_0 being the isotropic pressure corresponding to the weak field limit with $p_l = p_t = p_0$). Following Refs. [5, 7, 8], for finding the threshold field H_{th} one can use the approximate criterion $\delta \simeq 1$. Then anisotropic regime enters at $H_{th} \approx 5.5 \cdot 10^{17}$ G for $\varrho_B = 3\varrho_0, B = 100\text{MeV/fm}^3$, and at $H_{th} \approx 9.9 \cdot 10^{17}$ G for $\varrho_B = 4\varrho_0, B = 120\text{MeV/fm}^3$. The anisotropy parameter δ reaches its maximum $\delta_c \sim 2$ in the critical field H_c, corresponding to the onset of the longitudinal instability in SQM. Thus, as follows from the previous discussions, the effects of the pressure anisotropy are important at $H_{th} < H < H_c$.

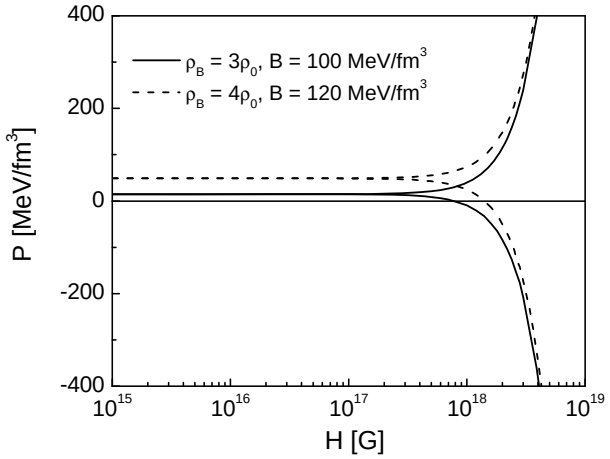

Fig. 1. Transverse (ascending branches) and longitudinal (descending branches) pressures in magnetized SQM at zero temperature as functions of the magnetic field strength for $\varrho_B = 3\varrho_0, B = 100\text{MeV/fm}^3$ (solid lines) and $\varrho_B = 4\varrho_0, B = 120\text{MeV/fm}^3$ (dashed lines).

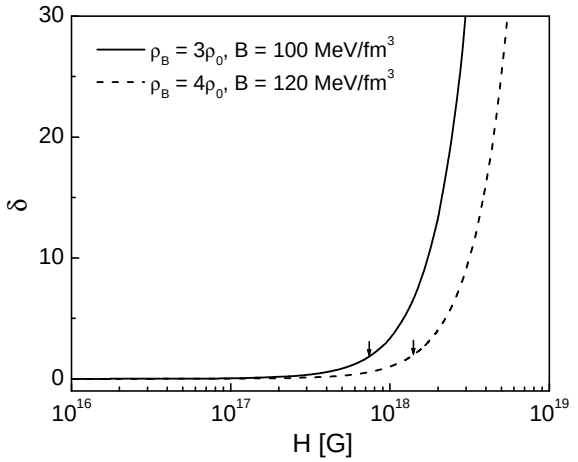

Fig. 2. Same as in Fig. 1, but for the normalized difference $\delta = (p_t - p_l)/p_0$ between the transverse and longitudinal pressures. The vertical arrows show the maximum normalized splitting δ_c at the corresponding critical field H_c.

Fig. 3 shows the energy density E of the system as a function of the magnetic field strength at zero temperature without the pure magnetic field energy contribution $E_f = \dfrac{H^2}{8\pi}$ (left panel) and with account of it (right panel). It is seen that the energy density of solely magnetized SQM decreases with H. However, the overall effect of the magnetic field, with account of the Maxwell term, is to increase the energy density of the system. Nevertheless, this effect of the magnetic field is, in fact, insignificant because the magnetic field in SQM is bound from above by the critical magnetic field H_c.

Because of the pressure anisotropy, the equation of state of SQM in a strong magnetic field is also anisotropic. Fig. 4 shows the dependence of the energy density E of the system on the transverse pressure p_t (left panel) and on the longitudinal pressure p_l (right panel) after excluding the dependence on H in these quantities. In particular, the anisotropic character of the pressure is reflected in the fact that the energy density is the increasing function of p_t while it decreases with p_l. This is because the dominant Maxwell term enters the transverse pressure p_t and the energy density E with positive sign while it enters the longitudinal pressure p_l with negative sign. In the right panel, the physical region corresponds to $p_l > 0$.

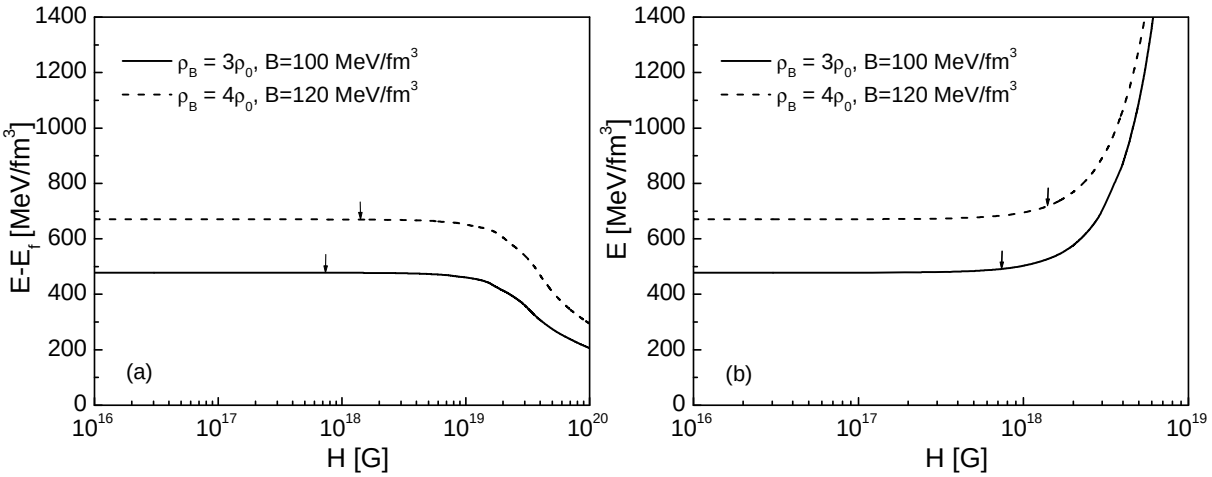

Fig. 3. Same as in Fig. 1, but for the energy density E of the system at zero temperature (a) without the magnetic field energy contribution $E_f = H^2/8\pi$ and (b) with account of E_f. The vertical arrows indicate the points corresponding to the critical field H_c.

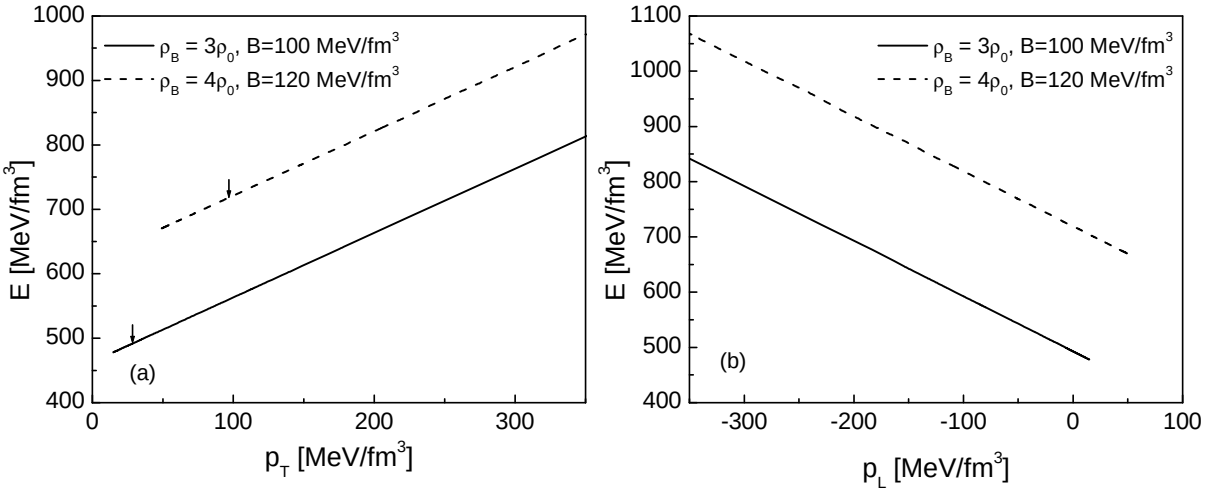

Fig. 4. The energy density E of the system at zero temperature as a function of: (a) the transverse pressure p_t and (b) the longitudinal pressure p_l. The meaning of the vertical arrows in the left panel is the same as in Fig. 3. In the right panel, the physical region corresponds to $p_l > 0$.

In summary, we have considered the impact of strong magnetic fields up to 10^{20} G on the EoS of SQM at zero temperature under additional constraints of total baryon number conservation, charge neutrality and chemical equilibrium with respect to various weak processes occurring in the system. The study has been done within the framework of the MIT bag model. In the numerical calculations, we have adopted two sets of the total baryon number density and bag pressure, $\varrho_B = 3\varrho_0, B = 100\text{MeV/fm}^3$ and $\varrho_B = 4\varrho_0, B = 120\text{MeV/fm}^3$. It has been shown that the longitudinal pressure decreases with the magnetic field (contrary to the transverse pressure increasing with H) and vanishes in the critical field H_c, resulting in the longitudinal instability of SQM. The value of the critical field H_c depends on the total baryon number density of SQM and the bag pressure B, and it turns out to be somewhat less or larger than 10^{18} G for the two sets of the parameters, considered in the given study. The longitudinal and transverse pressures as well as the anisotropic EoS of magnetized SQM have been determined at the total baryon number densities and magnetic field strengths relevant to the interiors of magnetars.

J.Y. was supported by grant 2010-0011378 from Basic Science Research Program through NRF of Korea funded by MEST and by grant R32-10130 from WCU project of MEST and NRF.

REFERENCES

1. *Bodmer A.* Collapsed Nuclei // Phys. Rev. D - 1971. - Vol. 4. - P. 1601 - 1606.
2. *Witten E.* Cosmic separation of phases // Phys. Rev. D - 1984. - Vol. 30. - P. 272 - 285.
3. *Farhi E., Jaffe R. L.* Strange matter // Phys. Rev. D - 1984. - Vol. 30. - P. 2379 - 2390.
4. *Alcock C., Farhi E., Olinto A. V.* Strange stars // Astrophys. J. - 1986. - Vol. 310. - P. 261 - 272.
5. *Ferrer E.J., de la Incera V., Keith J.P. et al.* Equation of state of a dense and magnetized fermion system // Phys. Rev. C - 2010. - Vol. 82. - P. 065802.
6. *Khalilov V.R.* Macroscopic effects in cold magnetized nucleons and electrons with anomalous magnetic moments // Phys. Rev. D - 2002. - Vol. 65. - P. 056001.
7. *Isayev A.A., Yang J.* Anisotropic pressure in dense neutron matter under the presence of a strong magnetic field // Phys. Lett. B - 2012. - Vol. 707. - P. 163 - 168.
8. *Isayev A.A., Yang J.* Finite temperature effects on anisotropic pressure and equation of state of dense neutron matter in an ultrastrong magnetic field // Phys. Rev. C - 2011. - Vol. 84. - P. 065802.
9. *Chakrabarty S.* Quark matter in a strong magnetic field // Phys. Rev. D - 1996. - Vol. 54. - P. 1306 - 1316.
10. *Paulucci L., Ferrer E. J., de la Incera V., Horvath J. E.* Equation of state for the magnetic-color-flavor-locked phase and its implications for compact star models // Phys. Rev. D - 2011. - Vol. 83. - P. 043009.

COMPARISON OF VARIOUS SCINTILLATION DETECTORS WITH n-γ PULSE SHAPE DISCRIMINATION

E. S. Konobeevski, M. V. Mordovskoy, I. M. Sharapov, S. V. Zuyev

Institute for Nuclear Research, Russian Academy of Sciences, Moscow, Russia

The possibility of using liquid scintillators and stilbene for digital n-γ discrimination using CAEN Waveform Digitizer is examined. The charge-integration and the charge-decay methods was employed to compare the pulse shape discrimination properties of four scintillators: EJ-301, EJ-315 (C_6D_6), NE-213 and stilbene. It is proposed to use the new shape-parameters to improve the n-γ discrimination.

To obtain new data on neutron-neutron interaction in a wide energy range (20 - 100 MeV) a setup for study the nd-breakup reaction was installed at the Institute for Nuclear Research (INR) of Russian Academy of Sciences [1]. This setup allows one to detect the three final particles - two neutrons and proton and determine their energies. The experiment is performed at the neutron beam channel RADEX of Moscow meson factory of INR [2].

In our study of the deuteron breakup reaction we use various scintillation detectors of neutrons. As an active target-detector we used liquid deuterated (C_6D_6) EJ-315-scintillator produced by Eljen Technology Company (analog of NE-230 and BC-537 scintillators). Behind the target along the beam of primary neutrons was placed neutron beam monitor on the base of stilbene crystal.

As the monitor and the active target detectors operate in the presence of background gamma rays, it is necessary to apply scintillators, allowing pulse-shape discrimination of neutrons and gamma rays. In our work we compared various organic scintillators based on stilbene crystals and liquid scintillators (EJ-301, EJ-315 and NE-213). Some characteristics of the tested scintillators are presented in Table 1.

Table 1. **The main characteristics of tested scintillators**

Scintillator	Light Output (% of Anthracene)	Mean Decay Times			References
		τ_1	τ_2	τ_3	
Stilbene	50 %	4.05 ns	33 ns	270 ns	[2]
EJ-301	78 %	3.16 ns	32.3 ns	270 ns	[3, 4]
EJ-315	60 %	3. 5 ns	?	?	[3, 4]
NE-213	78 %	3.16 ns	32.3 ns	270 ns	[2]

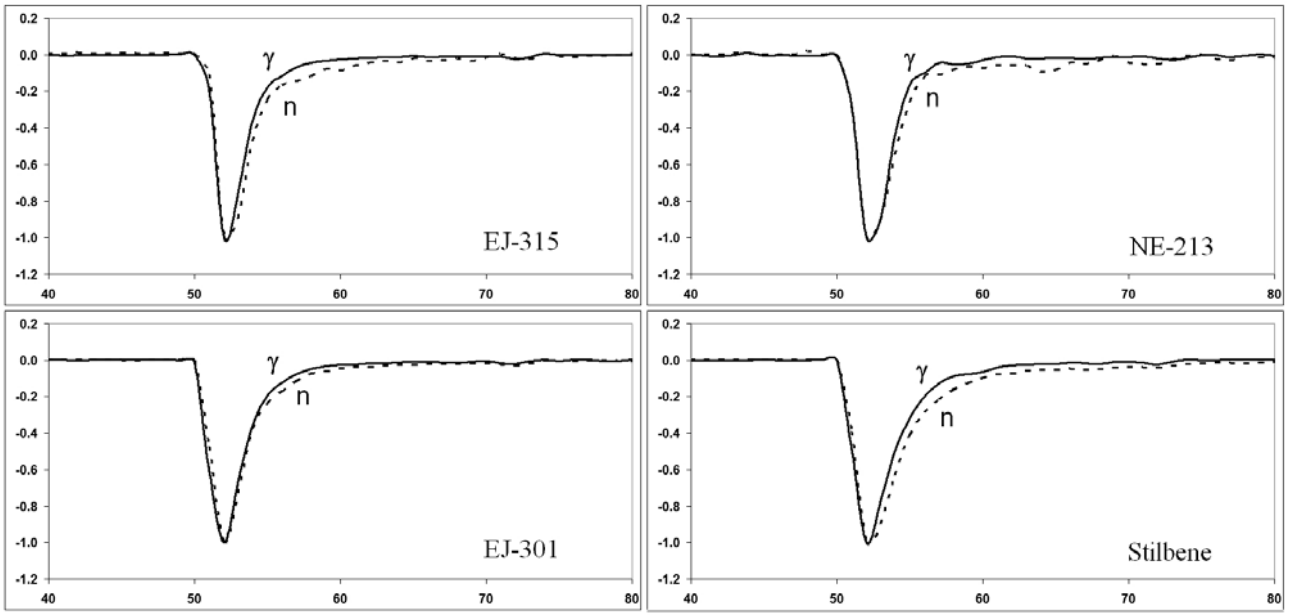

Fig. 1. Oscillograms of γ- and n-pulses reduced to the unit amplitude for tested scintillators irradiated by PuBe source. Scale interval of the horizontal axis is equal to 4 ns.

The most widely used methods for neutron detection in the presence of gamma radiation background utilizes the difference in the shapes of the scintillation pulses induced by neutrons (recoil protons) and γ-rays in organic scintillators. Pulse shape discrimination (PSD) phenomena discovered and demonstrated many decades ago are based on the existence of two-decay component fluorescence, in which, in addition to the main component decaying exponentially

(prompt fluorescence), there is usually a slower emission that has the same wavelength, but longer decay time (delayed emission) [5]. The short range of the energetic protons produced from neutron collisions yields a high concentration of exited molecules, compared to the longer range of the electrons from the gamma interactions, leading to the enhanced level of delayed emission with longer decay times in neutron-induced pulses in comparison to those produced by the gamma excitation. This leads to a somewhat different form of the scintillation signal from neutrons and gamma rays. The difference in the slow decay component of the light emission induced by neutrons and gamma-rays is the basis of digital pulse-shape discrimination in the scintillating detectors. The typical pulses from the scintillators tested, reduced to the unit amplitude, are shown in Fig. 1.

The associated photomultiplier signals were digitized by means of the Mod. DT5720C (2 Channel, 12bit, 250MS/s) Waveform Digitizer developed by CAEN - Costruzioni Apparecchiature Elettroniche Nucleari SpA [6]. Signals with amplitude up to 2 V were parallel digitized by 4096-channel FLASH-ADC with periodicity of 4 ns.

For different signals (see Fig. 1) some parameters characterizing the shape of the pulse were considered. Typical parameters of the pulse are shown in Fig. 2. We used them in the charge-integration and the charge-decay methods for the n-γ discrimination.

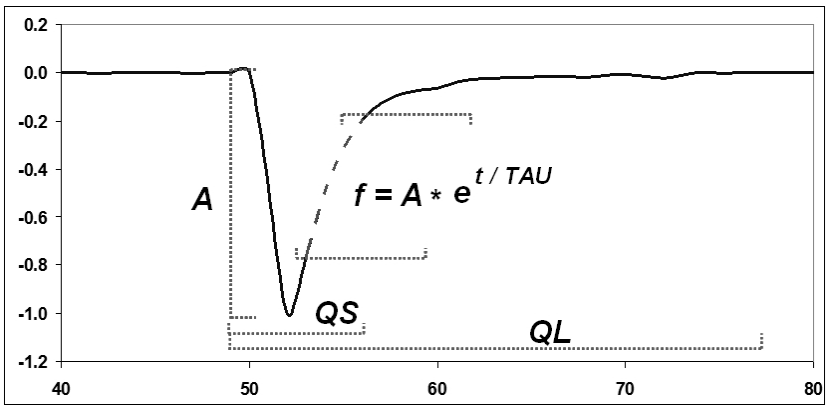

Fig. 2. Parameters characterizing the pulses of the scintillators.

The shape of the trailing edge of different pulses may be fitted using the function

$$f(t) = A \cdot e^{t/TAU}, \tag{1}$$

where $f(t)$ is the digitized value of the pulse at time t, A is the maximum amplitude, TAU is the decay time of the slow pulse component, different for neutrons and γ-rays. We also used QL/A-parameter, characterizing the effective width of the pulse and also different for neutrons and γ-rays, and PSD [6] parameter defined as:

$$PSD = \frac{QL - QS}{QL}, \tag{2}$$

where QL and QS are "long" and "short" parts of the integral of the pulse. The decay time TAU, effective width QL/A and PSD are the shape-parameters. For n-γ discrimination, usually, two-dimensional scatter-plots of the shape-parameters vs. pulse height are used.

For quantitative comparison of the quality of separation between γ-rays and neutrons one consider the Figure of merit (FOM) which is defined [6] as

$$FOM = \frac{\Delta Peak}{FWHM_n + FWHM_\gamma}, \tag{3}$$

where $\Delta Peak$ is the separation between the neutron and gamma peaks and $FWHM_n$ and $FWHM_\gamma$ are the full widths at half maximum of the neutron and gamma peaks in the n-γ spectrum, which is the projection of the two dimensional scatter plot onto the shape parameter axis. Therefore, a larger FOM value means a better separation between neutron and γ-ray events.

In Fig. 3 the typical two-dimensional scatter-plots of the shape-parameters PSD, QL/A and TAU vs. pulse-height A are shown for the stilbene irradiated by PuBe source. It is shown, that the scatter-plot PSD vs. A and its projection onto PSD-axis demonstrate the best n-γ discrimination with $FOM \sim 1.15$. All studied scintillators demonstrate such dependence.

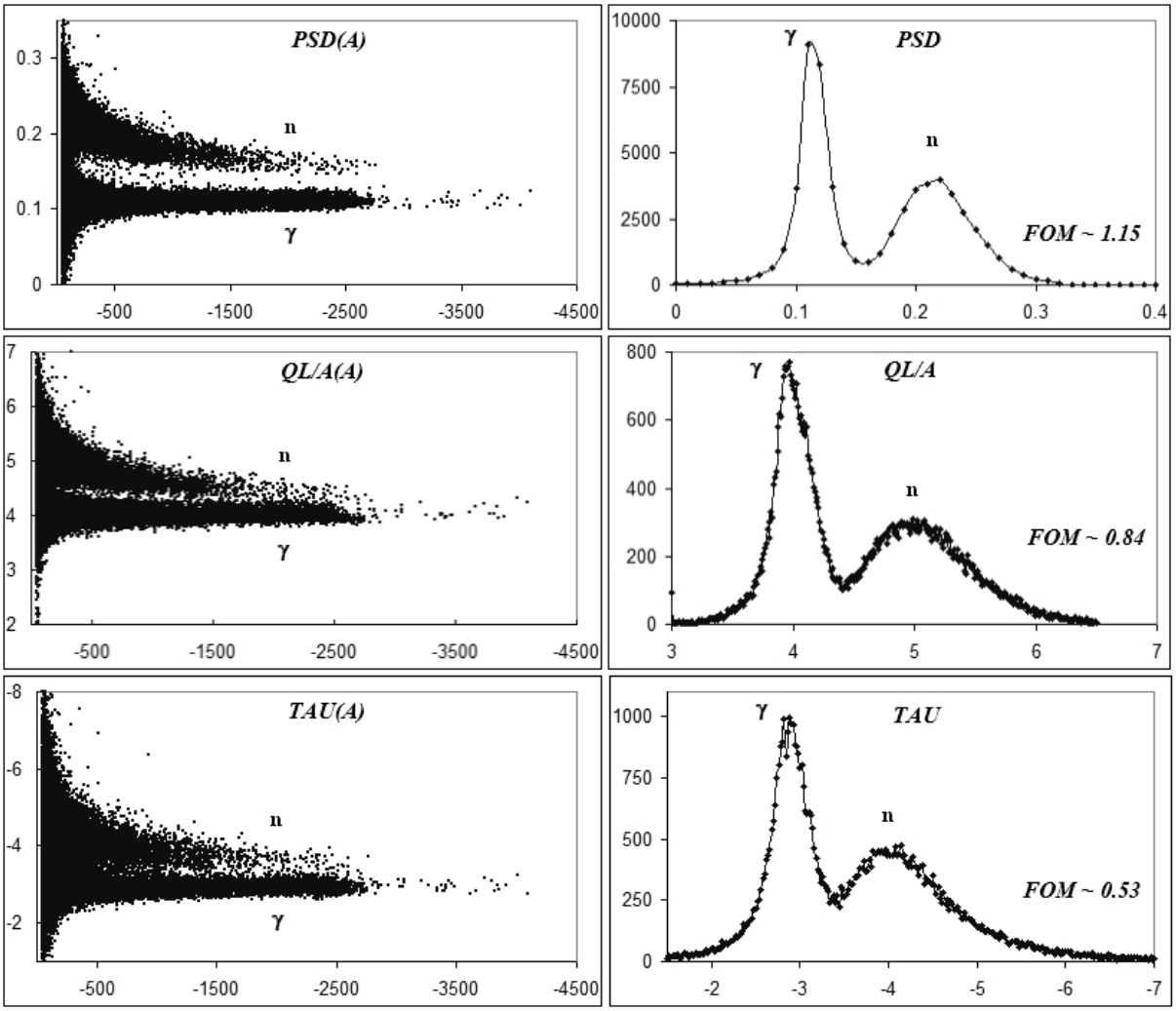

Fig. 3. Two-dimensional diagrams of the shape-parameters *PSD, QL*/*A* and *TAU* vs. *A* (*left*) and the corresponding projections on the *Y*-axis (*right*) obtained for the stilbene scintillator irradiated by PuBe source.

In addition to two-dimensional scatter-plots of the shape-parameters vs. pulse-height, *QL* or *QS* may also be considered two-dimensional scatter-plots of one shape-parameter to another. Examples of such two-dimensional scatter-plots for the cases *PSD* vs. *QL/A*, *PSD* vs. *TAU* and *TAU* vs. *QL/A* are shown in Fig. 4.

These diagrams show that the projections on the axes will give not very good separation. However, it is clear that the n- and γ-events are grouped in spots symmetrically around a some center. Further optimization of the separation can be achieved by a rotation around this center at an angle at which the line connecting the centers of n- and γ-spots becomes parallel to one of the axes of the two-dimensional diagram. This operation is equivalent to the rotation of primary axis at the same angle, and leads to some new variables, which are the new shape-parameters. Such coordinate transformation results in the diagram shown in Fig. 5. After the projection on the shape parameter axis we obtain the new spectra and can estimate the quality of separation using *FOM*, defined as above (2).

The data in Figs. 4 and 5 suggest the possibility of an improvement in n-γ separation with the introduction of the new shape-parameters with respect to the standard methods of n-γ discrimination.

It should be noted that the shape of the peaks in the shape parameter spectra is different from the Gaussian ones. In particular, there is a broad "tail" (a slow decrease far away from the center of the peak). Consequently, the use of FOM parameter, based on the half-width of the Gaussian peaks, does not fully reflect the quality of n-γ separation. In our view, it would be more appropriate to characterize the separation by the number of gamma-ray events that fall into the area of selection for neutron events, and vice versa. In this case, as the quality criteria of separation one can use the ratio of gamma peak to valley between neutron and gamma peak – A_{PV}. Table 2 shows that the rotation of the coordinate system can significantly increase this ratio, and, consequently, improve the quality of n-γ separation.

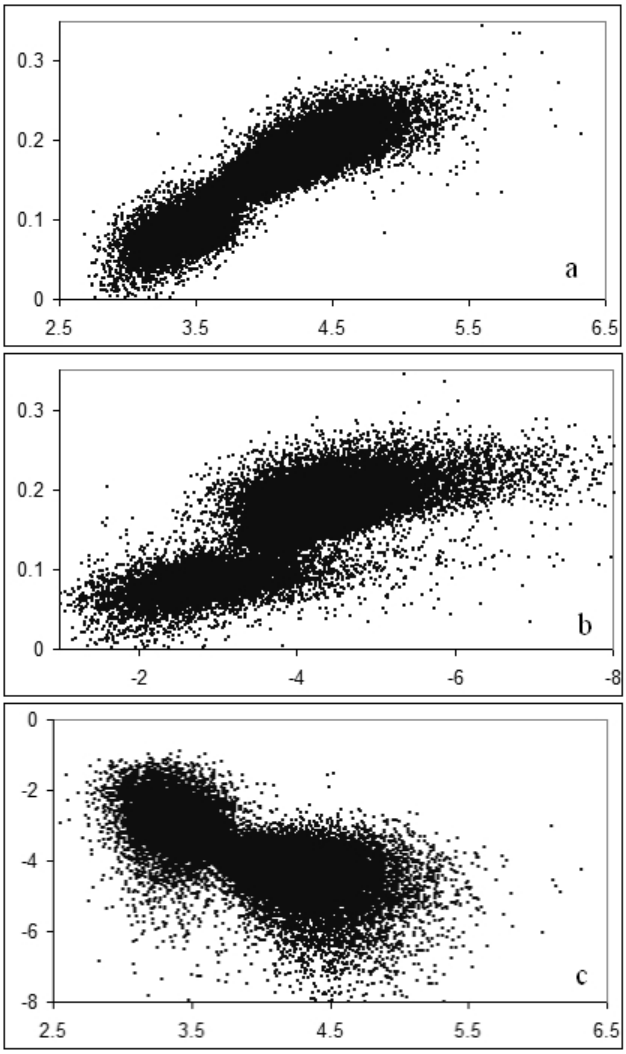

Fig. 4. The two-dimensional scatter-plots of the shape-parameters: *a – PSD* vs. *QL/A* (*FOM*(*PSD*)~1.17, *FOM*(*QL/A*)~0.73); *b – PSD* vs. *TAU* (*FOM*(*PSD*)~1.17, *FOM*(*TAU*)~0.52); *c – TAU* vs. *QL/A* (*FOM*(*TAU*)~0.52, *FOM*(*QL/A*)~0.73) are shown for the EJ-301 scintillator irradiating by PuBe source.

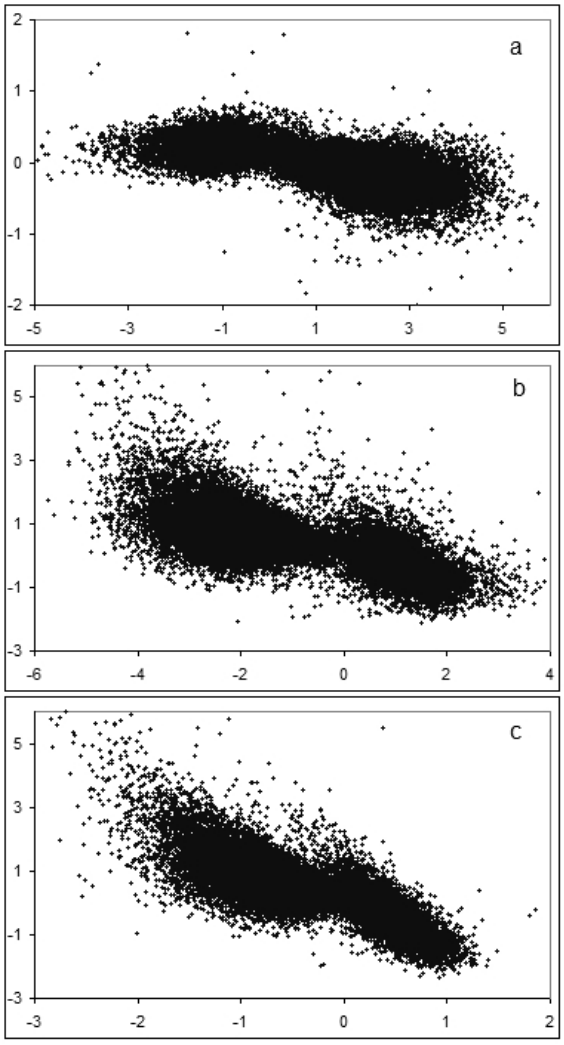

Fig. 5. The two-dimensional scatter-plots as in Fig. 4, after the transformation of variables: *a – PSD'* vs. *QL/A'* (*FOM*(*PSD'*)~1.17, *FOM*(*QL/A'*)~1.17); *b – PSD'* vs. *TAU'* (*FOM*(*PSD'*)~1.18, *FOM*(*TAU'*)~1.18); *c – TAU'* vs. *QL/A'* (*FOM*(*TAU'*)~0.85, *FOM*(*QL/A'*)~0.85).

Table 2. **The ratio of A_{PV} parameter after the coordinate transformation to the initial one**

Scintillator	$A_{PV}^{transf} / A_{PV}^{init}$
Stilbene	1.49
EJ-301	1.37
EJ-315	1.19
NE-213	1.57

So, one can note that the use of new variables *PSD'* vs. *QL/A'* and the *PSD'* vs. *TAU'* improves the quality of n-γ-separation. Data obtained using PuBe source, as well as those obtained at neutron channel RADEX show a good n-γ-separation in the energy region of 0.5-30 MeV.

This work was supported by RFBR grant number 10-02-00603.

REFERENCES

1. *Burmistrov Yu. M., Zuyev S. V., Konobeevski E. S., Mordovskoy M. V. et al.* An Experimental Setup for Studying Neutron–Neutron Final State Interaction on the Neutron Channel of the Moscow Meson Factory // Instruments and Experimental Techniques – 2009. – Vol. 52, No. 6. – P. 769 – 773.
2. *Koptelov E.A. et al.* A complex of complementary pulsed neutron sources, neutron and radiographic nanodiagnostic instruments at the Institute for Nuclear Research RAS // J. Phys.: Conf. Ser. – 2011. – Vol. 291. – P. 012012. – P. 1 – 6.
3. *Kuchnir F.T., Lynch F.J.* Time-Dependence of Scintillators and the Effect on P.S.D // IEEE Trans. Nucl. Sci. – 1968. – NS-15, No. 3 – P. 107 - 113.
4. *Eljen Technology Products* // http://www.eljentechnology.com.
5. *Zaitseva N, Glenn A, Carman L. et al.* Pulse Shape Discrimination in Impure and Mixed Single-Crystal Organic Scintillators // IEEE Trans. Nucl. Sci. – 2011. –Vol. 58, No. 6. – P. 3411 – 3420.
6. *CAEN. Application Note AN2506*. Digital Gamma Neutron discrimination with Liquid Scintillators // http://www.caen.it.

SEARCHING FOR PHYSICS BEYOND THE STANDARD MODEL AT THE LHC

T. V. Obikhod

Institute for Nuclear Research, National Academy of Sciences of Ukraine, Kyiv, Ukraine

We develop the necessary tools for building GUT models in F-theory. This approach is flexible because the local geometrical properties of singularities in F-theory compactifications encode the physical content of the theory. We see that geometry determines the gauge group, matter content and Yukawa coupling of a given model. These features are captured by a four-dimensional theory. Searches for SUSY in the context of the Minimal supersymmetric extension of the Standard Model (the MSSM) at the quark/string level of scale at the LHC are explained by unifying the fundamental interactions in the context of string theory. There are encouraging signs that string theory naturally includes many of the qualitative features of the Standard Model. Both gauge coupling unification as well as the matter content of the Standard Model hint at the presence of a unified gauge group structure at high energies. In order to use simulations to assess the prospects for detecting and measuring new particles at accelerators, MSSM model must be adopted. It seems necessary to reduce the size of the parameter space, by adopting one of the more restricted models for SUSY breaking, such as the mSUGRA one. Such models typically have only three or four parameters. The analysis of recent experimental data received from LHC (CMS) restricts the range of MSSM parameters to the new five parameters. Using computer programs SOFTSUSY, SDECAY and PYTHIA the mass spectrum, partial width and production cross sections of superpartners are calculated.

1. Introduction

The searches for new physics at the LHC motivated the necessary tools for building Grand Unification Theory (GUT) models in F-theory [1]. It is known that Minimal Supersymmetric Standard Model (MSSM) [2] through its connection to string theory improves the Standard Model (SM). There are several problems of SM, connected with our experimental knowledge and with some theoretical aspects:

1. there is the neutrino mass problem - the SM predicts neutrinos having zero mass, whereas we have experimental evidence for massive neutrinos;
2. SM field theory which include gravity ends up being non-renormalizable without predictions below the Planck scale;
3. SM has 19 free parameters to be determined experimentally;
4. the hierarchy problem;
5. the unification problem.

These problems can be decided with the help of MSSM model. In this model each particle, for example fermion, has its superpartner - boson with appropriate masses and couplings. MSSM includes new symmetry called R-parity. This gives us some usefull phenomenological results:

- the lightest sparticle, LSP must be stable and then it would be an excellent candidate for dark matter;
- the LSP interacts very weakly with matter;
- supersymmetric particles are produced in pairs;
- all supersymmetric particles are unstable and decay.

2. Category of D-branes

To construct the MSSM model from superstring theory we must use the notion of derived category [3]. We will give the short review of the theory of category.

A category $\cdots$ consists of the following data:

1. A class Ob$\cdots$ of objects $A, B, C, \ldots$;
2. A family of disjoint sets of morphisms $Hom(A,B)$ one for each ordered pair A,B of objects;
3. A family of maps

$$Hom(A,B)\cdot Hom(B,C)\to Hom(A,C)$$

one for each ordered triplet A,B,C of objects.

These data obey the axioms:

a) If $f: A\to B$, $g: B\to C$, $h: C\to D$, then composition of morphisms is associative, that is, $h(g\ f)=(h\ g)f$;

b) To each object B there exists a morphism $1_B: B\to B$ such that $1_B f = f$, $g1_B = g$ for $f: A\to B$ and $g: B\to C$.

There are several aspects that are necessary for construction the category of D-branes [3]:

- D-brane is associated to the locally-free sheaf;

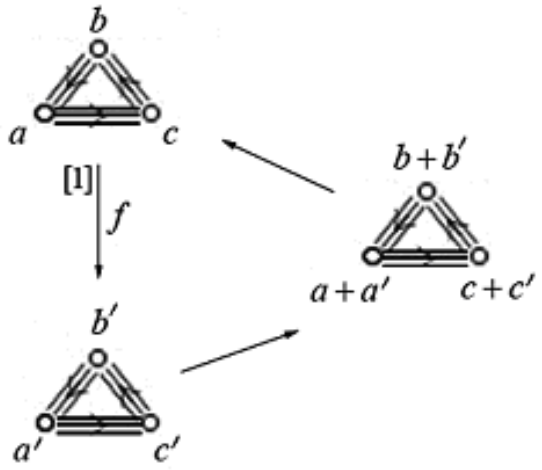

Distinguished triangle of derived category.

- An open string from one D-brane (sheaf E) to another D-brane (sheaf F) is given by an element of the group $Ext^q(E,F)$;
- the category of D-branes is the derived category of coherent sheaves $D(X)$;
- If X and Y are mirror Calabi-Yau threefolds then the category $D(X)$ is equivalent to the triangulated category $Tr_{-}(Y)$;
- D-branes on the orbifold C/G and open strings between them are described by the derived category of McKay quiver representations.

We consider the derived category of distinguished triangles over the abelian category of McKay quivers [3]. Objects of this category are distinguished triangles (numbers a,b,c and a',b',c' denote orbifold charges [4] characterizing McKay quivers); morphisms of this category are morphisms of distinguished triangles.

3. Particle content

The module space of an open superstring [5] has the form

$$Ext^0(Q,Q') = C^{aa'+bb'+cc'},$$
$$Ext^1(Q,Q') = C^{3ab'+3bc'+3ca'}. \quad (1)$$

Substituting in (1) orbifold charges

$$a=b=c=a'=b'=c'=4$$

and using the Langlands hypothesis [6], we obtain the realization of (1) in terms of SU(5) multiplets

$$3\cdot\left(24+5_H+\overline{5}_H+5_M+\overline{5}_M+10_M+\overline{10}_M\right).$$

This result determines the particle content of the MSSM.

4. Superpotential

The gauge invariant MSSM superpotential takes the form

$$W_{SU(5)} = \lambda^{d}_{ij}\cdot\overline{5}_H\cdot\overline{5}^{(i)}_M\cdot 10^{(j)}_M + \lambda^{u}_{ij}\cdot 5_H\cdot 10^{(i)}_M\cdot 10^{(j)}_M + \mu\cdot 5_H\cdot\overline{5}_H, \quad (2)$$

where 5_H and $\overline{5}_H$ are Higgs multiplets, $\overline{5}^{(i)}_M$ and $10^{(j)}_M$ are multiplets of quark and lepton superpartners, λ^{d}_{ij}, λ^{u}_{ij} are Yukawa coupling constants and μ is the Higgs mixing parameter.

5. Mass spectrum

The analysis of Yukawa coupling constants, based on observational hints and theoretical considerations, allows to restrict the parameter space in (2) to five free parameters [7]:

$$M_0 = 450\ \text{GeV},\ M_{1/2} = 425\ \text{GeV},$$
$$A_0 = 0,\quad \tan\beta = 10,\quad \operatorname{sgn}(\mu) = +1. \quad (3)$$

Using this restricted parameter set it is possible to calculate the mass spectrum of superpartners by application of the computer program SOFTSUSY [8]. This MSSM spectrum is shown in Table 1.

Table 1. **Mass spectrum of superpartners**

	GeV		GeV		GeV
$\tilde{u}_R$	974			$\tilde{g}$	1006
$\tilde{u}_L$	1000	$\tilde{\nu}_e$	525	$\tilde{\chi}_1^0$	174
$\tilde{d}_R$	972	$\tilde{e}_R$	477	$\tilde{d}_R$	327
$\tilde{d}_L$	1003	$\tilde{e}_L$	531	$\tilde{\chi}_3^0$	546
$\tilde{c}_R$	974			$\tilde{\chi}_4^0$	562
$\tilde{c}_L$	1000	$\tilde{\nu}_\mu$	525	$\tilde{\chi}_1^\pm$	327
$\tilde{s}_R$	972	$\tilde{\mu}_R$	477	$\tilde{\chi}_2^\pm$	562
$\tilde{s}_L$	1003	$\tilde{\mu}_L$	531		
$\tilde{t}_1$	741			h^0	114
$\tilde{t}_2$	947	$\tilde{\nu}_\tau$	523	A^0	749
$\tilde{b}_1$	910	$\tilde{\tau}_1$	471	H^0	749
$\tilde{b}_2$	968	$\tilde{\tau}_2$	531	$H^\pm$	753

6. Partial widths

Using the parameter set (3) it is possible to calculate partial widths of superpartners by application of the computer program SDECAY [9]. These partial widths are shown in Tables 2, 3.

Table 2. **Partial widths of superpartners**

	Channel	BR	Channel	BR
$\tilde{u}_R$	$\tilde{\chi}_1^0 u$	0.993	$\tilde{\chi}_4^0 u$	0.004
	$\tilde{\chi}_2^0 u$	0.002		
$\tilde{d}_R$	$\tilde{\chi}_1^0 d$	0.993	$\tilde{\chi}_4^0 d$	0.004
	$\tilde{\chi}_2^0 d$	0.002		
$\tilde{c}_R$	$\tilde{\chi}_1^0 c$	0.993	$\tilde{\chi}_4^0 c$	0.004
	$\tilde{\chi}_2^0 c$	0.002		
$\tilde{s}_R$	$\tilde{\chi}_1^0 s$	0.993	$\tilde{\chi}_4^0 s$	0.004
	$\tilde{\chi}_2^0 s$	0.002		

Table 3. **Partial widths of superpartners**

	Channel	BR	Channel	BR
$\tilde{g}$	$\tilde{d}_R d^*$	0.017	$\tilde{b}_1 b^*$	0.119
	$\tilde{d}_R^* d$	0.017	$\tilde{b}_1^* b$	0.119
	$\tilde{u}_R u^*$	0.015	$\tilde{b}_2 b^*$	0.021
	$\tilde{u}_R^* u$	0.015	$\tilde{b}_2^* b$	0.021
	$\tilde{s}_R s^*$	0.017	$\tilde{t}_1 t^*$	0.294
	$\tilde{s}_R^* s$	0.017	$\tilde{t}_1^* t$	0.294
	$\tilde{c}_R c^*$	0.015		
	$\tilde{c}_R^* c$	0.015		

7. Cross sections

Using the parameter set (3) it is possible to calculate production cross sections of superpartners by application of the computer program PYTHIA [10]. These cross sections at center-of-mass energy $\sqrt{s}$ =14 TeV are shown in Table 4.

Table 4. **Cross sections of superpartners**

Channel	Cross section, pb
$g\,g \to \tilde{g}\,\tilde{g}$	$\sigma_{\tilde{g}\tilde{g}} = 0.323$
$q\,g \to \tilde{d}_R\,\tilde{g}$	$\sigma_{\tilde{d}_R\tilde{g}} = 0.260$
$q\,g \to \tilde{u}_R\,\tilde{g}$	$\sigma_{\tilde{u}_R\tilde{g}} = 0.489$
$q\,q' \to \tilde{u}_R\,\tilde{d}_R$	$\sigma_{\tilde{u}_R\tilde{d}_R} = 0.132$

REFERENCES

1. *Beasley, C., Heckman, J.J., Vafa, C.* GUTs and exceptional branes in F-theory-I // arXiv:0802.3391 [hep-th].
2. *Haber H.E.* Introductory low-energy supersymmetry // arXiv: hep-ph/9306207.
3. *Aspinwall P.S.* D-branes on Calabi-Yau manifolds // arXiv: hep-th/0403166.

4. *Douglas M.R., Fiol B., Römelsberger C.* The spectrum of BPS branes on a noncompact Calabi-Yau // JHEP. - 2005. - Vol. 09. - P. 1 - 57.
5. *Katz S., Pantev T. and Sharpe E.* D-branes, orbifolds, and Ext groups // Nucl. Phys. - 2003. - Vol. B673. - P. 263 - 300.
6. *Schmid W.* Homogeneous complex manifolds and representations of semisimple Lie groups // Proc. Natl. Acad. Sci. USA. - 1968. - Vol. 69. - P. 56 - 59.
7. *Heckman J.J., Vafa C.* F-theory, GUTs, and the weak scale // arXiv:0809.1098 [hep-th].
8. *Allanach B.C.* SOFTSUSY2.0: a program for calculating supersymmetric spectra // Comput. Phys. Commun. - 2002. - Vol. 143. - P. 305 - 331.
9. *Muhlleitner M., Djouadi A., Mambrini Y.* SDECAY: a fortran code for the decays of the supersymmetric particles in the MSSM // Comput. Phys. Commun. - 2005. - Vol. 168. - P. 46 - 70.
10. *Sjöstrand T., Mrenna S., Skands P.* PYTHIA 6.4 Physics and Manual // JHEP. - 2006. - Vol. 05. - P. 1 - 26.

SPIN DETERMINATION OF HEAVY NONSTANDARD DILEPTON AND DIPHOTON RESONANCES AT THE LHC

A. A. Pankov, A. V. Tsytrinov

The Abdus Salam ICTP Affiliated Centre, Gomel State Technical University, Gomel, Belarus

New Physics scenarios generally predict the existence of very heavy quantum states that can possibly manifest themselves as peaks (or bumps) in the cross sections at the LHC. For values of the parameters in certain domains, different nonstandard models can generate peaks with the same mass and same number of events. In this case, the spin determination of a peak, requiring the angular analysis of the events, becomes crucial in order to identify the relevant nonstandard source. We discuss, using a particularly suitable symmetrically integrated angular asymmetry applied to Drell-Yan dilepton and diphoton events at LHC, the identification reach on the exchanges in these reactions of the following heavy bosons: spin-2 Randall-Sundrum graviton excitations; spin-1 heavy neutral gauge bosons *Z'*; and spin-0 SUSY *R*-parity violating sneutrinos.

1. Introduction

The existence of new heavy bosons predicted by many models beyond the standard model, with mass scales $M \gg M_{W,Z}$. They can be signalled by the observation of (narrow) peaks in the cross sections for reactions among standard model particles at the LHC. However, the observation of a peak/resonance at some large mass $M = M_R$ may not be sufficient to identify its underlying nonstandard model, in the multitude of potential sources of such a signal. Indeed, in 'confusion regions' of the parameters, different models can give the same M_R and same number of events under the peak. In that case, the test of the peak/resonance quantum numbers, the spin first, is needed to discriminate the models against each other in the confusion regions. Specifically, one defines for the individual nonstandard scenarios a *discovery reach* as the maximum value of M_R for peak observation over the standard model (SM) background, and an *identification reach* as the maximum value of M_R for which the model can be unambiguously discriminated from the other competing ones as the source of the peak. Particularly clean signals of heavy neutral resonances are expected in the inclusive reactions at the LHC:

$$p + p \to l^+ l^- + X \ \ (l = e, \mu) \quad \text{and} \quad p + p \to \gamma\gamma + X, \tag{1}$$

where they can show up as peaks in the dilepton and diphoton invariant mass M. While the total resonant cross section determines the number of events, hence the discovery reaches on the considered models, the angular analysis of the events allows to discriminate the spin-hypotheses from each other, due to the (very) different characteristic angular distributions. In the next sections we discuss the identification of the spin-2 against spin-1 and spin-0 hypotheses (and spin-0 only for diphoton case), modelled by the Randall - Sundrum model with one warped extra dimension [1], a set of Z' models [2], and the R-parity violating sneutrino exchange [3] (spin-0 scalar [4] for diphoton final states), respectively.

2. Cross sections and center-edge asymmetry

The total cross section for a heavy resonance discovery in the events (1) at an invariant dilepton (or diphoton) mass $M = M_R$ (with $R = G, Z', \tilde{\nu}$ denoting graviton, Z' and sneutrino, respectively) is:

$$\sigma(pp \to R) \cdot \mathrm{BR}(R \to l^+ l^-) = \int_{-z_{\mathrm{cut}}}^{z_{\mathrm{cut}}} \mathrm{d}z \int_{M_R - \Delta M/2}^{M_R + \Delta M/2} \mathrm{d}M \int_{y_{\min}}^{y_{\max}} \mathrm{d}y \frac{\mathrm{d}\sigma}{\mathrm{d}M\, \mathrm{d}y\, \mathrm{d}z}. \tag{2}$$

Resonance spin-diagnosis makes use of the comparison between the different differential angular distributions:

$$\frac{\mathrm{d}\sigma}{\mathrm{d}z} = \int_{M_R - \Delta M/2}^{M_R + \Delta M/2} \mathrm{d}M \int_{y_{\min}}^{y_{\max}} \frac{\mathrm{d}\sigma}{\mathrm{d}M\, \mathrm{d}y\, \mathrm{d}z} \mathrm{d}y. \tag{3}$$

In Eqs. (2) and (3), $z = \cos\theta_{\mathrm{cm}}$ and y are the lepton-quark (or photon-quark) angle in the dilepton (or diphoton) center-of-mass and the dilepton rapidity, respectively, and cuts on phase space due to detector acceptance are indicated. For integration over the full phase space, the limits would be $z_{\mathrm{cut}} = 1$ and $y_{\max} = -y_{\min} = \log(\sqrt{s}/M)$ with $\sqrt{s}$ the LHC collider center-of-mass energy. Furthermore, ΔM is an invariant mass bin around M_R, reflecting the detector energy resolution [5]. To evaluate the number N_S of resonant signal events time-integrated luminosities of 100 fb^{-1} for 14 TeV LHC (the ultimate expectations) and 20 fb^{-1} for 8 TeV LHC (expected to be archived before long shutdown) will be

assumed, and reconstruction efficiencies of 90 % for both electrons and muons and 80 % for photons). Typical experimental cuts are: $p_\perp > 20$ GeV and pseudorapidity $|\eta| < 2.5$ for both leptons; $p_\perp > 40$ GeV and $|\eta| < 2.4$ for photons. Finally, with N_B the number of 'background' events in the ΔM bin, determined by the SM predictions, the criterion $N_S = 5\sqrt{N_B}$ or 10 events, whichever is larger, will be adopted as the minimum signal for the peak discovery. To evaluate Eqs. (2) and (3) the parton subprocesses cross sections will be convoluted with the CTEQ6.6 parton distributions of Ref. [6]. Next-to-leading QCD effects for dilepton case can be accounted for by K -factors, and for simplicity of the presentation we here adopt a flat value $K = 1.3$. For diphoton case the full NLO calculations were done [7]. In practice, due to the completely symmetric pp initial state, the event-by-event determination of the sign of z may at the LHC be not fully unambiguous. This difficulty may be avoided by using as the basic observable for angular analysis the z -evenly integrated center-edge angular asymmetry, defined as [8 - 10]:

$$A_{\rm CE} = \frac{\sigma_{\rm CE}}{\sigma} \quad \text{with} \quad \sigma_{\rm CE} \equiv \left[\int_{-z^*}^{z^*} - \left(\int_{-z_{\rm cut}}^{-z^*} + \int_{z^*}^{z_{\rm cut}} \right) \right] \frac{{\rm d}\sigma}{{\rm d}z} {\rm d}z. \tag{4}$$

In Eq. (4), $0 < z^* < z_{\rm cut}$ defines the separation between the 'center' and the 'edge' angular regions and is *a priori* arbitrary, but the numerical analysis shows that it can be 'optimized' to $z^* \simeq 0.5$. The additional advantage of using $A_{\rm CE}$ is that, being a ratio of integrated cross sections, it should be much less sensitive to systematic uncertainties than 'absolute' distributions (examples are the K -factor uncertainties from different possible sets of parton distributions and from the choice of factorization vs renormalization mass scales).

3. New physics models

RS model with one compactified extra dimension. Originally, this model was proposed to solve the so-called gauge hierarchy problem, $M_{\rm EW} \ll M_{\rm Pl} \simeq 10^{16}$ TeV. The simplest set-up, called RS, consists of one warped extra spatial dimension, y, two three-dimensional branes placed at a compactification relative distance $y_c = \pi R_c$, and the specific 5-D metric [1]

$$ds^2 = \exp(-2k|y|)\eta_{\mu\nu} dx^\mu dx^\nu - dy^2. \tag{5}$$

In (5), $\eta_{\mu\nu}$ is the usual Minkowski tensor and $k > 0$ is the 5-D curvature. SM fields are localized to the so-called TeV brane, and gravity can propagate in the full 5-D 'bulk', included the other, so-called Planck, brane. On this brane, the effective 4-D mass scale is related to the Newton constant by the relation $\overline{M}_{\rm Pl} = 1/\sqrt{8\pi G_{\rm N}} = 2.44 \times 10^{15}$ TeV. Denoting by M_* the 5-D effective mass scale, analogously related to the cubic root of the 5-D Newton constant, the relation can be derived: $\overline{M}_{\rm Pl}^2 = (M_*{}^3/k)(1 - \exp(-2k\pi R_c))$. Under the basic 'naturalness' assumption $\overline{M}_{\rm Pl} \sim M_* \sim k$, needed to avoid further fine tunings, for $kR_c \sim 11$ the geometry of Eq. (5) implies that the mass spectrum on the Planck brane, of the 10^{15} TeV order, can on the TeV brane where SM particles live and interact, be exponentially 'warped' down to the effective scale $\Lambda_\pi = \overline{M}_{\rm Pl} \exp(-k\pi R_c)$ of the one (or few) TeV order. Interestingly, this brings gravitational effects into the reach of LHC. Junction conditions on the graviton field at the branes y -positions imply the existence of a tower of spin-2 graviton excitations, $h_{\mu\nu}^{(n)}$, with a specifically spaced mass spectrum $M_n = x_n k \exp(-k\pi R_c)$ in the TeV range (x_n are the roots of $J_1(x_n) = 0$). Denoting by $T^{\mu\nu}$ the SM energy-momentum tensor, and by $h_{\mu\nu}^{(0)}$ the zero-mode, ordinary, graviton, the couplings of graviton excitations to the SM particles are only $(1/\Lambda_\pi)$ suppressed (not $1/\overline{M}_{\rm Pl}$):

$$L_{\rm TeV} = -\left[\frac{1}{\overline{M}_{\rm Pl}} h_{\mu\nu}^{(0)}(x) + \frac{1}{\Lambda_\pi} \sum_{n=1}^{\infty} h_{\mu\nu}^{(n)}(x) \right] T^{\mu\nu}(x). \tag{6}$$

The RS model can be conveniently parameterized by the mass of the lowest graviton excitation $M_G \equiv M_1$, the only one presumably in the reach of LHC, and the 'universal', dimensionless, coupling constant $c = k/\overline{M}_{\rm Pl}$. The scale Λ_π and the (narrow) widths $\Gamma_n = \rho M_n x_n^2 c^2$ (with $\rho \simeq 0.1$), are then derived quantities. Theoretically 'natural' ranges expected for these parameters are $0.01 \le c \le 0.1$ and $\Lambda_\pi < 10$ TeV. Current 95 % limits from ATLAS and CMS experiments are, at the 7 TeV, 5 fb^{-1} LHC [11,12]: $M_G > 910$ GeV ($c = 0.01$) up to $M_G > 2160$ GeV ($c = 0.1$).

Heavy neutral gauge bosons. The spin-1 hypothesis is in process (1) realised by $q\bar{q}$ annihilation into lepton pairs through Z' intermediate states [2]. Such bosons are generally predicted by electroweak models beyond the SM, based

on extended gauge symmetries. Generally, Z' models depend on $M_{Z'}$ and on the left- and right-handed couplings to SM fermions. Further results will be given for a popular class of models for which the values of these couplings are fixed theoretically, thus only $M_{Z'}$ is a free parameter. These are the Z'_χ, Z'_ψ, Z'_η, $Z'_{\rm LR}$, $Z'_{\rm ALR}$ models, and the 'sequential' $Z'_{\rm SSM}$ model with Z' couplings identical to the Z ones. Current experimental lower limits (95 % CL) on $M_{Z'}$ depend on models, and range from 2260 GeV for Z'_ψ up to 2590 TeV for $Z'_{\rm SSM}$ [13]. The leading z-even angular distributions for the LO partonic subprocess $\bar{q}q \to Z' \to l^+l^-$ has the same form as the SM and, therefore, the resulting $A_{\rm CE}$ is *the same for all* Z' models.

R-parity violating sneutrino exchange. R-parity is defined as $R_p = (-1)^{(2S+3B+L)}$, and distinguishes particles from their superpartners. In scenarios where this symmetry can be violated, supersymmetric particles can be singly produced from ordinary matter. In the dilepton process (1) of interest here, a spin-0 sneutrino can be exchanged through the subprocess $\bar{d}d \to \tilde{\nu} \to l^+l^-$ and manifest itself as a peak at $M = M_{\tilde{\nu}}$ with a flat angular distribution [3]. Results on next-to-leading QCD orders available in the literature indicate the possibility of somewhat large K-factors, in particular due to supersymmetric QCD corrections. Besides $M_{\tilde{\nu}}$, the cross section is proportional to the R-parity violating product $X = (\lambda')^2 B_l$ where B_l is the sneutrino leptonic branching ratio and λ' the relevant sneutrino coupling to the $\bar{d}d$ quarks. Current limits on the relevant λ's are of the order of 10^{-2}, and the experimental 95 % CL lower limits on $M_{\tilde{\nu}}$ range from 397 GeV (for $X = 10^{-4}$) to 866 GeV (for $X = 10^{-2}$) [14]. We take for X, presently not really constrained for sneutrino masses of order 1 TeV or higher, the (rather generous) interval $10^{-5} < X < 10^{-1}$.

Model for scalar particle exchange. For the process with diphoton final states we consider the simple model of a scalar particle S, singlet under the SM gauge group and with mass $M \equiv M_S$ of the TeV order, proposed in Ref. [4]. The trilinear couplings of S with gluons, electroweak gauge bosons and fermions, are in this model:

$$L_{\rm Scalar} = c_3 \frac{g_s^2}{\Lambda} G^a_{\mu\nu} G^{a\mu\nu} S + c_2 \frac{g^2}{\Lambda} W^i_{\mu\nu} W^{i\mu\nu} S + c_1 \frac{g'^2}{\Lambda} B_{\mu\nu} B^{\mu\nu} S + \sum_f c_f \frac{m_f}{\Lambda} \bar{f}\, f\, S. \tag{7}$$

In Eq. (15), Λ is a high mass scale, of the TeV order of magnitude, and c's are dimensionless coefficients that are assumed to be of order unity, reminiscent of a strong novel interaction. Following Ref. [4], we assume $\Lambda = 3$ TeV and allow the coefficients c_i to take values equal to, or less than, unity. The leading order diphoton production process is in this model dominated by the s-channel exchange $gg \to S \to \gamma\gamma$. Numerically, it turns out from the cross section that there exist a 'confusion region' of the c's where scalar diphoton states can be produced with same mass M_S and number of events as the RS gravitons, and the width Γ_S comparable to (or smaller than) the mass window ΔM. The difference lies in the differential cross section, which in this case has the flat z-behaviour.

4. Spin identification with center-edge asymmetry

The nonstandard models briefly described in the previous section can mimic each other as sources of an observed peak in M, for values of the parameters included in so-called 'confusion regions' (of course included in their respective experimental and/or theoretical discovery domains), where they can give same numbers of signal events N_S. The M_R - N_S plots in Fig. 1 show as an example 'confusion regions' between spin-2 graviton and spin-0 sneutrino, spin-1 Z' for dilepton process and spin-0 scalar for diphotons. The number of events needed for 5-σ discovery at the 8 TeV LHC with luminosity $L_{\rm int} = 20$ fb^{-1} and current limits on RS resonance obtained from 7 TeV LHC data are also shown. In such confusion regions, one can try to discriminate models from one another by means of the angular distributions of the events, directly reflecting the different spins of the exchanged particles. We continue with the examples of confusion regions in Fig. 1 and start from the assumption that an observed peak at $M = M_R$ is the lightest spin-2 graviton (thus, $M_R = M_G$). We define a 'distance' among models accordingly:

$$\Delta A^{Z'}_{\rm CE} = A^G_{\rm CE} - A^{Z'}_{\rm CE} \qquad \text{and} \qquad \Delta A^{\tilde{\nu}}_{\rm CE} = A^G_{\rm CE} - A^{\tilde{\nu}}_{\rm CE}. \tag{8}$$

To assess the domain in the (M_G, c) plane where the competitor spin-1 and spin-0 models giving the same N_S under the peak can be *excluded* by the starting RS graviton hypothesis, a simple-minded χ^2-like criterion can be applied, which compares the deviations (8) with the uncertainty (statistical and systematic combined) $\delta A^G_{\rm CE}$ pertinent to the RS model. We impose the two conditions

$$\chi^2 \equiv \left(\Delta A^{Z',\tilde{\nu}}_{\rm CE} / \delta A^G_{\rm CE} \right)^2 > \chi^2_{\rm CL}. \tag{9}$$

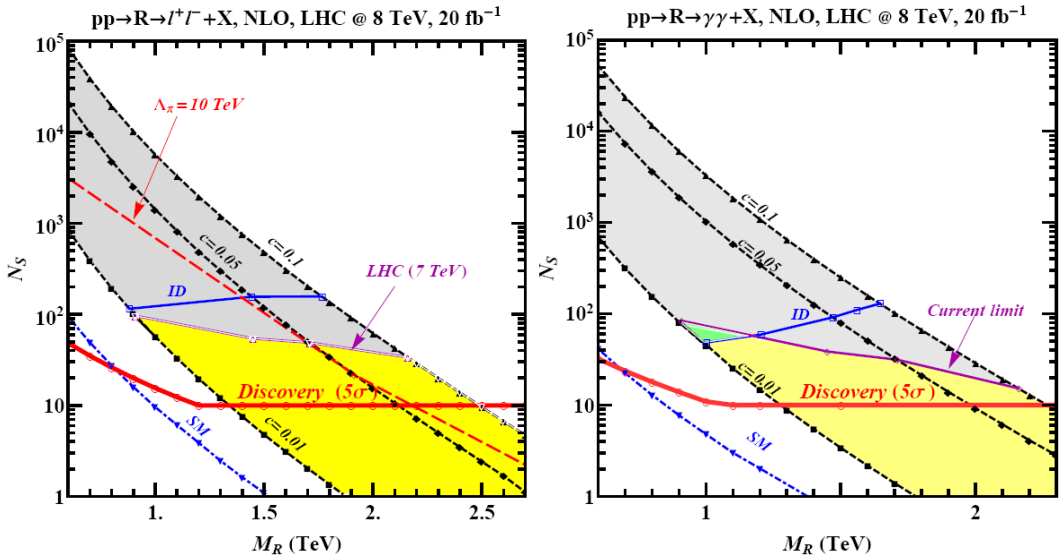

Fig. 1. Number of resonance (signal) events N_S *vs* M_R ($R = G$) at the LHC with $\sqrt{s} = 8$ TeV and $L_{int} = 20$ fb^{-1} for the process $pp \to G \to l^+l^- + X$ (left panel) and $pp \to G \to \gamma\gamma + X$ (right panel). The shaded area corresponds to the KK graviton signature space for $0.01 \le c \le 0.1$. Current experimental limits, 5σ discovery level and minimal number of events for RS graviton identification are also shown.

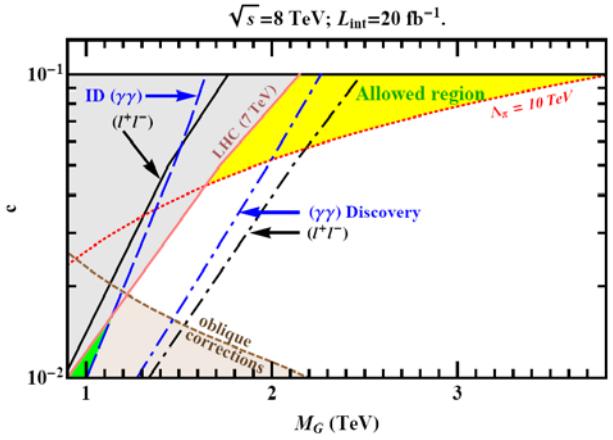

Fig. 2. Discovery and identification on RS graviton at the 8 TeV LHC with luminosity 20 fb^{-1}.

Eq. (18) contains the definition of χ^2, and the χ^2_{CL} specifies a desired confidence level (3.84 for 95 % CL). This condition determines the minimum number of events, N_S^{min}, needed to exclude the spin-1 and spin-0 hypotheses (hence to establish the graviton spin-2), and this in turn will determine the RS graviton *identification* domain in the (M_G, c) plane. Of course, an analogous procedure can be applied to the identification of Z' and $\tilde{\nu}$ exchanges against the two competing ones as sources of a peak in process. In process for RS graviton identification exploiting the same procedure one needs to exclude spin-0 only, since spin-1 resonance is forbidden by Landau-Yang theorem. Fig. 2 shows the identification domain for the RS graviton excitation, foreseeable from both the diphoton and the dilepton events, at the 8 TeV LHC with luminosity 20 fb^{-1}. Specifically: the regions to the left of the 'Discovery' lines are discovery domains at 5σ; the identification domains at 95 % CL are to the left of the 'ID' lines; the line 'LHC (7 TeV)' represents the current experimental lower limits from the 7 TeV LHC, the curve 'LHC (7 TeV)' delimits the 'allowed' region from below; the line 'oblique corrections' represents constraints (from below) from a fit to the oblique EW parameters. The Table represents the discovery (5σ) and identification (95 %) reaches on RS graviton at the 14 TeV LHC with luminosity 100 fb^{-1}. In conclusion, the Table shows that the χ^2-based angular analysis of dilepton and diphoton events described here can at the 14 TeV LHC provide identification limits on the RS graviton resonance ranging from $M_G = 2.0$ TeV ($c = 0.01$) up to $M_G = 3.3$ TeV ($c = 0.1$).

Discovery and identification reaches (in TeV) on RS graviton for 14 TeV LHC with L_{int} = 100 fb^{-1}.

c	Discovery	Identification
	$pp \to l^+l^- + X$	
0.01	2.5	1.6
0.1	4.6	3.2
	$pp \to \gamma\gamma + X$	
0.01	2.5	2.0
0.1	4.3	3.3

While, as one can see from Fig. 2, the spin angular analysis of RS graviton with the 8 TeV LHC and luminosity 20 fb^{-1} is not possible, but it still leaves some room for RS graviton resonance discovery up to $M_G = 2.5$ TeV for $c = 0.1$. The diphoton and dilepton channels can be considered as being complementary for both discovery and identification. The combination of their angular analyses, and the branching ratios prediction $\mathrm{Br}(\gamma\gamma)/\mathrm{Br}(l^+l^-) = 2$, should provide reliable method for identification of the RS graviton model.

REFERENCES

1. *Randall L., Sundrum R.* A large mass hierarchy from a small extra dimension // Phys. Rev. Lett. - 1999. - Vol. 83. - P. 3370 - 3373.
2. *Langacker P.* The Physics of Heavy Z' Gauge Bosons // Rev. Mod. Phys. - 2008. - Vol. 81. - P. 1199 - 1228.
3. *Kalinowski J., Rückl J.R., Spiesberger H., Zerwas P.M.* Supersymmetry with R-parity breaking: Contact interactions and resonance formation in leptonic processes at LEP2 // Phys. Lett. B. - 1997. - Vol. 406. - P. 314 - 320.
4. *Barbieri R., Torre R.* Signals of single particle production at the earliest // Phys. Lett. B. - 2011. - Vol. 695. - P. 259 - 263.
5. *ATLAS Collaboration*. ATLAS: Detector and physics performance technical design report. Volume 1 // CERN-LHCC-99-14. May 1999. 475 pp. ATLAS: Detector and physics performance technical design report. Volume 2 // CERN-LHCC-99-15. May 1999. 519 pp.
6. *Nadolsky P.M. et al.* Implications of CTEQ global analysis for collider observables // Phys. Rev. D. - 2008. - P. 013004.
7. *Kumar M.C., Mathews P., Pankov A.A. et al.* Spin-analysis of s-channel diphoton resonances at the LHC // Phys. Rev. D. - 2011. - P. 115008.
8. *Osland P., Pankov A.A., Paver N., Tsytrinov A.V.* Spin identification of the Randall-Sundrum resonance in lepton-pair production at the LHC // Phys. Rev. D. - 2008. - P. 035008.
9. *Osland P., Pankov A.A., Tsytrinov A.V., Paver N.* Spin and model identification of Z' bosons at the LHC // Phys. Rev. D. - 2009. - P. 115021.
10. *Osland P., Pankov A.A., Paver N., Tsytrinov A.V.* Sneutrino identification in dilepton events at the LHC // Phys. Rev. D. - 2010. - P. 115017.
11. *ATLAS Collaboration,* Search for high-mass dilepton resonances with 5/fb of pp collisions at sqrt(s) = 7 TeV with the ATLAS experiment // ATLAS-CONF-2012-007. - 2012; *ATLAS Collaboration,* Search for Extra Dimensions in the Diphoton Channel using 4.9/fb of Proton-Proton Collisions recorded at 7 TeV with the ATLAS Detector // ATLAS-CONF-2012-087. - 2012.
12. *CMS Collaboration*. Search for narrow resonances in dilepton mass spectra in pp collisions at sqrt(s) = 7 TeV // Phys. Lett. B. - 2012. - Vol. 714. - P. 158 - 179.
13. *CMS Collaboration*. Search for Resonances in the Dilepton Mass Distribution in pp Collisions at sqrt(s) = 8 TeV // CMS-PAS-EXO-12-015. - 2012; *ATLAS Collaboration*. Search for high-mass dilepton resonances with 5 fb-1 of pp collisions at sqrt(s) = 7 TeV with the ATLAS experiment // ATLAS-CONF-2012-007. - 2012.
14. *CDF Collaboration*. "A search for high-mass resonances decaying to dimuons at CDF // Phys. Rev. Lett. - 2009. - P. 091805.

SEARCH FOR ASSOCIATED HIGGS BOSON PRODUCTION WITH A W OR Z BOSON AND DECAYING TO A $b\bar{b}$ PAIR WITH THE ATLAS DETECTOR

Y. Pylypchenko (on behalf of the ATLAS collaboration)

University of Iowa, Iowa City, Iowa, USA

A summary of the ATLAS search for Higgs boson decaying into a pair of b-quarks and produced in association with W or Z boson is presented. No evidence of $H \to b\bar{b}$ signal is observed in $\sqrt{s}$ =7 TeV proton-proton collision data collected by the ATLAS detector in 2011 LHC run, corresponding to 4.7 fb^{-1} of integrated luminosity. The upper limits on Higgs boson production cross-section are reported for the mass range between 110 and 130 GeV.

1. Introduction

In the Standard Model (SM) of elementary particles the origin of the mass is explained by the Higgs mechanism, which also predicts the existence of the Higgs scalar boson. The search for the SM Higgs boson is one of the main goals of the ATLAS experiment [1] at the Large Hadron Collider (LHC) [2].

Recently, ATLAS reported a conclusive evidence of a new particle with mass 126 ± 0.4(stat) ± 0.4 (syst) GeV using the combination of data recorded during 2011 in $\sqrt{s}$ = 7 TeV proton-proton collisions, corresponding to 4.8 fb^{-1}, and early 2012 data recorded in $\sqrt{s}$ =8 TeV proton-proton collisions, corresponding to 5.8 fb^{-1} [3]. The observed decays to a pair of vector bosons indicate that the new particle is a neutral boson. Within the experimental uncertainties the observed new particle has characteristics that are compatible with the expectations for SM Higgs boson. However, at present a wide variety of interpretations of the observed signal are still possible. Combining the results from all the search channels ATLAS excluded SM Higgs bosons with masses outside a narrow range near the observed signal. The decays to SM fermions have not been observed so far.

Here, we present a summary of the results of the ATLAS search for associated Higgs boson production with a W or Z and decaying to $b\bar{b}$, in three channels, $WH \to l\nu b\bar{b}$, $ZH \to l^+l^-b\bar{b}$ (where l = e, μ) and $ZH \to \nu\bar{\nu}b\bar{b}$, using the data collected by ATLAS during 2011 in proton-proton collisions at $\sqrt{s}$ =7 TeV, corresponding to 4.6 - 4.7 fb^{-1} depending on the search channel [4]. The production of Higgs boson in association with a vector gauge boson W or Z is used in order to discriminate against the large multi-jet background.

2. The ATLAS Detector

ATLAS is one of the two large multipurpose detectors built at the LHC to explore physics at the TeV scale [1]. It consists of several detector subsystems. Closest to the interaction point is the Inner Detector (ID), the charged particle tracker immersed in a 2 T axial magnetic field provided by a superconducting solenoid magnet. The ID comprises three different technologies: Pixel detectors, SemiConductor Tracker (SCT) based on silicon micro-strip detectors and a straw-tube tracker with transition radiation detection capacity (TRT). The ID provides the reconstruction of charged particle tracks within a pseudorapidity range $|\eta| < 2.5$ [1].

The high granularity liquid argon (LAr) electromagnetic calorimeters surround the ID. The electromagnetic calorimeter is divided into a central barrel ($|\eta| < 1.475$) and end-cap ($1.375 < |\eta| < 3.2$) parts. In the regions adjacent to the inner detector ($|\eta| < 2.5$), it is radially segmented into three layers, to facilitate e/γ from π^0 separation and to provide required resolution of the electromagnetic shower position and direction measurements. In the region of $|\eta| < 1.8$, a presampler detector is placed in front of the electromagnetic calorimeter in order to correct for the upstream energy losses. The electromagnetic calorimeters are in turn surrounded by hadronic calorimeters. An iron-scintillator tile calorimeter provides coverage in the central region of $|\eta| < 1.5$, while the region of $1.5 < |\eta| < 3.2$ is covered by a LAr hadronic end-cap calorimeters. The forward regions ($3.2 < |\eta| < 4.9$) are instrumented with LAr calorimeters for both electromagnetic and hadronic measurements.

The outermost system of the ATLAS detector is the Muon Spectrometer (MS) which relies on a set of massive superconducting air-core toroid magnets. The MS utilizes a system of precision tracking chambers and fast detectors for triggering.

Electron candidates are reconstructed from energy deposits in the electromagnetic calorimeters and are required to

[1] ATLAS uses a right-handed coordinate system with its origin at the nominal interaction point. The counterclockwise beam direction defines the z-axis, the positive x-axis points towards the center of the LHC ring and the positive y-axis points upwards. Cylindrical coordinates (r, ϕ) are used in the transverse plane with respect to the beam, and the pseudorapidity η is defined in terms of the polar angle θ as η = -ln tan(θ/2).

pass identification criteria based on the shower shapes. Muons are seeded from the measurements in the MS.

The combination of all systems provides charged particle measurements together with efficient and precise lepton (e, μ) and photon identification in the pseudorapidity range $|\eta| < 2.5$.

Energy deposits measured in the whole acceptance range ($|\eta| < 4.9$) of the calorimeter system are used to reconstruct jets and missing transverse energy, E_T^{miss}.

3. Event Selection

The event selection utilizes a robust cut-based approach and is driven by the final state topologies of the search channels. Selected events are required to have one or two high-transverse momentum lepton (e or μ), or large missing transverse energy.

In all channels, events are required to contain exactly two jets consistent with the b-quark hadronization (b-jets), one of which with reconstructed transverse momentum $p_T > 45$ GeV and the other with $p_T > 25$ GeV. To identify a jet as a b-jet, a single discriminant ω is calculated based on the information from the secondary vertices reconstructed using the ID tracks associated to the jet as well as impact parameter information of the associated tracks [5]. The applied selection cut on ω corresponds to a 70% efficiency for b-jet identification and have a rejection factor of about 5 for jets originating from c-quark hadronization and a rejection factor of about 130 for jets due to u-, d-, s-quark or gluon [5].

Additional cuts that are applied in order to suppress background processes which can mimic signal events, are described in details in [4]. Significant sources of background include top production ($t\bar{t}$ and single top), production of W or Z boson in association with one or more jets (W+jet, Z+jet), di-boson production (WW, WZ and ZZ) and, in case of $WH \to l\nu b\bar{b}$ channel, multi-jet production.

The search for $H \to b\bar{b}$ decays is performed by looking for an excess of events above the background expectations in the invariant mass distribution of the b-jet pair, $m_{b\bar{b}}$ (Fig. 1). The background rates are estimated by using both data-driven techniques and from Monte Carlo simulations [4].

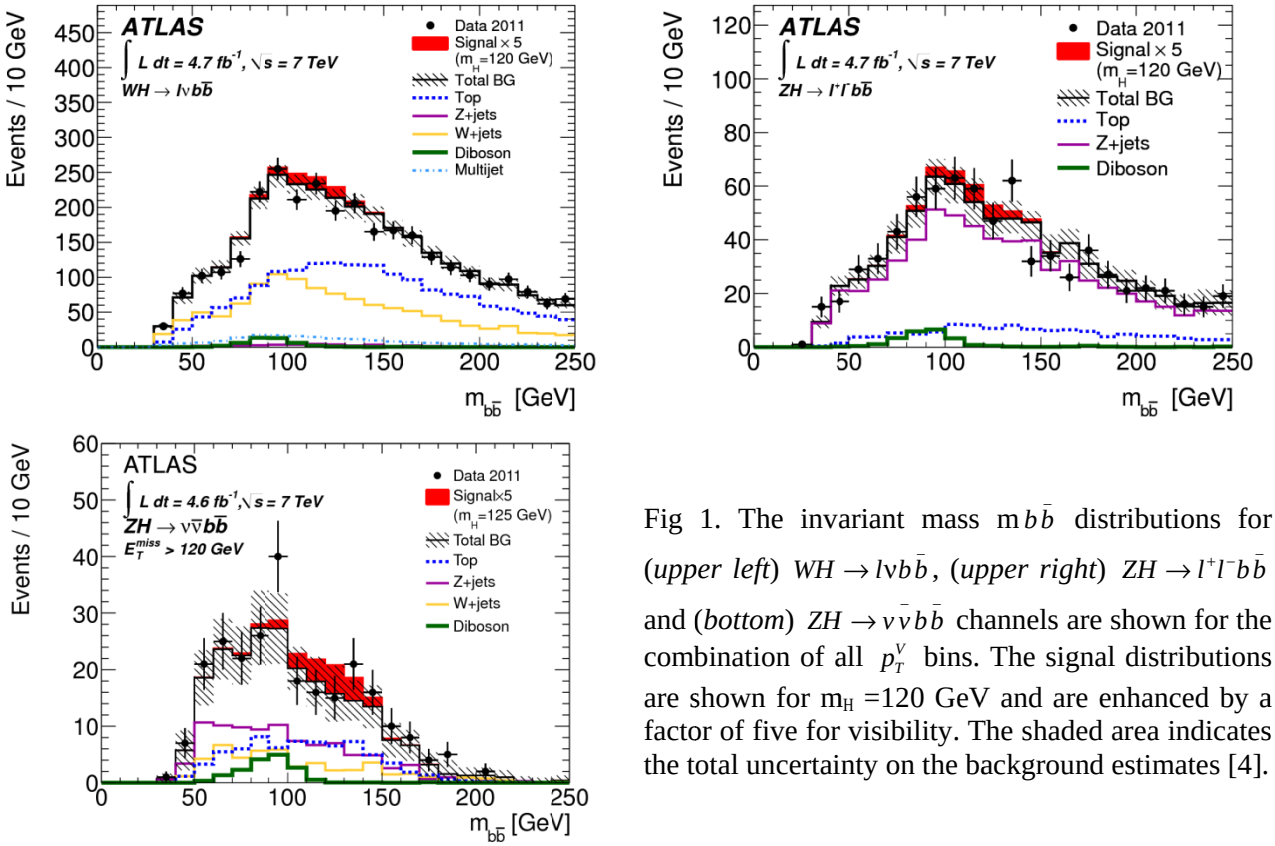

Fig 1. The invariant mass $m_{b\bar{b}}$ distributions for (*upper left*) $WH \to l\nu b\bar{b}$, (*upper right*) $ZH \to l^+l^-b\bar{b}$ and (*bottom*) $ZH \to \nu\bar{\nu}b\bar{b}$ channels are shown for the combination of all p_T^V bins. The signal distributions are shown for m_H =120 GeV and are enhanced by a factor of five for visibility. The shaded area indicates the total uncertainty on the background estimates [4].

To increase the sensitivity of the search, the $m_{b\bar{b}}$ distribution is examined in bins of the vector boson transverse momentum, p_T^V (V = W, Z). The expected signal is characterized by a relatively hard p_T^V spectrum, such that the signal

to background ratio increases with the transverse momentum of the vector boson. p_T^V is reconstructed from the lepton and E_T^{miss} in the $WH \to l\nu b\bar{b}$ channel, from the two leptons in the $ZH \to l^+l^-b\bar{b}$ channel and from E_T^{miss} in $ZH \to \nu\bar{\nu}b\bar{b}$ channel.

In the $WH \to l\nu b\bar{b}$ and $ZH \to l^+l^-b\bar{b}$ channels, there are four p_T^V bins: 0 GeV < p_T^V <50 GeV, 50 GeV < p_T^V < < 100 GeV, 100 GeV < p_T^V <200 GeV and p_T^V >200 GeV. In the $ZH \to \nu\bar{\nu}b\bar{b}$ channel, three p_T^V bins are defined: 120 GeV < p_T^V <160 GeV, 160 GeV < p_T^V <200 GeV and p_T^V >200 GeV. The numbers of the observed events in each p_T^V bin (N_{data}) are listed in Table 1 for the three search channels. The expected numbers of the signal events (N_{signal}) and the corresponding estimations for the background ($N_{background}$) are also presented in Table 1 [4].

4. Systematic Uncertainties

The systematic uncertainties related to the signal and background yields arise from b-tagging efficiency and mistagging rate, from uncertainties associated with jet and E_T^{miss} reconstruction, from lepton reconstruction and identification uncertainties, from integrated luminosity measurement as well as due to the overlaid collision events (pile-up). Additional uncertainties arise from the theoretical predictions on the SM Higgs boson inclusive cross-section, from background normalizations and the modeling of m$b\bar{b}$ and p_T^V distributions.

The number of the observed, simulated signal and estimated background events in each p_T^V bin for the $WH \to l\nu b\bar{b}$, $ZH \to l^+l^-b\bar{b}$ and $ZH \to \nu\bar{\nu}b\bar{b}$ search channels. The relative systematic uncertainties on the hypothesized signal and estimated total background yields are also shown. The simulated signal corresponds to a Higgs boson mass of m_H = 120 GeV. The number of events is shown in the full signal region defined as m$b\bar{b}$ ∈ [80 GeV, 150 GeV] [4].

p_T^V bin (GeV)	N_{signal}	$N_{background}$	N_{data}	Systematic Uncertainty (%)	
				Signal	Background
$WH \to l\nu b\bar{b}$ search channel					
0 - 50	5.0 ± 0.6	596 ± 23	614	11.4	3.9
50 - 100	5.1 ± 0.6	598 ± 16	588	10.8	2.7
100 - 200	3.7 ± 0.4	302 ± 10	271	11.0	3.4
>200	1.2 ± 0.2	27 ± 5	15	16.0	19.6
$ZH \to l^+l^-b\bar{b}$ search channel					
0 - 50	1.3 ± 0.1	148 ± 10	141	10.1	6.9
50 - 100	1.8 ± 0.2	150 ± 6	163	9.1	4.3
100 - 200	1.6 ± 0.2	67 ± 4	61	9.6	6.6
>200	0.4 ± 0.1	6.9 ± 1.2	13	16.5	17.3
$ZH \to \nu\bar{\nu}b\bar{b}$ search channel					
120 - 160	2.0 ± 0.2	85 ± 8	105	11.8	9.7
160 - 200	1.2 ± 0.1	32 ± 3	22	11.4	10.6
>200	1.5 ± 0.2	20 ± 3	25	13.4	16.0

For all channels, the uncertainty on the b-tagging efficiency, which varies between 5 % and 19 % depending on b-jet p_T, and the uncertainty on b-jet energy calibration, which varies between 3 % and 14 % depending on the jet p_T and η, are the leading uncertainties related to the detector performance. The largest non-instrumental contributions are from the top, Z+jet and W+jet background normalizations (2 - 5 %), and Monte Carlo predictions (≤15 %). The total systematic uncertainties on background and signal yields are summarized in the Table [4].

4. Results

The search is performed for five Higgs boson mass hypotheses in the range between 110 GeV and 130 GeV. The signal hypothesis is tested using a fit to the m$b\bar{b}$ distribution in the range 80 GeV < m$b\bar{b}$ <150 GeV. For each mass hypothesis a one-sided upper limit is placed on the ratio of the Higgs boson production cross-section to its SM value,

σ/σ_{SM}, at the 95 % confidence level. The exclusion limits are derived from the CL_s [6] treatment of the p-values computed with the profile likelihood ratio [7] using the binned m $b\bar{b}$ distribution.

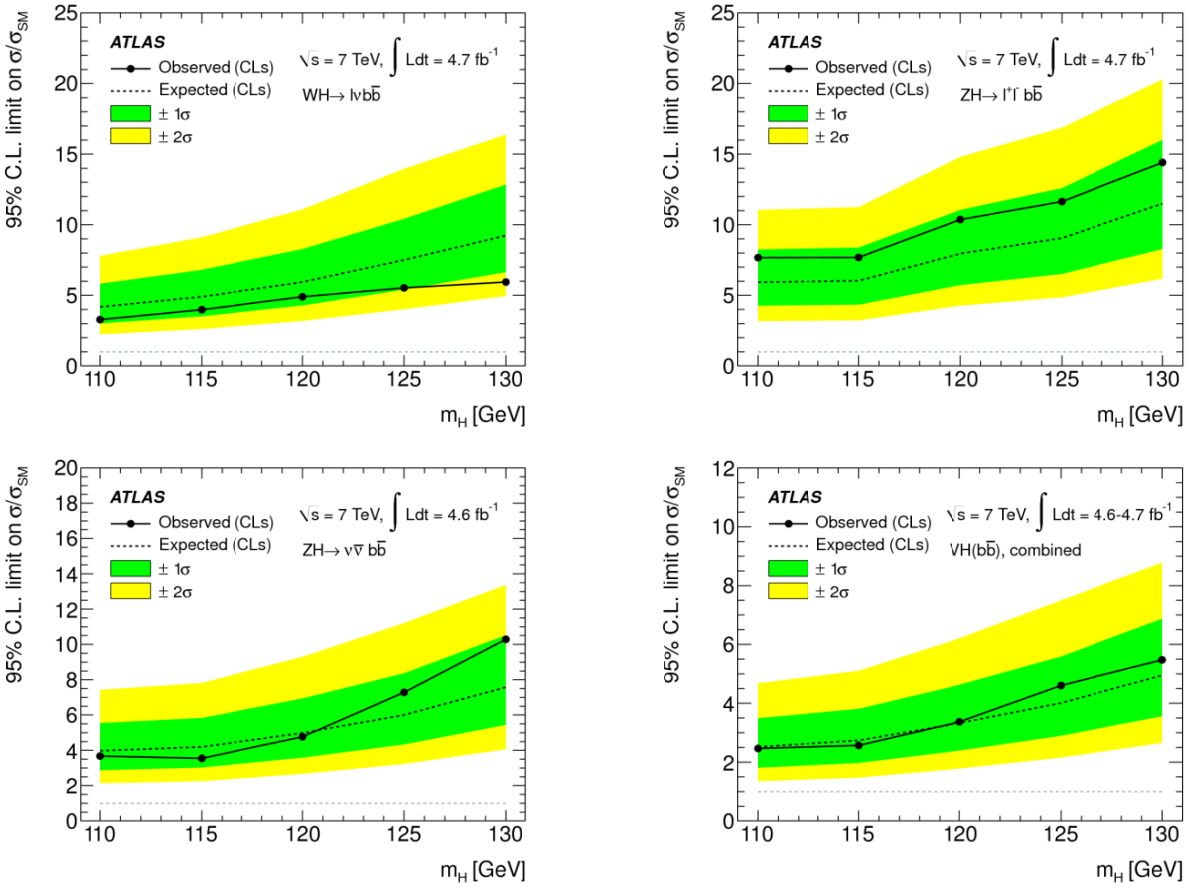

Fig. 2. Expected (dashed line) and observed (solid line) exclusion limits for $WH \to l\nu b\bar{b}$ (upper left), $ZH \to l^+l^-b\bar{b}$ (upper right) and $ZH \to \nu\bar{\nu}b\bar{b}$ (bottom left) channels expressed as the ratio to the SM Higgs boson cross-section, using the profile-likelihood method with CL_s. The dark (green) and light (yellow) areas represent 1σ and 2σ ranges of the expectations in the absence of a signal. The 95 % confidence level exclusion limits obtained from the combination of the three channels are shown on the bottom right plot [4].

The resulting exclusion limits on σ/σ_{SM} are plotted in Fig. 2 for each hypothesis of Higgs boson mass. The observed upper limits range between 3.3 and 5.9 for $WH \to l\nu b\bar{b}$ channel, 7.7 and 14.4 for $ZH \to l^+l^-b\bar{b}$ channel and between 3.7 and 10.3 for the $ZH \to \nu\bar{\nu}b\bar{b}$ channel, depending on the Higgs boson mass. The combined exclusion limit for the three channels ranges from 2.5 to 5.5 times the SM Higgs boson cross-section, depending on the Higgs boson mass. The limits include systematic uncertainties which weaken the estimates by 25-40 % depending on the search channel.

4. Conclusions

The achieved sensitivity, in terms of the ratio to the SM Higgs boson production cross-section, expressed as the exclusion limit at 95 % confidence level, varies in the mass range 110 GeV < m_H< 130 GeV between 2.5 and 5.5, depending on the mass hypothesis. The expected exclusion limits range between 2.5 and 4.9 for the same mass interval.

The current LHC run will continue until early 2013 and it is expected to deliver 20 fb^{-1} data to ATLAS, at $\sqrt{s}$ = 8 TeV. With the larger dataset and improved analyses in $WH \to l\nu b\bar{b}$, $ZH \to l^+l^-b\bar{b}$ and $ZH \to \nu\bar{\nu}b\bar{b}$ channels, ATLAS is expected to be able to constrain the branching ratio of the important decay of SM Higgs boson to a $b\bar{b}$ pair.

REFERENCES

1. *ATLAS Collaboration*. The ATLAS Experiment at the CERN Large Hadron Collider // JINST. - 2008. - Vol. 3. - P. S8003
2. *L. Evans, P. Bryant* (*editors*). LHC Machine // JINST. - 2008. - Vol. 3. - P. S8001
3. *ATLAS Collaboration.* Observation of a New Particle in the Search for the Standard Model Higgs Boson with the ATLAS Detector at the LHC // Phys. Lett. B. - 2012. - Vol. 716. - P. 1 - 29. [arXiv:1207.7214v2].
4. *ATLAS Collaboration.* Search for the Standard Model Higgs boson produced in association with a vector boson and decaying to a b-quark pair with the ATLAS detector // Submitted to Physics Letters. B. - 2012. - P. 1 - 29. [arXiv:1207.0210v1].
5. *ATLAS Collaboration*. Commissioning of the ATLAS high-performance b-tagging algorithms in the 7 TeV collision data // ATLAS-CONF-2011-102. - 2011. - P. 1 - 22. [http://cdsweb.cern.ch/record/1369219].
6. *Read A. L.* Presentation of earch results: the CL_s technique // J. Phys. - 2002. - Vol. G28. - P. 2693 - 2704.
7. *Cowan G., Cranmer K., Gross E., Vittels O*. Asymptotic formulae for likelihood-based test of new physics // Eur. Phys. J. - 2011. - Vol. C71. - P. 1554.

GLUON LOOPS IN THE INELASTIC PROCESSES IN QCD

I. V. Sharf[1], K. K. Merkotan[1], N. A. Podolyan[1], D. A. Ptashynskyy[1], A. V. Tykhonov[2], M. A. Deliyergiyev[2], G. O. Sokhrannyi[1], V. D. Rusov[1,3]

[1] *Department of Theoretical and Experimental Nuclear Physics, Odesa National Polytechnic University, Odesa, Ukraine*
[2] *Department of Experimental Particle Physics, Jozef Stefan Institute, Ljubljana, Slovenia*
[3] *Department of Mathematics, Bielefeld University, Bielefeld, Germany*

It is shown that inelastic process of the exchange with two massless gluons is formally equivalent to the process of the exchange with one massive particle. Thus, using the Laplace's method, a new mechanism of mass generation in inelastic processes is discovered, which is described by the non-Abelian gauge theory. Furthermore, it is shown that in the QCD perturbation theory, the same mechanisms of cross-sections growth take place, similar to the ones discovered before in the effective scalar theories.

1. Introduction

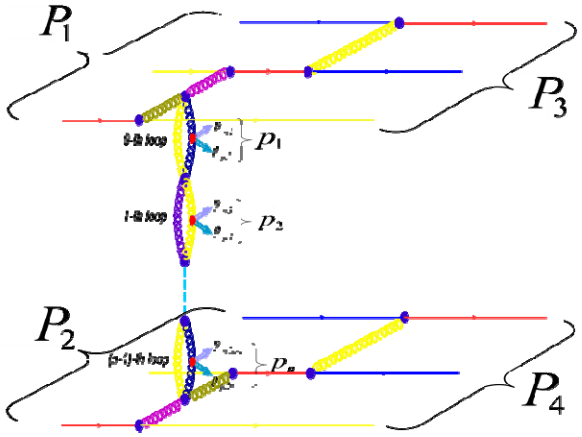

Fig. 1. The simplest diagram of the inelastic scattering with gluon loops.

In previous works [1 - 5] the permissibility of applying the Laplace's method to calculation of the inelastic scattering cross-sections has been demonstrated on the example of Feynman diagrams for effective scalar field theories. The aim of the work is the application of this method to a more realistic theory, i.e. QCD. The simplest diagrams of the inelastic scattering which gives a non-zero contribution to scattering amplitude are the diagrams with gluon loops, shown in Fig. 1. The detailed proof of this statement is given in Ref. [6].

The further simplification is that the diagrams in Fig. 4 correspond to the analytical expressions, which are the product of multipliers that are matched to each of two proton units (top and bottom in Fig. 1) and also a multiplier, that is matched a set of gluon loops (Fig. 2).

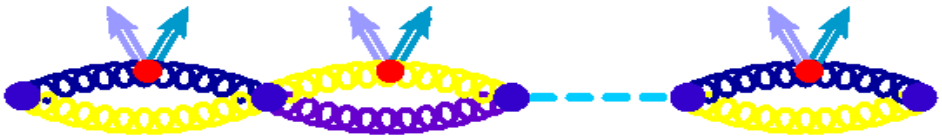

Fig. 2. Inside part of diagram in Fig. 4, which contains a set of gluon loops.

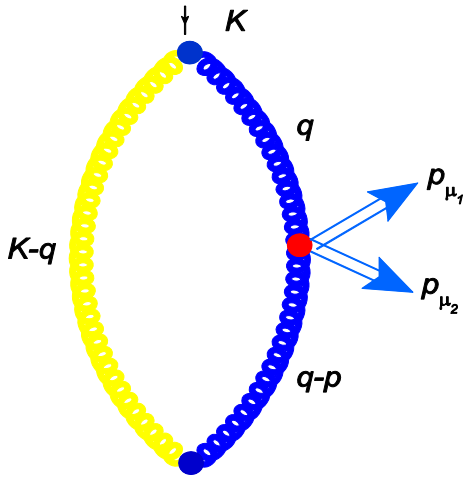

Fig. 3. Four-momentum lines of a gluon loop.

It allows exploring and maximizing modulus of these multipliers separately. In addition, an expression that is a product of multipliers, each of which corresponds to the single gluon loop, corresponds to the part of the diagram in Fig. 2. The integration by four-momenta that circulate through loops can also be performed separately from each other.

The aim of this work is to find the maximum point of the scattering amplitude modulus squared and to study its properties for the inside parts of the diagram (Fig. 1), shown in Fig. 2.

2. Calculation of the gluon loop integral

According to Feynman's diagram technique, up to a constant term, the expression corresponding to the gluon loop (Fig. 3) has the form:

$$A=\int d^4q\frac{1}{(K-q)^2+i\varepsilon}\frac{1}{q^2+i\varepsilon}\frac{1}{(q-p)^2+i\varepsilon}. \tag{1}$$

Hereinafter the sum is denoted by p

$$p=p_{\mu_1}+p_{\mu_2}. \tag{2}$$

Similarly to what has been proved in Ref. [1] we can show that the scalar squares of four-momentum K, entering each gluon loop, are negative.

Applying the Feynman identity to Eq.(1), and performing the transformation, it can be reduced to a two-dimensional integral over the triangle $\triangle ABC$ of the Fig. 4, *a*:

$$A=\frac{\pi^2 i}{p^2\sqrt{3}}\iint\limits_{\Delta ABC}dy_1dy_2\frac{1}{\left(-\sqrt{\frac{2}{3}}y_1+\frac{Kp}{p^2}\left(\sqrt{\frac{1}{6}}y_1-\frac{1}{\sqrt{2}}y_2+\frac{1}{3}\right)-\frac{1}{6}\right)^2-b\left(\sqrt{\frac{1}{6}}y_1-\frac{1}{\sqrt{2}}y_2+\frac{1}{3}-l\right)^2+d+i\varepsilon}, \tag{3}$$

where

$$b=\frac{(Kp)^2-K^2p^2}{\left(p^2\right)^2},d=\frac{1}{4}\left(\frac{\left(Kp-K^2\right)^2}{(Kp)^2-K^2p^2}-1\right),l=\frac{p^2\left(Kp-K^2\right)}{2\left((Kp)^2-K^2p^2\right)}. \tag{4}$$

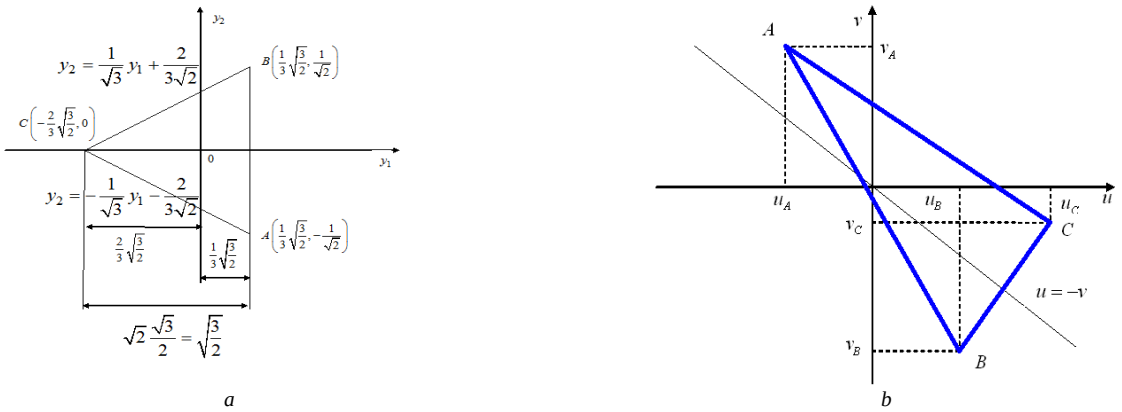

Fig. 4. The domain of integration: *a* - for Eq. 3; *b* - for Eq. 6.

As one can see from Eq. (4), considering the negativity of scalar square of four-vector K, entering the loop (see Fig. 3), we have $b>0$. That means the quadratic form in the denominator of the integral (3) is the difference of squares. Therefore, for the further calculation of the integral (3), it is convenient to pass to new variables

$$u=\left(-\sqrt{\frac{2}{3}}y_1+\frac{Kp}{p^2}\left(\sqrt{\frac{1}{6}}y_1-\frac{1}{\sqrt{2}}y_2+\frac{1}{3}\right)-\frac{1}{6}\right)-\sqrt{b}\left(\sqrt{\frac{1}{6}}y_1-\frac{1}{\sqrt{2}}y_2+\frac{1}{3}-l\right),$$

$$v=\left(-\sqrt{\frac{2}{3}}y_1+\frac{Kp}{p^2}\left(\sqrt{\frac{1}{6}}y_1-\frac{1}{\sqrt{2}}y_2+\frac{1}{3}\right)-\frac{1}{6}\right)+\sqrt{b}\left(\sqrt{\frac{1}{6}}y_1-\frac{1}{\sqrt{2}}y_2+\frac{1}{3}-l\right). \tag{5}$$

In these variables, instead of expression (3) we get:

$$A=\frac{-\pi^2 i}{2\sqrt{(Kp)^2-K^2p^2}}\iint\limits_{\Delta ABC}dudv\frac{1}{uv+c^2+i\varepsilon}, \tag{6}$$

where the following notation is used:

$$c^2=\frac{K^2(K-p)^2}{4\left((Kp)^2-p^2K^2\right)}>0. \tag{7}$$

The triangle $\triangle ABC$ maps on the triangle which is shown in Fig. 4, *b*. Furthermore, the coordinates of vertices C and B of the triangle fig.4a are expressed through the outer four-momentum of loop in Fig. 3:

$$u_C = \frac{1}{2} + \frac{1}{2}\frac{Kp - K^2}{\left(\sqrt{(Kp)^2 - K^2 p^2}\right)} > 0, v_C = \frac{1}{2}\left(1 - \frac{Kp - K^2}{\sqrt{\left(Kp - K^2\right)^2 - K^2 (K-p)^2}}\right) < 0,$$

$$u_B = -\frac{1}{2} + \frac{1}{2}\frac{\left(Kp - K^2\right)}{\sqrt{(Kp)^2 - K^2 p^2}} = -v_C > 0, v_B = -\frac{1}{2} - \frac{1}{2}\frac{\left(Kp - K^2\right)}{\sqrt{(Kp)^2 - K^2 p^2}} < 0. \quad (8)$$

The expression for the coordinate v_A can be written in the form:

$$v_A = \frac{1}{2}\left(\frac{K^2 - (K-p)^2}{p^2} + \frac{\left(\frac{K^2 - (K-p)^2}{p^2}\right)^2 - \left(\frac{K^2 + (K-p)^2}{p^2}\right)}{\sqrt{1 - 2\left(\frac{K^2 + (K-p)^2}{p^2}\right) + \left(\frac{K^2 - (K-p)^2}{p^2}\right)^2}}\right). \quad (9)$$

Taking into account the negativity of K^2 and $(K-p)^2$, one can see that second term in Eq. (9) is positive. After the calculation of the difference of two squares terms in parentheses, we get:

$$\left(\frac{\left(\frac{K^2 - (K-p)^2}{p^2}\right)^2 - \left(\frac{K^2 + (K-p)^2}{p^2}\right)}{\sqrt{1 - 2\left(\frac{K^2 + (K-p)^2}{p^2}\right) + \left(\frac{K^2 - (K-p)^2}{p^2}\right)^2}}\right)^2 - \left(\frac{K^2 - (K-p)^2}{p^2}\right)^2 = \frac{4K^2 (K-p)^2}{\left(p^2\right)^2} > 0. \quad (10)$$

For this we draw a conclusion that the absolute value of second positive term in parentheses Eq. (9) is greater than the first one. Therefore, in spite of the sign of the first term, we have $v_A > 0$.

The expression for the coordinate u_A has the form:

$$u_A = \frac{1}{2}\left(\frac{K^2 - (K-p)^2}{p^2} - \frac{\left(\frac{K^2 - (K-p)^2}{p^2}\right)^2 - \left(\frac{K^2 + (K-p)^2}{p^2}\right)}{\sqrt{1 - 2\left(\frac{K^2 + (K-p)^2}{p^2}\right) + \left(\frac{K^2 - (K-p)^2}{p^2}\right)^2}}\right), \quad (11)$$

which differs from the Eq. (9) for v_A only by its sign. Now, the largest modulus in the parentheses of (11) is negative. Therefore $u_A < 0$.

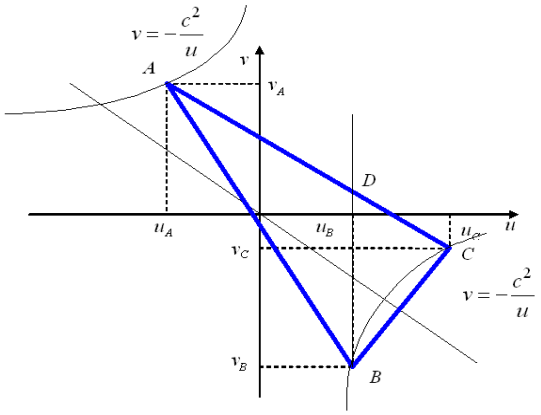

Fig. 5 The relative position of the integration domain in Eq. (6) and hyperbola Eq.(13), on which the real part of the denominator in Eq. (6) changes its sign.

As will be shown below, the Jacobian of the transformation (5) plays a significant role for each of the loops Fig. 5. The expression for the Jacobian of this transformation has the form

$$J = \frac{\partial(u,v)}{\partial(y_1, y_2)} = \frac{2}{\sqrt{3}}\frac{\sqrt{(Kp)^2 - K^2 p^2}}{p^2}. \quad (12)$$

Let's consider the further calculation of the integral (6). The real part of the denominator of the integrand expression in (6) turns to zero along the hyperbola

$$uv + c^2 = 0. \quad (13)$$

Inserting Eqs. (8), (9) and (11) into this expression demonstrates that the hyperbola includes all three

vertices of the triangle $\triangle ABC$ in Fig. 4, *a* (see Fig. 5). As a result, within the region, bounded by the segments *AB* and *AC* and the arc of hyperbola *BC* , one gets the inequality

$$uv + c^2 > 0, \tag{14}$$

and in the region between the arc *BC* and segment *BC* :

$$uv + c^2 < 0. \tag{15}$$

Hence, due to the presence of region, in which the relations (15) take place, multiplier A, which corresponds to each loop in Fig. 2, and which is expressed by Eq. (6), has a nonzero imaginary part. It can be represented as follows:

$$A = \frac{i\pi^2}{2} A', \quad \mathrm{Im}(A') = \frac{\pi}{\sqrt{(Kp)^2 - K^2 p^2}} \ln\left(\frac{u_C}{u_B}\right),$$

$$\mathrm{Re}(A') = \frac{1}{\sqrt{(Kp)^2 - K^2 p^2}} \left(\int_{u_A}^{u_B} \frac{1}{u} \ln\left(\frac{k_{AC}(u - u_C)}{k_{AB}(u - u_B)}\right) du + \int_{u_B}^{u_C} du \frac{1}{u} \ln\left(\frac{k_{AC}(u_A - u)}{(u - u_B)}\right) \right). \tag{16}$$

Here k_{AB} and k_{AC} denote the angular coefficients of the lines *AB* and *AC* in Fig. 5.

The expression (16) includes one-dimensional integrals, which can be calculated numerically. This allows to numerically calculate the multipliers, each of which corresponds to one of the loops in Fig. 5, and to numerically maximize the square modulus of their product. The maximization procedure is described in details in Ref. [6]. Its main results are given below.

3. The results of numerical maximization.

The results of the numerical maximization of the squared modulus of scattering amplitude Fig. 2 appeared to be very similar to the results for the diagram in simple scalar models, obtained in [1, 5]. In particular, as shown in Ref. [6], the magnitude of scattering amplitude squared modulus in the point of maximum increase with the growth energy $\sqrt{s}$, and the rapidities in the point of maximum produce an arithmetic progression.

The values of K^2 for different loops (see Fig. 4) are given in Fig. 6 with respect to the index of gluon loop. These are calculated using the rapidities at the point of maximum for different $\sqrt{s}$.

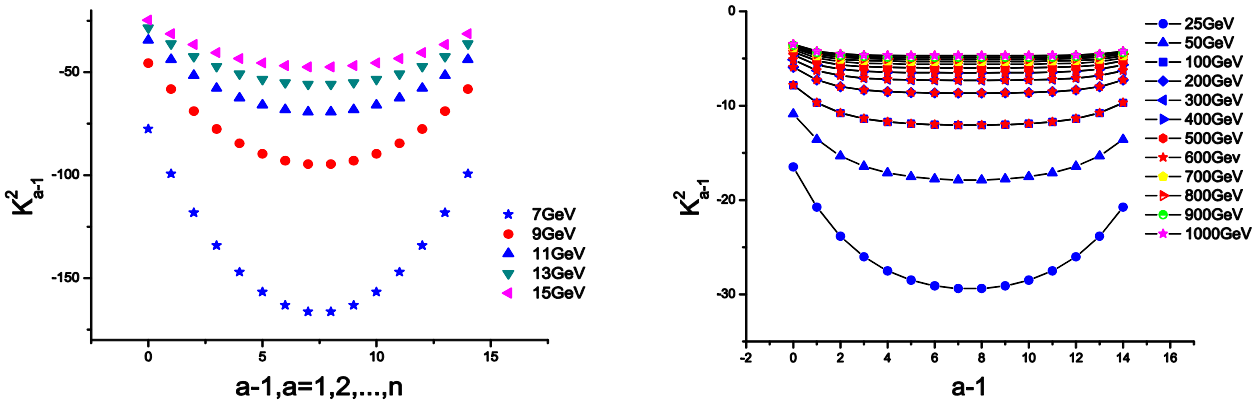

Fig. 6. The scalar square of four-momenta K^2_{a-1} entering the loop in Fig. 4 (herewith, the loop containing the a-th vertex is labeled as "a-1") as a function of number of loop at different energies $\sqrt{s}$.

These graphs are quite similar to the ones in Fig. 6 of Ref. (Sharf, et al., Description of Hadron Inelastic Scattering by the Laplace Method and New Mechanisms of Cross-section Growth, 2011), obtained for the simplest multi-peripheral "comb" diagrams in φ^3 theory. The origin of the analogy between the model, based on the diagrams with loops in QCD, and the one based on loop-less diagrams in φ^3 theory can be explained from the following concerns.

At the numerical maximization it has been observed that the outcome only slightly differs from the one, which would have been obtained if the multiplier corresponding to each loop Eq. (16) would be replaced with the expression for the inverse Jacobian only Eq. (12). This expression enters Eq. (16) as a factor in front of the integral in the real part, and before the logarithm of the imaginary part. Above illustrated graphs are shown in Fig. 7.

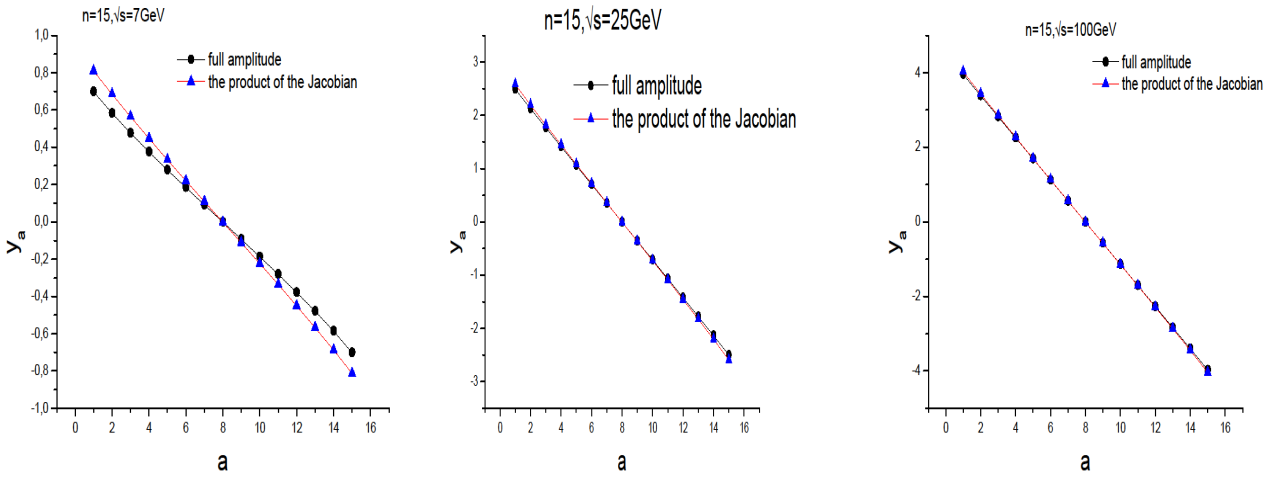

Fig. 7. Comparison of the results of maximization the total amplitudes (circles) and the products of Jacobians only, given at different energies.

Thus, instead of the full scattering amplitude, with good accuracy one can maximize the logarithm of the product of the Jacobians. Dropping out the multipliers and the constant summands, which are irrelevant to the maximization, this logarithm can be reduced to the form:

$$\tilde{A} = -\sum_{a=1}^{N} \ln\left(\left(K_{a-1} p_a \right)^2 - K_{a-1}^2 p_a{}^2 \right). \tag{17}$$

As shown in Fig. 7 in the vicinity of the point of maximum the values K_{a-1}^2 are almost equal between themselves. Namely

$$K_{a-1}^2 \approx \left(K_{a-1} - p_a \right)^2. \tag{18}$$

Consequently

$$\left(K_{a-1} p_a \right) \approx \frac{p_a{}^2}{2} = 2, \tag{19}$$

Here the mass-shell condition is taken into account, and momenta are nondimensionalized with mass of secondary particle.

These considerations are confirmed by the results of the direct calculation of the values $\left(K_{a-1} p_a \right)$, given in Ref. [6]. Given the approximation (19) instead of (17) we get:

$$\tilde{A} = -N \ln(4) - \sum_{a=1}^{N} \ln\left(1 - K_{a-1}^2\right). \tag{20}$$

This expression up to the first term, which is nonessential for the maximization, coincides with the expression that occurs in the simplest version of φ^3 theory for the "comb" diagrams, and which was previously employed in Refs. [1-5].

4. Conclusions and discussion

The main conclusion from the above results is that the inelastic process of exchange with two massless gluons in QCD (see Fig. 6) is equivalent to exchange with one massive particle in a scalar φ^3 theory. However, we by no means employ the features of QCD, i.e. such an outcome will occur in any arbitrary non-Abelian gauge theory, which features the massive secondary particles.

Moreover, as one can see from Ref. [6], within the considered model, the mechanism of cross-sections growth, which was discovered earlier for the effective scalar theories [2, 5], remains. The essence of this mechanism is as follows.

The scalar square of each four-momentum K_{a-1}^2 is negative. This means that the three-dimensional momentum, which runs through the loop, can't be reduced to zero in any reference frame. The value of $\left| K_{a-1}^2 \right|$ is equal to the square of this three-dimensional momentum in the reference frame, in which the momentum is minimal. According to the uncertainty relation, the smaller is this momentum the bigger is the spatial region, in which one can find during the measurement the particles involved in the process, described by loop in Fig. 2, or the particle that transfers the four-momentum K_{a-1} along the scalar "comb". The growth of this region defines the growth of scattering cross-section of initial particles.

REFERENCES

1. *Sharf I., Tykhonov A., Sokhrannyi G. et al.*Mechanisms of Proton-Proton Inelastic Cross-Section Growth in Multi-Peripheral Model within the Framework of Perturbation Theory. Part 1 // Journal of Modern Physics. - 2011. - P. 1480 - 1506.
2. *Sharf I., Tykhonov A., Sokhrannyi G. et al.* Mechanisms of Proton-Proton Inelastic Cross-Section Growth in Multi-Peripheral Model within the Framework of Perturbation Theory. Part 2 // Journal of Modern Physics. - 2012. - P. 16 - 27.
3. *Sharf I., Tykhonov A., Sokhrannyi G. et al.* Mechanisms of Proton-Proton Inelastic Cross-Section Growth in Multi-Peripheral Model within the Framework of Perturbation Theory. Part 3 // Journal of Modern Physics. - 2012. - P. 129 - 144.
4. *Sharf I., Tykhonov A., Sokhrannyi G. et al.* On the role of longitudinal momenta in high energy hadron-hadron scattering // Central European Journal of Physics. - 2012. - P. 858 - 887.
5. *Sharf I., Tykhonov A., Sokhrannyi G. et al.* Description of Hadron Inelastic Scattering by the Laplace Method and New Mechanisms of Cross-section Growth // Ukrainian Journal of Physics. - 2011. - P. 1151 - 1164.
6. *Sharf I., Merkotan K., Ptashynskyy D. et al.* Gluon Loops in the Inelastic Processes in QCD. - 2012. - arxiv:1210.3490.

Closing remarks

Five days of the 4-th International Conference on “Current Problems in Nuclear Physics and Atomic Energy” passed quickly.

NPAE-Kyiv2012 Conference covered the following topics:

- Collective processes in atomic nuclei;
- Nuclear reactions;
- Nuclear structure and decay processes;
- Rare nuclear processes;
- Neutron and reactor physics, nuclear data;
- Problems of atomic energy;
- Applied nuclear physics, experimental facilities and detection techniques;
- High-energy physics.

These topics are closely related to the researches which are carried out in the Institute for Nuclear Research of the National Academy of Sciences of Ukraine, Kyiv and in the Department of Physics of Taras Shevchenko National University of Kyiv. The large variety and richness of subjects ranged from applied nuclear physics (reactors, neutron physics, application of nuclear techniques in medicine, data acquisition, etc.) to the subjects of pure nuclear physics (nuclear reactions, nuclear structure, neutrino physics, etc.) and to the fundamental high-energy physics (compressed baryonic matter, dibaryons, hadronic fireball, etc.) have been presented by the Conference participants.

175 participants from 20 countries were registered. 136 oral reports (19 plenary and 117 section reports) and 44 posters were presented during the Conference. So, the multinational audience consisted of the outstanding specialists from various nuclear physics directions. The participants may extend scientific horizon due to very broad scope of the Conference topics. We hope new ideas will be inspired due to interdisciplinary interplay. Nuclear power will be the important component of our electricity generation during the 21st century, and therefore, nuclear physics, nuclear engineering and nuclear fundamental researches will have the significant role in the nearest future. We hope that informal contacts of participants induce future collaborations concerning different fields of scientific researches.

During the Closing ceremony we hear nice words from Prof. Rita Bernabei (INFN & University of Roma 2), Prof. Sarkis Karamian (JINR, Dubna), Prof. Jan Toke (University of Rochester, Rochester), Prof. Adam Sobiczewski, (Warsaw University, Warsaw), Prof. Peter Ring (TU München).

We are closing the Conference with fruitful scientific results and useful discussions.

We hope that participants spent nice time in Kyiv. There were possibilities for scientific discussions, refreshments and time to see very ancient city, Kyiv, city with rich history.

We wish everyone a safe journey home.

Thank you all for participation. Hope to see you at our next meeting!

Ivan M. Vyshnevskyi

Chairman of the NPAE-Kyiv2012 Conference,
Director of the Institute for Nuclear Research

Author Index

For notes

Scientific publication

The 4-th International Conference "Current Problems in Nuclear Physics and Atomic Energy" (NPAE-Kyiv2012)

Proceedings
Part II

Presentations are published in authors' edition

Cover's design *T. O. Margitych*
Computer-aided makeup *O. D. Grygorenko*

Підп. до друку 21.02.2013. Формат 60×84/8. Ум. друк. арк. 38,4
Тираж 200 пр. Зам. № 3

Інститут ядерних досліджень НАН України,
просп. Науки, 47, м. Київ, 03680, тел. 525-14-56
Свідоцтво суб'єкта видавничої справи ДК № 4051 від 18 квітня 2011 р.

Надруковано у ЦСТРІ м. Києва, філія № 7 «КОПІ ЦЕНТР»,
просп. Перемоги, 37, м. Київ, 03056, тел.: 277-88-93, 277-37-49
Свідоцтво суб'єкта видавничої справи ДК № 37096928 від 15 березня 2005 р.